Aix*Marseille université
Socialement engagée

NNT/NL : 2020AIXM0001/001ED000

THÈSE DE DOCTORAT

Soutenue à Aix-Marseille Université
le 15 novembre 2021 par

Romain Paviot

Étude cosmologique de la structure à grande échelle dans le sondage spectroscopique eBOSS

Cosmological analysis of the large-scale structure in the eBOSS spectroscopic survey

Discipline
Physique

Spécialité
Astrophysique et Cosmologie

École doctorale
Physique et Sciences de la Matière - 352

Laboratoire/Partenaires de recherche
Laboratoire d'Astrophysique de Marseille
Centre de Physique des Particules de Marseille
Centre National de la Recherche Scientifique

Composition du jury

Alain Blanchard Institut de Recherche en Astrophysique et Planétologie	Rapporteur
Luigi Guzzo Università di Milano	Rapporteur
Sandrine Codis AIM - Laboratoire Cosmologie et Evolution des Galaxies	Examinatrice
Guilaine Lagache Laboratoire d'Astrophysique de Marseille	Présidente du jury
Stéphanie Escoffier Centre de Physique des Particules de Marseille	Directrice de thèse
Sylvain de la Torre Laboratoire d'Astrophysique de Marseille	Co-directeur de thèse

LAM LABORATOIRE D'ASTROPHYSIQUE DE MARSEILLE

CENTRE DE PHYSIQUE DES PARTICULES DE MARSEILLE CPPM

cnrs

Je soussigné, Romain Paviot, déclare par la présente que le travail présenté dans ce manuscrit est mon propre travail, réalisé sous la direction scientifique de Stéphanie Escoffier et Sylvain de la Torre, dans le respect des principes d'honnêteté, d'intégrité et de responsabilité inhérents à la mission de recherche. Les travaux de recherche et la rédaction de ce manuscrit ont été réalisés dans le respect à la fois de la charte nationale de déontologie des métiers de la recherche et de la charte d'Aix-Marseille Université relative à la lutte contre le plagiat.

Ce travail n'a pas été précédemment soumis en France ou à l'étranger dans une version identique ou similaire à un organisme examinateur.

Fait à Marseille le 08/09/2021

Résumé

L'étude de la distribution à grande échelle des galaxies fournit des informations uniques sur la nature et les constituants de l'Univers. Les sondages spectroscopiques de galaxies cartographient cette distribution tridimensionnelle dans l'espace des décalages spectraux, distribution qui est déformée en raison des vitesses particulières des galaxies. Ces déformations apparentes, appelées distorsions dans l'espace des décalages spectraux (RSD), nous permettent de sonder la croissance de la structure cosmique au fil du temps et de poser des contraintes sur la nature de la gravité. En outre, les ondes acoustiques qui se sont propagées dans le fluide primordial avant le découplage matière-rayonnement, impriment une échelle caractéristique de 150 mégaparsecs dans la distribution spatiale de la matière : les oscillations acoustiques baryoniques (BAO). Cette échelle caractéristique peut être mesurée dans la distribution des galaxies pour fournir des informations sur l'histoire du taux d'expansion de l'Univers. Cette thèse est dédiée à l'étude cosmologique des RSD et BAO à partir de la fonction de corrélation à deux points de plus de 300 000 galaxies rouges et lumineuses observées par le sondage eBOSS du Sloan Digital Sky Survey. Les principales systématiques observationnelles sur la détermination du taux de croissance des structures et du taux d'expansion proviennent des fluctuations du nombre de galaxies observées et sont liées à la variation de la qualité de l'échantillon photométrique utilisé pour le ciblage spectroscopique des galaxies. La validation du modèle théorique, ainsi que l'estimation des corrections des systématiques observationnelles, ont été réalisées à l'aide de simulations très réalistes du sondage. J'ai développé une approche alternative à la statistique à deux points standard, où les modes angulaires sont annulés. Cette nouvelle statistique est exempte de contamination angulaire au prix d'une modeste perte d'information. Je présente dans ce manuscrit un modèle précis permettant de modéliser cette nouvelle statistique. Enfin, je présente les contraintes cosmologiques obtenues à partir des BAO et RSD sur l'échantillon de galaxies rouges et en combinaison avec les autres échantillons, ainsi que les implications sur le modèle cosmologique. Ce manuscrit se termine par une discussion sur les défis et perspectives des sondages de prochaine génération tels que DESI.

Mots clés : structure à grande échelle, sondage spectroscopique de galaxies, distorsions dans l'espace des décalages spectraux, oscillations acoustiques baryoniques, croissance des structures

Abstract

The study of the large-scale distribution of galaxies provides unique information about the nature and constituents of the Universe. Spectroscopic surveys of galaxies map this three-dimensional distribution in redshift space, which is distorted due to the peculiar velocity of galaxies. These apparent distortions, called redshift-space distortions (RSD), allow us to probe the growth of cosmic structure over time and to place constraints on the nature of gravity. In addition, the acoustic waves that propagated in the primordial fluid prior to the matter-radiation decoupling imprint a characteristic scale of 150 megaparsecs in the spatial distribution of matter: baryonic acoustic oscillations (BAO). This characteristic scale can be measured in the distribution of galaxies to provide information about the expansion rate history of the Universe. This thesis is dedicated to the cosmological study of RSD and BAO from the two-point correlation function of more than 300,000 luminous red galaxies observed by the eBOSS survey, part of the Sloan Digital Sky Survey. The main observational systematic errors in the determination of the structure growth rate and expansion rate arise from fluctuations in the number of observed galaxies and are related to the variation in the quality of the photometric sample used for the spectroscopic targeting of galaxies. The validation of the theoretical model, as well as the estimation of observational systematic errors corrections, were performed using very realistic survey simulations. I have developed an alternative approach to the standard two-point statistics, where the angular modes are cancelled. This new statistic is free of angular contamination at the cost of a modest loss of information. In this manuscript, I present a precise model for this new statistic. Finally, I present the cosmological constraints obtained from the BAO and RSD analysis of the sample of red luminous galaxies and in combination with the other samples, as well as the implications on the cosmological model. The manuscript concludes with a discussion of the challenges and prospects for next generation surveys such as DESI.

Keywords: large-scale structure, galaxy spectroscopic survey, redshift-space distortions, baryon acoustic oscillations, growth of structure

Remerciements

2 mois après ma soutenance de thèse, je me retrouve enfin à écrire mes remerciements. Et ils sont nombreux! Ainsi, je vais donc être ordonné, comme dans ma thèse, et aller d'étape en étape.

Tout d'abord, j'aimerais remercier les membres du jury pour être venu assister à ma thèse à Marseille. Je remercie également les rapporteurs pour avoir pris le temps de lire et corriger le manuscrit. Je remercie également tous les membres du 1er étage aile cosmologie. Vous êtes une équipe super, très sympathique et j'ai pris du plaisir à passer du temps (même si c'était très peu) avec vous pendant ma thèse. Je remercie également mes deux directeurs de thèse Stéphanie et Sylvain pour m'avoir pris sous votre tutelle pendant ces trois années. Merci Sylvain pour tout ton travail, tout ton aide durant ces trois années. Tu as su me canaliser, me motiver durant les périodes difficiles et je pense sérieusement avoir été chanceux de t'avoir comme chef.

Passons maintenant à la mifa. Je tiens d'abord, forcément, à remercier mes parents. D'abord pour m'avoir mis au monde et pour m'avoir permis de vivre sur cette magnifique planète bleu (qui cependant est en déclin, mais c'est une autre histoire!) Mais surtout, pour tout le chemin que vous m'avez permit d'accomplir. Vous m'avez toujours soutenue et encourager dans toutes les étapes de ma vie. Cela n'a pas été facile tous les jours, car jusqu'à la vingtaine (voir plus!), je n'ai jamais été très famille. Je préférai geeker et sortir avec mes copains. À la maison, j'étais froid, je ne parlais que très peu, et je ne rendais pas toute l'attention que vous me portiez. Je vous remercie donc également pour votre patience, et merci à Papa pour avoir parlé pour moi et Alban à table durant toutes ces années. Un grand merci à ma Mamou qui m'a aidé pour corriger mon résumé en français : J'aurai probablement laissé toutes les fautes d'orthographe! Viens donc Alban, le sang de la veine, mon petit frère que je remercie également, pourquoi? Alors la aucune idée, mais merci quand même Alban! Viennent ensuite le reste de ma famille, mes tantes, mes oncles, mes grands-parents, que je remercie également pour tout leur soutien et leur amour. Je garderai des souvenirs formidables de Saint-Michel l'observatoire et de Six-Fours les plages.

Maintenant, les copains! D'abord, en lien avec mon travail, je remercie toutes les personnes avec lesquelles j'ai travaillé dans la collaboration eBOSS, merci à tous les espaniques des LRGs, Julian Hector et Mariana, je vous embrasse et je vous souhaite plein de bonne choses! Merci aussi à tous les autres thésards FR d'eBOSS : Marie (ou sont les voids? bah on les voit pas!), Sylvain (a donde esta los neutrinos?), Arnaud (merci pour ton manuscrit très constructif :)). Cette petite semaine au Mexique restera graver dans ma mémoire! Bonne chance à vous par la suite!

Maintenant les autres copains, ce qui ne mérite pas forcément de remerciement, juste un peu d'amour. D'abord, je remercie tous les copains de Lycée, vous êtes les sangs, challah vous avez comprit le sujet de ma thèse! Vivement nos prochaines vacances tout ensemble. De gros bisous à tous les copains de la prépa : Seb Cyril et Bruno. La ou la majeure partie des étudiants détestaient la prépa, nous, on était à 5 sigmas au-dessus de la moyenne niveau hapiness!! Un grand merci également à Sébastien. Pour la petite histoire, en quittant mon école d'ingénieur de Chasseneuil-du Poitou, Sébastien m'appelle et me dit qu'il reste un jour pour s'inscrire pour rejoindre le master SPaCE. C'est de l'astrophysique, il me dit, donc moi ça m'intéresse pas mal vu que je suis perdu. Bilan, j'ai maintenant réussi ma thèse et j'ai trouvé un post-doc au CEA (merci Sandrine;), c'est fou!

Merci également à tous les copains du Labo, du master : Val Adri et Cédric, et de la thèse : Vincent et Paul. On a galéré ensemble, et on réussira tout ensemble ! De gros bisous.

Et pour finir sur mes remerciements, je me dois de garder le meilleur pour la fin. Merci beaucoup à ma chérie, Clémence, d'avoir été avec moi pendant toutes ces années. Tu es la seule qui me comprend vraiment, et qui me connaît sous toutes mes facettes. J'ai toujours pu compter sur toi, même dans les moments de doute et de stress, et je chéris chaque moment en ta compagnie. Merci beaucoup a ma belle-famille, c'est principalement grâce à vous que j'ai appris à être famille, ce qui m'a permis de ma rapprocher de la mienne.

THE END

Table des matières

Introduction

Cosmology is the field of physics that aims at describing the formation, evolution and content of the Universe. The standard model of cosmology provides a theoretical background in which matter structure on the largest scales can form and evolve in a way that is close to what we observe. This branch of physics has made astonishing improvements over the last century. In the early twentieth century, Einstein, with the development of the theory of General Relativity in particular, provided the fundamental principles and theoretical framework for its mathematical description. About ten years later, Lemaître and Hubble found the evidence that the Universe was in expansion. Later, the prediction and discovery of the cosmic microwave background (almost) isotropic radiation has been, among others, a big step forward. This evidence that the early Universe was hot and dense, in agreement with the prediction of the Hot Big-Bang model, led to the establishment of the standard model for cosmology. In this model, the observed tiny temperature anisotropies in the cosmic microwave background, are understood to be the early-universe density fluctuations seeding the large-scale structure that we observe today.

Numerous cosmological observations in the last decades have suggested the existence of a dark matter, and possibly, a dark energy component. Without dark matter, we fail to understand the dynamics of galaxies and clusters of galaxies, as well as the formation of the most massive structures. A major breakdown in cosmology was the discovery of the acceleration of the expansion of the Universe at the turn of the millennium. Dark energy, or in its simplest form the cosmological constant, is associated to the observed recent acceleration of universal expansion. The exact nature of dark energy, and truthfulness, are still debated nowadays, while accounting for about 70% of the energy budget in the currently favoured cosmological model, the ΛCDM model. The baryonic matter, which refers to the matter as described by the standard model of particle physics, only represents 5%, the remaining of matter being associated to dark matter. By formation, galaxies trace the cosmic matter density field. Because of their abundance, they are the best observable astronomical objects to trace the history of expansion and structure growth. This comes from the fact that the evolution of the spatial distribution of matter and galaxies is governed on the largest scales by a balance between gravitational attraction and universal expansion.

The improvement in extragalactic instrumentation in the last decades has enabled the detection of galaxies deeper and deeper into the early Universe. The invention of multi-fibre or muli-slit spectroscopy in the end of the 1990s, was a huge step forward. It enabled us to measure spectra for a large number of targeted galaxies within one exposure. Since then, the number of observed galaxy spectra has increased tremendously, covering large cosmological volumes. The angular positions of galaxies combined with redshift measurements in galaxy spectra, enable us to characterize the three-dimensional distribution of galaxies. The so-called clustering analysis of the galaxy spatial distribution uses particular features to constrain cosmological parameters : the baryon acoustic oscillations and redshift-space distortions. The former, which are observed very early on in the cosmic microwave background, have imprinted the large-scale distribution of matter and galaxy, at scales of approximately 150 megaparsecs. This characteristic scale can be used as a standard ruler, and when measured at different cosmic times, allows putting constraints on the curvature of the Universe and the nature of dark energy. In addition, galaxies tend to fall onto overdense regions under the action of gravity, inducing peculiar velocities that deviate from pure expansion. This

impacts the observed redshifts of galaxies and thus, their apparent spatial distribution. This leads to the so-called redshift-space distortions, which are directly sensitive to the growth rate of structure, namely how fast structure grows in the Universe. Therefore, those features in the three-dimensional clustering of galaxies provide constraints on both the nature of gravity and dark energy.

In 2018, the currently largest spectroscopic survey of galaxies ended its observations : the extended Baryon Oscillations Spectroscopic Survey (eBOSS), part of the Sloan Digital Sky Survey (SDSS) IV programme. In total, SDSS observed more than 3 millions galaxy spectra, which revealed the largest three-dimensional map of the Universe that the human ever observed. This manuscript presents my PhD work, which aim was to analyse the final galaxy sample, by performing a cosmological analysis of their spatial distribution, and derive new constraints on the expansion rate of the Universe and gravity on cosmological scales. I performed the clustering analysis of the eBOSS sample of luminous red galaxies (LRGs), at redshift $0.6 < z < 1.0$, where the Universe was half younger than today. These brights galaxies are strongly clustered, mostly living in overdense regions, and therefore are ideal for the study of large scale structure over large volumes. I dedicated a significant effort in the development and improvement of the analysis pipeline, in order to measure robust cosmological constraints. I also developed a new model for an alternative statistic to be used in cosmological redshift survey analysis, which is free from any angular systematic errors. Finally, I participated to the cosmological interpretation of these results.

This manuscript is divided into 4 chapters. In Chapter 1, I introduce the standard model of cosmology, which I will assume throughout the manuscript. The theoretical background of structure formation is presented in Chapter 2. I then describe in Chapter 3 the observational strategy of the eBOSS survey and associated clustering analysis in Chapter 4 for the luminous red sample. I finally conclude on cosmological implications of the 20 year of galaxy clustering observations of the SDSS programme, and discuss the future challenges and prospects for the DESI survey.

1 The concordance model of cosmology

Sommaire

The study of the large-scale galaxy distribution first requires an overview of the structure of the Universe and its evolution in time. I present in this chapter how the Universe can be described in the standard model of cosmology and the cosmological constraints that have been derived from observations. This chapter is mainly based on the lectures from CARROLL 1997 and SCHUTZ 2009 and on the textbook of MO, BOSCH et WHITE 2012.

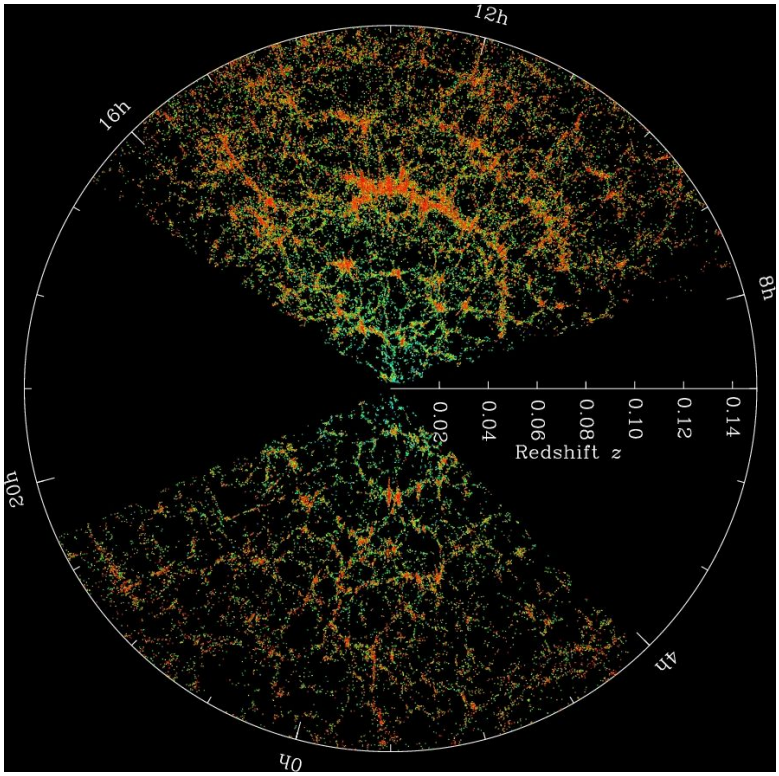

FIGURE 1.1 – The distribution of galaxies observed by the Sloan Digital Sky Survey (SDSS)-III Baryon Oscillations Spectroscopic Survey (BOSS). Credit : Taken from https://www.sdss.org/science/

1.1 The homogeneous and isotropic Universe

I present in this section the pillars upon which is based our physical understanding of cosmology.

1.1.1 The Cosmological Principle

The Cosmological Principle states that, on sufficiently large scales, the Universe can be considered as spatially homogeneous and isotropic. This can be seen on Fig. 1.1. On scales below about 100 Mpc, the Universe appears anisotropic : we observe large-scale structures probed by galaxies redshift surveys such as the Sloan Digital Sky Survey (SDSS). However, at scales larger than about 100 Mpc, the Universe appears isotropic and homogeneous. This is even more true when we observe the cosmic microwave background (CMB), a picture of the sky at redshift $z = 1090$, where relative temperature fluctuations of the order of 10^{-3} are measured. The Cosmological Principle can also be stated as the presence of a fundamental observer at each location in space, for which the Universe appears isotropic. The fundamental observer thus defines a cosmological rest frame. In such a frame, the CMB should appear isotropic. It is indeed the case as the CMB dipole, observed for the first time by the Cosmic Background Explorer (COBE) launched by NASA in 1989, is best explained by the local group motion of galaxies with a velocity of (627 ± 22) kms^{-1} relative to the CMB (LINEWEAVER et AL. 1996). Subtracting the dipole to the CMB yield fluctuations of the order of 10^{-5}. In the framework

of General Relativity, the Cosmological Principle allows us to derive the equations that govern the evolution of the background smooth universe. The small-scale inhomogeneities are treated as perturbations on top of this background.

1.1.2 General Relativity

In General Relativity, space-time is described as a four-dimensional manifold with a metric. Any metric theory of gravitation is based on Einstein's equivalence principle :

1. Weak equivalence principle : all particles fall at the same rate in a gravitational field, independently of their mass or composition.
2. Einstein's equivalence principle : any non-gravitational local experiment will have the same result if performed in a free falling inertial frame as if it were performed in the flat space-time of Special Relativity.

Under these assumptions, gravitation results from a curved space-time, whose geometry is described by a metric **g**. A metric **g** defines the distance between any points of a manifold. The length element between two space-time events separated by dx^μ is,

$$\mathrm{d}s^2 = g_{\mu\nu}\mathrm{d}x^\mu \mathrm{d}x^\nu. \tag{1.1}$$

Following Einstein's tensor notation, the Greek indices go from 0 to 3, while the Latin indices are used for the spatial component of the metric only, i.e. from 1 to 3. $g_{\mu\nu}$ is a symmetric tensor with inverse $g^{\mu\nu}$ and determinant g [1]. In Special Relativity, the length element $\mathrm{d}s^2$ is

$$\mathrm{d}s^2 = -c^2\mathrm{d}t^2 + (\mathrm{d}x^1)^2 + (\mathrm{d}x^2)^2 + (\mathrm{d}x^3)^2. \tag{1.2}$$

In the following, we will set c = 1, unless otherwise stated. In this case, the metric has the simple form, $g_{\mu\nu} = \eta_{\mu\nu} = \mathrm{diag}(-1,1,1,1)$. We note that, although Minkowski spaces are flat, they are not Euclidean, because their metrics are different : photons travel on straight lines of zero proper length. The equation of motion of a photon is given by

$$\nabla \cdot \mathbf{U} = 0, \tag{1.3}$$

where ∇ is the nabla operator [2] and **U** is the fourth velocity vector, tangent to the photon particle path. In component notation and pecial Relativity, this reduces to

$$U^\beta U^\alpha_{,\beta} = 0, \tag{1.4}$$

where we denote $\partial\phi/\partial x^\beta = \phi_{,\beta}$. Einstein's equivalence principle means that, in local region of space-time, one can find an inertial and comoving reference in which the measurements of physical properties will be identical to those of Special Relativity. Since gravitation results from a curved space-time, this means that gravity adds nothing locally, all the effects of gravity are felt over extended regions of space-time. The only detectable aspect of gravity are the tidal forces, which correspond to the non-uniformity of the gravitational field. For example, tides effect arise from the difference between the Moon and Sun gravitational fields across Earth's diameter. These forces prevent the construction of a global inertial framework. We have already said that space-time is described as a four-dimensional manifold with a metric. A 3-dimensional manifold is a topological space that is locally Euclidean. In 4 dimensions, our curved manifold will be locally like a Minkowski

1. A tensor noted $T^{i_1,\ldots,i_m}_{j_1,\ldots,j_n}$ corresponds to a linear function of M unique forms and N vectors in the real number. For example, a one-form is a (0,1) tensor, the scalar product is a (0,2) tensor and so on.

2. $\mathrm{div} \equiv \nabla \cdot \mathbf{U}$, $\overrightarrow{\mathrm{grad}} \equiv \nabla U, \triangle \equiv \nabla^2 = \mathrm{div}(\overrightarrow{\mathrm{grad}} U)$

space. Einstein principle therefore guarantees that, locally, the physical laws expressed in a curved space-time will have the same form as those of Special Relativity. Einstein principle thus assumes the non-coupling between gravitation and the other physical forces, otherwise we could not make such an equivalence.

In Special Relativity, it is quite straightforward to derive the equation of the photon trajectory in a flat Minkowski space. In general relativity, we have to describe the trajectory of the photon in a curved space-time. The equivalent of Eq. 1.4 is

$$U^\beta U^\alpha_{;\beta} = U^\beta U^\alpha_{,\beta} + \Gamma^\alpha_{\mu\beta} U^\mu U^\beta = 0, \tag{1.5}$$

where $;\beta$ is the covariant derivative. The covariant derivative specifies the derivative along tangent vectors on the manifold. $\Gamma^\alpha_{\mu\beta}$ corresponds to the Christoffel symbols that can be derived from the metric as

$$\Gamma^\alpha_{\mu\beta} = \frac{1}{2} g^{\delta\alpha} (g_{\delta\beta,\mu} + g_{\mu\delta,\beta} - g_{\mu\beta,\delta}). \tag{1.6}$$

Denoting by τ (the proper time) the parameter of the curve, then $U^\alpha = \mathrm{d}x^\alpha/\mathrm{d}\tau$,$U^\beta_{,\beta} = \mathrm{d}/\mathrm{d}\tau$ and Eq. 1.5 simplify to

$$\frac{\mathrm{d}}{\mathrm{d}\tau}\left(\frac{\mathrm{d}x^\alpha}{\mathrm{d}\tau}\right) + \Gamma^\alpha_{\mu\beta} \frac{\mathrm{d}x^\mu}{\mathrm{d}\tau} \frac{\mathrm{d}x^\beta}{\mathrm{d}\tau} = 0. \tag{1.7}$$

This is the geodesic equation of straight line in General Relativity. The curvature of the space-time is described with the Riemann tensor. Its expression is constructed from the metric first and second derivatives

$$R^\alpha_{\beta\mu\nu} = \Gamma^\alpha_{\beta\nu,\mu} - \Gamma^\alpha_{\beta\mu,\nu} + \Gamma^\alpha_{\sigma\nu}\Gamma^\sigma_{\beta\mu} - \Gamma^\alpha_{\sigma\mu}\Gamma^\sigma_{\beta\nu}. \tag{1.8}$$

The only contraction leading to a tensor of order 2 is the Ricci tensor :

$$R_{\mu\nu} = R^\alpha_{\mu\alpha\nu}, \tag{1.9}$$

whose trace $R = g^{\mu\nu} R_{\mu\nu}$ is called the Ricci scalar.

The Einstein field equations relate the space time geometry to the distribution of matter-energy within it as

$$G_{\mu\nu} = 8\pi G T_{\mu\nu} - \Lambda g_{\mu\nu}, \tag{1.10}$$

where we introduced the cosmological constant Λ. G is the Newton constant, $G_{\mu\nu}$ is the Einstein tensor and $T^{\mu\nu}$ is the stress-energy tensor, which corresponds to the flux of the μ component of the momentum vector through a surface of constant x^ν. The Einstein tensor can be written as

$$G_{\mu\nu} = R_{\mu\nu} - \frac{1}{2} R g_{\mu\nu}. \tag{1.11}$$

The left side of Eq. 1.10 represents the curvature of space-time as defined by the metric while the right side expression refers to the matter-energy content. Einstein equation therefore implies an equivalence between the space-time geometry and the distribution of matter-energy content.

The stress-energy tensor for a perfect isotropic fluid can be written as

$$T^{\mu\nu} = (\rho + p) U^\mu U^\nu + p g^{\mu\nu}, \tag{1.12}$$

where ρ and p correspond to the density and pressure of the fluid. Finally Einstein equivalence principle ensures the conservation of the total energy momentum tensor,

$$T^{\mu\nu}_{;\mu} = 0. \tag{1.13}$$

The Einstein field equations 1.10-1.11 can be directly determined by applying the principle of

least action ($\delta S = 0$) to the Universe, which determines the motion of each point in space. The Einstein-Hilbert action reads

$$S = \frac{1}{16\pi G}\int d^4x\sqrt{-g}(R-2\Lambda) + \int d^4\sqrt{-g}\mathscr{L}_m. \tag{1.14}$$

The first term on the right side corresponds to the Lagrangian of the metric from which we subtract the Lagrangian of Λ. We have also introduced the total Lagrangian of matter $\mathscr{L}_m$. More generally, these equations can be modified to provide new models of gravity called $f(R)$ theories, where the Lagrangian of $g_{\mu\nu}$ takes different forms. These modifications to standard gravity try to explain the recent accelerated expansion of the Universe, see Section 1.1.4, without invoking the cosmological constant, instead by considering a different action of matter on the curvature of space-time.

1.1.3 Friedmann-Lemaître-Robertson-Walker metric

Since the Universe is isotropic to a fundamental observer, the velocity field cannot have any preferred direction. The only allowed motions are therefore either pure contraction or expansion, i.e.

$$\delta\mathbf{v} = H\delta\mathbf{x}, \tag{1.15}$$

where $\delta\mathbf{v}$ and $\delta\mathbf{x}$ are the velocity and position of a particle with respect to the fundamental observer, and H is a constant. If we consider all the observers O' equidistant from an fundamental observer O, each of the observers O' must observe the same local values of the expansion rate and all physical quantities due to the isotropy of the Universe. Since any O' observer remains equidistant from O at any subsequent time, each observer can synchronize its clock with a light signal, and once synchronized the clocks must remain the same. Since this is true for any observer O, it means that there is a three-dimensional hypersurface in space-time in which all physical observables are uniform and evolve according to a universal time. Such a time is called the cosmic time. Of course, such cosmic time only makes sense on large scales, because space-time is curved in local high-density environments. In an homogeneous and isotropic Universe, three-dimensional surfaces are therefore space-like hyperspaces of constant proper time t, the metric can be written as

$$\mathrm{d}s^2 = -c^2\mathrm{d}t^2 + a^2(t)\left(\frac{\mathrm{d}x^2}{1-Kx^2} + x^2\mathrm{d}\Omega^2\right). \tag{1.16}$$

This is the Friedmann-Lemaître-Robertson-Walker (FLRW) metric. $a(t)$ is the cosmic scale factor, x is a radial coordinate and $d\Omega^2 = \mathrm{d}\theta^2 + \sin^2\theta\mathrm{d}\phi^2$ is the infinitesimal solid angle element. We will also set c=1 following the convention previously adopted. K corresponds to the curvature parameter. For $K > 0$, the spatial part of the metric is closed, when $K > 0$ it is open, and when $K = 0$ it is flat. Here, the coordinates (x,θ,ϕ) are called the comoving coordinates in any fundamental observer frame. A proper distance between 2 observers can be defined at any time by $l = \int dl$. Assuming one at the origin and the other at at coordinates (x_1,θ,ϕ), we get

$$l = \int_0^{x_1}\frac{\mathrm{d}x}{1-Kx^2} = a(t)\chi(x_1), \tag{1.17}$$

where

$$\chi(x) = \begin{cases} K^{-1/2}\sin^{-1}(\sqrt{K}x) & \text{if } K > 0, \\ x & if\, K = 0, \\ -K^{-1/2}\sinh^{-1}(\sqrt{-K}x) & \text{if } K < 0. \end{cases} \tag{1.18}$$

χ is the comoving distance between any 2 observers. It corresponds to the proper distance measured in units of the scale factor. It is often useful to rewrite the metric in term of the conformal time

$$\tau(t) = \int_0^t \frac{\mathrm{d}t'}{a'(t)}, \tag{1.19}$$

yielding

$$\mathrm{d}s^2 = a^2(\tau)[-\mathrm{d}\tau^2 + \mathrm{d}\chi^2 + f_k^2(\chi)(\mathrm{d}\theta^2 + \sin^2\theta \mathrm{d}\phi^2)], \tag{1.20}$$

where

$$f_k(\chi) = x = \begin{cases} K^{-1/2}\sin(\sqrt{K}\chi) & \text{if } K > 0, \\ \chi & \text{if } K = 0, \\ -K^{-1/2}\sinh(\sqrt{-K}\chi) & \text{if } K < 0. \end{cases} \tag{1.21}$$

We see that χ corresponds to a comoving geodesic distance as it measures the length of the shortest path connecting two points on the three-dimensional hypersurface. Only when $K = 0$ and thus $x = \chi$, the radial coordinate x corresponds to a geodesic distance.

The Hubble parameter $H(t)$ is defined as the infinitesimal variation of the proper time distance l at time t between any two fundamental observers, expressed in unit of the proper distance, $H(t)l \equiv \mathrm{d}l/\mathrm{d}t$. Given Eq. 1.17, it follows that

$$H(t) = \frac{\dot{a}}{a}, \tag{1.22}$$

where the dot is used for time derivative.

Almost all astrophysical observations are made through light. Is it therefore important to determine how photons travel in a isotropic and homogeneous Universe. Without loss of generality, let us consider a radial signal ($\mathrm{d}\phi = \mathrm{d}\theta = 0$) propagating to the origin. Since photons follow the geodesics $\mathrm{d}s^2 = 0$, their trajectory can be written as

$$\mathrm{d}\tau = \mathrm{d}\chi. \tag{1.23}$$

If a light signal is emitted at time t_e from a position x_e, it will reach the origin at time

$$\tau(t_o) - \tau(t_e) = \chi(x_e) - \chi(t_o) = \chi(x_e). \tag{1.24}$$

Since the comoving distance between the 2 points remain the same, another signal emitted at $t_e + \delta t_e$ will reach the origin at

$$\tau(t_o + \delta t_o) - \tau(t_e + \delta t_e) = \chi(x_e). \tag{1.25}$$

It follows that

$$\tau(t_o + \delta t_o) - \tau(t_e + \delta t_e) = \tau(t_o) - \tau(t_e), \tag{1.26}$$

by using the definition of τ and assuming $\delta t_e \ll t_e$ and $\delta t_o \ll t_o$, a valid assumption for astronomical observations. We obtain

$$\frac{\delta t_o}{a(t_o)} = \frac{\delta t_e)}{a(t_e)}. \tag{1.27}$$

Thus, the period of a wave, or equivalently its wavelength, increases proportionally to the scale factor

$$\frac{\lambda_o}{\lambda_e} = \frac{a(t_o)}{a(t_e)}. \tag{1.28}$$

Introducing the redshift parameter, $z \equiv (\lambda_o - \lambda_e)/\lambda_e$ as the relative change in wavelength we have,

$$1 + z \equiv \frac{\lambda_o}{\lambda_e} = \frac{a(t_o)}{a(t_e)}, \tag{1.29}$$

where we will set $a(t_o) = 1$. If the Universe is expanding, $a(t_o) > a(t_e)$, then spectral features of galaxies should appear redshifted, while they would be blueshifted in a contracting universe.

1.1.4 The expansion of the Universe

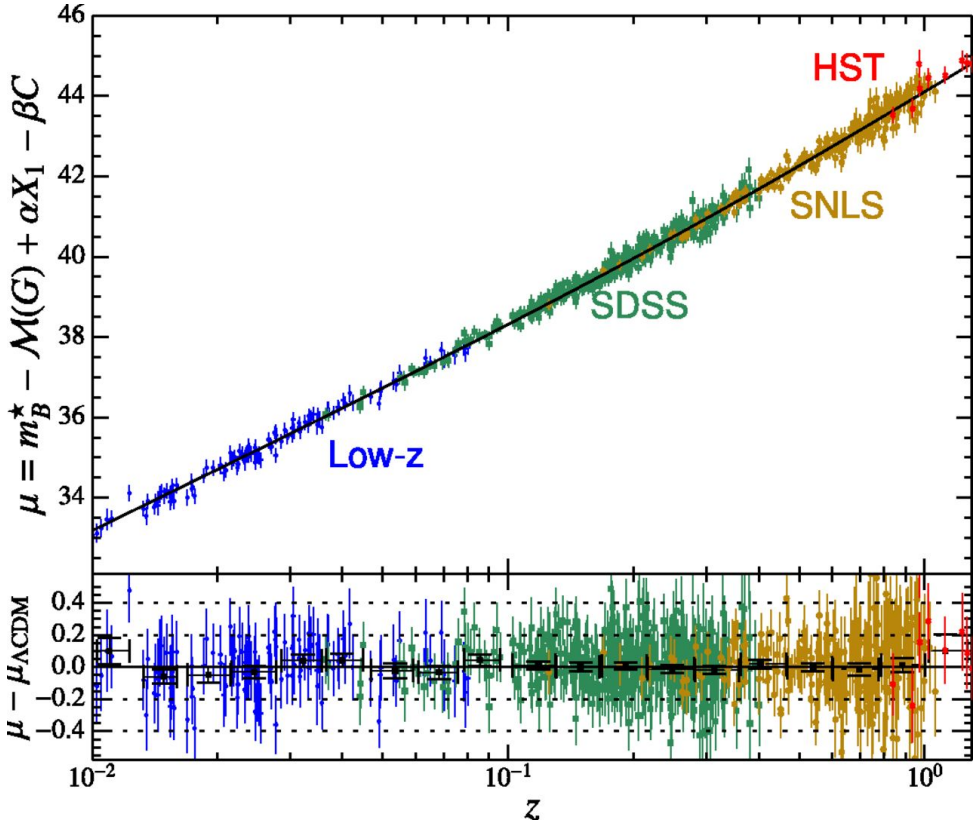

FIGURE 1.2 – The observed Hubble diagram at redshift below z<1 of SNIa observed with SDSS-II (KESSLER et AL. 2009), the Supernova Legacy Survey (SNLS) (ASTIER et AL. 2006) and the Hubble Space Telescope (HST) (RIESS et AL. 2007) Credit :(BÉTOULE et AL. 2014)

As we will see later, small perturbations in the background density field induce velocities that deviate from pure expansion. These velocities relative to a rest cosmological frame are what we called proper or peculiar velocities. The proper velocity of an object relative to a cosmological observer at the origin is defined as $v = \mathrm{d}v/dt$ with $l(t)$ the proper distance between the object and observer. From Eq. 1.17 we get

$$v(t) = \dot{a}(t)\chi(t) + a(t)\dot{\chi}(t) = H(t)l + \dot{\chi}(t) = H(t)l + v_p. \tag{1.30}$$

Let us now consider a non-relativistic object moving freely at velocity $v_p \ll c$. The object passes in front of a fundamental observer O_1 at time t and travels a distance $\mathrm{d}l = v\mathrm{d}t$. At that time, the object passes a second fundamental observer who has a relative velocity $\mathrm{d}v = H\mathrm{d}l = Hv\mathrm{d}t$ with respect to O_1. O_2 will therefore measure $v(t + \mathrm{d}t) = v(t) - \mathrm{d}v$. The equation of motion of this particle is therefore

$$\frac{\mathrm{d}v_p}{\mathrm{d}t} + \frac{\dot{a}}{a}v_p = 0. \tag{1.31}$$

The peculiar velocity of a free non-relativistic particle decreases as the inverse of the scale factor

$$v_p(t) \propto a^{-1}(t). \tag{1.32}$$

For a photon with zero mass, we have that $pc = E = h\nu$. Since $\nu \propto a^{-1}$, we also have that $p(t) \propto a^{-1}(t)$ for photons. This scaling relation holds for both massive particles and relativistic species. If the Universe is expanding then particle velocity will tend towards zero : all particles will eventually become at rest with respect to the cosmological frame. Since $a\dot{\chi}$ is due to peculiar velocities, with directions randomly distributed, it is zero on average. Therefore, $\langle V \rangle = Hl$. This demonstrates Hubble-Lemaître law (HUBBLE 1929) : the relative velocity between two objects is proportional to their distance, most commonly written in the form

$$v = H_0 D, \tag{1.33}$$

where $H_0 = H(z = 0)$ is the Hubble constant and D is the proper distance.

In the local Universe, the velocity of an object can be directly determined from its redshift as $v = cz$. The value of the Hubble parameter at the present epoch can thus be determined by measuring separately the redshift and the distance of galaxies. This method, called the Hubble diagram, is the most direct evidence for the expansion of the Universe. A fundamental task in astronomy is the correct determination of distances, required to convert observables into physical quantities. There are mainly two ways of determining the distance to an object : by looking at its apparent flux or angular size. The most direct distance measurement relies on trigonometric parallax (LURI et AL. 2018). Its principle is very simple : by looking at the change of orientation θ of a close object relative to another at infinity, we can determine the distance d to that object, given the relative distance traveled by the observer b, $\theta = b/d$. However, this method can only be used for close stars in the Milky Way (up to a few kpc). Astronomical objects direct observable properties are the angular size and the energy flux received at the observer's position. Thus, the distance of an object can be estimated if its physical size or luminosity can be obtained independently of the distance. Objects whose physical size and luminosity can be obtained in this way are called standard rulers and standard candles respectively. We will briefly describe some of these objects :

1. Cepheids variable stars. These stars exhibit an apparent change in luminosity with period varying from 2 to 150 days. The period has been found to correlate with the intrinsic luminosity of Cepheids, with a 20% scatter. Once the luminosity-period relation is calibrated using the parallax distance of Cepheids in the Milky Way, it can be used (assuming a universal relation) to calculate the distance to Cepheids in other galaxy for distances below 20 Mpc/h (RIESS et AL. 2018).
2. Type Ia supernovae (SNIa). SNIa supernovae corresponds to the stellar explosion of a white dwarf in a binary system. Such object can reach a luminosity up to $\sim 10^{10}$ $L_\odot$, with $L_\odot$ the luminosity of the Sun, comparable to the luminosity of a galaxy. The SNIa luminosity peaks are remarkably similar (BRANCH et MILLER 2014) and is correlated with the characteristic time associated to their light curves, with a 12% scatter. Once again, the SN1a absolute magnitude is calibrated using Cepheids (DHAWAN et AL. 2018)
3. Baryon acoustic oscillations (BAO). These oscillations are imprinted in the distribution of matter in the early Universe. The size of the fluctuations are directly observable in the cosmic microwave background. As the comoving angular size of these fluctuations remains the same with cosmic time, we can use this standard ruler to constrain the expansion rate.
4. Galaxies. The observed velocities of spiral galaxies are correlated with their rotational velocity, $L \propto V^4$. This is the Tully-fisher relation (TULLY et R. FISHER 1977). For elliptical galaxies, luminosity is correlated with the velocity dispersion instead $L \propto \sigma_v^4$.

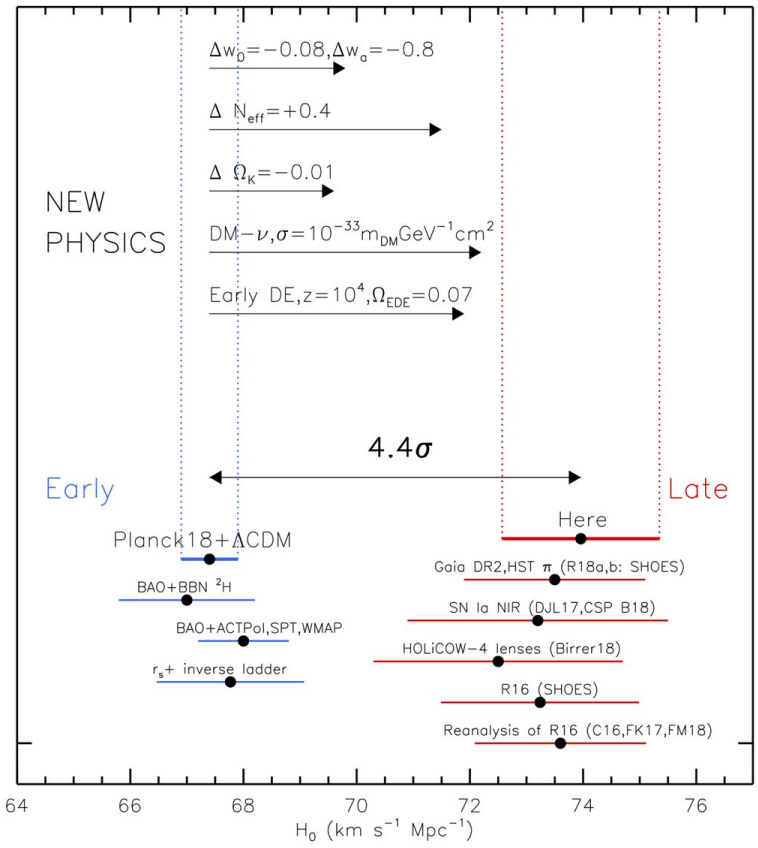

FIGURE 1.3 – H_0 tension between measurements in the early and late Universe. H_0 in the early Universe is measured by (PLANCK COLLABORATION 2018). See for details in RIESS et AL. 2019 for details on the sample involved. Taken from (RIESS et AL. 2019)

In order to measure H_0 in the local Universe, we must target local galaxies whose peculiar velocity are negligible compared to the Hubble flow. Since peculiar velocities of galaxies are typically of the order of 200 km/s, a Hubble flow of at least about 4 10^3 km/s is needed to ensure that peculiar velocities are negligible, which corresponds to $z_{\min} \approx 0.01$. Fig. 1.2 presents the SNIa Hubble diagram, which combines observations from several SNIa surveys. The black line represents the modelled distance luminosity for a flat Universe, with $H_0 = 70$ km/s/ Mpc^{-1}. As we can see on Fig. 1.3 there are currently tension between early and late-time measurements of H_0. The latest measurements lead to a 5.3σ discrepancy (WONG et AL. 2019) that is still debated.

1.1.5 Cosmological distances

Let us now determine how distances can be measured on cosmological scales. If we consider an object of intrinsic size s and luminosity L at a distance d of an observer, the observed properties of this object will be its angular size θ and flux F. This allows us to define the angular diameter distance D_A and the luminosity distance D_L such that

$$\theta = \frac{s}{D_A}, \quad F = \frac{L}{4\pi D_L^2}. \tag{1.34}$$

In a static space, $d = D_A = D_L$, but in a expanding Universe D_A, D_L and d may have entirely different values. The radial comoving distance D_c of an object emitted at time t_e and observed at the origin

at time t_0 is obtained by integrating along a radial light geodesic

$$D_c(t_e) = \tau(t_e) = \int_{t_e}^{t_0} \frac{\mathrm{d}t'}{a(t')}. \tag{1.35}$$

From Eq. 1.22, we have that $\mathrm{d}t = \mathrm{d}a/aH(a) = -dz/((1+z)H(z))$, and therefore

$$D_c(z) = \int_0^z \frac{\mathrm{d}z'}{H(z')}. \tag{1.36}$$

The comoving angular distance D_M relates the transverse comoving size of an object with comoving surface area dS_e to the observed solid angle $d\Omega_o$

$$dS_e = D_M^2 d\Omega_o^2. \tag{1.37}$$

It follows from the metric expression that

$$D_M(z) = f_k(D_c(z)). \tag{1.38}$$

The angular diameter distance D_A relates the transverse physical size of an object to the observed solid angle. Since the physical surface area is $dS_p = a(t_e)^2 dS_e$, we have that

$$D_A(z) = \frac{D_M(z)}{1+z}. \tag{1.39}$$

The luminosity distance D_L relates the luminosity L_e of a source located at a radial comoving distance D_c to the flux ϕ_0 measured by the observer such that

$$\phi_0 = \frac{L_e}{4\pi D_L^2}. \tag{1.40}$$

The luminosity scales as $\mathrm{d}E/\mathrm{d}t$. Since the time interval $\mathrm{d}t \propto a(\tau)d\tau$ scales as a and the received energy λ_o scales as a^{-1}, we have

$$\phi_0 = \frac{L_e(1+z)^{-2}}{4\pi f_k^2(D_c(z))}, \tag{1.41}$$

and therefore

$$D_L(z) = D_M(z)(1+z). \tag{1.42}$$

All the cosmological distances described here are expressed in terms of the curvature and Hubble parameter $K(t)$ and $H(t)$, expressions that are related to the energy content in the Universe. To determine the evolution of H with time, one needs to know the time evolution of the scale factor. This can be determine in a isotropic and homogeneous Universe with the Einstein field equations, which describe the geometrical properties of space-time as a function of the energy content of the Universe. In the local Universe, we can have an approximation for the evolution of the scale factor by using a Taylor expansion

$$a(t) = 1 + H_0(t-t_0) - \frac{1}{2}q_0 H_0^2 (t-t_0)^2 + \mathcal{O}(t^3), \tag{1.43}$$

where $q_0 = -\ddot{a}_0 a_0/\dot{a}_0{}^2 = -\ddot{a}_0/H_0^2$. The sign of q_0 comes from the natural expectation that the Universe will decelerate at some point. The expansion of the Hubble parameter gives

$$H(z) = H_0[1 + (q_0+1)z] + \mathcal{O}(z^2), \tag{1.44}$$

At first order, the luminosity distance can be written as

$$D_L = \frac{1}{H_0}[z - \frac{1}{2}(q_0 - 1)z] + \mathcal{O}(z^2). \tag{1.45}$$

The luminosity distance only depend on H_0 for $z \ll 1$, on q_0 for $z < 0.2$, and on all cosmological parameter for $z \sim 0.3$. Of course, the Taylor expansion is just an approximation for small perturbations around the local Hubble flow H_0, and in general one needs to properly determine the evolution of the expansion rate history $H(z)$.

1.1.6 Friedmann equations

As seen previously, the geometrical properties of space-time in a homogeneous and isotropic Universe are described by the FLRW metric, whose parameterization depends on the curvature parameter K and on the temporal evolution of the scale factor $a(t)$. The Einstein field equations 1.10-1.11 can be written as

$$R_{\mu\nu} + g_{\mu\nu}\Lambda = 8\pi G\left(T_{\mu\nu} - \frac{1}{2}g_{\mu\nu}T\right), \tag{1.46}$$

where $T = T^{\nu}_{\nu}$ is the trace of the energy-momentum tensor. In General Relativity, essentially all types of matter can be approximated as a perfect fluid. Non-relativistic matter can be treated as a perfect fluid with zero pressure, which we will refer to as as "dust" in the following. A star can be modelled locally as a perfect fluid with isotropic pressure, and more generally, any isotropic fluid (which therefore has neither thermal conduction nor viscosity) can be seen as a perfect fluid. These fluids are entirely characterized by their density and pressure. The expression of a perfect fluid is already given by Eq. 1.12. In an homogeneous and isotropic Universe, density and pressure depend only on cosmic time, and the four-velocity vector in the comoving frame of the fluid takes the form $U = (1,0,0,0)$ [3]. For an isotropic fluid, this further reduces to $T^{\mu\nu}$= diag(ρ,p,p,p), with $T_{\mu\nu} = T^{\alpha\beta}g_{\alpha\mu}g_{\beta\nu}$ and $T = T^{\alpha}_{\alpha} = g_{\alpha\beta}T^{\beta\alpha} = 3p - \rho$. For the FLRW metric, the non-zero components of the Ricci tensor are given by

$$R_{00} = -3\frac{\ddot{a}}{a} \quad \text{and} \quad R_{ij} = \left(\frac{\ddot{a}}{a} + 2\frac{\dot{a}^2}{a^2} + \frac{2K}{a^2}\right)g_{ij}, \tag{1.47}$$

and the curvature scalar is

$$R = 6\left(\frac{\ddot{a}}{a} + \frac{\dot{a}^2}{a^2} + \frac{K}{a^2}\right). \tag{1.48}$$

Inserting the expression for the stress-energy and Ricci tensors into the Einstein field equation 1.46 yields

$$\frac{\ddot{a}}{a} = -\frac{4\pi G}{3}(\rho + 3P) + \frac{\Lambda}{3}, \tag{1.49}$$

for the time component, and

$$\frac{\ddot{a}}{a} + 2\frac{\dot{a}^2}{a^2} + 2\frac{K}{a^2} = 4\pi G(\rho - P) + \Lambda, \tag{1.50}$$

for the space component. It then follows from inserting Eq. 1.49 into Eq. 1.50

$$H^2(z) \equiv \frac{\dot{a}^2}{a^2} = \frac{8\pi G}{3}\rho - \frac{K}{a^2} + \frac{\Lambda}{3}, \tag{1.51}$$

3. Remember that when $c = 1$, time is equivalent to distance, while ρ and p are equivalent to energy density

Tableau 1.1 – Scaling relations for the differents energy components in the Universe

Energy component	w	ρ	a
vacuum	-1	$\propto a^0$	$\propto e^{Ht}$
matter	0	$\propto a^{-3}$	$\propto t^{2/3}$
Relativistic components	1/3	$\propto a^{-4}$	$\propto t^{1/2}$
Curvature	$-1/3$	$\propto a^{-2}$	$\propto t$

Eqs. 1.49 and 1.51 are the Friedmann equations and any cosmology that obeys to these two equations is called a FLRW cosmology. It is a set of two equations with three unknown quantities, $a(t)$, $\rho(t)$ and $P(t)$. To resolve this system one needs a third equation, an equation of state that relates pressure and density.

Let us consider a small comoving volume V. In an isotropic and homogeneous Universe, there should be no heat flow through the boundaries of V. Therefore V can be treated as a adiabatic volume, and its thermodynamical properties do not follow General Relativity, as long as its volume is small enough. For our adiabatic expanding volume ($V \propto a^3$) we have that

$$\mathrm{d}U + p\mathrm{d}V = 0, \mathrm{d}S = 0, \tag{1.52}$$

where U is the internal energy, p is the pressure and S is the entropy. In term of energy density, this can be written as

$$V\mathrm{d}\rho + (\rho + P)\mathrm{d}V = 0. \tag{1.53}$$

Since $V \propto a^3$, differentiating the latter equation with respect to a yields

$$\frac{\mathrm{d}\rho}{\mathrm{d}a} + 3\left(\frac{\rho + p}{a}\right) = 0, \tag{1.54}$$

which can be written as

$$\dot{\rho} + 3H(\rho + p) = 0. \tag{1.55}$$

This corresponds to the continuity equation for fluid elements in a expanding Universe. Is is common to introduce the equation of state parameter w such that $P = w\rho$. if w is time independent, then

$$\rho \propto a^{-3(1+w)}. \tag{1.56}$$

The cosmological constant Λ is equivalent to a fluid whose equation of state is $w = -1$. Non-relativistic matter will be treated as a dust fluid, which has no pressure, so $w = 0$. Radiation and relativistic matter will be treated as fluid with $w = 1/3$. Inserting Eq. 1.56 into Eq. 1.49 gives the scaling relations given in Table 1.1. We denote the energy density of a fluid Y at the present time by $\rho_{\mathrm{Y},0}$. The total density of non-relativistic matter in the Universe is usually express as

$$\rho_{\mathrm{m},0} = \Omega_{\mathrm{m},0}\rho_{\mathrm{crit},0}, \tag{1.57}$$

where

$$\rho_{\mathrm{crit}}(t) \equiv \frac{3H^2(t)}{8\pi G}, \tag{1.58}$$

is known as the critical density at time t. $\Omega_{\mathrm{m},0}$ is a dimensionless quantity that represents the density parameter of non-relativistic matter at the present time. From Friedmann equations 1.49 and 1.51, we can see that the cosmological constant and the curvature can be considered as two energy components with

$$\rho_\Lambda = \frac{\Lambda}{8\pi G}, \quad \rho_\mathrm{K} = \frac{-3K}{8\pi G a^2}. \tag{1.59}$$

The density ρ that appears in Eq. 1.51 can be decomposed into its different energy components, which scale with a in different ways. This allows us to rewrite Eq. 1.51 in terms of densities at present time as

$$H^2(t) = \frac{8\pi G}{3}\left[\rho_{\mathrm{m},0}\left(\frac{a_0}{a(t)}\right)^3 + \rho_{\mathrm{r},0}\left(\frac{a_0}{a(t)}\right)^4 + \rho_{\mathrm{k},0}\left(\frac{a_0}{a(t)}\right)^2 + \rho_{\Lambda,0}\right]. \tag{1.60}$$

By dividing each term by $H^2(t)$, and taking $t = t_0$ gives

$$\Omega_{\mathrm{m},0} + \Omega_{\mathrm{r},0} + \Omega_{\Lambda,0} + \Omega_{\mathrm{k},0} = 1, \tag{1.61}$$

which can be rewritten as

$$\Omega_{\mathrm{k},0} = 1 - \Omega_0, \quad \text{where} \quad \Omega_0 = \Omega_{\mathrm{m},0} + \Omega_{\mathrm{r},0} + \Omega_{\Lambda,0}. \tag{1.62}$$

Ω_0 is the total density parameter at present time. Ω_0 is less than 1 for a open Universe, equals to unity for a flat Universe and is more than 1 for a closed Universe. Since Ω_0 corresponds to the total energy density in unit of $\rho_{\mathrm{crit},0}$, it means that $\rho_{\mathrm{crit},0}$ defines a critical density for closure. From the definition of redshift, $1 + z \equiv a_0/a(t)$, we can rewrite Eq. 1.60 as

$$H^2(z) = \left(\frac{\dot{a}}{a}\right)^2 = \frac{8\pi G}{3}\left[\rho_{\mathrm{m},0}(1+z)^3 + \rho_{\mathrm{r},0}(1+z)^4 + \rho_{\mathrm{k},0}(1+z)^2 + \rho_{\Lambda,0}\right], \tag{1.63}$$

with

$$H(z) = H_0 E(z) = H_0\sqrt{\Omega_{\mathrm{m},0}(1+z)^3 + \Omega_{\mathrm{r},0}(1+z)^4 + \Omega_{\mathrm{k},0}(1+z)^2 + \Omega_{\Lambda,0}}. \tag{1.64}$$

If we define the density parameter at time t as $\Omega_{y,t} = \rho_{y,t}/\rho_{\mathrm{crit},t}$ we have that

$$\Omega_\Lambda(t) = \frac{\Omega_{\Lambda,0}}{E^2(z)}, \quad \Omega_{\mathrm{m}}(t) = \frac{\Omega_{\mathrm{m},0}(1+z)^3}{E^2(z)}, \quad \Omega_{\mathrm{k}}(t) = \frac{\Omega_{\mathrm{k},0}(1+z)^2}{E^2(z)}. \tag{1.65}$$

Once H, Ω_{m},Ω_Λ, Ω_{r} and Ω_{k} are know at present time, their value can be extrapolated at any earlier time.

Finally, another important distance in cosmology is the horizon. Light emitted by an event at r_e, t_e will reach the origin at time t_0 such as

$$\chi(r_e) = \int_{t_e}^{t_0}\frac{c\,\mathrm{d}t}{a(t)} = \int_{a_e}^{a_0}\frac{\mathrm{d}a}{\dot{a}}\left[\frac{8\pi G\rho(a)a^2}{3} - K\right]^{-1/2}, \tag{1.66}$$

where we have used $\rho = \rho_{\mathrm{m}} + \rho_{\mathrm{r}} + \rho_\Lambda$, $\mathrm{d}t = \mathrm{d}a/\dot{a}$, and Friedmann equation 1.51. If the integral converges to a given value χ_h, they may exist particles for which $\chi(r) > \chi_h$, from which no signal could be have been received at r_0. Such particles are said to be beyond the particle horizon at the origin at time t_0. The convergence criteria requires that $\rho a^2 \to \infty$ when $a \to 0$. Particle horizon only exists in universes that are radiation- or matter-dominated at early times.

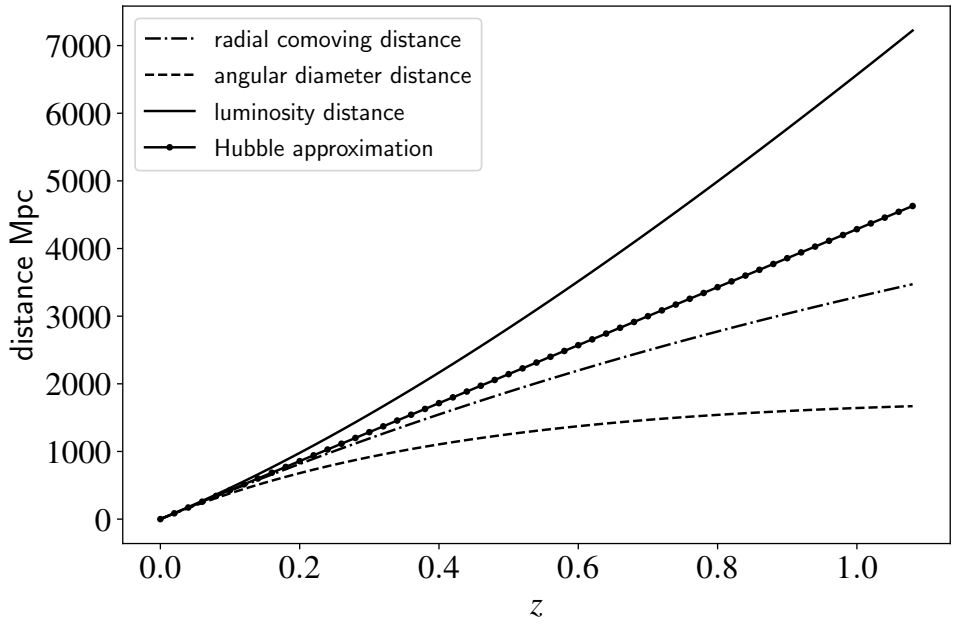

FIGURE 1.4 – Distance measurements in a flat Universe. We have used Eqs. 4.36, 1.39, 1.42 with Eq. 4.38, assuming $h = 0.6776, \Omega_{\Lambda,0} = 0.7, \Omega_{\mathrm{m},0} = 1 - \Omega_{\Lambda,0}$ in a flat Universe.

A representation of the cosmological distances is shown in Fig. 1.4. At a redshift below 0.1, all distances are equivalent and can be estimated in the Hubble approximation. At a redshift above 0.2, we can already see that the Hubble approximation is below the luminosity distance, and is caused by the expansion rate of the Universe induced by the cosmological constant (here $\Omega_\Lambda = 0.7$). To calculate the cosmological distances introduced in 1.1.5, we need to provide the value of the current density parameters and the value of the Hubble constant H_0 to determine the evolution of H as in the Eq. 1.63. A usual convention is to take $H_0 = 100\ h$ km s^{-1}Mpc^{-1}, where h is the reduced Hubble constant. The density parameters can also be expressed in terms of physical quantities, $\omega_{\mathrm{Y},0} = \Omega_{\mathrm{Y},0} h^{-2}$.

The deceleration parameter q_0 can be written in term of the current densities as

$$q_0 = \frac{\Omega_{\mathrm{m},0}}{2} + \Omega_{\mathrm{r},0} - \Omega_{\Lambda,0}. \tag{1.67}$$

Finally, from the definitions of $E(z)$ and Ω_0 we can express the total density parameter at any redshift as

$$\Omega(z) - 1 = (\Omega_0 - 1)\frac{(1+z)^2}{E^2(z)}. \tag{1.68}$$

Age of the Universe

Since $\dot{a} > 0$ for the entire history of the Universe, we can obtain an expression for the age of the Universe at redshift z from Eqs. 1.29 and 1.63,

$$t(z) \equiv \int_0^{a(z)} \frac{\mathrm{d}a}{\dot{a}} = \frac{1}{H_0}\int_z^\infty \frac{\mathrm{d}z}{(1+z)E(z)}. \tag{1.69}$$

Given the cosmological parameter values given in Table 1.2, we can numerically integrate the above integral to determine the age of the Universe, $t \approx 13.8$ Gyr (PLANCK COLLABORATION 2018).

Radiation dominated era

Within the Hot Big Bang scenario, the radiation component dominates at early time. Thus, we can integrate Eq. 1.63 neglecting the matter component.

$$\frac{a}{a_0} = \left(\frac{32\pi G\rho_{\mathrm{r},0}}{3}\right)^{1/4} t^{1/2}, \tag{1.70}$$

and therefore $a \propto t^{1/2}$ for relativistic species. For radiation $\rho_{\mathrm{r}} \propto a^{-4}$, since the volume scales as $V \propto a^{-3}$ and the photon energy as $E = h\nu \propto a^{-1}$. From the equation of state, it follows that $P_{\mathrm{r}} \propto a^{-4}$ and since a black-body radiation has $\rho_r \propto T^4$, $T \propto a^{-1}$. Therefore, a black-body radiation remains black-body as the Universe expands. This gives the following scaling relations

$$\frac{T}{10^{10}K} \approx \left(\frac{\rho}{10^{7}\mathrm{gcm}^{-3}}\right)^{1/4} \approx \frac{1+z}{10^{10}} \approx \left(\frac{t}{1s}\right)^{-1/2}. \tag{1.71}$$

These relations can be used to approximate the temperature of density of the Universe for $z > 10^5$ ($t < 10^{10}s$).

Matter-dominated era

Non-relativistic matter density has $\rho_{\mathrm{m}} \propto a^{-3}$ and therefore the Universe will become matter-dominated after decoupling with CMB photons. For $\Omega_{\Lambda,0} = 0$ and $K = 0$, Eq. 1.63 reduces to

$$\frac{a}{a_0} = \left(\frac{3}{2}H_0 t\right)^{2/3}, \tag{1.72}$$

as $a \propto t^{2/3}$ for non-relativistic matter. This is the solution for a Einstein-de-Sitter (EdS) universe.

Cosmological constant-dominated era

For a flat model where $\Omega_{\mathrm{m},0} + \Omega_{\Lambda,0} = 1$, Eq. 1.63 can be rewritten as

$$\frac{\dot{a}}{a} = H_0^2\left[\Omega_{\mathrm{m},0}\left(\frac{a_0}{a}\right) + \Omega_{\Lambda,0}\right], \tag{1.73}$$

where the solution neglecting matter contribution is

$$\frac{a}{a_0} = \exp\left(\sqrt{\frac{\Lambda}{3}}(t - t_0)\right). \tag{1.74}$$

This model is called a de Sitter universe. We can see that if the late Universe is dominated by a cosmological constant, its expansion will be exponential.

1.2 The early Universe

We present in this section the physics of the early Universe, just after the Big Bang, which is considered as the initial state of the Universe. As we have seen previously, the observed expansion in the Universe is a natural result of a cosmological constant in a homogeneous and isotropic universe, whose dynamics on large-scale is described by General Relativity. However the expansion of the Universe is not enough to prove the Hot Big-Bang model of cosmology.

1.2.1 Timeline of the early Universe

The formulation of the Hot Big-Bang model began in the early 1940s with Gamow, Alpher and Herman. They proposed that if the abundances of elements have a cosmological origin, the early stage of the Universe should be hot and dense enough to allow for primordial nucleosynthesis, before the cooling down due to expansion. In 1948, Alpher and Hermann predicted the presence of a thermal relic with a temperature of the order of a few Kelvins. This radiation was eventually observed 16 years later and named the cosmic microwave background (CMB). The Planck 2018 observations of CMB temperature fluctuations are shown in Fig. 1.6, where colors from red to blue correspond to tiny relative temperature fluctuations of the order of 10^{-5} K. The first observation of this radiation that singled out the Hot Big-Bang model as the prime candidate to describe the early Universe.

Atomic and particle physics allow a detailed prediction of the matter content of the Universe in the era dominated by radiation. When the temperature of the Universe is higher than the rest mass energy of a given charged particle, the interactions between photons are energetic enough to create that particle and its antiparticle, which in turn can give rise to other types of particle. For example, when the temperature of the Universe is higher than the rest mass energy of an electron ($T > 6\ 10^9$ K), electrons and positrons can be generated in pairs, producing self-generating neutrinos.

$$\gamma + \gamma \longleftrightarrow e + \bar{e}, \quad e + \bar{e} \longleftrightarrow \mu_e + \bar{\mu}_e. \tag{1.75}$$

If the density of the Universe is high enough, the creation of the positron and the electron, and their Compton scattering with photons, might establish a thermal equilibrium along these species. In order to maintain such an equilibrium, the frequency of interactions between the different particle species must be sufficiently high. The interaction rate is $\tau \equiv n\langle v\sigma\rangle$ where n is the number density of particle, v is their relative velocity and σ is the interaction cross-section (which usually depends on v). As the Universe expands and cools, this rate generally decreases. When it becomes less than the expansion rate of the Universe $H(t)$, particles decouple from the photon fluid and their density freezes at its current value, as long as the particles are stable. Except for particles created by high-energy processes, the present Universe is filled with matter that decoupled from the photon fluid in the past.

We will briefly review the chronology of the big bang. Since the early Universe was dominated by radiation, we can use the scaling relation in Eq. 1.71 to derive the temperature T at any given cosmic time. In this section we use the natural unit system in which $c = \hbar = k_B = 1$. Making these constants dimensionless implies that [energy] = [mass] = [temperature] = [time]$^{-1}$,[length]$^{-1}$. We will only consider temperatures below $10^{13}K$. This temperature is higher than the binding energy of hadrons.

1. At T $\approx 3\times10^{12}K$ ($t \approx 10^{-5}$ s) corresponding to an energy of 200-300 MeV, the quarks-hadrons phase occurs confining quarks in hadrons. Once this transition was completed, the Universe was filled with a hot plasma consisting of three types of particle : relativistic pions π^+,π^-,π^0, non-relativistic protons p and neutrons n, leptons e,$\bar{e}$,μ,$\bar{\mu}$ and their associated neutrinos $\mu_e,\bar{\mu}_e,\mu_u,\bar{\mu}_u$, and photons.
2. At T $\approx10^{12}K$ ($t \approx 10^{-4}$ s), (π^+,π^-) pairs annihilate and π^0 decay into protons. Nucleons are thus the only remaining hadronic species. At around the same time, muons start to annihilate and become negligible. Their corresponding neutrinos decouple from the plasma and expand freely in the Universe.
3. At T $\approx 5\times10^9K$ ($t \approx 4$ s), electrons and positrons pairs annihilates and $\mu_e,\bar{\mu}_e$ expand out of the plasma. The n/p ratio freezes at the value of $\exp(-\Delta m/T)$ where $\Delta m \approx 1.3MeV$, corresponding to a factor 0.1.
4. At T $\approx10^9K$ ($t \approx 1$ min) Primordial nucleosynthesis begins to synthesize protons and neutrons

and produces Deuterium, Helium and other elements. As the temperature is still very high, all these elements are ionized. The Universe is thus filled with free-moving neutrinos and highly-ionized atoms.

5. At T ≈4000 K (t ≈ 2 10^5 yr) almost half of the baryonic matter is in form of neutral atoms. This is what is called recombination (even if it is the first time in the Universe that neutral atoms appear). Because of the sudden drop in the number density of free electrons, the Universe becomes transparent to photons. The CMB is emitted. Once all CMB photons moves freely in the Universe, baryon becomes free from the influence radiation, this corresponds to the drag redshift, r_d. The Universe is then filled with neutral atoms that become opaque to light, this corresponds to the dark ages. During that time, gravitational instability grows primordial density fluctuations. The baryonic gas in high-density regions cools down and condensates to high-enough pressure to produce the first stars, which will form later the first galaxies. Once a large-enough amount of blue star has been formed in the early Universe, the UV photons will eventually ionize all the intergalactic medium, and the Universe will become transparent to light again. This corresponds to the re-ionization redshift.

1.2.2 The primordial nucleosynthesis

As already discussed, at any given epoch, particles are either in thermal equilibrium with the hot plasma, or in free expansion in the Universe. The number density n, pressure P, and energy density ρ of a given specie can be written in term of its distribution function f($\mathbf{x}$,$\mathbf{p}$, t). Since the Universe is homogeneous and isotropic, $f(\mathbf{x},\mathbf{p},t) = f(p,t)$ where $p = |\mathbf{p}|$ and

$$n(t) = 4\pi \int f(p,t)p^2 \mathrm{d}p \tag{1.76}$$

$$\rho(t) = 4\pi \int E(p)f(p,t)p^2 \mathrm{d}p \tag{1.77}$$

$$p(t) = 4\pi \int \frac{p^2}{3E(p)} f(p,t)p^2 \mathrm{d}p \tag{1.78}$$

where the energy E is related to the momentum p as $E(p) = (p^2 + m^2)^{1/2}$. Eq. 1.78 comes from kinetic theory, according to which the pressure is related to the velocity and momentum as $P = 1/3n\langle pv\rangle$. For particle in thermal equilibrium we have

$$f(\mathbf{p},t)\mathrm{d}\mathbf{p}^3 = \frac{g}{2\pi^3}\left(\exp\left(\frac{E(p)-\mu}{T(t)}\right) \pm 1\right)^{-1} \mathrm{d}p, \tag{1.79}$$

where μ is the chemical potential and $T(t)$ is the temperature at time t. The sign ± takes positive value for Fermi-Dirac species (spin of half integer value) and negative value for Bose-Einstein species (integer spin). g is the degeneracy factor : $g = 1$ for neutrinos, $g = 2$ for photons and charged leptons). The factor $1/2\pi^3$ is due to Heisenberg's uncertainties principle : no particle can be localized in a phase-space volume smaller than the fundamental volume $1/2\pi^3\hbar$. Inserting this equation into Eqs. 1.76 and 1.78 yields

$$n_{eq} = \frac{g}{2\pi^2}\int_m^\infty \frac{(E^2-m^2)^{1/2}E\mathrm{d}E}{exp[(E-\mu)T] \pm 1} \tag{1.80}$$

$$\rho_{eq} = \frac{g}{2\pi^2}\int_m^\infty \frac{(E^2-m^2)^{1/2}E^2\mathrm{d}E}{exp[(E-\mu)T] \pm 1} \tag{1.81}$$

$$p_{eq} = \frac{g}{6\pi^2}\int_m^\infty \frac{(E^2-m^2)^{3/2}\mathrm{d}E}{exp[(E-\mu)T] \pm 1}. \tag{1.82}$$

When $T \ll m$, particles are non-relativistic, their statistical properties are same for Fermi-Dirac and Bose-Einstein species

$$n_{eq} = g\frac{mT}{2\pi}^{3/2} e^{(\mu-m)/T}, \quad \rho_{eq} = nm, \quad p_{eq} = nT \tag{1.83}$$

For non-degenerated $\mu \ll T$ relativistic species ($m \ll T$ $E = p$) the analytical solution are

$$n_{eq} = \begin{cases} [\zeta(3)/\pi^2]gT^3 & \text{(Bose-Einstein)} \\ (3/4)[\zeta(3)/\pi^2]gT^3 & \text{(Fermi-Dirac)} \end{cases} \tag{1.84}$$

$$\rho_{eq} = \begin{cases} [\pi^2/30]gT^4 & \text{(Bose-Einstein)} \\ (7/8)[\pi^2/30]gT^4 & \text{(Fermi-Dirac)} \end{cases} \tag{1.85}$$

$$p_{eq} = \rho_{eq}/3, \tag{1.86}$$

where ζ is the Riemann zeta function. In general, we need to know the chemical potential μ of the species. The chemical potential is an additive quantity that is conserved during a reaction (LANDAU et LIFSHITZ 1959). Since the photon is not a conserved quantity, its chemical potential must be zero. Because the number density of baryon and leptons are found to be much smaller than that of photons, the chemical potential can be approximated to zero, when computing the mean thermodynamical quantities of the fluid in the early Universe (this is no longer true once the temperature drops and allows nuclear reactions). We note that Eq. 1.86 explains why $w = 1/3$ for relativistic species. Before looking at the abundances of atoms, we need to examine the abundance of their constituting elements : neutrons and protons. They have a comparable rest mass of ≈ 940 MeV, which implies that they become non-relativistic at very early times ($t \approx 10^{-6}s$). They maintain equilibrium through weak interactions

$$p + e \longleftrightarrow n + \mu_e \quad n + \bar{e} \longleftrightarrow p + \bar{\mu}_e. \tag{1.87}$$

Since $g_n = g_p = 2$, we obtain by using Eq. 1.83 the ratio between the number density of proton and that of neutron :

$$\frac{n_n}{n_p} = \exp\left(-\frac{Q}{T} + \frac{\mu_n - \mu_p}{T}\right) \approx \exp\left(-\frac{Q}{T}\right), \tag{1.88}$$

where Q is the mass difference between neutron and proton. $Q \equiv m_n - m_p = 1.294$ MeV. When the temperature decreases toward ≈ 1 MeV, the neutron density starts to drop compared to that of protons. At about the same temperature, neutrinos decouples from the fluid, and this ratio freezes out at value $n_n/n_p \approx 0.2$ (neutrons are unstable to beta decay but end up fast enough in helium 4 nuclei so that this number is a correct approximation overall). The binding energies of the lightest nuclei, such as deuterium and helium, are of the order of a few MeV, corresponding to a temperature of $\approx$ a few $10^{10}K$. However, because of the high entropy per baryon, the Universe has to cool down to a temperature of a few $(1-3)10^9K$. At such low temperatures, the number densities of protons and neutrons are too low to form heavy elements by many-body reactions. Nucleosynthesis must proceed through two-body interactions. Deuterium forms first, and then combine to form Helium, much favoured due to its higher binding energy. Elements heavier than helium are rare because of the instability of nuclei with $A = 5$ and $A = 8$, and because of the temperature already too low to overcome Coulomb barrier. As a result, almost all neutrons will end up in helium nuclei, and the helium abundance can then be approximated as

$$Y \equiv X_{He} \approx \frac{2n_n}{n_n + n_p} = \frac{n_n/n_p}{n_n/n_p + 1} \approx 1/4. \tag{1.89}$$

For a given specie Y with atomic number A, $X_Y \equiv A n_Y / n_b$ with $n_b = n_n + n_p + \sum_i A_i n_{A,i}$. The summation is performed over the densities of all baryonic species with mass number $A_i = \sum_i (n_p + n_n)_{nuc}$. To get the abundance for non-relativistic species other than helium, we first need compute their number density with Eq. 1.83. For a specie of mass number A and charge number Z, this corresponds to

$$n_A = g_A \frac{m_A T}{2\pi}^{3/2} e^{(\mu_A - m_A)/T}, \tag{1.90}$$

where $\mu_A = Z\mu_p + (A-Z)\mu_n$. Since we can express the chemical potential of neutron and proton given their number density with 1.83, the latter equation can be recast as

$$n_A = \frac{g_A A^{3/2}}{2^A} n_p^Z n_n^{A-Z} \left(\frac{m_N T}{2\pi}\right)^{3(1-A)/2} \exp\left(\frac{B_A}{T}\right), \tag{1.91}$$

where $B_A = Z m_p + (A-Z) m_n - m_A$ is the binding energy of species A(Z), and $m_N = m_A / A$ is the nucleon mass. It then follows that $X_A = A n_a / n_b$. However the total baryonic density n_b at early time is not directly detectable. What is know however is the relativistic photon density n_γ at any temperature $n_\gamma = 2[\zeta(3)/\pi^2] g T^3$. The final abundance of any non-relativistic species can be written as

$$n_A = \frac{g_A A^{5/2}}{2} \left(\frac{4\zeta(3)}{\sqrt{2\pi}}\right)^{A-1} X_p^Z X_n^{A-Z} \eta^{A-1} \left(\frac{m_N}{T}\right)^{3(1-A)/2} \exp\left(\frac{B_A}{T}\right), \tag{1.92}$$

where $\eta = n_b / n_\gamma$.

At the end of the Big Bang nucleosynthesis, T≈ 0.03 MeV ($t \approx 1000$ s), apart from helium-4, traces of helium-3, deuterium (mass abundance of $\approx 10^{-4}$), and lithium-7 ($\approx 10^{-9}$) remain. Is is instructive to look at the distribution function of particles that have decoupled from the plasma. After decoupling at a temperature t_e, the mean interaction rate drops below the expansion rate, and particles moves freely on geodesics. As we have seen, $p \propto a^{-1}$ for relativistic and non-relativistic particle. As a consequence, relative momenta are conserved and the distribution function at a time $t > t_e$ is

$$f(\mathbf{p}, t) = f\left(\mathbf{p}\frac{a(t)}{a(t_e)}, t_f\right), \tag{1.93}$$

thus the form of the distribution is "frozen" at the moment when particles decouple from the hot plasma.

1.2.3 The cosmic microwave background

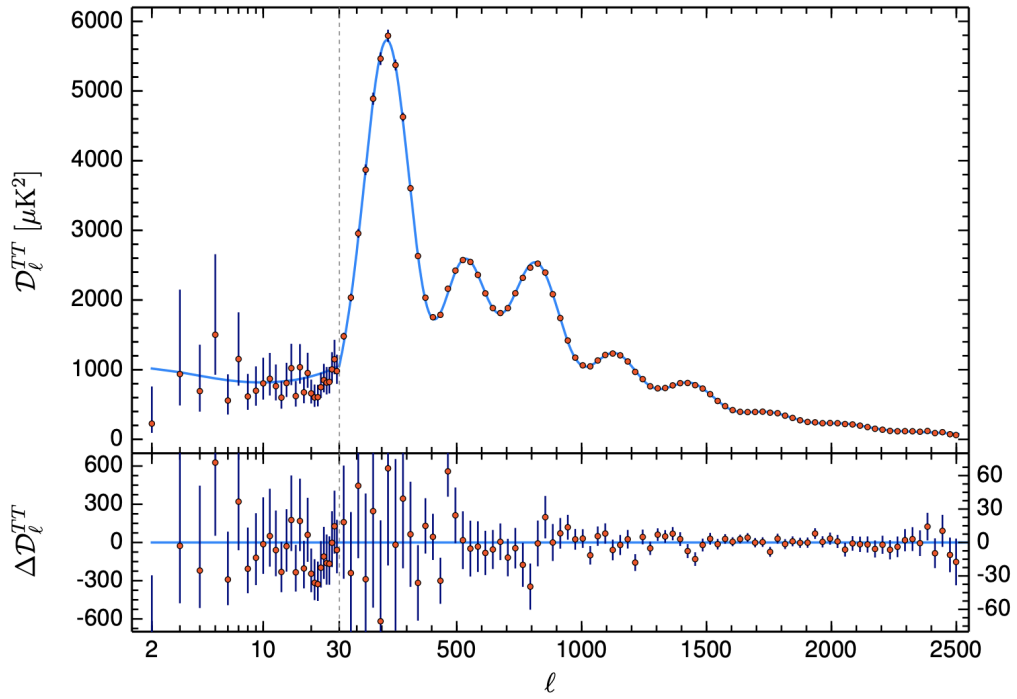

FIGURE 1.5 – The CMB temperature power spectrum as measured by (PLANCK COLLABORATION 2018). The black lines corresponds to the bestfit model using TT, TE, EE, lowE and lensing data. The axis changes from logarithms scale to linear scale at ℓ=30

After primordial nucleosynthesis, all particles (except for free neutrinos) interact through electromagnetic processes such as free-free interactions, Compton scattering, and recombination of ions with electrons. When the temperature drops below 13.6 eV, electrons and protons begin to combine to form hydrogen atoms.

$$p + e \longleftrightarrow H + \gamma. \tag{1.94}$$

Photons are less and less scattered with free electrons and start to move freely in the Universe from a last scattering surface. This corresponds to the CMB radiation.

CMB radiation was firstly discovered in 1965 by Penzias and Wilson, and it was quickly found that this radiation was highly isotropic and a black-body radiation at a temperature of about 3 K. The current CMB temperature was measured to an extreme precision by COBE (FIXSEN 2009) at a value of

$$T_{\rm CMB} = 2.7255 \pm 0.0006 {\rm K}. \tag{1.95}$$

However, tiny temperature fluctuations of the order of 10^{-5} are detectable in the CMB as shown in Fig. 1.5. These fluctuations correspond to the fluctuations of the underlying matter in the photon-baryon fluid at the time of recombination. Today, the best constraint on the energy densities come from the observed anisotropies of the CMB.

Usually, the fluctuations observed on the sphere are expanded in spherical harmonics as

$$\frac{\Delta T}{T}(\theta,\phi) \equiv = \frac{T(\theta,\phi) - \bar{T}}{\bar{T}} = \sum_{\ell=0}^{\infty} \sum_{m=-\ell}^{\ell} a_{\ell {\rm m}} Y_{\ell {\rm m}}(\theta,\phi). \tag{1.96}$$

The spherical harmonics form an orthogonal basis on a sphere and are defined as

$$Y_{\ell \mathrm{m}} = \sqrt{\frac{2l+1}{4\pi}\frac{(\ell-\mathrm{m})!}{(\ell+\mathrm{m})!}} P_\ell^{\mathrm{m}}(\cos\theta)\exp^{i\mathrm{m}\phi}, \tag{1.97}$$

where P_ℓ^{m} are the Legendre polynomials and the coefficients $a_{\ell \mathrm{m}}$ are given by

$$a_{\ell \mathrm{m}} = \int_{\theta=\pi}^{\pi}\int_{\phi=0}^{2\pi} \frac{\Delta T}{T}(\theta,\phi)\, Y_{\ell \mathrm{m}}\, d\Phi, \tag{1.98}$$

where $d\Phi$ is the infinitesimal solid angle element. We can define the angular power spectrum of fluctuations as the variance of the harmonic coefficients $C_\ell \equiv \langle a_{\ell \mathrm{m}} a_{\ell' \mathrm{m}'} \rangle$, which are equal to

$$C_\ell = \frac{1}{2\ell+1}\sum_{m=-\ell}^{\ell} \langle |a_{\ell \mathrm{m}}|^2 \rangle. \tag{1.99}$$

ℓ is called a multipole and corresponds to a given angular scale on the sky. $\ell = 10$ and $\ell = 100$ corresponds to approximately 10 and 1 degrees on the sky. The angular power spectrum observed by (PLANCK COLLABORATION 2018) is shown in Fig. 1.5. The position and height of the peaks seen in the spectrum provide direct constraints on curvature and energy content parameters in the early Universe.

I will not review in details CMB physics, but I will give an overview of baryon acoustic oscillations in Section 2.1.3.4.

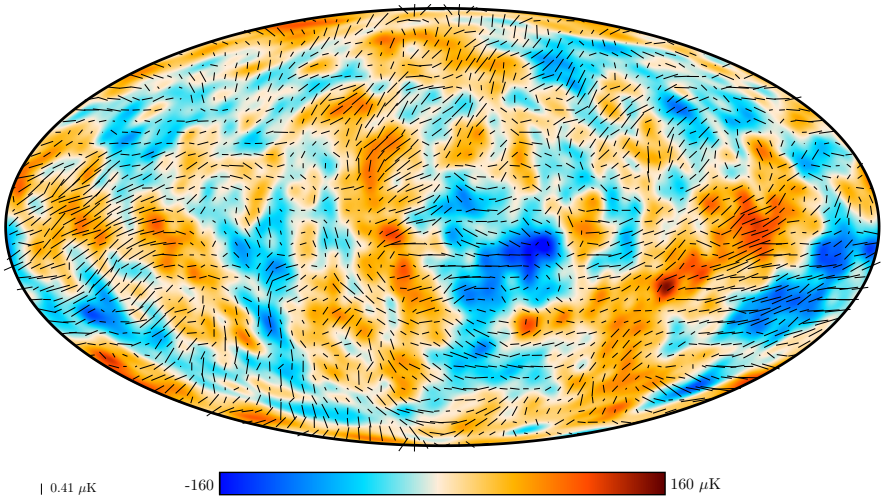

FIGURE 1.6 – Planck 2018 map of the polarized CMB anisotropies. The direction and lengths of the rods represents the direction and amplitude of the polarized photons. With this map, (PLANCK COLLABORATION 2018) measured the cosmological parameters given in Table 1.2. Taken from https://www.cosmos.esa.int/web/planck/picture-gallery

1.2.4 Inflation

Current cosmological parameter constraints suggest that the Universe is spatially flat. The time evolution of the density parameters gives us insight into the evolution of the curvature over time. The evolution of the total density parameter Ω is

$$\Omega_{\mathrm{K}} = \Omega_{\mathrm{K},0}\frac{(1+z)^2}{E^2(z)}. \tag{1.100}$$

Neglecting the cosmological constant at early time yields

$$\Omega_{\rm K} = \Omega_{\rm K,0}\left[\Omega_{\rm m,0}(1+z) + \Omega_{\rm r,0}(1+z)^2 + \Omega_{\rm K,0}\right]^{-1}. \tag{1.101}$$

The value of $\Omega_{\rm K}$ becomes smaller and smaller as we go back in time. When matter density equals radiation density,

$$\Omega_{\rm m,0}(1+z)^3 = \Omega_{\rm r,0}(1+z)^4, \tag{1.102}$$

(at a redshift $z \approx 3500$), we find that $|\Omega_k| < 5\ 10^{-6}$. At Planck time, when $z_{\rm Pl} \approx 5^{31}$, we find that $|\Omega_k| < 2\ 10^{-62}$. Such values are so small that they are considered as fine tuning, and an extra mechanics is required to make the early value of the curvature density more natural, i.e. of the order of unity.

An other puzzling issue is the remarkable homogeneity of the CMB. The last scattering surface is measured to be at $z = 1089.80 \pm 0.21$. Assuming only matter and radiation at the end of recombination, the corresponding horizon of particle as defined in Eq. 1.66 is

$$\chi(r_*) = \int_{z_*}^{\infty} \frac{dz}{H(z)} = \int_0^{a_*} \frac{da}{\dot{a}} \left[\frac{8\pi G\rho(a)a^2}{3} - K\right]^{-1/2}, \tag{1.103}$$

where $\chi(r_*) \approx 3 \times 10^2$ Mpc. Dividing by the angular diameter distance at that redshift yields an angular scale of approximately 1 degree. The fact that the CMB temperature appears so homogeneous on larger scales is concerning, this is called the horizon problem. A mechanism is required to causally connect these regions, which can be achieved through an early phase of accelerated expansion. This mechanism is dubbed *inflation*. In the standard model, the Universe is radiation-dominated in the early Universe $\rho \propto a^{-4}$, and the comoving horizon is finite. This integral must diverge to resolve the horizon problem. This requires $\rho \propto a^{\beta}$ with $\beta < -2$. Given the a dependence in the first law of thermodynamics Eq. 1.54, we have

$$\rho + 3P < 0. \tag{1.104}$$

Inserting this equation into the Eq. 1.49 gives $\ddot{a} > 0$. The acceleration of the expansion of the Universe at early time is what we call the inflation, and occurs when an energy density that satisfies the latter equation dominates. Since observations suggest that dark energy is negligible at early times, vacuum energy could corresponds to such an energy with $P = -\rho_v$. In that case, the expansion of the Universe is exponential, similarly to what is excepted when the cosmological constant dominates the total energy budget,

$$a \propto e^{Ht} \quad \text{where} \quad H = \sqrt{8\pi G\rho_v}/3. \tag{1.105}$$

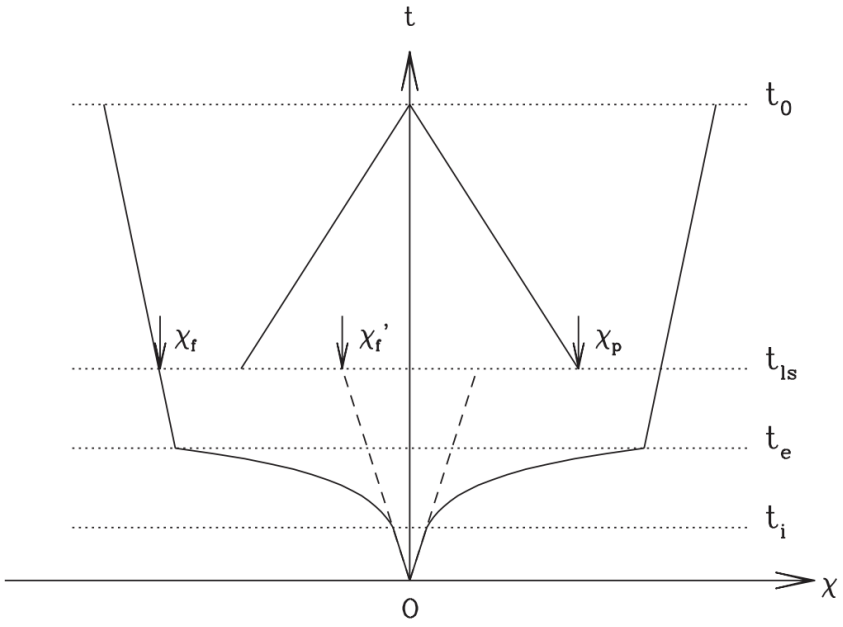

FIGURE 1.7 – A illustration of the lightcone structure in an inflationary universe. The Big Bang is labeled by 0, and time flows from bottom to top. In the absence of inflation, the light cone represented in dashed lines would be smaller than our past light cone χ_p at the last scattering surface (at time t_{ls}) resulting in the causality problem discussed. The inflation solve this tension, by extending the light cone to much larger distance, $\chi > \chi_p$. (MO, BOSCH et WHITE 2012)

Fig. 1.7 illustrates how inflation can solve the horizon problem. If we assume that inflation starts at a time t_i for a small period of time $\mathrm{d}t$ such as it ends at time $t_e = t_i + \mathrm{d}t$. If $\mathrm{d}t$ is large enough, the size of the forward light-cone $\chi_f(t_{ls})$ on the last scattering surface will be larger than the size of the past light-cone. Defining the number of e-folds as

$$N = \log\left(\frac{at_e}{at_i}\right), \tag{1.106}$$

we can express the ratio of curvature density before and after inflation as

$$\left|\frac{\Omega_{t_e}}{\Omega_{t_i}}\right| = \left(\frac{at_e}{at_i}\frac{Ht_f}{Ht_e}\right)^{-2} > \left(\frac{at_e}{at_i}\right)^{-2} = e^{-2N}. \tag{1.107}$$

In order to have about $|\Omega_k(t_f)| < 10^{-60}$ at the end of inflation, as predicted by the standard model, and a natural value of$|\Omega_k(t_i)|$ at the beginning of the inflation $\mathcal{O}(1)$, one needs to set $N \approx 70$. We have already seen that the acceleration of the expansion of the Universe at the present time could be due to a scalar field $\phi(\mathbf{x}, t)$. In the same way, inflation could be due to scalar field. The scalar fields that cause inflation are dubbed inflatons. Varying the inflaton field ϕ and the metric in the Einstein-Hilbert action, and neglecting the Lagrangian of matter, yields the Friedmann and Klein-Gordon equations (PETER et UZAN 2012)

$$H^2 = \frac{8\pi G}{3}\left(\frac{1}{2}\dot{\phi}^2 + V(\phi)\right) - \frac{K}{a^2}, \tag{1.108}$$

$$\frac{\ddot{a}}{a} = \frac{8\pi G}{3}\left(V(\phi) - \dot{\phi}^2\right), \tag{1.109}$$

$$0 = \ddot{\phi} + 3H\dot{\phi} + V_{,\phi}. \tag{1.110}$$

Neglecting the curvature at early time yields

$$\dot{H} = \frac{\ddot{a}}{a} - H^2 = -4\pi G\dot{\phi}^2. \tag{1.111}$$

A phase of accelerated expansion requires $\ddot{a}/a$ to be large and therefore the field ϕ should approximately be constant and satisfies

$$\dot{\phi}^2 \ll V(\phi), \quad \ddot{\phi} \ll 3H\dot{\phi}. \tag{1.112}$$

The inflationary models that match this requirement are called **slow roll** inflation models. Using Eqs. 1.108 and 1.110, this condition can be rewritten in terms of the inflaton potential $V(\phi)$ such that

$$\left(\frac{V_{,\phi}}{V}\right)^2 \ll 24\pi G, \quad \frac{|V_{,\phi,\phi}|}{V} \ll 24\pi G. \tag{1.113}$$

This implies that the potential $V(\phi)$ of the inflaton in the slow-roll scenario should be nearly flat.

One of the most important features of inflation is the associated production of tiny perturbations, acting as density seeds for late structures of the Universe. While inflation smooths classical inhomogeneities by stretching them on very large scales, it cannot remove quantum fluctuations : stretching them will only produce new ones because of the Heisenberg uncertainty principle. Inflation is needed because the amplitude of vacuum metric fluctuations in a Minkowski space are typically very small and only large near the Planck scale. Therefore the observed fluctuations of the order of 10^{-5} in the CMB can only be produced by an accelerated phase of expansion at early time. Fluctuations within the horizon will have a decreasing amplitude as they stretch, but as soon as they cross the horizon, they become frozen. This means that they become stretched to galactic scale without any change in amplitude. Slow-roll inflation predicts adiabatic, nearly Gaussian, and scale-invariant perturbations. The power spectrum of these fluctuation (see Table 2.2 for a definition) is predicted to have the form of

$$P(k) \propto k^{n_s}, n_s = 1 - 6\epsilon + 2\eta, \tag{1.114}$$

where n_s is called the spectral index, and ϵ and η are called the slow-roll parameters. Current constraints from CMB gives $n_s = 0.9665 \pm 0.0036$, in good agreement with basic inflationary predictions. In the single-scalar-field scenario of inflation, some non-Gaussianities are excepted to be produced at second-order in the perturbations. Detection of such departure would allow to further constrain inflationary models, which are the cornerstone of modern cosmology. Primordial non-Gaussianities (PNG) are usually described in term of a constant called f_{NL}. Assuming that non-Gaussianities only depend on the local value of the potential, the primordial potential can be written as (MUELLER et AL. 2021)

$$\phi = \phi + f_{NL}\langle\phi^2 - \langle\phi^2\rangle\rangle, \tag{1.115}$$

where ϕ is a Gaussian random field and f_{NL} describes the amplitude of the quadratic non-Gaussian term. $f_{NL} = 0$ corresponds to a pure Gaussian field. CMB and large-scale structure (LSS) provide constraints on f_{NL}, in particular, Planck CMB anisotropies predict $f_{NL} = 0.9 \pm 5.1$ at 68% confidence level. Latest measurement of f_{NL} with quasars observed by the extended Baryon Oscillation Spectroscopic Survey (eBOSS, DAWSON et AL. 2016) yields $f_{\rm NL} = -12 \pm 21$ at 68% confidence level (MUELLER et AL. 2021).

1.3 Cosmological facts

In the concordance model of cosmology, the so-called ΛCDM model, the energy content of the Universe is as follows :

— The cosmological constant Λ, or more generally, dark energy. It is responsible for the acceleration of the expansion of the Universe at current epoch,
— Radiation. This corresponds to photons and relativistic neutrinos.
— Baryonic matter. This corresponds to the matter that interacts with light. Baryonic matter is composed of all elements of the standard model of particle physics. There may exist non-relativistic species of massive neutrinos that would contribute to the baryonic energy content,
— Cold dark matter. This type of matter does not interact with radiation and interact weakly with baryonic matter. Nonetheless, it is needed to understand the formation of LSS and the dynamics of galaxies and clusters of galaxies.

1.3.1 Relativistic species

Given the CMB temperature at current epoch, we can get an estimate of the current radiation density at present time :

$$\omega_{\gamma,0} = 2.4729 \pm 0.0022 \times 10^{-5}. \tag{1.116}$$

Neutrinos decouple from the primordial fluid at a temperature of $T \approx 1$ MeV. As the temperature decreases, electrons annihilate and the entropy released is given to the photon. The increase in temperature of T_γ is given by entropy conservation by $T_\nu = (4/11)^{1/3} T_\gamma$. Assuming that the neutrinos temperature did not changed at decoupling, we have that (for relativistic neutrinos)

$$\rho_\nu = \frac{7}{8}\left(\frac{4}{11}\right)^{4/3} \rho_\gamma. \tag{1.117}$$

The factor 7/8 comes from the fact that neutrinos are fermions while photons are bosons. This gives the density parameter for massless neutrinos :

$$\omega_{\nu,0} = 5.6161 \pm 0.0049 \times 10^{-6} \times N_\nu, \tag{1.118}$$

where N_ν corresponds to the number of distinct species of neutrinos, 3 in the standard model. However, neutrinos are not totally decoupled at $e^\pm$ annihilation, the effective number of neutrinos is $N_{\text{eff}} = 3.045$ rather than $N = 3$ (MANGANO et AL. 2002, SALAS et PASTOR 2016). The effective number of degree of freedom of relativistic neutrinos was measured by (PLANCK COLLABORATION 2018) and BAO measurements at lower redshift to be $N_{\text{eff}} = 2.99 \pm 0.17$, which is consistent with the theoretical value of N_{eff}. Eq. 1.118 ignores neutrinos mass, however neutrino oscillations detected by the Super-Kamiokande and Sudbury Neutrino Observatory experiments (KAJITA 1998,AHMAD et AL. 2001) require that at least one neutrino eigenstate has a mass greater than 0.05 eV.

1.3.2 Baryonic matter

One way to determine the baryonic density is to constraint η, the ratio of the number density of baryons over the number density of relativistic CMB photons. To high accuracy, this ratio is unchanged from the end of the Big Bang nucleosynthesis (BBN) to present time (STEIGMAN 2006). The baryonic energy density Ω_b can be expressed as

$$274\omega_{\text{b},0} = 10^{10}\eta. \tag{1.119}$$

Observations of the absorption lines of quasars at redshift $z = 2.52$ (COOKE et AL. 2018) have provided measurements of deuterium abundances corresponding to

$$5.810^{-10} < \eta < 6.610^{-10}, \quad 0.021. < \omega_{\gamma,0} < 0.024 \tag{1.120}$$

These measurements are consistent with measurement of helium abundance (AVER et AL. 2015) in the local metal-poor extragalactic medium and are also in very good agreement with the observed baryonic density infered from CMB anistropies, as seen in Table 1.2.

1.3.3 Dark matter

Clusters of galaxies are the most massive gravitationally-bounded structures in the Universe, spanning the range $10^{12} - 10^{15} M_\odot$. ZWICKY 1937 was the first to detect a dark, invisible component of matter in the mass distribution of the Coma cluster of galaxies (A1656). The virial theorem states that a for a stable system

$$\langle E_c \rangle = -2\langle E_p \rangle, \tag{1.121}$$

where $\langle E_c \rangle$ and $\langle E_p \rangle$ are the kinetic and potential energies of the system. Based on his observations, ZWICKY 1937 suggested that the total mass was much larger than the luminous mass of the clusters. There is different ways of tracing the baryonic component within a cluster. Gas in the intercluster medium is heated up to extreme temperatures of the order of $10^7 - 10^9$ Kelvins and emit in X-rays. Observations of the density and temperature profile of the gas in clusters, with a estimation of the luminosity of galaxies, can provide an estimate of the baryonic mass of the cluster. Other ways to constrain the mass of clusters is with using gravitational lensing effects. Photons are distorted along the line of sight due to the presence of matter. Within the strong gravitational lensing regime, we can measure the mass in the central region of clusters ($< 50 - 200$kpc), while in the weak gravitational lensing regime (image distortions as in Fig. 1.8) we can have an estimation of the density profile of matter up to the edges of clusters ($< 1 - 3$Mpc). The observed ratio $\omega_{b,0}/\omega_{c,0}$ is expected to be $> 17\%$ (BAHCALL 1996). Given the value $\omega_{b,0}$ from BBN, $\omega_{c,0} \approx 25\%$.

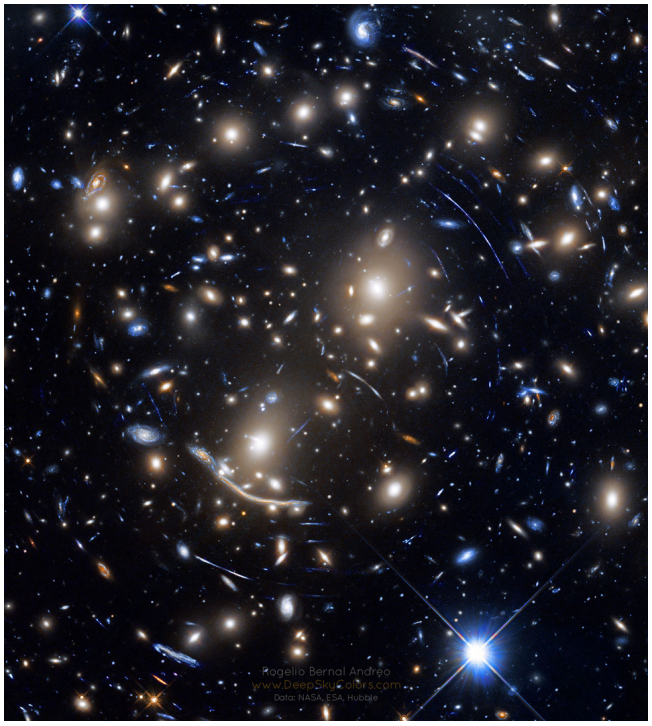

FIGURE 1.8 – The Abell 370 cluster. Within the center of the cluster, one can observe the weak lensing distortions of the background galaxies. Credit : NASA, ESA, Hubble ; Processing Copyright : Rogelio Bernal Andreo. Taken from https://science.nasa.gov/abell-370-galaxy-cluster-gravitational-lens

Observations of galaxies also show evidences for the existence of a dark matter component. Assuming that the gravitational field is weak, we can use Newtonian dynamics to link the observed

rotation velocity to the amount of mass within the orbit as

$$\frac{v^2(r)}{r} = -\frac{GM(<r)}{r^2}. \tag{1.122}$$

The luminosity distance of spiral galaxies decreases exponentially with distance from the center, with a typical scale R_d. Above $2-3\ R_d$ we expect the mass at r to be constant, which would imply

$$v(r) \propto \frac{1}{\sqrt{r}}, \quad r > 3R_d. \tag{1.123}$$

This is not what we observe in Fig. 1.9 : The rotation curves of spiral galaxies converge toward a value v_∞, outside of a few optical radii. The missing mass is attributed to dark matter. For galaxies, baryonic matter represents $\approx 15\%$ of the total mass, very similarly as what is found for galaxy clusters. Another way to trace dark matter is through the so-called cosmic shear signal, the average weak lensing distortions of background source by galaxies along the line of sight (LoS). The distortions of the foreground galaxies can be used to infer the distribution of matter between the lens and the source.

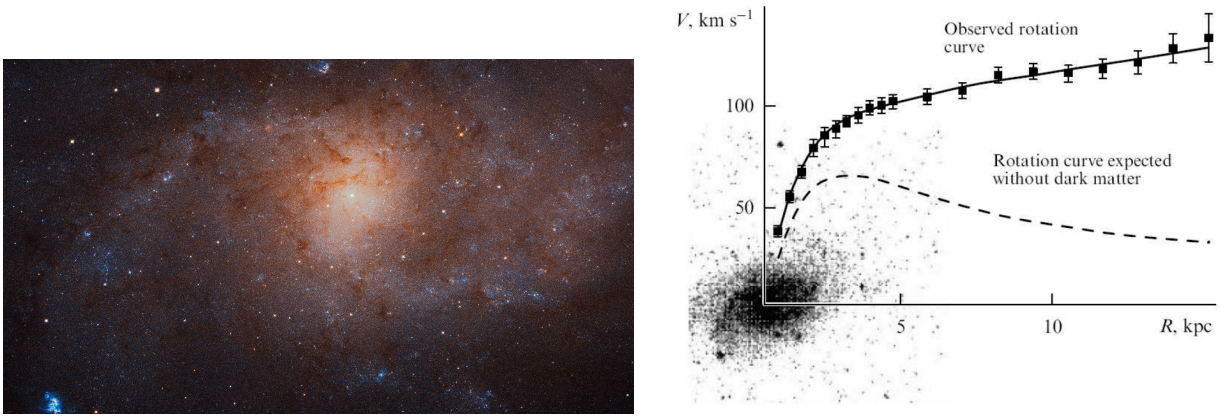

FIGURE 1.9 – Left panel : M33, observed by NASA https://www.nasa.gov/feature/goddard/2019/messier-33-the-triangulum-galaxy. Right : Rotation curve of M33. Taken from (ZASOV et AL. 2017)

Candidates for dark matter

One possible nature of dark matter is in form of particles. In that case, we expected massive particles that interact weekly with baryons, radiation and themselves. As we will see in the next chapter, observed fluctuations in the cosmic microwave background will grow after recombination due to gravitational instability. Since dark matter weakly interacts with radiation, it decouples earlier from the plasma and forms potential wells in which baryonic matter will fall into once decoupled. Without the formation of these potential wells at early times, it is difficult to explain the formation of structures that we observe today. Dark matter is either cold or hot when it decoupled from the hot plasma. In the warm dark matter scenario, particles are light and their high speed suppress the growth of perturbations smaller than the size of a super clusters, which are the most massive structures observed in the Universe. Smaller structures are created by fragmentation. In a cold dark matter scenario, galaxies and clusters of galaxies evolve within dark matter halos. First small structures such as globular clusters and galaxies form, and then merge to form larger and larger structures, connected by nodes and filaments. The hot dark matter scenario predicts too many massive structures, with galaxies forming at much later times, $z \approx 2$. The cold dark matter is favoured as it allows the formation of small structures : the dark matter halos.

Therefore, a serious candidate for dark matter is weakly interacting massive particles (WIMPs), with a mass of about 100GeV and that interact weakly through gravity and weak nuclear force. However, this particle has not be observed yet, and its nature is still unknown. The density profile $\rho(r)$ of dark matter halos has been studied in depth with N-Body simulations. Those simulations help in determining the shape of $\rho(r)$, for instance the Navarro-Frenk-White profile (NAVARRO, FRENK et WHITE 1996). However, some issues remain with dark matter particles :

— Analytical density profiles overestimate the amount of matter in the centre of dark matter halos compared to what observations suggest (BLOK 2010),

— In numerical simulations, the number of satellites in our local group should ≈ 1000 and we only observe 36 galaxies within 0.5 Mpc.

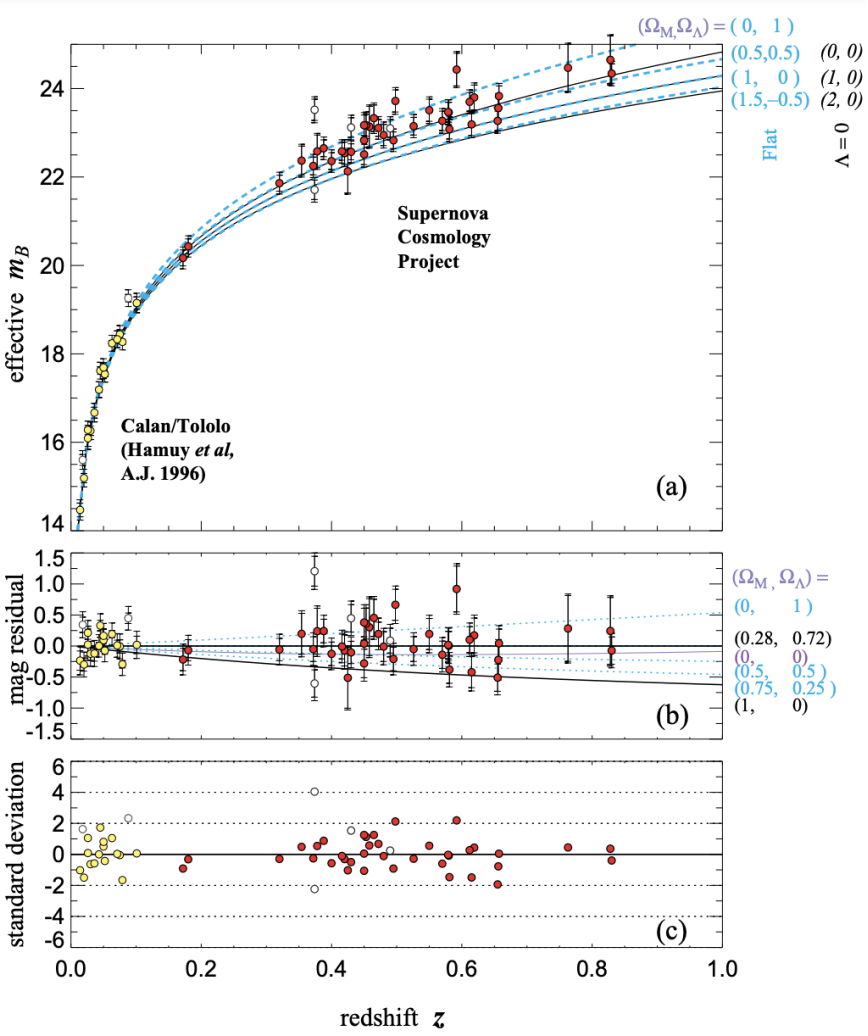

FIGURE 1.10 – Supernovae Hubble diagram. The red points correspond to the supernovae observed by the Supernovae Cosmology Project (PERLMUTTER et AL. 1999), while the yellow points are the observations of the Calan/Tololo survey (HAMUY et AL. 1996). Taken from PERLMUTTER et AL. 1999

Many other dark matter scenarios have been proposed to solve these issue, for instance warm dark matter or decaying dark matter. Neutrinos could also be a candidate for dark matter since they interact weekly with baryonic matter, but given their current density (see Eq.1.118) they cannot represent the total dark matter budget. Other scenarios also fail to solve the observed tensions. In the rest of this manuscript, we will only refer to dark matter as cold dark matter.

1.3.4 Dark energy

The first evidence of a non-null cosmological constant, or more generally of the possible existence of dark energy, comes from the observation of the luminosity of SNIa up to $z \approx 1$, see Fig. 1.10. PERLMUTTER et AL. 1999 put a decisive constraint on the deceleration parameter :

$$0.8\Omega_{\mathrm{m},0} - 0.6\,\Omega_{\Lambda,0} \approx -0.2 \pm 0.1. \tag{1.124}$$

As seen previously, the radiation can be neglected at present time and the deceleration parameter in Eq. 1.67 can be written as

$$q_0 = \frac{\Omega_{\mathrm{m},0}}{2} - \Omega_{\Lambda,0}, \tag{1.125}$$

which gives for the above relation

$$q_0 \approx -0.33 - 0.83\Omega_{\mathrm{m},0}. \tag{1.126}$$

Since $\Omega_{m,0} > 0$, we have q_0<0, meaning that the universal expansion is accelerating at present time. Today, the best constraints from Pantheon SNIa alone gives

$$\Omega_{\Lambda,0} = 0.702 \pm 0.022, \tag{1.127}$$

within the flat ΛCDM model (SCOLNIC et AL. 2018). As already emphasized, the cosmological constant can be interpreted as a fluid with equation of state $p = -\rho$, i.e. a fluid with negative pressure. Although such a fluid cannot be found in classical physics, it is excepted in quantum physics.

The energy-momentum tensor of the vacuum energy in an isotropic and homogeneous universe can be written as follows

$$T^{\mu\nu} = -\rho_v g^{\mu\nu}. \tag{1.128}$$

However, quantum field theory predicts an energy density associated to the cosmological constant in for of vacuum energy that is 60 to 120 orders of magnitude larger than what we observe. This is known as the cosmological constant problem. Given up on the vacuum energy as a source of dark energy, one can explore deviation from a pure cosmological constant $w = -1$ by leaving w free. Using CMB anisotropies, CMB lensing, BAO and SNIa data PLANCK COLLABORATION 2018 measure $w = 1.028 \pm 0.032$ within a flat CDM model, compatible with a cosmological constant. Another approach consists in allowing for a time variation of w, as in the Chevallier-Polarski-Linder parameterization (CHEVALLIER et POLARSKI 2001) of dark energy given by

$$w(a) = w_0 + (1-a)\,w_a. \tag{1.129}$$

With the same data, PLANCK COLLABORATION 2018 find $w_0 = 0.961 \pm 0.077$ and $w_a = 0.28^{0.31}_{-0.27}$, still compatible with a cosmological constant. However, this model does not provide a physical explanation for dark energy. A more natural explanation for dark energy would be the existence of scalar field ϕ called quintessence field evolving in a potential V (ϕ) such that the Einstein-Hilbert action can be written as :

$$S = \frac{1}{16\pi G}\int \mathrm{d}^4x\sqrt{-g}R - \frac{1}{16\pi G}\int \mathrm{d}^4x(\partial_\mu\partial^\mu\phi + 2V(\phi)) + \int \mathrm{d}^4\sqrt{-g}\mathscr{L}_m. \tag{1.130}$$

The important point to mention is that the vacuum energy in these fields mimics the contribution of the cosmological constant Λ. The equation of state of the scalar field is given by

$$w_\phi = \frac{\dot\phi^2 - 2V(\phi)}{\dot\phi^2 + 2V(\phi)}. \tag{1.131}$$

Tableau 1.2 – PLANCK COLLABORATION 2018 CMB (TT, TE, EE, lowE + lensing + BAO) derived cosmological parameters.

Parameter	Notation	Value
reduced Hubble constant	h	0.6766 ± 0.0042
matter density	$\omega_{\mathrm{m},0}$	0.14240 ± 0.00087
cold dark matter density	$\omega_{\mathrm{c},0}$	0.11933 ± 0.00091
baryon density	$\omega_{\mathrm{b},0}$	0.02242 ± 0.00014
photon density	$\omega_{\gamma,0}$	$(2.4729 \pm 0.0022) \times 10^5$
curvature density	$\Omega_{\mathrm{K},0}$	0.0007 ± 0.0019
cosmological constant/dark energy density	$\Omega_{\Lambda,0}$	0.6889 ± 0.0056
index of the primordial power spectrum	n_s	0.9665 ± 0.0038
amplitude the primordial power spectrum	$10^9 A_s$	2.105 ± 0.030
redshift of last scattering surface	z_*	1089.80 ± 0.21
sound horizon at last scattering surface	r_*	144.57 ± 0.22 Mpc
redshift of drag	z_{d}	1060.01 ± 0.29
sound horizon at drag	r_{d}	147.21 ± 0.23Mpc
redshift of reionization	z_{rei}	7.82 ± 0.71

To obtain a value $w_\phi \approx 1$ at present time, the potential term must dominate over the kinetic term. Neither quintessence field theory nor a cosmological constant provides an explanation on why dark energy starts to dominate at late time, see Fig. 1.11.

As we have seen, the nature of dark matter and dark energy are still poorly constraints nowadays, even though they represent about 95% of the total energy in the Universe today. COLIN et AL. 2019 used different samples of SNIa over the whole sky at redshifts $0 < z < 1$ and by decomposing the deceleration parameter into a monopole and a dipole components $q_0 = q_m + q_d \mathscr{F}(z, s)$, where $\mathscr{F}(z, s)$ describes the scale dependence of the dipole ,they find

$$q_m = -0.157 \quad q_a = -8.03. \tag{1.132}$$

This is consistent with zero acceleration $q_m = 0$ at 1.4σ and reject the isotropy of the Universe ($q_a = 0$ for a isotropic Universe) at 3.9σ. The conclusion of this work is that the observed expansion rate in the Universe might result from a poor knowledge of our local dynamics. Dark matter also arised in observations that could not explain the observed dynamics of galaxies and galaxy clusters.

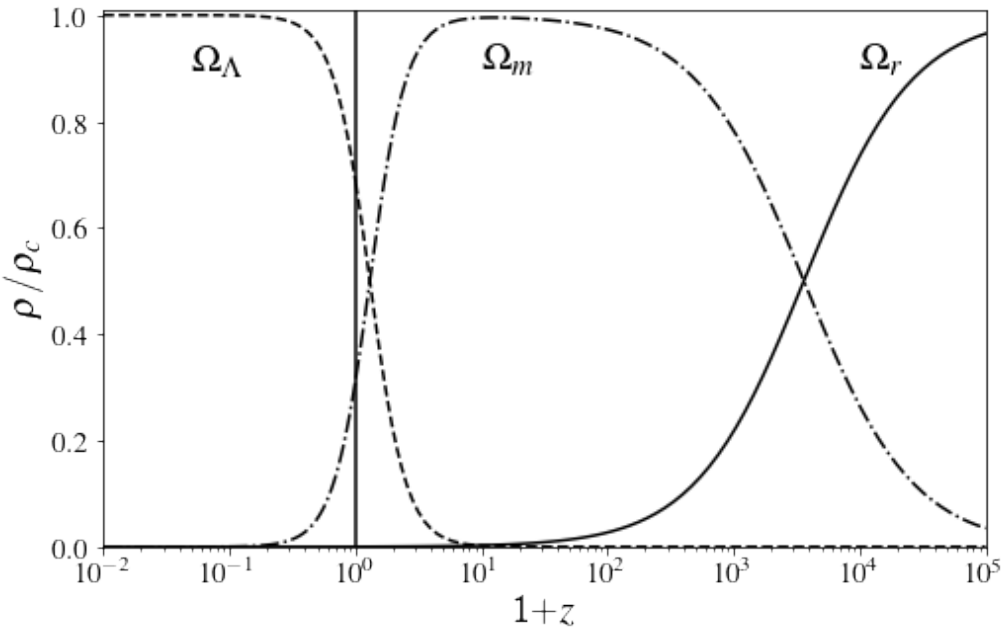

FIGURE 1.11 – Variation of densities parameters as a function of redshift given the cosmological constraints of Table 1.2. We used Eqs. 1.65 and 4.38 assuming massless neutrinos for simplicity.

An alternative to dark energy and dark matter is to consider modified gravity models. Many models have been proposed, such as

— f(R) theories. The contribution of curvature to the total action of the system is replaced by a function of the Ricci scalar. f is chosen such that modified gravity effects are suppressed in the large or rapidly changing curvature limit through the so-called Chameleon mechanism.

— Theories with extra dimensions. The acceleration of the Universe is driven by extra dimensions, and standard General Relativity is recovered on small scales, through the so-called Vainshtein mechanism.

— Horndeski theories. They are the most general theory of gravity involving a four-dimensional metric along with a scalar field such that equations of motion are second order.

For a model to be viable, it must be consistent with all observations that we described previously. While modified gravity can be effective in descriving the dynamics of galaxies, most of them fail to reproduce all observations, such as the anisotropies in the CMB. In addition, many gravity models have been ruled out by the constraint on the speed of gravitational waves, which is nearly equal to the speed of light, as imposed by the recent observation of a gravitational wave with an electromagnetic counterpart (LIGO-COLLABORATION et VIRGO-COLLABORATION 2017). Therefore, the most probable model right now remains ΛCDM, being the one that fulfills most of the requirements. We will therefore consider this model through the rest of the manuscript keeping in mind the observed tensions for some cosmological parameters.

2 The large-scale structure of the Universe

Sommaire

In the previous chapter, I described the evolution of the Universe *background* within the framework of the standard model of cosmology. The early Universe is well described with the Hot Big Bang model, where the inflation field is responsible for the acceleration of the expansion just after the Big Bang. Quantum theory provides the framework to explain this acceleration phase that led to the primordial fluctuations in the Universe. These fluctuations are directly observable in the CMB in form of temperature anisotropies. Once CMB photons moved freely in the Universe, fluctuations grew up under gravitational instability to form the structure that we see today (see Fig. 1.1). The theory that connects CMB anisotropies caused by inflation and the observed large structure of the Universe today is the theory of cosmological perturbations. Matter perturbations are treated as density fluctuations with respect to the mean background density of the Universe ,

$$\delta \equiv \frac{\rho - \bar{\rho}}{\bar{\rho}}, \tag{2.1}$$

which evolve with time under gravity.

In the following, I will present the theory of linear perturbations, valid in the limit of small perturbations $\delta \ll 1$, and which can be treated at first order. This chapter is based on the review of Bernardeau et al. 2002, the lecture notes from Kurki-Suonio 2020, and the textbook of Mo, Bosch et White 2012. We will assume the case where the background is the flat FLRW universe. The constant-time hypersurface will thus have an Euclidean geometry, which will allow us to decompose the observed structure of the Universe into Fourier modes.

2.1 Linear perturbation theory

I will first review linear Newtonian and Lagrangian perturbation theories in Sections 2.1.1 and 2.1.2. The relativistic effects that arise when perturbations are large will be reviewed in Section 2.1.3. Higher-order perturbation theory corrections are discussed in Section 2.1.4.

2.1.1 Newtonian theory of perturbations

The Newtonian theory of perturbations applies when the size of the perturbations is much smaller than the horizon size, such that causality is considered as instantaneous. Let us suppose that the Universe is composed of an inhomogeneous ideal fluid with density $\rho(t,\mathbf{r})$, velocity $u(t,\mathbf{r})$, pressure $p(t,\mathbf{r})$, and gravitational potential $\phi(t,\mathbf{r})$, where t designate the cosmic time and $\mathbf{r}$ corresponds to the physical (proper) coordinates. This fluid evolution is determined by the hydrodynamical equations of classical physics :

$$\text{Continuity equation :} \quad \frac{\mathrm{d}\rho}{\mathrm{d}t} + \rho \nabla \mathbf{v} = 0, \tag{2.2}$$

$$\text{Euler equation :} \quad \frac{\mathrm{d}\mathbf{u}}{\mathrm{d}t} + \frac{\nabla p}{\rho} + \nabla\phi = 0, \tag{2.3}$$

$$\text{Poisson equation :} \quad \nabla^2\phi = 4\pi G\rho, \tag{2.4}$$

where

$$\frac{\mathrm{d}}{\mathrm{d}t} \equiv \frac{\partial}{\partial t} + \mathbf{u}\cdot\nabla, \tag{2.5}$$

and $\partial/\partial t$ is the partial derivative at fixed $\mathbf{r}$. Together with the equation of state of the gas $p = p(\rho, S)$, this set of equations forms a closed system from which we can determine the unknown properties of the fluid. This treatment is only valid in the non-relativistic regime where $|v| \ll c$ and $p \ll \rho c^2$. In the Newtonian fluid approach, a single velocity vector is assigned to each point in space. This means that the fluid motion must be in a single flow regime, with adjacent particles moving in

parallel paths and not crossing each other. Although this seems to be a reasonable approximation in the linear regime, this assumption breaks down when non-linear structures form, from the mixing of different streams, what is often called *shell crossing*. This treatment is valid for a dark matter that does not interact with baryonic matter and radiation. For baryons we would need to take into account dissipative effects such as free-streaming damping that occurs when collisionless particles with large random velocities move in and out of the perturbations. The set of Eqs. 2.2-2.4 are non-linear and therefore hard to solve analytically. Assuming the Universe background as an expanding FLRW universe, we can perturb the fluid properties around the Hubble flow at linear order :

$$\rho(t,\mathbf{r}) = \bar{\rho}(t) + \delta p(t,\mathbf{r}) = \bar{\rho}(t)(1+\delta(t,\mathbf{r})), \quad u(t,\mathbf{r}) = \bar{v}(t,\mathbf{r}) + v(t,\mathbf{r}), \tag{2.6}$$

The background velocity field is given by the Hubble law

$$\bar{v}(t,\mathbf{r}) = H(t)\mathbf{r} = \dot{a}x, \tag{2.7}$$

with x in comoving coordinates. The velocity perturbations $v(t,\mathbf{r}) \equiv \delta u(t,\mathbf{r})$ correspond to the **peculiar** velocities induced by gravitational instability. The transformation from proper to comoving coordinates is given by

$$\nabla_r = \frac{\nabla_x}{a} \quad , \frac{\partial}{\partial t}|_x = \frac{\partial}{\partial t}|_r - \frac{\dot{a}}{a}\mathbf{x}\cdot\nabla_x. \tag{2.8}$$

Since $\bar{\rho} \propto a^{-3}$ we can rewrite Eqs. 2.2-2.4 as (Mo, Bosch et White 2012)

$$\frac{\partial \delta}{\partial t} + \nabla\cdot[(1+\delta)\mathbf{v}] = 0, \tag{2.9}$$

$$\frac{\partial \mathbf{v}}{\partial t} + H\mathbf{v} + \frac{1}{a}(\mathbf{v}\cdot\nabla)\mathbf{v} + \frac{1}{a\bar{\rho}}(c_s^2\nabla\rho + \sigma\nabla S) + \frac{\nabla\Phi}{a} = 0 \tag{2.10}$$

$$\nabla^2\Phi = 4\pi G\bar{\rho}a^2\delta, \quad \Phi = \phi + \frac{a\ddot{a}x^2}{2}, \tag{2.11}$$

where we have used the expansion at first order $1/(\bar{\rho}+\delta\rho) = 1/\bar{\rho} + \delta\rho/\bar{\rho}^2 + \mathcal{O}(\delta\rho^2)$ and the equation of state at first order

$$\nabla p = c_s^2\nabla\rho + \sigma\nabla S, \tag{2.12}$$

where $c_s^2 = \delta p/\delta\rho$ is the square of the sound speed and $\sigma = \delta p/\delta S$. The other energy contributions that do not interact with the matter fluid, such as an homogeneous radiation field or the cosmological constant Λ, enter the formalism only in the background Poisson field equations and thus do not alter the linear perturbation calculation. Even if these fluids can introduce relativistic pressure, we will assume that the set of hydrodynamical equations is correct and that the expansion of the Universe is governed by the Friedmann equation, taking into account the contribution of additional energy sources. To solve the above system, initial conditions must be specified. The perturbations can then be decomposed into a linear combination of different modes of perturbations, each of them having analytical solutions.

2.1.1.1 Entropy modes

Entropy (S) conservation allows steady entropy perturbations

$$\delta S(t,\mathbf{k}) = \delta S(\mathbf{k}), \quad \delta(t,\mathbf{k}) = 0. \tag{2.13}$$

Entropy conservation can only take place in multi-component fluids such as the baryon-photon fluid before recombination. Since dark matter, which dominates the matter budget, couples weakly

with photons and baryons, it is unlikely that entropy perturbations arose in the early Universe. Moreover, slow-roll inflation models do not predict entropy perturbations, therefore we will not consider these perturbations in the following. These modes are also called isocurvature modes, since $\delta_{\rm i} = 0$ implies $\delta\Phi_i = 0$ from Poisson equation.

2.1.1.2 Adiabatic modes

Initial perturbations correspond to density perturbations $\delta \neq 0$. If we set $\delta S = 0$, at first order, Eqs. 2.9 and 2.10 take the form

$$\frac{\partial \delta}{\partial t} + \frac{1}{a}\nabla \cdot \mathbf{v} = 0, \tag{2.14}$$

$$\frac{\partial \mathbf{v}}{\partial t} + H\mathbf{v} + \frac{c_s^2}{a}\nabla\delta + \frac{\nabla\Phi}{a} = 0. \tag{2.15}$$

By defining the Fourier transform of a field $A(\mathbf{k}, t)$ as

$$A(\mathbf{k}, t) = \int \frac{\mathrm{d}\mathbf{x}^3}{(2\pi)^3} \exp(-i\mathbf{k}\cdot\mathbf{x}) A(\mathbf{x}, t), \quad A(\mathbf{x}, t) = \int \mathrm{d}\mathbf{k}^3 \exp(i\mathbf{k}\cdot\mathbf{x}) A(\mathbf{k}, t), \tag{2.16}$$

with $\mathbf{k}$ the comoving Fourier modes, we can rewrite Eq. 2.14 as

$$\dot{\delta}_{\mathbf{k}} + \frac{i\mathbf{k}}{a}\mathbf{v}_{\mathbf{k}} = 0. \tag{2.17}$$

By differentiating this equation, we find that

$$\ddot{\delta}_{\mathbf{k}} + 2H\dot{\delta}_{\mathbf{k}} + \left(\frac{c_s^2 k^2}{a^2} - 4\pi G\bar{\rho}\right)\delta_{\mathbf{k}} = 0, \tag{2.18}$$

where we have used Eqs. 2.15 and 2.17 to eliminate $\dot{\mathbf{v}}$ and $\mathbf{v}$. This corresponds to a second order differential equation that gives two independent solutions. Given these solutions, one can directly compute the velocity field given in Eq. 2.14. If we decompose the velocity into a gradient and a curl part as

$$\mathbf{v} = \mathbf{v}_g + \mathbf{v}_c, \tag{2.19}$$

then, by applying the rotational operator to the Euler equation 2.15 we find that

$$\nabla \times \mathbf{v} \propto a^{-1}. \tag{2.20}$$

In the linear regime, the curl of the velocity field tends towards zero as the Universe expands. Thus, we can express $\mathbf{v}$ as the gradient of a velocity potential $\mathbf{v} = -\nabla\mathbf{V}$ such that $\nabla \cdot v_{\mathbf{k}} = -\nabla^2 V_{\mathbf{k}} = k^2 V_{\mathbf{k}}$ and $v_{\mathbf{k}} = -i\mathbf{k}V_{\mathbf{k}}$. The continuity equation 2.14 then takes thus form in Fourier space of

$$\mathbf{v}_{\mathbf{k}} = \frac{i\mathbf{k}}{k^2} a\dot{\delta}_{\mathbf{k}}. \tag{2.21}$$

2.1.1.3 Linear growth factor

To understand how adiabatic perturbations evolve, let us consider a static universe where $H = 0$. In that case, Eq. 2.18 has simple analytical solutions. If the second term is negative, the solutions will correspond to a growing exponential and a decaying exponential, while if is positive, both solutions correspond to oscillations. This is what is called the **Jeans criterion**. Only modes with

physical wavelength λ larger than the Jeans length λ_J can grow as

$$\lambda = \frac{2\pi a}{k} > \lambda_J \equiv c_s \sqrt{\frac{\pi}{G\rho}}. \tag{2.22}$$

In the same way, we can define the Jeans mass as

$$M > M_J = \frac{4\pi}{3}\frac{\lambda_J}{2}\rho. \tag{2.23}$$

Only perturbations with mass higher than the Jeans mass can grow. The Jeans mass is proportional to the sound speed c_s. Before recombination, the sound speed is high because of photon pressure, but decreases rapidly once photons freely exit the plasma. However, dark matter is not coupled to the photon-baryon fluid, whose sound speed is negligible at any time. This means that dark matter perturbations can grow right after inflation, while baryonic perturbations cannot grow before recombination. In an expanding Universe, the evolution of perturbations will be similar to the case of a static Universe. The only difference comes from the H term, the Hubble flow, which acts as a friction term that will prevent the growth of perturbations. If we only consider modes whose wavelength is much larger than the Jeans length, Eq. 2.18 reduces to

$$\ddot{\delta}_{\mathbf{k}} + 2H\dot{\delta}_{\mathbf{k}} - 4\pi G\bar{\rho}\delta_{\mathbf{k}} = 0. \tag{2.24}$$

This has for general solution

$$\delta(t,\mathbf{k}) = \delta_+(\mathbf{k})D_+(t) + \delta_-(\mathbf{k})D_-(t), \tag{2.25}$$

where the subscripts $-$ and $+$ denote the decaying and growing modes respectively. $\delta_+(\mathbf{k})$ and $\delta_-(\mathbf{k})$ correspond to complex valued initial conditions, while the functions $D_+(t)$ and $D_-(t)$ are independent of the wavenumber k. The growing solution $D_+(t)$ is called the *linear growth function*, and is usually normalised such that $D_+(z=0)=1$. The growing mode in the EdS universe is given by $D_+(t) \propto t^{2/3}$, thus

$$D_+(t) \propto a(t) \propto t^{2/3}, \tag{2.26}$$

where we have used the scaling relation in Table 1.1 for the matter-dominated universe. From the growing mode D_+, we define

$$g(a) \equiv \frac{D(a)}{a}, \quad f \equiv \frac{\mathrm{d}\ln D}{\mathrm{d}\ln a}, \tag{2.27}$$

where g is the *linear growth factor* and f its logarithmic derivative, the dimensionless *linear growth rate*. For an arbitrary ΛCDM model with given Ω_Λ and Ω_m, the growth factor g can be written as (HEATH 1977)

$$g(a) = \frac{5\Omega_m}{2}\int_0^a \frac{d\tilde{a}}{\tilde{a}^3 H(\tilde{a})^3}. \tag{2.28}$$

CARROLL 1992 provided an approximate solution at low redshift. This formula is accurate at below 1% for realistic values of Ω_m and Ω_Λ, and at any redshift as long as the radiation term is negligible. It is given by

$$g(z) = \frac{5\Omega_\mathrm{m}(z)}{2\Omega_\mathrm{m}(z)^{4/7} - \Omega_\Lambda + (1+\Omega_\mathrm{m}(z)/2)((1+\Omega_\Lambda(z)/70)}, \quad D_+(z) = \frac{1}{1+z}\frac{g(z)}{g(0)}, \tag{2.29}$$

such that D_+ is normalised by construction. The linear growth rate depends on the nature of gravity and is given by

$$f(\Omega_\mathrm{m}) \approx \Omega_m^\gamma. \tag{2.30}$$

For ΛCDM and General Relativity, it was found that $\gamma \approx 0.6$ (P. PEEBLES 1980), most accurate approximations yielding $\alpha \approx 0.545$. This γ value, the growth index, is sensitive to gravity and can differ by at least 30% in modified gravity models with respect to General Relativity (LINDER et CAHN 2007). Inserting the growing solution into the continuity equation 2.14 yields

$$\nabla \cdot \mathbf{v} = -a\dot{\delta} = -a\delta \frac{\dot{D}}{D} = -aH\delta \frac{1}{H}\frac{\dot{D}}{D} = -aH\delta f(\Omega_{\rm m}), \tag{2.31}$$

where we have used the fact that, at later time, only the growing modes dominate, see Eq. 2.34. Thus, the continuity equation in 2.14 takes the form

$$\delta(\mathbf{x}) = -\frac{\nabla \cdot \mathbf{v}}{Haf(\Omega_{\rm m})}, \quad \mathbf{v}_{\mathbf{k}} = \frac{i\mathbf{k}}{k^2} Ha\delta_{\mathbf{k}} f(\Omega_{\rm m}). \tag{2.32}$$

Therefore, if one can observe both the velocity and density perturbations, then one can derive f and constrain gravity through γ value.

2.1.2 Lagrangian theory of perturbations

In the Newtonian framework, the dynamics of the fluid is determined at discrete positions in space by solving the fluids equation Eqs. 2.9-2.11. In the Lagrangian framework, the fluid is instead described by the evolution of the trajectories of its particles. The Euclidean position $\mathbf{x}$ of a particle at time t can be written as

$$\mathbf{x}(\mathbf{q}, t) = \mathbf{q} + \Psi(\mathbf{q}, t), \tag{2.33}$$

where $\mathbf{q}$ is the position in Lagrangian space and Ψ is the displacement field. Since fluctuations were small at early time, it makes sense to assume that at recent times, only the growing mode of perturbations has a significant amplitude. Thus

$$\delta(t, \mathbf{x}) = \frac{D(t)}{D(t_i)} \delta(\mathbf{x}, t_i), \tag{2.34}$$

where we have dropped the + subscript for conciseness. This statement also holds for peculiar velocity and gravitational fields. Inserting the above relation in the Poisson equation 2.11 yields

$$\Phi(t, \mathbf{x}) = \frac{D(t)}{t} \Phi(\mathbf{x}). \tag{2.35}$$

Since in a matter-dominated universe, $D(t) \propto a$, this equation implies that the gravitational potential is independent of the scale factor. At linear order, the Euler equation for pressureless matter is

$$\dot{\mathbf{v}} + \frac{\dot{a}}{a}\mathbf{v} = -\frac{\nabla\Phi}{a}, \tag{2.36}$$

which can be integrated to give

$$\mathbf{v} = -\frac{\nabla\Phi}{a} \int \frac{D}{a} \mathrm{d}t. \tag{2.37}$$

Since $D(a)$ satisfies Eq. 2.24, $\int (D/a)\mathrm{d}t = \dot{D}/4\pi G\rho_m a$, we can rewrite the later equation as

$$\mathbf{v} = -\frac{\dot{D(a)}}{4\pi G\rho_m a^2} \Phi(\mathbf{x}). \tag{2.38}$$

This shows that peculiar velocities are proportional to the gravitational field. Integrating the above equation at first order such that $\phi(\mathbf{x})$ is replaced by $\phi(\mathbf{x}_i)$, where $\mathbf{x}_i$ are the initial position of the

mass element at position x, yields

$$\mathbf{x} = \mathbf{x}_i - \frac{D(a)}{4\pi G\rho_m a^3}\nabla\Phi(\mathbf{x}_i). \tag{2.39}$$

The first-order Lagrangian approach to linear perturbations theory is due to Zel'dovich (ZEL'DOVICH et AL. 1970). It specifies the growth of perturbations, given the displacement $\mathbf{x}-\mathbf{x}_i$ and the velocity $\mathbf{v}$ of each mass element with initial position $\mathbf{x}_i$. Zel'dovich suggested that this formalism could be applied to structure, where perturbations are no longer small $\delta \sim 1$. This is known as the Zel'dovich approximation. Particle trajectories are straight lines whose displacements are proportional to the growth factor. The density field is given by mass conservation through the Jacobian of the mapping from $\mathbf{x}_i$ to $\mathbf{x}$:

$$1+\delta = \left|\frac{\partial \mathbf{x}}{\partial \mathbf{x}_i}\right| = \frac{1}{(1-\lambda_1 D)(1-\lambda_2 D)(1-\lambda_3 D)}, \tag{2.40}$$

where $\lambda_1 > \lambda_2 > \lambda_3$ are the eigenvalues of the deformation tensor $\partial_j\partial_k\Phi_i/4\pi G\rho_m a^3$. This approximation is no longer valid once the first non-linear structures have formed. In reality, particles moving in a structure where $\delta \approx 1$ will oscillate in the gravitational potential instead of moving in straight line. At shell crossing, fluid elements with different initial positions will have the same Eulerian position, the Jacobian vanishes, and the density field becomes singular. The description of the fluid in terms of this mapping will no longer be valid.

2.1.3 Relativistic theory of perturbations

As long as the Cosmological Principle holds, the Universe *background* evolves according to a FLRW cosmology. In the relativistic theory of perturbation, small inhomogeneities in the distribution of matter density will lead to local perturbations of space-time. As long as the perturbations are small, this space-time will be similar to the homogeneous and isotropic Universe that we just described. The perturbed metric takes the form

$$g_{\mu\nu} = \bar{g}_{\mu\nu} + \delta g_{\mu\nu}, \tag{2.41}$$

and the perturbed curvature and energy tensors equal

$$G_{\mu\nu} = \bar{G}_{\mu\nu} + \delta G_{\mu\nu}, \tag{2.42}$$
$$T_{\mu\nu} = \bar{T}_{\mu\nu} + \delta T_{\mu\nu}, \tag{2.43}$$

which further reduce to the field equation of perturbations

$$\delta G_{\mu\nu} = 8\pi G\delta T_{\mu\nu}. \tag{2.44}$$

Both the background and perturbed space-time quantities are calculated at the same coordinate values (x^0, x^1, x^2, x^3), this is what allows us to the do the substitutions in Eq. 2.44. Given a metric $\bar{g}_{\mu\nu}$ on the background space-time, there may exist many coordinates systems for which Eq.2.41 holds. This choice of coordinate system corresponds to a gauge choice. In linear (first-order) perturbation theory, one keeps only the first order terms of the metric perturbation $\delta g_{\mu\nu}$ and their corresponding derivatives $\delta g_{\mu\nu,\alpha}, \delta g_{\mu\nu,\alpha,\beta}$. In higher-order perturbation theory one would need to keep the higher-order perturbation terms of the metric. The FLRW metric in a flat universe takes the form

$$\mathrm{d}s^2 = a^2(\tau)(-\mathrm{d}\tau^2 + \delta_{ij}\mathrm{d}x^i\mathrm{d}x^j), \tag{2.45}$$

and the energy-momentum tensor for a perfect fluid in the Universe background is

$$T_{\mu\nu} = (\bar{\rho} + \bar{p})U_\mu U_\nu + \bar{p}\bar{g}^{\mu\nu} = \mathrm{diag}(\bar{\rho}, \bar{p}, \bar{p}, \bar{p}), \tag{2.46}$$

where $\bar{\rho}, \bar{p}$ and U_μ are the density pressure and four-velocity vector of the fluid. In perturbation theory, the dynamics of the Universe background is also expressed in term of the conformal Hubble parameter, $\mathscr{H} = a'/a$, where the prime corresponds to time derivative with respect to the conformal time. The Friedmann equations 1.50 and 1.51 take the form

$$\mathscr{H}^2 = \frac{8\pi G}{3}\bar{\rho}a^2, \quad \mathscr{H}' = -\frac{4\pi G}{3}a^2(\bar{\rho} + \bar{p}), \tag{2.47}$$

and the equation of motion reads

$$\bar{\rho}' + 3\mathscr{H}(\bar{\rho} + \bar{p}) = 0. \tag{2.48}$$

Given Eq. 2.41, the metric perturbations is defined as

$$\delta g_{\mu\nu} \equiv g_{\mu\nu} - \bar{g}_{\mu\nu}. \tag{2.49}$$

In its most general form, the perturbed metric takes the form

$$\delta g_{\mu\nu}\mathrm{d}x^\mu \mathrm{d}x^\nu = a^2(\tau)[-2A\mathrm{d}\tau^2 - B_i\mathrm{d}\tau\mathrm{d}x^i + (-2D\delta_{ij} + 2E_{ij})\mathrm{d}x^i\mathrm{d}x^j] \tag{2.50}$$

where $A(\tau,\mathbf{x}), B_i(\tau,\mathbf{x}), D(\tau,\mathbf{x})$ are scalar and vector quantities and $E_{ij}(\tau,\mathbf{x})$ is a traceless symmetric tensor. At linear order, $\bar{a}(\tau) = a(\tau)$ and we will omit the bar on the scale factor to ease the notation. In a block matrix notation, the perturbed metric takes the form

$$\delta g_{\mu\nu} = a^2 \begin{pmatrix} -2A & -B_i \\ -B_i & -2D\delta_{ij} + 2E_{ij} \end{pmatrix} \tag{2.51}$$

and the line element in the perturbed space-time is

$$\mathrm{d}s^2 = a^2(\tau)[-(1+2A)\mathrm{d}\tau^2 - B_i\mathrm{d}\tau\mathrm{d}x^i + (1-2D)\delta_{ij} + 2E_{ij})\mathrm{d}x^i\mathrm{d}x^j] \tag{2.52}$$

The (4×4) metric perturbation is symmetric and has therefore 10 degrees of freedom : 1 for the scalar A, 3 for the vector B_i, and 6 for the symmetric tensor E_{ij}. Four of them correspond to a choice of coordinates in Eq. 2.41, these are called gauge freedom. In this manuscript we will work with scalar modes only. The metric then takes the form

$$\mathrm{d}s^2 = a^2(\tau)[-(1+2A)\mathrm{d}\tau^2 - B_{,i}\mathrm{d}\tau\mathrm{d}x^i + (1-2\psi)\delta_{ij} + 2E_{,ij})\mathrm{d}x^i\mathrm{d}x^j], \tag{2.53}$$

where we have introduced the curvature perturbation $\psi \equiv D + 1/3\nabla^2 E$. We will work mainly with the Newtonian conformal gauge, symmetric for scalar modes and defined as follows

$$B = E = 0. \tag{2.54}$$

The perturbed metric then takes the forms

$$\mathrm{d}s^2 = a^2(\tau)[-(1+2\Phi)\mathrm{d}\tau^2 + (1-2\Psi)\delta_{ij}\mathrm{d}x^i\mathrm{d}x^j], \tag{2.55}$$

where $\Phi \equiv A$ and $\Psi \equiv D$ are called the Bardeen potentials (BARDEEN 1980) [1] In the same way, the perturbed stress-energy tensor and the Einstein tensor are defined as Eq. 2.43

$$\delta T_{\mu\nu} \equiv T_{\mu\nu} - \bar{T}_{\mu\nu}, \tag{2.56}$$
$$\delta G_{\mu\nu} \equiv G_{\mu\nu} - \bar{G}_{\mu\nu}. \tag{2.57}$$

In a perturbed space-time, matter cannot be treated as a perfect fluid anymore and the stress-energy tensor takes the form

$$T_{\mu\nu} = (\rho + p)U_\mu U_\nu + p g_{\mu\nu} + \Pi_{\mu\nu} \tag{2.58}$$

where $\Pi_{\mu\nu}$ is the anisotropic stress tensor of the real fluid. It is a traceless symmetric tensor perpendicular to the fourth-velocity U_μ. The quantities in the perturbed space time are

$$\rho(\tau, \mathbf{x}) = \bar{\rho}(\tau) + \delta\rho(\tau, \mathbf{x}), \tag{2.59}$$
$$p(\tau, \mathbf{x}) = \bar{p}(\tau) + \delta p(\tau, \mathbf{x}) \tag{2.60}$$
$$U_\mu(\tau, \mathbf{x}) = \bar{U}_\mu(\tau) + \delta U_\mu(\mathbf{x}), \tag{2.61}$$

where $\delta\rho$, δp, and δU_μ are perturbations treated at linear order. Since $\Pi_{\mu\nu}$ is assumed to be zero in a FLRW Universe, this quantity is treated as a perturbation as well. The complete expression of $\delta G_{\mu\nu}$ $\delta T_{\mu\nu}$ can then be determined from the metric expression, Eq. 2.55, and from Eqs. 2.56 and 2.56. Detailed calculation of these terms can be found in KURKI-SUONIO 2020. The expression for the Einstein equations of the perturbation $\delta G_{\mu\nu} = 8\pi G \delta T_{\mu\nu}$ at linear order are given by (KURKI-SUONIO 2020)

$$\nabla^2\Psi = 4\pi G a^2 \bar{\rho}\left[\delta + 3(1+w)\mathcal{H}v\right], \tag{2.62}$$
$$\Phi' + \mathcal{H}\Phi = 4\pi G a^2 (\bar{\rho} + \bar{p})\, v \tag{2.63}$$
$$\Phi'' + \mathcal{H}(\Phi' + 2\Psi') + (2\mathcal{H}' + \mathcal{H}^2)\Phi + \frac{1}{3}\nabla^2(\Phi - \Psi) = 4\pi G a^2 \delta p \tag{2.64}$$
$$\Psi - \Phi = 8\pi G a^2 \bar{p}\Pi, \tag{2.65}$$

which translate in the following set of equations in Fourier space [2]

$$\left(\frac{k}{\mathcal{H}}\right)^2 \Psi_{\mathbf{k}} = -\frac{3}{2}\left[\delta_{\mathbf{k}} + 3(1+w)\frac{\mathcal{H}}{k} v_{\mathbf{k}}\right], \tag{2.66}$$
$$\mathcal{H}^{-1}\Psi_{\mathbf{k}} + \Phi_{\mathbf{k}} = \frac{3}{2}(1+w)\frac{\mathcal{H}}{k} v_{\mathbf{k}} \tag{2.67}$$
$$\mathcal{H}^{-2}\Psi''_{\mathbf{k}} + \mathcal{H}^{-1}(\Phi'_{\mathbf{k}} + 2\Psi'_{\mathbf{k}}) + \left(1 + \frac{2\mathcal{H}'}{\mathcal{H}}\right)\Phi_{\mathbf{k}} - \frac{1}{3}\left(\frac{k}{\mathcal{H}}\right)^2 (\Psi_{\mathbf{k}} - \Phi_{\mathbf{k}}) = \frac{3}{2}\frac{\delta p_{\mathbf{k}}}{\bar{\rho}} \tag{2.68}$$
$$\left(\frac{k}{\mathcal{H}}\right)^2 (\Psi_{\mathbf{k}} - \Phi_{\mathbf{k}}) = 3w\Pi_{\mathbf{k}}, \tag{2.69}$$

where we have used the background relations in Eq. 2.47. v corresponds to the peculiar velocity perturbation of the fluid $v_i \equiv aU^i$, whose scalar part is the velocity potential $v^S = -\nabla\mathbf{v}$. δ corresponds to the relative density perturbation of the fluid and $w \equiv \bar{p}/\bar{\rho}$. As we can see, all $\mathbf{k}$-modes will evolve independently in the linear regime. The conservation of the stress-energy tensor $T^{\mu}_{\nu;\mu} = 0$ gives the

1. The Bardeen potentials are defined as $\Phi \equiv A + \mathcal{H}(B - E') + (B - E')' and \Psi \equiv D + 1/3\nabla^2 E - \mathcal{H}(B - E') = \psi - \mathcal{H}(B - E')$.
2. We adopted the following notation in Fourier space : vectors and tensors are respectively scaled by a factor $1/k$ and $1/k^2$ respectively, such that scalars, vectors, and tensors modes have the same dimension in Fourier space. The other convention is that $v_{\mathbf{k}} = -i\, v_{\mathbf{k}}$ keeping in mind we do refer to the scalar part of the vector field.

following set of energy conservation equations in x-space (KURKI-SUONIO 2020)

$$\delta' = (1+w)(\nabla^2 v + 3\Psi') + 3\mathscr{H}\left(w\delta - \frac{\delta p}{\bar{\rho}}\right), \tag{2.70}$$

$$v' = -\mathscr{H}(1-3w)v - \frac{w'}{1+w}v + \frac{\delta p}{\bar{\rho}+\bar{p}} + \frac{2}{3}\frac{w}{1+w}\nabla^2\Pi + \Phi. \tag{2.71}$$

We introduce the comoving gauge with gauge conditions $v = B = 0$. We will denote quantities in that gauge with a subscript C. Perturbations in the comoving gauge are related to those in the Newtonian gauge by

$$\delta p^C = \delta p + 3H(1+w)c_s^2\bar{\rho}v, \tag{2.72}$$

$$\delta^C = \delta + 3H(1+w)\bar{\rho}v, \tag{2.73}$$

such that Eq. 2.62 reduces to Poisson equation

$$\nabla^2\Psi = 4\pi G a^2 \bar{\rho}\delta^C. \tag{2.74}$$

We also introduce the comoving curvature perturbation $\mathscr{R}$

$$\mathscr{R} \equiv -\psi^C = -\psi - \mathscr{H}(v - B). \tag{2.75}$$

Using Eq. 2.63 to get rid of the velocity perturbation, we can express $\mathscr{R}$ as

$$\mathscr{R} = -\Psi - \frac{2}{3(1+w)}(\mathscr{H}^{-1}\Psi' + \Phi). \tag{2.76}$$

2.1.3.1 Perfect fluid

From Eq. 2.69, we can see that outside the horizon $k/\mathscr{H} \ll 1$ and

$$\left(\frac{k}{\mathscr{H}}\right)^2(\Psi - \Phi) = 3w\Pi \approx 0. \tag{2.77}$$

Outside the horizon, dissipative effects can be neglected and the fluid can be approximated with a perfect fluid where $\Pi = 0$. In that case, it also implies $\Psi = \Phi$. As we do not aim at giving a precise, but rather a quantitative evolution of fluctuations on large scales, we will consider the case of a perfect fluid in the following. In that case, Einstein field equations 2.62-2.65 take the form

$$\nabla^2\Phi = 4\pi G a^2\bar{\rho}\left[\delta + 3(1+w)\mathscr{H}v\right], \tag{2.78}$$

$$= \frac{3}{2}\mathscr{H}^2\left[\delta + 3(1+w)\mathscr{H}v\right] \tag{2.79}$$

$$\Phi' + \mathscr{H}\Phi = 4\pi G a^2(\bar{\rho}+\bar{p})v = \frac{3}{2}\mathscr{H}^2(1+w)v \tag{2.80}$$

$$\Phi'' + 3\mathscr{H}\Phi' + (2\mathscr{H}' + \mathscr{H}^2)\Phi = 4\pi G a^2\delta p = \frac{3}{2}\mathscr{H}^2\frac{\delta p}{\bar{\rho}}, \tag{2.81}$$

and the conservation equation 2.70,2.71 reads

$$\delta' = (1+w)(\nabla^2 v + 3\Phi') + 3\mathscr{H}\left(w\delta - \frac{\delta p}{\bar{\rho}}\right),$$

$$v' = -\mathscr{H}(1-3w)v - \frac{w'}{1+w}v + \frac{\delta p}{\bar{\rho}+\bar{p}} + \Phi. \tag{2.82}$$

Adiabatic modes

The total entropy perturbation $\boldsymbol{S}$ is defined as

$$\boldsymbol{S} = \mathscr{H}\left(\frac{\delta p}{\bar{p}'} - \frac{\delta\rho}{\bar{\rho}'}\right) \tag{2.83}$$

and is gauge invariant. From the background relations in Eq. 2.48, $\bar{\rho}' = -3\mathscr{H}(1+w)\bar{\rho}$ and $\bar{p}' = c_s^2\bar{\rho}'$, we can express the entropy perturbation as

$$\boldsymbol{S} = \frac{1}{3(1+w)}\left(\frac{\delta\rho}{\bar{\rho}} - \frac{1}{c_s^2}\frac{\delta p}{\bar{\rho}}\right). \tag{2.84}$$

We can then express the right term of Eq. 2.81 as

$$\frac{\delta p}{\bar{\rho}} = c_s^2\left[\delta - 3(1+w)\boldsymbol{S}\right]. \tag{2.85}$$

With the use of background relations, this allow us to rewrite Eq. 2.81 as

$$\mathscr{H}^{-2}\Phi'' + 3(1+c_s^2)\mathscr{H}^{-1}\Phi' + 3(c_s^2 - w)\Phi = c_s^2\mathscr{H}^{-2}\nabla^2\Phi - \frac{9}{2}c_s^2(1+w)S. \tag{2.86}$$

Perturbations where entropy perturbation vanish

$$\boldsymbol{S} = 0, \Leftrightarrow \delta p = c_s^2\delta\rho \tag{2.87}$$

are called adiabatic perturbations (or equivalently adiabatic modes as in the last section). For such perturbations, we can rewrite Eq. 2.86 in Fourier space as

$$\mathscr{H}^{-2}\Phi_{\mathbf{k}}'' + 3(1+c_s^2)\mathscr{H}^{-1}\Phi_{\mathbf{k}}' + 3(c_s^2 - w)\Phi_{\mathbf{k}} = \left(\frac{-c_s^2k^2}{\mathscr{H}^{-2}}\right)\Phi_{\mathbf{k}}, \tag{2.88}$$

from which $\Phi_{\mathbf{k}}$ can be solved, given initial conditions. We can express the density and velocity perturbations with Eqs. 2.79 and 2.80 as

$$v_{\mathbf{k}} = \frac{2k}{3(1+w)}(\mathscr{H}^{-2}\Phi_{\mathbf{k}}' + \mathscr{H}^{-1}\Phi_{\mathbf{k}}), \tag{2.89}$$

$$\delta_{\mathbf{k}} = -\frac{2}{3}\left(\frac{k}{\mathscr{H}}\right)^2 - 3(1+w)\left(\frac{\mathscr{H}}{k}\right)v_{\mathbf{k}} = -\frac{2}{3}\left(\frac{k}{\mathscr{H}}\right)^2 - 2(\mathscr{H}\Phi_{\mathbf{k}}' + \Phi_{\mathbf{k}}), \tag{2.90}$$

If the fluid is made up of various perfect fluid components, such that $T_\nu^\mu = \sum_{i=1}^N [T_\nu^\mu]_i$

$$\bar{\rho} = \sum\bar{\rho}_i, \quad \bar{p} = \sum w_i\bar{\rho}_i, \quad w = \sum\frac{\bar{\rho}_i}{\bar{\rho}}w_i, \quad c_s^2 = \sum\frac{\bar{\rho}_i'}{\bar{\rho}'}c_i^2, \tag{2.91}$$

$$\delta p = \sum\delta p_i, \quad \delta = \sum\frac{\bar{\rho}_i}{\bar{\rho}}\delta_i, \quad v_l = \sum\frac{1+w_i}{1+w}\frac{\bar{\rho}_i}{\bar{\rho}}(v_i)_l, \tag{2.92}$$

with $w_i \equiv \bar{p}_i/\bar{\rho}_i$ and $c_i \equiv \bar{p}_i'/\bar{\rho}_i'$. We also introduce the *relative* entropy perturbations between two fluids elements by

$$S_{ij} \equiv -3\mathscr{H}\left(\frac{\delta p_i}{\bar{\rho}_i{}'} - \frac{\delta p_j}{\bar{\rho}_j{}'}\right). \tag{2.93}$$

If there is no energy transfer between the fluid elements in the Universe background, each of them evolve according to their equation of motion given by Eq. 2.48 such that $c_s^2 = \sum(\bar{\rho}_i + \bar{p}_i)/(\bar{\rho} + \bar{p}))c_s^2$.

We can then rewrite the relative entropy conservation as

$$S_{ij} = \frac{\delta_i}{1+w_i} - \frac{\delta_j}{1+w_j}. \tag{2.94}$$

Given the background relation in Eq. 2.48 and the continuity equation in 2.82, we can express the derivative of the relative entropy as

$$S'_{ij} = \nabla^2(v_i - v_j) - 9\mathscr{H}(c_i^2 \boldsymbol{S}_i - c_j^2 \boldsymbol{S}_j). \tag{2.95}$$

Finally we can express the variation of the comoving curvature defined in Eq. 2.76 for a perfect fluid as (KURKI-SUONIO 2020),

$$\frac{3}{2}(1+w)\mathscr{H}^{-1}\mathscr{R}'_{\mathbf{k}} = \left(\frac{k}{H}\right)^2 c_s^2 \Phi_{\mathbf{k}}^2 + \frac{9}{2}c_s^2(1+w)\boldsymbol{S}. \tag{2.96}$$

For isentropic perturbations and super-horizon scales, $\boldsymbol{S} = 0$ and $k/\mathscr{H} \ll 1$ we obtain the important result that $R' \approx 0$: the comoving curvature stays constant above the horizon. Any perturbation can be decomposed into a linear combination of isentropic ($\delta S = 0$) and isocurvature ($\mathscr{R} = 0$) modes. As already pointed out, we will only refer to isentropic initial solutions such that Eq. 2.88 always holds.

2.1.3.2 Evolution of perturbations in the radiation-dominated era

Now that we have defined our mathematical background, we can study how matter fluctuations evolve in the radiation-dominated era. At early time, one needs to take into account relativistic effects and interaction between the different energy components. The total energy density ρ reads

$$\rho = \rho_{\rm b} + \rho_{\rm c} + \rho_\nu + \rho_\gamma + \rho_{\rm DE}. \tag{2.97}$$

In the following we will make the following assumptions :

— There is no perturbation in dark energy.
— Baryon and dark matter have no pressure $p_{\rm b} = p_{\rm c} = 0$, for both the background and the perturbation, i.e. $\delta_{\rm p} = 0$. This means that $w_c = w_b = c_s^2 = c_b^2 = 0$ We assume neutrinos to be massless and therefore we have for both photons and neutrinos, $w_\gamma = w_\nu = c_\gamma^2 = c_\nu^2 = 1/3$, and $p_\gamma = 1/3\rho_\gamma$, which implies $\delta p_\gamma = 1/3\delta_\gamma$
— We neglect photons and neutrinos anisotropy such that $\Pi = 0$ and $\Psi = \Phi$. We can therefore treat neutrinos and radiation as a single radiation component $\delta_\gamma = \delta_\nu = \delta_r$.
— We ignore baryon contribution : since baryons are coupled to photons, their perturbations do not grow during the radiation era. After decoupling, baryons will fall into the gravitational potentials of dark matter and $\delta_{\rm b} \approx \delta_{\rm c}$.

In that case, we have

$$\rho = \rho_{\rm m} + \rho_{\rm r}. \tag{2.98}$$

It is common to express the densities as a function of the scale factor at matter-radiation equality. If we define

$$y \equiv \frac{a}{a_{eq}} \quad \text{with} \quad \Omega_{\rm m,0}(1+z_{eq})^3 = \Omega_{\rm r,0}(1+z_{eq})^4, \tag{2.99}$$

then

$$\Omega_{\rm m,0} = \frac{1}{1+y}, \quad \Omega_{\rm r,0} = \frac{y}{1+y} \tag{2.100}$$

and Friedmann equations 1.50,1.51 yield

$$\mathscr{H}^2 = \frac{1+y}{y^2}, \frac{\mathscr{H}_{eq}}{2} \quad \mathscr{H}_{eq}^2 = 2\frac{\Omega_{\mathrm{m},0}^2}{\Omega_{\mathrm{r},0}} H_0 \tag{2.101}$$

where H_{eq} corresponds to the Hubble radius at which the mode k enters the horizon. Conservation equations 2.82 take the form

$$\begin{aligned} \delta'_{\mathrm{m}} + k v_{\mathrm{m}} &= 3\Phi'_{\mathbf{k}}, \\ v'_{\mathrm{m}} + \mathscr{H} v_{\mathrm{m}} &= k\Phi_{\mathbf{k}} \\ \delta'_{\mathrm{r}} + \frac{4}{3} k v_{\mathrm{r}} &= 4\Phi'_{\mathbf{k}} \\ v'_{\mathrm{r}} - \frac{1}{4} k\delta_{\mathrm{r}} &= k\Phi_{\mathbf{k}}, \end{aligned} \tag{2.102}$$

and Eq. 2.66 yield

$$k^2\Phi''_{\mathbf{k}} + 3\mathscr{H}(\Phi'_{\mathbf{k}} + \mathscr{H}\Phi_{\mathbf{k}}) = -4\pi G a^2 \delta_{\mathbf{k}} = -4\pi G a^2(\rho_{\mathrm{m}}\delta_{\mathrm{m}} + \rho_{\mathrm{r}}\delta_{\mathrm{r}}). \tag{2.103}$$

We will drop the subscript **k** on the density and velocity field if the fluid is made up of various components to ease the notation. Eqs. 2.102 and Eq. 2.103 form a closed set of five equations and five unknowns. To solve this system, one needs to specifies initial conditions.

Initial conditions

We choose pure adiabatic initial conditions and impose $\boldsymbol{S} = S = S' = 0$. In a radiation-dominated universe $y \ll 1$, the Universe is dominated by radiation $\bar{\rho} \propto a^{-4}$ and $w = c_s^2 = 1/3$. From the Friedmann equations 2.47 we find $\mathscr{H}^2 \propto a^{-2}$, which implies that a' is constant and

$$a \propto \tau \Rightarrow \mathscr{H} = \frac{1}{\tau} \quad \text{and} \quad \mathscr{H}' = -\frac{1}{\tau^2}. \tag{2.104}$$

For radiation, Eq. 2.88 can be recast as

$$\Phi''_{\mathrm{rad}} + \frac{4}{\tau}\Phi'_{\mathrm{rad}} + \frac{1}{3}k^2\Phi_{\mathrm{rad}} = 0, \tag{2.105}$$

where Φ_{rad} refers to the gravitational potential induced by photons pressure. This equation can be rewritten into a first order Bessel equation by setting $u \equiv \Phi\tau$:

$$u'' + \frac{2}{\tau}u' + \left(\frac{k^2}{3} - \frac{2}{\tau^2}\right)u = 0. \tag{2.106}$$

The non-decaying solution is given by

$$\Phi_{\mathrm{rad}}(k,\tau) = \frac{1}{\tau}u = A_{\mathbf{k}}\frac{\sqrt{3}}{k\tau} j_1\left(\frac{k\tau}{\sqrt{3}}\right), \tag{2.107}$$

where $A_{\mathbf{k}} = A \times k/\sqrt{3}$, A is given by initial conditions, and j_1 is the Bessel function of order 1. At really early times $k\tau \ll 1$, $\Phi(\tau) \approx 1/3 A_{\mathbf{k}} = \text{const}$ and therefore we have $\Phi' = 0, \Phi = \Phi_i$. From Eqs. 2.89

and 2.90 we obtain for the scalar perturbations δ and v

$$v_{\rm r} = \frac{1}{2}\left(k\tau^2\Phi' + k\tau\Phi\right) = \frac{1}{2}k\tau\Phi, \tag{2.108}$$

$$\delta_{\rm r} = -\frac{2}{3}(k\tau)^2\Phi - \frac{4}{k\tau}v_r = -\left[2 + \frac{2}{3}\left(\frac{k}{H}\right)^2\right]\Phi. \tag{2.109}$$

For $\tau \ll k^{-1}$ $\delta_r = -2\Phi = \text{const}$ while $v = 1/2k\tau\Phi$ grows as τ. The relative entropy of the matter-radiation fluid is by definition

$$S_{\rm mr} \equiv \delta_{\rm m} - \frac{3}{4}\delta_{\rm r}. \tag{2.110}$$

The conditions $S = 0$ and $S' = 0$ then translates into $\delta_{\rm m} = 3/4\delta_{\rm r}$ and $v = v_{\rm r} = v_{\rm m}$. Thus given pure adiabatic initial conditions, we have for each k-mode

$$\Phi = \Phi_i, \quad \Phi' = 0, \quad \delta_{{\rm r},i} = -2\Phi, \quad \delta_{{\rm m},i} = \frac{3}{4}\delta_{{\rm m},i}, \quad v = v_{\rm m} = v_{\rm r} = 1/2k\tau\Phi. \tag{2.111}$$

Sub-horizon scale in the radiation-dominated era

Here we are will only interest in the evolution of the matter perturbations during the radiation-dominated era. Given 2.104 we can rewrite the continuity equation for dark energy as

$$\tau\delta'_{\rm m} + k\tau v_{\rm m} = 3\tau\Phi'_{\mathbf{k}}, \tag{2.112}$$

$$\tau v'_{\rm m} + v_{\rm m} = k\tau\Phi_{\mathbf{k}}. \tag{2.113}$$

Taking the derivative of Eq. 2.112 and using Eq. 2.113 to get rid of the velocity perturbation yields

$$\delta''_{\rm m} + \frac{1}{\tau}\delta'_{\rm m} = 3\Phi''_{\mathbf{k}} + \frac{3}{\tau}\Phi'_{\mathbf{k}} - k^2\Phi_{\mathbf{k}} \equiv F(k,\tau). \tag{2.114}$$

The homogeneous system has for solution

$$\delta_{\rm m} = C_1 + C_2\log(k\tau), \tag{2.115}$$

and with Green's method the full solution reads

$$\delta_{\rm m} = C_1 + C_2\log(k\tau) - \int_0^\tau d\tau' F(k,\tau')\tau'(\log(k\tau') - \log(k\tau)). \tag{2.116}$$

When $\tau \to 0$ the integral converges. Therefore one needs $C_2 = 0$ for physically motivated initial perturbations. This imply that $A = \delta_{\rm m}(\text{ini}) = -3/2\Phi_{\rm ini}$. Using numerical integration yields for sub-horizon scale $k/\mathscr{H} \gg 1$

$$\delta_{\rm m} \approx= -9\Phi\log 0.6k\tau \propto \log(\tau) \propto \ln a \tag{2.117}$$

Transition from radiation- to matter-dominated era

For a perfect fluid, we can rewrite 2.76 as

$$\frac{2}{3}\mathscr{H}^{-1}\Phi' + \frac{5+3w}{3}\Phi = -(1+w)\mathscr{R}. \tag{2.118}$$

We already saw that for adiabatic conditions, $\mathscr{R} = \text{const}$ at super-horizon scale. Then for both radiation- and matter-dominated eras we have $w = \text{const}$, and the general solution for the differen-

tial Eq. 2.118 is

$$\Phi = -\frac{3+3w}{5+3w}\mathscr{R} + Ca^{-\frac{5+3w}{2}}. \tag{2.119}$$

If w is constant for sufficiently enough time, we can neglect the homogeneous solution and finally

$$\Phi = -\frac{3+3w}{5+3w}\mathscr{R},$$
$$\Phi_{\mathbf{k}} = -\frac{2}{3}\mathscr{R}_{\mathbf{k}} \quad (w = 1/3, \quad \text{adiabatic}, \quad k/\mathscr{H} \ll 1) \tag{2.120}$$
$$\Phi_{\mathbf{k}} = -\frac{3}{5}\mathscr{R}_{\mathbf{k}}. \quad (w = 0, \quad \text{adiabatic}, \quad k/\mathscr{H} \ll 1). \tag{2.121}$$

The change of gravitational potential between the radiation- and matter-dominated era is

$$\Phi = \frac{9}{10}\Phi_i. \tag{2.122}$$

2.1.3.3 Evolution of perturbations in the matter-dominated era

In the matter-dominated era ($y \gg 1$)

$$\bar{p} = w = c_s^2 = 0, \quad \delta_p = \Pi = 0. \tag{2.123}$$

From Friedmann equations 2.47 written in terms of conformal time we have that

$$2\mathscr{H}' + \mathscr{H} = 0. \tag{2.124}$$

We already saw the solution of such a system in proper time, i.e. $a(t) \propto t^{2/3}$. In conformal time, using the second equation in 2.47 for matter ($\bar{\rho} \propto a^{-3}$), we obtain that $a' \propto a^{1/2}$, which gives

$$a(\tau) \propto \tau^2. \tag{2.125}$$

Therefore, we have $\mathscr{H} = 2/\tau$ and $\mathscr{H}' = -2/\tau^2$ and

$$4\pi G a^2 \bar{\rho} = \frac{3}{2}\mathscr{H}^2 = \frac{6}{\tau^2}. \tag{2.126}$$

Einstein equations 2.78-2.81 in the matter-dominated era are

$$\nabla^2\Phi = 4\pi G a^2 \bar{\rho}\,[\delta + 3\mathscr{H}v] \tag{2.127}$$
$$\Phi' + \mathscr{H}\Phi = 4\pi G a^2(\bar{\rho})\,v, \tag{2.128}$$
$$\Phi'' + 3\mathscr{H}\Phi' + (2\mathscr{H}' + \mathscr{H}^2)\Phi = 0. \tag{2.129}$$

Using Eq. 2.124 we can rewrite 2.129 as (or equivalently using Eq. 2.88 for entropy modes)

$$\Phi'' + \frac{6}{\tau}\Phi' = 0, \tag{2.130}$$

with solution

$$\Phi(\tau, \mathbf{x}) = C_1(\mathbf{x}) + C_2(\mathbf{x})\tau^{-5}. \tag{2.131}$$

The second term corresponds to the decaying mode and thus can be neglected at late time. $C_1(\mathbf{x})$ and $C_2(\mathbf{x})$ can be determined from the initial values of $\Phi_{\rm ini}(\mathbf{x}), \Phi'_{\rm ini}(\mathbf{x})$ at some initial time τ_{in}.

$$\Phi_{\rm ini}(\mathbf{x}) = C_1(\mathbf{x}) + C_2(\mathbf{x})\tau_{\rm ini}^{-5}, \tag{2.132}$$

$$\Phi'_{\rm ini}(\mathbf{x}) = -5C_2(\mathbf{x})\tau_{\rm ini}^{-6}. \tag{2.133}$$

The linear combination of these two equations gives

$$C_1(\mathbf{x}) = \Phi_{\rm ini} + \frac{1}{5}\tau_{\rm ini}\Phi'_{\rm ini}, \tag{2.134}$$

$$C_2(\mathbf{x}) = -\frac{1}{5}\tau_{\rm ini}^{-6}\Phi'_{\rm ini}. \tag{2.135}$$

$$\tag{2.136}$$

As the decaying part $C_2(\mathbf{x})$ will become negligible compared to $C_1(\mathbf{x})$, we have that

$$\Phi(\tau, \mathbf{x}) = \Phi(\mathbf{x}), \tag{2.137}$$

meaning that the Bardeen potential Φ is constant for perturbations in the matter-dominated era and therefore $\Phi' = 0$. From 2.128 we obtain for the velocity perturbation

$$v = \frac{2\Phi}{3\mathscr{H}} = \frac{1}{3}\Phi\tau \propto \tau \propto a^{1/2} \tag{2.138}$$

and the Poisson equation 2.78 reads

$$\nabla^2\Phi = \frac{3}{2}\mathscr{H}^2\left(\delta + 2\Phi\right), \tag{2.139}$$

which gives in Fourier space

$$\delta_{\mathbf{k}} = -\left[2 + \frac{2}{3}\left(\frac{k}{H}\right)^2\right]\Phi_{\mathbf{k}}. \tag{2.140}$$

For super-horizon scales $k/\mathscr{H} \ll 1$ perturbations stay constant

$$\delta_{\mathbf{k}} = -2\Phi_{\mathbf{k}} = \text{const}, \tag{2.141}$$

whereas for sub-horizon scales $k/\mathscr{H} \gg 1$ perturbations grow proportionally to the scale factor as

$$\delta_{\mathbf{k}} = -\frac{2}{3}\left(\frac{k}{\mathscr{H}}\right)^2\Phi_{\mathbf{k}} \propto \tau^2 \propto a. \tag{2.142}$$

Since the comoving Hubble length $\mathscr{H}$ grows with time, perturbations that were initially outside of the horizon will eventually cross the horizon and grow proportionally to the scale factor. This conclusion is only valid in the Newtonian Gauge as scalar quantities are not conserved by gauge transformations. Switching to the comoving gauge yields, we use Eqs. 2.140 and 2.138, and

$$\delta^C_{\mathbf{k}} = \delta^N_{\mathbf{k}} + 3\mathscr{H}v^N_{\mathbf{k}} = -2\Phi_{\mathbf{k}} + \frac{2}{3}\left(\frac{k}{H}\right)^2\Phi_{\mathbf{k}} + 2\Phi_{\mathbf{k}} = \frac{2}{3}\left(\frac{k}{H}\right)^2\Phi_{\mathbf{k}}, \tag{2.143}$$

which also holds in the radiation-dominated era. In that case, perturbations outside of the horizon grow proportionally with the scale factor as $\mathscr{H}^{-2} \propto a$.

2.1.3.4 Baryon acoustic oscillations

Let us look at how baryon and photons interact during the radiation-dominated era. We do not consider dark matter here, as it falls under its own gravitational potential and interact weakly with the baryon-photon fluid. Conservation equations 2.70 and 2.71 take the form

$$\delta_{\rm b}' = -kv_{\rm b} + 3\Psi_{\mathbf{k}}', \tag{2.144}$$

$$v_{\rm b}' = -\mathscr{H}v_{\rm b} + k\Psi_{\mathbf{k}} + \frac{1}{R\tau_{\rm coll}}(v_\gamma - v_{\rm b}) \tag{2.145}$$

$$\delta_\gamma' = -\frac{4}{3}kv_\gamma + 4\Psi_{\mathbf{k}}' \tag{2.146}$$

$$v_\gamma' = \frac{1}{4}k\delta_\gamma - \frac{1}{6}k\Pi_\gamma + k\Phi_{\mathbf{k}} + \frac{1}{\tau_{\rm coll}}(v_{\rm b} - v_\gamma), \tag{2.147}$$

where

$$R \equiv \frac{3\rho_b}{4\rho_\gamma}, R' = \mathscr{H}R, \quad \tau_{\rm coll} = \frac{1}{an_e\sigma_T}, \tag{2.148}$$

with $\tau_{\rm coll}$ the mean conformal time of collision between electrons and photons. We will assume Π_γ and $v_{\rm b} - v_\gamma$ to be small, only keeping the velocity difference at first order, such that $\Psi = \Phi$, $v_{\rm b} - v_\gamma \neq 0$ in the tight coupling limit where $\tau_{\rm coll} \ll \mathscr{H}^{-1}$. This approximation will break once photons decouple from the hot plasma at $t_{\rm rec}$. From these approximations we can rewrite Eq. 2.145 as

$$v_{\rm b} = v_\gamma - R\tau_{\rm coll}(v_{\rm b}' + Hv_{\rm b} - k\Phi_{\mathbf{k}}) \approx v_\gamma - R\tau_{\rm coll}(v_\gamma' + Hv_\gamma - k\Phi_{\mathbf{k}}) \tag{2.149}$$

and Eq. 2.147 becomes

$$v_\gamma' \approx \frac{1}{4}k\delta_\gamma + k\Phi_{\mathbf{k}} - R(v_\gamma' + Hv_\gamma - k\Phi_{\mathbf{k}}) \tag{2.150}$$

or equivalently,

$$\left[(1+R)v_\gamma\right]' = k\left(\frac{1}{4}\delta_\gamma + (1+R)\Phi_{\mathbf{k}}\right). \tag{2.151}$$

Taking the derivative with respect to conformal time and multiplying Eq. 2.146 by $(1+R)$ gives

$$\delta_\gamma'' + \frac{R'}{1+R}\delta_\gamma' + c_s^2k^2\delta_\gamma = -\frac{4}{3}k^2\Phi_{\mathbf{k}} + 4\Phi_{\mathbf{k}}'' + \frac{4R'}{1+R}\Phi_{\mathbf{k}}, \tag{2.152}$$

where $c_s^2 = (1+R)/3$ is the sound speed of the fluid. Defining temperature fluctuations as $\Theta \equiv \frac{1}{4}\delta_\gamma$ the latter equation becomes

$$\Theta'' + \frac{R'}{1+R}\Theta' + c_s^2k^2\Theta = -\frac{1}{3}k^2\Phi_{\mathbf{k}} + \Phi_{\mathbf{k}}'' + \frac{R'}{1+R}\Phi_{\mathbf{k}} \equiv F_{\mathbf{k}}(\tau). \tag{2.153}$$

Eq. 2.153 has the form of an harmonic oscillator with a forcing term induced by the potential and a friction term due to the variation of the baryon-to-photon density ratio. Well within the horizon, the oscillations will be much faster compared to the change in amplitude of background quantities, such that the contribution of the friction and forcing terms is approximately constant over the scales of interest, i.e. the time variation of the amplitude of the acoustic oscillations are small. Furthermore, we will assume that $\Phi' = \Phi'' = 0$. To solve the homogeneous equation we write $\Theta = Ae^{iB}$, where $A(\tau)$ and $B(\tau)$ are real functions representing the amplitude and oscillations of θ. The real and imaginary part of the homogeneous equation then gives (neglecting the time variation of A)

$$(B')^2 = \frac{k^2}{3(1+R)} = c_s^2k^2, \quad A = -\frac{1}{2}\frac{B''}{B} - \frac{1}{2}\frac{R'}{1+R}. \tag{2.154}$$

First equality gives

$$B(\tau) = k\int_{t_0}^{\tau} c_s(\tau)d\tau + C = kr_s(\tau) + C, \tag{2.155}$$

where C is a constant,

$$r_s = \int_{t_0}^{\tau} c_s(\tau)d\tau \tag{2.156}$$

corresponds to the sound horizon of baryon acoustic oscillations. Inserting $B(\tau)$ into the right equation of 2.154, we find $A \propto (1+R)^{-1/4}$ that implies that

$$\Theta_{\mathbf{k}}(\tau) = A_{\mathbf{k}}(1+R)^{-1/4}e^{ikr_s+C}, \tag{2.157}$$

with $A_{\mathbf{k}}$ given by initial conditions. The solutions of the equation can be directly determined by writing Eq. 2.153 into the more convenient form,

$$(\Theta_{\mathbf{k}} + (1+R))'' + \frac{R'}{1+R}(\Theta_{\mathbf{k}} + (1+R))' + \frac{k^2}{3(1+R)}(\Theta_{\mathbf{k}} + (1+R)) = 0, \tag{2.158}$$

where $\Phi' = (1+R)\Phi' = 0$. This directly corresponds to the case of homogeneous solutions, with now the variable $\Theta + (1+R)\Phi$ instead of Θ. Therefore, the full solutions read

$$\Theta_{\mathbf{k}}(\tau) = -(1+R)\Phi_{\mathbf{k}} + A_{\mathbf{k}}(1+R)^{-1/4}e^{ikr_s+C}. \tag{2.159}$$

The oscillations of the photon-baryon fluid stop after recombination, and these are directly observable in the CMB power spectrum. The sound horizon at recombination is measured up to an extreme precision by Planck and can therefore be used as a standard ruler. It represents the mean distance that matter travels in the plasma around initial perturbations in the photon-baryon fluid. Once photons are fully decoupled (at $r_{\rm drag}$), the baryonic distribution will be frozen in the Universe, and we can therefore expect to observe clusters of matter around overdensities of comoving size of $\approx$ 100 h^{-1} Mpc. Of course, the baryons will fall into the gravitational potential of the dark matter field, and overtime these oscillations will be damped and have a smaller amplitude due to non-linear effects.

2.1.3.5 Linear transfer function

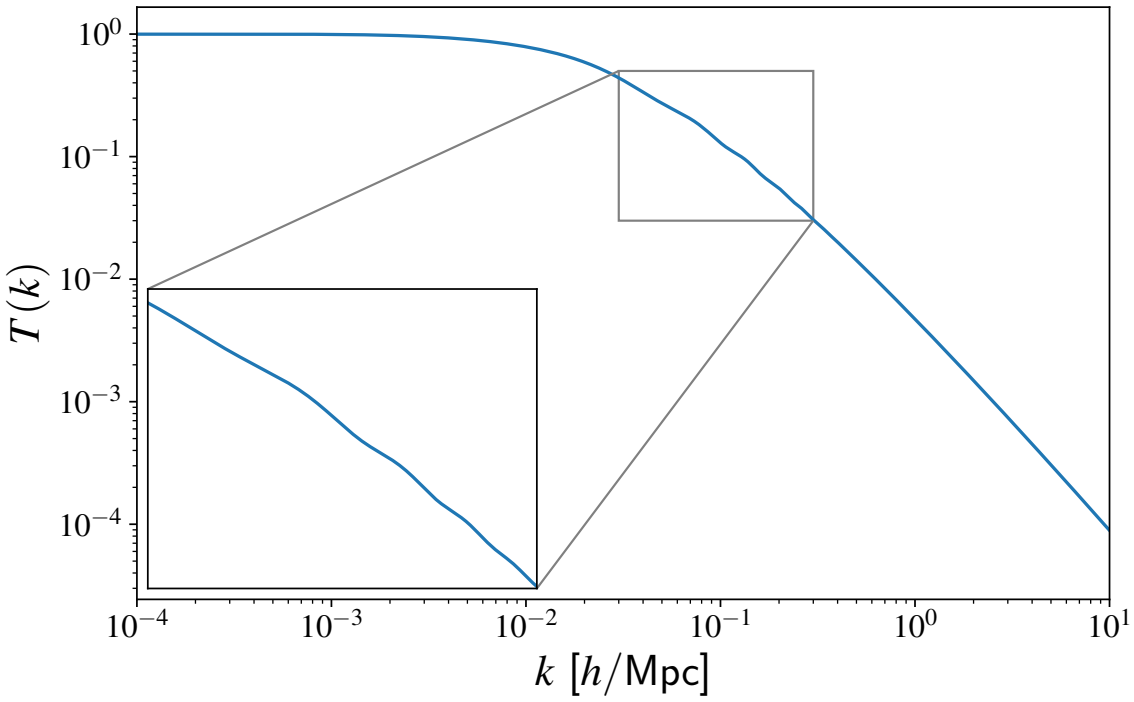

FIGURE 2.1 – Linear transfer function computed with the Boltzmann solver CAMB (LEWIS et AL. 2000) for the fiducial cosmology used in this manuscript, see Eq. 2.281

If we summarize the results of the last sections we have that :
— the initial perturbations $\delta_{\mathrm{ini}}(k)$ are quantum perturbations imprinted into the distribution of matter by inflation. In slow-roll inflation models, these perturbations are initially adiabatic,
— when $k \ll k_{eq}$, perturbations outside of the horizon grow $\propto \mathscr{H}^{-2} \propto a$. After k enters the Hubble radius in the matter-dominated era, it also grows proportionally to the scale factor,
— when $k \gg k_{eq}$, perturbations that cross the horizon in the radiation-dominated era grow logarithmically. Sub-horizon perturbations in the radiation-dominated era only grow by a factor $(k/k_{eq})^{-2}\ln(k/k_{eq})$ compared to perturbations still outside the horizon.

Following the above statements, we can introduce the linear transfer function $T(k)$ that relates the amplitude of sub-horizon perturbations in the matter-dominated era to the initial conditions we already described. For isentropic perturbations we have that

$$\delta(k,t) = \frac{9}{10}\frac{T(k,t)}{T(k\to 0,t)}\frac{D(t)}{D(t_i)}\delta_{\mathrm{i}}(k,t=0), \tag{2.160}$$

where D is the linear growth factor. The transfer function is normalized by construction. On large scales, it will have the form

$$T(k) \approx \begin{cases} 1 & \left(\frac{k}{k_{eq}}\right) \ll 1, \\ \left(\frac{k}{k_{eq}}\right)^{-2}\ln\left(\frac{k}{k_{eq}}\right) & \left(\frac{k}{k_{eq}}\right) \gg 1. \end{cases} \tag{2.161}$$

Nonetheless, the results obtained in the last section are approximations. To get an accurate expression for the transfer function $T(k)$, we need to take into account for the contributions of each energy component and their interactions. EISENSTEIN et HU 1998 provided numerical simulations-based

fitting formula that describe the matter transfer function as

$$T(k) = \frac{\Omega_\mathrm{c}}{\Omega_\mathrm{m}} T_c(k) + \frac{\Omega_\mathrm{b}}{\Omega_\mathrm{m}} T_b(k). \tag{2.162}$$

Dividing the matter contribution in both baryonic matter (T_b) and dark matter (T_c) seems a reasonable approximation before the drag epoch, as these two components were dynamically independent. After the drag epoch, both are weighted by their fractional density. This formula includes the baryonic processes that shape the matter transfer function. In addition to acoustic features and baryon infall, it includes the effect of *Silk damping* that damp the growth of matter perturbations due to photon diffusion in the primordial fluid. At the drag epoch, it also includes the *Compton drag* effect and *velocity overshoot* : once decoupled from photons, baryons will move from overdensities to underdensities, thus generating new perturbations.

Another way of determining the evolution of perturbations is through the direct numerical resolution of the relativistic Boltzmann equation for the primordial fluid :

$$\left(p^\mu \delta_\mu - \Gamma^i_{\mu\nu} p^\mu p^\nu \frac{\delta}{\delta p^\mu} \right) f = C(f), \tag{2.163}$$

where $f(x, \mathbf{p})$ is the distribution function, $p^\mu = (p^0, \mathbf{p})$ is the momentum and $C(f)$ corresponds to the collision term. Since the distribution function is a function of the direction $\mathbf{p}$, we can decompose it into the Legendre basis as

$$f(k, \tau, \mu) = \sum_{i=0}^{\infty} (2\ell + 1) i^{-\ell} P_\ell(\mu) f_\ell(k, \mu), \quad \mu = \mathbf{k} \cdot \mathbf{p}. \tag{2.164}$$

From Legendre polynomial $P_\ell(\mu)$ relations :

$$\int_{-1}^{1} L_\ell(\mu) L_\mathrm{q}(\mu) d\mu = \delta_{\ell \mathrm{q}}, \quad (2\ell + 1)\mu P_\ell(\mu) = (\ell + 1) P_{\ell+1}(\mu) + \ell P_{\ell-1}(\mu), \tag{2.165}$$

we can convert the Boltzmann equation into a set of coupled differential equations in which each ℓ couples $f_\ell(k, \tau)$, $f_{\ell-1}(k, \tau)$, and $f_{\ell+1}(k, \tau)$. To get an accurate modelling of CMB multipoles C_ℓ, one needs to reach $\ell \approx 1000$. There are several public codes that computes realistic transfer functions by solving this set of Bolzmann equations, such as CAMB (LEWIS et AL. 2000) or CLASS (LESGOURGUES 2011). A example of dark matter transfer function computed with CAMB is shown in Fig. 2.1. The transfer function is normalized such that $T(k \to 0) = 1$. The logarithmic part of the transfer function, for $k > k_{eq}$, is due to the growth of dark matter perturbations during the radiation-dominated era, while at $k < k_{eq}$, sub-horizon perturbations grow as a during the matter-dominated era. We can clearly see an oscillating pattern in the regime $k > k_{eq}$. It corresponds to the baryon acoustic oscillations in the primordial fluid as different k modes were at different phases of the oscillations before the end of recombination at t_dec.

2.1.4 Higher-order corrections

So far, we have only considered small perturbations $\delta_m \ll 1$ in the linear regime. Since we know that density perturbations in the CMB δ are of the order of$\approx 10^{-5}$, this is a reasonable approximation for the early Universe. As time evolves, matter perturbations δ_m will grow to the point where $\delta \sim 1$ and where non-linear effects become important. It is then useful to decompose the density perturbations as a function of linear and non-linear parts at any time as

$$\delta(t, k) = \delta_\mathrm{lin}(t, k) + \delta_\mathrm{N\text{-}loop}(t, k), \tag{2.166}$$

where the linear perturbation is given by 2.160. Non-linear perturbations can be derived by inserting the lower-order solution into the non-linear terms that appear in the fluid equation [3]. Non-linear effects will mix different k modes and lead to the cosmic structures that we see at later time, filaments connected by nodes and surrounded by voids.

In the Eulerian standand perturbation theory (SPT), the density and velocity fields are expanded around the linear solution, treating the variance of the linear fluctuations as a small parameter. Since the linear solution simply corresponds to a time-dependent $D(a)$ scaling of the initial density field, we can expand fluctuations at higher orders as (BERNARDEAU et AL. 2002)

$$\delta(\mathbf{x},t) = \sum_{i=1}^{n} \delta^{(n)}(\mathbf{x},t), \quad \theta(\mathbf{x},t) = \sum_{i=1}^{n} \theta^{(n)}(\mathbf{x},t), \tag{2.168}$$

where $\theta(\mathbf{x},t)$ corresponds to the divergence of the velocity field $\theta(\mathbf{x},t) \equiv \nabla\cdot\mathbf{v}$, $\delta^{(1)}(\mathbf{x},t)$ and $\theta^{(1)}(\mathbf{x},t)$ are linear in the initial density field, $\delta^{(2)}(\mathbf{x},t)$ and $\theta^{(2)}(\mathbf{x},t)$ are quadratic in the initial density field, and so on. We will follow the notation of (BERNARDEAU et AL. 2002). In term of conformal time, we can first rewrite Poisson equation 2.11 as,

$$\nabla^2\Phi = \frac{3}{2}\Omega_{\rm m}(\tau)\mathscr{H}^2\delta, \tag{2.169}$$

where we have used the definition of the critical density in Eq. 1.58. The fluid equations 2.14-2.15 then take the form

$$\frac{\partial\delta}{\partial\tau} + \theta = 0, \tag{2.170}$$

$$\frac{\partial\theta}{\partial\tau} + \mathscr{H}\theta + \frac{3}{2}\Omega_{\rm m}(\tau)\mathscr{H}^2\delta = 0. \tag{2.171}$$

The second Eq. 2.171 is the divergence of Eq. 2.15, with the approximation $c_s^2 = 0$ in a EdS universe. At two-loop order, fluid equations become non-linear as a consequence of the coupling between different k modes. In Fourier space, the latter equations reduce to (BERNARDEAU et AL. 2002; ASSASSI et AL. 2014)

$$\frac{\partial\delta}{\partial\tau} + \theta = [\delta * \theta], \tag{2.172}$$

$$\frac{\partial\mathbf{v}}{\partial\tau} + \mathscr{H}\mathbf{v} + \frac{3}{2}\Omega_{\rm m}(\tau)\mathscr{H}^2\delta = [\theta * \theta], \tag{2.173}$$

where the left side corresponds to the linear solution and the right side contains non-linear convolutions

$$[\delta * \theta]_{\mathbf{q}} = \int_{\mathbf{q}_1} \alpha(\mathbf{q},\mathbf{q}_1)\theta_{\mathbf{q}_1}\delta_{\mathbf{q}-\mathbf{q}_1}, \quad \alpha(\mathbf{q},\mathbf{q}_1) \equiv \frac{\mathbf{k}\cdot\mathbf{q}_1}{\mathbf{q}_1^2}, \tag{2.174}$$

$$[\theta * \theta]_{\mathbf{q}} = \int_{\mathbf{q}_1} \beta(\mathbf{q},\mathbf{q}_1,\mathbf{q}_1-\mathbf{q})\theta_{\mathbf{q}_1}\delta_{\mathbf{q}-\mathbf{q}_1}, \quad \beta(\mathbf{q},\mathbf{q}_1,\mathbf{q}_1-\mathbf{q}) \equiv \frac{q^2\mathbf{q}_1\cdot\mathbf{q}_2}{2q_1^2q_2^2}. \tag{2.175}$$

3. We note that the Newtonian approach that we described is only valid when the mean free path of particles is much smaller than the scale of perturbations. In a more general case, the evolution of the fluid is determined by the Vlasov equation

$$\frac{df}{dt} + \frac{1}{ma^2}\mathbf{p}.\nabla f - m\nabla\Phi.\frac{\partial f}{\partial\mathbf{p}} = 0, \tag{2.167}$$

where f corresponds to the distribution $f(t,\mathbf{x},\mathbf{p})$. Although exact, this equation is non-linear due to the presence of the gravitational potential in the equation.

In the EdS universe, $\Omega_{\rm m} = 1$ and the above equations can be solved with the following perturbative expansion (BERNARDEAU et AL. 2002) [4]

$$\delta(\mathbf{x},\tau) = \sum_{i=1}^{n} a^n(\tau)\delta^{(n)}(\mathbf{x},\tau_{\rm ini}), \quad \theta(\mathbf{x},t) = -\mathscr{H}\sum_{i=1}^{n} a^n(\tau)\theta^{(n)}(\mathbf{x},\tau_{\rm ini}), \tag{2.176}$$

where the fields $\delta^{(n)}$ and $\theta^{(n)}$ can be written in Fourier space as

$$\delta^{(n)}(\mathbf{k},\tau_{\rm ini}) = \int_{\mathbf{q}_1} .. \int_{\mathbf{q}_n} (2\pi)^3\delta^{\rm D}(\mathbf{q}_1 + ..\mathbf{q}_n - \mathbf{q})F_n(\mathbf{q}_1,...,\mathbf{q}_n)\delta_{\mathbf{q}_1}\delta^{(1)}_{\mathbf{q}_1}(\mathbf{k},\tau_{\rm ini})..\delta^{(1)}_{\mathbf{q}_n}(\mathbf{k},\tau_{\rm ini}), \tag{2.177}$$

$$\theta^{(n)}(\mathbf{k},\tau_{\rm ini}) = \int_{\mathbf{q}_1} .. \int_{\mathbf{q}_n} (2\pi)^3\delta^{\rm D}(\mathbf{q}_1 + ..\mathbf{q}_n - \mathbf{q})G_n(\mathbf{q}_1,...,\mathbf{q}_n)\delta_{\mathbf{q}_1}\delta^{(1)}_{\mathbf{q}_1}(\mathbf{k},\tau_{\rm ini})..\delta^{(1)}_{\mathbf{q}_n}(\mathbf{k},\tau_{\rm ini}), \tag{2.178}$$

and the kernels F_n and G_n can be computed iteratively (BERNARDEAU et AL. 2002). In particular, $F_1 = G_1 = 1$ and

$$F_2(\mathbf{q}_1,\mathbf{q}_2) = \frac{5}{7} + \frac{\mu_{12}}{2}\left(\frac{q_1}{q_2} + \frac{q_2}{q_1}\right) + \frac{2}{7}\mu_{12}^2, \tag{2.179}$$

$$G_2(\mathbf{q}_1,\mathbf{q}_2) = \frac{3}{7} + \frac{\mu_{12}}{2}\left(\frac{q_1}{q_2} + \frac{q_2}{q_1}\right) + \frac{4}{7}\mu_{12}^2, \tag{2.180}$$

$$\tag{2.181}$$

with $\mu_{12} = (\mathbf{q}_1\cdot\mathbf{q}_2)/q_1q_2$. Following the same approach than in Eulerian dynamics, one can also go beyond the Zel'dovich approximation in Lagrangian space by expanding the displacement field as

$$\Psi(\mathbf{q},t) = \Psi^{(1)}(\mathbf{q},t) + \Psi^{(2)}(\mathbf{q},t) + .. + \Psi^{(n)}(\mathbf{q},t), \tag{2.182}$$

see for example the review of(BOUCHET 1996).

2.2 Two-point statistics of density fields

2.2.1 Definition

Now that we have described how the initial perturbations $\delta(\mathbf{x},t)$ evolve in the Universe, we will focus our attention to the statistical properties of the cosmic density field. To specify such a field, one could in principle specify $\delta(\mathbf{x},t)$ at each position in space $\mathbf{x}$, but this is impossible as the number of field and $\mathbf{x}$ values are infinite. Instead, it is more relevant to think of δ as the realization of a stochastic process and to specify the random process that generated the density field δ. This treatment looks similar to what is done in statistical mechanics : we do not aim at deriving the positions of velocities of each particle but rather try to determine the statistical properties of the distribution function of the particles. By analogy, for n points at position $x_1,..,x_n$, the random field is characterized by the probability distribution function

$$\mathscr{P}_x(\delta(x_1),\delta(x_2),..\delta(x_{\rm n}))\,{\rm d}\delta_1{\rm d}\delta_2...{\rm d}\delta_{\rm n},$$

4. This result is only valid for an EdS universe, but can be approximated to any ΛCDM cosmology by replacing the EdS linear growth factor by the corresponding ΛCDM one.

which gives the probability to observe δ in the range $\delta_i + \mathrm{d}\delta_i$ (i=1,..,n). This distribution is fully determined if all its moments

$$\langle \delta(x_1)^{l_1}, \delta(x_2)^{l_2}, ..\delta(x_\mathrm{n})^{l_\mathrm{n}} \rangle \equiv \int \delta(x_1)^{l_1}, \delta(x_2)^{l_2}, ..\delta(x_\mathrm{n})^{l_\mathrm{n}} \mathscr{P}_x(\delta(x_1), \delta(x_2), ..\delta(x_\mathrm{n}))\, \mathrm{d}\delta_1 \mathrm{d}\delta_2 ... \mathrm{d}\delta_\mathrm{n}, \tag{2.183}$$

are known, with l_i non-zero positive value.

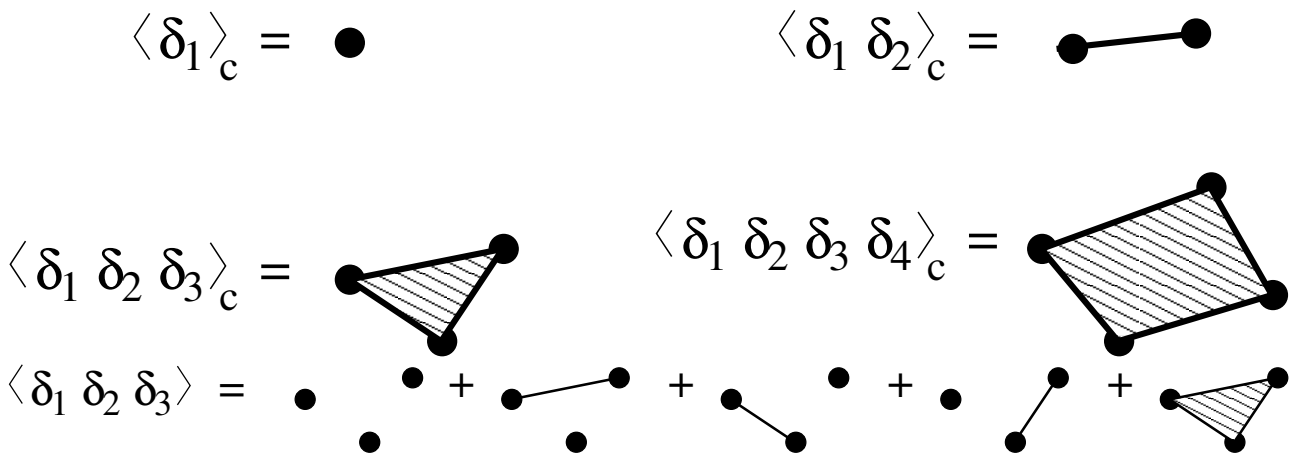

FIGURE 2.2 – Illustration of the different moments of the density field. The bottom plot shows the decomposition of the $\ell = 3$ moment. Taken from (BERNARDEAU et AL. 2002)

An illustration of the four first moments is presented in Fig. 2.2. Following the Cosmological Principle, we consider δ as the realization of a homogeneous and isotropic random process such that the first moment of the distribution function, i.e. expectation value, is $\langle\delta\rangle = 0$. The variance of the density field is given by $\sigma^2 = \langle\delta^2(x)\rangle$ and the moment

$$\xi(\mathbf{x}, \mathbf{x}') \equiv \langle \delta(\mathbf{x}), \delta(\mathbf{x'})) \rangle \tag{2.184}$$

is the so-called *two-point correlation function*. It can be defined as the excess probability, compared to a Poisson point process, of finding two objects separated by a distance s,

$$\delta P = \bar{n}^2 \delta V_1 \delta V_2 (1 + \xi(s)), \tag{2.185}$$

where $\bar{n}$ is the mean number density and δV_i are infinitesimal volume elements. Since the Universe is homogeneous and isotropic, ξ depends only on r, $\xi(r) \equiv \xi(\mathbf{x}, \mathbf{x}')$ where $r = |\mathbf{x} - \mathbf{x}'|$. If $\xi(r)$ is continuous at $r = 0$, then the field can be decomposed into Fourier modes such that

$$\langle \delta(\mathbf{k}, \mathbf{k}') \rangle = (2\pi)^3 \delta^D(\mathbf{k} - \mathbf{k}') P(\mathbf{k}), \quad P(\mathbf{k}) = \int \xi(x) \exp^{-i\mathbf{k}\mathbf{x}} \mathrm{d}x^3, \tag{2.186}$$

where δ^D is the Dirac delta function. The function $P(\mathbf{k})$ is called the *power spectrum* of the fluctuations. Since $\xi(r)$ is real and the Universe is isotropic, $P(k)$ is a real function that depends only on the norm $\mathbf{k}$. It corresponds to the Fourier transform of the two-point correlation $\xi(r)$. As the simplest inflation models predict nearly Gaussian initial perturbations, random fields in cosmology are usually referred to as Gaussian random fields. Further, if the field is homogeneous with zero mean, the probability distribution function of the Gaussian field is a multivariate Gaussian,

$$\mathscr{P}_x(\delta(x_1), \delta(x_2), ..\delta(x_n))\, d\delta_1 d\delta_2 ... \delta_n = \frac{1}{(2\pi)^{n/2}\sqrt{det(C)}} \exp\left(-\frac{1}{2} \sum_{i,j=1}^{n} \delta(\mathbf{x}_i)(C_{ij}^{-1})\delta(\mathbf{x}_j) \right), \tag{2.187}$$

where the covariance matrix is given by $C_{ij} = \xi(|x_j - x_i|)$. This means that a Gaussian random field is entirely determined by the correlation function $\xi(r)$ (or equivalently the power spectrum $P(k)$). As already pointed out, the brackets $\langle . \rangle$ correspond to the expectation value of the random field. Since the observed large-scale structure is the result of a single realization, we need to assume ergodicity. Ergodicity assume that volume averages converge towards ensemble averages as the volume goes to infinity. It has been shown (ALDER 1981) that zero mean Gaussian random fields are ergodic. For other types of random fields, the **fair sample hypothesis** of (P. PEEBLES 1980) states that separated-enough parts of the Universe may be realizations of different stochastic process such that we can observe them as individual realisations. However, most of galaxy surveys to date still provide modest volumes, whose ensemble average are subject to statistical fluctuations. This is what we call the **sample variance**. This issue will hopefully be overcome with now-operating DESI (DESI COLLABORATION 2016) survey and the future EUCLID survey (AMENDOLA et AL. 2018) [5], which will observe hundreds more galaxy redshifts than we have today, over huge cosmological volumes.

Eq. 2.161 gives an approximation of the linear matter power spectrum and its evolution as a function of cosmic time is given by

$$P_{\rm lin}(t,k) = A_s \left(\frac{k}{k_0}\right)^{n_s} T^2(k) D_+^2(t), \tag{2.188}$$

where A_s is the normalization of the power spectrum at pivot $k_0 = 0.05\ h^{-1}$Mpc. In observational cosmology, the power spectrum is often normalized by the averaged power in spheres of size $r = 8h^{-1}$Mpc such as

$$\sigma_8(z)^2 = \frac{1}{2\pi^2} \int k^2 {\rm d}k P_{\rm lin}(k,z) W(rk), \tag{2.189}$$

where $W(x) = 3(\sin(x)x\cos(x))/x^3$ is a top-hat window function. We simply denote its value at $z = 0 : \sigma_8 \equiv \sigma_8(z = 0)$. Inflation models also predict a small running power-law spectral index with wavenumber, $\alpha_s \equiv dn_s/dk$. The CMB measurements of (PLANCK COLLABORATION 2018) measured $\alpha_s = -0.0045 \pm 0.0067$. Including the running of the spectral index yields in the latter equation

$$P_{\rm lin}(t,k) = A_s \left(\frac{k}{k_0}\right)^{ns+0.5\alpha \ln k/k_0} T^2(k) D_+^2(t). \tag{2.190}$$

In the rest of the manuscript, linear power spectra are computed with CAMB (LEWIS et AL. 2000) at any desired redshift. CAMB calculate the linear transfer $T(k)$ in a ΛCDM cosmology, and evolves the linear power spectrum using Eq. 2.188. We checked that using CLASS (LESGOURGUES 2011) instead provides the same result.

Galaxies trace the luminous component of the matter density field. This is where we are going to focus our attention in the following, since the main goal of this thesis is to analyse the luminous red galaxy spectroscopic sample of eBOSS. The observation of galaxy two-point correlations shows amplitude variations in galaxy clustering, depending on galaxy intrinsic properties and selections. This mean that there exist a bias between the observed galaxy density field δ_g and the underlying matter density field δ_m. On large scales ($r > 20\ ^{-1}$Mpc), the bias between galaxy and matter density fields, b, is assumed to be scale-independent such that,

$$\delta_{\rm g} = b\delta_{\rm m} \rightarrow P_{\rm gg} = b^2 P_{\rm lin}. \tag{2.191}$$

5. The DESI and Euclid surveys are specifically designed to study the LSS of the Universe, see 4.4.4

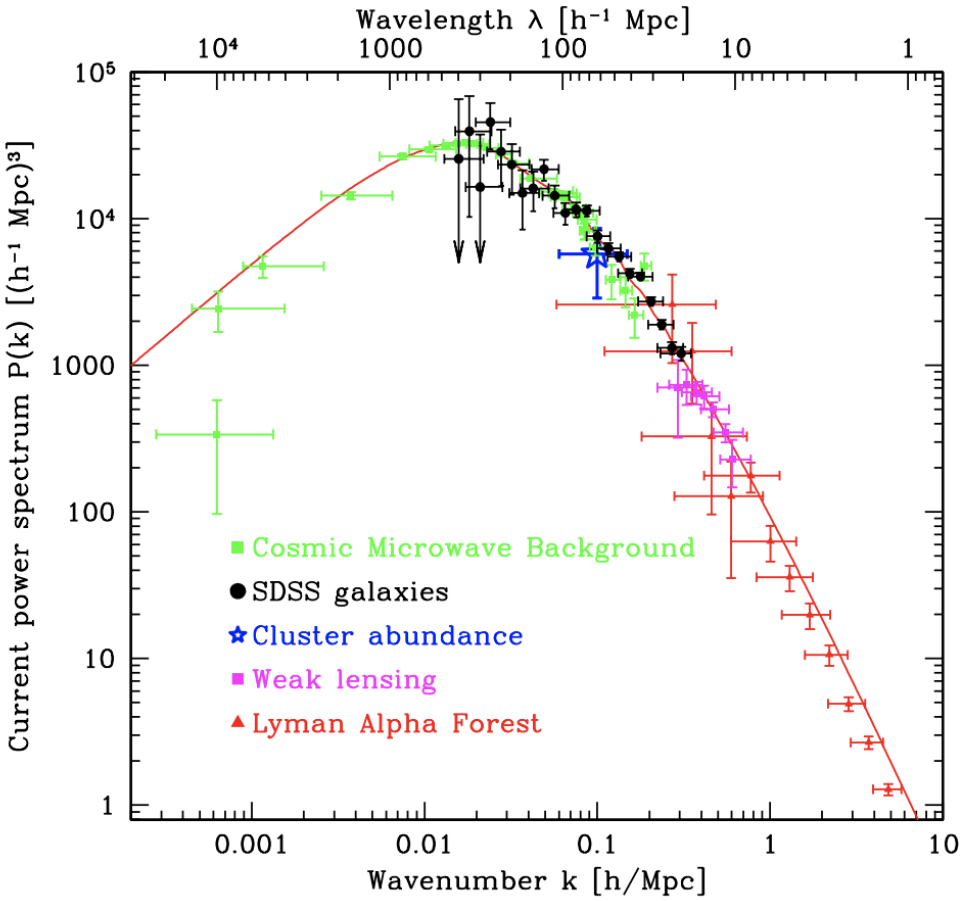

FIGURE 2.3 – Matter power spectrum prediction (red curve) and matter tracers observations (points). The details on the power spectrum measurements for the different matter tracers shown with different colours can be found in TEGMARK et AL. 2012. Taken from (TEGMARK et AL. 2012).

We can see an example of the matter power spectrum and related observations in Fig. 2.3. On large scales, the power spectrum spectrum has the same slope as during inflation, i.e. $P(k) \propto k^{ns}$, while on smaller scales, the shape of the power spectrum is affected by the different physical processes occurring during the radiation-dominated era. The turnaround of the amplitude marks the transition from radiation- to matter-dominated era. We can see that the power spectrum has been measured with different tracers, each of them providing information at different scales. On very large scales, matter fluctuations are observed through CMB anisotropies. At large, semi-linear scales, matter fluctuations are observed through the galaxy distribution. The associated galaxy linear bias has been corrected for in the figure. The highly non-linear scales can be probed by the Lyman-α forest. This forest corresponds to the different absorption lines that can be observed in quasars (QSOs) spectra, due to the presence of cold hydrogen gas along the LoS.

2.2.2 Non-linear matter power spectrum

Following the decomposition of Eq. 2.166, we can express the total power spectrum $P_{\delta\delta}(t,k)$ in perturbation theory as

$$P_{\delta\delta}(t,k) = P_{\rm lin}(t,k) + P_{\text{N-Loop}}(t,k). \tag{2.192}$$

We also introduce the velocity divergence power spectrum $P_{\theta\theta}$ and the cross power spectrum between matter and velocity divergence $P_{\delta\theta}$. In the linear regime $P_{\theta\theta} = P_{\theta\delta} = P_{\rm lin}$. This of course will not hold in the non-linear regime : tidal effects will damp the velocity power spectra at small

scale. The 1-loop power spectra take the form (BERNARDEAU et AL. 2002; SCOCCIMARRO 2004)

$$P_{\delta\delta} = P(k) + 2\int [F_2(\mathbf{p},\mathbf{q})]^2 P(p)P(q)\mathrm{d}^3q + 6P(k)\int F_3(k,q)P(q)\mathrm{d}^3q, \tag{2.193}$$

$$P_{\theta\theta} = P(k) + 2\int [G_2(\mathbf{p},\mathbf{q})]^2 P(p)P(q)\mathrm{d}^3q + 6P(k)\int G_3(k,q)P(q)\mathrm{d}^3q \tag{2.194}$$

$$P_{\theta\delta} = P(k) + 2\int F_2(\mathbf{p},\mathbf{q})G_2(\mathbf{p},\mathbf{q})P(p)P(q)\mathrm{d}^3q + 3P(k)\int [F_3(p,q)+G_3(k,q)]P(q)\mathrm{d}^3q, \tag{2.195}$$

where $\mathbf{p} = \mathbf{k} - \mathbf{q}$, the expressions for F_3 and G_3 kernels can be found in SCOCCIMARRO 2004, and $P(k) \equiv P_{\rm lin}(k)$. The linear power spectrum is cut at small wavenumbers (infrared) and high wavenumbers (ultraviolet) to control the divergences that appear in the calculation when $P(k) = 0$. It has been show in (CROCCE et Román SCOCCIMARRO 2006) that linear and 1-loop [6] perturbation theory corrections gives biased estimates of the power spectrum, even at the BAO scale, requiring higher-order corrections to obtain a fair estimate of the non-linear matter power spectrum. A way of recovering small-scale, non-linear information is directly through the use of cosmological simulations, which we will review in Section 2.4.

RegPT

REGPT is a 2-loop prescription for the density and velocity divergence power spectra, which formalism is based on a multi-point propagator expansion (TARUYA et AL. 2012). In that case, we can rewrite Eqs. 4.51 and 4.52 in term of the two-component multiplet

$$\Psi_a(\mathbf{k};t) = \left(\delta(\mathbf{k};t), -\frac{\theta(\mathbf{k};t)}{f}\right), \tag{2.196}$$

where the subscripts $a = 1,2$ denote the density and velocity divergence components of the matter fluid. Here, θ is defined as $\theta \equiv \nabla\cdot\mathbf{v}/(aH(a))$. A new time variable, $\eta \equiv \ln D$ with D the linear growth factor, is defined and the evolution of $\Psi_a(\mathbf{k};t)$ is given by (TARUYA et AL. 2012)

$$\left[\delta_{ab}\frac{\partial}{\partial\eta} + \Omega_{ab}(\eta)\right]\Psi_b(\mathbf{k};t) = \int \frac{\mathrm{d}^3\mathbf{k}_1^2\mathrm{d}\mathbf{k}_2^3}{(2\pi)^3}\delta^D(\mathbf{k}-\mathbf{k}_1-\mathbf{k}_2)\gamma_{abc}(\mathbf{k}_1,\mathbf{k}_2)\Psi_b(\mathbf{k}_1;t)\Psi_c(\mathbf{k}_2;t), \tag{2.197}$$

where the repetition of the same subscripts indicates a sum over multiplet components. The time-dependent matrix $\Omega_{ab}(\eta)$ is given by

$$\Omega_{ab}(\eta) = \begin{pmatrix} 0 & -1 \\ -\frac{3}{2f^2}\Omega_m(\eta) & \frac{3}{2f^2}\Omega_m(\eta) - 1 \end{pmatrix} \tag{2.198}$$

with f the linear growth rate. The vertex functions $\gamma_{abc}(\mathbf{k}_1,\mathbf{k}_2)$ are given by

$$\gamma_{abc}(\mathbf{k}_1,\mathbf{k}_2) = \begin{cases} \frac{1}{2}\left(1 + \frac{\mathbf{k}_1\cdot\mathbf{k}_2}{k_2^2}\right), & (a,b,c) = (1,1,2), \\ \frac{1}{2}\left(1 + \frac{\mathbf{k}_1\cdot\mathbf{k}_2}{k_2^1}\right), & (a,b,c) = (1,2,1), \\ \frac{1}{2}\left(\frac{(\mathbf{k}_1\cdot\mathbf{k}_2)|\mathbf{k}_1\cdot\mathbf{k}_2|^2}{2k_2^1k_2^2}\right), & (a,b,c) = (2,2,2), \\ 0, & \text{otherwise.} \end{cases} \tag{2.199}$$

6. 1-loop corresponds to second-order corrections, 2-loop to third-order corrections etc.

Eq. 2.197 can be recast as an integral equation

$$\Psi_a(\mathbf{k};t) = g_{ab}(\eta,\eta_0)\phi_b(\mathbf{k}) + \int_{\eta_0}^{\eta} \mathrm{d}\eta' g_{ab}(\eta,\eta') \frac{\mathrm{d}^3\mathbf{k}_1^2 \mathrm{d}\mathbf{k}_2^3}{(2\pi)^3} \delta^D(\mathbf{k}-\mathbf{k}_1-\mathbf{k}_2)\gamma_{bcd}(\mathbf{k}_1,\mathbf{k}_2)\Psi_c(\mathbf{k}_1;\tau)\Psi_d(\mathbf{k}_2;\tau), \tag{2.200}$$

where the quantity $\phi_b(\mathbf{k}) \equiv \Psi_a(\mathbf{k};\eta_0)$ denotes the initial conditions, and the function g_{ab} denotes the linear propagator satisfying the equation

$$\left[\delta_{ab}\frac{\partial}{\partial\eta} + \Omega_{ab}(\eta)\right] g_{ab}(\tau,\tau') = 0, \tag{2.201}$$

with the condition that $g_{ab}(\tau,\tau) = 1$. It is straightforward to obtain a perturbative solution for Eq. 2.200 by perturbing the field as

$$\Psi_a(\mathbf{k};\tau) = \sum_{n=1}^{\infty} \Psi_a^{(n)}(\mathbf{k},\eta_0). \tag{2.202}$$

As an alternative approach, TARUYA et AL. 2012 considered the multi-point propagator expansion introduced by (Francis BERNARDEAU et AL. 2008), in which multi-point propagators are the building blocks of the expansion. They are fully non-pertubative objects, which correspond to the ensemble average of small variations of the evolved cosmic density field with respect to its initial conditions. The $(p+1)$ multi-point propagator $\Gamma^{(p)}$ can be defined as (TARUYA et AL. 2012)

$$\frac{1}{p!}\left\langle \frac{\delta^p\Psi_a(\mathbf{k};\tau)}{\delta\phi_{c_1}(\mathbf{k}_1)..\delta\phi_{c_p}(\mathbf{k}_p)} \right\rangle = \delta^D(\mathbf{k}-\mathbf{k}_1..-\mathbf{k}_p)\frac{1}{(2\pi)^{3(p-1)}}\Gamma^{(p)}(\mathbf{k}_1..\mathbf{k}_p;\eta). \tag{2.203}$$

In term of multi-point propagators, the non-linear matter spectrum reads (Francis BERNARDEAU et AL. 2008; TARUYA et AL. 2012; NISHIMICHI et AL. 2017)

$$P(k) = \sum_{n=1}^{\infty} n! \int \frac{\mathrm{d}^3\mathrm{k}_1..\mathrm{d}^3\mathrm{k}_n}{2\pi^{3(n-1)}} [\Gamma^{(n)}(\mathrm{k}_1,..,\mathrm{k}_n))]^2 P_{\rm lin}(\mathrm{k}_1)..P_{\rm lin}(\mathrm{k}_n). \tag{2.204}$$

This formalism is accurate and has been used in the Fourier-space analysis of emission lines galaxies (ELG, DE MATTIA et AL. 2021) and QSOs (NEVEUX et AL. 2020) in eBOSS. It provides 2-loop theoretical predictions for $P_{\delta\delta}$, $P_{\theta\theta}$, and $P_{\delta\theta}$, valid up to $\mathrm{k} \approx 0.3\ h\ \mathrm{Mpc}^{-1}$ in real space.

RESPRESSO

RESPRESSO (Rapid and Efficient SPectrum calculation based on RESponSe functiOn) is a 2-loop formalism based on the non-linear response function formalism (NISHIMICHI et AL. 2017). The response function plays a similar role as the multipoint propagator expansion : it determines the variation of the non-linear matter power spectrum with respect to small variations of the linear power spectrum. Formally this can be written as

$$\delta P_{\delta\delta}(k;z) = \int \mathrm{d}\ln q K(q,k;z)\delta P_{\rm lin}(k;z), \tag{2.205}$$

where K is the response function that can alternatively be defined as

$$K(q,k;z) = q\frac{\delta P_{\delta\delta}(k;z)}{\delta P_{\rm lin}(k;z)}. \tag{2.206}$$

Based on numerical simulation measurements of the response function, (NISHIMICHI et AL. 2017) proposed the following phenomenological model

$$K_{\rm model}(k,q) = \left[\left(1+\beta_{k,q}+\frac{1}{2}\beta_{k,q}^2\right)K_{\rm tree}^{\rm SPT}(k,q) + (1+\beta_{k,q})K_{\rm 1\text{-}loop}^{\rm SPT}(k,q) + K_{\rm 2\text{-}loop}^{\rm SPT}\right] D(\beta_{k,q}), \quad (2.207)$$

where $\beta_{k,q} = \alpha_k + \alpha_q$ and

$$\alpha_k = \frac{k^2}{2}\int \frac{{\rm d}k}{6\pi^2} P_{\rm lin}. \quad (2.208)$$

The damping function is defined as

$$D(x) = \begin{cases} \exp(-x), & \text{if} \quad K_{\rm model}(k,q) > 0, \\ 1/(1+x) & \text{if} \quad K_{\rm model}(k,q) < 0, \end{cases} \quad (2.209)$$

and the explicit expressions for the response function, $K^{\rm SPT}$, using SPT at the 2-loop level, can be found in (NISHIMICHI et AL. 2017). The RESPRESSO formalism is designed to recover SPT predictions, while keeping the features of the regularized perturbation theory calculation. The response function is cosmology- and time-dependent through the shape and amplitude of the linear power spectrum. This formalism basically extends the range of validity of REGPT to higher non-linear k of $k \approx 1\ h$ Mpc^{-1}. This model for the non-linear matter power spectrum has been used in the configuration space analysis of eBOSS QSOs (HOU et AL. 2021) and LRG (BAUTISTA et AL. 2021).

Convolutional Lagrangian Perturbation Theory

The Convolutional Lagrangian Perturbation Theory (CLPT) provides an alternative non-perturbative resummation of Lagrangian perturbations in configuration space for biased tracers. The Lagrangian coordinates are related to Eulerian coordinates with Eq. 2.33. The two-point correlation function can be expanded in its Lagrangian coordinates by considering galaxies to be locally biased with respect to the matter density $\delta(\vec{q})$. The expansion is performed at different orders of the Lagrangian bias function $F[\delta(\vec{q})]$, defined as

$$1 + \delta_X(\vec{q}, t) = F[\delta(\vec{q})]. \quad (2.210)$$

The Eulerian density field is computed by convolving the Lagrangian one with the displacement field ψ as

$$1 + \delta_X(\vec{x}) = \int {\rm d}^3q\, F\left[\delta(\vec{q})\right] \int \frac{{\rm d}^3k}{(2\pi)^3} e^{i\vec{k}(\vec{x}-\vec{q}-\vec{\psi}(\vec{q}))}. \quad (2.211)$$

The local Lagrangian bias function F is approximated by a non-local expansion using its first and second derivatives, where the n^{th} derivative is given by

$$\langle F^n \rangle = \int \frac{{\rm d}\delta}{\sqrt{2\pi}\sigma} e^{-\delta^2/2\sigma^2} \frac{{\rm d}^n F}{{\rm d}\delta^n}. \quad (2.212)$$

The two-point correlation function is then obtained by evaluating the expression $\xi_X(\vec{r}) = \langle \delta_X(\vec{x})\delta_X(\vec{x}+\vec{r})\rangle$ (CARLSON et AL. 2013)

$$1 + \xi_X(\vec{r}) = \int {\rm d}^3q M(\vec{r},\vec{q}), \quad (2.213)$$

where $M(\vec{r},\vec{q})$ is the kernel of convolution that takes into account the displacement and bias expansion up to its second derivative.

The CLPT can also provide predictions for the pairwise mean velocity $v_{12}(r)$ and pairwise velocity dispersion $\sigma_{12}(r)$ as a function of the real-space separation, which will be important for the modelling of the redshift-space power spectrum. These are computed following the formalism developed by L. WANG et AL. 2014, which is similar to the one describe above but modifying the convolution

kernels to take into account the velocity rather than the density :

$$v_{12}(r) = (1+\xi(\vec{r}))^{-1} \int M_1(\vec{r},\vec{q}) \mathrm{d}^3 q, \tag{2.214}$$

and

$$\sigma_{12}(r) = (1+\xi(\vec{r}))^{-1} \int M_2(\vec{r},\vec{q}) \mathrm{d}^3 q. \tag{2.215}$$

The kernels $M_{1,2}(\vec{r},\vec{q})$ also depend on the first two non-local derivatives of the Lagrangian bias function $\langle F' \rangle$ and $\langle F'' \rangle$, which are free parameters in the model. Hereafter, we eliminate the angle brackets around the Lagrangian bias terms to simplify the notation.

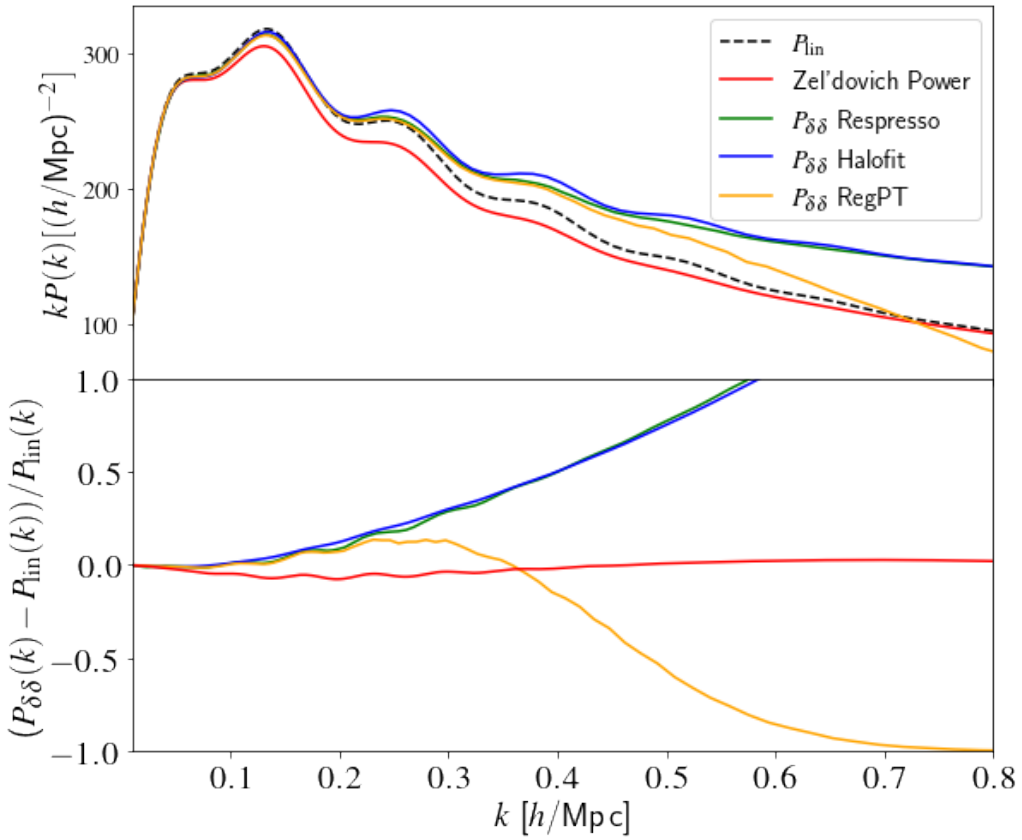

FIGURE 2.4 – Comparison between different methods which compute the real space non-linear matter power spectrum at redshift $z = 0.55$ in the fiducial cosmology, see Eq. 2.281. The black dashed corresponds to the linear power spectrum, computed with CAMB. The Zel'Dovich power spectrum is in red, the RESPRESSO power in green, the HALOFIT power in blue, and the REGPT power in yellow

Model power spectra calibrated on simulations

HALOFIT is the only model described in this manuscript that predicts the non-linear matter power spectrum without using perturbation theory (TAKAHASHI et AL. 2012). The total dimensionless power spectrum $\Delta \equiv k^3 P(k)/(2\pi)^2$ is modelled and decomposed into a 1-halo (matter correlations within the same dark matter halo) and a 2-halo term (correlations between different halos). It is calibrated using N-body simulations. This non-linear matter power spectrum was not used directly in the eBOSS analysis but is an ingredient for the velocity divergence power spectrum formalism described in the following.

BEL et AL. 2018 provides fitting functions based on N-body simulation and valid up to k $\approx 0.7\ h$

Mpc^{-1}, which describe the non-linear $P_{\theta\theta}$ and $P_{\delta\theta}$. These are given by

$$\begin{aligned} P_{\theta\theta}(k) &= P_L(k) e^{-k(a_1 + a_2 k + a_3 k^2)}, \\ P_{\delta\theta}(k) &= \left(P^{HF}_{\delta\delta}(k) P_{\rm lin}(k)\right)^{\frac{1}{2}} e^{-\frac{k}{k_\delta} - bk^6}, \end{aligned} \tag{2.216}$$

where $P^{HF}_{\delta\delta}$ is the non-linear matter power spectrum estimated with HALOFIT.

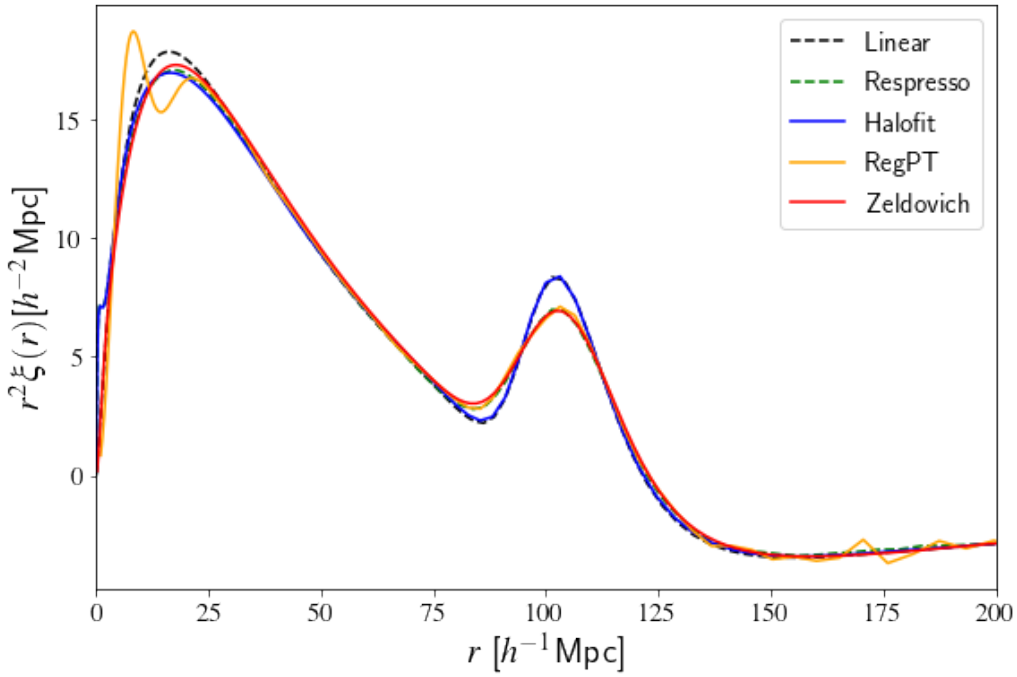

FIGURE 2.5 – Two-point correlation functions associated to the power spectrum predictions presented in Fig. 2.4.

The overall degree of non-linearity is determined by the amplitude of matter fluctuation at the considered redshift. The dependence of the fitting function coefficients on σ_8 is given by

$$\begin{aligned} a_1 &= -0.817 + 3.198\sigma_8, \\ a_2 &= 0.877 - 4.191\sigma_8 \\ a_3 &= -1.199 + 4.629\sigma_8 \\ 1/k_\delta &= -0.017 + 1.496\sigma_8^2 \\ b &= 0.091 + 0.702\sigma_8^2. \end{aligned} \tag{2.217}$$

These fitting functions have been used in the configuration-space analysis of QSOs (HOU et AL. 2021) and LRGs (BAUTISTA et AL. 2021).

We present in Figs. 2.4 and 2.5 the non-linear power spectra and their corresponding non-linear two-point correlation functions at $z = 0.55$. As we can see, non-linear prescriptions have enhanced power on non-linear scales, above $k \approx 0.1\ h\ \mathrm{Mpc}^{-1}$. Below that scale, all predictions are equivalent. Because of non-linearity in the velocities, 2-loop prescriptions damp the baryonic acoustic oscillations in the spectra. REGPT and RESPRESSO are equivalent up $k \approx 0.2$-$0.3\ h\ \mathrm{Mpc}^{-1}$. At higher k, we can see that the power in the REGPT prediction is damped, due to the presence of a UV cutoff in the propagator expansion TARUYA et AL. 2012. On the other hand, RESPRESSO provides both a similar high-k amplitude as HALOFIT model, and the expected BAO non-linear damping. This is crucial to derive unbiased cosmological parameters estimation. We can see that the BAO damping is absent

from the HALOFIT prediction, since at the BAO scales (in the 2-halo term) this prescription relies only on linear theory.

Let's now focus our attention to the two-point correlation function. As one expect, REGPT and RESPRESSO provide similar predictions up to 20 h^{-1}Mpc and a damped BAO peak due to non-linear effects. However, we can see some wiggles in REGPT prediction below 20 h^{-1}Mpc. TARUYA et AL. 2012 showed that as the redshift z decreases, the effect of the UV cutoff increases, and the small-scale correlation function is more and more underestimated. This is one of the main reason why RESPRESSO is used other REGPT in the eBOSS configuration space analysis, while REGPT formalism is robust enough for the Fourier-space analysis. We will omit the comparison of $P_{\theta\theta} and P_{\delta\theta}$ but refer to HOU et AL. 2021 for a comparison of BEL et AL. 2018 fitting functions with other perturbation theory predictions. Overall, those predictions are found to be very similar.

2.2.3 Non-linear galaxy bias

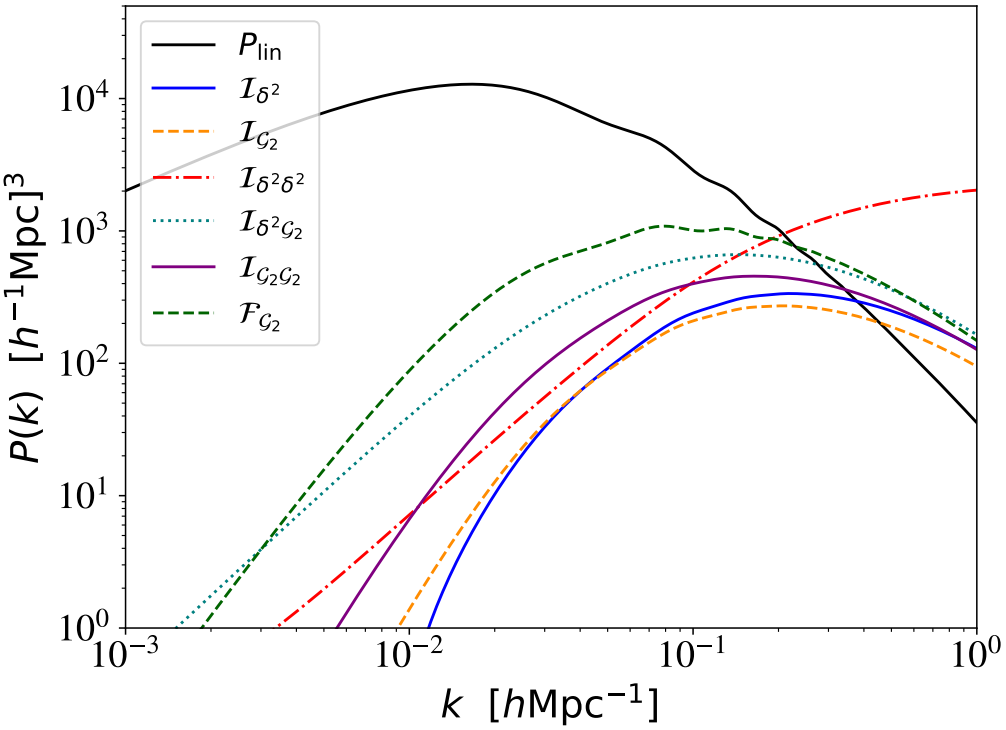

FIGURE 2.6 – Linear galaxy power spectrum and 1-loop integrals used to construct the non-linear galaxy power spectrum. Taken from (CHUDAYKIN et AL. 2020)

On large scales, the linear bias provides a simple scaling between the matter and galaxy density fields. In the local Eulerian biasing scheme, one further assumes that the galaxy density field is a local function of the matter density field. At semi-linear scales ($r \approx 20h^{-1}$ Mpc), where fluctuations are still expected to be small, we can Taylor expand the galaxy density field

$$\delta_g(\mathbf{x}) = b_1\delta_1(\mathbf{x}) + \frac{b_2}{2!}\delta_2(\mathbf{x}) + .. + \frac{b_n}{n!}\delta_n(\mathbf{x}). \tag{2.218}$$

The issue with this formulation is that high-order terms receive a contribution from all scales and are not necessarily small. A first approach to avoid this issue is to smooth out the density field on scales above a characteristic smoothing scale. However, the choice of smoothing scale is arbitrary, and should not appear in any local bias prescription. Instead, MCDONALD et AL. 2009 introduced the so-called renormalisation procedure, the idea being to add local counter terms to high-order δ_n

to suppress their amplitude. In the above Taylor expansion, such approach includes dependencies on the local values of the gravitational and velocity potentials, Φ and Φ_v respectively.

Here we follow the renormalisation scheme described in ASSASSI et AL. 2014 and SIMONOVIĆ 2018, where the expression for the biased density field at 1-loop is given by

$$\delta_{\rm g} = b_1\delta + \frac{b_2}{2}\delta^2 + b_{\mathcal{G}_2}\mathcal{G}_2 + b_{\Gamma_3}\Gamma_3. \tag{2.219}$$

The operators $\mathcal{G}_2$ and Γ_3 are defined as

$$\mathcal{G}_2(\phi) \equiv (\partial_i\partial_j\phi)^2 - (\partial^2\phi)^2, \tag{2.220}$$

$$\Gamma_3(\phi,\phi_v) \equiv \mathcal{G}_2(\phi) - \mathcal{G}_2(\phi_v). \tag{2.221}$$

In the local Lagrangian picture, the non-local bias parameters $b_{\mathcal{G}_2}$ and b_{Γ_3} are related to the linear bias parameter b_1 as

$$b_{\mathcal{G}_2} = -\frac{2}{7}(b_1-1), \quad b_{\Gamma_3} = \frac{11}{42}(b_1-1). \tag{2.222}$$

With this biasing model, the galaxy-galaxy and galaxy-velocity divergence power spectra read (ASSASSI et AL. 2014, SIMONOVIĆ 2018)

$$\begin{aligned} P_{gg}(k) &= b_1^2 P_{\delta\delta}(k) + b_2 b_1 I_{\delta^2}(k) + 2b_1 b_{\mathcal{G}_2} I_{\mathcal{G}_2}(k) \\ &\quad + 2\left(b_1 b_{\mathcal{G}_2} + \frac{2}{5}b_1 b_{\Gamma_3}\right) F_{\mathcal{G}_2}(k) + \frac{1}{4}b_2^2 I_{\delta^2\delta^2}(k) \\ &\quad + b_{\mathcal{G}_2}^2 I_{\mathcal{G}_2\mathcal{G}_2}(k) + \frac{1}{2}b_2 b_{\mathcal{G}_2} I_{\delta_2\mathcal{G}_2}(k) \end{aligned} \tag{2.223}$$

$$\begin{aligned} P_{g\theta}(k) &= b_1 P_{\delta\theta}(k) + \frac{b_2}{4} I_{\delta^2\theta}(k) + b_{\mathcal{G}_2} I_{\mathcal{G}_2\theta}(k) \\ &\quad + \left(b_{\mathcal{G}_2} + \frac{2}{5}b_{\Gamma_3}\right) F_{\mathcal{G}_2\theta}(k). \end{aligned} \tag{2.224}$$

In the above equations, $I_{\delta^2}(k)$, $I_{\mathcal{G}_2}(k)$, $F_{\mathcal{G}_2}(k)$, $I_{\delta^2\delta^2}(k)$, $I_{\mathcal{G}_2\mathcal{G}_2}(k)$, $I_{\delta_2\mathcal{G}_2}(k)$, are 1-loop integrals, which expressions can be found in SIMONOVIĆ 2018. The expressions for $I_{\delta^2\theta}(k)$, $I_{\mathcal{G}_2\theta}(k)$, and $F_{\mathcal{G}_2\theta}(k)$ integrals are nearly identical as for $I_{\delta^2}(k)$, $I_{\mathcal{G}_2}(k)$, and $F_{\mathcal{G}_2}(k)$, except that the G_2 kernel replaces the F_2 kernel in $I_{\delta^2}(k)$, $I_{\mathcal{G}_2}(k)$ and $F_{\mathcal{G}_2}(k)$. These 1-loop integrals are computed using the method described in SIMONOVIĆ 2018, which uses a power-law decomposition of the input linear power spectrum to perform efficiently the integrals. We present in Fig. 2.6 a representation of these one-loop integrals. We note that the integral $I_{\delta^2\delta^2}(k)$ is divergent on large scales, and therefore the difference $|I_{\delta^2\delta^2}(k) - I_{\delta^2\delta^2}(0)|$ is shown in the figure. We also adopt this definition for the evaluation of $I_{\delta^2\delta^2}(k)$.

2.3 Two-point statistics in redshift space

2.3.1 Redshift-space distortions

In principle, the two-point correlation function provides the same amount of information as the power spectrum. In the eBOSS analysis described later in Chapter 4, both are measured with different methods, and cosmological measurements are afterwards combined to provide the most robust cosmological constraints. In this manuscript we will only consider the galaxy clustering in configuration space. Further information on the measurement of the power spectrum for a realistic survey geometry can be found in (GIL-MARIN et AL. 2020; DE MATTIA et AL. 2021; NEVEUX et AL. 2020).

In galaxy redshift surveys, we can determine for each galaxy the comoving distance $D_c(z)$ at the measured redshift z from the spectrum, assuming a fiducial cosmology. This, together with galaxy angular positions allows us to determine the three-dimensional positions of galaxies. These positions further allows measuring the galaxy two-point correlation function (2PCF), $\xi(r)$, which only depends depends on r in a isotropic Universe. However, we know that the evolution of matter perturbations induce peculiar velocities, which we cannot take into account when converting redshifts to distances. This introduces apparent distortions, which end up being a wonderful opportunity to probe both the density and velocity fields, which in turn enable inferring the growth rate of structure. This effect is called **redshift-space distortions**. The observed redshift of an object can be decomposed as

$$z_{\rm obs} = z_{\rm cosmo} + \delta z, \tag{2.225}$$

where $z_{\rm cosmo}$ is the Hubble flow, and δz is the redshift perturbation that can be written in a general way as (CHALLINOR et LEWIS 2011; H. ZHAO et AL. 2013; BRETON et AL. 2019),

$$\delta z = \frac{a_0}{a}\left[\frac{\mathbf{v}\cdot\mathbf{n}}{c} - \frac{(\psi-\psi_0)}{c^2} + \frac{1}{2}\left(\frac{v}{c}\right)^2 + \int_\tau^{\tau_0}\frac{\partial(\phi+\psi)}{\partial\tau}\mathrm{d}\tau\right], \tag{2.226}$$

where $\mathbf{n}$ is the unit LoS vector, $\mathbf{v}$ is the peculiar velocity of the object, and ϕ and Ψ are the Bardeen potentials (BARDEEN 1980). The first and third terms correspond to the non-relativistic and relativistic Doppler shifts. The second and fourth terms correspond to the relativistic gravitational shift and the integrated Sachs-Wolfe (ISW) effect, caused by time fluctuations of the Bardeen potentials along the LoS. BRETON et AL. 2019 investigated with simulations the contribution of each term and found that relativistic and lensing effects break the symmetry along the transverse direction, inducing a non-zero dipole moment of the 2PCF. However, these effects occurs at non-linear scale and are subdominant compared to the standard Doppler redshift. Thus we can approximate δz as

$$\delta z = \frac{\mathbf{v}\cdot\mathbf{n}}{c}(1+z_{\rm cosmo}). \tag{2.227}$$

We denote by s the distance in redshift space, $s \equiv D_c(z_{\rm obs})$, and r its (true) distance in real space. The latter equation reduces to

$$\mathbf{s} = \mathbf{r} + \frac{\mathbf{v}\cdot\mathbf{n}}{aH(a)}. \tag{2.228}$$

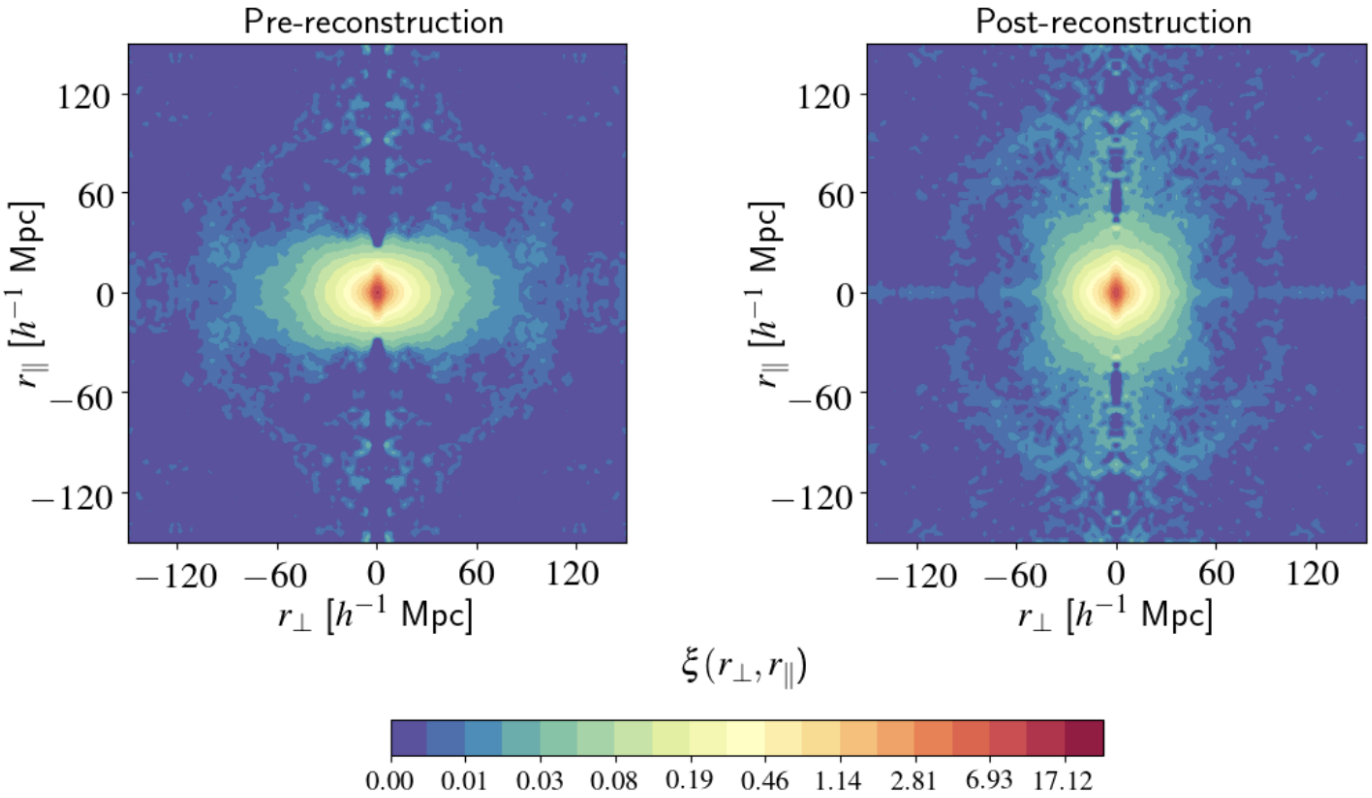

FIGURE 2.7 – Redshift-space two-point correlation function of the eBOSS luminous red galaxies (LRG) sample combined with the BOSS constant mass galaxies (CMASS) sample. in the redshift range $0.6 < z < 1.0$. The left (right) panel shows the (pre/post)-reconstruction 2PCF in bins $r_\parallel, r_\perp$. Bins of size 1.25 h^{-1}Mpc and bi-cubic interpolation have been used to produce the contours. Taken from (BAUTISTA et AL. 2021)

In Fig. 2.7 we illustrate the observed redshift-space 2PCF of the combined luminous red galaxies (LRG) and constant mass (CMASS) galaxy samples in the redshift range $0.6 < z < 1.0$. The distances between galaxies are decomposed into a radial $r_\parallel = r\mu$ and a transverse $r_\perp = \sqrt{r^2 - r_\parallel^2}$ component. The right panel applies a reconstruction technique to the density field to remove BAO non-linearity (see Section 2.3.2). This technique effectively eliminates most of the large-scale distortions and allows a clear detection of the BAO peak. Before reconstruction, one can look at the distortion pattern in the clustering of galaxies in redshift space.

On large separations, typically when $s > 40h^{-1}$Mpc, galaxies will have coherent peculiar motions induced by the growth of structure. They will tend to fall into the gravitational potentials of larger structures. Their apparent position will therefore be closer to the center of the potential Φ in redshift space than in real space, squashing the amplitude of the 2PCF along the LoS. This is the Kaiser effect. On smaller scales, galaxies trace the matter distribution of highly non-linear structures such as galaxy clusters, with size up between $r = 1-3\ h^{-1}$Mpc. In these virialized systems, galaxies have random motions with a velocity dispersion $\sigma_v \approx$ 200-500 km s^{-1} that is no longer negligible. These incoherent motions induce an elongation of the 2PCF amplitude along the LoS : the so-called Finger-of-God (JACKSON 1972)(FoG). For a biased tracer such as galaxies, the continuity equation 2.32 takes the form

$$\beta\delta + \frac{1}{Ha}\nabla\cdot\mathbf{v} = 0, \quad \beta \equiv \frac{f}{b}. \tag{2.229}$$

If we can measure the 2PCF of the galaxy density field δ_g at different redshifts and model it, then we can directly derived constraints on the time evolution of the linear growth rate f, and thus on the rate of the formation of cosmic structures over time.

Galaxy redshift surveys only probe a portion of the sky and are characterized by a radial selection function $\bar{n}(\mathbf{r})$, which corresponds to the mean number density of galaxies at comoving distance $\mathbf{r}$. The galaxy density field δ_g in real space is given by

$$\delta_g(\mathbf{r}) = \frac{n(\mathbf{r}) - \bar{n}(\mathbf{r})}{\bar{n}(\mathbf{r})}. \tag{2.230}$$

Since galaxies trace the underlying matter density field δ, which is a realisation of a random stochastic process, the galaxy distribution then forms a Poisson process and $\bar{\mathbf{n}}(\mathbf{r})$ actually corresponds to the probability of observing a galaxy at the position $\mathbf{r}$. The expectation value of the covariance of the overdensity field will thus be contaminated by a Poisson shot-noise term

$$\langle \delta_{\rm obs}(\mathbf{r}_1)\delta_{\rm obs}(\mathbf{r}_2)\rangle \equiv \delta^D(\mathbf{r}_1 - \mathbf{r}_2)[\bar{n}(\mathbf{r}_1)]^{-1}. \tag{2.231}$$

For a Poisson process and a finite separation $|\mathbf{r}_1 - \mathbf{r}_2| \neq 0$, we have that

$$\langle \delta_{\rm obs}(\mathbf{r}_1)\delta_{\rm obs}(\mathbf{r}_2)\rangle = \xi(r_{12}). \tag{2.232}$$

In redshift space, we drop the isotropic condition and therefore

$$\langle \delta_{\rm obs}(\mathbf{s}_1)\delta_{\rm obs}(\mathbf{s}_2)\rangle \equiv \xi^s(\mathbf{s}_1, \mathbf{s}_2, s_{12}). \tag{2.233}$$

If the angle between the positions $\mathbf{s}_1$ and $\mathbf{s}_2$ is small, the LoS distortions are plane-parallel, and the redshift-space correlation function can be decomposed in term of a parallel $s_\parallel$ and a transverse $s_\perp$ component,

$$\xi^s(\mathbf{s}_1, \mathbf{s}_2, s_{12}) \approx \xi^s(s_\parallel, s_\perp). \tag{2.234}$$

This is the plane-parallel approximation, widely used in both measurements of the anisotropic two-point statistics and in its theoretical modelling. Let us define the observed density field in redshift space as (Kaiser 1987; Andrew Hamilton 1998)

$$\delta^s_{\rm obs}(\mathbf{s}) = \frac{n^s(\mathbf{s}) - \bar{n}^s(\mathbf{s}))}{\bar{n}^s(\mathbf{s})}, \tag{2.235}$$

where $\bar{n}^s(\mathbf{s})$ and $n^s(\mathbf{s})$ are the *selection function* and the number density of galaxies at position $\mathbf{s}$ in redshift space. The selection function corresponds to the mean density of object at position $\mathbf{s}$. The conservation of the number of galaxies yields

$$n^s(\mathbf{s})d^3(\mathbf{s}) = n(\mathbf{r})d^3(\mathbf{r}). \tag{2.236}$$

We can re-express the latter equation in term of overdensities using 2.235 as

$$[1 + \delta^s(\mathbf{s})]\mathrm{d}^3 s = [1 + \delta(\mathbf{r})]\mathrm{d}^3 r, \tag{2.237}$$

where we have used the fact that the mean number density of galaxies is the same in both space. For convenience, we will express distance in velocity units as in (Andrew Hamilton 1998; Mo, Bosch et White 2012) such that Eq. 2.228 can be written as

$$\mathbf{s} = \mathbf{r} + v_r \mathbf{u}, \tag{2.238}$$

with v_r the velocity projected along the radial direction, $r \equiv H_0 d$, and $s \equiv cz$. Given Eq. 2.237 we find that

$$1 + \delta^s(\mathbf{s}) = \frac{r^2}{(r + v_r)^2}\left(1 + \frac{\partial v_r}{\partial r}\right)^{-1}[1 + \delta(\mathbf{r})]. \tag{2.239}$$

In the linear regime, the peculiar velocity field is related to the density field as

$$\delta(\mathbf{r}) = -\frac{\nabla_{\mathbf{r}} \cdot \mathbf{v}}{\beta} \tag{2.240}$$

This is the same as Eq. 2.229 except that the H factor have been reabsorbed into the distance $r = H_0 d$. We will now assume that peculiar velocities are small compared to the relative distance between the observer and the object $v_r \ll |r|$, in the linear regime $\delta \ll 1$, which also imply $\partial v_r / \partial r \ll 1$. Thus we have that

$$\delta^s(\mathbf{s}) = \delta(\mathbf{r}) - \left(\frac{\partial}{\partial r} + \frac{2}{r}\right) v_r. \tag{2.241}$$

In the linear regime, we can express v as a gradient of a potential such that Eq. 2.240 can be written as

$$v_r = -\beta \frac{\partial}{\partial r} \nabla_{\mathbf{r}}^{-2} \delta. \tag{2.242}$$

finally we have that

$$\delta^s = \mathbf{S}\delta, \tag{2.243}$$

where $\mathbf{S}$ is called the linear redshift operator :

$$S = 1 + \beta \left(\frac{\partial^2}{\partial r^2} + \frac{2\partial}{r\partial r}\right) \nabla_{\mathbf{r}}^{-2}. \tag{2.244}$$

In the plane-parallel approximation, this reduces to

$$\mathbf{S}^p = 1 + \beta \frac{\partial^2}{\partial z^2} \nabla_{\mathbf{z}}^{-2}, \tag{2.245}$$

where we have chosen z for the LoS vector. In Fourier space, $(\partial^2/\partial z^2)\nabla^{-2} = k_z^2/k^2 = \mu_{\mathbf{k}}^2$ with $\mu_{\mathbf{k}}$ the cosine of the angle between the wavevector $\mathbf{k}$ and the LoS $\mathbf{z}$. Strictly speaking, this angle is different from the angle in configuration space $s_\parallel = s\mu$, but we will keep the same notation in both space for simplicity. Thus,

$$\delta^s(\mathbf{k}) = (1 + \beta\mu_{\mathbf{k}}^2)\delta(\mathbf{k}), \tag{2.246}$$

i.e. $\delta^s(\mathbf{k})$ is enhanced by a factor $1 + \beta\mu_{\mathbf{k}}^2$. The linear power spectrum in redshift space δ^s is finally given by (KAISER 1987)

$$P^s(\mathbf{k}) = (1 + \beta\mu_{\mathbf{k}}^2)^2 P(k). \tag{2.247}$$

Since $P^s(\mathbf{k})$ is a function of μ, we can compress the 2D information into multipole moments using the Legendre basis,

$$P^s(\mathbf{k}) = \sum L_l(\mu) P_l^s(k), \quad P_l^s(k) = \frac{2l+1}{2} \int_{-1}^{1} P^s(\mathbf{k}) L_l(\mu) \mathrm{d}\mu. \tag{2.248}$$

The first non-zero multipole moments (even ℓ) are given by

$$\begin{aligned} P_0^s(k) &= \left(1 + \frac{2}{3}\beta + \frac{1}{5}\beta^2\right) P(k), \\ P_2^s(k) &= \left(\frac{4}{3}\beta + \frac{4}{7}\beta^2\right) P(k) \\ P_4^s(k) &= \left(\frac{8}{35}\beta^2\right) P(k). \end{aligned} \tag{2.249}$$

P_0^s, P_2^s and P_4^s are respectively the monopole, quadrupole and hexadecapole moments of the power spectrum. We note that for $\ell = 0$, $L_\ell(\mu) = 1$ meaning that P_0^s corresponds to the angle-averaged

of redshift-space power spectrum. As we can see, redshift-space power spectrum multipoles are enhanced by factors of β only : infall velocities will make the density constrast appear larger in redshift space, this again corresponds to the Kaiser effect. In real space, the only non-vanishing multipole moment is the monopole, often simply referred to as the three-dimensional power spectrum. The linear RSD model does not provide unbiased estimate of β or f, and we need to go beyond linear theory.

Let us rewrite Eq. 2.228 as (Román SCOCCIMARRO et AL 1999)

$$\mathbf{s} = \mathbf{x} - f u_z(\mathbf{x})\hat{\mathbf{z}}, \tag{2.250}$$

where $u_z(\mathbf{x}) \equiv -v(\mathbf{x})\cdot\hat{\mathbf{z}}/(aH(a)f)$ and $\hat{z}$ is the LoS unit vector. In the plane-parallel approximation, the Jacobian of the transformation between real and redshift spaces is exactly given by $J(\mathbf{x}) = 1 - f\Delta_z u_z(\mathbf{x})$, with by definition $\mathrm{d}s^3 = J(\mathbf{x})\mathrm{d}x^3$. The conservation of the number of galaxies, Eq. 2.237, yields

$$\delta^s(\mathbf{s}) = \frac{\delta(\mathbf{x}) + 1 - J(\mathbf{x})}{J(\mathbf{x})} = \frac{\delta(\mathbf{x}) + f\Delta_z u_z(\mathbf{x})}{1 - f\Delta_z u_z(\mathbf{x})}. \tag{2.251}$$

The expression for the density field in redshift space is thus given by

$$\delta^s(\mathbf{k}) = \int_0^\infty \frac{\mathrm{d}^3 s}{(2\pi)^3} e^{-i\mathbf{ks}}\delta^s(\mathbf{s}) = \int_0^\infty \frac{\mathrm{d}^3 x}{2\pi^3} e^{-i\mathbf{kx}} e^{if k_z u_z(\mathbf{x})}[\delta(\mathbf{x}) + f\Delta_z u_z(\mathbf{x}))], \tag{2.252}$$

and the matter power spectrum in redshift space is given by

$$P^s(\mathbf{k}) = \int_0^\infty \frac{\mathrm{d}^3 r}{(2\pi)^3} e^{-i\mathbf{kr}} \langle e^{if k\mu\Delta U_z}[\delta(\mathbf{x}) + f\Delta_z u_z(\mathbf{x})][\delta(\mathbf{x'}) + f\Delta_z u_z(\mathbf{x'})]\rangle, \tag{2.253}$$

where $\Delta U_z = u_z(\mathbf{x}) - u_z(\mathbf{x'})$ is the pairwise LOS velocity and $r \equiv |x - x'|$. This expression is exact in the plane-parallel approximation and is the starting point for several quasi-linear RSD models in Fourier space.

The terms in the brackets describs the large-scale power enhancements due to peculiar infall velocities, the Kaiser effect. On smaller scales, the exponential factor will damp the power due to the random motions in collapsed structures, corresponding to the FoG. Since these motions correspond to the highly non-linear regime, they cannot be modelled rigorously using perturbation theory. For instance $\delta \approx 200$ at the cluster scale, which is well above the density contrast $\delta \approx 1$ assumed in perturbation theory. Historically, FoG effects have been mainly modelled phenomenologically by using a Gaussian or Lorentzian form, the latter being more accurate for a large variety of galaxy populations. It takes the form

$$D(k\mu\sigma_v) = \frac{1}{1 + (k\mu\sigma_v)^2}, \tag{2.254}$$

where σ_v is the pairwise velocity dispersion that can be treated as a nuisance parameter. However, there exists other forms as used in (HOU et AL. 2021) for instance, although they are equivalent to the Lorentzian form. Perturbation theory treatments can provide high-order corrections to better approximate the term inside the brackets. Two quasi-linear RSD models were used in the eBOSS LRG DR16 analysis : a hybrid version of the 1-loop TNS model (TARUYA, NISHIMICHI et SAITO 2010; DE LA TORRE et AL. 2017) for biased tracers and the Convolutional Lagrangian Perturbation Theory combined with Gaussian streaming model (CPLT-GS).

2.3.1.1 Hybrid TNS

SCOCCIMARRO 2004 proposed a simple ansatz for the redshift-space power spectrum by making the assumption that the exponential factor inside the term inside the brackets (ensemble average)

involving the density and velocity fields, can be put out of the ensemble average. In that case Eq. 2.253 simplifies to

$$P_{\rm g}^{s}(k,\mu) = D(k\mu\sigma_v)\big[P_{\rm gg}(k) + 2\mu^2 f P_{{\rm g}\theta} + \mu^4 f^2 P_{\theta\theta}(k)\big], \tag{2.255}$$

TARUYA, NISHIMICHI et SAITO 2010 proposed an improved model that takes into account the coupling between the exponential prefactor and the terms involving density and velocity fields inside the ensemble average, leading to two new correction terms C_A and C_B. In that case the final redshift-space power spectrum for biased tracer can be written as

$$P_{\rm g}^{s}(k,\mu) = D(k\mu\sigma_v)\big[P_{\rm gg}(k) + 2\mu^2 f P_{{\rm g}\theta} + \mu^4 f^2 P_{\theta\theta}(k) + C_A(k,\mu,f,b_1) + C_B(k,\mu,f,b_1)\big], \tag{2.256}$$

where the explicit form of $C_A(k,\mu,f,b_1)$ and $C_B(k,\mu,f,b_1)$ at 1-loop level is given by (TARUYA, NISHIMICHI et SAITO 2010)

$$C_A(k,\mu,f,b) = \sum_{m,n=1}^{3} b^{3-n} f^n \mu^{2m} P_{A_{mn}}(k), \tag{2.257}$$

$$C_A(k,\mu,f,b) = \sum_{n=1}^{4}\sum_{a,b=1}^{2} b^{4-a-b}(-f)^{a+b}\mu^{2n} P_{B_{nab}}(k), \tag{2.258}$$

with,

$$P_{A_{mn}}(k) = \frac{k^3}{(2\pi)^2}\left[\int_0^\infty {\rm d}r \int_{-1}^{1} {\rm d}x \left(A_{mn}(r,x)P_{\rm lin}(k) + \tilde{A}_{mn}(r,x)P_{\rm lin}(kr)\right) + P_{\rm lin}(k)\int_0^\infty {\rm d}r\, a_{mn}(r) P_{\rm lin}(kr)\right], \tag{2.259}$$

and

$$P_{B_{nab}}(k) = \frac{k^3}{(2\pi)^2}\int_0^\infty {\rm d}r \int_{-1}^{1} {\rm d}x B^n_{ab}(r,x)\frac{P_{a2}(k\sqrt{1+r^2-2rx})P_{b2}(kr)}{(1+r^2-2rx)^a}, \tag{2.260}$$

where $P_{12}(k) = P_{\delta\theta}$ and $P_{22}(k) = P_{\theta\theta}$. $A_{mn}(r,x)$, $\tilde{A}_{mn}(r,x)$, $a_{mn}(r)$ and $B^n_{ab}(r,x)$ are given in Appendix A of (TARUYA, NISHIMICHI et SAITO 2010).

This corresponds to a hybrid model that we used for the analysis of eBOSS luminous red galaxies. We call it 'hybrid' since the real-space non-linear power spectra are estimated using RESPRESSO and Bel et al. 2017 fitting functions, rather than perturbation theory calculations as in (TARUYA, NISHIMICHI et SAITO 2010). In the following, we shall refer to it as the TNS model for simplification. The two-point correlation function multipole moments $\xi_\ell(s)$ are obtained from the multipole moments of the redshift-space power spectrum $P_\ell(k)$, defined as

$$P_\ell(k) = \frac{2\ell+1}{2}\int_{-1}^{1} P(k,\mu)L_\ell(\mu)\,{\rm d}\mu, \tag{2.261}$$

where L_ℓ are Legendre polynomials. The P_ℓ are then Hankel transformed to obtain ξ_ℓ. For a given power spectrum multipole moment of order ℓ, the Hankel transform is given by

$$\xi_\ell(r) = \frac{i^\ell}{2\pi^2}\int_0^\infty k^2 j_\ell(kr)P_\ell(k)\,{\rm d}k, \tag{2.262}$$

where j_ℓ are the spherical Bessel functions. The Hankel transforms can be computed efficiently with the Fast Fourier Transform in logarithmic space (FFTlog) formalism Andrew HAMILTON 2000. The TNS model predicts non-vanishing even multipoles up to $\ell = 8$.

We could have employed the 2-loop version of the correction terms derived in (TARUYA et AL. 2013) and used in Fourier space in DE MATTIA et AL. 2021 and NEVEUX et AL. 2020. Redshift-space

corrections at 2-loop in the TNS model can be estimated using the REGPT formalism, and by damping the amplitude of the corrections at high k. We computed the 2-loop corrections with the code of (DE MATTIA et AL. 2021) [7] but keeping for the non-linear power spectra RESPRESSO and Bel et al. 2017 fitting functions (which are in very good agreement with REGPT $P_{\delta\theta}$ and $P_{\theta\theta}$). At $z \approx 1$, we found using numerical simulations that 2-loop corrections perform better by $\approx 0.5\sigma$ on $f\sigma_8$ parameter. However, at $z = 0.55$, we found that the 2-loop corrections do not perform as well as the 1-loop correction, leading to 1.5σ shifts on $f\sigma_8$ and $\alpha_\perp$. Therefore, we will only consider 1-loop corrections for consistency at all cosmic time. We remark that cosmological constraints on the growth of structure are expressed in terms of $f\sigma_8$, since the amplitude of the power spectrum and growth of structure are strongly degenerate.

In the end, our TNS model has 6 free parameters $[f, b_1, b_2, b_{\Gamma_3}, b_{\mathcal{G}_2}\sigma_v]$, where b_{Γ_3} and $b_{\mathcal{G}_2}$ can be kept fixed following the relation given by Eq. 2.222. Bispectrum (see Section 2.3.1.3) analyses of N-body simulation show that those relations are reasonable approximations (CHAN et AL. 2012,SAITO et AL. 2014). However, as pointed out in SÁNCHEZ et AL. 2017, fixing b_{Γ_3} to the local Lagrangian prediction is not optimal because b_{Γ_3} partially absorbs the scale dependence in b_1, which should be present in the bias expansion. We investigate in Section4.2.2 whether fixing b_{Γ_3} or not is optimal for the specific case of eBOSS LRG using NSERIES mocks. $b_{\mathcal{G}_2}$ is kept fixed to its Lagrangian prediction as it cannot be well constrained by 2pt-statistics only, given the considered scales.

2.3.1.2 CLPT with Gaussian streaming model

In configuration space and under some assumptions, Eq. 2.253 can be equivalently written as a convolution as (SCOCCIMARRO 2004)

$$1 + \xi^s(s_\perp, s_\parallel) = \int_{-\infty}^{\infty} \mathrm{d}r_\parallel [1 + \xi(r)]\, p(s_\parallel - r_\parallel | \mathbf{r}), \tag{2.263}$$

where $s_\parallel = s\mu$ and $r_\parallel = r\mu$ are redshift- and real-space separations along the LoS and $s = \sqrt{s_\parallel^2 + s_\perp^2}$. ξ(r) is the real-space correlation function and p is the probability distribution function of pairwise LOS velocities at a separation $\mathbf{r}$. This type of model is usually referred to as the streaming model.

Although CLPT is more accurate than Lagrangian Resummation Theory from MATSUBARA 2008 in real space, the small-scale modelling is not good enough to describe redshift-space distortions. This is particularly important given that part of peculiar velocities are generated by interactions that occur at the typical scales of clusters of galaxies ($r \sim 1$ Mpc). This can be solved by mapping the real-space CLPT modelto redshift space using the Gaussian Streaming (GS) model proposed by (REID et AL. 2011). In this model, the small-scale pairwise velocity distribution is assumed to have a Gaussian form, whose moments depend on the separation r and the angle between the separation vector and the LoS μ. The final redshift-space correlation function is obtained as

$$\begin{aligned} 1 + \xi^s(r_\perp, r_\parallel) = \int & \frac{1}{\sqrt{2\pi\left[\sigma_{12}^2(r) + \sigma_{\mathrm{FoG}}^2\right]}} [1 + \xi_(r)] \\ & \times \exp\left\{ -\frac{[r_\parallel - y - \mu v_{12}(r)]^2}{2\left[\sigma_{12}^2(r) + \sigma_{\mathrm{FoG}}^2\right]} \right\} \mathrm{d}y, \end{aligned} \tag{2.264}$$

where $\xi(r)$, $v_{12}(r)$, and $\sigma_{12}(r)$ are predicted by CLPT. We will quote this model as CLPT-GS in the following. The last function in the integral takes into account the scale-dependent halo-halo pairwise velocity and we have to introduce an extra parameter σ_{FoG} describing the FoG effect. REID et AL. 2011 demonstrated that the CLPT-GS model can predict the redshift-space clustering with an accuracy of ≈ 2 per cent when dark matter halos are used as tracers. Using galaxies, the accuracy

7. https://github.com/adematti/pyRegPT

decreases as $\sigma_{\rm FoG}$ increases. Considering that about 85 percent of the galaxies from the LRG sample are central galaxies (ZHAI et AL. 2017), the accuracy remains close to the one obtained using halos. In summary, given a assumed cosmology, that we shall call a *fiducial* cosmology, this RSD model has four free parameters $[f, F', F'', \sigma_{\rm FoG}]$.

Since $f(z)$ and $\sigma_8(z)$ are highly degenerated, $\sigma_8(z)$ is kept fix to its fiducial value in the analysis. However, we will show in Section4.2.2 that constraints on $f\sigma_8$ are strongly cosmology-dependent when α deviates too much from unity. We can reduce this dependency by re-computing σ_8 using $R = 8\alpha h^{-1}$Mpc, where α is the isotropic dilation factor obtained in the fit, this actually keeps the scale at which σ_8 is measured fixed relative to the data in units of h^{-1}Mpc, which only depends on $\Omega_{\rm m}^{\rm fid}$.

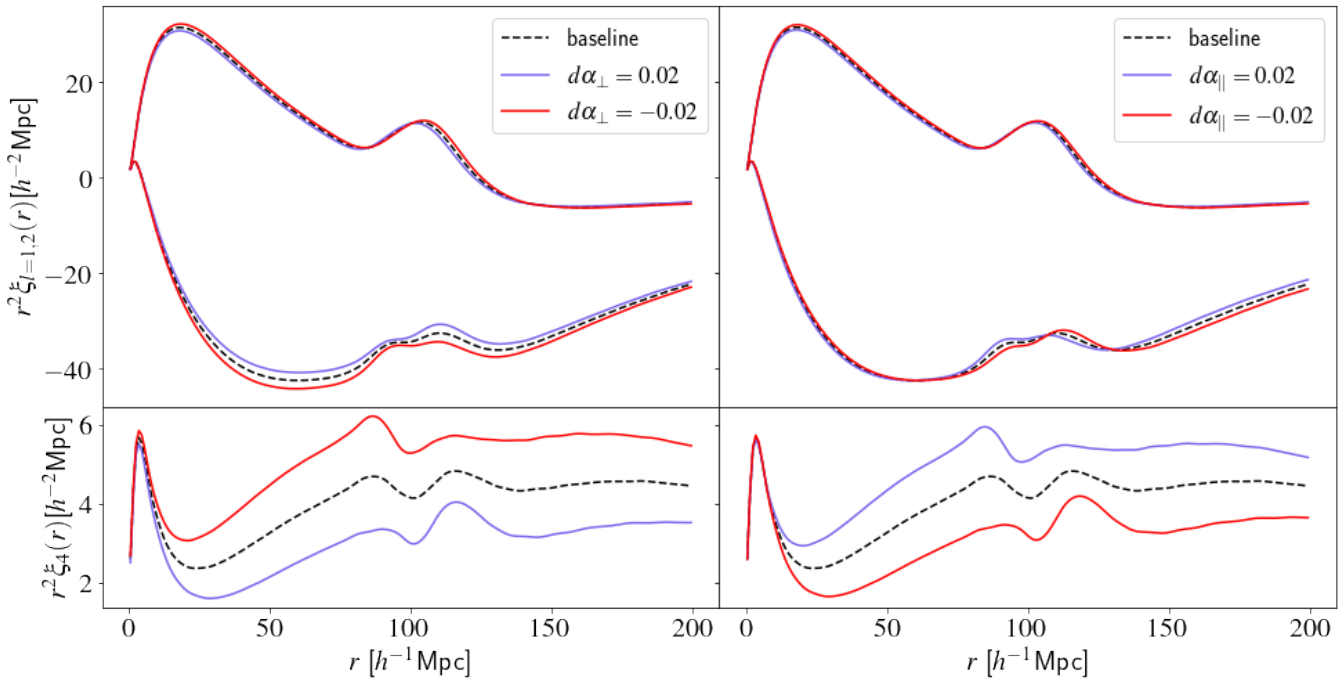

FIGURE 2.8 – Variation of the 2PCF TNS multipoles as a function of $\alpha_\perp$ (left) and $\alpha_\parallel$(right). The baseline configuration is at redshift $z = 0.7$ in the fiducial cosmology, see Eq. 2.281, with parameters $\alpha_\parallel = 1, = 1, \sigma_8 = 0.5, f = 0.88, b_1 = 1.0, b_2 = -0.2$, the other non-local bias parameters being fixed to Lagrangian prescription.

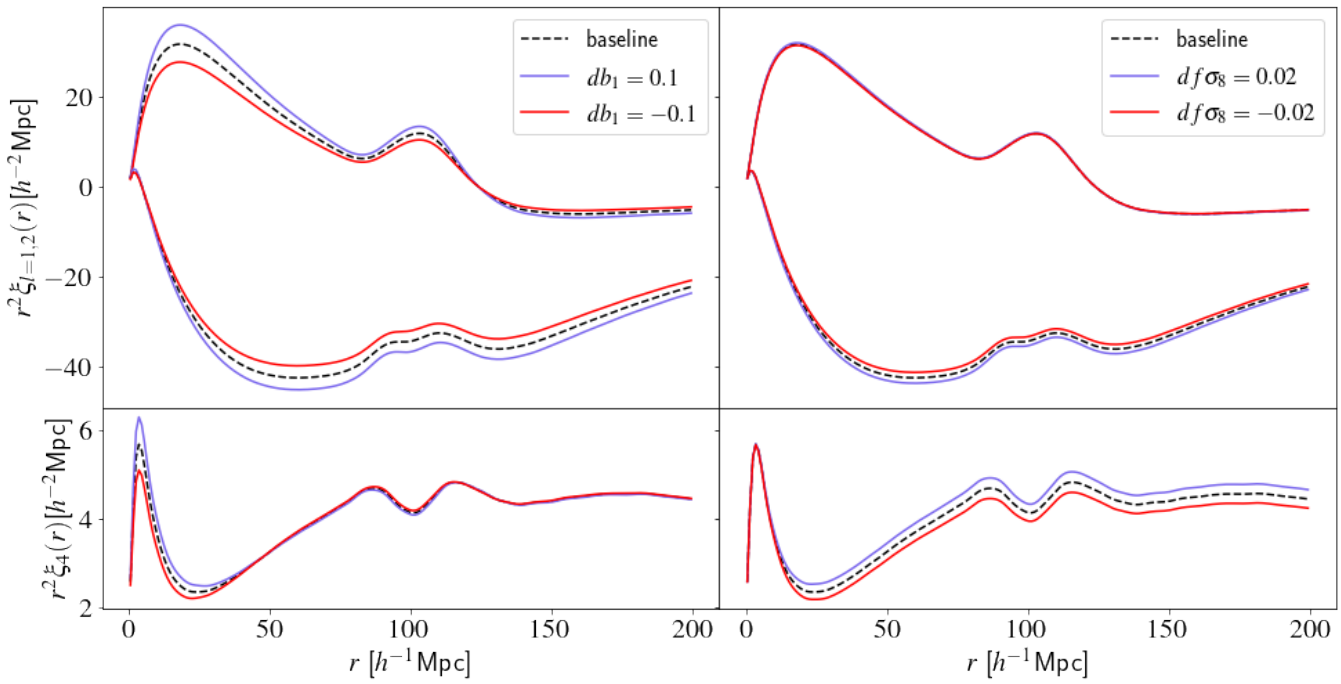

FIGURE 2.9 – Variation of the 2PCF TNS multipoles as a function of b_1 (left) and $f\sigma_8$ (right). Note that $f\sigma_8$ variations correspond to variations in f.

2.3.1.3 Visualisation of the TNS model

We will now illustrate the impact of each parameters on the shape of the predicted 2PCF by the TNS model. We present in Fig. 2.8 the variation of the anisotropic redshift space 2PCF as a function of $\alpha_\perp$ and $\alpha_\parallel$. The distortions perpendicular to the LoS, seem to have a larger impact on clustering than distortions parallel to the LoS, specially for the quadrupole. We can see an increase of all multipole amplitudes at semi-linear and BAO scales, with a small shift of BAO toward higher values, as $\alpha_\perp$ decreases. Variation in $\alpha_\parallel$ instead induces a shift of the BAO position in the quadrupole, with a positive correlation between $\alpha_\parallel$ and the hexadecapole amplitude. $\alpha_\parallel$ ($\alpha_\perp$) will preferentially affect separations with angle in the vicinity of $\mu \approx 1(0)$, and where Legendre moments $\ell = 2,4$ have different amplitudes. This explains the different impact of $\alpha_\perp$ and $\alpha_\parallel$ on the anisotropic multipole moments.

We present in Fig. 2.9 the variations of the 2PCF as a function of the linear bias b_1 and the growth rate $f\sigma_8$. As we can see, the amplitude of the monopole and quadrupole is strongly correlated with b_1. The linear bias has nearly no impact on the hexadecapole, except on small-scale, at $s < 40h^{-1}$ Mpc. Growth rate variations have a very small impact on the monopole amplitude, as excepted. $f\sigma_8$ only induces variation in the higher-order moments of the 2PCF, with an increase in amplitude in the quadrupole and hexadecapole as $f\sigma_8$ increases.

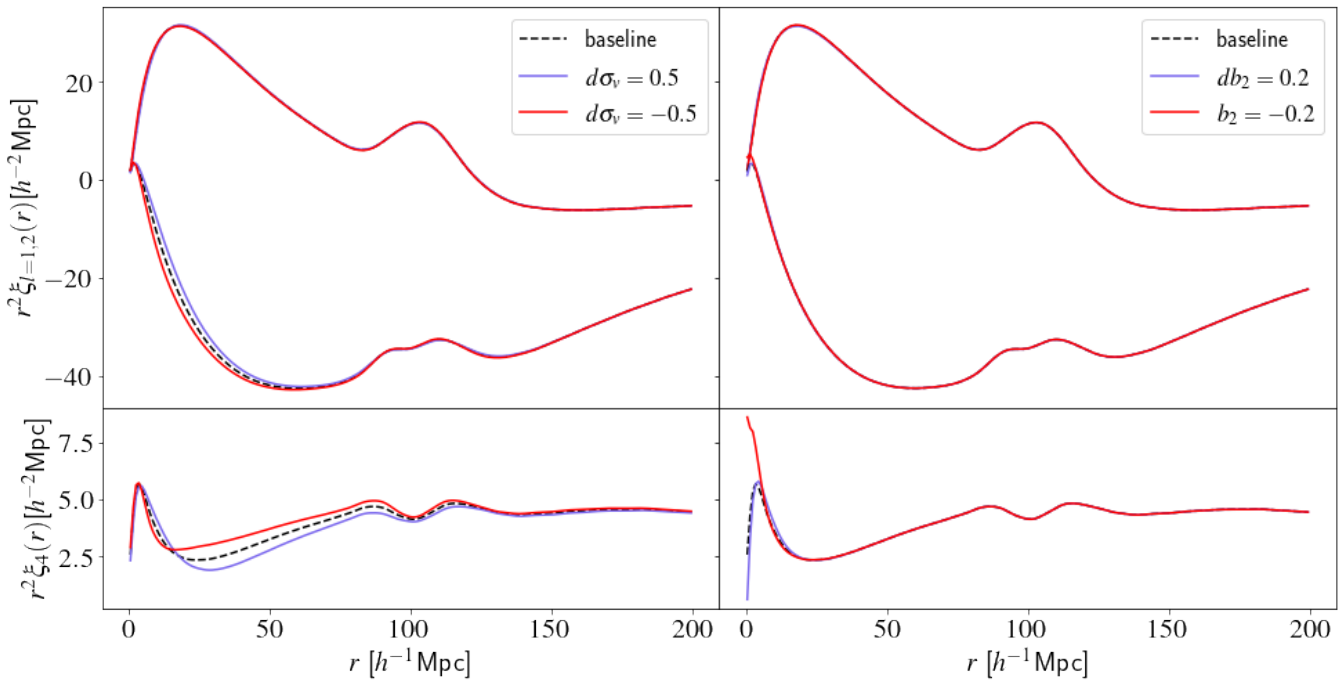

FIGURE 2.10 – Variation of the 2PCF TNS multipoles as a function of σ_v(left) andb_2(right).

We present in Fig. 2.10 the variation of the clustering as a function of the velocity dispersion, σ_v and the non-linear (quadratic) bias term b_2. Since σ_v models the velocities in the non-linear regime, it impact mostly the small-scale anisotropic multipoles. While the shape of the quadrupole does not strongly depend on the velocity dispersion, the hexadecapole moment is way more impacted, up to scale $s < 50h^{-1}$ Mpc. In addition it was reported in TARUYA et AL. 2013 that the modeling of these non-linear motions, through a phenomenological damping function, strongly affects the hexadecapole estimation. On the other hand, b_2 has a significant impact only on the very small scales of the hexadecapole, at $s < 30h^{-1}$ Mpc, nearly at the boundaries of typical full-shape RSD analysis in redshift surveys. Indeed this is due to the $I_{\delta^2\delta^2}$ integral being predominant at $k > 0.1\ h\mathrm{Mpc}^{-1}$.

We finally focus our attention at the impact of the b_{Γ_3} and $b_{\mathcal{G}_2}$ bias parameters presented in Fig. 2.11. Looking first at Eqs. 2.223 and 2.224, we see that both bias parameters multiply the same 1-loop integral for both power spectra. Actually, the kernel $F_{\mathcal{G}_2} \equiv 5/2F_{\Gamma_3}$ (ASSASSI et AL. 2014), which explains the 2/5 in front of b_{Γ_3}. Therefore, these two bias parameters are degenerated. Their effect on the 2PCF is thus exactly the same, except from the factor 2/5 in front. Variation of these bias parameters will influence the shape of all multipole moments on semi-linear scales, but mainly for the hexadecapole. We can also notice a non-negligible impact on the monopole BAO amplitude.

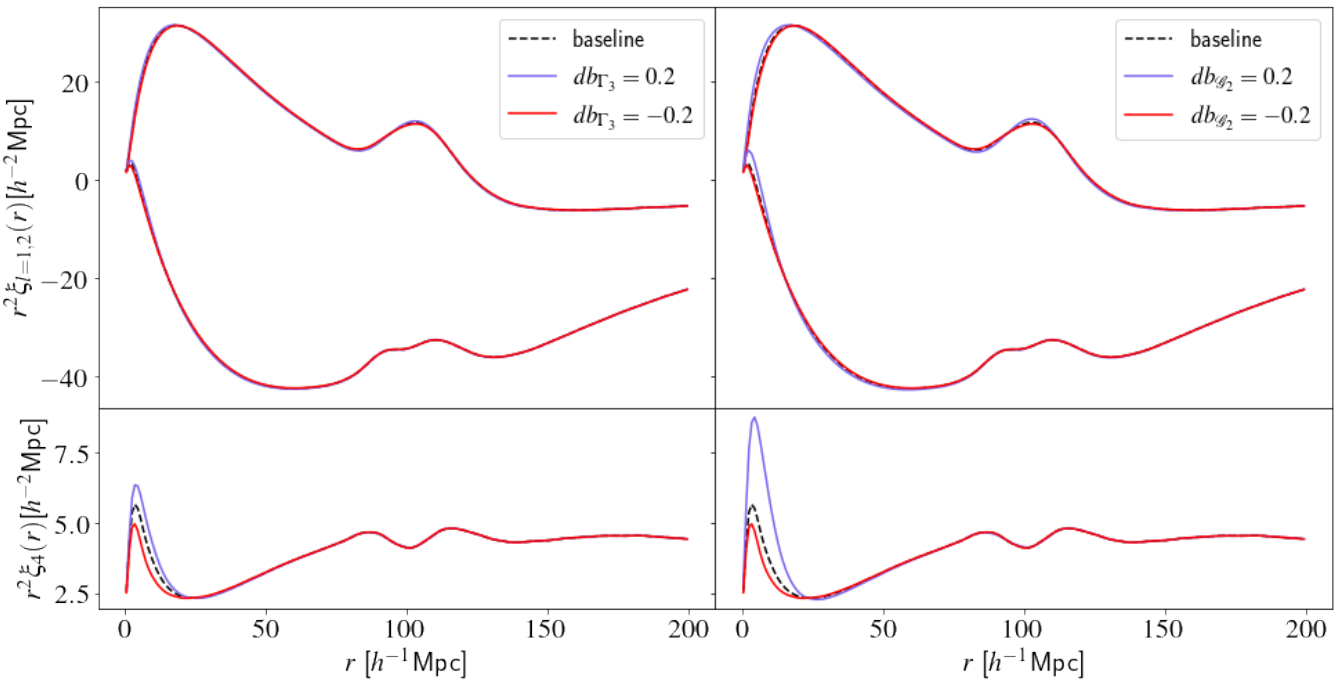

FIGURE 2.11 – Variation of the 2PCF TNS multipoles as a function of b_{Γ_3} (lef) and $b_{\mathcal{G}_2}$ (right).

2.3.2 Baryon acoustic oscillations

The sound horizon as already introduced in Eq. 2.156 can be written as

$$r_s = \int_{z_d}^{\infty} \frac{c_s(z)}{H(z)} \mathrm{d}z \tag{2.265}$$

and is measured up to extreme precision by PLANCK COLLABORATION 2018, $r_s = 147.21 \pm 0.23$ Mpc. One of the main goal of the BOSS and eBOSS collaboration (DAWSON et AL. 2013; DAWSON et AL. 2016) was to detect with great precision this feature, which was first observed by the pioneering large galaxy redshift surveys SDSS and 2dFGRS (COLE et AL. 2005). We illustrate in Fig. 2.12 the acoustic signal observed in the spatial distribution of galaxies probed by the BOSS survey (ALAM et AL. 2017). This acoustic feature is measured in all of the three overlapping redshift bins considered in the BOSS analysis, and provides precise geometrical constraints, when combined with Planck data, see Section 4.4.

2.3.2.1 The Alcock-Paczynski effect

In large spectroscopic surveys, one needs to assume a *fiducial* cosmology to convert observed angular positions and redshifts to cosmological distances. We usually consider a flat ΛCDM model as fiducal cosmology (but see in Section 4.4). In addition, a value for Ω_b, n_s, and A_s (or equivalently σ_8) is also needed to derive r_s and the power spectrum of fluctuations in the fiducial cosmology. BAO scale is measured anisotropically and decomposed into a transverse (sensitive to D_M) and a radial (sensitive to H) component. More specifically, one measure the observed shift in the BAO position with respect to its positions in the fiducial cosmology. This shift is associated to the so-called Alcock-Paczynski effect (ALCOCK et PACZYŃSKI 2001). Alcock-Paczynski distortions on observed galaxy separations are induced by using a wrong fiducial cosmology with respect to the

actual one. We thus introduce two dimensionless parameters

$$\alpha_\perp = \frac{D_M(z_{\rm eff})/r_d}{D_M^{\rm fid}(z_{\rm eff})/r_d^{\rm fid}}, \quad \alpha_\parallel = \frac{D_H(z_{\rm eff})/r_d}{D_H^{\rm fid}(z_{\rm eff})/r_d^{\rm fid}}, \tag{2.266}$$

with $D_H(z) = c/H(z)$, which describe the shift in separations parallel and perpendicular to the LoS. These shifts can be converted into a pure isotropic and anisotropic shift as these distortions are independent of redshift-space distortions, they are pure geometrical quantities. Thus we have

$$\alpha = \alpha_\parallel^{1/3}\alpha_\perp^{2/3}, \quad \epsilon = \left(\alpha_\parallel/\alpha_\perp\right)^{1/3} - 1. \tag{2.267}$$

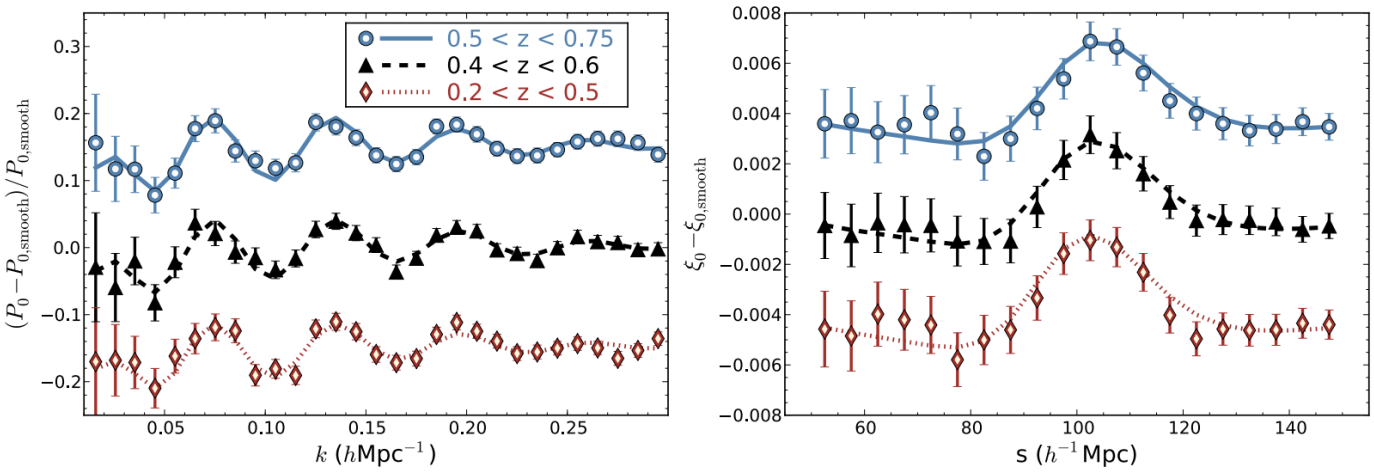

FIGURE 2.12 – BAO signals in the post-reconstruction power spectrum (left panel) and correlation function (right panel) and predictions of the best-fit models. Taken from (ALAM et AL. 2017)

2.3.2.2 Reconstruction

To remove non-linearities in the observed clustering of galaxies, and in particular the non-linear damping of the BAO peak, we can employ a reconstruction technique, which we will briefly describe in the following. The idea behind reconstruction is the go "backward" in time, by effectively removing peculiar velocities due to the growth of structure, and thus BAO non-linear damping. In BURDEN et AL. 2014, this is done using the first-order Lagrangian theory, the so-called Zel'dovich approximation. The relation between the Eulerian position $\mathbf{x}$ and the Lagrangian position $\mathbf{q}$ is

$$\mathbf{x}(\mathbf{q}, t) = \mathbf{q} + \Psi(\mathbf{q}, t), \tag{2.268}$$

with $\Psi(\mathbf{q}, t)$ the displacement field. Conservation of mass between the two spaces gives that the sum of the densities in Eulerian space is

$$\bar{\rho} d^3\mathbf{q} = \rho(\mathbf{x}, t) d^3\mathbf{x}, \tag{2.269}$$

where $\bar{\rho}$ is the mean number density in Lagrangian space, and $\rho(\mathbf{x}, t)$ is the density in Eulerian space at position $\mathbf{q}$. At linear order, the Eulerian overdensity is thus related to the displacement field as

$$\nabla_q \cdot \Psi_{(1)}(\mathbf{k}) = -\delta_{(1)}(\mathbf{k}) \tag{2.270}$$

with δ the overdensity in Eulerian space, and the subscript (1) denotes the fact that we are at first order. Once again, assuming that the displacement field is a gradient of the Lagrangian potential

we have that

$$\Psi(\mathbf{k}) = \frac{i\mathbf{k}}{k^2}\delta(\mathbf{k}), \tag{2.271}$$

which corresponds to the Lagrangian displacement field in the Zel'dovich approximation ZEL'DOVICH et AL. 1970. We can then displace galaxies given the real density contrast. To account for galaxy bias and RSD, Eq. 2.270 can be re-written as (PADMANABHAN et AL. 2012)

$$\nabla\Psi + \frac{f}{b}\nabla\cdot(\Psi\cdot\hat{r})\hat{r} = -\frac{\delta_g}{b}. \tag{2.272}$$

The galaxy sample used in BAUTISTA et AL. 2021 that we will introduce shortly, is composed of high-z CMASS galaxies observed by the BOSS survey combined with LRGs observed by eBOSS. Both are relatively biased with respect to the underlying density field and $b \approx 2-2.5$. Given the universal relation $f(\Omega_m) = \Omega_m^{6/11}$ for any ΛCDM cosmology, we can estimate f at the effective redshift (see Eq. 4.81) of our sample given our fiducial cosmology. We apply the reconstruction technique [8] with $b = 2.3$ and $f(z = 0.72) = 0.815$. Galaxies are point-like estimators of the underlying field. It is therefore necessary to smooth the observed spatial distribution to provide a continuous estimator of δ. In our analysis we use a smoothing scale of 15 h^{-1}Mpc. It has been show in CARTER et AL. 2020 that reconstruction results are insensitive to the choice of these parameters. There are other ways to reconstruct the density field than using the Lagrangian approach. One alternative is to apply the principle of least action directly to the galaxies, which can provide even more accurate reconstruction of the density field, see (SARPA et AL. 2019).

2.3.2.3 BAO modelling

The modelling of the BAO feature (only) in the 2PCF is more phenomenological than for redshift-space distortions. We describe here the standard modelling in configuration space used in previous SDSS analyses (e.g. ANDERSON et AL. 2014, ROSS et AL. 2017, BAUTISTA et AL. 2018) and in the final eBOSS analysis of BAUTISTA et AL. 2021. We aim at modelling the correlation function multipoles $\xi_\ell(r)$ on scales relevant to BAO ($40 < r < 180$ h^{-1}Mpc). The redshift-space anisotropic galaxy power-spectrum $P(k,\mu)$ is modelled as

$$P(k,\mu) = \frac{b^2\left[1+\beta(1-S(k))\mu^2\right]^2}{(1+k^2\mu^2\Sigma_s^2/2)} \times \left[P_{\text{no peak}}(k) + P_{\text{peak}}(k)e^{-k^2\Sigma_{\text{nl}}^2(\mu)/2}\right]. \tag{2.273}$$

where b is the linear bias, $\beta = f/b$ is the redshift-space distortions parameter. The non-linear broadening of the BAO peak is accounted for by multiplying the "peak-only" power spectrum P_{peak} (see below) by a Gaussian distribution with $\Sigma_{\text{nl}}^2(\mu) = \Sigma_\parallel^2\mu^2 + \Sigma_\perp^2(1-\mu^2)$. The non-linear random motions on small-scale are modeled by a Lorentzian distribution parametrised by Σ_s. In likelihood analysis, the values of $(\Sigma_\parallel, \Sigma_\perp, \Sigma_s)$ are held fixed to improve convergence. The values chosen for these damping terms were obtained from fits to the average correlation function in simulations. For the eBOSS analysis, we use the NSERIES mocks (see Section 3.1.5), which are based on N-body simulations. We show in Section 4.2.1 that our results are insensitive to small changes to those values. Following SEO et AL. 2016 theoretical considerations, we also apply a term $S(k) = e^{-k^2\Sigma_r^2/2}$ to the post-reconstruction modeling of the correlation function ($S(k) = 0$ for the pre-reconstruction BAO model). This term accounts for the smoothing used in our reconstruction technique.

We follow the procedure from KIRKBY et AL. 2013 to decompose the BAO peak component P_{peak} from the linear power-spectrum P_{lin}. We start by computing the correlation function by Fourier-transforming P_{lin}, then we model the correlations over the peak region by a polynomial function fitted using information outside the peak region ($50 < r < 80$ and $160 < r < 190 h^{-1}$Mpc).

8. https://github.com/julianbautista/eboss_clustering, this code is also used for DR16 results

The resulting correlation function is then Fourier-transformed back to get $P_{\text{no peak}}$. The analysis in Fourier space uses the same procedure GIL-MARIN et AL. 2020. Previous BOSS & eBOSS BAO analyses used the approximate formulae from EISENSTEIN et AL. 1998 for decomposing the peak. We have checked that both methods yield only negligibly different results. We estimate the correlation function multipoles $\xi_\ell(s)$ with Eqs. 2.261 and 2.262. The BAO peak position is parameterised via the dilation parameters $\alpha_\perp$ and $\alpha_\parallel$ such that the power spectrum multipoles take the form (GIL-MARIN et AL. 2020)

$$P_\ell(k) = \frac{2\ell+1}{2\alpha_\perp\alpha_\parallel^2}\int_{-1}^{1} \mathrm{d}\mu \mathscr{L}_\ell(\mu) P[k'(k,\mu),\mu'(\mu)], \tag{2.274}$$

with

$$k' = \frac{k}{\alpha_\perp}\left[1+\mu^2\left(\frac{1}{F_\epsilon^2}-1\right)\right]^{1/2}, \tag{2.275}$$

$$\mu' = \frac{\mu}{F_\epsilon}\left[1+\mu^2\left(\frac{1}{F_\epsilon^2}-1\right)\right]^{-1/2}, \tag{2.276}$$

and $F_\epsilon = \alpha_\parallel/\alpha_\perp$. In our implementation, we apply the scaling factors exclusively to the peak component of the power spectrum. As shown by KIRKBY et AL. 2013 the decoupling between the peak and broad-band shape of the correlation function makes the constraints on the dilation parameters only dependent on the BAO peak position, with no information coming from the broad-band shape as this the case in RSD analysis.

The final BAO model is a combination of the cosmological multipoles ξ_ℓ and a smooth function of separation. The smooth function is meant to account for unknown systematic effects in the survey that potentially create large-scale correlations, which could contaminate our measurements. It is worth noting that there are currently no accurate analytical models for the post-reconstruction multipoles, as the $S(k)$ term in Eq. 2.273 is generally not sufficient). Our final BAO template-model is

$$\xi_\ell^t(r) = \xi_\ell(\alpha_\perp,\alpha_\parallel,r) + \sum_{i=i_{\min}}^{i_{\max}} a_{\ell,i}\, r^i. \tag{2.277}$$

Our baseline analysis uses $i_{\min} = -2$ and $i_{\max} = 0$, corresponding to three nuisance parameters per multipole moment. We find that increasing the numbers of nuisance terms does not impact significantly the results. Note that this smooth function cannot be used in the full-shape RSD analysis, since these terms would be completely degenerate with the growth parameter.

The baseline BAO analysis uses the monopole ξ_0 and the quadrupole ξ_2 of the correlation function. Fits to mock samples including the hexadecapole show that ξ_4 does not add information (see Table 4.4). In likelihood data analysis, the broadband parameters are let free, while both dilation parameters are allowed to vary between 0.5 and 1.5. A total of 9 parameters are fitted simultaneously.

For the RSD models considered previously, we instead follow the Alcock-Paczynski implementation of (XU et AL. 2013). In RSD analysis, we are interested in the $\ell = \{0,2,4\}$ multipole moments.

Given a model ξ_0, ξ_2, and ξ_4, the same quantities in the fiducial cosmology are given by

$$\xi_0^{\rm fid}(r^{\rm fid}) = \xi_0(\alpha r) + \frac{2}{5}\epsilon\left[3\xi_2(\alpha r) + \frac{{\rm d}\xi_2(\alpha r)}{{\rm d}\ln(r)}\right], \tag{2.278}$$

$$\xi_2^{\rm fid}(r^{\rm fid}) = \left(1+\frac{6}{7}\epsilon\right)\xi_2(\alpha r) + 2\epsilon\frac{{\rm d}\xi_0(\alpha r)}{{\rm d}\ln(r)} + \frac{4}{7}\epsilon\frac{{\rm d}\xi_2(\alpha r)}{{\rm d}\ln(r)} + \frac{4}{7}\epsilon\left[5\xi_4(\alpha r) + \frac{d\xi_4(\alpha r)}{{\rm d}\ln(r)}\right], \tag{2.279}$$

$$\xi_4^{\rm fid}(r^{\rm fid}) = \xi_4(\alpha r) + \frac{36}{35}\epsilon\left[-2\xi_2(\alpha r) + \frac{{\rm d}\xi_2(\alpha r)}{{\rm d}\ln(r)}\right] + \frac{20}{77}\epsilon\left[3\xi_4(\alpha r) + 2\frac{{\rm d}\xi_4(\alpha r)}{{\rm d}\ln(r)}\right] + \frac{90}{143}\left[7\xi_6(\alpha r) + \frac{{\rm d}\xi_6(\alpha r)}{{\rm d}\ln(r)}\right]. \tag{2.280}$$

This corresponds to an approximation for small variations around $\alpha = 1$ and $\epsilon = 0$. We compared this implementation to the exact implementation of AP distortions given by Eq. 2.274. We found that both implementations give extremely similar results. Throughout the rest of the manuscript, the fiducial cosmology will refer to the one used in (BAUTISTA et AL. 2021),

$$\Omega_m = 0.310 \quad \Omega_c = 0.260 \quad \Omega_b = 0.048 \quad \Omega_\nu = 0.0014 \quad h = 0.676 \quad n_s = 0.970 \quad s_8 = 0.80. \tag{2.281}$$

2.3.3 Complementary large-scale structure analyses

So far, we only discussed two-point statistics of the galaxy density field. One can also use at higher-order statistics of the galaxy distribution, in particular the three-point correlation or its Fourier counterpart the bispectrum. Following the definition of the power spectrum, see Eq. 2.186, we can define the bispectrum as (GIL-MARIN, NOREÑA et AL. 2015)

$$(2\pi^3)\langle\delta_{\mathbf{k}_1}\delta_{\mathbf{k}_1}\delta_{\mathbf{k}_3}\rangle = B(k_1,k_2)\delta^D(\mathbf{k}_1+\mathbf{k}_2+\mathbf{k}_3). \tag{2.282}$$

As illustrated in Fig. 2.2, the three-point correlation function can be defined as (BERNARDEAU et AL. 2002)

$${\rm d}P_{123} = n^3[1+\xi(x_{12}+\xi(x_{23}+\xi(x_{31}+\xi_3(x_{12},x_{23},x_{31})]{\rm d}V_1{\rm d}V_2{\rm d}V_3. \tag{2.283}$$

In the work of (GIL-MARIN, NOREÑA et AL. 2015; GIL-MARIN et AL. 2015), the combination of $f\sigma_8$ measured with the power spectrum and $f^{0.43}\sigma_8$ measured with the bispectrum breaks the degeneracy between f and σ_8, allowing for tight constraints for these 2 parameters. Combining growth rate measurements from bispectrum with Planck measurements (PLANCK COLLABORATION 2014), also provides constraints on neutrino mass (GIL-MARIN, NOREÑA et AL. 2015).

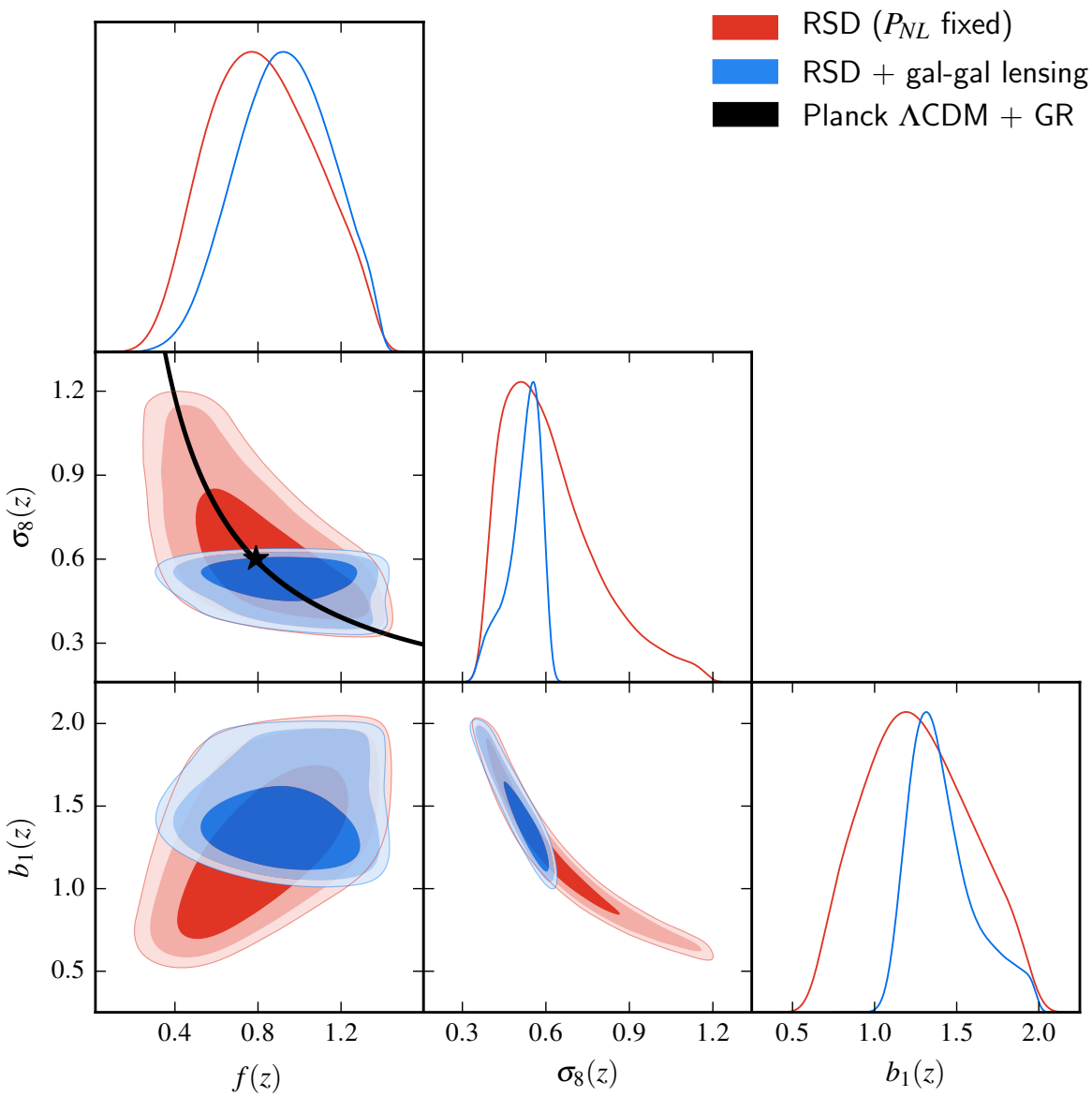

FIGURE 2.13 – Two-dimensional posterior contours for f and σ_8 at $0.5 < z < 0.7$, showing the impact of the additional galaxy-galaxy lensing constraint on the $f\ \sigma_8$ plane. Red contours represents the RSD fit only (with fixed power-spectrum template amplitude), Blue contours corresponds to the combination of RSD + galaxy-galaxy lensing. The black line shows the region of constant $f\sigma_8$ of (PLANCK COLLABORATION 2016) of the LCDM bestfit. The star corresponds to the combined $f\sigma_8$ measurement. Taken from (DE LA TORRE et AL. 2017)

Galaxy clustering measurements in redshift space can also be combined with galaxy-galaxy lensing measurements. Galaxy-galaxy lensing, i.e. the two-point correlation between the position of foreground galaxies and the shear of background galaxies, is sensitive $\xi_{\rm gm}$, the cross-correlation between galaxy and matter. Combining $\xi_{\rm gm}$ and $\xi_{\rm gg}$ measurements can break the degeneracy between f, b_1, σ_8, as we can see from Fig. 2.13 (DE LA TORRE et AL. 2017). Additionally, measurement of $\xi_{\rm gm}$ also breaks the degeneracy of the bias parameters b_{Γ_3} and $b_{\mathcal{G}_2}$ (ASSASSI et AL. 2014).

Finally, one can also probe the growth of structure in the linear regime through the growth of cosmic voids, see for example (AUBERT et AL. 2020). The statistical precision that will be achieved with future large-scale surveys (see Section4.4.4) will allows us to combine galaxy two-point statistics with these complementary LSS probes in a very efficient way.

2.4 Cosmological simulations

Beyond the analytical modelling of large-scale structure observables, it is important to introduce cosmological simulations. These are the cornerstone of modern cosmology and serve as an unique validation of the analytical theories that I described in Sections 2.1, 2.2, and 2.3. Numerical simulations uniquely allows us to probe non-linear structure formation in high-density environment, where perturbation theory breaks down. In this section, I will mainly review N-body simulations, which evolve only dark matter particle through gravity.

2.4.1 N-Body simulation

In general, N-body simulations evolve collisionless particles. Collisional N-body simulations on the other hand, allows collisions through momemtum exchange between particles. To do so, one needs to directly solve the Vlasov and Poisson equations, which describe the evolution of the phase-distribution function $f(\mathbf{x},\mathbf{p},t)$. However, solving these equations using a six-dimensional grid is computationally too expansive. This is why a discrete set of particles ($10^{10}-10^{12}$) are used in N-Body simulations.

Initial conditions

In N-body simulations, particles are evolved through gravity, starting from initial conditions specified at an early time ($z\approx 100$). There exists different ways of specifying the initial distribution of particles. One first solution is to use a random uniform sampling, however it generates spurious structure formation from sampling noise even when no perturbation are imposed. A second solution involves generating a regular grid of particles, but this lead to preferred directions and scales. WHITE 1994 introduces the glass-like distribution to overcome these issues. From a random uniform distribution, particles are evolved through gravity, but instead of assuming gravitational force to be positive, particles repulse each other. This step takes usually about 150 time steps and spans an expansion factor of 10^6. This results in a homogeneous distribution, which has no preferred scales or directions. Then a density field δ is generated following a Gaussian distribution, with variance given by a linear matter spectrum at the desired redshift using CLASS or CAMB for instance. Particles are assigned velocities, which can be done for example in the linear regime using Zel'dovich approximation. Once initial conditions are specified, different methods exists to describe the evolution of particles with gravity.

2.4.1.1 The particle-particle method

In the particle-particle (PP) method, the peculiar velocity of each particle is calculated as

$$\frac{d\mathbf{u}_i}{dt}+H\mathbf{u}_i=\frac{1}{m_i}\sum_{j\neq i}F_{ij} \tag{2.284}$$

where the gravitational force of particle j on particle i is

$$F_{ij}=-Gm_im_j\frac{\mathbf{r}_j-\mathbf{r}_i}{[|\mathbf{r}_j-\mathbf{r}_i|^2+\epsilon^2]^{3/2}}, \tag{2.285}$$

with ϵ a small, softening parameter. Softening reduces small-scale shot noise, and avoids divergence at null separations. This eases the calculation and allows for an increase of the number of particles of the simulation, by a few order of magnitude (DEHNEN 2001). Of course, softening introduces a bias with respect to Newtonian dynamics. The accuracy of the PP method scales as $\mathcal{O}(N^2)$, with N being the number of particles, thus faster techniques have been developed.

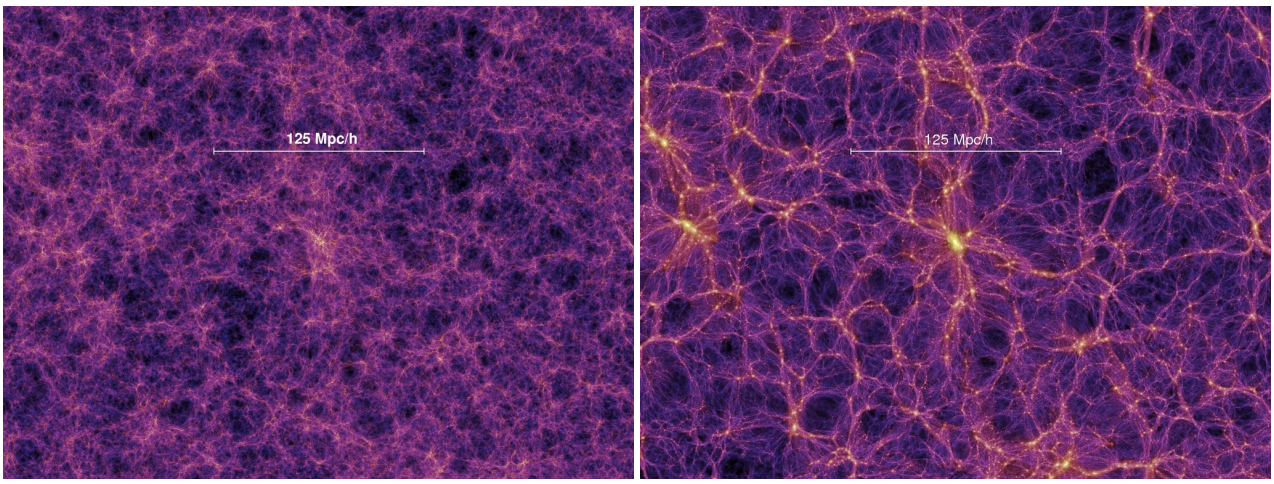

FIGURE 2.14 – Projected dark matter density field. Millennium simulation (SPRINGEL et AL. 2005) at redshift $z = 5.7$, $t = 1.0Gyr$ (left) and at redshift $z = 0$, $t = 13.6Gyr$ (right). Taken from https://wwwmpa.mpa-garching.mpg.de/galform/virgo/millennium/

2.4.1.2 The particle-mesh method

In the particle-mesh method (PM), the matter density field is evaluated on a grid with an interpolation kernel, typically cloud-in-cell or triangular shaped cloud (CUI et AL. 2008). The gravitational potential is evaluated on the grid using Poisson equation, solved in Fourier space with Fast Fourier Transforms (FFT), and softened at the grid cell size. This methods scales as FFT algorithms, i.e. $\mathcal{O}(N_c \ln N_c)$ with N_c the number of cells, plus the interpolation kernel that scales as $\prime(N)$. This method is fast, but inaccurate at scales below few cells sizes. The small-scale precision can be increase with adaptive mesh refinement methods (AMR), where the grid resolution is dynamically adapted in high-density environment. Another solution is the combination of PM and PP at small scale (a few cells sizes) leading to the P^3M method. If further combined with AMR in high-density regions, it leads to the AP^3M method (COUCHMAN 1991)

2.4.1.3 Tree codes

In tree codes, particles are grouped into hierarchically smaller and smaller cells, following a tree structure, which does not have to be recomputed at each time step. The gravitational potential of particle groups is expanded in multipoles around the groups center of mass. Smaller cells are considered until the opening angle (size over distance) is less than a given threshold parameter. These algorithms scale as $\mathcal{O}(N \log N)$ and can be coupled to PM codes. Hybrid Tree-PM codes are the most efficient algorithms for cosmological simulations (e.g. GADGET-2 SPRINGEL 2005). Alternatively, recent numerical simulations have been developed that directly solve the Vlasov-Poisson equation (O. HAHN et ANGULO 2016), thus eliminating the force softening and sampling noise.

2.4.1.4 Connection to galaxies

We present in Fig. 2.14 the projected density field of the Millenium Run simulation (SPRINGEL et AL. 2005) based on the GADGET-2 code. At early time, one can already observe the formation of the first structures that have grown from initial perturbations through gravitational instability. At later time, these structures (as well as voids) have further grown to form a clearly detectable cosmic web-like structure, with filaments of dark matter connecting nodes in overdense regions. Baryonic matter should fall into the most overdense structures, the halos, and eventually cool down and form

compact structures through dissipative processes, forming the first stars and galaxies. Halos are therefore the direct connection between the dark matter and galaxy density fields.

To take into account baryonic processes, one has to rely on hydrodynamical simulations. These simulation incorporate gas dynamics as well as photo-heating, radiative cooling, star formation, feedbacks (from stars, supernovae, active galactic-nuclei), magnetic fields, see for instance in the Illustris-TNG simulation (PILLEPICH et AL. 2018). There exists two types of hydrodynamical simulations : either using a Lagrangian framework with smooth particle hydrodynamical (SPH), which describes fluids with a discrete set of points, or using an Eulerian approach, by solving the fluid equations on a grid. Physical processes that take place below the simulation resolution are instead described with empirical models, tuned on observations with semi-analytical models of galaxy formation. Hydrodynamical simulations are nowadays one of the best approaches that we have to understand galaxy formation and evolution. However, they are numerically very expansive and limited in size, up to 300 h^{-1}Mpc for Illustris-TNG, and are therefore not suitable for the study of the large-scale structure. To link galaxies with halos, other approaches are possible, such as semi-analytical models or statistical models such as sub-halo abundance matching (SHAM) or halo occupation distribution (HOD) models. Before describing those models in more detail, it necessary to provide a theoretical description of a dark matter halo and to introduce the different methods developed to detect those halos in N-body simulations.

2.4.2 Structure formation

2.4.2.1 Spherical collapse

In the absence of cosmological constant, the radius of a mass shell in a spherical perturbation evolves according to the Newton equation

$$\frac{\mathrm{d}^2 r}{\mathrm{d}t^2} = -\frac{GM}{r^2}, \quad M = \frac{4}{3}\pi\rho R^3, \quad \rho = \bar{\rho}[1+\delta] \tag{2.286}$$

where M is the mass within the shell. M is independent of t before shell crossing, and the latter equation can be integrated once and yields

$$\frac{1}{2}\left(\frac{\mathrm{d}r}{\mathrm{d}t}\right)^2 - \frac{GM}{r} = E, \tag{2.287}$$

with E the energy of the mass shell. The system is bounded when the energy is negative, in this case the solution can be parametrised as follows :

$$R = \frac{R_m}{2}(1-\cos\theta), \quad t = \frac{t_m}{\pi}(\theta - \cos\theta), \tag{2.288}$$

where $R_m = -GM/E$ and $t_m = \pi(R_m)^{3/2}/(GM)^{1/2}$. First the radius grows up to $R = R_m$ at $t = t_m$ and then shrinks to $R = 0$ at $t = 2t_m$. In a EdS universe, the scaling relations in Table 1.1 and Friedmann equations 1.51 yield $\bar{\rho} = 1/(6\pi G t^2)$ and the density perturbation is

$$\delta = \frac{9MGt^2}{2R^3} - 1. \tag{2.289}$$

The solution given in Eq. 2.288 can be written at first order as

$$R(t) = \frac{R_m}{4}\left(\frac{6\pi t}{t_m}\right)^{2/3}\left[1 - \frac{1}{20}\left(\frac{6\pi t}{t_m}\right)^{2/3}\right]. \tag{2.290}$$

The spherical overdensity evolves in three phrases. First, it grows as $\delta \propto t^{2/3}$ until reaching its maximum at $t = t_m$. Then the structure collapse at $t = 2t_m$, where the model predicts $R = 0$. At linear order, this corresponds to $\delta_c \approx 1.686$, which is called the critical density for collapse. This value is nearly cosmology-independent (MO, BOSCH et WHITE 2012). In reality, the radius does not reach zero and the system reach an equilibrium at an overdensity $\delta_{\rm vir} = 177$ (MO, BOSCH et WHITE 2012).

2.4.2.2 Dark matter halos

Dark matter halos are defined as overdense gravitationally-bound systems. One can found other gravitationally-bound sub-structures, those are called sub-halos. In the literature, the halo boundary are usually express in terms of the virial radius $R_{\rm vir}$, defined as the radius where the mean matter density within the halo is $\Delta_{\rm vir}$ times the background density of the Universe, with $\Delta_{\rm vir} \sim 1+177 = 178$. However, this definition is sensitive to the expansion of the Universe, and halos will have an increasing size with time. Another definition for the halo boundary have been introduced by (MORE et AL. 2015) : the splashback radius, which segregates infalling from orbiting materials within a halo.

Within a simulation, halos can be found using multiples techniques. The most common methods are the spherical overdensity (SO) of PRESS et SCHECHTER 1974 and the Friends-of-Friend (FoF) algorithm of M. DAVIS et AL. 1985. SO algorithms locate density peaks and grow a spherical shell until the density falls below a threshold value (given by the spherical collapse model for example). The FoF algorithm instead identifies halo as a collection of particles. All particles below a given linking length are identified as members of the same halo. This approach can be extended to include velocity information. Then the halo center is either defined as the halo center of mass or the most bounded particle of the group. In N-body simulations, the *halo merger tree* keeps tracks of the halo merging history, it provides all the progenitors of a given halo. Merger trees are a powerful tool to investigate the so-called *halo assembly bias*. In the Millenium Run simulation, GAO, SPRINGEL et WHITE 2005 found that the amplitude of the 2PCF on large scales depends strongly on the halo formation time. For example, at a mass $10^{11} h^{-1}{\rm M}_\odot$ they found that 10% of the oldest halos are 5 times more clustered than the 10% younger. This assembly history have an impact on galaxy formation and evolution. For instance it has been shown in NAGAI et KRAVTSOV 2005 that sub-halos are rapidly stripped out of their material after accretion (by 30 % up to 70 %), while tidal stripping of galaxies occurs much later. Galaxies of similar stellar mass can therefore exhibit different clustering properties based on their formation history. By probing a large enough volume, we can mitigate the impact of assembly bias. Conversely, the statistical precision of next-generation survey such as DESI will allow us to directly detect this assembly bias in the large-scale structure.

2.4.2.3 Semi-analytical models of galaxy formation

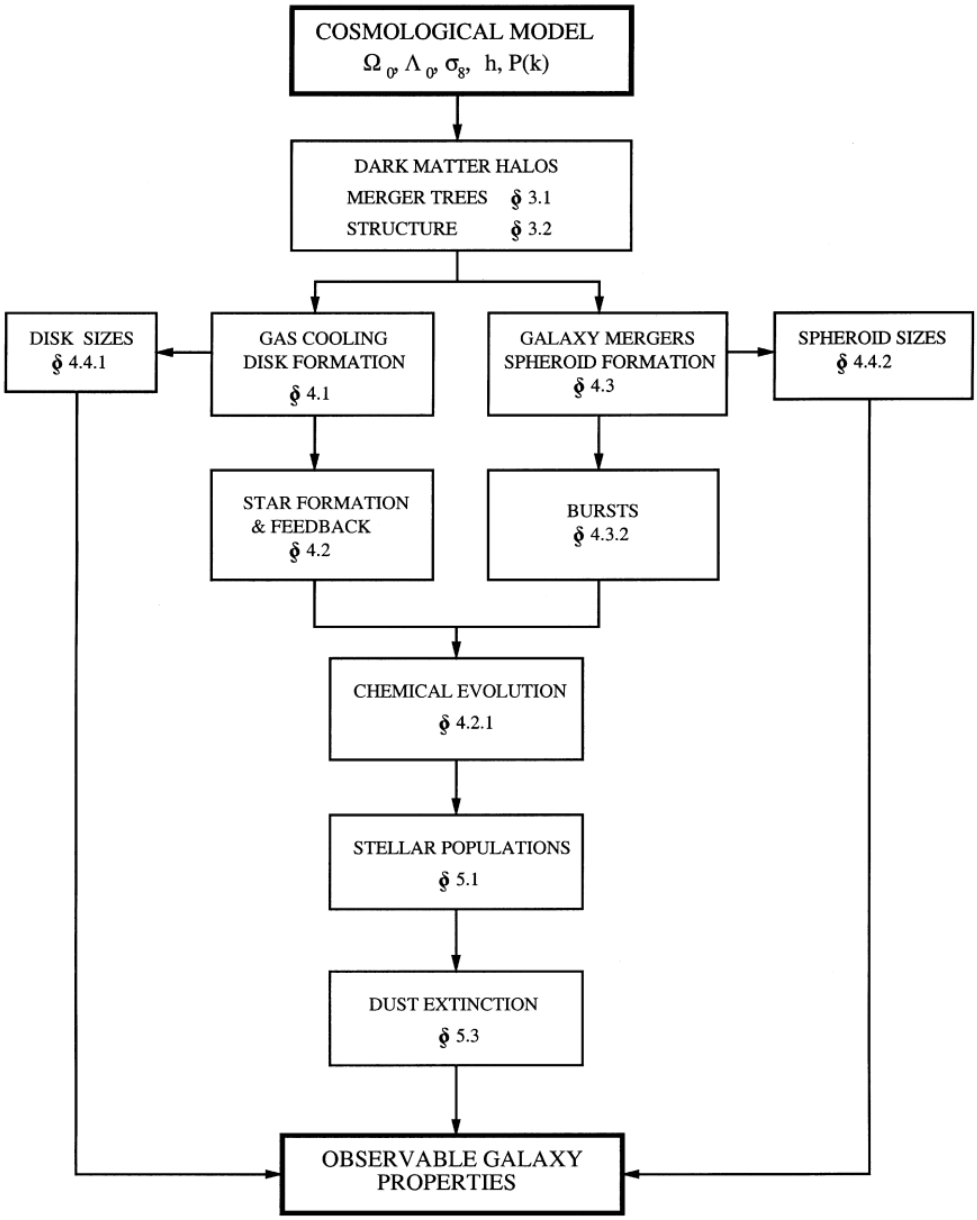

FIGURE 2.15 – Schematic description of a semi-analytical model of structure formation. Taken from COLE et AL 2000

The formation and evolution of galaxies depend on the ability of the gas to cool down and form stars. In turn, gas is reheated by different feedback processes. The stellar-to-halo mass function peaks around at mass $10^{12}h^{-1}\mathrm{M}_{\odot}$, above this mass AGN feedback heats the gas of the interstellar medium, preventing further star formation (SILK et REES 1998). In low-mass halos, supernovae feedback can also prevent/enhance the formation of stars in the ISM and ejects materials outside of the halo. *Semi-analytical models* of galaxy formation provide a set of equations that describe the flow between stars, cold and hot gas and predict star formation history and metallicity of galaxies (COLE et AL 2000). These models typically rely on a few dozens of parameters, some of them that can be directly tuned to observed relations. However, semi-analytical models require halos merger trees, which can be time-consuming to compute for very large N-body simulation. Therefore, for the study of LSS, SHAM and HOD prescriptions are usually favoured.

2.4.2.4 SHAM and HOD

Sub-halo abundance matching populates dark matter sub-halos in N-body simulations in a statistical way, assuming a monotonic relation between galaxy properties (stellar mass, luminosity) and the mass of the parent halo or subhalo. For a sub-halo, galaxy properties are described in term of the mass of the subhalo, or either in term of the maximum velocity $v_{\rm max}$, at the time of accretion. This quantity is more robust as sub-halos loose mass due to tidal stripping after becoming satellite in a larger halo. It has been shown in SIMHA et AL. 2012 that SHAM is in good agreement with the halo occupation distribution in SPH simulations, but does not incorporate (due to the assumed monotonic relation) the stellar-mass loss in galaxies due to stripping effect. Halo occupation distribution model describes the probability distribution function $P(N_{\rm g}|M_{\rm h})$ of having a number $N_{\rm g}$ of galaxies in halos of mass $M_{\rm h}$. This probability is often split between central and satellite galaxies, orbiting around the central galaxies, such that

$$\langle N_{\rm g}|M_{\rm h}\rangle = \langle N_{\rm cen}|M_{\rm h}\rangle + \langle N_{\rm sat}|M_{\rm h}\rangle. \tag{2.291}$$

To provide this description, one has to infer to full probability law (Poisson, Gaussian, negative binomial etc., see AVILA et AL. 2020 and ROSSI et AL. 2021) for both central and satellite galaxies. HOD parameters can be determined given semi-analytical models of galaxy formation (AVILA et AL. 2020) and/or observed galaxy clustering properties. On small scales, at $r \approx 1h^{-1}$Mpc, the 2PCF is sensitive to the number of satellites, and on large scales it is sensitive to the average mass of parent halos (WECHSLER et TINKER 2018). Note that HOD prescriptions assume that the occupation of galaxies inside halos is independent of the large-scale environment, which seems to be in disagreement with the findings of GAO, SPRINGEL et WHITE 2005 on the existence of assembly bias.

3 Analysis of the eBOSS survey

Sommaire

3.1 Construction of a galaxy redshift sample

In order to extract the most stringent cosmological information from the observed distribution of galaxies, one needs to have a redshift measurement for all observed galaxies. However, billions of galaxies are observable in principle, and it is too much of an effort to measure a redshift for each galaxy. Instead, we select a target galaxy population based on photometric observations, in a way that maximises our ability to obtain a spectrum, and in turn extract a reliable redshift measurement from it, given the specificity of the spectrograph at disposal. Galaxies can be classified into different types according to their observed morphology, colour, luminosity, or stellar mass. Overall, two main classes emerge : blue spiral and red elliptical galaxies. Each of these galaxy populations has different stellar populations and dust extinction properties, which will influence the way that we see them. Given the redshifts and volume that we want to efficiently probe in cosmological redshift surveys, the target selection and type of galaxies to be targeted in spectroscopy are crucial parameters.

3.1.1 Target selection

In a galaxy spectrum, we have information about the spectral energy distribution (SED) at a given spectral resolution. In photometry, the SED is averaged over pass-band filters, and the color of a galaxy represents the amplitude difference between those filters. The flux received in a pass-band l is expressed in terms of its *relative* apparent magnitude m_l as

$$m_l = -2.5\log_{10}\left(\frac{F_l}{F_{l,0}}\right), \tag{3.1}$$

where $F_{l,0}$ corresponds to the reference flux in that filter. Historically, Vega star flux was used to calibrate the flux for visible and near-infrared wavelength. AB magnitudes corresponds to an *absolute* reference magnitude system for which the reference flux is set to 3631 Jy where 1 Jy = 10^{-26} W Hz^{-1} m^{-2}. The AB magnitude in a given pass-band is given by

$$m_{AB} = -2.5\log_{10}\left(\frac{\int f_\nu (h\nu)^{-1} e(\nu) d\nu}{\int 3631\text{Jy}(h_\nu)^{-1} e(\nu) d\nu}\right) \tag{3.2}$$

where f_ν is the spectral energy density at frenquency ν, h is the Planck constant and e_ν is the filter response function. Galactic extinction modifies the observed apparent magnitude of an extra-galactic object depending on its angular position on the sky. Therefore, observed AB magnitudes are corrected by galactic extinction as is the case in this manuscript. The correction is based on the galactic E(B-V) extinction map of (SCHLEGEL et AL. 1998). The imaging depth is expressed as the AB magnitude of a point source object detected at 5σ, while the seeing is defined as the full width at half maximum (FWHM) of the point spread function (PSF) of the point source object.

To carry out spectroscopic observations we first focus on a specific population of galaxies, either blue galaxies, red galaxies, or all galaxies up to limiting magnitude for instance, from which observed colours or magnitudes are known. We can then define a color or/and magnitude criterion to observe that galaxy population at any desired redshift interval. Once galaxies are selected from a photometric survey, the three-dimensional information can be obtained from spectroscopic observations.

The SDSS survey (YORK et AL. 2000) was designed in the 80's as a wide-area (10,000 square degree) multi-band imaging and spectroscopic survey with primary goal to understand the large-scale structure in the Universe. A dedicated 2.5-meters telescope (GUNN et AL. 2006) was designed and built by the SDSS colaboration at the Apache Point Observatory (APO), Sunspot, New Mexico. Spectroscopic observations were performed with two multi-object fiber-fed twin spectrographs (SMEE et AL. 2013). The spectrograph started operating in 1999 and observed more than 1,500,000 spectra during the stage I and stage II of the SDSS survey, from which the first BAO signal was

detected in a sample of approximately 46,000 luminous red galaxies in the range $0.16 < z < 0.47$ (EISENSTEIN et AL. 2005). The SDSS spectrograph was then upgraded (SMEE et AL. 2013) for the SDSS-III BOSS survey (AIHARA et AL. 2011) in order to detect fainter objects at higher redshifts. The detailed description of the spectroscopic and photometric set up can be found in (GUNN et AL. 2006,SMEE et AL. 2013).

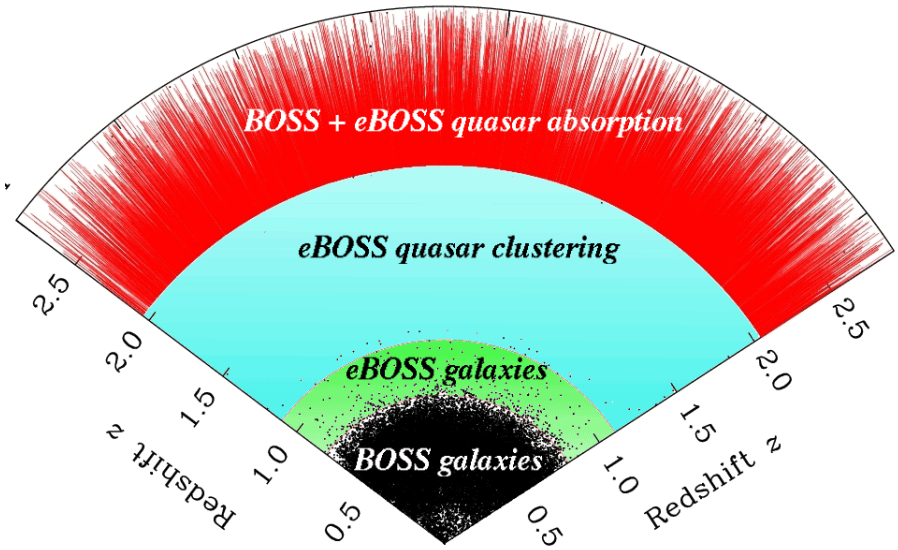

FIGURE 3.1 – Radial distribution of the different types of galaxies observed with BOSS and eBOSS, credit : SDSS

In addition to SDSS optical imaging,SDSS-III BOSS and SDSS-IV eBOSS surveys (DAWSON et AL. 2013; DAWSON et AL. 2016) galaxies have near-infrared photometric data from the full-sky coverage of the Wide-field Infrared Survey Explorer (WISE) survey (WRIGHT et AL. 2010). Emission line galaxies (ELG) (RAICHOOR et AL. 2017) were selected from the data release 3 and 5 of the Dark Energy Camera Legacy Survey (DECaLS, DEY et AL. 2019). This choice was motivated by the fact that DeCaLs photometry was at least one magnitude deeper than SDSS imaging, allowing us to select fainter galaxies. We present in Fig. 3.1 the different types of galaxies observed by SDSS. The BOSS survey observed around 360,000 galaxies at low redshift (the LOWZ galaxy sample) in the redshift range $0.15 < z < 0.43$, and more than 770,000 galaxies (CMASS) in the redshift range $0.43 < z < 0.70$. At redshift between $2.15 < z < 3.15$, BOSS observed more than 150,000 spectra of quasars to probe the large-scale structure through the Lyman-α forest. BOSS spectrograph was re-used by eBOSS, the 5-year extension of the BOSS program. eBOSS was designed to allow precise clustering measurements at higher redshifts compared to BOSS, with 174,000 LRG in the redshift range $0.6 < z < 1.0$, 173,000 ELG redshifts in $0.6 < z < 1.1$, and 330,000 quasars (QSOs) in $0.8 < z < 2.2$. The number of high-redshift $z > 2.1$ Lyman-α quasars was also increased by 60,000.

We will now focus our attention on the CMASS and LRG galaxies observed respectively with the BOSS and eBOSS surveys. Further information on target selection of SDSS galaxies can be found in (EISENSTEIN et AL. 2001, EISENSTEIN et AL. 2011,ROSS et AL. 2014,REID et AL. 2016 ,PRAKASH et AL. 2016,ROSS et AL. 2020) and are briefly summarised in the following.

CMASS

It has been showed in (M. STRAUSS et AL. 2002) that a selection based solely on an apparent magnitude cut selects too many low-redshift and low-luminosity galaxies. This is why the selections of BOSS and eBOSS galaxies rely on both a color-color and a color-magnitude selections in the similar way as for the selection of luminous red galaxies in SDSS-II (EISENSTEIN et AL. 2001). SDSS

colours are defined from magnitudes (denoted with the subscript *mod*) modelled using the best fit, psf convolved, of either a de Vancouleurs or exponential profile fit in the r band. This best fit is then used to determine the magnitudes in the other band, see ABAZAJIAN et AL. 2004. Apparent magnitude cuts are made with cmodel magnitude (denoted with the subscript *cmod*), which are determined by the best fit of the linear combination of a de Vancouleurs and a exponential profile in each band separately. During SDSS-III, different colour and magnitude selections were used to select CMASS galaxies, here we will only refer to the final selection criterion as given by REID et AL. 2016. We first introduce the variable $d_\perp$

$$d_\perp = (r_{\rm mod} - i_{\rm mod}) - (g_{\rm mod} - r_{\rm mod})/8 \tag{3.3}$$

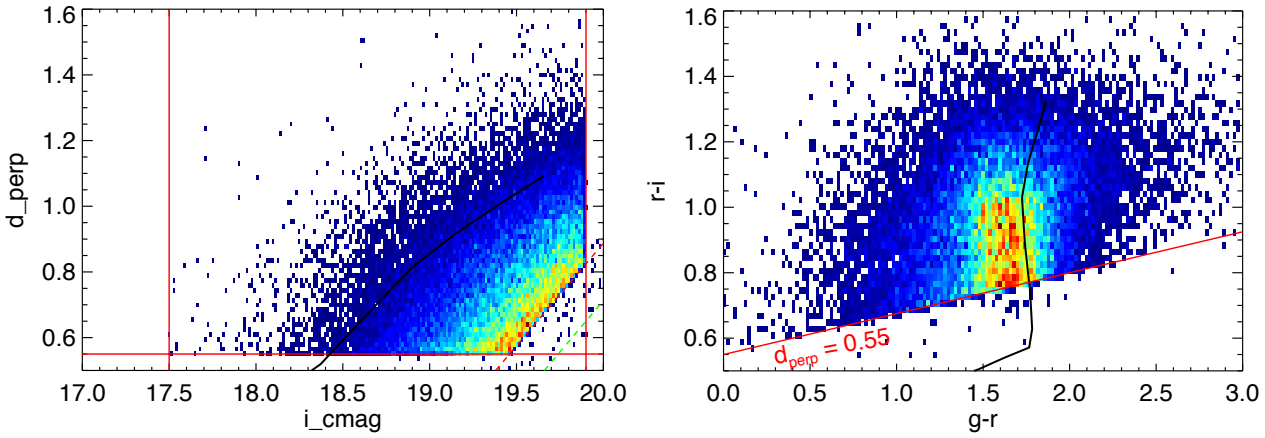

FIGURE 3.2 – Density plot of CMASS galaxies in the $i_{\rm cmod}$ $d_\perp$ plane (left) and in the $(g-r)$,$(r-i)$ color plane. Red corresponds to high density regions while blue and black correspond to lower density regions. The black line corresponds to the passively LRG model of MARASTON et AL. 2009 while the green line vertical lines correspond to an additional cut in magnitude. Taken from REID et AL. 2016

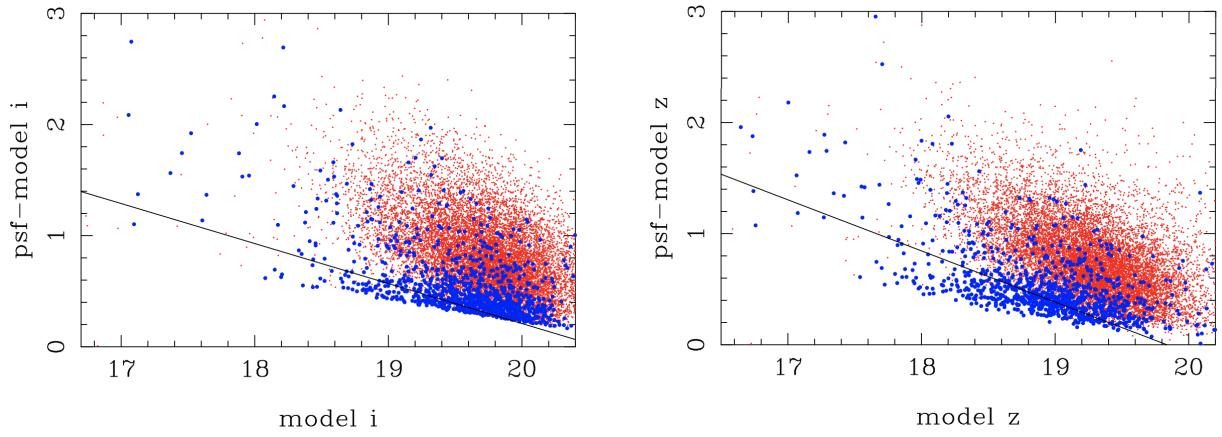

FIGURE 3.3 – Distribution of spectroscopically confirmed stars (blue points) and galaxies (red points) in the psf-model vs model i-band (left) and z-band (right). The black lines are the linear cut that remove most of the star while removing less than 1% of the galaxies. Taken from REID et AL. 2016

Fig. 3.2 represents the density of CMASS galaxies in two different colour planes. On the left panel is represented the sliding cut in $d_\perp$, the i-band plane designed to select an approximate stellar-mass complete sample. Stellar mass increases with the perpendicular distance to the sliding cut

represented by the red dashed line [1]. Vertical lines represent the magnitude limit cuts in the i-band. In each panel, the black solid lines represent the color evolution of passively evolving LRG according to the model of MARASTON et AL. 2009,

$$i_{\rm cmod} = 19.86 + 1.6(d_\perp - 0.8). \tag{3.4}$$

The right panel represents CMASS color distribution in the $(g-r)$,$(r-i)$ plane. The redshift of galaxies increase upward, starting at a redshift $z = 0.40$ for $d_\perp = 0.55$. The criterion $d_\perp > 0.55$ discards low redshift galaxies.

Fig. 3.3 represents stars (red) and galaxies (blue) in the magnitude versus psf minus magnitude plane for the i and z bands. The difference between the psf and magnitude measures the extendedness of a source, making it a useful criterion to separate star from galaxies. The black lines represent the linear cut for the CMASS sample, which removes most of the stars. The explicit color and magnitude cuts for the final CMASS sample are given by

$$d_\perp > 0.55, \tag{3.5}$$
$$i_{\rm cmod} < 19.86 + 1.6(d_\perp - 0.8) \tag{3.6}$$
$$17.5 < i_{\rm cmod} < 19.9 \tag{3.7}$$
$$i_{\rm psf} - i_{\rm mod} > 0.2 + 0.2(20 - i_{\rm mod}) \tag{3.8}$$
$$z_{\rm psf} - z_{\rm mod} > 9.125 - 0.46 z_{\rm mod} \tag{3.9}$$
$$i_{\rm fib2} < 21.5 \tag{3.10}$$
$$r_{\rm mod} - i_{\rm mod} < 2 \tag{3.11}$$
$$r_{\rm dev,i} < 20.0 {\rm pix}, \tag{3.12}$$

where $r_{\rm dev,i}$ corresponds to the effective radius of the best-fit de Vaucouleurs profile for the i-band magnitude, measured in pixels. The subscript fib2 corresponds to the total flux within a $2''$ diameter of the object center, corresponding to the aperture of BOSS spectrograph fiber (SMEE et AL. 2013). Eqs. 3.5, 3.6 and 3.7 correspond to the cut illustrated in Fig. 3.2, while Eqs. 3.8 and 3.9 refer to the linear cut of Fig. 3.3. The faint magnitude cut in Eqs. 3.7 and 3.10 are used to provide a high redshift success rate, while the bright limit in Eq. 3.7 is used to discard low-z galaxies. Eqs. 3.11 and 3.12 are used to exclude outliers with deblending issues. These selections provide a approximate stellar-mass-limited sample (REID et AL. 2016). MASTERS 2011 showed that 26% of CMASS galaxies have a late-type morphology, i.e. are blue galaxies. ROSS et AL. 2014 showed that consistent cosmological measurements result from both dataset.

LRG

It is well know that massive, red elliptical galaxies live in high density environments and clusters strongly (DRESSLER 1980). These galaxies, which are the most luminous and reddest, are often referred to as luminous red galaxies (LRG) and have been widely studied in SDSS-I and SDSS-II surveys (EISENSTEIN et AL. 2001,EISENSTEIN et AL. 2005). Using optical photometry alone, one can target galaxy LRGs at redshift $z < 0.7$. Since the primary goal of eBOSS was to observe LRGs in the redshift range $0.6 < z < 1.1$ we need to target fainter objects. To to do so, PRAKASH et AL. 2016 proposed to use the WISE photometry in the near-infrared. WISE observed the full sky in four infrared channels centered at 3.4, 4.6, 12, and 22 µm, which are referred to as $W1, W2, W3, W4$ in PRAKASH et AL. 2016. For eBOSS, only the $W1$ band is used in the LRG selection. We present in Fig. 3.4 the color-color dispersion of galaxies observed by WISE and CFHTLS. As the redshift increases, we can see a clear distinction between stars and galaxy in near-infrared/optical at $z > 0.6$. We can

1. The red dashed line is in the bottom right corner of the plot, near the high-density region.

also see that $r-i$ color increases with redshift. Given these observations, PRAKASH et AL. 2016 proposed a color-color selection given by

$$r_{\rm mod} - i_{\rm mod} > 0.98, \tag{3.13}$$
$$r_{\rm mod} - W1 > 2(r_{\rm mod} - i_{\rm mod}) \tag{3.14}$$
$$i_{\rm mod} - z_{\rm mod} > 0.625. \tag{3.15}$$

The color criterion given in Eq. 3.15 have been introduced by (PRAKASH et AL. 2016) to reduce the contamination of $z < 0.6$ galaxies. The 5σ depth for photometric observations of points source in SDSS are $u = 22.15$, $g = 23.13$, $r = 22.70, i = 22.20, z = 20.71$ (DAWSON et AL. 2016). In order to detect high-redshift galaxy with a correct S/N ratio, the following magnitude cut was imposed

$$IVARx_{\rm mod} \neq 0, \quad x = r, i, z, \tag{3.16}$$
$$z_{\rm fib2} < 21.7 \tag{3.17}$$
$$19.9 < i_{\rm cmod} < 21.8 \tag{3.18}$$
$$W1_{vega} \neq 0 \tag{3.19}$$
$$W1_{AB} < 20.299, \tag{3.20}$$

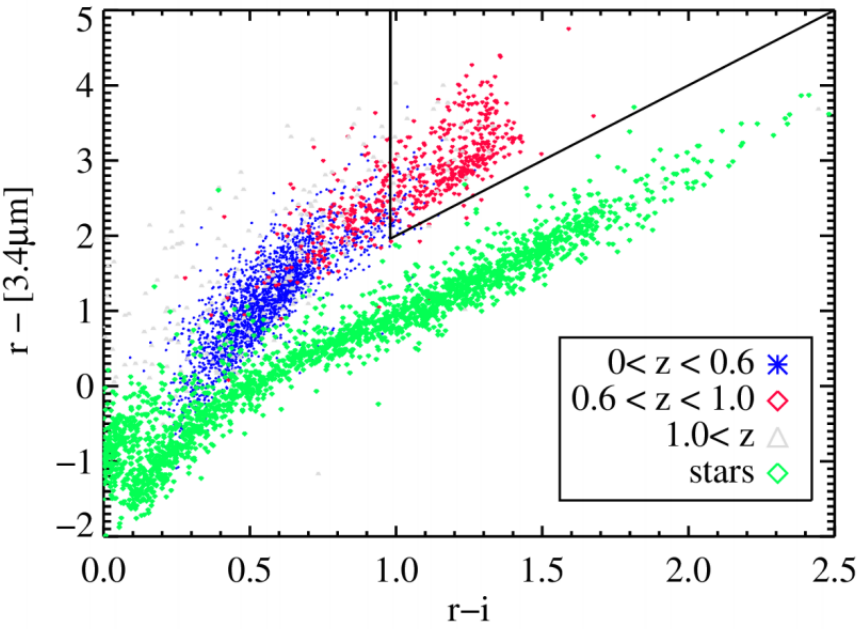

FIGURE 3.4 – Optical–infrared color–color plot for galaxies observed by WISE and CFHTLS. Red diamonds display galaxies at 0.6 < z < 1.0, blue symbols represent galaxies with redshift z < 0.6, and cyan triangles represent galaxies at z > 1.0. Stars are represented by green diamonds. The triangular area depicts the LRG selection effect. Photometric redshifts are taken from the COSMOS photo-z catalog of ILBERT et AL. 2009 and optical photometry is taken from the catalog of (GWYN et AL. 2012). Taken from PRAKASH et AL. 2016

where $IVAR$ corresponds to the inverse variance of the model flux. Eq. 3.18 ensures that we do not target CMASS galaxies, $W1_{vega}$ being different from zero means that the photometry is reliable and Eq. 3.20 implies that WISE measurements have a S/N ratio greater than 5 (WRIGHT et AL. 2010).

3.1.2 Spectroscopic observations

Once galaxies are selected out of the photometric survey, their spectra can be measured by assigning a fiber to each target. The *fiber assignment* corresponds to the action of assigning spectroscopic fibers to target galaxies and is performed in such a way to maximize the fraction of targets which receive a fiber, the so-called *tiling algorithm* (BLANTON et AL. 2003). First, the sky is divided into a set of rectangles in spherical coordinates, the so-called *chunks*. The tiling algorithm then assigns target galaxies to spectroscopic tiles in each chunk. These tiles have a central location on the sky and a list of target to be observed. They have a circular field of view of radius 1.49 degrees. The observation of the tiles are carried out with plates [2], with holes drilled and fiber assigned at each target location. Fibers of the same tile cannot lie closer than 62″ one another, because of the physical sheathing of each fiber.

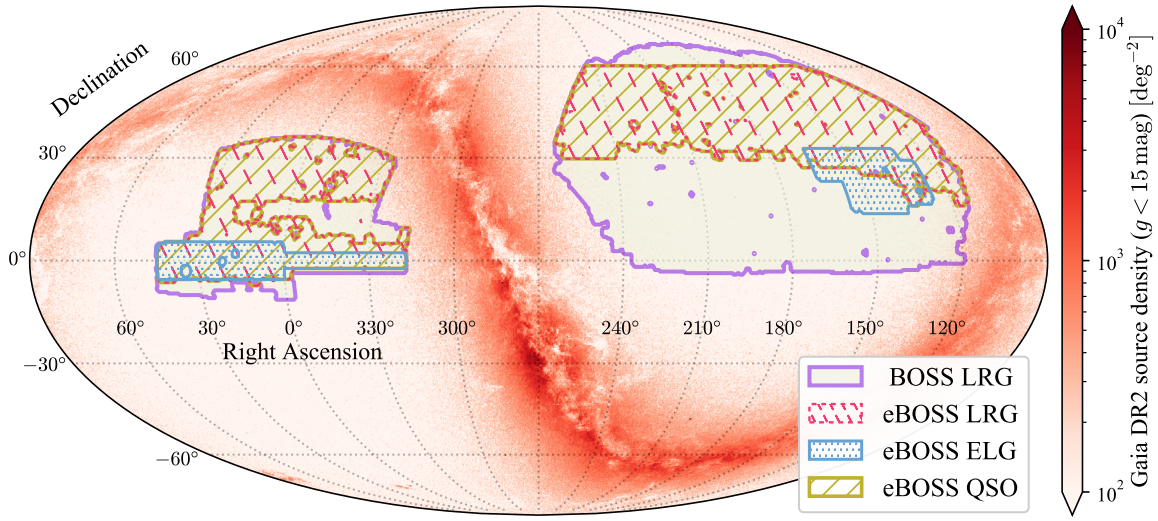

FIGURE 3.5 – The sky coverage of eBOSS DR16 tracers and BOSS DR12 CMASS galaxies. The density map is constructed from Gaia DR2 (GAIA COLLABORATION 2018) sources with $g< 15$ mag. Taken from (C. ZHAO et AL. 2021)

The BOSS and eBOSS survey geometry are described in terms of spherical polygons with the MANGLE software (SWANSON et AL. 2008). A *sector* is defined as the union of the polygons as a unique intersection of spectroscopic tiles. These polygons form the basic unit of geometrical decomposition of the survey footprint, represent the boundaries of the imaging surveys, the circular fields of the tiles, as well as regions to be masked (for instance the center of each spectroscopic tile, see REID et AL. 2016). Then, regions with bad photometric properties (high extinction,bright objects) inside the survey geometry are masked (REID et AL. 2016,BAUTISTA et AL. 2018,BAUTISTA et AL. 2021). In addition, QS0s had priority during the fiber assignment procedure (DAWSON et AL. 2016), and so LRG targets closer than 62″ to a quasar couldn't be observed, thus these regions were masked as well. In total, all masks combined cover 17 % of the initial footprint, with the quasar collision mask accounting for 11 %. We present in Fig. 3.5 the sky coverage of eBOSS and CMASS BOSS galaxies. The final sample DR16 LRG sample is composed of 202 642 CMASS combined with 174 816 LRGs in a effective area of 9493deg^2 (ROSS et AL. 2020).

3.1.3 Redshift estimation

The IDLSPEC2D (BOLTON et AL. 2012) software reduces BOSS and eBOSS spectra from two dimensional images (spatial and spectral) that span multiple exposures into single 1D spectrum. This

2. Spectroscopic tiles in high density environment can also be observed with multiples plates.

software was originally designed for BOSS galaxies and was afterward updated for eBOSS data, see AHUMADA et AL. 2020. In BOSS, the best redshift is estimated from the 1D spectrum with the IDLSPEC1D software (BOLTON et AL. 2012) based on a χ^2 minimization approach.

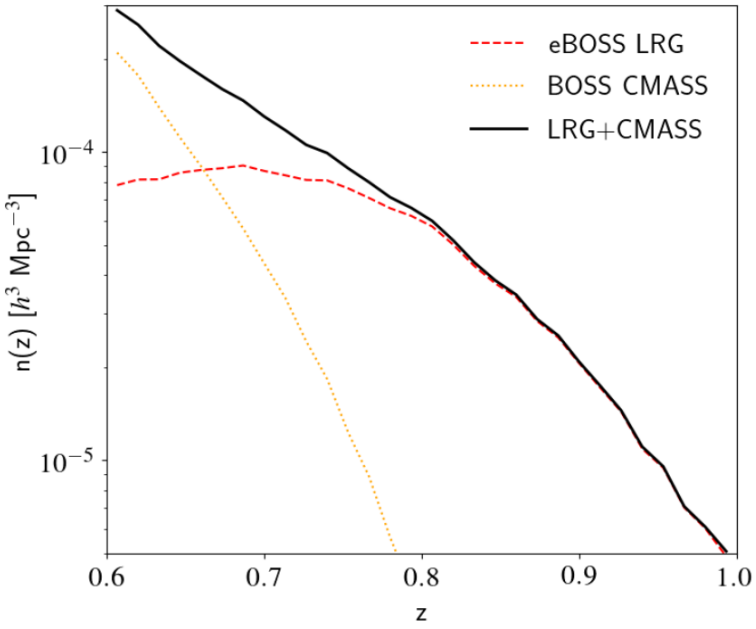

FIGURE 3.6 – Radial distribution of the LRG plus CMASS sample. The continuous black line corresponds to the eBOSS sample, the yellow dashed line corresponds to the CMASS sample, and the red dashed line corresponds to the combined sample. Taken from (BAUTISTA et AL. 2021)

The measured spectrum is compared to a linear combination of spectral templates plus a low order polynomial to marginalize over calibration errors and inhomogeneous extinctions. The spectral templates are constructed from 3 differents classes, **STAR**, **GALAXY** and **QSO**, using a rest-frame principal component analysis (PCA) applied to a training sample based on observed spectra from stars, quasars, and galaxies. The best measurement (redshift, redshift error and spectral class) is taken to be the one which minimizes the χ^2. The χ^2 difference between the first and the second best fit solutions is used to derive the confidence of the redshift measurement, given by the ZWARNING flag. [3] IDLSPEC1D provides robust redshift estimations for 99 % of CMASS galaxies but performed poorly for eBOSS galaxies, being fainter at higher redshift, with only 70% of accurate redshift for LRGs. Since the primary goal was to have at least 90% good redshifts for eBOSS (DAWSON et AL. 2016), a new redshift pipeline was used. Called REDROCK, this pipeline was originally designed for DESI, and is based on a combination of IDLSPEC1D and the archetype method of HUTCHINSON et AL. 2016. The first step of REDROCK is similar to what is done with IDLSPEC1D : spectra are fitted to a linear combination of PCA templates of star, galaxies and quasars without the polynomial marginalization. The templates for stars and galaxies are constructed at a higher resolution than that of the BOSS spectrograph. The high resolution templates are then convolved with the instrument resolution and position in the focal plane to match BOSS/eBOSS obeservations. In addition to BOSS empirical templates, new PCA templates were derived from 20 000 theoretical galaxy spectra that span stellar age, metallicity and star formation (ROSS et AL. 2020). 30 000 spectra were also produced for stars of different mass and evolutionary stages. In a second step, spectra are fitted to a single spectrum template, called *archetype*. The goal of this additional step is to remove solutions

3. https://www.sdss.org/dr16/algorithms/bitmasks/#ZWARNING

involving non physical linear combination of PCA templates. This procedure is performed in the vicinity of at most three best-fit solutions in each class. Then, the redshift is given by the template which minimizes the χ^2, and once again, the χ^2 difference between the first and second fit gives the reliability criterion. The REDROCK algorithm provides 90.5 % of good redshifts for the eBOSS LRG sample. We present in Fig. 3.6 the radial distribution of the eBOSS LRG and BOSS CMASS samples, with redshift measured with REDROCK and IDLSPEC1D, respectively.

3.1.4 Estimation of the 2PCF

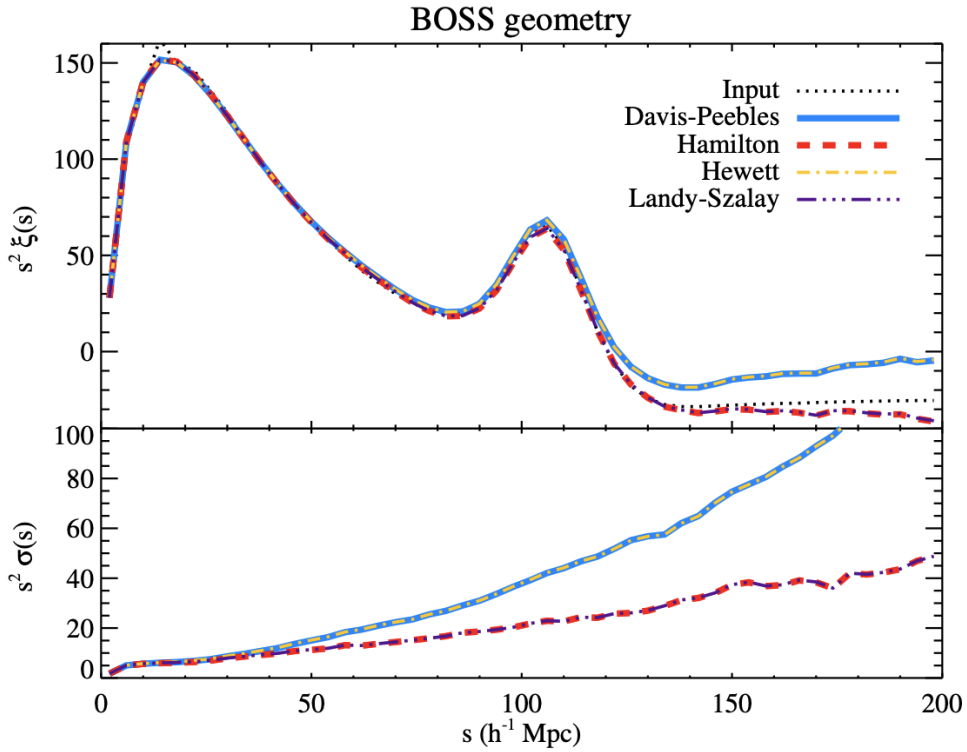

FIGURE 3.7 – Comparison between the different estimators of Eqs. 3.21 for the BOSS DR9 geometry. The top panel represents the real space correlation function, $\xi(r)$ while the bottom panel represents the variance $\sigma^2 = \langle\langle\xi\rangle - \xi\rangle$. The Input (dotted line) corresponds to a set of galaxy generated from lognormal density field simulations (COLES et JONES 1991) Taken from VARGAS-MAGAÑA et AL. 2013

Now that we have described the observational procedure to build a galaxy redshift survey sample, we can proceed with the estimation of the 2PCF. From the measured redshifts with REDROCK, we can determine the radial comoving distance in our fiducial cosmology. It gives us the 3D positions of galaxies. As a reminder, galaxies are biased tracers of the underlying density field δ, which result from a stochastic process. Thought cosmic times, galaxies dynamics will be governed by both gravitation and dark energy (or a modified theory of gravitation that would absorb both contribution) to form the LSS we see today. From the direct comparison to a random point process, we can trace the overdense regions of the galaxy density field (positive correlation on small scales) as well as underdense dense (negative correlation on large scales). Thus it became clear that the 2PCF could be computed effectively by comparing pairs of galaxy to pairs of a random point process (see Fig. 2.2 for 2pt-statistics). The most common estimators used in the literature are given by

(H. PEEBLES 1974,HEWETT 1982,DAVIS et P. PEEBLES 1983,HAMILTON 1993,LANDY et SZALAY 1993)

$$\begin{aligned}
\xi_{PH}(s) &= \frac{DD}{RR} - 1 \\
\xi_{Hew}(s) &= \frac{DD - DR}{RR} \\
\xi_{DP}(s) &= \frac{DD}{DR} - 1 \\
\xi_{H}(s) &= \frac{DD \times RR}{DR^2} - 1 \\
\xi_{LS}(s) &= \frac{DD - 2DR}{RR} + 1
\end{aligned} \tag{3.21}$$

where DD,RR(auto-correlation), DR and DR^2(cross-correlation) are the number of pairs in the range $[s-ds, s+ds]$. We present in Fig. 3.7 a comparison between the different estimators and the exact two-point correlation, which can be determined from the initial conditions of a log-normal simulation (COLES et JONES 1991) for a realistic survey geometry. The Hamilton and Landy-Szalay estimators as well as the Davis-Peebles and Hewett estimators are equivalent between each others. We can see that the Hamilton and Landy-Szalay provides unbiased measurements up to $150h^{-1}$Mpc with no increase in variance. The most frequently used estimator in the literature in the Landy-Szalay estimator (here after called LS) that we will use in this manuscript. In the estimators above, all the paircounts are normalized. For the auto-correlation, the total number of pairs corresponds to the binomial $\binom{N}{2} = N(N-1)/2$ with N the number of of object. For the cross-correlation DR the total number of pairs is given by $DR = N_d N_r$ with N_d and N_r the number of galaxy and randoms points respectively. If we furthermore apply weights to the galaxy and random catalogues, the normalization of the number of pairs is given by $((\sum w_i)^2 - \sum w_i^2)/2$ for the auto-correlation and by $\sum w_{d,i} \sum w_{r,i}$ for the cross-correlation. In general, the correlation function is estimated in two dimension, either by binning the paircounts in terms of distance parallel r_π and transverse r_p to the LoS (like in Fig. 2.7), or in terms of distance s and angle μ

$$\xi(s,\mu) = \frac{DD(s,\mu) - 2DR(s,\mu) + RR(s,\mu)}{RR(s,\mu)} \tag{3.22}$$

Formally, the random catalog will corresponds by construction, to an discrete representation of the selection function $\bar{n}^s(\mathbf{s})$, already introduced in Eq. 2.235, which gives the excepted density of galaxies at position $\mathbf{s}$, in the absence of clustering. Random catalogs are usually created with 50 times the number of galaxy, to reduces shot noise. To construct a random catalog, we first randomly populate the survey geometry, as defined by the union of the polygons of the corresponding MANGLE map, such that galaxies and randoms have the exact same angular footprint. The radial selection function is taken to be exactly the one of the galaxy catalog : this is done by randomly assigning redshift positions of galaxies to the randoms, the so-called shuffling-technic. ROSS et AL. 2012 compares this method to an alternative approach which fit spline with varying knot number to the measured galaxy distribution, and then sample directly from the spline. Their Fig. 19 shows that the former method provides the most unbiased measurements on mock catalogs. However with this technic, the inferred radial selection function is taken to be exactly the observed radial distribution of the data. Similarly, the norm of the selection function, the expected mean number density of galaxies, is often taken to be the observed mean density of galaxies. This matching between selection functions and observations will lead to the so-called global and radial integral constraint effects. The global integral constraint effect has no impact on configuration space analysis, as the mean density of galaxy over the whole footprint will only influence the shot-noise contribution of the power spectrum. However, the radial integral constraint effect (here-after called RIC) has a larger impact on clustering modes, and needs to be corrected for. In DE MATTIA et RUHLMANN-KLEIDER

2019, both integral constraints are modelled and corrected for any survey geometry and selection function. We refer the reader to this paper for further details. Similarly to what is done in Fourier space (Eq. 2.248), we can compress the 2d information in configuration space into multipoles

$$\xi_\ell(s) = \frac{(2\ell+1)}{2}\int_{-1}^{1}\xi(s,\mu)L_\ell(\mu)\mathrm{d}\mu. \tag{3.23}$$

However estimating the paircounts in bins provide a discrete estimation of $\xi(s,\mu)$. We therefore approximate the integral as a Riemann sum

$$\xi_\ell(s) = (2\ell+1)\sum_i \xi(s,\mu_i)L_\ell(\mu_i)\mathrm{d}\mu \tag{3.24}$$

where the factor of 2 has dropped out of the assumed symmetry between positive and negative μ. In this manuscript, we consider either CUTE (ALONSO 2012) or CORRFUNC (SINHA et GARRISON 2020), two highly optimized code to compute the paircounts. Both codes gives the exact same results (as expected) with CORRFUNC being faster for $N \gtrapprox 10^5$ particles.

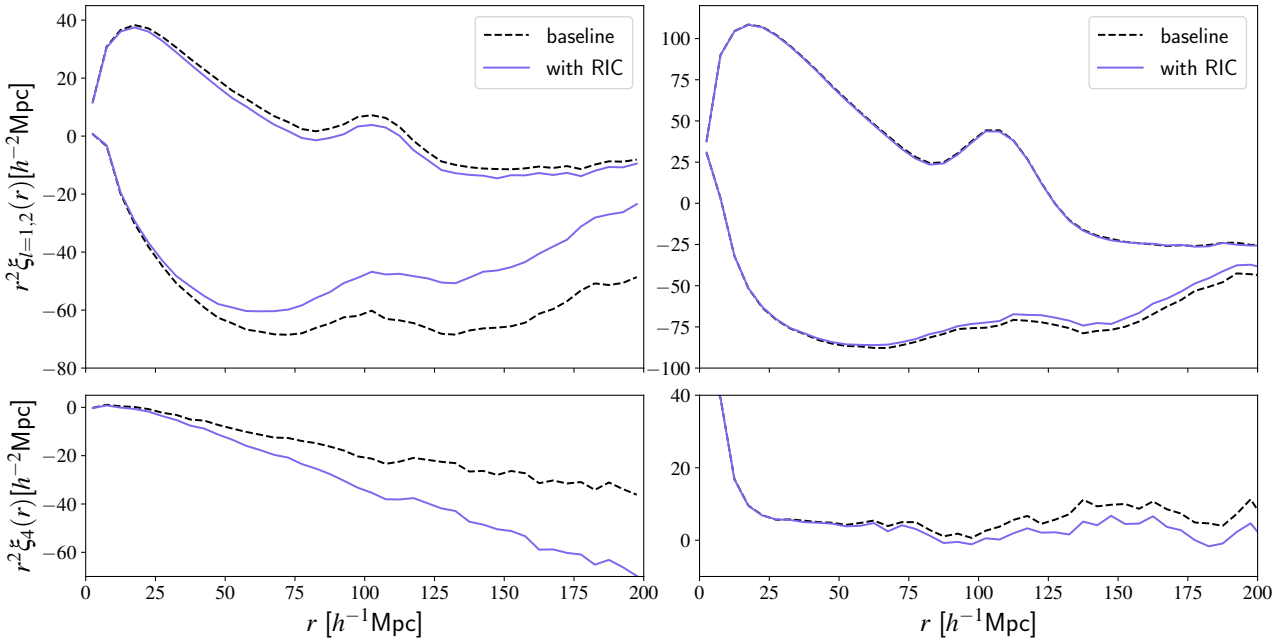

FIGURE 3.8 – RIC effect for two different types of tracer. The left (right) panel, represents the mean 2PCF for the ELG SGC EZMOCKS (CMASS NSERIES) mocks over 500 (84) realizations. (monopole plus quadrupole on the top, hexadecapole on the bottom). The mocks are presented in Section 3.1.5.

We present in Fig. 3.8 the mean 2PCF multipoles measured for ELG and CMASS mock catalogs (see next Section). In the baseline case, a single random catalog, and thus selection function, is used for the estimation of the 2PCF. The RIC effect is added by considering a single random catalog per mock, with the radial distribution of each random catalog draw randomly from each realization, as for the data. As one can see, the RIC effect is stronger for ELG tracers compared to CMASS galaxy. The ELG SGC footprint covers approximately 400 deg^2 while the CMASS NGC footprint covers approximately 7000 deg^2, and smaller effective area will produce higher fluctuations in the estimation of the radial selection function. Since the RIC effect is large for ELG, this effect has been modelled in DR16 ELG analysis (DE MATTIA et AL. 2021 ; TAMONE et AL. 2020) following the modelization of (DE MATTIA et RUHLMANN-KLEIDER 2019). For the eBOSS plus CMASS DR16 analysis, the impact of RIC is smaller, and therefore we chose not to include it in our modelling. We

instead add in quadrature the bias observed for this methodology, to the statistical errors of our cosmological measurements, see Chapter 4. In addition to the integral constraints, the so-called wide-angle effect need to be corrected for on large scales. This effect arises due to the plane-parallel approximation which assume that the galaxy separation is negligible compared to the LoS distance. This issue is more problematic for Fourrier space analysis which aim to derive constraints on primordial non-Gaussianity from large-scale modes of the monopole.

3.1.5 Simulations used in the eBOSS LRG analysis

In this work, we used 3 different kinds of simulations in order to simulate the clustering properties of the galaxy samples under consideration.

Nseries

The NSERIES mocks (see ALAM et AL. 2017, Sec 7.2), are a set high-resolution N-Body simulations run with the GADGET-2 code, and populated with a single HOD model, designed to match the clustering properties of the CMASS DR12 NGC sample. The mocks have same radial and angular selection functions than the data within the redshift range $0.43 < z < 0.70$. There are 84 independent mocks in total generated out of 7 independent periodic boxes of size $2.6h^{-1}$Gpc. While this sample is not fully representative of the eBOSS LRG sample, we use these N-body mocks to test the RSD models down to semi-linear scales. The number of realizations and their large volume ($84 \times 3.67\text{Gpc}^3$) are ideal to test model accuracy with high precision. The covariance matrix for these mocks were computed from 2048 realisations of the same volume with the MD-Patchy approximated method (KITAURA et AL. 2014). The effective redshift of these mocks, as defined in Eq. 4.81, is $z_{\rm eff} = 0.56$.

OuterRim

We then considered the OuterRim simulation (HEITMANN et AL. 2019), a N-Body simulation with cubic size $3h^{-1}$Gpc with 10240^3 DM particles at a mass resolution $1.85 \times 10^9 h^{-1}\text{M}_\odot$. The simulation was run with HACC (Hardware/Hybrid Accelerrated Cosmology Code, HABIB et AL. 2016), which consist of a combination of PM methods for large scales, and architecture-tunable part for small scales, based on the PP or PPTree method. From this cubic mock, we extract 27 realisations with size $1h^{-1}$Gpc. The DM halos have been populated using four different HODs (ZHENG et AL. 2007, LEAUTHAUD et AL. 2011, TINKER et AL. 2013, HEARIN et AL. 2015) at 3 different luminosity thresholds to cover a large range of galaxy populations. These mocks are part of the Mock Challenge which aim is to quantify potential systematic errors originating from the HODs. The first HOD introduced in (ROSSI et AL. 2021), is the HOD presented in (ZHENG et AL. 2007) which represents the cornerstone for other HOD frameworks. The central occupation distribution is given by a nearest integer distribution with first moment given by an error function [4]

$$\langle N_{\rm cen}(M_{\rm h})\rangle = \frac{1}{2}\left[1 + \text{erf}\left\{\frac{\log(M_{\rm h}) - \log(M_{\rm min})}{\sigma_{\log_{\rm M}}}\right\}\right] \tag{3.25}$$

with M_h the halo mass, $M_{\rm min}$ is the minimum mass for a halo to host a galaxy at given luminosity threshold and $\sigma_{\log_{\rm M}}$ is the rate of transition from $\langle N_{\rm cen}(M_{\rm h})\rangle = 0$ to $\langle N_{\rm cen}(M_{\rm h})\rangle = 1$. The satellite occupation fraction is given by a Poisson distribution with first moment given by a power law truncated at the low-mass end

$$\langle N_{\rm sat}(M_{\rm h})\rangle = \left(\frac{M_{\rm h} - M_0}{M_1}\right)^{\alpha} \tag{3.26}$$

where α is the power law slope. The Zheng HOD has therefore 5 parameters, $M_{\rm min}, \sigma_{\log_{\rm M}}, M_0, M_1, \alpha$.

4. In (ROSSI et AL. 2021), $\ln \equiv \ln_{10}$

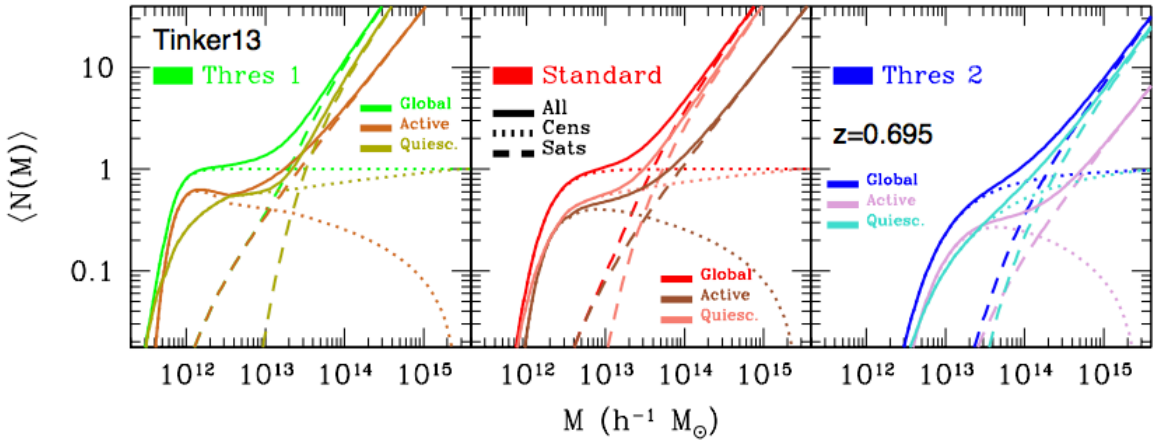

FIGURE 3.9 – Tinker HOD model at $z = 0.695$, for 3 mass threshold, denoted as 'Thres 1' ($M_*^{\rm thr} = 10^{10}h^{-1}M_\odot$), 'Standard' ($M_*^{\rm thr} = 10^{10.5}h^{-1}M_\odot$), and 'Thres 2' ($M_*^{\rm thr} = 10^{11}h^{-1}M_\odot$). Taken from (ROSSI et AL. 2021)

The Leauthaud HOD prescription (LEAUTHAUD et AL. 2011), extends the Zheng formalism by including a parameterization of the underlying stellar-to-halo mass relation (SHMR). The conditional stellar mass function (CSMF) is decomposed as $\Phi(M_*|M_{\rm h}) = \Phi_{\rm cen}(M_*|M_{\rm h}) + \Phi_{\rm sat}(M_*|M_{\rm h})$ since centrals and satellites experience different star formation history. $\Phi_{\rm cen}(M_*|M_{\rm h})$ is modelled as a log normal distribution, and is normalized such that (LEAUTHAUD et AL. 2011 ; ROSSI et AL. 2021)

$$\Phi_{\rm cen}(M_*|M_{\rm h}) \quad = \quad \frac{1}{\ln 10 \sigma_{\log M_*}\sqrt{2\pi}} \cdot \exp\left[- \frac{\{\log(M_*) - \log[f_{\rm SHMR}(M_{\rm h})]\}^2}{2\sigma^2_{\log M_*}} \right]$$

with $\sigma_{\log M_*}$, a log-normal scatter and $f_{\rm SHMR}$ is the logarithmic mean of the stellar mass, see (ROSSI et AL. 2021). The form of $f_{\rm SHMR}$ is described by 5 additional parameters. The satellite occupation function is parameterized as a power law with an exponential cutoff

$$\langle N_{\rm sat}(M_{\rm h}|M_*^{\rm thr})\rangle = \left(\frac{M_{\rm h}}{M_{\rm sat}}\right)^{\alpha_{\rm sat}} \exp\left(-\frac{M_{\rm cut}}{M_{\rm h}}\right) \tag{3.27}$$

where $M_{\rm sat}$ and $M_{\rm cut}$ define the amplitude of the power law and the scale of the exponential cutoff. This HOD models has a total of 11 to 16 parameters. The Tinker HOD (TINKER et AL. 2013) is an extension of the Leauthaud HOD to galaxy samples defined by both stellar mass, and star formation (SF). Galaxies are divided into a star-forming sequence, and a quenching sequence of red galaxies ; this color bimodality is already observed at $z \approx 1$ (TINKER et AL. 2013). The Tinker model basically extend the Leauthaud prescription to these two sub samples. The occupation statistics are the same as for the Leauthaud model, although the satellite occupation of star-forming and quenched galaxies subsamples are treated independently, for a total of 27 parameters, see TINKER et AL. 2013 ; ROSSI et AL. 2021 for more details. The final model considered is the Hearin HOD (HEARIN et AL. 2015), which extend the standard HOD framework by including the effect of the galaxy assembly bias, see (HEARIN et AL. 2015) for details. More information on the simulation, the HOD, and the Mock Challenge can be found in ROSSI et AL. 2021. The redshift of these mocks is $z = 0.695$.

EZmocks

The final set of mocks used in the analysis are the EZMOCKS (CHUANG et AL. 2015). These mocks evolves DM particles with Zel´dovich approximation, including a non-linear, non-local, and scale-dependent galaxy bias prescription to populate the DM field with galaxies. The two-point statistics

Tableau 3.1 – Sets of cosmological parameters within the ΛCDM used in this work. All models are parameterised with the set of paramaters Ω_m, Ω_c, Ω_b, Ω_ν, $h = H_0/(100\text{km/s/Mpc})$, n_s and A_s. With these parameters we compute the normalisation of the linear power spectrum σ_8 at $z = 0$ and the comoving sound horizon scale at drag epoch r_{drag}. The different labels refer to our baseline choice (Base), the EZMOCKS (EZ), the NSERIES (NS), the OUTERRIM (OR) cosmologies, and an additional model (X) with larger value for Ω_m.

	Base	EZ	NS	OR	X
Ω_m	0.310	0.307	0.286	0.265	0.350
Ω_c	0.260	0.259	0.239	0.220	0.300
Ω_b	0.048	0.048	0.047	0.045	0.048
Ω_ν	0.0014	0	0	0	0.0014
h	0.676	0.678	0.700	0.710	0.676
n_s	0.970	0.961	0.960	0.963	0.970
A_s $[10^{-9}]$	2.041	2.116	2.147	2.160	2.041
$\sigma_8(z=0)$	0.800	0.823	0.820	0.800	0.874
r_{drag} [Mpc]	147.78	147.66	147.15	149.35	143.17

Tableau 3.2 – Values for the comoving angular diameter distance D_M and the Hubble distance $D_H = c/H(z)$ in unit of r_d and the normalised growth rate of structures $f\sigma_8$. These values are predictions from the cosmological models in Table 3.1

Model	z_{eff}	$\frac{D_M}{r_{\text{drag}}}$	$\frac{D_H}{r_{\text{drag}}}$	$f\sigma_8$
Base	0.698	17.436	20.194	0.456
Base	0.560	14.529	21.960	0.465
EZ	0.698	17.429	20.211	0.467
NS	0.560	14.221	21.692	0.469
OR	0.695	16.717	19.866	0.447
X	0.698	17.685	20.146	0.504
X	0.560	14.778	22.019	0.518

(monopole and quadrupole) in these mocks agree with N-body simulation within 1% down to 10 h^{-1} Mpc. The angular and radial distributions of the eBOSS LRG sample in combination with the $z > 0.6$ CMASS galaxies were reproduced in these mock catalogs. The full description of these mocks can be found in the paper (C. ZHAO et AL. 2021). These mocks are really fast to compute, and hence are perfect for the estimations of the covariance matrix. We also use these mocks to study the impact of observational systematic effects on cosmological measurements, and for the correlations between different methods for the calculation of the consensus results between configuration and Fourier space. A total of 1000 independents realizations is used in the analysis. Since the EZMOCKS mimics our data sample, they have the same z_{eff}. The cosmological parameters for each simulation are listed in Table 3.1, and their corresponding equivalents in terms of distance measurements and growth of structure are listed in Table 3.2.

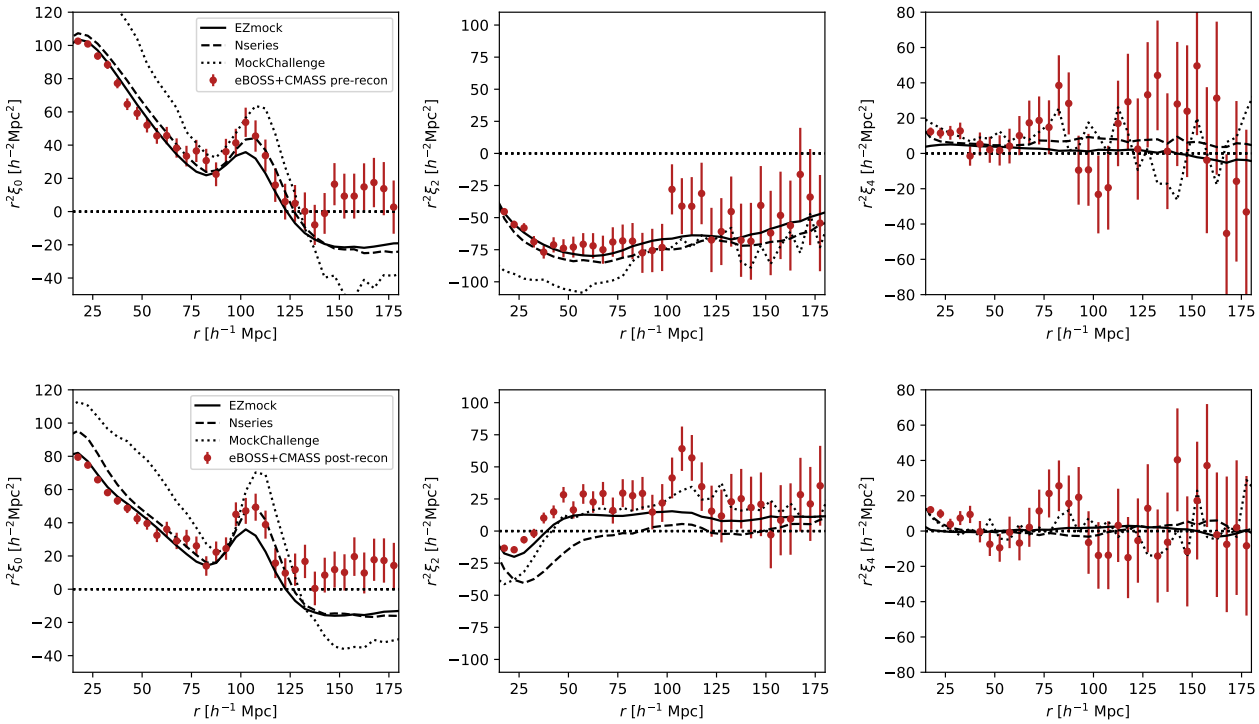

FIGURE 3.10 – Multipoles of the correlation function of data compared to the mock catalogs for pre-reconstruction (top panel) and post-reconstruction (bottom panel). The data is the combined eBOSS LRG + CMASS (NGC+SGC) samples and the mocks are the average multipoles of 1000 EZMOCKS realisations (solid line), 84 NSERIES realisations (dashed line) and 27 MOCKCHALLENGE mocks populated with L11 HOD model (dotted lines).Taken from (BAUTISTA et AL. 2021)

The red points with error bars in Fig. 3.10 show the even multipoles of the correlation function from the eBOSS LRG sample. The solid, dashed, and dotted black curves display the average multipoles in the different mock datasets used in this study : EZMOCKS, NSERIES, and MOCKCHALLENGE. The error bars are obtained from the dispersion of the 1000 EZMOCKS multipoles around their mean. By construction, the amplitude of the EZMOCKS multipoles matches the data at separations $s < 70h^{-1}$Mpc. A slight mismatch in the BAO peak amplitudes between data and EZMOCKS is visible. This mismatch does not impact cosmological results from the data since the covariance matrix dependency on the peak amplitude is small. However, the comparison of the precision of BAO peak measurements between mocks and data needs to account for this mismatch : the expected errors of our BAO measurement are smaller for data than for the ensemble of EZMOCKS. For comparison, the average multipoles of the NSERIES mocks, also shown in Fig. 3.10, are a better match to the peak amplitude seen in the data. N-Body simulations are therefore a nearly perfect tool to confront theories with observations. Almost, because they do not include the observational constraints that we experience on Earth [5].

3.2 Observational systematic errors

In large-scale structure analysis, the basic assumption is the large-scale homogeneity and isotropy of the Universe. Thus, the Universe has no preferred directions and the excepted mean number density of galaxies, averaged over a large volume, should be the same in every direction. However observational features such as galaxy extinction or star density are inhomogeneous, inducing a non

5. Although we will include contamination on EZMOCKS to validated our methodology, see Section 4.2.2.3.

homogeneous pattern in galaxy clustering that we need to correct for. Additionally, one needs to correct for inhomogeneous targeting of galaxies due to the fiber assignment.

3.2.1 Correction for completeness

For each sector (as defined in Section 3.1.2, the fiber assignment completeness is defined as (BAUTISTA et AL. 2018)

$$C = \frac{N_{\rm gal} + N_{\rm qso} + N_{\rm star} + N_{\rm cp} + N_{\rm fail}}{N_{\rm targ}}, \tag{3.28}$$

where $N_{\rm gal}$ is the number of LRGs with good redshift, $N_{\rm star}$ and $N_{\rm qso}$ are the number of QSOs and stars found among LRGs targets, $N_{\rm cp}$ is the number of LRGs without spectra due to collision with a galaxy with a know redshift, $N_{\rm fail}$ is the number of target without correct redshift estimation and $N_{\rm targ}$ is the total number of LRGs target. Sections with regions $C < 0.5$ are discarded from the analysis to avoid spurious clustering due to low completeness. We downweight each point in the random catalog by the completeness of its corresponding sky sector.

3.2.2 Correction for redshift failures and fiber collisions

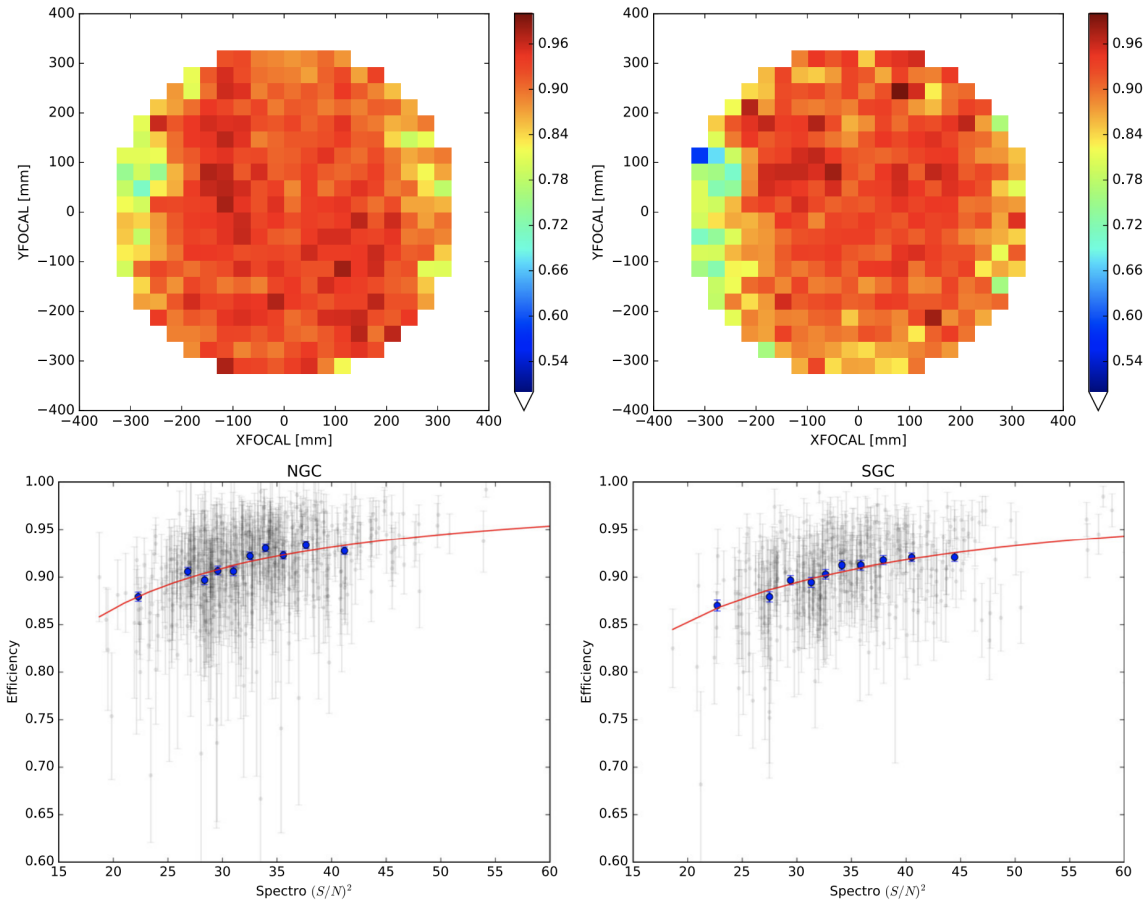

FIGURE 3.11 – Top panel : Average redshift efficiency as a function of the position of the fiber in the focal plane. YFOCAL < 0 corrsponds to the spectrograph 1 while YFOCAL > 0 corrresponds to the spectrograph 2. Bottom panel : Average redshift efficiency per spectrograph as a function of $(S/N)^2$ binned (blue points) and unbinned (gray points). Red lines show the best-fit models. The left panel shows the results for the NGC, while the right panel shows the SGC, taken from BAUTISTA et AL. 2018

In BOSS, REID et AL. 2016 found a correlation between i_{fib2} and the redshift success rate, i.e, fainter galaxies with a lower S/N ratio yield less accurate redshifts than their counterpart. To correct this issue, a similar neighboor up-weighting schema is adopted where the neighrest neighbor observed on the same plate and on the same date, is up-weighted. This restricts the neighbor search to galaxies observed under the same conditions. To take into account the correlation between redshift failure and i_{fib2}, those weights are redshift-magnitude dependant, see (REID et AL. 2016). The analysis of the LSS catalog is restricted only to data from plate with flag PLATEQUALITY set to good. A plate is considered good enough if there is no more than 10% of catastrophic redshift, with a minimum S/N ratio for the blue and red arm of the spectrograph (DAWSON et AL. 2013). It has been shown by BAUTISTA et AL. 2018 that the up-weighting scheme introduces a bias of at least 5% on all scales in the amplitude of the quadrupole for the eBOSS LRG sample. This bias is likely caused by the larger fraction of failures and lower densities of objects compared to the CMASS sample. This is why in eBOSS spectra with bad redshift, i.e with bad S/N ratio are used. The redshift efficiency is defined per sector as BAUTISTA et AL. 2018

$$\eta = \frac{N_{\rm gal}}{N_{\rm zfail} + N_{\rm gal}}. \tag{3.29}$$

The bottom panel of Fig. 3.11 represents the redshift efficiency as a function on the galaxy separation in the focal plane. We observe a decrease of the efficiency near the edges of the focal plane. The reason is that light transmitted by fibers at the edges of the focal plane ends up at the edges of the CCD, where the optical performance of the spectrograph is degraded, which lead to larger PSF and optical aberrations, such as coma (SMEE et AL. 2013). The top panel shows that, on average, lower S/N spectra yields lower confident redshift. The efficiency η is fitted to a simple model of the form

$$\eta(x) = \frac{1}{1 + 1/p(x)}, \tag{3.30}$$

where $x = (S/N)^2$ and p is a first-order polynomial. The final efficiency model is equal to the product of the efficiency in the focal plane (top panel of Fig. 3.11) and the efficiency given by Eq. 3.30. For each random galaxy with a position (RA,DEC) in the sky, a plate and a position XFOCAL, YFOCAL is assigned to the random. Galaxies and randoms are up-weighted depending on the efficiency of the model. About 4% of the LRGs targets were not observed due to fiber collisions. These collisions can bias the clustering measurements so we applied the following correction : for $N_{\rm targ}$ objects in a given collision group for which $N_{\rm spec}$ have a spectrum, all objects are up-weighted by $w_{\rm cp} = N_{\rm targ}/N_{\rm targ}$,

3.2.3 Systematics due to Photometry

In BOSS, it has been showed by ROSS et AL. 2012 than galaxy density is correlated with star density and seeing. These correlations contaminates clustering measurements by introducing large-scale power not associated to the true spatial distribution of galaxies. In DR12 (REID et AL. 2016), weights are computed for each galaxy to counteract the dependence of this correlations, assuming that the systematics are independent. In eBOSS, this assumption was dropped and multiple linear regression was instead used to correct for non cosmological fluctuations. The multiple linear regression models the observed density field $\delta_{\rm phot}$ as a linear combination of maps m_i

$$\delta_{\rm phot}(RA, Dec) = p_0 + \sum_{i=1}^{n} p_i m_i(RA, Dec), \tag{3.31}$$

where p_0 is the average density over the whole survey, and the p_i are the coefficient which minimize the $\chi^2 = (\delta - \delta_{\rm phot})^2/\sigma_i^2$. Each map is produced with HEALPIX [6] with pixels of size 189 arcmin^2. The fluctuations δ are estimated from the data (from the normalized ratio of the number of galaxies over the number of randoms) as a function of a given systematic quantity. Fig. 3.12 shows the results of the multiple linear regression for the DR14 LRG catalog, using seven differents maps, five of which from SDSS (AIHARA et AL. 2011) : stellar density, i-band depth, z-band sky flux, z-FWHM and r-band extinction, and two from WISE (WRIGHT et AL. 2010) : median number of single-exposure frames per pixel in the WISE W1 band (WISE W1 Cov Med) and median of accumulated flux per pixel in the WISE W1 band (WISE W1 Med).

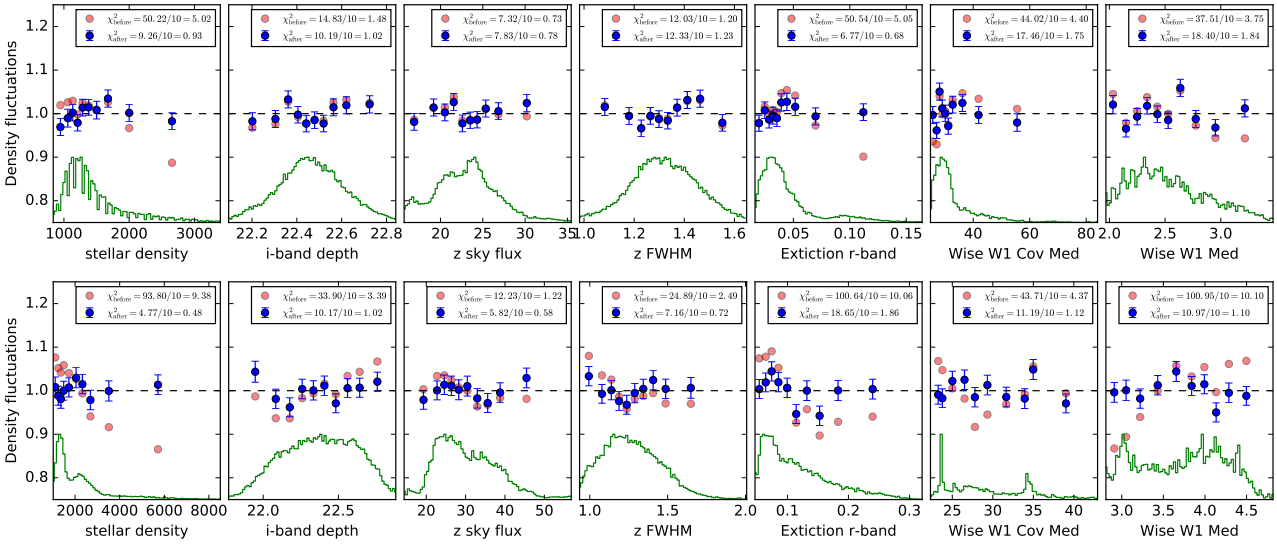

FIGURE 3.12 – Fluctuations in the number density of galaxy with respect to different photometric variables for the NGC (top panels) and the SGC (bottom panels). Red (blue) points indicate fluctuations prior/after corrections. The galaxy histogram with respect to the same quantities is shown in green. The fit is made simultaneously across all maps, taken from BAUTISTA et AL. 2018

Since differents SDSS bands are strongly correlated, the analysis is restricted to a single band : the i-band covering most of the observed flux in the optical for the LRGs. In the NGC, the χ^2 improves from $\chi^2/dof = 192/(70-8)$ before corrections to $\chi^2/dof = 80.6/(70-8)$ after corrections. For SGC, it improves from $\chi^2/dof = 365.8/(70-8)$ to $\chi^2/dof = 68.2/(70-8)$. With this method, the predominant improvement are related to dependencies with stellar density, extinction and WISE quantities. Once the density model is determined, one can correct the observed fluctuations with two differents ways : either by assigning to each galaxy a weight $w_{\rm syst} = 1/\delta_{\rm phot}$ or by sub-sampling the randoms to match the observed pattern in the data. Fig. 3.13 presents both implementations compared to the case where no correction is applied. We can see that both methods provides very similar results, well below the statisticals errors. We can see that on the monopole, the high scale power is supresssed with this method, while the correction has nearly zero impact on the quadrupole. In eBOSS DR16, we have chosen to up-weight each galaxy by $w_{\rm syst}$.

3.2.4 FKP weight

In addition to the weights we just described, we also used in our analysis the weight introduced by (FELDMAN, KAISER et PEACOCK 1994) which optimizes the clustering signal-to-noise ratio for a

6. https ://healpix.jpl.nasa.gov/

survey with varying average mean density $\bar{n}(z)$ as a function of redshift. FKP weight are defined as

$$w_{\rm fkp}(z) = \frac{1}{1+\bar{n}(z)P_0}. \tag{3.32}$$

We compute $\bar{n}(z)$ by linear interpolation over redshifts bins of size $dz = 0.005$. P_0 corresponds to the amplitude of the power-spectrum at the scale of interest $k \approx 0.15 h\mathrm{Mpc}^{-1}$ (Reid et al. 2016). We take $P_0 = 10000 h^3\mathrm{Mpc}^{-3}$, the same value used in the final DR12 analysis of CMASS galaxies. We apply these weights to both the data and to the randoms catalogs. To resume, we weight each galaxy and random by the total weight [7]

$$w = w_{\rm cp}\, w_{\rm noz}\, w_{\rm syst}\, w_{\rm fkp} \tag{3.33}$$

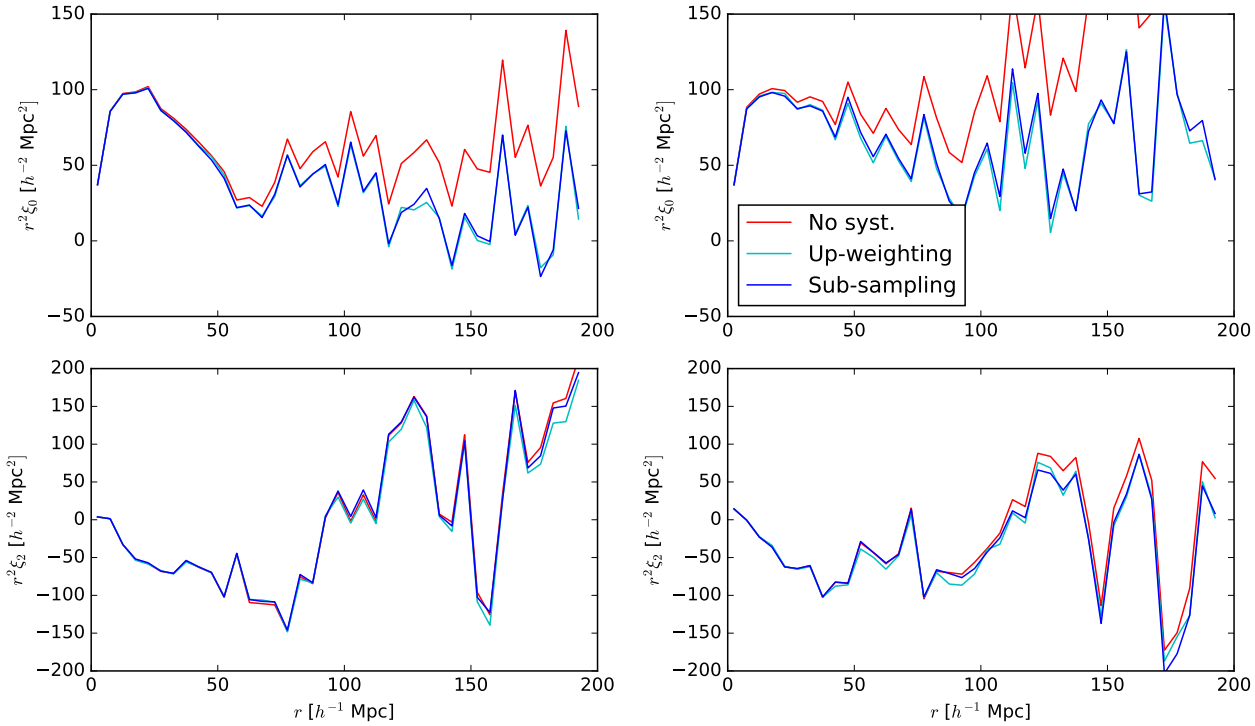

Figure 3.13 – Monopole and quadrupole (top and bottom) of the correlation function for the North pole (left) and the South pole (right). The red lines shows the 2PCF without any corrections. The cyan line shows the result when up-weighting galaxies, and the blue line shows the sub-sampling of randoms, taken from Bautista et al. 2018

to account for both fiber collision, redshifts failure, and spurious fluctuations due to systematics maps. The effective redshift of data and mock catalogs is defined as the weighted mean redshift of galaxy pairs,

$$z_{\rm eff} = \frac{\sum_{i>j} w_i w_j (z_i + z_j)/2}{\sum_{i>j} w_i w_j}, \tag{3.34}$$

where w_i is the total weight of the galaxy i and the indices i, j run over the galaxies in the considered catalog. We only include pairs of galaxies with separations between 25 and 130 h^{-1} Mpc, which correspond to the range used in our full-shape analysis (see Section 4.2.2.1). We obtain $z_{\rm eff} = 0.698$ for the combined eBOSS + CMASS sample. Given the total weight of Eq. 3.33 we defined the effective

7. For BOSS, the convention is different, $w = w_{\rm syst}\, w_{\rm fkp}(w_{\rm cp} + w_{\rm noz} - 1)$

volume of a galaxy sample by

$$V_{\rm eff} = \int_{z=z_{\rm min}}^{z_{\rm max}} \left(\frac{\bar{n}(z)P_0}{1+\bar{n}(z)P_0} \right)^2 A_{\rm eff} R^2(z) dR(z), \tag{3.35}$$

with $R(z)$ the comoving distance at redshift z and $A_{\rm eff}$ the effective area of the sample. For the combined North plus South poles, we find an effective volume of 2.72 Gpc^3.

3.2.5 PIP and ANG weights

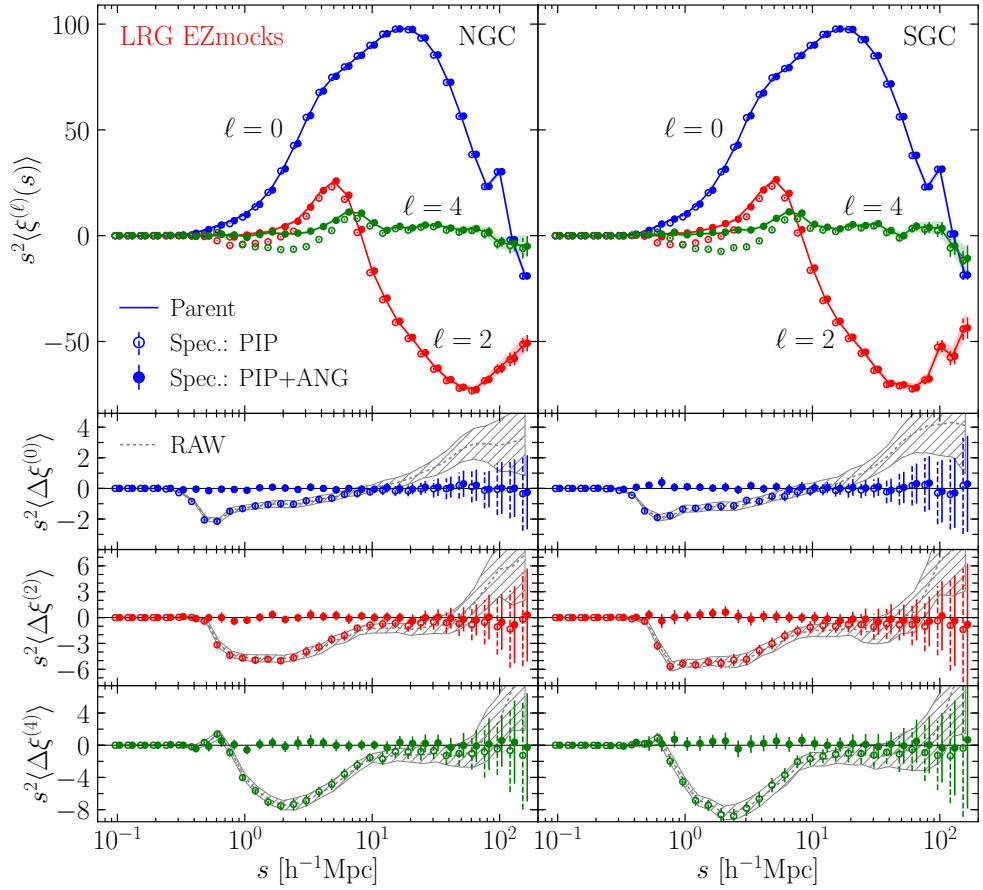

FIGURE 3.14 – The top panel represents the multipoles of the mean 2PCF averaged over 100 EZMOCKS for the LRG sample. The parent measurement is in continuous lines while unfilled/filled markers corresponds to the sample of assigned targets with PIP/PIP+ANG weights respectively. The shaded area and the errors bars represents the 1σ standard deviation for each case. The bottom panel represents the mean difference among the 3 cases, also considering the RAW measurement, where no weight are applied to the target catalog. Taken from (MOHAMMAD et AL. 2020)

The weight $w_{\rm cp}$ used in eBOSS to correct for fiber assignment is an approximation only valid for angular scale above 62″. An alternative approach, the 'pairwise-inverse probability' weighting scheme have been introduced by (BIANCHI et PERCIVAL 2017) and have been applied to the VIPERS (The VImos Public Extragalactic Redshift Survey,DE LA TORRE et AL. 2013) and eBOSS surveys in the analysis of (MOHAMMAD et AL. 2018; MOHAMMAD et AL. 2020). The technique calculates the selection probability for each observed pair by generating multiple random survey realisations statistically equivalent to the actual observation. Then, each observed pair is weighted by the

inverse of this probability. However, this method rely on the assumption that no pairs have zero probability of being observed, which is not true due to physical size of fiber. To recover the small clustering below fiber collision scale, PERCIVAL et BIANCHI 2017 combines this method with an angular up-weighting scheme (ANG). All galaxy and galaxy-random pairs are weighted by

$$w_{\rm ang}^{DD}(\theta) = \frac{DD^{\rm par}(\theta)}{DD^{\rm fib}_{\rm PIP}(\theta)}, \tag{3.36}$$

$$w_{\rm ang}^{DR}(\theta) = \frac{DR^{\rm par}(\theta)}{DR^{\rm fib}_{\rm IPP}(\theta)}, \tag{3.37}$$

$$\tag{3.38}$$

where the subscripts par and fib denote the pair of galaxies of the parent catalog and pair of galaxies that receive fibers. The PIP and IIP subscripts denote the 'pairwise-inverse probability' and the 'inverse-probability' weights given by Eq. 6 of (MOHAMMAD et AL. 2020). This assumption is valid if the set of unobserved pairs is statistically equivalent to the set of observed pairs. Survey design such as that of eBOSS might not entirely fulfill this requirement as area where tiles overlap might correlate to high density environments. The efficiency of such weighting scheme is presented in Fig. 3.14. Above the fiber collision scale, PIP weights effectively correct for the missing number of unobserved targets. The inclusion of ANG weights provide unbiased measurements up to the smallest scales. In Section 4.3.5, we investigate the potential gain of using these weights for the cosmological analysis of the eBOSS LRG DR16 sample.

3.3 The angular modes-free correlation function

3.3.1 Definition

In order to mitigate angular systematics, we describe in PAVIOT et AL. 2021 an alternative approach that consists in analysing the galaxy two-point statistics in configuration space, with nulled angular modes. We will refer to this modified statistics in the following as the *angular modes-free* (AMF) two-point correlation function. This is possible by modifying the standard estimator of the two-point correlation function. This idea was first introduced by BURDEN et AL. 2017 to mitigate the impact of DESI fiber assignment. They proposed an estimator similar to the standard LS estimator, but that includes an additional random catalogue where angular positions are randomly drawn from the galaxy catalogue. This effectively permits removing the angular clustering, as angular correlations are canceled by the new random catalogue. The amplitude of this new statistic is suppressed with respect to the standard two-point correlation function, but is blind to any systematic angular selection effects. A similar method was also developed in Fourier space in PINOL et AL. 2017. The first real-life application of such estimator was performed on the eBOSS ELG sample by TAMONE et AL. 2020. Alternatively, DE MATTIA et RUHLMANN-KLEIDER 2019 proposed an alternative approach to mitigate angular systematics with the so-called pixelization schema. The sky is divided into pixels with HEALPIX (GÓRSKI et AL. 2005) and randoms are assigned weights in order to null observed density fluctuations in each pixels.

In this work, we derive a full model for the modified two-point correlation function in redshift space, assess its accuracy, and perform a full analysis of baryonic acoustic oscillations and redshift-space distortions on CMASS and ELG mock samples, as a proof of concept. We will refer to this modified statistic in the following as the angular modes-free (AMF) two-point correlation function. In order to suppress the angular clustering, one can modify the LS estimator by introducing an auxiliary random catalogue. The latter has exactly the same angular clustering pattern as the data but with a random realisation of the radial distribution. It is easily constructed by randomly

assigning galaxy angular positions from the data catalogue to the random points. We will refer to it as the shuffled random catalogue, S, in the following. One can thus design a modified LS estimator such that (BURDEN et AL. 2017)

$$\tilde{\xi}(s,\mu) = \frac{DD(s,\mu) - 2DS(s,\mu) + SS(s,\mu)}{RR(s,\mu)}. \tag{3.39}$$

In this estimator the standard random catalogue in the numerator is replaced by the shuffled random catalogue, while is kept in the denominator. It is clear that by imprinting the angular clustering of the galaxies in the random catalogue, one suppresses the angular clustering and associated potential systematic errors, but at the price of removing part of the cosmological information. As for the standard correlation function, the AMF correlation function can be expanded in multipole moments. In the case of the shuffled random catalogue, since angular positions are drawn from observed galaxy positions, some angular positions will be repeated. This leads to some SS or DS pairs with vanishing angular separation, or equivalently with $\mu = 1$. Keeping these pairs in the pair counts can introduce additional noise and bias in the estimation of the AMF correlation function multipole moments. In practice however, by adopting a proper binning in μ in the pair counts, these pairs can be discarded. This effect is more problematic in Fourier space where $\mu = 1$ associated modes cannot be discarded in the estimator and introduce an additional shot-noise term, as discussed in (DE MATTIA et RUHLMANN-KLEIDER 2019).

3.3.2 Modelling

3.3.2.1 Approximated model

In order to model the AMF correlation function, we follow (BURDEN et AL. 2017) and define the AMF overdensity field

$$\tilde{\delta}(\mathbf{r}) \equiv \frac{n(\mathbf{r}) - \tilde{n}(\mathbf{r})}{\bar{n}(\mathbf{r})} \tag{3.40}$$

where $n(\mathbf{r})$, $\tilde{n}(\mathbf{r})$ and $\bar{n}(\mathbf{r})$ correspond respectively to the number density of galaxies, shuffled random points, and standard random points at comoving position $\mathbf{r}$. By construction, the shuffled random number density is

$$\tilde{n}(\mathbf{r}) = \frac{\int n(\chi',\gamma)\mathrm{d}\chi' \int \bar{n}(\chi,\gamma')\mathrm{d}\gamma'}{\int\int \bar{n}(\chi',\gamma')\mathrm{d}\chi'\mathrm{d}\gamma'} \tag{3.41}$$

where γ corresponds to the two-dimensional angular coordinates and χ to the radial coordinate. We assume that the random catalogue is uniform across the sky in γ, and can thus express the AMF overdensity field,

$$\tilde{\delta}(\mathbf{r}) = \delta(\mathbf{r}) - \frac{\int \delta(\chi,\gamma)\bar{n}(\chi)\mathrm{d}\chi}{\int \bar{n}(\chi)\mathrm{d}\chi}. \tag{3.42}$$

In the following, in order to simplify the notation, $\bar{n}$ is normalized so that $\int \bar{n}(\chi)d\chi = 1$. In Eq. 3.42, the second term on the right-hand side corresponds in fact to the projected overdensity at angular position γ on the sky,

$$\hat{\delta}(\gamma) = \int \delta(\chi,\gamma)\bar{n}(\chi)\mathrm{d}\chi. \tag{3.43}$$

The AMF correlation function corresponds to the auto-correlation of the AMF overdensity field,

$$\tilde{\xi}(\mathbf{s}) \equiv \langle\tilde{\delta}(\mathbf{r})\tilde{\delta}(\mathbf{r}')\rangle = \langle\delta(\mathbf{r})\delta(\mathbf{r}')\rangle - 2\left\langle\delta(\mathbf{r})\hat{\delta}(\gamma')\right\rangle + \left\langle\hat{\delta}(\gamma)\hat{\delta}(\gamma')\right\rangle, \tag{3.44}$$

where we have defined $\mathbf{s} = \mathbf{r}' - \mathbf{r}$ and $\langle.\rangle$ denotes the ensemble average. In the latter equation, the first and third terms correspond respectively to the three-dimensional and angular correlation functions, while the second term is the cross-correlation between the three-dimensional overdensity and

projected angular overdensity fields.

The angular correlation term is defined as

$$w(\theta) \equiv \left\langle \int \delta(\chi,\gamma)\bar{n}(\chi)\mathrm{d}\chi \int \delta(\chi',\gamma')\bar{n}(\chi')\mathrm{d}\chi' \right\rangle \tag{3.45}$$

and is related to the three-dimensional correlation function ξ as (P. PEEBLES 1980),

$$w(\theta) = \int_0^\infty \mathrm{d}\chi \int_0^\infty \mathrm{d}\chi' \xi(\theta,\Delta\chi)\bar{n}(\chi)\bar{n}(\chi'), \tag{3.46}$$

where $\theta = |\gamma' - \gamma|$ is the angular separation and $\Delta\chi = \chi' - \chi$ is the radial separation. Further defining $\bar{\chi} = (\chi + \chi')/2$ and changing the variable of integration in the integrals leads to (SIMON 2007)

$$w(\theta) = \int_0^\infty \mathrm{d}\bar{\chi} \int_{-2\bar{\chi}}^{2\bar{\chi}} \mathrm{d}\Delta\chi\, \xi(\theta,\Delta\chi)\bar{n}\left(\bar{\chi} - \frac{\Delta\chi}{2}\right)\bar{n}\left(\bar{\chi} + \frac{\Delta\chi}{2}\right). \tag{3.47}$$

If we assume that $\bar{n}$ weakly varies over the typical $\Delta\chi/2$ scale in $\xi(\theta,\Delta\chi)$ so that $\bar{n}\left(\bar{\chi} - \Delta\chi/2\right) \simeq \bar{n}\left(\bar{\chi} + \Delta\chi/2\right) \simeq \bar{n}(\chi)$ in the inner integral, Eq. 3.47 simplifies to the well-known Limber approximation (LIMBER 1953) :

$$w(\theta) \simeq \int_0^\infty \mathrm{d}\bar{\chi}\, \bar{n}^2(\chi) \int_{-\infty}^\infty \mathrm{d}\Delta\chi\, \xi(\theta,\Delta\chi). \tag{3.48}$$

The cross-correlation term can be written as (BURDEN et AL. 2017)

$$\left\langle \delta(\chi,\gamma) \int \delta(\chi',\gamma')\bar{n}(\chi')d\chi' \right\rangle \simeq \int_0^\infty \mathrm{d}\chi'\, \bar{n}(\chi')\,\xi(\theta,\Delta\chi), \tag{3.49}$$

and by adopting the same changes of variable as previously, the right-hand side of Eq. 3.49 becomes

$$\int_{-\infty}^\infty \mathrm{d}\Delta\chi\, \bar{n}\left(\bar{\chi} + \frac{\Delta\chi}{2}\right)\xi(\theta,\Delta\chi). \tag{3.50}$$

In this equation, $\bar{\chi}$ is an undefined constant, which is related at first order to the mean radial distance of the sample. The right-hand side of Eq. 3.49 used to obtain this result should in reality be averaged over the observed volume, introducing a further integral over $\mathrm{d}^3\chi$. In fact, this approximation can be avoided by making explicit the volume integral over the survey window function as shown in Section 3.3.2.2. We note that if we use Limber-type approximation in Eq. 3.50, the mean number density goes out of the integral and the expression reduces to a constant times the projected correlation function.

In practice, we are seeking an expression for the anisotropic three-dimensional correlation function that can be used to model observed multipole moments. In the plane-parallel approximation, the separation vector $\mathbf{s}$ can be decomposed in terms of the transverse and radial comoving separations, $s_\perp$ and $s_\parallel$ respectively, using for instance the mid-point line-of-sight definition (K. B. FISHER, Marc DAVIS, M. A. STRAUSS et al. 1994). We can thus use the previous model defined for $\xi(\theta,\Delta\chi)$ and make the substitutions : $\Delta\chi \to s_\parallel$ and $\theta \to s_\perp$. This holds when the radial distance is large with respect to the pair separation and effectively assumes a flat sky. In this case, we obtain that

$$\tilde{\xi}(s_\perp, s_\parallel) = \xi(s_\perp, s_\parallel) - 2C(s_\perp, s_\parallel) + A(s_\perp) \tag{3.51}$$

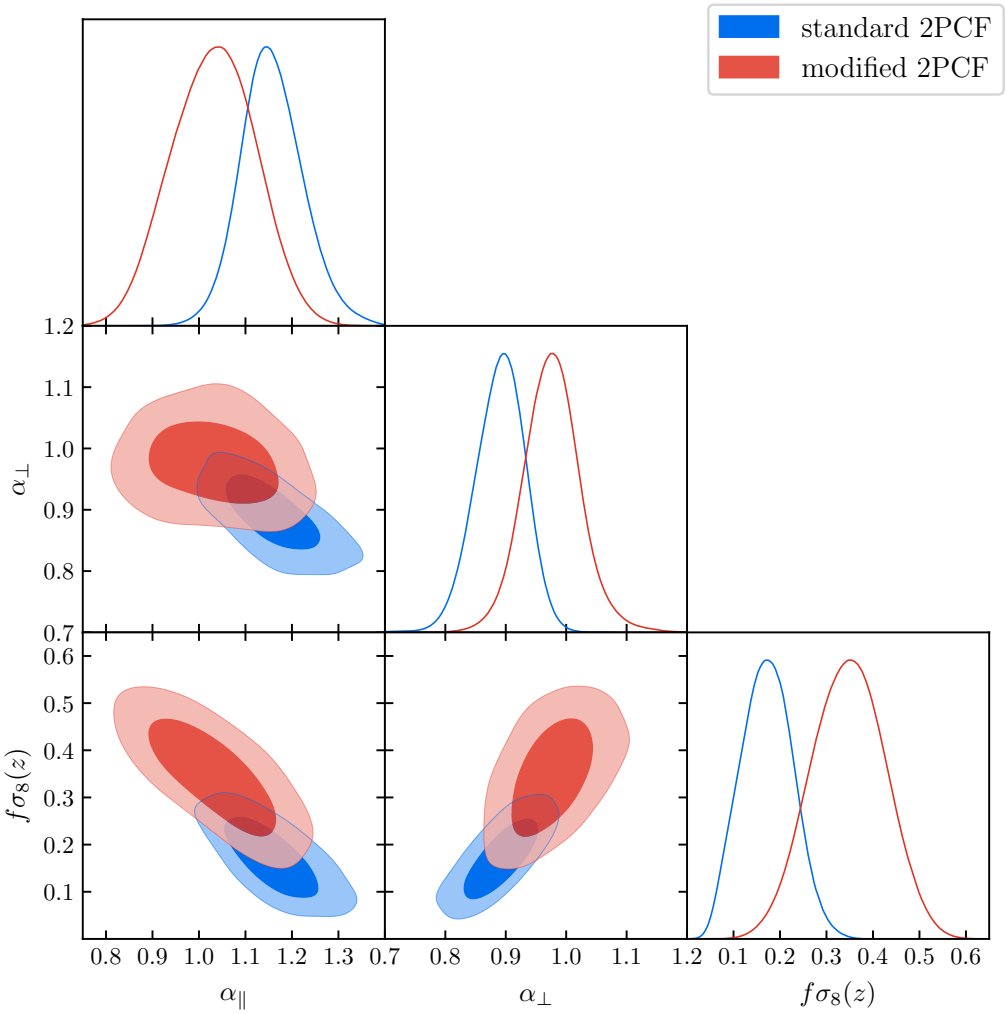

FIGURE 3.15 – RSD + BAO contours for the DR16 ELG sample. The blue contours corresponds to the fit of the standard 2PCF, while red contours corresponds to the fit to the AMF 2PCF. Taken from (TAMONE et AL. 2020)

where

$$C(s_\perp, s_\parallel) = \int_{-\infty}^{\infty} \mathrm{d}s_\parallel \, \bar{n}\left(\bar{\chi} + \frac{s_\parallel}{2}\right) \xi(s_\perp, s_\parallel), \tag{3.52}$$

$$A(s_\perp) = \int_0^{\infty} \mathrm{d}\bar{\chi} \int_{-\infty}^{\infty} \mathrm{d}s_\parallel \xi(s_\perp, s_\parallel) \, \bar{n}\left(\bar{\chi} - \frac{s_\parallel}{2}\right) \bar{n}\left(\bar{\chi} + \frac{s_\parallel}{2}\right), \tag{3.53}$$

or with Limber approximation,

$$C_\mathrm{L}(s_\perp, s_\parallel) = \bar{n}(\bar{\chi}) \int_{-\infty}^{\infty} \mathrm{d}s_\parallel \, \xi(s_\perp, s_\parallel), \tag{3.54}$$

$$A_\mathrm{L}(s_\perp) = \int_0^{\infty} \mathrm{d}\bar{\chi} \bar{n}^2(\bar{\chi}) \int_{-\infty}^{\infty} \mathrm{d}s_\parallel \xi(s_\perp, s_\parallel). \tag{3.55}$$

By substituting A and C by A_L and C_L in Eq. 3.51 one defines the simplest model, where both Limber and flat-sky approximations are used. In the eBOSS ELG analysis of (TAMONE et AL. 2020), where i have been involved in the AMF modelling, C and A_L are used as the cross-correlation and angular terms, respectively. In those approximate models, $\bar{\chi}$ is a free parameter that can be determined empirically from simulations for the specific galaxy sample under consideration. Eventually, the AMF correlation function multipole moments can be obtained by remapping $\tilde{\xi}(s_\perp, s_\parallel)$ into $\tilde{\xi}(s, \mu)$

using that $s_\perp = s\sqrt{1-\mu^2}$ and $s_\parallel = s\mu$, and integrating $\tilde{\xi}(s,\mu)$ over μ as in Eq. 3.23. In order to stregthen the cosmological measurement due to a low signal to noise ratio, isotropic BAO and RSD analyses are combined at the likelihood level for the eBOSS ELG sample (TAMONE et AL. 2020; DE MATTIA et AL. 2021). I present in Fig. 3.15 the posteriors of the BAO+RSD analysis of the ELG DR16 sample in configuration space (TAMONE et AL. 2020). The fit to the standard 2PCF provides non physicals constraints for the growth of structures $f\sigma_8 = 0.171^{+0.058}_{-0.059}$ while the fit of the AMF 2PCF provides a more robust estimate of $f\sigma_8 = 0.348^{+0.082}_{-0.089}$ in better agreement with expectations for current gravity models.

3.3.2.2 Full model

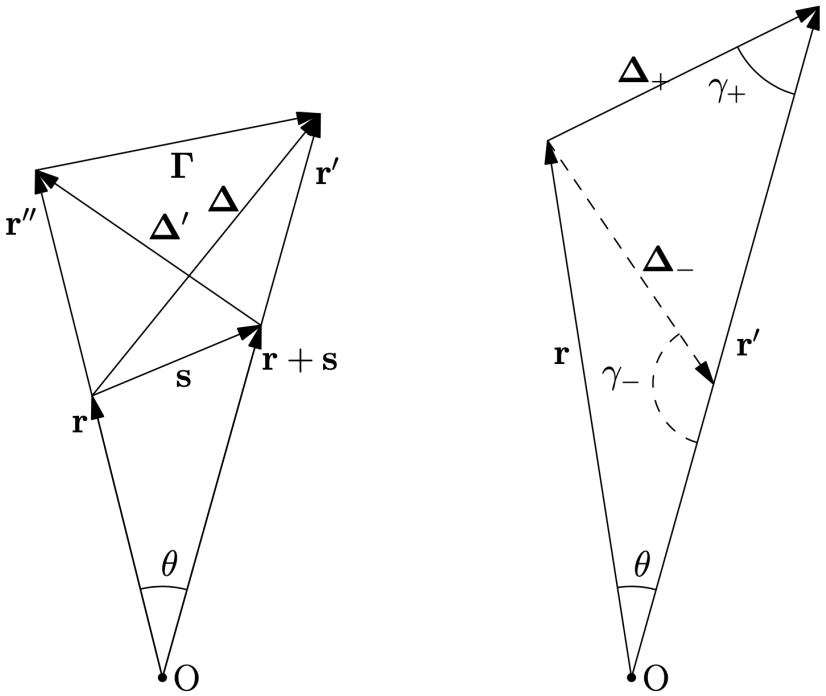

FIGURE 3.16 – Left : geometrical setting. Right : illustration of the two solutions of the triangle defined by the vectors $(\mathbf{r}, \Delta, \mathbf{r}')$. For given r, θ, and $\Delta = |\Delta_-| = |\Delta_+|$, it exists two possible lengths for r' and associated included angle : γ_+ or γ_-.

In fact, the flat-sky approximation and the approximation made in Eq. 3.49 can be avoided. Precisely, the AMF estimator in Eq. 4.83 corresponds to the auto-correlation of the AMF overdensity times the survey window function, divided by the survey window correlation function. The window function $P(\mathbf{r})$ is the probability of seeing an object at any position $\mathbf{r}$ in the survey.

$$F(\mathbf{r}) = P(\mathbf{r})\delta(\mathbf{r}) - P(\mathbf{r}) \int \mathrm{d}r'' \bar{n}(r'')\delta(\mathbf{r}''), \tag{3.56}$$

where $\mathbf{r}$ and $\mathbf{r}''$ share the same line of sight, the AMF correlation function is

$$\tilde{\xi}(\mathbf{s}) \equiv \frac{\langle F(\mathbf{r})F(\mathbf{r}+\mathbf{s})\rangle}{\langle P(\mathbf{r})P(\mathbf{r}+\mathbf{s})\rangle}. \tag{3.57}$$

From the definition of $F(\mathbf{r})$, we have that

$$\begin{aligned} F(\mathbf{r})F(\mathbf{r}+\mathbf{s}) = & P(\mathbf{r})P(\mathbf{r}+\mathbf{s})\delta(\mathbf{r})\delta(\mathbf{r}+\mathbf{s}) \\ & - P(\mathbf{r})\delta(\mathbf{r})P(\mathbf{r}+\mathbf{s})\int \mathrm{d}r'\bar{n}(r')\delta(\mathbf{r}') \\ & - P(\mathbf{r}+\mathbf{s})\delta(\mathbf{r}+\mathbf{s})P(\mathbf{r})\int \mathrm{d}r''\bar{n}(r'')\delta(\mathbf{r}'') \\ & + P(\mathbf{r})P(\mathbf{r}+\mathbf{s})\int \mathrm{d}r''\bar{n}(r'')\delta(\mathbf{r}'')\int \mathrm{d}r'\bar{n}(r')\delta(\mathbf{r}'), \end{aligned} \tag{3.58}$$

where $\mathbf{r}'$ and $\mathbf{r}+\mathbf{s}$ are colinear (as well as $\mathbf{r}$ and $\mathbf{r}''$). By taking the ensemble average of Eq. 3.58 we can identify four terms. The first one corresponds to the windowed correlation function, the second and third are associated to the cross term in the following, and the fourth term to the angular term. The denominator of Eq. 3.57 is the window correlation function. Putting all terms together we find that the AMF correlation function can be written as

$$\tilde{\xi}(\mathbf{s}) = \xi(\mathbf{s}) - \frac{C(\mathbf{s})}{W(\mathbf{s})} + \frac{A(\mathbf{s})}{W(\mathbf{s})}, \tag{3.59}$$

where

$$\xi(\mathbf{s}) = \langle\delta(\mathbf{r})\delta(\mathbf{r}+\mathbf{s})\rangle \tag{3.60}$$

$$C(\mathbf{s}) = \int \mathrm{d}^3r\, P(\mathbf{r})P(\mathbf{r}+\mathbf{s})\left[\int \mathrm{d}r'\bar{n}(r')\xi(\mathbf{r}'-\mathbf{r}) + \int \mathrm{d}r''\bar{n}(r'')\xi\left(\mathbf{r}''-\mathbf{r}-\mathbf{s}\right)\right], \tag{3.61}$$

$$A(\mathbf{s}) = \int \mathrm{d}^3r\, P(\mathbf{r})P(\mathbf{r}+\mathbf{s})\int \mathrm{d}r''\bar{n}(r'')\int \mathrm{d}r'\bar{n}(r')\xi(\mathbf{r}'-\mathbf{r}''), \tag{3.62}$$

$$W(\mathbf{s}) = \int \mathrm{d}^3r\, P(\mathbf{r})P(\mathbf{r}+\mathbf{s}). \tag{3.63}$$

The geometrical configuration is presented in Fig. 3.16. By introducing $\mathbf{r_s}$, Δ, Δ', and Γ such that

$$\begin{aligned} \mathbf{r_s} &= \mathbf{r}+\mathbf{s} \\ \Delta &= \mathbf{r}'-\mathbf{r} \\ \Delta' &= \mathbf{r}''-\mathbf{r_s} \\ \Gamma &= \mathbf{r}'-\mathbf{r}'', \end{aligned} \tag{3.64}$$

A and C simplifie to

$$C(\mathbf{s}) = \int \mathrm{d}^3r P(\mathbf{r})P(\mathbf{r_s})\left[\int \mathrm{d}r'\bar{n}(r')\xi(\Delta) + \int \mathrm{d}r''\bar{n}(r'')\xi(\Delta')\right] = C_1(\mathbf{s}) + C_2(\mathbf{s}) \tag{3.65}$$

$$A(\mathbf{s}) = \int \mathrm{d}^3r P(\mathbf{r})P(\mathbf{r_s})\int \mathrm{d}r''\bar{n}(r'')\int \mathrm{d}r'\bar{n}(r')\xi(\Gamma). \tag{3.66}$$

In order to calculate those terms we have to solve for three triangles with sides $(\mathbf{r},\Delta,\mathbf{r}')$,$(\mathbf{r}'',\Delta',\mathbf{r_s})$, and $(\mathbf{r}'',\Gamma,\mathbf{r}')$. We need to express r' and r'' as a function of r, r_s, θ, Δ, Δ', and Γ. This involves solving the general case when two sides and a non-included angle of a triangle are given. In this configuration, there is one or two solutions depending on the relative size of the two given sides. However, since separations are generally smaller than the distance to galaxies, we are always in the

case with two solutions. We thus have

$$r' = r\cos\theta \pm \sqrt{\Delta^2 - r^2\sin^2\theta}, \tag{3.67}$$

$$r'' = r_s\cos\theta \pm \sqrt{\Delta'^2 - r_s^2\sin^2\theta}, \tag{3.68}$$

$$r' = r''\cos\theta \pm \sqrt{\Gamma^2 - r''^2\sin^2\theta}. \tag{3.69}$$

Using those relations in Eq. 3.65 and 3.66 leads to

$$C_1(\mathbf{s}) = \int \mathrm{d}^3 r P(\mathbf{r})P(\mathbf{r_s}) \int_{-r}^{\infty} \mathrm{d}\Delta \frac{\pm\Delta}{\sqrt{\Delta^2 - r^2\sin^2\theta}} \bar{n}\left(r\cos\theta \pm \sqrt{\Delta^2 - r^2\sin^2\theta}\right)\xi(\Delta), \tag{3.70}$$

$$C_2(\mathbf{s}) = \int \mathrm{d}^3 r P(\mathbf{r})P(\mathbf{r_s}) \int_{-r_s}^{\infty} \mathrm{d}\Delta' \frac{\pm\Delta'}{\sqrt{\Delta'^2 - r_s^2\sin^2\theta}} \bar{n}\left(r_s\cos\theta \pm \sqrt{\Delta'^2 - r_s^2\sin^2\theta}\right)\xi(\Delta'), \tag{3.71}$$

$$A(\mathbf{s}) = \int \mathrm{d}^3 r P(\mathbf{r})P(\mathbf{r_s}) \int_0^{\infty} \mathrm{d}r'' \bar{n}(r'') \int_{-r''}^{\infty} d\Gamma \frac{\pm\Gamma}{\sqrt{\Gamma^2 - r''^2\sin^2\theta}} \bar{n}\left(r''\cos\theta \pm \sqrt{\Gamma^2 - r''^2\sin^2\theta}\right)\xi(\Gamma). \tag{3.72}$$

If we expand $\xi(\Delta)$ in multipole moments in the local plane-parallel approximation such that $\xi(\Delta) = \sum_{p=0}^{\infty}\xi_p(\Delta)L_\ell(\mu_\Delta)$, the term C_1 can be re-expressed as

$$C_1(\mathbf{s}) = 2\int_0^{\infty} \mathrm{d}\Delta \sum_{p=0}^{\infty} \Delta\xi_p(\Delta) \int \mathrm{d}^3 r P(\mathbf{r})P(\mathbf{r_s}) \frac{\pm\bar{n}\left(r\cos\theta \pm \sqrt{\Delta^2 - r^2\sin^2\theta}\right)}{\sqrt{\Delta^2 - r^2\sin^2\theta}} L_p(\mu_{\Delta\pm}). \tag{3.73}$$

By making the change of variable $\Delta \to -\Delta$ in Eq. 3.70, the solution with smallest r' (with minus sign) becomes

$$C_{1-}(\mathbf{s}) = 2\int_0^{\infty} \mathrm{d}\Delta \sum_{p=0}^{\infty} \Delta\xi_p(\Delta) \int \mathrm{d}^3 r P(\mathbf{r})P(\mathbf{r_s}) \frac{\bar{n}\left(r\cos\theta - \sqrt{\Delta^2 - r^2\sin^2\theta}\right)}{\sqrt{\Delta^2 - r^2\sin^2\theta}} L_p(\mu_{\Delta-}). \tag{3.74}$$

Therefore, assuming that the two geometrical configurations are equiprobable, we can take the average contribution and

$$C_1(\mathbf{s}) = \int_0^{\infty} \mathrm{d}\Delta \sum_{p=0}^{\infty} \Delta\xi_p(\Delta) \left(\int \mathrm{d}^3 r P(\mathbf{r})P(\mathbf{r_s}) \times \frac{\bar{n}\left(r\cos\theta + \sqrt{\Delta^2 - r^2\sin^2\theta}\right)L_p(\mu_{\Delta+}) + \bar{n}\left(r\cos\theta - \sqrt{\Delta^2 - r^2\sin^2\theta}\right)L_p(\mu_{\Delta-})}{\sqrt{\Delta^2 - r^2\sin^2\theta}} \right). \tag{3.75}$$

By further expanding in multipole moments, the latter read

$$C_{1\ell}(s) = \int_0^{\infty} \mathrm{d}\Delta \sum_{p=0}^{\infty} \Delta\xi_p(\Delta) \left(\frac{2\ell+1}{2} \int_{-1}^{1} \mathrm{d}\mu_s \int \mathrm{d}^3 r P(\mathbf{r})P(\mathbf{r_s}) \times \frac{\bar{n}\left(r\cos\theta + \sqrt{\Delta^2 - r^2\sin^2\theta}\right)L_p(\mu_{\Delta+}) + \bar{n}\left(r\cos\theta - \sqrt{\Delta^2 - r^2\sin^2\theta}\right)L_p(\mu_{\Delta-})}{\sqrt{\Delta^2 - r^2\sin^2\theta}} L_\ell(\mu_s) \right). \tag{3.76}$$

Carrying out in a similar fashion with the other terms we eventually find that

$$X_\ell(s) = \int_0^\infty \mathrm{d}\Delta \sum_{p=0}^{\infty} \Delta\,\xi_p(\Delta)\mathcal{W}_{X\ell p}(s,\Delta), \tag{3.77}$$

where X stands for C_1, C_2, or A and

$$\mathcal{W}_{C_1\ell p}(s,\Delta) = \frac{2\ell+1}{2}\int_{-1}^{1}\mathrm{d}\mu_s \int \mathrm{d}^3 r\, P(\mathbf{r})P(\mathbf{r_s}) \times \frac{\bar{n}\left(r\cos\theta + \sqrt{\Delta^2 - r^2\sin^2\theta}\right)L_p(\mu_{\Delta-}) + \bar{n}\left(r\cos\theta - \sqrt{\Delta^2 - r^2\sin^2\theta}\right)L_p(\mu_{\Delta-})}{\sqrt{\Delta^2 - r^2\sin^2\theta}} L_\ell(\mu_s), \tag{3.78}$$

$$\mathcal{W}_{C_2\ell p}(s,\Delta) = \frac{2\ell+1}{2}\int_{-1}^{1}\mathrm{d}\mu_s \int \mathrm{d}^3 r\, P(\mathbf{r})P(\mathbf{r_s}) \times \frac{\bar{n}\left(r_s\cos\theta + \sqrt{\Delta^2 - r_s^2\sin^2\theta}\right)L_p(\mu_{\Delta'+}) + \bar{n}\left(r_s\cos\theta - \sqrt{\Delta^2 - r_s^2\sin^2\theta}\right)L_p(\mu_{\Delta'-})}{\sqrt{\Delta^2 - r_s^2\sin^2\theta}} L_\ell(\mu_s), \tag{3.79}$$

$$\mathcal{W}_{A\ell p}(s,\Delta) = \frac{2\ell+1}{2}\int_{-1}^{1}\mathrm{d}\mu_s \int \mathrm{d}^3 r\, P(\mathbf{r})P(\mathbf{r_s}) \int_0^\infty \mathrm{d}r'\bar{n}(r') \times \frac{\bar{n}\left(r'\cos\theta + \sqrt{\Delta^2 - r'^2\sin^2\theta}\right)L_p(\mu_{\Gamma+}) + \bar{n}\left(r'\cos\theta - \sqrt{\Delta^2 - r'^2\sin^2\theta}\right)L_p(\mu_{\Gamma-})}{\sqrt{\Delta^2 - r'^2\sin^2\theta}} L_\ell(\mu_s). \tag{3.80}$$

Similarly, the window correlation function multipole moments can be written as

$$\mathcal{W}_\ell(s) = \frac{2\ell+1}{2}\int_{-1}^{1}\mathrm{d}\mu_s \int \mathrm{d}^3 r P(\mathbf{r})P(\mathbf{r_s})L_\ell(\mu_s). \tag{3.81}$$

In the above multipole expansions, we use the mid-point line-of-sight convention so that μ_Δ, $\mu_{\Delta'}$, μ_Γ correspond to the cosine angles between the separation vectors and their mid-point directions, e.g. $\mu_s = \hat{\mathbf{p}}_s\cdot\hat{\mathbf{s}}$, where $\mathbf{p}_s$ is the position of the median point of $\mathbf{s}$. Those cosine angles can be deduced by solving the half triangle delineated by the median point direction. We thus have that

$$\mu_{\Delta\pm} = \frac{\pm r'\cos\gamma_\Delta - \Delta/2}{\sqrt{r'^2 + \Delta^2/4 \mp r'\Delta\cos\gamma_\Delta}} \text{ with } \gamma_\Delta = \arcsin\frac{r\sin\theta}{\Delta}, \tag{3.82}$$

$$\mu_{\Delta'\pm} = \frac{\pm r''\cos\gamma_{\Delta'} - \Delta'/2}{\sqrt{r''^2 + \Delta'^2/4 \mp r''\Delta'\cos\gamma_{\Delta'}}} \text{ with } \gamma_{\Delta'} = \arcsin\frac{r_s\sin\theta}{\Delta'}, \tag{3.83}$$

$$\mu_{\Gamma\pm} = \frac{\pm r'\cos\gamma_\Gamma - \Gamma/2}{\sqrt{r'^2 + \Gamma^2/4 \mp r'\Gamma\cos\gamma_\Gamma}} \text{ with } \gamma_\Gamma = \arcsin\frac{r''\sin\theta}{\Gamma}. \tag{3.84}$$

The kernels in Eqs. 3.78, 3.79, 3.80, and 3.81 are purely geometrical functions that depend on the window function and number density of the sample. They are weighted integrals over the observed volume and can be evaluated with a Monte Carlo method by making use of random catalogues as in (DE MATTIA et RUHLMANN-KLEIDER 2019). The weighting of each pair is given by the functions in the inner integrands in Eqs. 3.78, 3.79, 3.80, and 3.81. For instance in the case of $\mathcal{W}_\ell$, an estimate can

be obtained by computing

$$\mathcal{W}_\ell(s) = \frac{2\ell+1}{2}\frac{1}{2\pi s^2 \Delta s\, N_\mathrm{p}}\sum_{i,j}\delta_D(|\mathbf{r}_j-\mathbf{r}_i|-s)L_\ell(\mu_s), \tag{3.85}$$

where the sum goes over the i^{th} and j^{th} random objects of the catalogue, Δs is the bin size in s, N_p is total number of pairs, and δ_D denotes the Dirac delta function. An alternative and efficient method to calculate those kernels in a realistic survey configuration, i.e. in a lightcone, is to follow the method of (Breton et de la Torre 2021). The latter, use two nested spherical volume integrals to sample all pair configurations in the lightcone. It necessitates the a priori knowledge of the angular selection correlation function, which can be efficiently estimated with angular maps of the survey, as well as the mean number density of galaxies as function of distance. Applying a similar approach to the case of the above kernels involves computing the following integrals numerically :

$$\begin{aligned}\mathcal{W}_{C_1\ell p}(s_\mathrm{min},s_\mathrm{max},\Delta) = \frac{2\ell+1}{2}\int_0^\infty \mathrm{d}r\, r^2\bar{n}(r)\int_{s_\mathrm{min}}^{s_\mathrm{max}}\mathrm{d}s\int_{-1}^{1}\mathrm{d}\mu\,\Phi(\theta)\,\bar{n}(r_s)L_\ell(\mu_s)\\ \times\frac{\bar{n}\left(r\cos\theta+\sqrt{\Delta^2-r^2\sin^2\theta}\right)L_p(\mu_{\Delta-})+\bar{n}\left(r\cos\theta-\sqrt{\Delta^2-r^2\sin^2\theta}\right)L_p(\mu_{\Delta-})}{\sqrt{\Delta^2-r^2\sin^2\theta}},\end{aligned} \tag{3.86}$$

$$\begin{aligned}\mathcal{W}_{C_2\ell p}(s_\mathrm{min},s_\mathrm{max},\Delta) = \frac{2\ell+1}{2}\int_0^\infty \mathrm{d}r\, r^2\bar{n}(r)\int_{s_\mathrm{min}}^{s_\mathrm{max}}\mathrm{d}s\int_{-1}^{1}\mathrm{d}\mu\,\Phi(\theta)\,\bar{n}(r_s)L_\ell(\mu_s)\\ \times\frac{\bar{n}\left(r_s\cos\theta+\sqrt{\Delta^2-r_s^2\sin^2\theta}\right)L_p(\mu_{\Delta'+})+\bar{n}\left(r_s\cos\theta-\sqrt{\Delta^2-r_s^2\sin^2\theta}\right)L_p(\mu_{\Delta'-})}{\sqrt{\Delta^2-r_s^2\sin^2\theta}},\end{aligned} \tag{3.87}$$

$$\begin{aligned}\mathcal{W}_{A\ell p}(s_\mathrm{min},s_\mathrm{max},\Delta) = \frac{2\ell+1}{2}\int_0^\infty \mathrm{d}r\, r^2\bar{n}(r)\int_{s_\mathrm{min}}^{s_\mathrm{max}}\mathrm{d}s\int_{-1}^{1}\mathrm{d}\mu\,\Phi(\theta)\,\bar{n}(r_s)\int_0^\infty\mathrm{d}r'\bar{n}(r')L_\ell(\mu_s)\\ \times\frac{\bar{n}\left(r'\cos\theta+\sqrt{\Delta^2-r'^2\sin^2\theta}\right)L_p(\mu_{\Gamma+})+\bar{n}\left(r'\cos\theta-\sqrt{\Delta^2-r'^2\sin^2\theta}\right)L_p(\mu_{\Gamma-})}{\sqrt{\Delta^2-r'^2\sin^2\theta}},\end{aligned} \tag{3.88}$$

where $\Phi(\theta)$ is the angular selection function correlation function, θ and r_s can be expressed in terms of r, s, and μ_s, and $(s_\mathrm{min}, s_\mathrm{max})$ defines the s bin under consideration. These three- and four-dimensional integrals can be computed efficiently using the CUBA library (T. Hahn 2005) as described in (Breton et de la Torre 2021). Finally, the AMF anisotropic correlation function can be expressed as

$$\tilde{\xi}(s,\mu) = \xi(s,\mu) - \frac{C(s,\mu)}{W(s,\mu)} + \frac{A(s,\mu)}{W(s,\mu)} \tag{3.89}$$

where

$$C(s,\mu) = \sum_{\ell=0}^{\infty}\left(\int_0^\infty \mathrm{d}\Delta\sum_{p=0}^{\infty}\Delta\xi_p(\Delta)\mathcal{W}_{C\ell p}(s,\Delta)\right)L_\ell(\mu) \tag{3.90}$$

$$A(s,\mu) = \sum_{\ell=0}^{\infty}\left(\int_0^\infty \mathrm{d}\Delta\sum_{p=0}^{\infty}\Delta\xi_p(\Delta)\mathcal{W}_{A\ell p}(s,\Delta)\right)L_\ell(\mu) \tag{3.91}$$

$$W(s,\mu) = \sum_{\ell=0}^{\infty}\mathcal{W}_\ell(s)L_\ell(\mu). \tag{3.92}$$

and

$$\mathcal{W}_{C\ell p}(s,\Delta) = \mathcal{W}_{C_1\ell p}(s,\Delta) + \mathcal{W}_{C_2\ell p}(s,\Delta). \tag{3.93}$$

The multipole moments of the AMF correlation function are obtained from $\tilde{\xi}(s,\mu)$ as

$$\tilde{\xi}_\ell(s) = \frac{(2\ell+1)}{2}\int_{-1}^{1}\tilde{\xi}(s,\mu)L_\ell(\mu)\mathrm{d}\mu. \tag{3.94}$$

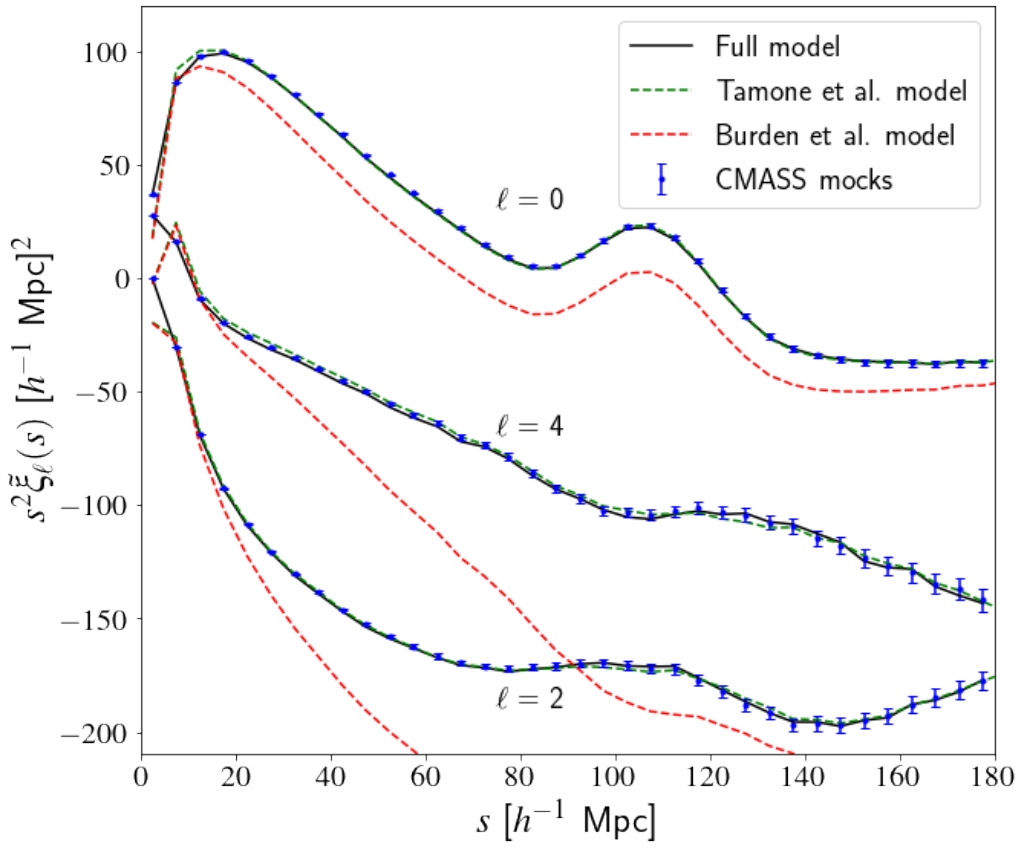

FIGURE 3.17 – Comparison of the monopole, quadrupole, and hexadecapole AMF correlation function model predictions and CMASS mocks mean measurement. The black solid line corresponds to the full model, the green short-dashed line to the TAMONE et AL. 2020 model, and the red long-dashed line to the original BURDEN et AL. 2017 ansatz.

3.3.2.3 Implementation of the full model

We use a similar method as that presented in BRETON et DE LA TORRE 2021 to calculate the full model kernels. We first build angular HEALPIX (GÓRSKI et AL. 2005) maps from the survey footprints used to create the mocks. These maps are used to estimate the angular selection correlation function, $\Phi(\theta)$, with POLSPICE code (SZAPUDI, PRUNET et COLOMBI 2001; CHON et AL. 2004). The $\bar{n}(\chi)$ are estimated from CMASS and ELG random catalogues and shown in Fig. 3.18. Redshifts are converted to comoving distances using the corresponding fiducial cosmology of the simulation, given in Table 3.1. From these two ingredients, the kernels can be evaluated numerically using multi-dimensional Monte-Carlo integration methods. Specifically, we use the CUBA library (T. HAHN 2005) in a similar way as in BRETON et DE LA TORRE 2021 to solve numerically the kernel integrals. A code to compute those kernels for any survey geometry is publicly available[8]. Once kernels are computed, the cross-correlation and angular terms are obtained by integrating over Δ the kernels times the model

8. https://github.com/mianbreton/RR_code

standard correlation function. In practice, this integral is performed as a Riemmann sum. We find that a Δ binning of 1 Mpc/h is sufficient to have a numerically stable model estimation.

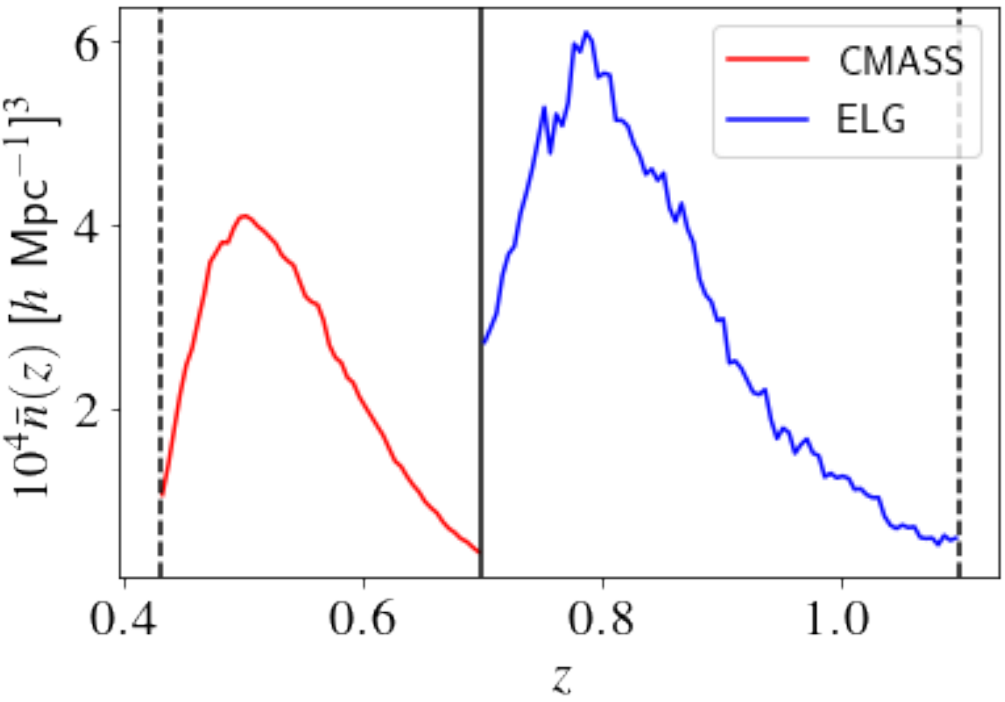

FIGURE 3.18 – Galaxy number density in CMASS (red curve) and ELG (blue curve) mock samples.

3.3.2.4 Sensitivity to angular systematics

It is interesting to see formally that the AMF overdensity removes any additive angular contamination. Indeed, if we write the contaminated overdensity $\delta(\mathbf{r}) + c(\mathbf{r})$, where c is a contamination field that only depends on the line-of-sight direction, we have for the windowed AMF overdensity,

$$F(\mathbf{r}) = P(\mathbf{r})\,(\delta(\mathbf{r}) + c(\mathbf{r})) - P(\mathbf{r}) \int \mathrm{d}r'\,\bar{n}(r')\,\big(\delta(\mathbf{r}') + c(\mathbf{r}')\big) \tag{3.95}$$

$$= P(\mathbf{r})\delta(\mathbf{r}) - P(\mathbf{r}) \int \mathrm{d}r'\,\bar{n}(r')\delta(\mathbf{r}'). \tag{3.96}$$

To obtain the latter equation we have used that, by definition of c and the fact that $\mathbf{r}$ and $\mathbf{r}'$ share the same line of sight, $c(\mathbf{r}') = c(\mathbf{r})$. Nonetheless, if the contamination field modulates the observed number of galaxies, as for instance in the case of varying survey depth or galactic extinction (SHAFER et HUTERER 2015), both additive and multiplicative components will arise, and the multiplicative one will not be erased (it will factorise $F(\mathbf{r})$). In order to verify previous statements, we test the efficiency of the AMF two-point correlation function estimator at removing a spurious angular modulation in galaxy number using the galaxy CMASS mocks introduced in Section 3.1.5. We instil an artificial angular modulation in the number of galaxies N, such that $N \to N(1+\epsilon)$, in a similar fashion as in DE MATTIA et RUHLMANN-KLEIDER 2019. This is done by weighting each galaxy at angular position (RA, Dec) by

$$w_{\mathrm{ang}}(\mathrm{R.A}, \mathrm{Dec}) = 1 + 0.2 \sin\left(\frac{2\pi}{10} \times \mathrm{RA}\right) \sin\left(\frac{2\pi}{5} \times \mathrm{Dec}\right). \tag{3.97}$$

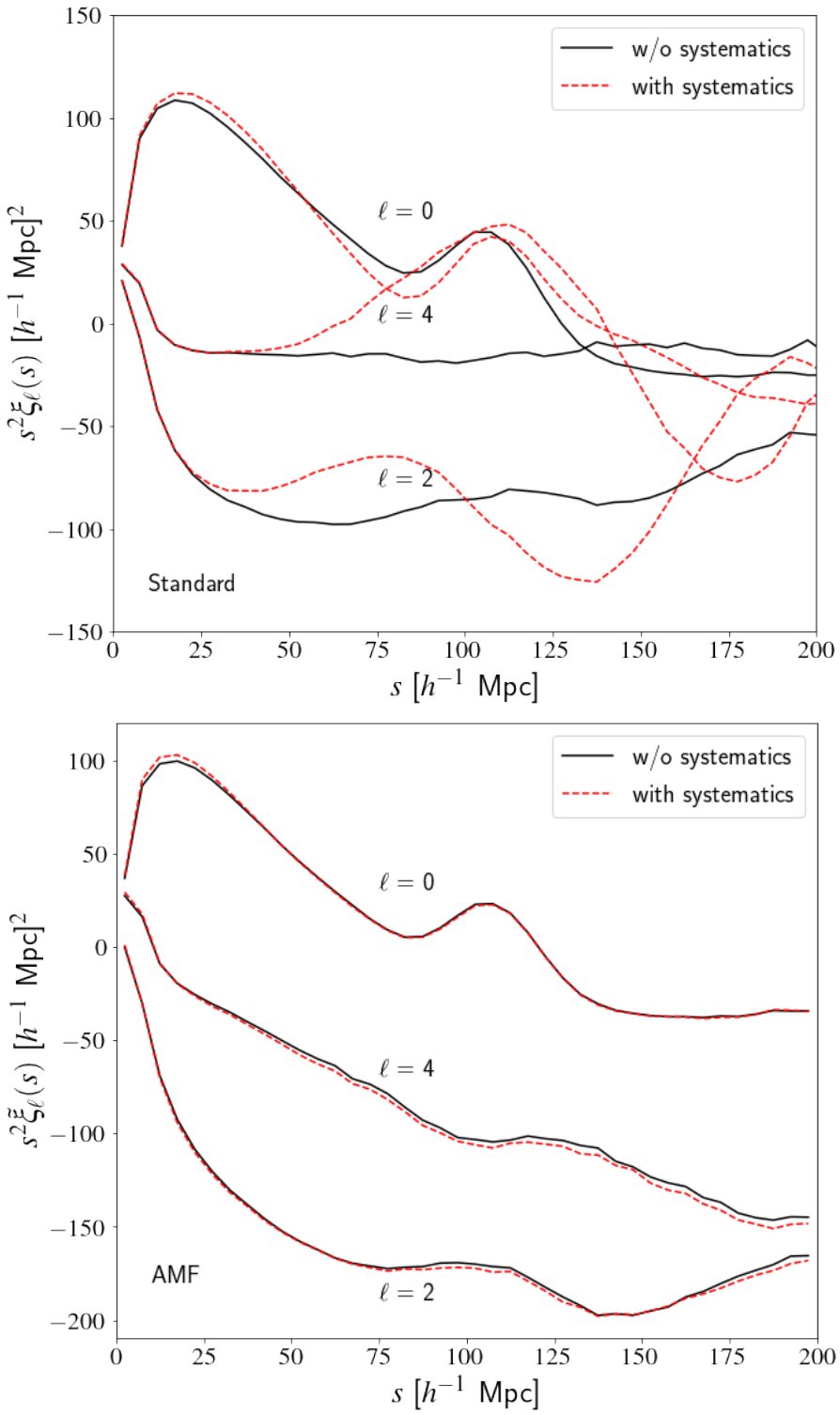

FIGURE 3.19 – CMASS mocks mean measurements of the standard (top figure) and AMF (bottom figure) correlation function multipole moments with (solid lines) and without (dashed lines) angular systematics.

We choose here a modulation amplitude of 20%, which is typical of the observed level. The standard and AMF correlation function multipole moments are measured in each mock and later averaged, including or not galaxy weights $w_{\rm ang}$. In the standard two-point correlation function estimator, the angular weights are only applied to the galaxy catalogue, while in the AMF estimator, they are applied in the galaxy and shuffled random catalogues. The resulting measurements are shown in Fig. 3.19. We can see for the standard two-point correlation function that angular

systematics significantly affect all the multipole moments. On the other hand, the AMF multipole moments are nearly unaffected by angular systematics. We only see a negligible shift in amplitude on the small scales of the monopole and on the hexadecapole. This demonstrates that the multiplicative component of the angular contamination is very small, and most of the effect of the angular modulation is removed in the AMF estimator.

3.3.3 Test on mock samples

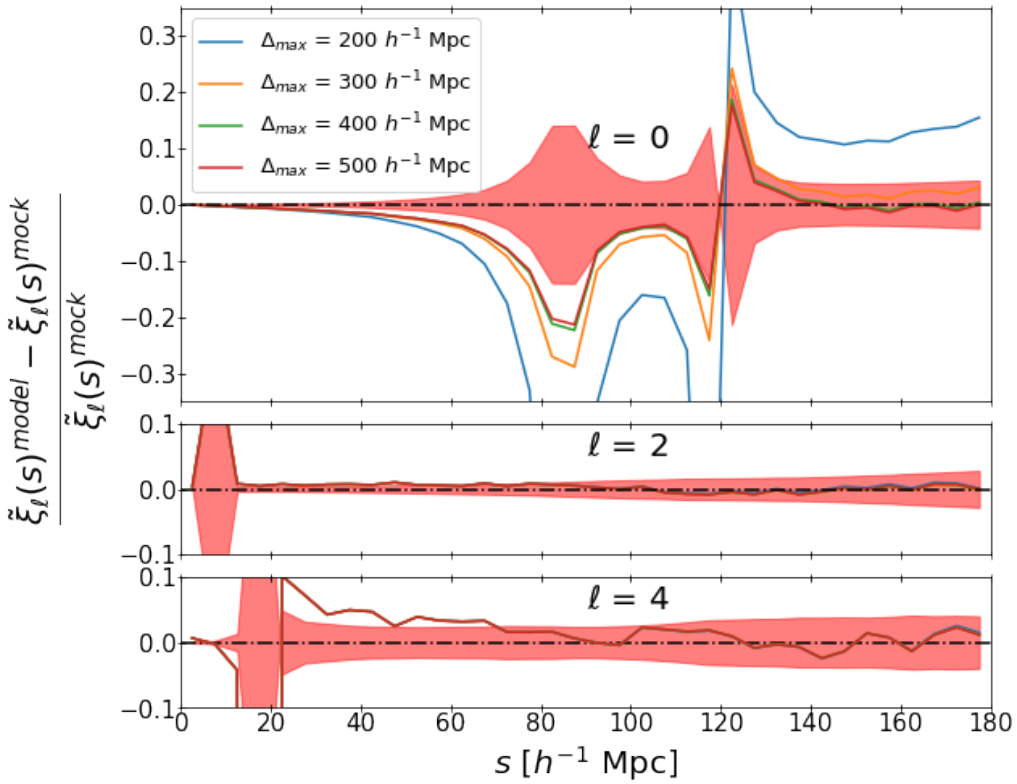

FIGURE 3.20 – Relative difference between the full model (black solid line in Fig. 3.17) and the mean of CMASS mocks measurements as a function of $\Delta_{\max}$ (the maximum Δ value for the integration of Eqs. 3.90, 3.91) for the monopole (top), quadrupole (middle), and hexadecapole (bottom) AMF correlation function. The red shade area represents the 1σ statistical uncertainty.

In order to test the AMF correlation function model presented in the previous section, we make use of NSERIES and EZmocks (see section 3.1.5 which reproduce CMASS and eBOSS ELG samples and cover the redshift intervals $0.43 < z < 0.7$ and $0.7 < z < 1.1$ respectively. First, we compare model predictions to the mean AMF correlation function measured in the CMASS mocks. The models take as input the redshift-space galaxy correlation function and sample number density as a function of radial distance. For the purpose of testing AMF models, we fix those to their mean mocks values.

We present in Fig. 3.17 the comparison between the original ansatz from BURDEN et AL. 2017, the model used in TAMONE et AL. 2020, the full model presented in this thesis, and mock predictions. We can see that the original ansatz allows us to recover only qualitatively the mock AMF correlation function mutipole moments, with a significant shift in amplitude. Conversely, TAMONE et AL. 2020 and the full model yield similar predictions, very close to the mock measurements. In fact, looking closely at the differences between these two models, we see that the full model performs best, particularly on the smallest scales of the monopole and on the hexadecapole. It is worth recalling

that the TAMONE et AL. 2020 model has a free parameter, $\bar{\chi}$, which we optimised here to best reproduce the measured AMF correlation in the mocks.

In evaluating the models, we have in practice to define the limit of integration for the integral over χ or Δ, as in Eqs. 3.90-3.91. The impact of this choice on the full model accuracy is presented in Fig. 3.20. The latter shows the relative difference of the full model prediction with respect to the mock prediction, for different values of $\Delta_{\rm max}$ varying from 200 to 500 Mpc/h. $\Delta_{\rm max}$ = 500 Mpc/h corresponds approximately to the maximum scale possibly probed in the mock survey volume. The red area in Fig. 3.20 represents the 1σ deviation from the mean of the mocks.

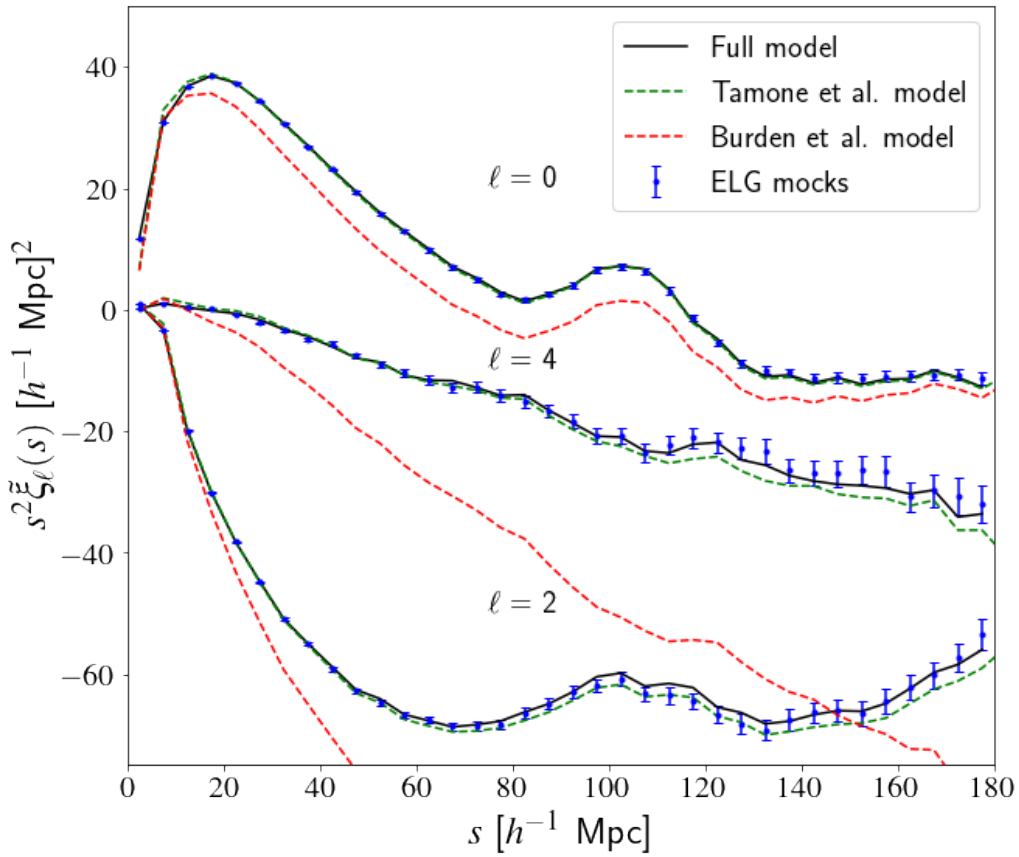

FIGURE 3.21 – Comparison of the monopole, quadrupole, and hexadecapole AMF correlation function model predictions and ELG mocks mean measurement. The black solid line corresponds to the full model, the green short-dashed line to the TAMONE et AL. 2020 model, and the red long-dashed line to the original (BURDEN et AL. 2017) ansatz.

We find that, as expected, by increasing $\Delta_{\rm max}$, the prediction converges to the expected signal, particularly for the monopole. For the quadrupole and hexadecapole, the prediction already converges for $\Delta_{\rm max}$ = 200 Mpc/h. We note that the two strong departures from zero around the BAO peak in the monopole, and on small-scale in the quadrupole and hexadecapole, are artifacts due to the zero crossing of these functions. Overall, in the case of the CMASS sample, we find that $\Delta_{\rm max}$ = 400 Mpc/h allows the recovery of the mocks prediction within a percent. While the quadrupole signal is retrieved at all scales below 1 σ, we can see larger shifts for the monopole and hexadecapole. The impact of these shifts on the determination of cosmological parameters will be presented in section 3.3.3.1.

We repeat the comparison for the ELG, a population of galaxies that has a very different intrinsic clustering properties with respect to CMASS. In that case, the correlation function measurements are less precise, mainly due to the smaller volume probed by the ELG mock samples. The mean AMF correlation function in the ELG mocks is shown in Fig. 3.21 together with the prediction of

the full model. Similarly as for CMASS, the agreement is very good, with the full model prediction falling within the 1σ measurement errors. We note that the ELG sample selection function is more complex as the sample is made of different patches (TAMONE et AL. 2020), with slightly different $\bar{n}(z)$. In the modelling we use instead single averaged $\bar{n}(z)$, which can explain the small difference seen on large scales with respect to the mock prediction and that were not present in the CMASS case.

3.3.3.1 Cosmological analysis of CMASS and ELG AMF clustering

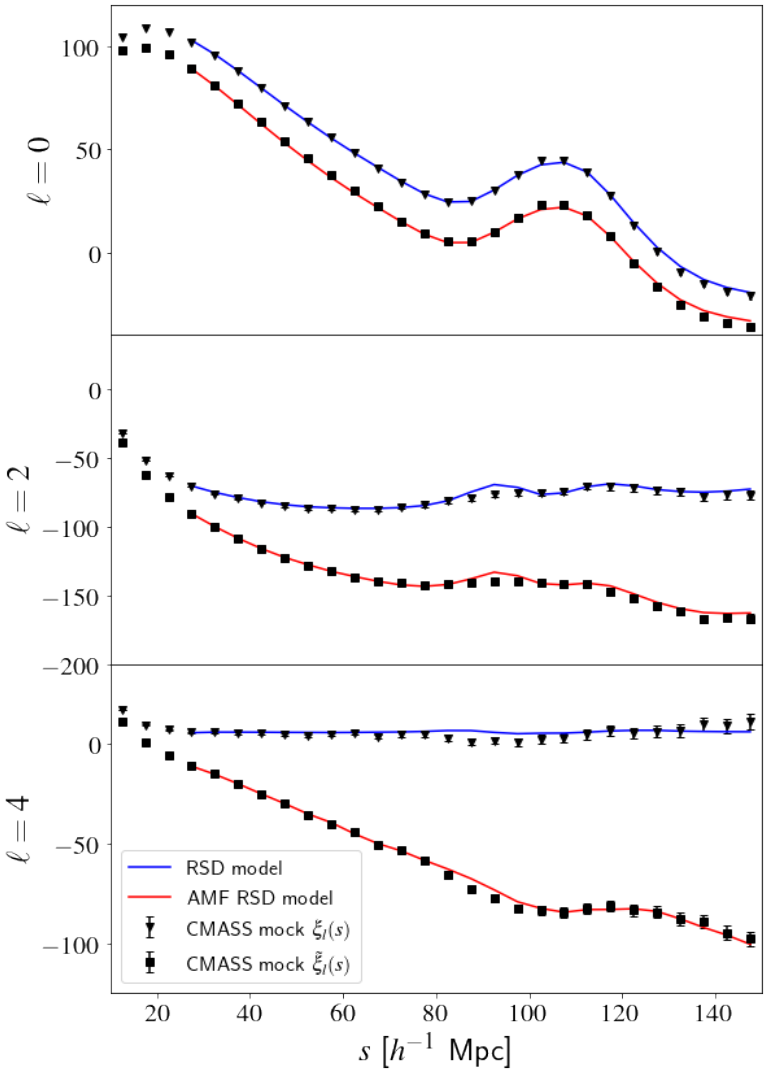

FIGURE 3.22 – Best-fit RSD models to the standard and AMF mean mock monopole and quadrupole, and hexadecapole for the CMASS sample.

The models for the AMF TNS correlation moments are evaluated using Eq. 3.89, where $\xi(s,\mu)$ in Eqs. 3.90 and 3.91 is replaced by $\xi^{\rm TNS}(s,\mu)$, given by the hankel transform of Eq. 2.256. The sum over TNS multipoles is limited to even multipole moments up to $\ell = 8$, since the other moments vanish. Moreover, we parameterise the Alcock-Paczyński (AP) distortions induced by the assumed fiducial cosmology in the measurements via Eq. 2.274. We apply these dilation parameters to the theoretical TNS power spectrum $P^s(k,\mu)$ defined in Eq. 2.256. In this way, we do not have to recompute the kernels at each iteration of the data likelihood analysis. We have checked that this implementation gives unbiased cosmological measurements when fitting the modelled AMF correlation function, which should in principle give the exact same result as the one of the standard correlation function,

regardless of the correctness of the considered AMF model. The model for the AMF BAO correlation function multipole moments is obtained from Hankel transform 2.262 of Eq. 2.273, where $\xi(s,\mu)$ in Eqs. 3.90 and 3.91 is replaced by $\xi^{\rm BAO}(s,\mu)$ and

$$\xi^{\rm BAO}(s,\mu) = \sum_{\ell=0}^{\ell=4} \xi_\ell^{\rm BAO}(s) L_\ell(\mu) \tag{3.98}$$

with $P^s_{\rm BAO}(k,\mu)$ given by Eq. 2.273.

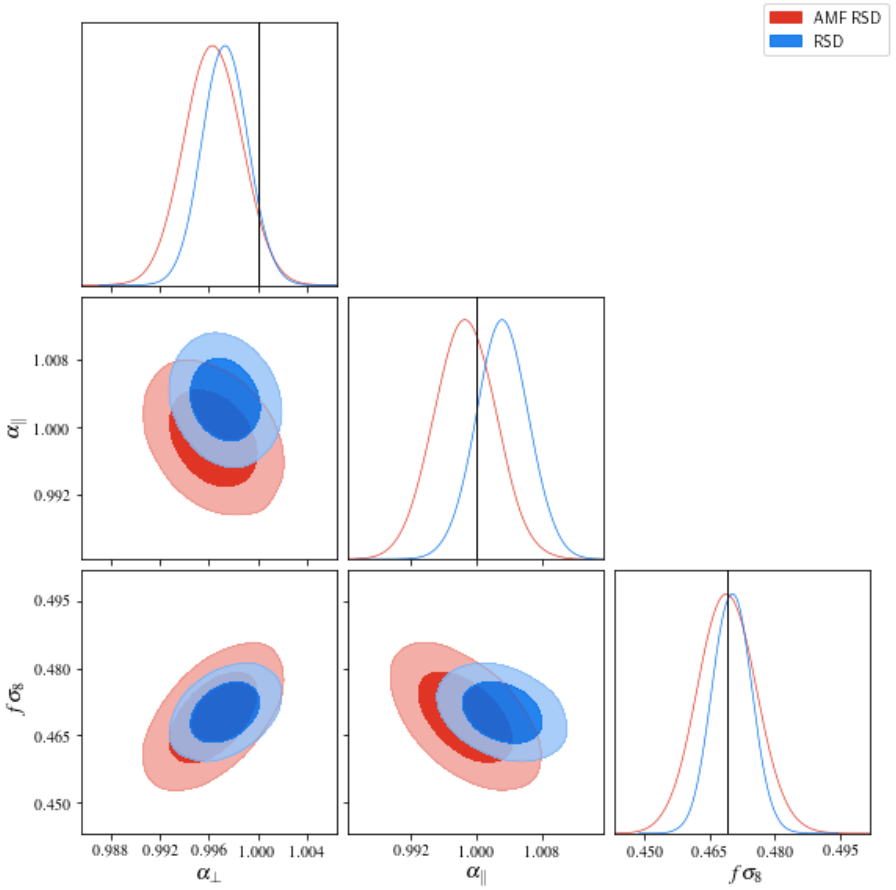

FIGURE 3.23 – Posterior likelihood contours on $\alpha_\parallel$, $\alpha_\perp$ and $f\sigma_8$ obtained when fitting standard (blue) and AMF (red) multipole moments in the full-shape RSD analysis on the CMASS sample

In the BAO modelling, a linear RSD model is implicitly assumed, which only predicts non-vanishing even multipole moments up to $\ell = 4$. The implementation of AP dilation parameters is exactly the same as previously for the RSD modelling. In order to model the AMF BAO multipoles, we apply the broadband parameters in Eq. 2.277 after the AMF modelling. This is mainly to avoid adding two extra broadband parameters to the model hexadecapole, which cannot be well constrained when fitting only the BAO feature in the monopole and quadrupole moments of the correlation function.

3.3.3.2 Full-shape redshift-space distortions results

We derive cosmological constraints from both standard and AMF two-point correlation functions in the mocks. We perform a full-shape RSD analysis of the monopole, quadrupole and hexadecapole moments in the range $25 < r < 150\ h^{-1}$Mpc based on the TNS model. We run a likelihood analysis (see Section 4.1)and constraints on $\alpha_\parallel, \alpha_\perp, f\sigma_8$ parameters. AMF kernels are precomputed up to a

Tableau 3.3 – RSD and BAO results for the mean of NSeries (CMASS sample) and EZmocks (ELG sample). We assume in each analysis the corresponding fiducial cosmology of the mocks. We therefore expect the AP distortions parameters $\alpha_\parallel$ and $\alpha_\perp$ to be equal to 1. For the growth rate, we expect $f\sigma_8 = 0.469$ and $f\sigma_8 = 0.449$ for CMASS and ELG respectively. For full-shape analysis, we also present the statistical error corresponding to one realisation after the slash. The last column correspond to the rescaled $f\sigma_8$ as defined in Section 2.3.1.2

Method	$\alpha_\perp$	$\alpha_\parallel$	$f\sigma_8$	$f\sigma_{8\mathrm{rs}}$
CMASS				
RSD M+Q+H standard	$0.9972 \pm (0.0019/0.017)$	$1.0032 \pm (0.0032/0.029)$	$0.4700 \pm (0.0044/0.04)$	0.4694 ± 0.0044
RSD M+Q+H AMF	0.9962 ± 0.0023	0.9987 ± 0.0038	0.4686 ± 0.0067	0.4696 ± 0.0067
BAO standard	1.0056 ± 0.0022	1.0007 ± 0.0044		
BAO AMF	1.0043 ± 0.0026	1.0011 ± 0.0046		
ELG				
RSD M+Q standard	$1.0038 \pm (0.0043/0.096)$	$1.0089 \pm (0.0066/0.147)$	$0.4556 \pm (0.0053/0.118)$	0.4523 ± 0.0053
RSD M+Q AMF	1.0028 ± 0.0049	1.0142 ± 0.0067	0.4616 ± 0.0065	0.4567 ± 0.0065
BAO standard	1.0023 ± 0.0043	1.0063 ± 0.0062		
BAO AMF	1.0009 ± 0.0051	1.0171 ± 0.0066		

maximum value of $\Delta_{\mathrm{max}} = 500$ Mpc/h, necessary to provide a robust modelling of the BAO feature as discussed in the previous section.

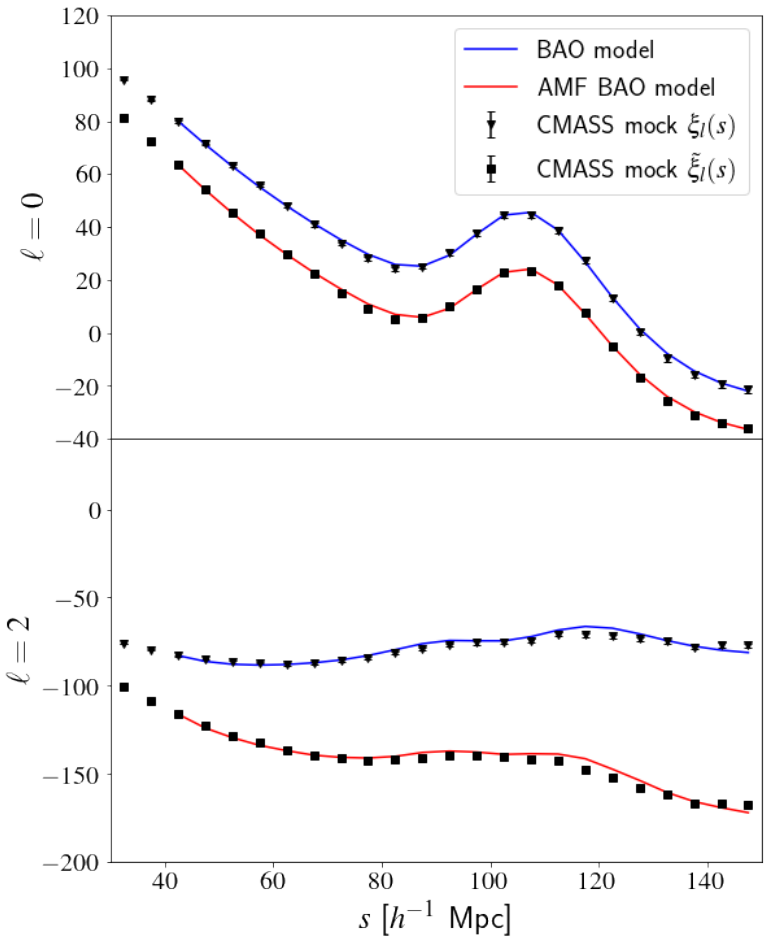

FIGURE 3.24 – Best-fit BAO models to the standard and AMF mean mock monopole and quadrupole for the CMASS sample.

The constraints on $\alpha_\parallel, \alpha_\perp, f\sigma_8$ that we obtain are given in Table 3.3 for the CMASS sample and the best-fitting models are shown in Fig. 3.22. We find that the AMF correlation function, compared to the standard correlation function, provides a robust and unbiased estimate of $f\sigma_8$ and $\alpha_\perp$. They lie within 1σ of the statistical uncertainty on the mean of the mocks.

However we find a small 1.4σ shift for $\alpha_\parallel$ with respect to the standard analysis. This shift is due to the small difference shown in the monopole and in the hexadecapole on quasilinear scale, and remains a small effect. The 1σ statistical errors obtained on the parameters from the AMF analysis increase by 20 %, 18 % and 50 % for $\alpha_\parallel, \alpha_\perp, f\sigma_8$, respectively. As expected, the signal is decreased in the AMF correlation function leading to worse constraints. The most affected parameter constraints are those for $f\sigma_8$. The joint posterior contours for all combinations of parameters is shown in Fig. 3.23. These contours were obtained with the ensemble sampler ZEUS (KARAMANIS et AL. 2020; KARAMANIS et AL. 2021) [9]. We can see that, while AMF analysis exhibits larger contours compared to the standard analysis, the direction of degeneracy between the different parameters is similar.

For the ELG mocks, we only consider the monopole and quadrupole in the likelihood analysis. Indeed, we found that including the hexadecapole in the standard analysis introduces a 3σ shift on $\alpha_\parallel$. Since this shift is not present in the N-Body CMASS mocks, we conclude that we cannot safely compare standard and AMF cosmological measurements when the hexadecapole is included. This is likely due to the approximated method used to produce EZmocks. It is important to emphasise that EZmocks were not meant to reproduce the observed ELG clustering with highest accuracy, instead to reach an accuracy comparable to the statistical precision of the eBOSS ELG sample, where statistical 1σ relative precisions on $\alpha_\parallel$, , and $f\sigma_8$ are 9.6%, 14.7%, and 26.3% respectively (ROSS et AL. 2020; TAMONE et AL. 2020; DE MATTIA et AL. 2021). Consequently, we can hardly judge from systematic deviations on the parameters below typically 1σ in these mocks.

The ELG constraints on $\alpha_\parallel, \alpha_\perp, f\sigma_8$ that we obtain are given in Table 3.3. We find that the AMF analysis provides similar constraints on as the standard analysis. The AMF central values for $\alpha_\parallel$ and $f\sigma_8$ lie within 1σ of the standard analysis uncertainty. We note that the close to 1σ shift in $f\sigma_8$ almost disappear when considering $f\sigma_{8\mathrm{rs}}$. The posterior probability contours for all combinations of parameters are shown in Fig. 3.25. As for CMASS mocks, the degeneracy directions between the parameters are similar in the standard and AMF analyses.

9. https://zeus-mcmc.readthedocs.io/en/latest/

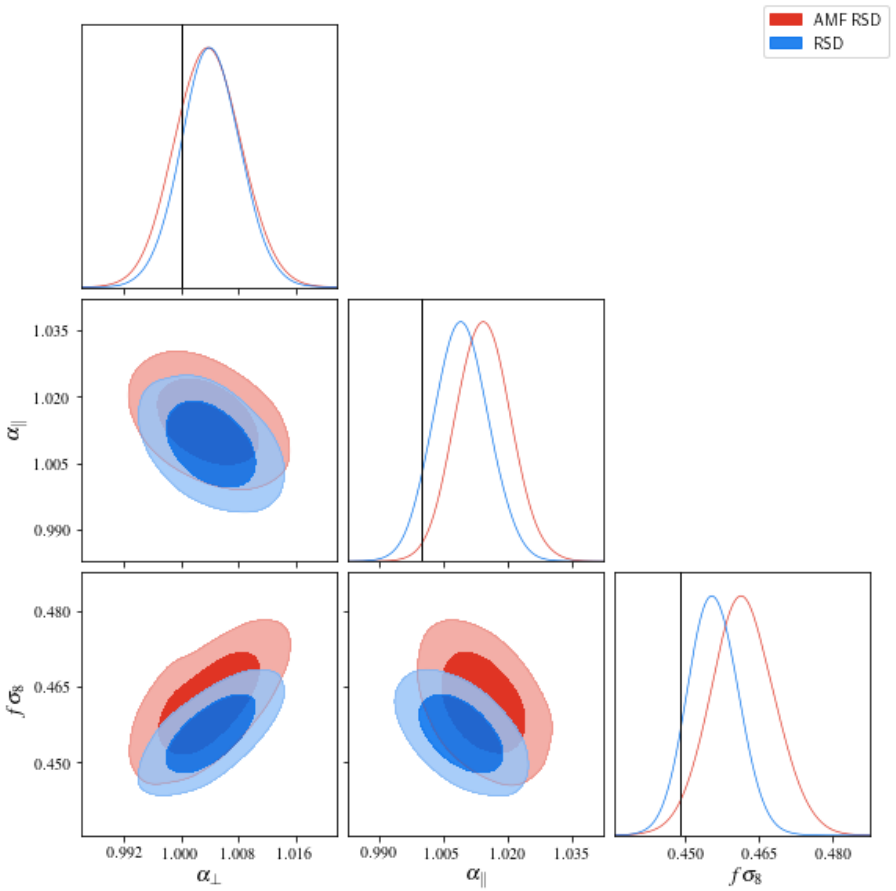

FIGURE 3.25 – Same as Figure 3.23 but for ELG mocks.

3.3.3.3 BAO-only results

We perform a BAO-only analysis on the mean mock AMF and standard correlation function. We only consider pre-reconstruction correlation functions, i.e. we do not apply any BAO reconstruction scheme as usually done in real data (BAUTISTA et AL. 2021). Only the monopole and quadrupole are used, as the hexadecapole does not add much constraints in a BAO fit, (BAUTISTA et AL. 2021). We fit both multipoles in the range $40 < s < 150\ h^{-1}$Mpc. The constraints on $\alpha_\parallel, \alpha_\perp$ that we obtain are given in Table 3.3 for the CMASS sample and the best-fitting models are shown in Fig. 3.24. In the BAO-only case as well, we find that we can recover almost the same constraints with the AMF and standard analyses. Here, central values on $\alpha_\parallel, \alpha_\perp$ are within less than 1σ of that from the standard analysis. The statistical uncertainty on the parameters increases by less than 5%. Overall, the BAO-only analysis of the AMF correlation function is almost as efficient as the standard BAO pre-reconstruction analysis. The joint posterior likelihood contours for $\alpha_\parallel$ and $\alpha_\perp$ is shown in Fig. 3.26. These contours were computed using the minimization algorithm IMINUIT (JAMES et ROOS 1975) [10]. As for the RSD case, we see that, while AMF analysis exhibit slightly larger uncertainty compared to the standard case, the direction of degeneracy is the same. In the ELG mocks, while the AMF is very close to that obtained in the standard analysis, we observe a 1.6σ shift on $\alpha_\parallel$. This shift is partially related to the observed shift on the model AMF correlation function shown in Fig. 3.21. It can be explained by the way the AMF model accounts for the varying galaxy radial distribution in the ELG SGC sample. Each ELG SGC mock covers 358 deg^2 over an effective volume of 0.5 Gpc^3. The SGC footprint is composed of two adjacent chunks : eboss21 and eboss22, respectively covering 117 and 240 deg^2. These chunks exhibit slightly different radial distributions as illustrated in Fig. **??**. If we perform a BAO-only AMF analysis only on the eboss21 chunk, we find that the shift on

10. https://iminuit.readthedocs.io/

Tableau 3.4 – Absolute difference between the derived parameters in the AMF ELG analysis of the BAO and those obtained in the standard analysis. The results are shown for the case of the entire SGC footprint and that of only the chunk eboss21. The provided errors correspond to the variance obtained by summing up in quadrature the parameter variance from the AMF and standard analyses.

Field	$\Delta\alpha_\perp$	$\Delta\alpha_\parallel$
ELG SGC	-0.0014 ±0.0066	0.0108 ±0.0091
ELG eboss21	0.0051 ±0.0143	0.0009 ±0.0175

$\alpha_\parallel$ disappears. This is shown in Table 3.4, where the absolute differences between parameters obtained with the standard and AMF analyses are given. Therefore, the shift on $\alpha_\parallel$ can be attributed to the adopted methodology to derived AMF kernels for the ELG. Overall, and given the intrinsic uncertainty on the clustering in the EZmocks, we can conclude that the AMF does not show any significant bias on the recovered cosmological parameters with respect to the standard analysis.

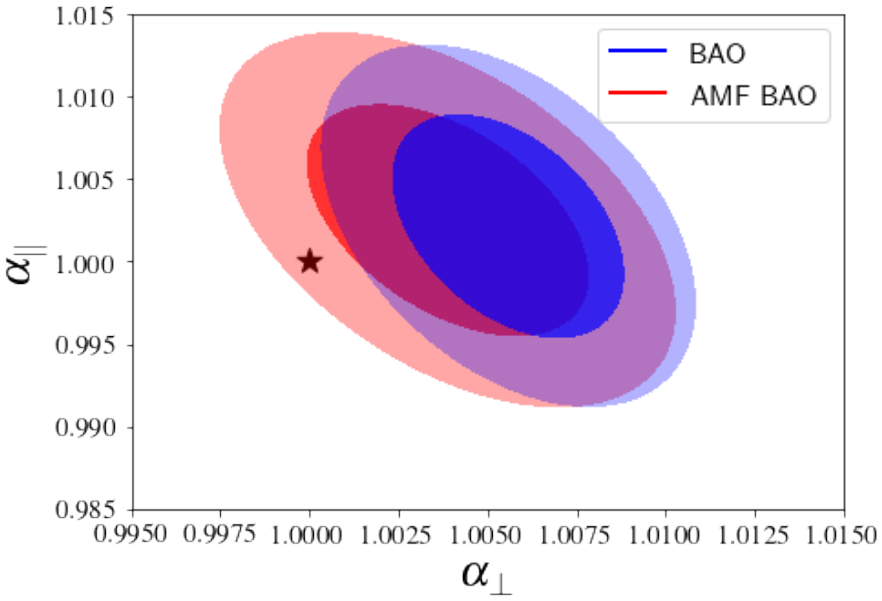

FIGURE 3.26 – Posterior likelihood contours on $\alpha_\parallel$, $\alpha_\perp$ when fitting standard (blue) and AMF (red) multipole moments (monopole and quadrupole only) in the BAO-only analysis on the CMASS sample.

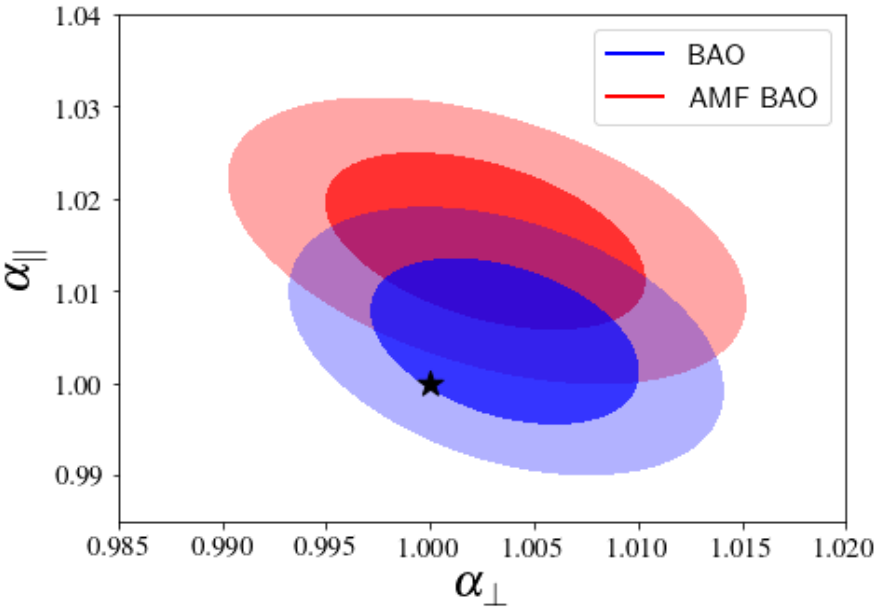

FIGURE 3.27 – Same as Fig. 3.26, but for ELG mocks

3.3.4 Discussion

In this section, we studied the use of a modified galaxy two-point correlation function for cosmological inference, whose particularity is to suppress angular modes, and in turn, any potential angular observational systematic errors. This statistic, the AMF two-point correlation function, was first introduced by BURDEN et AL. 2017. We extended the latter work and derived a full model to describe this statistic, given a model of the standard redshift-space two-point correlation function. We compared the model to mock galaxy samples of luminous red and emission-line galaxies measurements at $0.43 < z < 1.1$ and found that it outperforms all previous proposed approximate models. Moreover, it uniquely allows reproducing the full shape of the AMF correlation function, when the underlying correlation function is known, without introducing any new nuisance parameter. This makes possible the performance of a full-shape redshift-space distortions analysis using this statistic. As a proof of concept, we performed a cosmological analysis of the AMF correlation function in the CMASS and ELG mocks, in a similar fashion as we would do with real survey data. We found that we can recover nearly unbiased $\alpha_\parallel$, $\alpha_\perp$, $f\sigma_8$ parameters with respect to the standard method. There is an increase of $18-20\%$ on $\alpha_\perp$ and $\alpha_\parallel$ statistical uncertainty, and of 50% on $f\sigma_8$ in those mock samples. Current and future large spectroscopic surveys such as DESI or Euclid will probe much larger universal volumes. This will allow reducing considerably the statistical errors on cosmological parameters. For those, it will be crucial to control the systematic errors at a extremely low level. Today, this is a challenge and the work presented here paves the way towards achieving this goal. By construction, the AMF two-point correlation function is less constraining compared to the standard correlation function. Nonetheless, this approach can be advantageously used in the case of inhomogeneous or incomplete samples, or in the case of surveys with a complex angular selection function that is poorly understood (DE MATTIA et AL. 2021 ; TAMONE et AL. 2020). A direct possible application is the cosmological analysis of early-stage dataset from future large redshift surveys, such as DESI or Euclid. The latter will suffer from low completeness in the first years of observation (BURDEN et AL. 2017) and the AMF correlation function should allow robust cosmological measurements from these early data. Finally, it is important to emphasize that the AMF approach is complementary to the standard one, in the sense that it can be used as a cross-validation test. In fact, it allows studying the impact of angular systematic errors in the standard analysis and can be used as a benchmark to check whether all angular systematic errors are well accounted for. If

one finds that the recovered cosmological parameters are the same with the two approaches, this validates the accuracy of the observational bias correction scheme used in the standard analysis.

4 Cosmological implications

Sommaire

Tableau 4.1 – List of fitted parameters and their priors used in full-shape analysis for the two models

Par. TNS	Prior TNS	Par. CLPT-GS	Prior CLPT-GS
$\alpha_\perp$	[0.5, 1.5]	$\alpha_\perp$	[0.5, 1.5]
$\alpha_\parallel$	[0.5, 1.5]	$\alpha_\parallel$	[0.5, 1.5]
f	[0, 2]	f	[0, 2]
b_1	[0.2, 4]	$\langle F' \rangle$	[0,3]
b_2	[−10, 10]	$\langle F'' \rangle$	[-10,10]
b_{Γ_3}	[−2, 4]	$\sigma_{\rm FoG}$	[0,40]
σ_v	[0.1, 8]		

I present now the cosmological analysis of the eBOSS plus CMASS DR16 sample in the redshift range $0.6 < z < 1.0$ (BAUTISTA et AL. 2021). In this section, i have tested my implementation of the TNS model against mocks, and derived full-shape constraints on the data.

4.1 Parameter Inference

4.1.1 Likelihood

The cosmological parameter inference is performed by means of the likelihood analysis of the data. The likelihood $\mathscr{L}$ is assumed to be Gaussian

$$-2\ln\mathscr{L}(\theta) = \sum_{i,j}^{N_p} \vec{\Delta}_i(\theta)\hat{\Psi}_{ij}\vec{\Delta}_j(\theta), \tag{4.1}$$

where θ is the vector of parameters, $\vec{\Delta}$ is the data-model difference vector, N_p is the total number of data points. An estimate of the precision matrix $\hat{\Psi} = (1-D)\hat{C}^{-1}$ is obtained from the covariance $\hat{C}$ from 1000 realisation of EZmocks, where $D = (N_p+1)/(N_{\rm mocks}-1)$ is a factor that accounts for the skewed nature of the Wishart distribution (HARTLAP et AL. 2007) The data vector that enters in $\vec{\Delta}$ includes, in the baseline configuration, the monopole and quadrupole correlation functions for the BAO analysis, and the monopole, quadrupole, and hexadecapole correlation functions for the RSD analysis.

In the BAO analysis, the best-fit parameters $(\alpha_\perp, \alpha_\parallel)$ are found in a frequentist approach, by minimizing $-2\ln\mathscr{L} = \chi^2$ with a quasi-Newton minimum finder algorithm IMINUIT (JAMES et ROOS 1975) [1]. The errors in $\alpha_\parallel$ and $\alpha_\perp$ are found by computing the intervals where χ^2 increases by unity. Gaussianity is not assumed in the error calculation, but we find that on average, errors are symmetric and correctly described by a Gaussian. The 2D errors in $(\alpha_\perp, \alpha_\parallel)$, such as those presented in Fig. 4.10, are found by scanning χ^2 values in a regular grid in $\alpha_\perp$ and $\alpha_\parallel$. In the case of the full-shape analysis, we explore the likelihood of the data in a Bayesian approach with the Markov chain Monte Carlo ensemble sampler EMCEE(FOREMAN-MACKEY et AL. 2013) [2]. For individual mock realizations, we follow the same frequentist approach as for the BAO analysis. The input power spectrum shape parameters are fixed at the fiducial cosmology and any deviations are accounted for through the Alcock-Paczynski parameters $\alpha_\perp$ and $\alpha_\parallel$. We assume the uniform priors on model parameters given in Table 4.1.

The final parameter constraints are obtained by marginalizing the full posterior likelihood over the nuisance parameters. The marginal posterior is approximated by a multivariate Gaussian distribution with central values given by best-fitting parameter values $\theta^* = (\alpha_\perp, \alpha_\parallel, f\sigma_8)$ and parameter

1. https://iminuit.readthedocs.io/
2. https://emcee.readthedocs.io/

Tableau 4.2 – Characteristics of the baseline fits for all models in this work, where $N_{\rm mock}$ is the number of mocks used in the estimation of the covariance matrix, $N_{\rm par}$ is the total number of parameters fitted, $N_{\rm bins}$ is the total size of the data vector, $(1-D)$ is the correction factor to the precision matrix (HARTLAP et AL. 2007), m_1 is the factor to be applied to the estimated error matrix and m_2 is the factor that scales the scatter of best-fit parameters of a set of mocks (if these were used in the calculation of the covariance matrix). The derivation of m_1 and m_2 can be found in (PERCIVAL et AL. 2014).

	BAO	RSD TNS	RSD CLPT-GS
$N_{\rm mock}$	1000	1000	1000
$N_{\rm par}$	9	7	6
$N_{\rm bins}$	40	65	63
$(1-D)$	0.96	0.93	0.94
m_1	1.022	1.053	1.053
m_2	1.065	1.128	1.125

covariance matrix C_θ. Since the covariance matrix is computed from a finite number of mock realisations, we need to apply correction factors to the obtained C_θ. These factors are described by Eqs. 18 and 22 from PERCIVAL et AL. 2014 to be applied to uncertainties and to the scatter over best-fit values, respectively. These factors, which depend on the number of mocks, parameters and bins in the data vectors, are given in Table 4.2. The final parameter constraints from this work are available to the public in this format [3].

4.1.2 Combining BAO and RSD constraints

From the same input LRG catalog, we produced BAO-only and full-shape RSD constraints, both in configuration and Fourier space (GIL-MARIN et AL. 2020). Each measurement yields a marginal posterior on $(\alpha_\perp, \alpha_\parallel)$ for BAO-only or $(\alpha_\perp, \alpha_\parallel, f\sigma_8)$ for the full-shape RSD analyses. In the following we describe the procedure to combine all these posteriors into a single consensus constraint, while correctly accounting for their covariances. This consensus result is the one used for the final cosmological constraints described in (EBOSS COLLABORATION 2021) and summarized in Section 4.4

We follow closely the method presented in (SÁNCHEZ et AL. 2017) to derive the consensus result. The idea is to compress M data vectors x_m containing p parameters and their $p \times p$ covariance matrices C_{mm} from different methods into a single vector x_c and covariance C_c, assuming that the χ^2 between individual measurements is the same as the one from the compressed result. The expression for the combined covariance matrix is

$$C_c \equiv \left(\sum_{m=1}^{M} \sum_{n=1}^{M} C_{mn}^{-1} \right)^{-1} \tag{4.2}$$

and the combined data vector is

$$x_c = C_c \sum_{m=1}^{M} \left(\sum_{n=1}^{M} C_{nm}^{-1} \right) x_m \tag{4.3}$$

where C_{mn} is a $p \times p$ block from the full covariance matrix between all parameters and methods C,

3. sdss.org/

defined as

$$C = \begin{pmatrix} C_{11} & C_{12} & \cdots & C_{1M} \\ C_{21} & C_{22} & \cdots & C_{2M} \\ \vdots & \vdots & \ddots & \vdots \\ C_{M1} & C_{M2} & \cdots & C_{MM} \end{pmatrix} \tag{4.4}$$

The diagonal blocks C_{mm} are obtained from the Gaussian approximation of the marginal posterior from each method. The off-diagonal blocks C_{mn} with $m \neq n$ cannot be estimated from our fits. We derive these off-diagonal blocks from results from each method applied to the 1000 EZMOCKS realisations. More precisely, we compute the correlation coefficients $\rho^{\rm mocks}_{p_1,p_2,m,n}$ between parameters p_1, p_2 and methods m, n using the mocks and scale these coefficients by the diagonal errors from the data. It is worth emphasizing that the correlation coefficients between parameters depend on the given realisation of the data, while the ones derived from mock measurements are ensemble averaged coefficients. Therefore, we scale the correlations coefficients from the mocks in order to match the maximum correlation coefficient that would be possible with the data (ROSS et AL. 2015b) For the same parameter p_1 measured by two different methods m and n, we assume that the maximum correlation between them is given by $\rho_{\rm max} = \sigma_{p1,m}/\sigma_{p1,n}$, where σ_p is the error of parameter p. This number is computed for the data realisation $\rho^{\rm data}_{\rm max}$ and for the ensemble of mocks $\rho^{\rm mocks}_{\rm max}$. We can write the adjusted correlation coefficients as

$$\rho^{\rm data}_{p_1,p_1,m,n} = \rho^{\rm mocks}_{p_1,p_1,m,n} \frac{\rho^{\rm data}_{\rm max}}{\rho^{\rm mocks}_{\rm max}} \tag{4.5}$$

The equation above accounts for the diagonal terms of the off-diagonal block C_{mn}. For the off-diagonal terms, we use

$$\rho^{\rm data}_{p_1,p_2,m,n} = \frac{1}{4}\left(\rho^{\rm data}_{p_1,p_1,m,n} + \rho^{\rm data}_{p_2,p_2,m,n}\right)\left(\rho^{\rm data}_{p_1,p_2,m,m} + \rho^{\rm data}_{p_1,p_2,n,n}\right) \tag{4.6}$$

We use the method described above to perform all the constraint combinations, except for the combination of results from CLPT-GS and TNS RSD models, which use the same input data vector (pre-reconstruction multipoles in configuration space). For this particular combination, we simply assume that $C_c^{-1} = 0.5(C_{mm}^{-1} + C_{nn}^{-1})$ and $x_c = 2C_c^{-1}\left(C_{mm}^{-1}x_m + C_{nn}^{-1}x_n\right)$. For all combinations, we chose to use the results from at most two methods at once ($M = 2$) in order to reduce the potential noise introduced by the procedure.

Denoting ξ_ℓ the results from the configuration space analysis and P_ℓ that from the Fourier space analysis, our recipe to obtain the consensus result for the LRG sample is as follows :

— Combine RSD ξ_ℓ TNS and RSD ξ_ℓ CLPT-GS results into RSD ξ_ℓ,
— Combine BAO ξ_ℓ with BAO P_ℓ into BAO $(\xi_\ell + P_\ell)$,
— Combine RSD ξ_ℓ with RSD P_ℓ into RSD $(\xi_\ell + P_\ell)$,
— Combine BAO $(\xi_\ell + P_\ell)$ with RSD $(\xi_\ell + P_\ell)$ into BAO+RSD $(\xi_\ell + P_\ell)$

Alternatively, we can proceed as

— Combine BAO ξ_ℓ with RSD ξ_ℓ into (BAO+RSD) ξ_ℓ,
— Combine BAO P_ℓ with RSD P_ℓ into (BAO+RSD) P_ℓ
— Combine BAO+RSD ξ_ℓ with BAO+RSD P_ℓ into (BAO+RSD) $\xi_\ell + P_\ell$

In Section 4.2.3 we test this procedure on the mock catalogues.

4.2 Robustness of the analysis to systematic errors

In this section we perform a comprehensive set of tests of the adopted methodology using all the simulated datasets available. We estimate the biases in the measurement of the cosmological

parameters $(\alpha_\perp, \alpha_\parallel, f\sigma_8)$ and derive the systematic errors for both BAO-only and full-shape RSD analyses. For a given parameter, we define the systematic error $\sigma_{p,\mathrm{syst}}$ as follows. We compare the estimated value of the parameter x_p to a reference value x_p^{ref} and set the systematic error value to

$$\sigma_{p,\mathrm{syst}} = 2\sigma_p, \quad \text{if } |x_p - x_p^{\mathrm{ref}}| < 2\sigma_p, \tag{4.7}$$

$$\sigma_{p,\mathrm{syst}} = |x_p - x_p^{\mathrm{ref}}|, \quad \text{if } |x_p - x_p^{\mathrm{ref}}| > 2\sigma_p, \tag{4.8}$$

where σ_p is the estimated statistical error on x_p. As a conservative approach, we use the maximum value of the bias amongst the several cases studied.

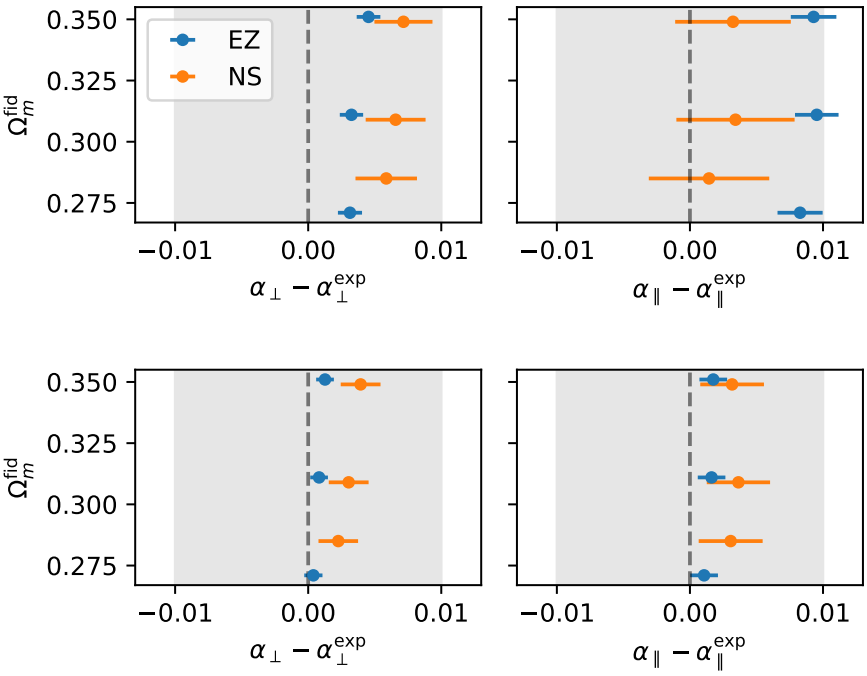

FIGURE 4.1 – Impact of choice of fiducial cosmology in the recovered values of $\alpha_\parallel$ and $\alpha_\perp$ from the stacks of 1000 multipoles from the EZMOCKS (blue) and 84 NSERIES mocks (orange), for pre- (top panels) and post- (bottom panels) reconstruction. Associated error bars correspond to the error on the mean of the mocks. The gray shaded areas correspond to one per cent errors. For comparison, the error on real data is near 1.9 per cent for $\alpha_\perp$ and 2.6 per cent for $\alpha_\parallel$ in the post-reconstruction case.

4.2.1 BAO systematics

The methodology described in Section 2.3.2 was tested using the 1000 EZMOCKS mock survey realisations and 84 NSERIES realisations. For each realisation, we compute the correlation function and its multipoles, and fit for the BAO peak position to determine the dilation parameters $\alpha_\parallel$, $\alpha_\perp$ and associated errors. We compare the best-fit $\alpha_\perp, \alpha_\parallel$ to their expected values, which are obtained from the cosmological models described in Table 3.1. The effective redshift of the EZMOCKS is $z_{\mathrm{eff}} = 0.698$ and $z_{\mathrm{eff}} = 0.56$ for NSERIES.

In Fig. 4.1 we summarize the systematic biases from pre- and post-reconstruction mocks for a few choices of fiducial cosmology, parameterised by Ω_m^{fid}. In pre-reconstruction mocks, biases in the recovered α values reach up to 0.5 per cent in $\alpha_\perp$ and 1.0 per cent in $\alpha_\parallel$. These biases are expected due to the impact of non-linear effects on the position of the peak that cannot be correctly accounted for with the Gaussian damping terms in Eq. 2.273 at this level of precision (SEO et AL. 2016). We recall that we are fitting the average of all realisations. The reconstruction procedure

Tableau 4.3 – Average biases from BAO fits on the stacked multipoles of 1000 EZMOCKS and 84 NSERIES realisations. All results are based on post-reconstruction correlation functions.

Sample	$\Omega_m^{\rm fid}$	$\ell_{\rm max}$	$\alpha_\perp - \alpha_\perp^{\rm exp}$ $[10^{-3}]$	$\alpha_\parallel - \alpha_\parallel^{\rm exp}$ $[10^{-3}]$
EZ	0.27	2	0.4 ± 0.7	1.1 ± 1.0
EZ	0.27	4	0.5 ± 0.7	1.4 ± 1.0
EZ	0.31	2	0.9 ± 0.7	0.3 ± 1.1
EZ	0.31	4	1.0 ± 0.7	0.4 ± 1.1
EZ	0.35	2	1.3 ± 0.7	1.8 ± 1.0
EZ	0.35	4	1.2 ± 0.7	1.5 ± 1.0
NS	0.286	2	2.3 ± 1.5	3.1 ± 2.4
NS	0.286	4	2.2 ± 1.5	3.0 ± 2.4
NS	0.31	2	3.0 ± 1.5	3.6 ± 2.4
NS	0.31	4	3.0 ± 1.5	3.7 ± 2.4
NS	0.35	2	3.9 ± 1.5	3.2 ± 2.4
NS	0.35	4	3.9 ± 1.5	3.5 ± 2.4

removes in part the non-linear effects and this is seen as a reduction of the biases to less than 0.2 per cent. The bias reduction is also seen in the NSERIES mocks, particularly on $\alpha_\perp$, confirming that the bias reduction is not related to a feature of the mocks induced by the approximate method used to build them.

Table 4.3 shows results from Fig. 4.1 for the post-reconstruction case only, including the fits with the hexadecapole $\xi_{\ell=4}$. The impact of the hexadecapole is negligible even in this very low-noise regime, for both types of mocks. The reported dilation parameters for almost all cases are consistent with expected values within 2σ. We see a 2.6σ deviation on $\alpha_\perp$ for the NSERIES case analysed with $\Omega_m^{\rm fid} = 0.35$. However this choice of $\Omega_m^{\rm fid}$ is the most distant from the true value of the simulation and its observed bias is still less than half a per cent, which is small compared to the statistical power of our sample. For the EZMOCKS, which have smaller errors, the biases are up to 0.13 per cent for $\alpha_\perp$ and 0.18 per cent for $\alpha_\parallel$. These biases are much smaller than the expected statistical errors in our data, i.e. ~1.9 per cent for $\alpha_\perp$ and ~2.6 per cent for $\alpha_\parallel$, showing that our methodology is robust at this statistical level. In these fits, all parameters except $\Sigma_{\rm rec} = 15 h^{-1}$Mpc were left free. The best-fit values of $\Sigma_\perp, \Sigma_\parallel$ and Σ_s were used and held fixed in the fits of individual realisations.

Results from Table 4.3 and Fig. 4.1 show no statistically significant dependence of results with the choice of fiducial cosmology. We derived the systematic errors for the BAO analysis using the values from Table 4.3 and Eqs. 4.7 and 4.8. We used only the fits to the EZMOCKS, which have better precision. The systematic errors for $\alpha_\perp$ and $\alpha_\parallel$ are respectively :

$$\text{BAO}: \ \sigma_{\rm syst,model} = (0.0014, 0.0021), \tag{4.9}$$

which are negligible compared to statistical errors of one realisation of our data. Note that the fiducial cosmologies considered are all flat and assume general relativity . CARTER et AL. 2020 and BERNAL et AL. 2020 find that BAO measurements are robust to a larger variety of fiducial cosmologies (but all close to the assumed one). Additional systematic errors should be anticipated when extrapolating to cosmologies that are significantly different than the truth, for instance yielding dilation parameters significantly different than unity.

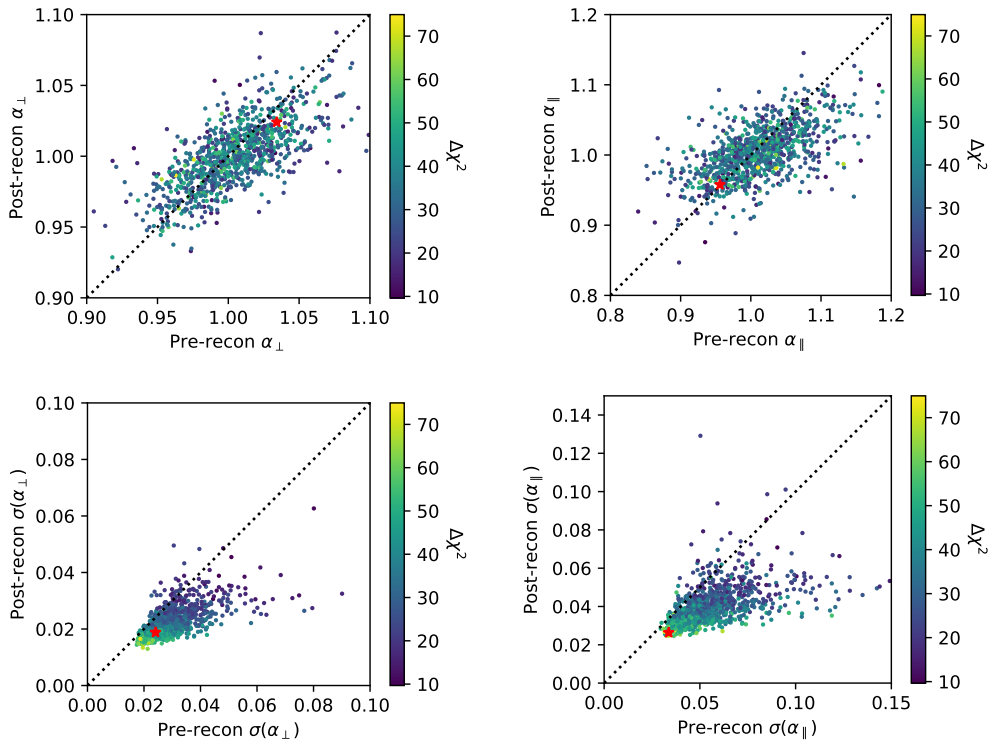

FIGURE 4.2 – Distribution of dilation parameters $\alpha_\perp$ and $\alpha_\parallel$ and its estimated errors for pre and post reconstruction EZMOCK catalogs with systematic effects. The color scale indicates the difference in χ^2 values between a model with and without BAO peak. The red stars shows results with real data. There is a known mismatch in the BAO peak amplitude between data and EZmocks causing the accuracy of the data point to be slightly smaller than the error distribution in the EZmocks (see Section 3.1.5).

Fig. 4.2 displays the distribution of recovered $\alpha_\perp$, $\alpha_\parallel$ and their respective errors measured from each of the individual EZMOCKS. The error distribution shows that reconstruction improves the constraints on $\alpha_\perp$ or $\alpha_\parallel$ in 94 per cent of the realisations (89 per cent have both errors improved). As expected, realisations with smaller errors generally exhibit larger values of $\Delta\chi^2 = \chi^2_{\text{no peak}} - \chi^2_{\text{peak}}$, meaning a more pronounced BAO peak and higher detection significance. We see no particular trend in the best-fit α values with $\Delta\chi^2$ in the two top panels. The red stars in Fig. 4.2 indicate the values obtained in real data. The error in $\alpha_\perp$ in the data is typical of what is found in mocks, although for $\alpha_\parallel$ it is found at the extreme of the mocks distribution. As discussed in Section 3.1.5 and displayed in Fig. 3.10, the BAO peak amplitude in the data multipoles is slightly larger than the one seen in this EZMOCK sample. A similar behaviour is observed in the eBOSS QSO sample (HOU et AL. 2021; NEVEUX et AL. 2020) who also use EZMOCKS and in the BOSS DR12 CMASS sample (ROSS et AL. 2017).

Table 4.4 presents a statistical summary of the fits performed on the EZMOCKS. We tested several changes to our baseline analysis : include the hexadecapole, change the separation range $[r_{\text{min}}, r_{\text{max}}] = [50, 150]\,h^{-1}$Mpc, allow BAO damping parameters $\Sigma_\perp$ and $\Sigma_\parallel$ to vary within a Gaussian prior ($5.5 \pm 2\,h^{-1}$Mpc), and fit the pre-reconstruction multipoles. We remove realisations with fits that did not converge or with extreme error values (more than 5σ of their distribution, where σ is defined as the half the range covered by 68 per cent of values). The total number of valid realisations is given by N_{good} in Table 4.4. In most cases studied, the observed standard deviation of the best-fit parameters $\sigma(\alpha)$ is consistent with the average per-mock error estimates $\langle\sigma_\alpha\rangle$, indicating that our errors are correctly estimated. We also see that the dispersion of dilation parameters is not significantly reduced when adding the hexadecapole ξ_4 to the BAO fits, showing that most of the

Tableau 4.4 – Statistics on errors from BAO fits on 1000 EZMOCKS realisations. All results are based on post-reconstruction correlation functions. σ is the scatter of best-fit values x_i amongst the $N_{\rm good}$ realisations with confident detection or non-extreme values or errors (out of the 1000), $\langle\sigma_i\rangle$ is the mean estimated error per mock, $Z = (x_i - \langle x_i\rangle)/\sigma_i$ is the pull quantity for which we show the mean $\langle Z_i\rangle$ and standard deviation $\sigma(Z)$. First row corresponds to our baseline analysis.

Analysis	$N_{\rm good}$	$\alpha_\perp$				$\alpha_\parallel$			
		σ	$\langle\sigma_i\rangle$	$\langle Z_i\rangle$	$\sigma(Z_i)$	σ	$\langle\sigma_i\rangle$	$\langle Z_i\rangle$	$\sigma(Z_i)$
baseline	990	0.022	0.023	-0.02	0.99	0.035	0.036	-0.03	0.96
$\ell_{\rm max} = 4$	995	0.022	0.023	-0.02	0.99	0.035	0.035	-0.03	0.97
pre-recon	968	0.030	0.030	-0.05	1.07	0.055	0.056	-0.06	0.97
pre-recon $\ell_{\rm max} = 4$	968	0.029	0.028	-0.03	1.04	0.054	0.054	-0.07	1.02
$r_{\rm min} = 20h^{-1}$Mpc	979	0.023	0.026	-0.01	0.93	0.035	0.040	0.04	1.26
$r_{\rm min} = 30h^{-1}$Mpc	987	0.023	0.024	-0.02	0.95	0.036	0.038	-0.02	0.92
$r_{\rm min} = 40h^{-1}$Mpc	995	0.022	0.023	-0.02	0.98	0.035	0.036	-0.02	0.94
$r_{\rm max} = 160h^{-1}$Mpc	989	0.022	0.023	-0.02	0.99	0.036	0.036	-0.03	0.96
$r_{\rm max} = 170h^{-1}$Mpc	989	0.022	0.023	-0.02	0.99	0.036	0.036	-0.03	0.96
$r_{\rm max} = 180h^{-1}$Mpc	990	0.022	0.023	-0.02	0.98	0.035	0.036	-0.03	0.95
Prior $\Sigma_{\perp,\parallel}$	993	0.022	0.023	-0.02	1.00	0.035	0.035	-0.03	0.96

BAO information is contained in the monopole and quadrupole at this level of precision. The mean and dispersion of the pull parameter, defined as $Z_\alpha = (\alpha - \langle\alpha\rangle)/\sigma_\alpha$, are consistent with an unit Gaussian for almost all cases, which further validates our error estimates.

All the tests performed in this section show that our BAO analysis is unbiased and provides correct error estimates. We apply our baseline analysis to the real data and report results in Section 4.3.1.

4.2.2 RSD systematics

We present in this section the systematic error budget of the full-shape RSD analysis. Particularly, we discuss the impact of the choice of scales used in the fit, the bias introduced by each model, the bias introduced by varying the fiducial cosmology, the bias associated to the choice of the LRG halo occupation distribution model, and the impact of observational effects. These are quantified through the analysis of the various sets of mocks with both TNS and CLPT-GS models, which are described in Section 2.3.1.

4.2.2.1 Optimal fitting ranges

We first study the optimal range of scales in the fit for the two RSD models considered in this work. It is worth noting that the optimal range of scales is not necessarily the same for the two models. Generally, full-shape RSD analyses use scales going from tens of h^{-1}Mpc to about $130-150\,h^{-1}$Mpc. Including smaller scales potentially increases the precision of the constraints but at the expense of stronger biases on the recovered parameters. This is related to the limitations of current RSD models to fully describe the non-linear regime. On the other hand, including scales larger than $\sim 130\ h^{-1}$Mpc does not significantly improve the precision, since the variations of the model on those scales are small.

In order to determine the optimal range of scales for our RSD models, we performed fits to the mean correlation function of the NSERIES mocks, which are those that most accurately predict the expected RSD in the data. Fig. 4.3 shows the best-fit values of $f\sigma_8$, $\alpha_\parallel$, and $\alpha_\perp$ as a function of the minimum scale used in the fit, $r_{\rm min}$. In each panel, the grey bands show 1 per cent errors in

$\alpha_\perp, \alpha_\parallel$ and 3 per cent errors in $f\sigma_8$ for reference. Top panels present the measurements from the TNS model when the parameter $b_{\Gamma 3}$ fixed to the value given by Eq. 2.222, while in the mid panels this parameter is let free. Bottom panels show best-fit values for the CLPT-GS model as studied in ICAZA-LIZAOLA et AL. 2020. As noted in ZARROUK et AL. 2018, the hexadecapole is more sensitive to the difference between the true and fiducial cosmologies and is generally less well modelled on small scales compared to the monopole and quadrupole. We therefore consider the possibility of having a different minimum fitting scale for the hexadecapole with respect to the monopole and quadrupole that share the same $r_{\rm min}$. For consistency with the other systematic tests, we performed this analysis using two choices of fiducial cosmologies, $\Omega_m^{\rm fid} = 0.286$ (blue) and $\Omega_m^{\rm fid} = 0.31$ (red). The maximum separation in all cases is $r_{\rm max} = 130 h^{-1}$Mpc, as we find that using larger $r_{\rm max}$ has a negligible impact on the recovered parameter values and associated errors.

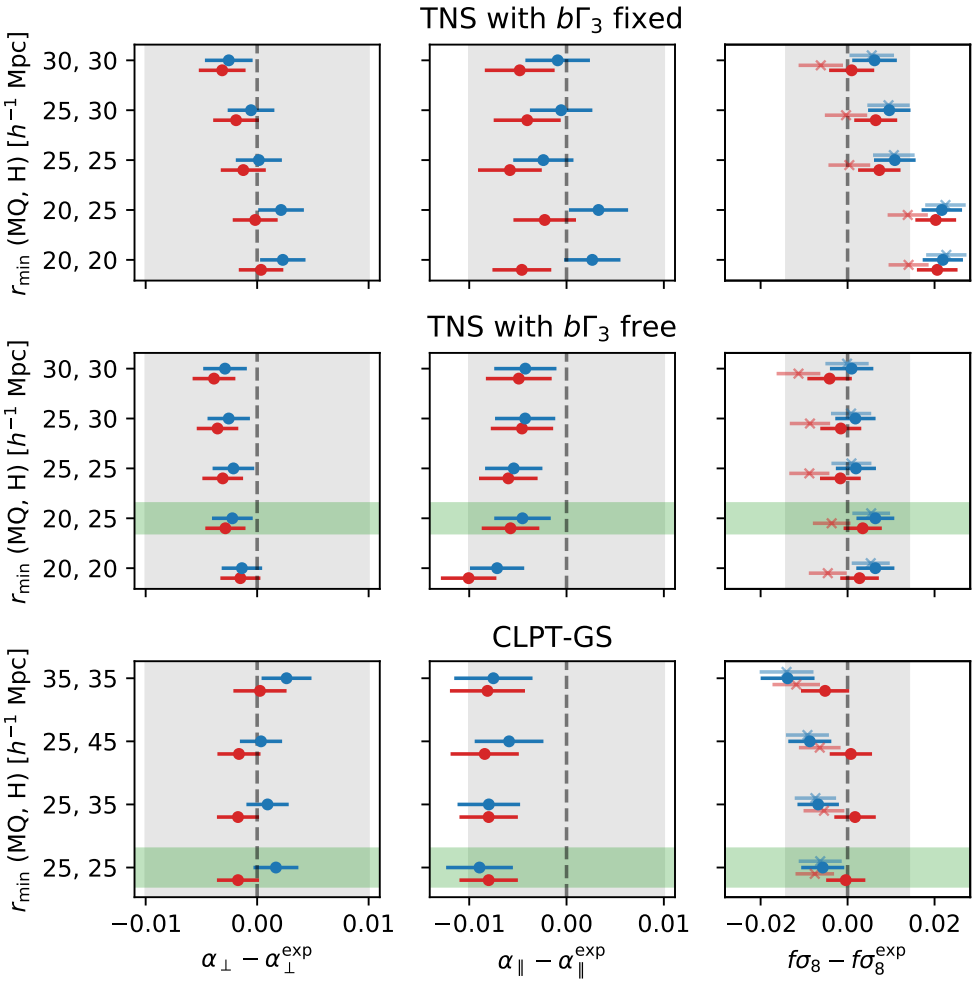

FIGURE 4.3 – Biases in the measurement of $f\sigma_8, \alpha_\parallel, \alpha_\perp$ obtained from full-shape fits to the average of 84 multipoles from the NSERIES mocks as a function of the separation range used. The y-axis displays the value of the minimal separation $r_{\rm min}$ used in fits of the monopole, quadrupole (MQ) and hexadecapole (H). Top and mid rows display results for the TNS model when fixing or letting free the parameter $b\Gamma_3$ respectively. Bottom row presents results for the CLPT-GS model. The blue circles correspond to the analysis using $\Omega_m^{\rm fid} = 0.286$ (the true value of simulations) while the red squares correspond to $\Omega_m^{\rm fid} = 0.31$. The gray shaded areas correspond to 1 per cent errors in $\alpha_\perp, \alpha_\parallel$ and to 3 per cent in $f\sigma_8$. The green shared area shows our choice for baseline analysis for TNS and CLPT-GS models.

In the case of the TNS model, I consider two different cases that correspond to when $b_{\Gamma 3}$ is fixed to its Lagrangian prediction and when $b_{\Gamma 3}$ is allowed to vary. In the case of $\Omega_m^{\rm fid} = 0.286$ and when $b_{\Gamma 3}$ is fixed, in the top panels of Fig. 4.3, we can see that $f\sigma_8$ is overestimated by 1.5 per cent when using scales above $25h^{-1}$Mpc and by 2 per cent below. Using $r_{\rm min} > 25h^{-1}$Mpc reduces the bias to about 1 per cent on $f\sigma_8$. For $\alpha_\parallel$ and $\alpha_\perp$ parameters, biases range from 0.3 to 0.5 per cent and are all statistically consistent with zero. When $b_{\Gamma 3}$ is let free, in the mid panels of Fig. 4.3, the model provide more robust measurements of $f\sigma_8$ at all tested ranges. The biases in $f\sigma_8$ over all ranges does not exceed 0.6σ, compared to approx 2.5σ for the fixed $b_{\Gamma 3}$ case. We also remark that letting b_{Γ_3} free also provides a better fit to the BAO amplitude and the hexadecapole on the scales of $20-25h^{-1}$Mpc. We see a 1 per cent bias on $\alpha_\parallel$ when $r_{\rm min} = 20h^{-1}$Mpc for all three multipoles. This bias is however reduced by increasing the hexadecapole minimum scale to $r_{\rm min} = 25h^{-1}$Mpc. The most optimal configuration for the TNS model is to let $b\Gamma_3$ free and fit the monopole and quadrupole in the range $20 \leq r \leq 130h^{-1}$Mpc and the hexadecapole in the range $25 \leq r \leq 130h^{-1}$Mpc, as marked by the green band in Fig. 4.3. If we use $\Omega_m^{\rm fid} = 0.31$, the trends and quantitative results are similar to the case with $\Omega_m^{\rm fid} = 0.286$.

For the CLPT-GS model, an exploration of the optimal fitting range was done in (Icaza-Lizaola et al. 2020). Two sets of tests have been performed. The first set consisted of fitting the mean of the mocks when varying $r_{\rm min}$ and the second, fitting the 84 individual mocks and measuring the bias and variance of the best fits when varying $r_{\rm min}$. We revisit the first set of tests, but this time performing a full MCMC analysis to determine best fits and errors. The bottom panels of Fig. 4.3 summarise the results. In the case of $\Omega_m^{\rm fid} = 0.286$, we see that using $r_{\rm min} = 25h^{-1}$Mpc for all multipoles yields to biases of 0.1, 1.1 and 1.6 per cent in $\alpha_\perp$, $\alpha_\parallel$, and $f\sigma_8$. Increasing $r_{\rm min}$ for the hexadecapole while fixing $r_{\rm min} = 25h^{-1}$Mpc for the monopole and quadrupole, does not change the results significantly, the biases are 0.1 per cent for all ranges in $\alpha_\perp$, and 1 per cent also for all ranges in $\alpha_\parallel$. For $f\sigma_8$ variations of 0.1-0.2 per cent arises when varying the range, but this variation in statistically consistent with zero. In the case of $\Omega_m^{\rm fid} = 0.31$, we find very similar trends. Using $r_{\rm min} = 25h^{-1}$Mpc for all multipoles yields biases of 0.2, 0.9 and 1.6 in $\alpha_\perp$, $\alpha_\parallel$ and $f\sigma_8$ respectively. When we decrease the range of the fits, the biases on $(\alpha_\perp, \alpha_\parallel, f\sigma_8)$ varies by (0.1-0.2, 0.2-0.3, 0.3-0.4) per cent. These variations are not significant and we decide to keep the lowest considered minimum scales on the hexadecapole in the fits.

Compared with previous BOSS full-shape RSD analysis in configuration space, we used for CLPT-GS model the same minimum scale for the monopole and quadrupole (Satpathy et al. 2017; Alam et al. 2017). The hexadecapole was not included in BOSS analyses. The exploration for the optimal minimum scale to be used for the hexadecapole was done in Icaza-Lizaola et al. 2020 and revisited in this work. The systematic error associated to the adopted fitting range is also consistent with previous results for the case where only the monopole and quadrupole are used, as reported in Icaza-Lizaola et al. 2020. The TNS model was not used in configuration space for analysing previous SDSS samples. However, as we describe in Section 4.2.2.2, the bias associated with both models when using their optimal fitting range is consistent between them, as well as consistent with previous BOSS results.

Overall, these tests performed on the Nseries mocks allow us to define the optimal fitting ranges of scales for both RSD models. Minimizing the bias of the models while keeping $r_{\rm min}$ as small as possible, we eventually adopt the following optimal ranges :

— TNS model : $20 < r < 130h^{-1}$Mpc for ξ_0 and ξ_2, and $25 < r < 130h^{-1}$Mpc for ξ_4

— CLPT-GS model : $25 < r < 130h^{-1}$Mpc for all multipoles,

which serve as baseline in the following. We compare the performance of the two models using these ranges in the following sections.

4.2.2.2 Systematic errors from RSD modeling and adopted fiducial cosmology

We quantify in this section the systematic error introduced by the RSD modelling and the choice of fiducial cosmology. For this, we used the NSERIES mocks [4]. The measurements of $\alpha_\perp$, $\alpha_\parallel$ and $f\sigma_8$ from fits to the average multipoles are given in Table 4.5 and shown in Fig. 4.4. The shaded area in the figure corresponds to 1 per cent deviation for $\alpha_\perp, \alpha_\parallel$ expected values and 3 per cent for $f\sigma_8$ expected value. We used both TNS (red) and CLPT-GS (blue) models and consider three choices of fiducial cosmologies parameterised by their value of $\Omega_m^{\rm fid}$. Note that, as for the BAO analysis, we only test flat ΛCDM models close to the most probable one. We expect the full-shape analysis to be biased if the fiducial cosmology is too different from the truth (the parametrisation with $\alpha_\perp$ and $\alpha_\parallel$ would not fully account for the distortions and the template power spectrum would differ significantly).

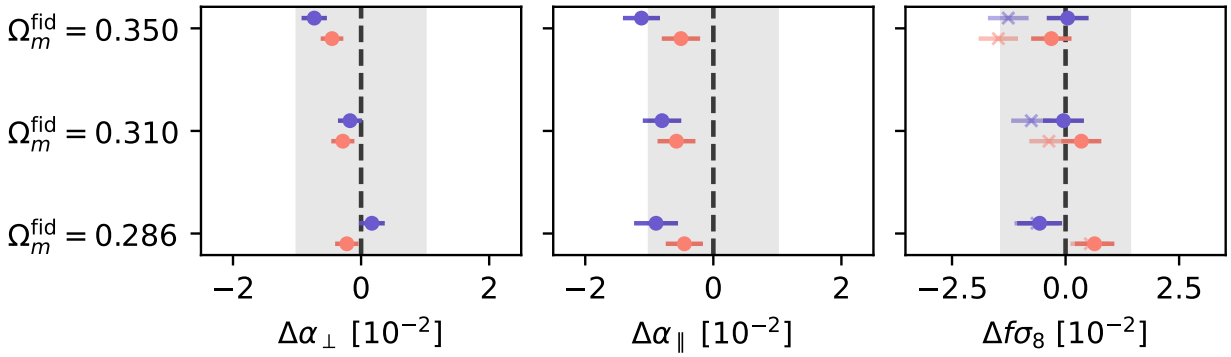

FIGURE 4.4 – Biases in best-fit parameters for both CLPT-GS (blue) and TNS (red) models from fits to the average multipoles of 84 NSERIES mocks. Shaded grey areas show the equivalent of 1 per cent error for $\alpha_\perp, \alpha_\parallel$ and 3 per cent for $f\sigma_8$. In the right panel, crosses indicate $f\sigma_8$ values when σ_8 is not recomputed as described in Section 2.3.1.2. The true cosmology of the mocks is $\Omega_m = 0.286$. For reference, the errors on our data sample are ∼ 2, 3 and 10 per cent for $\alpha_\perp, \alpha_\parallel, f\sigma_8$ respectively.

We find that both RSD models are able to recover the true parameter values within these bounds. We estimate the systematic errors related to RSD modelling using Eq. 4.7 and 4.8 by considering the shifts for the case where $\Omega_m^{\rm fid} = 0.286$ which is the true cosmology of the NSERIES mocks. We obtain, for $\alpha_\perp$, $\alpha_\parallel$ and $f\sigma_8$, respectively :

$$\text{CLPT} - \text{GS} : \sigma_{\rm syst,model} = (0.4,\ 0.9,\ 1.0) \times 10^{-2} \tag{4.10}$$

$$\text{TNS} : \sigma_{\rm syst,model} = (0.4,\ 0.6,\ 0.9) \times 10^{-2}. \tag{4.11}$$

The biases on the recovered parameters shown in Figure. 4.4 induced by the choice of fiducial cosmology remain within 1, 1, and 3 per cent for $\alpha_\perp, \alpha_\parallel$, and $f\sigma_8$ respectively. For $\alpha_\perp$, both CLPT-GS and TNS models produces biases lower than 2σ for all cosmologies except $\Omega_m^{\rm fid} = 0.35$, which is the most distant value from the true cosmology of the simulation $\Omega_m = 0.286$. For $\alpha_\parallel$, all biases are consistent with zero at 2σ level for the TNS model, while CLPT-GS shows biases slightly larger than 2σ for all $\Omega_m^{\rm fid}$.

The right panel of Fig. 4.4 shows the measured $f\sigma_8$ when using the original value of σ_8 from the template (crosses) and when recomputing it with the scaling of $R = 8h^{-1}$Mpc by the isotropic

4. Given the mismatch between the clustering of the MOCKCHALLENGE mocks and data, and its larger cosmic variance compared to NSERIES mocks, we decided to use MOCKCHALLENGE only for the quantification of systematic errors related to the halo occupation models.

Tableau 4.5 – Performance of the two full-shape models on the NSERIES mocks. Fits were performed on the the average of 84 multipoles. We report the shifts of best-fit parameters relative to their expected values. For $\Omega_m^{\rm fid} = 0.286$ we expect that both the α parameters are equal to 1. For $\Omega_m^{\rm fid} = 0.31$, $\alpha_\perp^{\rm exp} = 0.9788$, $\alpha_\parallel^{\rm exp} = 0.9878$ while for $\Omega_m^{\rm fid} = 0.35$ we expect $\alpha_\perp^{\rm exp} = 0.9623$, $\alpha_\parallel^{\rm exp} = 0.9851$. Since the growth rate of structures does not depend on the assumed cosmology, we expect to recover $f\sigma_8^{\rm exp} = 0.469$ for all cases.

Model	$\Omega_m^{\rm fid}$	$\Delta\alpha_\perp$ $[10^{-2}]$	$\Delta\alpha_\parallel$ $[10^{-2}]$	$\Delta f\sigma_8$ $[10^{-2}]$
CLPT-GS	0.286	0.2 ± 0.2	-0.9 ± 0.3	-0.6 ± 0.5
CLPT-GS	0.31	-0.2 ± 0.2	-0.8 ± 0.3	-0.0 ± 0.5
CLPT-GS	0.35	-0.7 ± 0.2	-1.1 ± 0.3	0.0 ± 0.5
TNS	0.286	-0.2 ± 0.2	-0.5 ± 0.3	0.6 ± 0.4
TNS	0.31	-0.3 ± 0.2	-0.6 ± 0.3	0.3 ± 0.4
TNS	0.35	-0.5 ± 0.2	-0.5 ± 0.3	-0.3 ± 0.4

dilation factor $\alpha = \alpha_\perp^{2/3}\alpha_\parallel^{1/3}$ (filled circles) as described in Section 2.3.1. Both TNS and CLPT-GS models show a consistent dependency with $\Omega_m^{\rm fid}$ when σ_8 is not re-evaluated : larger $\Omega_m^{\rm fid}$ yields smaller $f\sigma_8$. This is also found in the Fourier-space analysis of (GIL-MARIN et AL. 2020) and in Figure 14 of (SMITH et AL. 2020). As we recompute σ_8, this dependency is considerably reduced, which in turn reduces the contribution of the choice of fiducial cosmology to the systematic error budget. Using Eq. 4.7 and 4.8, with the entries of Table 4.5 (with σ_8 re-computed) where $\Omega_m^{\rm fid} \neq 0.286$ compared to the entries where $\Omega_m^{\rm fid} = 0.286$, we obtain the following systematic errors associated with the choice of fiducial cosmology for $\alpha_\perp$, $\alpha_\parallel$ and $f\sigma_8$, respectively :

$$\mathrm{CLPT-GS} : \sigma_{\rm syst,fid} = (0.9,\ 1.0,\ 1.4) \times 10^{-2} \tag{4.12}$$

$$\mathrm{TNS} : \sigma_{\rm syst,fid} = (0.5,\ 0.8,\ 1.2) \times 10^{-2} \tag{4.13}$$

These systematic errors would be twice as large if σ_8 was not recomputed as described in Section 2.3.1.2.

4.2.2.3 Systematics errors from observational effects

We investigate in this section the observational systematics. We used a set of 100 EZMOCKS to quantify their impact on our measurements. From the same set, we added different observational effects. For simplicity, those samples were made from mocks reproducing only the eBOSS component of the survey, neglecting the CMASS component. We consider that the systematic errors estimated this way can be extrapolated to the full eBOSS+CMASS sample by assuming that their contribution is the same over the CMASS volume. We thus produced the following samples :

1. no observational effects included, which we use as reference,
2. including the effect of the radial integral constraint (RIC,DE MATTIA et RUHLMANN-KLEIDER 2019), where the redshifts of the random catalog are randomly chosen from the redshifts of the data catalog,
3. including RIC and all angular features : fiber collisions, redshift failures, and photometric corrections.

For each set, we computed the average multipoles and fitted them using our two RSD models. The covariance matrix is held fixed among the various cases. Table 4.6 summarises the biases in $\alpha_\perp, \alpha_\parallel, f\sigma_8$ caused by the different observational effects. The shifts are relative to results of mocks without observational effects. We find that the radial integral constraint produces the greatest effect, particularly for the CLPT-GS model for which the deviation on $f\sigma_8$ is slightly larger than 2σ. Indeed,

Tableau 4.6 – Impact of observational effects on the full-shape analysis using EZMOCKS. Each row displays the shifts of best-fit parameters with respect to the case without observational effects ("no syst") : $\Delta x = x - x^{\text{no syst}}$. Fits are performed on the average multipoles of 100 realisations. We test the cases of mocks with radial integral constraint (RIC) and mocks with the combination of RIC and all angular observational effects (fiber collisions, redshift failures and photometric fluctuations). The angular effects introduced in mocks are corrected using the same procedure used in data. For simplicity, the mocks used here are only for the eBOSS part of the survey.

Type	Model	$\Delta\alpha_\perp$ $[10^{-2}]$	$\Delta\alpha_\parallel$ $[10^{-2}]$	$\Delta f\sigma_8$ $[10^{-2}]$
RIC	CLPT-GS	-0.3 ± 0.5	1.1 ± 0.6	-1.7 ± 0.8
+Ang. Sys.	CLPT-GS	0.0 ± 0.4	0.3 ± 0.6	0.0 ± 0.9
RIC	TNS	0.6 ± 0.5	-0.1 ± 0.7	-0.8 ± 0.9
+Ang. Sys.	TNS	0.8 ± 0.5	-0.2 ± 0.7	0.1 ± 0.9

the quadrupole for mocks with RIC has smaller absolute amplitude, which translates into small $f\sigma_8$ values. However, when adding angular observational effects the shifts are all broadly consistent with zero, which indicates that the two effects partially cancel each other.

Using values from the Table 4.6 and Eqs. 4.7 and 4.8, we derive the following systematic errors from observational effects for $\alpha_\perp$, $\alpha_\parallel$ and $f\sigma_8$, respectively :

$$\text{CLPT} - \text{GS} : \sigma_{\text{syst,obs}} = (0.9,\ 1.2,\ 1.7) \times 10^{-2} \tag{4.14}$$

$$\text{TNS} : \sigma_{\text{syst,obs}} = (1.0,\ 1.3,\ 1.8) \times 10^{-2} \tag{4.15}$$

These systematic errors are about 50 per cent of the statistical errors for each parameter, which corresponds to the most significant contribution to the systematic error budget.

4.2.2.4 Systematics Errors for HOD variation

We quantify in this section the potential systematic errors introduced by the models with respect to how LRGs occupy dark matter halos. This is done by analysing mock catalogs produced with different halo occupation distribution (HOD) models that mimic different underlying galaxy clustering properties. The same input dark matter field is used when varying the HOD model. We use the OUTERRIM mocks described in Section 3.1.5 and in (ROSSI et AL. 2021). Specifically, we analysed the mocks constructed using the "Threshold 2" for the HOD models from (LEAUTHAUD et AL. 2011; TINKER et AL. 2013; HEARIN et AL. 2015) and performed fits to the average multipoles over the 27 realisations available for each HOD model.

Fig. 4.5 and Table 4.7 shows the results. In this figure, each best-fit parameter is compared to the average best-fit over all HOD models in order to quantify the relative impact of each HOD (instead of comparing with their true value). The biases with respect to the true values were quantified in the previous section. The shaded regions represent 1 per cent error for $\alpha_\perp$ and $\alpha_\parallel$, and 3 per cent error for $f\sigma_8$.

We find that the biases for both RSD models are all within 1σ from the mean, although statistical errors are quite large (around one per cent for $\alpha_\perp, \alpha_\parallel$) compared to NSERIES mocks for instance. Also, the observed shifts are all smaller than the systematic errors estimated in the previous section. If we were to use the same definition for the systematic error introduced in Section 4.2, the relatively large errors from these measurements would produce a significant contribution to the error budget (because of the 2σ threshold). Therefore we consider that HOD has a negligible contribution to the total systematic error budget.

Tableau 4.7 – Performance of the full-shape analyses on the OUTERIM mocks produced using different HOD recipes. For each HOD Leauthaud2011,Tinker2013,Hearin2015 we display results obtained from our two RSD models (CLPT-GS and TNS). All results are from fits to the average multipoles of 27 realisations. Each row displays the shift of best-fit parameters with respect to the average parameters over the three HOD models : $\Delta x = x - \langle x \rangle_{\rm HOD}$. We found that these shifts are not significant and therefore do not contribute to systematic errors.

HOD	Model	$\Delta\alpha_\perp$ $[10^{-2}]$	$\Delta\alpha_\parallel$ $[10^{-2}]$	$\Delta f\sigma_8$ $[10^{-2}]$
L11	CLPT-GS	0.0 ± 0.7	0.0 ± 1.1	-0.1 ± 1.7
T13	CLPT-GS	0.1 ± 0.8	-0.2 ± 1.2	-0.6 ± 1.8
H15	CLPT-GS	0.0 ± 0.7	0.3 ± 1.1	0.6 ± 1.8
L11	TNS	-0.4 ± 0.5	-0.7 ± 1.1	0.7 ± 1.5
T13	TNS	0.2 ± 0.6	0.8 ± 1.0	-0.9 ± 1.4
H15	TNS	0.2 ± 0.6	-0.1 ± 1.0	0.2 ± 1.5

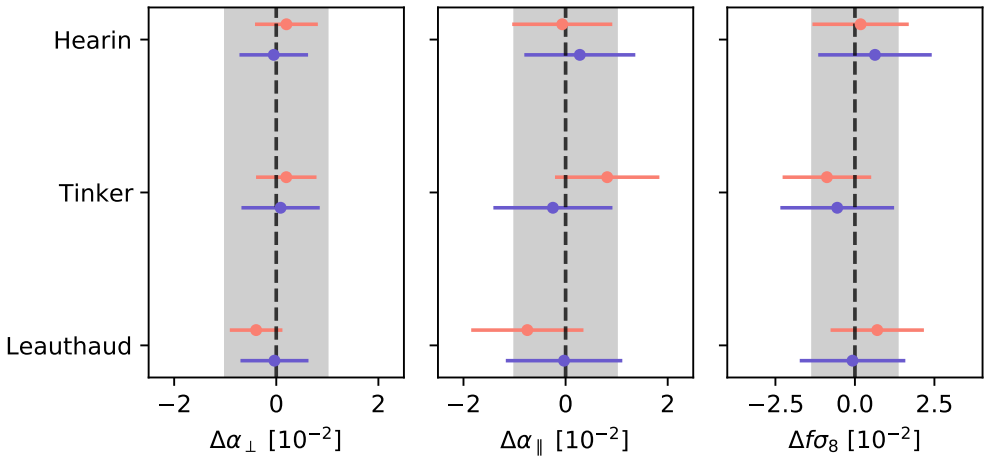

FIGURE 4.5 – Best-fit values of $\alpha_\perp$, $\alpha_\parallel$ and $f\sigma_8$ from fitting the average multipoles of the OUTERRIM mocks compared to their average over all HOD models. Blue points show results for the CLPT-GS model and red points show results for the TNS model. The shaded area shows 1% error for $\alpha_\perp, \alpha_\parallel$ and 3% for $f\sigma_8$.

4.2.2.5 Total systematic error of the full-shape RSD analysis

Table 4.8 summarises all systematic error contributions to the full-shape measurements discussed in the previous sections. We show the results for our two configuration-space RSD models TNS and CLPT-GS and for the Fourier space analysis of (GIL-MARIN et AL. 2020). We compute the total systematic error $\sigma_{\rm syst}$ by summing up all the contributions in quadrature, assuming that they are all independent. By comparing the systematic errors with the statistical error from the baseline fits to the data (see Section 4.3.2), we find that the systematic errors are far from being negligible : more than 50 per cent of the statistical errors for all parameters. The systematic errors are add in quadrature to the diagonal of the covariance of each measurement. We do not attempt to compute the covariance between systematic errors and this approach is more conservative (it does not underestimate errors).

Tableau 4.8 – Summary of systematic errors obtained from tests with mock catalogs. The total systematic error $\sigma_{\rm syst}$ is the quadratic sum of each contribution. The last rows display the final error which is a quadratic sum of statistical and systematic errors. The P_ℓ row correspond to the Fourrier space analysis of GIL-MARIN et AL. 2020.

Type	Model	$\sigma_{\alpha_\perp}$	$\sigma_{\alpha_\parallel}$	$\sigma_{f\sigma_8}$
Modelling	CLPT-GS	0.004	0.009	0.010
	TNS	0.004	0.006	0.009
Fid. cosmology	CLPT-GS	0.009	0.010	0.014
	TNS	0.005	0.008	0.012
Obs. effects	CLPT-GS	0.009	0.012	0.017
	TNS	0.010	0.014	0.018
$\sigma_{\rm syst}$	CLPT-GS	0.013	0.018	0.024
	TNS	0.012	0.017	0.023
	P_ℓ	0.012	0.013	0.024
$\sigma_{\rm stat}$	CLPT-GS	0.020	0.028	0.045
	TNS	0.018	0.031	0.040
	P_ℓ	0.027	0.036	0.042
$\sigma_{\rm syst}/\sigma_{\rm stat}$	CLPT-GS	0.66	0.63	0.54
	TNS	0.65	0.55	0.58
	P_ℓ	0.43	0.37	0.58
$\sigma_{\rm tot} = \sqrt{\sigma^2_{\rm syst} + \sigma^2_{\rm stat}}$	CLPT-GS	0.024	0.033	0.051
	TNS	0.021	0.035	0.046
	P_ℓ	0.029	0.038	0.048

4.2.3 Statistical properties of the LRG sample

We can also use the EZMOCKS for evaluating the statistical properties of the LRG sample, in particular to quantify how typical is our data compared with EZMOCKS, but also for measuring the correlations among the different methods and globally validating our error estimation.

The left panel of the Fig. 4.6 presents a comparison between the best-fit $(\alpha_\perp, \alpha_\parallel, f\sigma_8)$ and their estimated errors from fits of the TNS and the CLPT-GS models. The confidence contours contain approximately 68 per cent and 95 per cent of the results around the mean. The contours and histograms reveal a good agreement for the two models. Stars indicate the corresponding best fit values obtained from the data. The correlations between best-fit parameters of both models are 86, 83 and 93 per cent for $\alpha_\perp$, $\alpha_\parallel$ and $f\sigma_8$ respectively. A similar comparison for the errors is presented in the right panel of the Fig. 4.6. The errors inferred from the data analysis, shown as stars, are in good agreement with the 2D distributions from the mocks, lying within the 68 per cent contours. This excepted as we are using the EZMOCK covariance when fitting the data. The histograms comparing the distributions of errors for both methods also show a good agreement, in particular for $\alpha_\parallel$ and $f\sigma_8$. For $\alpha_\perp$, we observe that the distribution from CLPT-GS is slightly peaked towards smaller errors, while for TNS the error distribution has a larger dispersion for this parameter. The correlation coefficients between estimated errors from the two models are : 56, 38, and 39 per cent for $\alpha_\perp, \alpha_\parallel, f\sigma_8$, respectively.

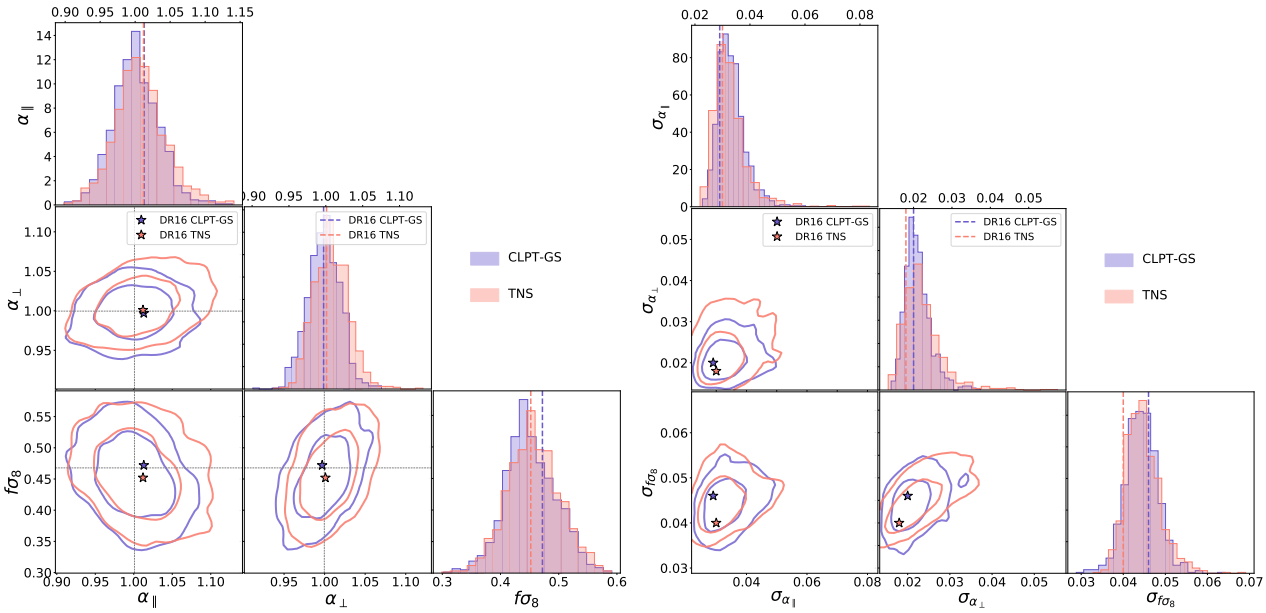

FIGURE 4.6 – Comparison between best-fit values (left panels) and estimated errors (right panel) for $(\alpha_\perp, \alpha_\parallel, f\sigma_8)$ using 1000 realisations of EZMOCKS fitted with the TNS and CLPT-GS models. The values obtained with real data are indicated by stars in each panel or as coloured vertical lines in the histograms. The thin black dashed line on the 2D plots refer to the true values of each parameter in the EZMOCKS.

Table 4.9 summarizes the statistical properties of errors for $\alpha_\perp, \alpha_\parallel, f\sigma_8$ for both BAO and full shape RSD analysis in configuration space (noted ξ_ℓ). We also include for reference the results from Fourier space analysis of (GIL-MARIN et AL. 2020), noted P_ℓ. For each parameter we show the standard deviation of the best fits values, σ, the mean estimated error $\langle\sigma\rangle$, the mean of the pull, $Z_i = (x_i - \langle x\rangle)/\sigma_x$ where $x = \alpha_\perp, \alpha_\parallel, f\sigma_8$, and its standard deviation $\sigma(Z)$. If errors are correctly estimated and follow a Gaussian distribution, we expect that $\sigma = \langle\sigma_i\rangle$, $\langle Z_i\rangle = 0$ and $\sigma(Z) = 1$. We remove results from non-converged chains and 5σ outliers in both best-fit values and errors (with σ defined as half of the range covered by the central 68 per cent values). Table 4.9 also shows the results from combining different methods employing the procedure described in Section 4.1.2. For each combination, we create the covariance matrix C (Eq. 4.4) from the correlation coefficients obtained from 1000 EZMOCKS fits, with small adjustments to account for the observed errors of a given realisation. The correlation coefficients (before this adjustement) is shown in Fig. 4.8 for all five methods. The BAO measurements from configuration and Fourier spaces are 87 and 88 per cent correlated for $\alpha_\perp$ and $\alpha_\parallel$, respectively. In RSD analyses these correlations reduce to slightly less than 80 per cent between $\alpha_\perp, \alpha_\parallel$ of both spaces, while $f\sigma_8$ correlations reach 84 per cent. The fact that these correlations are not exactly 100 per cent indicates that there is potential gain combining them.

For the BAO results (top three rows of Table 4.9), we see good agreement between σ_x and $\langle\sigma\rangle$ for all the parameters in both spaces. The mean of the pull $\langle Z_i\rangle$ is consistent with zero (their errors are roughly 0.02) and the standard deviation $\sigma(Z_i)$ is slightly smaller than unity for all variables, indicating that errors might be slightly overestimated. The combined BAO results of $(\xi_\ell + P_\ell)$ have errors slightly reduced to 2.2% for $\alpha_\perp$ and 3.4% in $\alpha_\parallel$ (based on the scatter σ of the best-fit values). The $\sigma(Z_i)$ are both closer to 1.0, indicating better estimate of errors for the combined case. As a conservative approach, the BAO errors on data (Section 4.3.1) are therefore not corrected by this overestimation.

Full shape RSD results (4th to 8th rows in Table 4.9) also show good agreement between σ_x and $\langle\sigma\rangle$ for all the parameters for both models and both spaces. Fig. 4.7 shows the pull distributions for both CLPT-GS and TNS models.

Tableau 4.9 – Statistics on errors from consensus results on 1000 EZMOCKS realisations. For each parameter, we show the standard deviation of best-fit values, $\sigma(x_i)$, the mean estimated error $\langle\sigma_i\rangle$, the mean of the pull, $Z_i = (x_i - \langle x_i\rangle)/\sigma_i$ and its standard deviation $\sigma(Z_i)$. $N_{\rm good}$ shows the number of valid realisations for each case after removing extreme values and errors at 5σ level.

Observable	$N_{\rm good}$	$\alpha_\perp$				$\alpha_\parallel$				$f\sigma_8$			
		σ	$\langle\sigma_i\rangle$	$\langle Z_i\rangle$	$\sigma(Z_i)$	σ	$\langle\sigma_i\rangle$	$\langle Z_i\rangle$	$\sigma(Z_i)$	σ	$\langle\sigma_i\rangle$	$\langle Z_i\rangle$	$\sigma(Z_i)$
BAO ξ_ℓ	987	0.023	0.023	-0.02	0.98	0.036	0.035	-0.02	0.96	-	-	-	-
BAO P_ℓ	978	0.024	0.024	-0.02	0.95	0.039	0.040	0.00	0.90	-	-	-	-
BAO $\xi_\ell + P_\ell$	970	0.022	0.022	-0.02	1.01	0.034	0.034	-0.02	0.97	-	-	-	-
RSD ξ_ℓ CLPT	819	0.023	0.021	0.01	1.03	0.033	0.033	-0.04	0.95	0.046	0.045	-0.01	0.97
RSD ξ_ℓ TNS	951	0.024	0.023	-0.05	1.03	0.037	0.033	-0.05	1.07	0.046	0.045	-0.01	0.95
RSD ξ_ℓ	781	0.021	0.021	-0.01	0.99	0.031	0.032	-0.03	0.96	0.042	0.045	-0.01	0.95
RSD P_ℓ	977	0.025	0.026	0.02	0.94	0.037	0.036	-0.04	1.00	0.046	0.046	0.01	0.96
RSD $\xi_\ell + P_\ell$	767	0.019	0.020	0.00	0.98	0.030	0.031	-0.03	0.97	0.041	0.043	-0.00	0.97
BAO+RSD ξ_ℓ	772	0.018	0.019	-0.01	1.00	0.024	0.025	-0.03	0.97	0.043	0.040	-0.02	1.06
BAO+RSD P_ℓ	955	0.019	0.020	0.00	0.96	0.028	0.029	-0.03	0.96	0.044	0.042	-0.01	1.05
BAO×RSD P_ℓ	986	0.019	0.019	0.03	0.99	0.029	0.028	-0.06	1.02	0.041	0.045	-0.01	0.92
BAO $(\xi_\ell + P_\ell)$ + RSD $(\xi_\ell + P_\ell)$	747	0.017	0.018	-0.01	1.00	0.024	0.025	-0.03	0.97	0.042	0.039	-0.02	1.09
(BAO+RSD) ξ_ℓ + (BAO+RSD) P_ℓ	747	0.017	0.018	-0.01	1.01	0.024	0.025	-0.03	0.99	0.042	0.039	-0.02	1.09

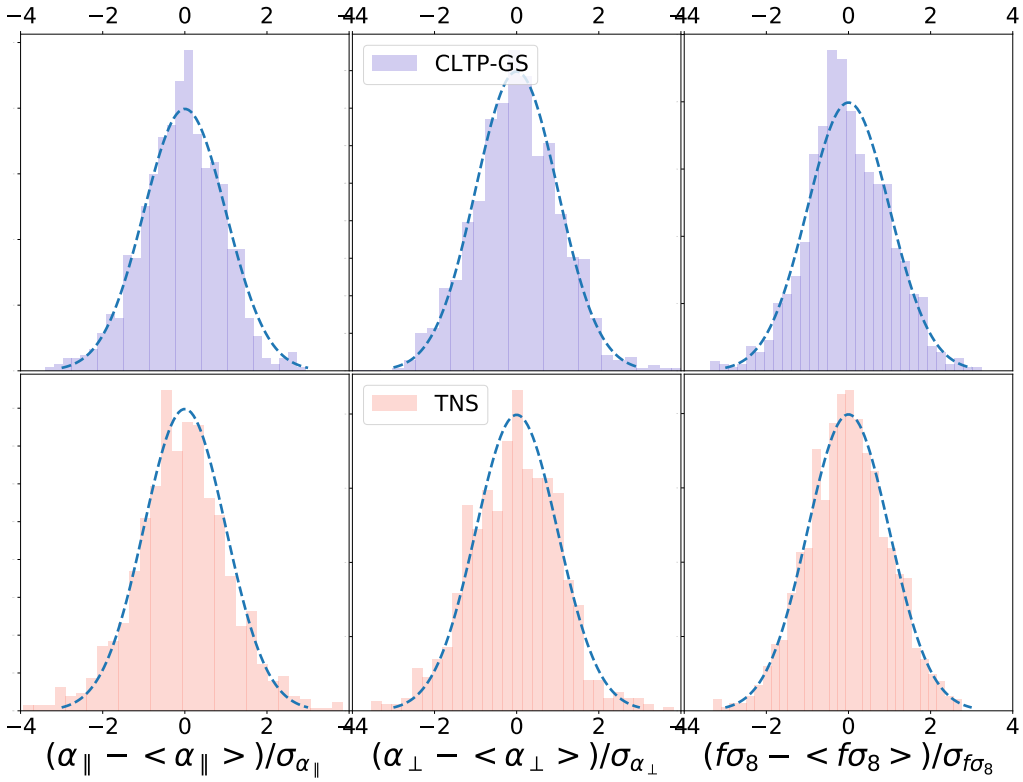

FIGURE 4.7 – Normalized distributions of the pull for the $\alpha_\parallel$, $\alpha_\perp$ and $f\sigma_8$ from fits of TNS and CLPT-GS models on EZMOCKS. The blue dashed lines represent the centered normalized Gaussian distribution.

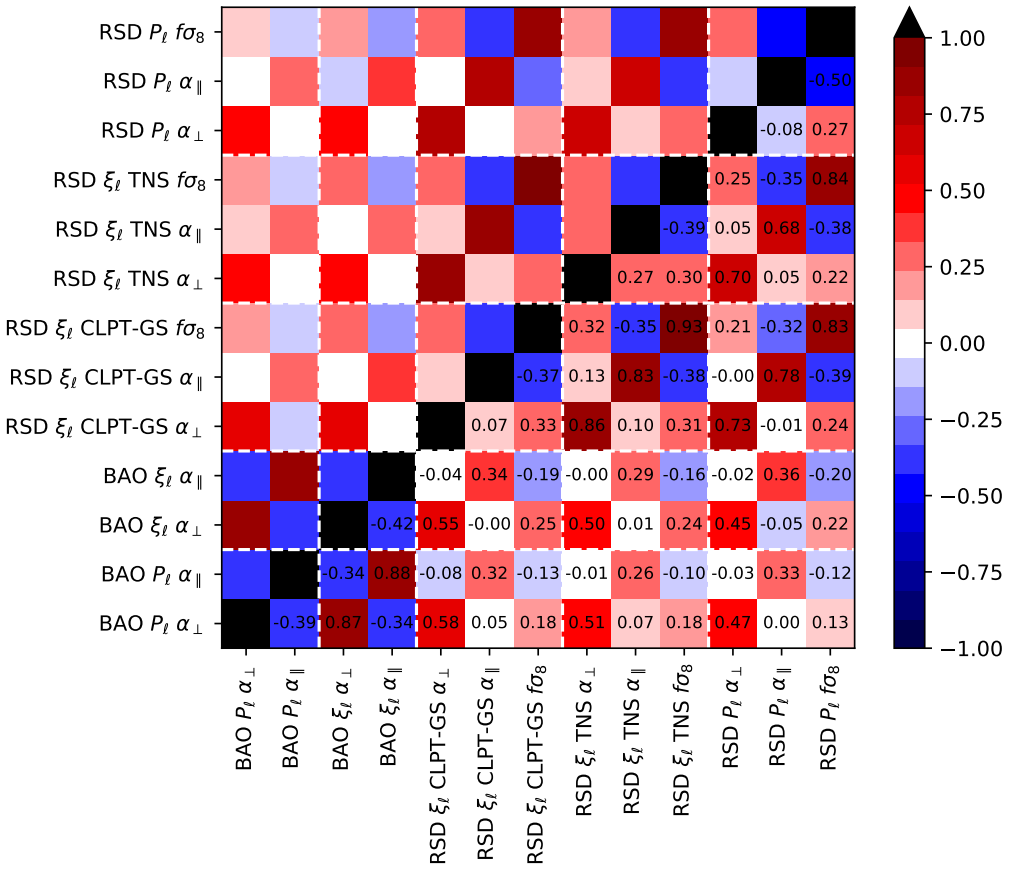

FIGURE 4.8 – Correlation coefficients between $\alpha_\perp, \alpha_\parallel, f\sigma_8$ for all methods and models obtained from fits to 1000 EZMOCK realisation of the eBOSS LRG+CMASS sample.

The mean of the pull for $\alpha_\perp$ and $f\sigma_8$ are consistent with zero in all cases though the mean pull for $\alpha_\parallel$ is negative, indicating a slightly skewed distribution. The $\sigma(Z_i)$ values for CLPT-GS and TNS models are consistent with one for $\alpha_\perp$ and slightly different than one for $\alpha_\parallel$ and $f\sigma_8$. Their combination (6th row) with inverse variance weighing slightly compensates for these differences, yielding better estimated errors, with $\sigma(Z_i)$ closer to one for all three parameters. The full-shape measurements in Fourier space (7th row) show similar behaviour than the ones in configuration space, with errors larger than measurements in configuration space. This is due to the larger number of nuisance parameters in the Fourier space analysis and to the choice of scales used in the Fourier space fits ($0.02 \leq k \leq 0.15$ hMpc^{-1}), which do not exactly translate to the range in separation used in our fits ($25 < r < 130$ h^{-1}Mpc), and may contain less information in average. The combined $\xi_\ell + P_\ell$ full-shape results in the 8th row present smaller dispersion on all parameters relative to each individual method. The pull values indicating slightly overestimated errors, which we do not attempt to correct. The 9th and 10th row of Table 4.9 show results of combining BAO and full-shape RSD results for a given space, ξ_ℓ or P_ℓ, while fully accounting for their large covariance as described in Section 4.1.2. We see that the scatter of $\alpha_\perp$ and $\alpha_\parallel$ is reduced by ~ 20 and 30 per cent, respectively, relative to their BAO-only analyses. For $f\sigma_8$ the scatter of best-fit values is the same as the full-shape-only analyses, as expected (BAO only do not provide extra information on $f\sigma_8$). The values of $\sigma(Z_i)$ for the combined results are consistent with one for $\alpha_\perp, \alpha_\parallel$, though for $f\sigma_8$ they are more than 5 per cent larger than unity for both configuration and Fourier space. This would indicate that our combination procedure from Section 4.1.2 produces slightly underestimated errors for $f\sigma_8$. In (GIL-MARIN et AL. 2020), an alternative method was suggested to extract the consensus results from BAO and RSD analysis : a simultaneous fit. Both BAO and RSD models are fitted simultaneously to the concatenation of the pre- and post-reconstruction data vectors.

This fit requires the full covariance matrix between pre- and post-reconstruction multipoles and

is estimated from 1000 EZMOCKS. Results of simultaneous fits on mocks are shown in the 11th row of Table 4.9 and are noted "BAO×RSD P_ℓ". These are to be compared with our usual method of combining posteriors, noted "BAO+RSD" and shown in the 10th row. First, we see good agreement between the scatter of best-fit values of all three parameters between BAO×RSD and BAO+RSD. However, the simultaneous fit overestimates the errors in $f\sigma_8$ by 8 per cent, based on its $\sigma(Z_i)$ value. While in theory the simultaneous fit is a better procedure, accounting for all correlations, in practice we only use 1000 mocks to estimate a larger covariance matrix with large off-diagonal terms. Therefore we cannot conclude from this test, which method leads to better estimated errors. We use BAO+RSD entries for the consensus results.

The last two rows of Table 4.9 show statistics on the final consensus results from the LRG sample when combining BAO and full shape from both Fourier and configuration spaces. These results reflect the full statistical power of the LRG sample. The excellent agreement between the statistics of these two rows shows that the order of combination does not impact results. The dispersion σ on $\alpha_\perp$ and $\alpha_\parallel$ are reduced to 1.8 and 2.6 per cent respectively while we had 2.2 and 3.4 per cent for BAO only, and 2.0 and 3.2 per cent for full-shape only. The pull distributions for $\alpha_\perp$ and $\alpha_\parallel$ are consistent with a Gaussian distribution. The scatter in $f\sigma_8$ is not reduced compared to individual methods, which is expected since BAO does not add information on this parameter, so the consensus error should be equal to the one obtained from the full-shape fits. However, the $\sigma(Z_i)$ for $f\sigma_8$ indicates that our consensus errors on this parameter might be underestimated by 10 per cent. While this seems to be significant, this result can be a consequence of the Gaussian assumption of all individual likelihoods not holding for all realisations, or the combination procedure itself might lead to underestimated errors (as seen with $f\sigma_8$ in the 9th and 10th rows), though we would need more mocks to test these hypotheses carefully.

For this work, we consider the underestimation on $f\sigma_8$ consensus errors (last two rows of Table 4.9) as another source of systematic error. The simplest correction to this underestimation is to scale the estimated errors of $f\sigma_8$ in each realisation by $\sigma(Z_i) = 1.09$. We proceed to apply this correction factor to the consensus $f\sigma_8$ errors with our data sample. This factor is to be applied only to statistical errors. In Section 4.3.3 we describe how we apply with this scaling in the presence of systematic errors.

4.3 Results

We provide in this section the results of the BAO analysis, the full-shape RSD analysis and the combination of the two for the eBOSS LRG sample. The analysis assumes an effective redshift for the sample of $z_{\rm eff} = 0.698$.

4.3.1 Results from the BAO analysis

We present in Fig. 4.9 our best-fit BAO model to the post-reconstruction eBOSS LRG multipoles. The associated reduced chi-squared is $\chi^2/{\rm dof} = 39/(40-9) = 1.26$. By scaling the resulting $\alpha_\perp$ and $\alpha_\parallel$ by $(D_M/r_d)^{\rm fid}$ and $(D_H/r_d)^{\rm fid}$, respectively by Eq. 2.266 we obtain :

$$\mathbf{D}_{{\rm BAO},\xi_\ell} = \begin{pmatrix} D_M/r_d \\ D_H/r_d \end{pmatrix} = \begin{pmatrix} 17.86 \pm 0.33 \\ 19.34 \pm 0.54 \end{pmatrix} \tag{4.16}$$

and the covariance matrix is

$$\mathbf{C}_{{\rm BAO},\xi_\ell} = \begin{pmatrix} 1.11 \times 10^{-1} & -5.86 \times 10^{-2} \\ - & 2.92 \times 10^{-1} \end{pmatrix} \tag{4.17}$$

Tableau 4.10 – The BAO measurement with the DR16 eBOSS+CMASS LRG dataset using the standard pipeline described in Section 2.3.2 and other analysis choices. Note that for cases with different $\Omega_m^{\rm fid}$, we scale the obtained $\alpha_\perp, \alpha_\parallel$ by the distance ratios in order to make them comparable with the case where $\Omega_m^{\rm fid} = 0.31$.

case	$\alpha_\perp$	$\alpha_\parallel$	χ^2/d.o.f.
Baseline	1.024 ± 0.019	0.956 ± 0.023	$39.0/(40-9)$
$w_{\rm sys} w_{\rm cp} w_{\rm noz} = 1$	1.022 ± 0.018	0.954 ± 0.023	$30.1/(40-9)$
$\Sigma_\perp, \Sigma_\parallel$ free	1.027 ± 0.016	0.947 ± 0.019	$31.9/(40-11)$
$\Sigma_\perp, \Sigma_\parallel$ prior	1.025 ± 0.017	0.952 ± 0.021	$36.2/(40-11)$
$+\xi_4$	1.031 ± 0.019	0.949 ± 0.024	$53.5/(60-12)$
$\Omega_m^{\rm fid} = 0.27$	1.026 ± 0.020	0.950 ± 0.023	$33.3/(40-9)$
$\Omega_m^{\rm fid} = 0.35$	1.026 ± 0.019	0.951 ± 0.022	$39.6/(40-9)$
DR12 method	1.023 ± 0.019	0.955 ± 0.024	$34.5/(40-10)$
Pre-recon	1.035 ± 0.025	0.957 ± 0.035	$42.0/(40-9)$
NGC only	1.038 ± 0.024	0.943 ± 0.024	$42.3/(40-9)$
SGC only	0.993 ± 0.032	0.982 ± 0.070	$44.5/(40-9)$

The errors correspond to a BAO measurement at 1.9 per cent in the transverse direction and 2.8 per cent in the radial direction, the best constraints ever obtained from $z > 0.6$ galaxies. The correlation coefficient between both parameters is -0.33.

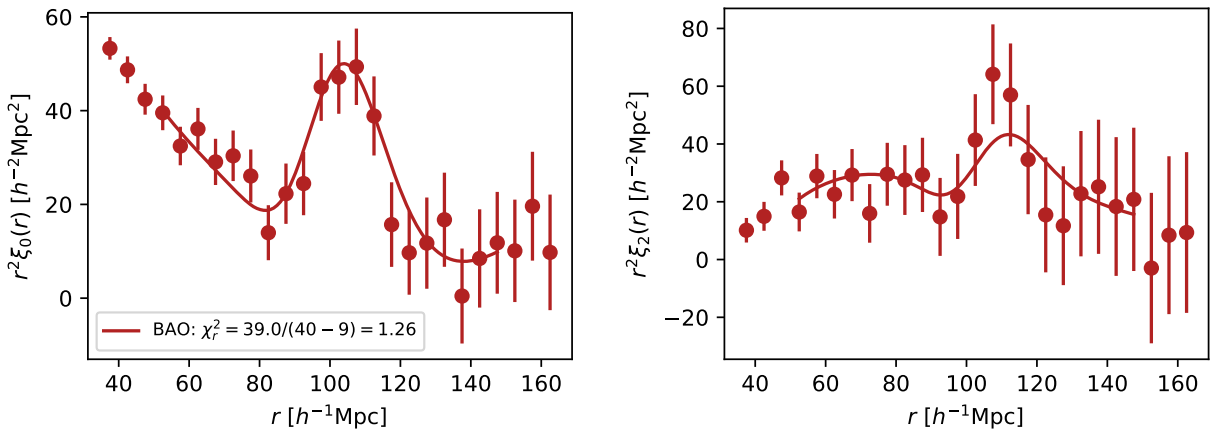

FIGURE 4.9 – Best-fit BAO model to the monopole (left) and quadrupole (right) of the post-reconstruction correlation function of the eBOSS + CMASS LRG sample. The legend displays the χ^2 value of the fit.

Fig. 4.10 shows in blue the 68 and 95% confidence contours in the $(D_M/r_d, D_H/r_d)$ space for the BAO measurement in configuration space. Our best-fit values are consistent within 1.26σ to the prediction of a flat ΛCDM model given by Planck 2018 best-fit parameters (PLANCK COLLABORATION 2018) assuming a χ^2 distribution with two degrees of freedom. This measurement is also in excellent agreement with the BAO analysis performed in Fourier space (GIL-MARIN et AL. 2020), shown as red contours in Fig. 4.10. Since Fourier and configuration space analyses use the same data, final measurements are highly correlated. Based on measurements of the same 1000 realisations of EZ-MOCKS, we obtain correlation coefficients of 0.86 for both D_M/r_d and D_H/r_d. As these correlations are not unity, there is some gain, in combining both measurements. Using the methods presented

in Section 4.1.2, we compute the combined BAO measurements between Fourier and configuration space. The result is displayed as grey contours in Fig. 4.10 and in Table 4.12 as "BAO $\xi_\ell + P_\ell$". The error of the combined result is only 2% smaller than the error of the configuration space analysis alone.

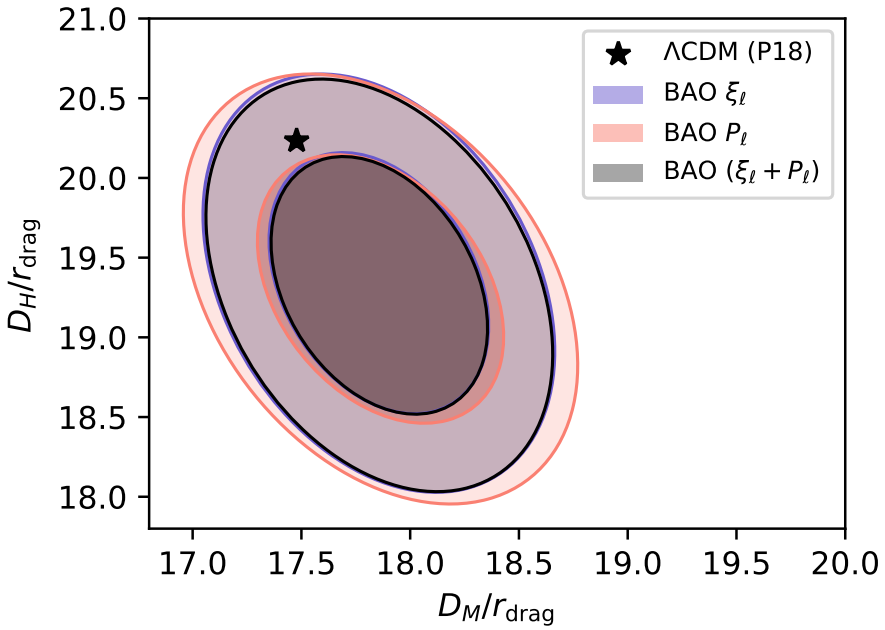

FIGURE 4.10 – Constraints on D_M/r_d and D_H/r_d at $z_{\rm eff} = 0.698$ from the BAO analysis of the eBOSS LRG sample post-reconstruction. Contours show 68 and 95 per cent confidence regions for the configuration space analysis in blue (this work), the Fourier space analysis from GIL-MARIN et AL. 2020 in salmon, and the consensus BAO result in grey. The expected values in a flat ΛCDM model with Planck 2018 best-fit parameters, shown by the black star, lies at 1.26σ from our best-fit parameters of the configuration space analysis.

Table 4.10 shows the impact on the BAO results in configuration space of different modifications in the methodology around the baseline configuration. The middle part of the table shows that our result is reasonably insensitive to some of these changes. Setting all systematic weights to unity causes only mild shifts to best-fit parameters while estimated errors are unchanged. Removing the corrections by weights significantly distorts the broad shape of the correlation function. The fact that our BAO results are insensitive to these corrections proves that practically all information comes uniquely from the BAO peak and not from the full-shape of the correlation function. This is a strong robustness validation of our BAO measurement. When leaving BAO damping parameters $(\Sigma_\perp, \Sigma_\parallel)$ free or constrained within a Gaussian prior, the best-fit values barely change while their errors are smaller than our baseline analysis. As observed on mocks, some realisations present sharper peaks due to noise and a sharper model could be considered as a better fit. However, we prefer to be conservative and not allow for this artificial increase in precision in our BAO analysis. Including the hexadecapole or changing the fiducial cosmology shifts alphas by less than one error bar, which is consistent to what is observed in mocks. We performed the BAO fits using the methods used in the BOSS DR12 analysis (ALAM et AL. 2017) which gives results in excellent agreement with our baseline method, with a slightly better χ^2. In the third part of Table 4.10 we present the pre-reconstruction result with similar best-fit $\alpha_\perp$ and $\alpha_\parallel$ but with errors larger by factors of 1.3 and 1.5, which is typical as seen in mocks (Fig. 4.2). Pre-reconstruction BAO-only fits using our methodology show biases of about 1 per cent in the mocks, therefore we do not recommend using

pre-reconstruction results without accounting for these biases. The NGC and SGC results are two independent samples and their best-fit $\alpha_\perp$ and $\alpha_\parallel$ are 0.25 and 0.53σ from each other respectively, therefore not representing a significant difference among hemispheres.

4.3.2 Results from the full-shape RSD analysis

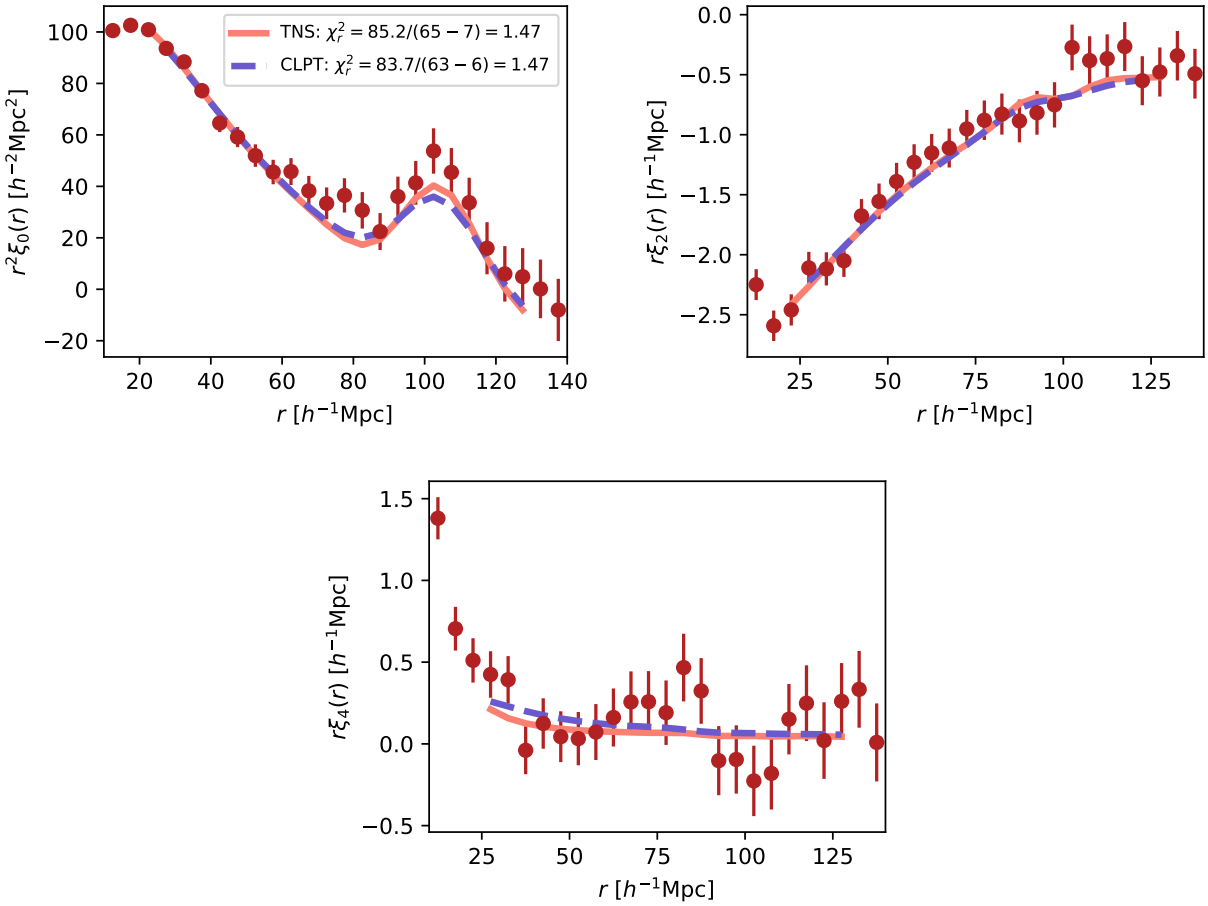

FIGURE 4.11 – Best-fits of the full-shape models to the eBOSS + CMASS multipoles. Left, mid and right panel display monopole, quadupole and hexadecapole, respectively. The monopole is scaled by r^2 while the other two are scaled by r. The CLPT-GS model is shown by the blue dashed line while the TNS model is shown by the red solid line. Note the baseline ranges used for each model are slightly different (see Fig. 4.3).

We present in Fig. 4.11 the best-fit TNS (red) and CLPT-GS (blue) RSD models to the pre-reconstruction eBOSS LRG multipoles. The associated reduced chi-squared values are $\chi^2/\mathrm{dof} = 85.2/(65-7) = 1.47$ for TNS and $\chi^2/\mathrm{dof} = 83.7/(63-6) = 1.47$ for CLPT-GS. While these values are unlikely explained by statistical fluctuations, we verified that the values reported for the χ^2 for both models are within EZMOCK χ^2 distributions. Both models perform similarly on data, but some differences are visible in Fig. 4.11. The TNS model produces a slightly sharper BAO peak than the CLPT-GS model, clearly visible in the monopole. This is due the fact that, intrinsically, the CLPT-GS model tends to predict a slightly higher BAO damping compared to Eulerian perturbation theory, as implemented here in the TNS model with RESPRESSO prescription. The CLPT-GS model has a slightly higher hexadecapole amplitude than the TNS model but both models seem to underestimate the hexadecapole amplitude below 35 h^{-1}Mpc by 1σ of the statistical uncertainties of the data. This underestimation in the amplitude of the hexadecapole is also present in the mocks for

Tableau 4.11 – The full-shape measurements with the DR16 eBOSS+CMASS LRG dataset from our baseline analysis described in Section 2.3.1 followed by results from other analysis choices. The presented errors are purely statistical and do not include systematic errors.

Model	Analysis	$\alpha_\perp$	$\alpha_\parallel$	$f\sigma_8$	χ^2/d.o.f.
CLPT-GS	baseline	0.997 ± 0.020	1.013 ± 0.028	0.471 ± 0.045	$83.7/(63-6) = 1.47$
CLPT-GS	$r_{\rm min} = 35h^{-1}$Mpc for ξ_4	1.017 ± 0.022	0.971 ± 0.031	0.499 ± 0.046	$79.3/(61-6) = 1.44$
CLPT-GS	NGC only	1.015 ± 0.025	1.009 ± 0.031	0.464 ± 0.055	$81.1/(63-6) = 1.40$
CLPT-GS	SGC only	0.985 ± 0.036	1.041 ± 0.062	0.439 ± 0.078	$71.3/(63-6) = 1.25$
TNS	baseline	1.001 ± 0.018	1.013 ± 0.031	0.451 ± 0.040	$85.2/(65-7) = 1.47$
TNS	$r_{\rm min} = 35h^{-1}$Mpc for ξ_4	1.013 ± 0.016	0.976 ± 0.027	0.458 ± 0.036	$73.7/(63-7) = 1.32$
TNS	Without ξ_4	1.019 ± 0.019	0.963 ± 0.035	0.472 ± 0.044	$50.1/(44-7) = 1.35$
TNS	NGC only	1.024 ± 0.029	1.013 ± 0.036	0.436 ± 0.053	$80.6/(65-7) = 1.39$
TNS	SGC only	0.993 ± 0.034	1.076 ± 0.070	0.423 ± 0.076	$69.1/(65-7) = 1.19$

both the NSERIES and EZMOCKS and was already reported in ICAZA-LIZAOLA et AL. 2020 explaining the relative high χ^2 of the data.

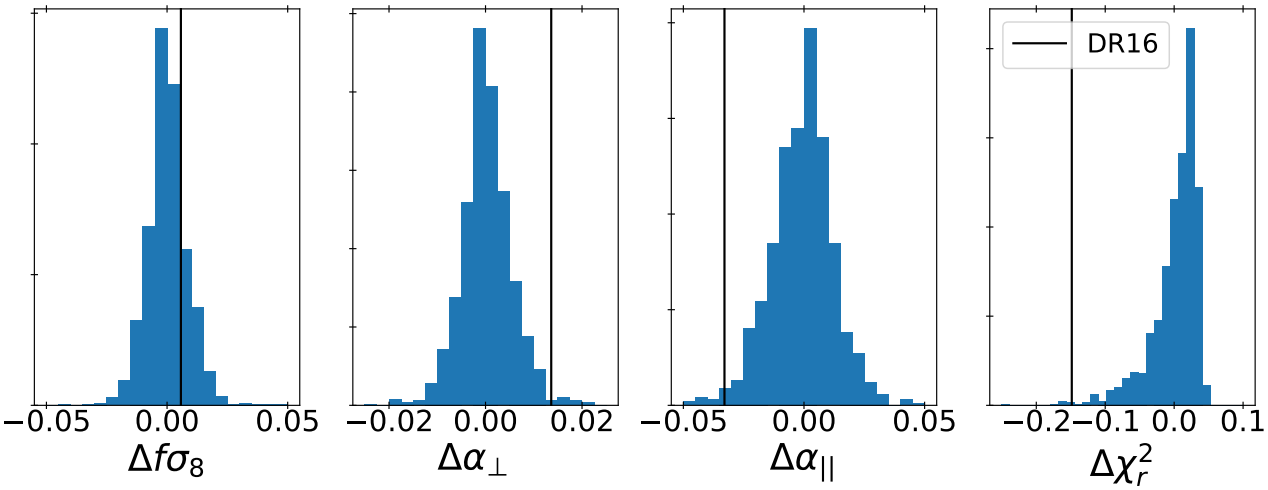

FIGURE 4.12 – Variation of the cosmological parameters and the reduced chi-squared as a function of the truncation scale of the hexadecapole for the TNS model. The normalisazed distributions corresponds to 1000 EZMOCKS while the vertical lines corresponds to the shift for the data.

Table 4.11 shows the impact of different modifications in the methodology around the baseline configuration. First, if we change the range of scales used in the hexadecapole by changing $r_{\rm min}$ from $25h^{-1}$Mpc to $35h^{-1}$Mpc. We see a decrease of the reduced chi-squared as we remove these scales from the hexedecapole, which are underestimated by the models. Removing those scales impact the measured cosmological parameters, particularly $\alpha_\parallel$, which is shifted by about 1 σ. We thus investigate if this shift is also present in the mocks. We present in Fig. 4.12 the distribution in the EZMOCKS of the difference on parameter constraints and reduced χ^2 induced by including or not the smallest scales of the hexadecapole in the fit. We find that the distribution for each of the parameters is centered on zero with a standard deviation of 0.006, 0.015 and 0.01 for $\alpha_\perp$, $\alpha_\parallel$ and $f\sigma_8$ respectively, which correspond to 0.3, 0.4 and 0.2 % of the uncertainties on the RSD TNS measurements in the data. This demonstrates that cosmological constraints are stable to the choice of the truncation scale for the hexadecapole. The vertical line shows the corresponding shift in the data. This shift remains within 1 σ of the EZMOCKS distribution for $f\sigma_8$ and reaches up to 2.3 σ for

$\alpha_\parallel$. For the reduced χ^2, the observed difference is on the edge of the EZMOCKS distribution. Even if few EZMOCKS realisations exhibit the same variation as in the data, the observed shifts are still statistically consistent.

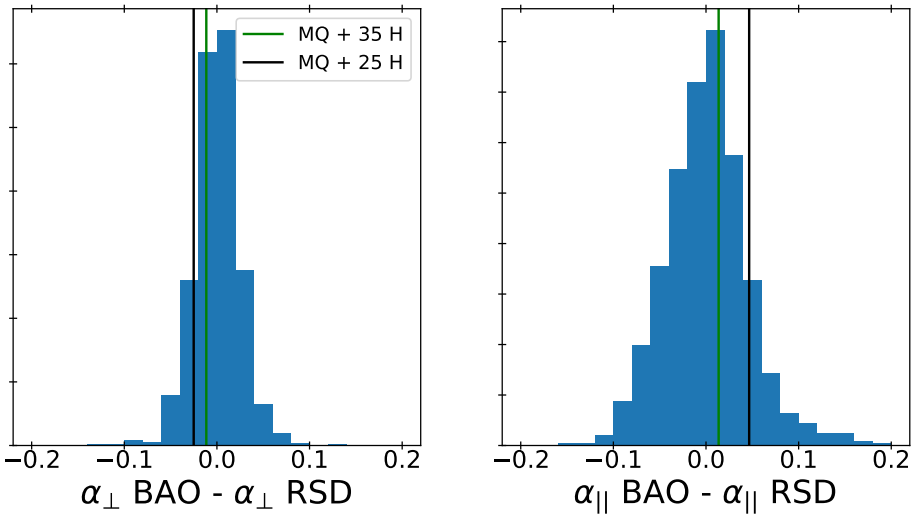

FIGURE 4.13 – Absolute difference between TNS and BAO post recon constraint on the alphas. The normalisazed distributions corresponds to 1000 EZMOCKS, while to the two vertical lines correspond to the two differents truncation scales for the hexadecapole.

Fig. 4.13 displays the difference on the geometrical distortion parameters between the BAO post-reconstruction and RSD TNS measurements in the EZMOCKS. Similarly as in the previous figure, the vertical line shows the difference found in the data. While the differences for $\alpha_\perp$ and $\alpha_\parallel$ are smaller when the smallest scales of the hexadecapole are removed from the RSD fits, both measurements seem to be consistent with BAO post-reconstruction measurements similarly as in the mocks. Both distributions are centered on zero with a standard deviation between BAO and RSD measurements of 0.04 and 0.06 for $\alpha_\perp$ and $\alpha_\parallel$ respectively. This shows that as expected RSD measurements provide a more uncertain determination of the geometrical distortion parameters than BAO measurements. We also perform fit on the data on both galactic poles, with measurements presented in Table 4.11. The NGC and SGC fields are two independent samples and we find that their individual best-fit $\alpha_\perp$ and $\alpha_\parallel$, and $f\sigma_8$ are 0.7σ, 0.5σ and 0.3σ from each other respectively for CLPT-GS and 0.7σ, 0.8σ and 0.1σ for TNS, which is not a significant difference.

The marginal posteriors on $\alpha_\perp, \alpha_\parallel, f\sigma_8$ and associated 68% and 95% confidence contours are shown in Fig. 4.14. The posteriors obtained from both models are in good agreement. Entries denoted as "RSD ξ_ℓ CLPT-GS" and "RSD ξ_ℓ TNS" in Table 4.12 gives the best-fit parameters and 1σ error (including systematic errors), translated into $D_M/r_d, D_H/r_d, f\sigma_8$. We find an excellent agreement in the best-fit parameters and errors between the two RSD models, as expected from the posteriors.

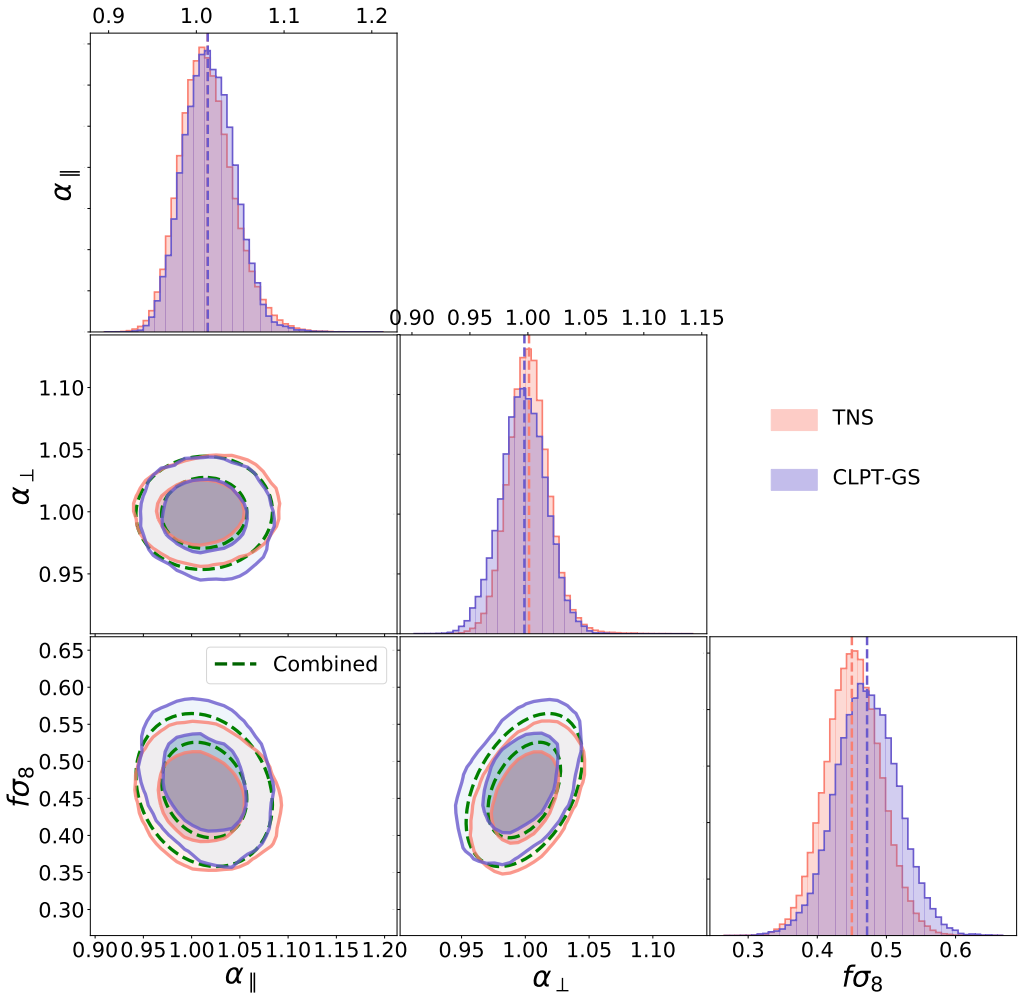

FIGURE 4.14 – Comparison between the TNS and CLPT-GS final posterior distributions over the three main parameters using the DR16 data. The distributions are in good agreement for the two models. The vertical dashed lines on the 1D distributions refer to the mean. Dashed line contours show the combined result from the two models, assumming Gaussian errors.

We combine the results from our two RSD models using a weighted average based on the individual covariance matrices (see Section 4.1.2). The combined measurement is indicated by "RSD ξ_ℓ" in Table 4.12 and shown with dashed contours in Fig. 4.14. Central values and errors of the combined result fall approximately in between the values of each individual measurement.

The combined best-fit parameters and covariance matrix of the full-shape RSD analysis in configuration space, including systematic errors, are

$$\mathbf{D}_{\mathrm{RSD},\xi_\ell} = \begin{pmatrix} D_M/r_d \\ D_H/r_d \\ f\sigma_8 \end{pmatrix} = \begin{pmatrix} 17.42 \pm 0.40 \\ 20.46 \pm 0.70 \\ 0.460 \pm 0.050 \end{pmatrix} \tag{4.18}$$

$$\mathbf{C}_{\mathrm{RSD},\xi_\ell} = \begin{pmatrix} 1.59 \times 10^{-1} & 6.28 \times 10^{-3} & 6.13 \times 10^{-3} \\ - & 4.88 \times 10^{-1} & -4.83 \times 10^{-3} \\ - & - & 2.46 \times 10^{-3} \end{pmatrix} \tag{4.19}$$

This corresponds to a 2.3 and 3.4 per cent measurements of the transverse and radial dilation parameters and a 11 per cent measurement of the growth rate of structure times σ_8. The errors on D_M/r_d and D_H/r_d are slightly larger than the ones from the BAO-only analysis, as expected, but the correlation coefficient between them is reduced from −0.33 to 0.02. This happens because

information on dilation parameters also come from the full-shape of the correlation function, rather than just the BAO peak. For instance, the correlation coefficient between $f\sigma_8$ and D_M/r_d is 0.31 and between $f\sigma_8$ and D_H/r_d is -0.14.

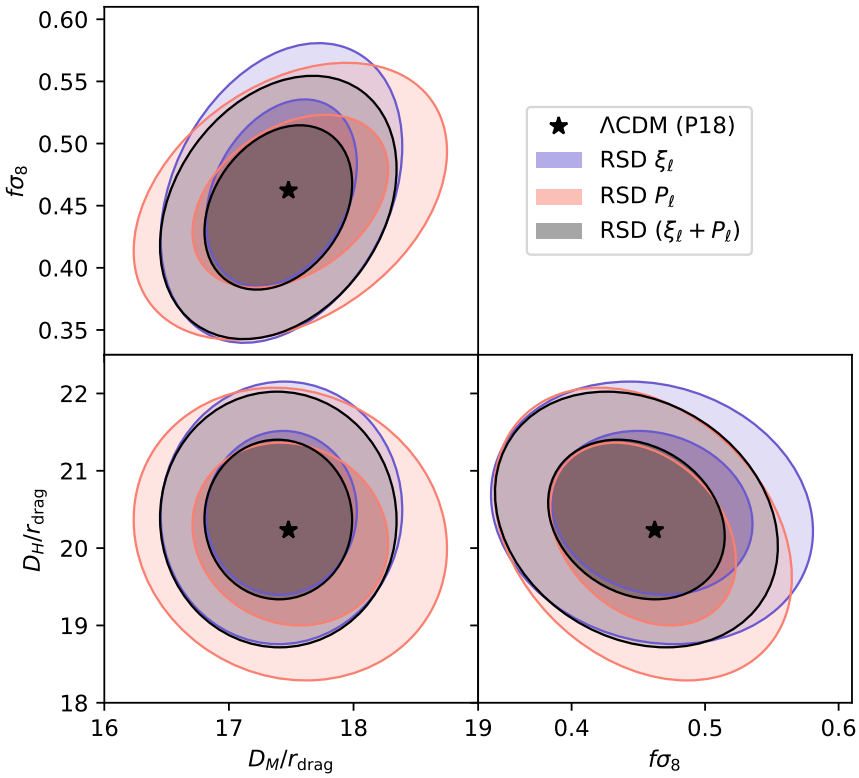

FIGURE 4.15 – Constraints on $D_M/r_d, D_H/r_d$ and $f\sigma_8$ $z_{\rm eff} = 0.698$ from the full-shape RSD analysis of the completed eBOSS LRG sample pre-reconstruction. Contours show 68 and 95 per cent confidence regions for the analyses in configuration space (blue), Fourier space (red) and the combined (grey). The expected values in a flat ΛCDM model with best-fit parameters from Planck 2018 results are indicated as a black star.

4.3.3 Consensus results

We present in Fig. 4.16 the final results of this work obtained by combining of BAO and full-shape RSD analyses in both configuration and Fourier spaces. Accounting for all sources of systematic error discussed in Section 4.2.2 and 4.2.3, the best-fit parameters and associated covariance matrix are :

$$\mathbf{D}_{\rm LRG} = \begin{pmatrix} D_M/r_d \\ D_H/r_d \\ f\sigma_8 \end{pmatrix} = \begin{pmatrix} 17.65 \pm 0.30 \\ 19.77 \pm 0.47 \\ 0.473 \pm 0.044 \end{pmatrix} \tag{4.20}$$

$$\mathbf{C}_{\rm LRG} = \begin{pmatrix} 9.11 \times 10^{-2} & -3.38 \times 10^{-2} & 2.47 \times 10^{-3} \\ - & 2.20 \times 10^{-1} & -3.61 \times 10^{-3} \\ - & - & 1.96 \times 10^{-3} \end{pmatrix} \tag{4.21}$$

which translate into a 1.7 and 2.4 per cent measurement of D_M/r_d and D_H/r_d respectively. The correlation between these two is −24 per cent. The error on $f\sigma_8$ is 9.4 per cent, which is the most precise measurement to date in this redshift range. We note that this final measurement is not sensitive to the order of combinations, as seen in the second panel of Fig. 4.16 and in the last row of Table 4.12. Those measurements agree well with the predictions from (PLANCK COLLABORATION

Tableau 4.12 – Summary table with results from this work, from (GIL-MARIN et AL. 2020), and their combination. All reported errors include the systematic component. The effective redshift of all measurements is $z_{\rm eff} = 0.698$.

Method	D_M/r_d	D_H/r_d	$f\sigma_8$
BAO ξ_ℓ	17.86 ± 0.33	19.34 ± 0.54	-
BAO P_ℓ	17.86 ± 0.37	19.30 ± 0.56	-
BAO $\xi_\ell + P_\ell$	17.86 ± 0.33	19.33 ± 0.53	-
RSD ξ_ℓ CLPT	17.39 ± 0.43	20.46 ± 0.68	0.471 ± 0.052
RSD ξ_ℓ TNS	17.45 ± 0.38	20.45 ± 0.72	0.451 ± 0.047
RSD ξ_ℓ	17.42 ± 0.40	20.46 ± 0.70	0.460 ± 0.050
RSD P_ℓ	17.49 ± 0.52	20.18 ± 0.78	0.454 ± 0.046
RSD $\xi_\ell + P_\ell$	17.40 ± 0.39	20.37 ± 0.68	0.449 ± 0.044
BAO+RSD ξ_ℓ	17.65 ± 0.31	19.81 ± 0.47	0.483 ± 0.047
BAO+RSD P_ℓ	17.72 ± 0.34	19.58 ± 0.50	0.474 ± 0.042
BAO $(\xi_\ell + P_\ell)$ + RSD $(\xi_\ell + P_\ell)$	17.65 ± 0.30	19.77 ± 0.47	0.473 ± 0.044
(BAO+RSD) ξ_ℓ + (BAO+RSD) P_ℓ	17.64 ± 0.30	19.78 ± 0.46	0.470 ± 0.044

2018), which predict at this redshift : 17.48, 20.23 and 0.462, respectively, for a flat ΛCDM model assuming gravity is described by General Relativity. These values are shown as stars in Fig. 4.16.

Systematic errors originating from observational effects, modelling and combination methods were carefully included in our measurements and are responsible for inflating final errors by 6, 13 and 20 per cent, respectively, on $D_M/r_d, D_H/r_d$ and $f\sigma_8$. In Section 4.2.3, we found that our statistical errors on the consensus $f\sigma_8$ were slightly underestimated. To apply this correction on the data consensus, we proceed as follows. First, we compute consensus with and without accounting for systematic errors from Table 4.8. The difference between their error matrices gives us the additive systematic matrix. Then, we scale the statistical errors on $f\sigma_8$ by 1.09 and we add back the additive systematic matrix. This procedure yields the results reported in Eq. 4.20 and 4.21.

4.3.4 Comparison with previous results

Our final consensus result for the DR16 LRG sample is shown in Eqs. 4.20 and 4.21, and used a total of 402,052 (weighted) galaxies over 9,463 deg^2 (with 4,242 deg^2 observed by eBOSS). (BAUTISTA et AL. 2018) and (ICAZA-LIZAOLA et AL. 2020) describe, respectively, the BAO and full-shape RSD measurements using the DR14 LRG sample, that contains 126,557 galaxies over 1,844 deg^2. In the DR14 sample, CMASS galaxies outside of the eBOSS footprint were not used. Because of that, the effective redshift of the DR14 measurements is slightly higher, at $z_{\rm eff} = 0.72$.

(BAUTISTA et AL. 2018) reported a 2.5 per cent measurement of the ratio of the spherically averaged distance to the sound horizon scale, $D_V(z = 0.72)/r_d = 16.08^{+0.41}_{-0.40}$. This result was obtained with isotropic fits to the monopole of the post-reconstruction correlation function. The statistical power of the DR14 sample is relatively low for anisotropic BAO constraints and has large non-Gaussian errors. Converting our DR16 anisotropic measurement of Eq. 4.20 into spherically averaged distances we obtain : $D_V(z = 0.698)/r_d = 16.26 \pm 0.20$, which is well within 1σ from the DR14 value. The error on D_V has reduced by a factor of two, slightly more than the square-root of the increase in effective volume, which gives a factor of $\sqrt{V_{\rm eff,DR16}/V_{\rm eff,DR14}} = \sqrt{2.73/0.9} \sim 1.74$. Note that in DR16 we combine BAO and full-shape analysis in Fourier and configuration spaces, which maximizes the

amount of extracted cosmological information.

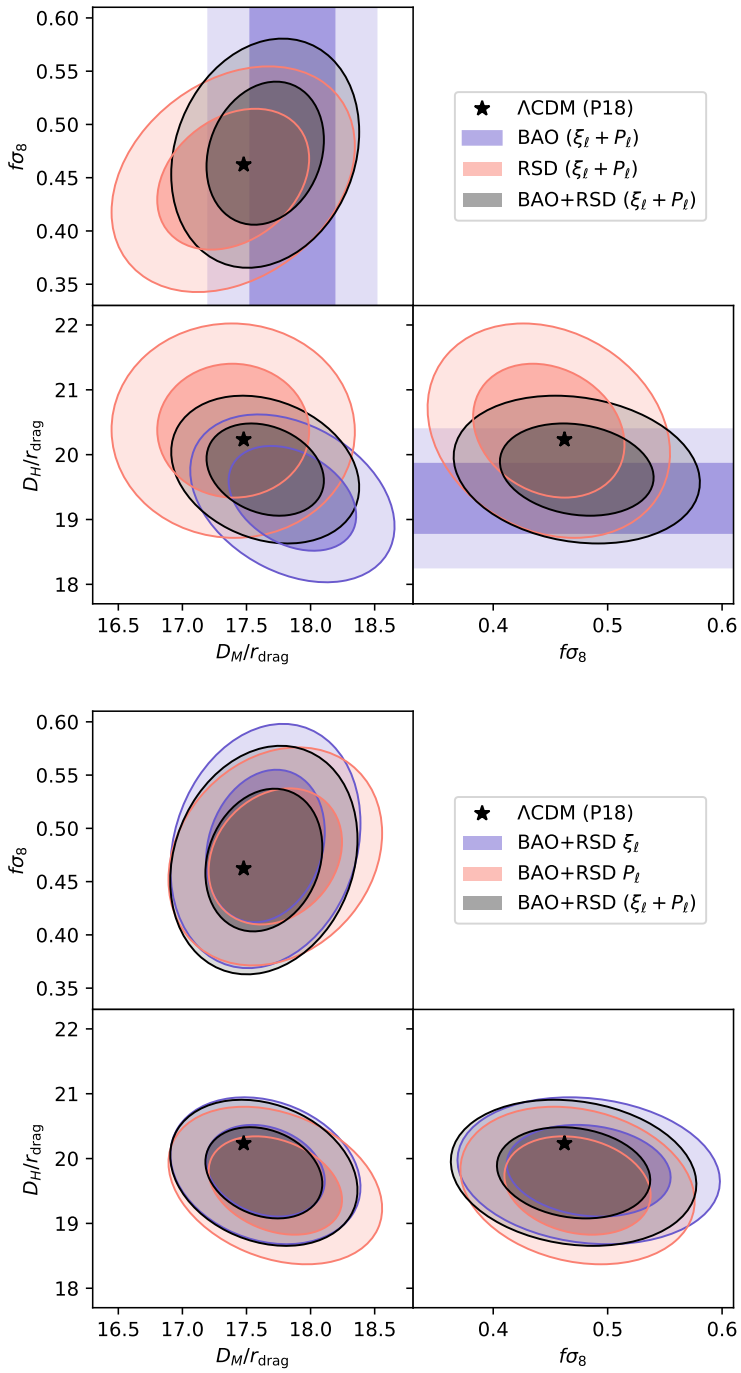

FIGURE 4.16 – Final measurements of $D_M/r_d, D_H/r_d, f\sigma_8$ from the completed eBOSS LRG sample at $z_{\rm eff} = 0.698$. Top and bottom panels show two possible procedures for obtaining the final result. The grey contours show the final results, which virtually the same in both panels (two bottom lines in Table 4.12). The black star indicates the prediction in a flat ΛCDM model with parameters from Planck 2018 results.

ICAZA-LIZAOLA et AL. 2020 presented the full-shape RSD analysis in the DR14 LRG sample in configuration space, yielding $f\sigma_8 = 0.454 \pm 0.134$, $D_M/r_d = 17.07 \pm 1.55$, and $D_H/r_d = 19.17 \pm 2.84$. All values are consistent within 1σ of DR16 results, even though errors for DR14 are quite large given the even lower significance of the BAO peak in the pre-reconstruction multipoles. The error on the growth rate of structure $f\sigma_8$ reduces by a factor of 3 in DR16 compared to DR14, clearly

Tableau 4.13 – Impact of the choice of fiber collision correction scheme on the recovered $\alpha_\perp$, $\alpha_\parallel$, and $f\sigma_8$ parameters in the eBOSS LRG sample without CMASS galaxies.

Model	Par	Base	PIP
BAO	$\alpha_\perp$	1.189 ± 0.062	1.199 ± 0.070
	$\alpha_\parallel$	0.850 ± 0.071	0.843 ± 0.074
	χ^2/dof	$47.7/48 = 0.99$	$51.7/48 = 1.08$
CLPT-GS	$\alpha_\perp$	1.009 ± 0.046	0.980 ± 0.044
	$\alpha_\parallel$	1.027 ± 0.056	1.035 ± 0.055
	$f\sigma_8$	0.473 ± 0.066	0.446 ± 0.066
	χ^2/dof	$67.8/54 = 1.26$	$71.5/54 = 1.32$
TNS	$\alpha_\perp$	1.024 ± 0.044	1.001 ± 0.041
	$\alpha_\parallel$	1.038 ± 0.050	1.032 ± 0.046
	$f\sigma_8$	0.451 ± 0.068	0.420 ± 0.065
	χ^2/dof	$71.1/58 = 1.23$	$74.8/58 = 1.29$

benefiting from the larger sample and the combination with post-reconstruction BAO results that help breaking model degeneracies.

Our DR16 LRG results at $0.6 < z < 1.0$ supersede the highest redshift results of the DR12 BOSS sample at $0.5 < z < 0.75$, which has an effective redshift of $z_{\rm eff} = 0.61$. (ALAM et AL. 2017) report a 1.4, 2.2 and 7.8 per cent measurements of $D_M/r_d, D_H/r_d$ and $f\sigma_8$ respectively. While the errors in the high-redshift bin are slightly smaller than our DR16 result, it has a large correlation with the intermediate-redshift bin at $0.4 < z < 0.6$. Our DR16 measurement is thus virtually independent of the first two DR12 BOSS redshift bins, and has effectively more weight in the final joint cosmological constraints. The cosmological implications of our DR16 LRG measurements are fully described in (EBOSS COLLABORATION 2021), and will be quickly summarized here.

4.3.5 Impact of fiber collision correction scheme

(MOHAMMAD et AL. 2020) provided PIP+ANG weights for the eBOSS LRG sample but without CMASS galaxies. We performed fits of our BAO and full-shape RSD models to the multipoles for this restricted sample. Note that this sample is about two thirds of the full sample used in our work. Table 4.13 compares the results on $\alpha_\perp$, $\alpha_\parallel$, and $f\sigma_8$ obtained with our baseline fiber collision correction to those using PIP weights. We see that the changes are small compared to the statistical errors for all methods and models. This is expected since PIP weights mostly impact the clustering on the smallest scales not used in our analysis ($r < 20h^{-1}$Mpc), while the baseline correction already well accounts for large-scale effects.

4.4 Cosmological implications

We will now discuss the cosmological implications of the SDSS redshift surveys measurements (eBOSS COLLABORATION 2021). Eight unique SDSS samples are considered. For galaxy and quasars clustering samples, BAO and RSD meausurements yields constraints on $D_M/r_d, D_H/r_d$ (or D_v/r_d) and $f\sigma_8$. For the Lyman-α forest, only the BAO measurement are considered. These measurements are presented in Fig. 4.17 and are taken from the different list of tracers :

— the Main Galaxy Sample (MGS, $0.07 < z < 0.2$) observed during stage I and II of SDSS. It contains 63163 galaxy from which BAO (D_V/r_d) and RSD measurements are provided in (ROSS et AL. 2015a; HOWLETT et AL. 2015).

— BOSS DR12 galaxies ($0.2 < z < 0.6$), 1.2 millions redshifts measured by BOSS during stage III. Three overlapping redshift bins were considered in the BOSS analysis : $0.2 < z < 0.5$, $0.4 < z < 0.6$ and $0.5 < z < 0.75$. Since $z > 0.6$ CMASS galaxies are combined with the eBOSS LRG sample, the last redshift bin from BOSS $0.5 < z < 0.75$ have been dropped. Bins $0.2 < z < 0.5$ and $0.4 < z < 0.6$ contain 604 001 and 686 370 galaxies, respectively. BAO ($D_M/r_d, D_H/r_d$) and RSD measurements are provided in (ALAM et AL. 2017).

— LRGs ($0.6 < z < 1.0$), targeted by eBOSS, with 174 816 detected redshifts combined with 202 642 CMASS galaxies. BAO ($D_M/r_d, D_H/r_d$) and RSD measurements are provided in Fourier space are provided in GIL-MARIN et AL. 2020. I have been involved in the full-shape analysis in configuration space BAUTISTA et AL. 2021

— ELGs ($0.6 < z < 1.1$) consisting of 173 736 galaxies. BAO (D_v/r_d) and RSD ($D_M/r_d, D_H/r_d, f\sigma_8$) measurements are given in (DE MATTIA et AL. 2021; TAMONE et AL. 2020). I have been involved in the AMF two-point function modelling described in TAMONE et AL. 2020.

— eBOSS QSOs ($0.8 < z < 2.2$), target by eBOSS, with 18% of galaxy from previous SDSS observation leading to a sample size of 343708 quasars. BAO ($D_M/r_d, D_H/r_d$) and RSD measurements are given in (NEVEUX et AL. 2020; HOU et AL. 2021)

— Lyman-α forests ($1.8 < z < 3.5$) found in quasar spectra. The BOSS sample of 157 845 spectra ($2 < z < 3.5$) without broad absorption lines has been complemented and partly re-observed by eBOSS, yielding a total sample of 210 005 spectra ($2.1 < z < 3.5$). Both an auto-correlation and a cross-correlation with 341 468 quasars ($z > 1.77$) were performed. BAO ($D_M/r_d, D_H/r_d$) measurements are given in (DU MAS DES BOURBOUX et AL. 2020)

In addition to the SDSS dataset, we used the measurements of the CMB (TT, TE, EE, lowE and lensing, PLANCK COLLABORATION 2018; PLANCK COLLABORATION 2020), the Pantheon supernovae SNIa (SCOLNIC et AL. 2018) and the year one observations of Dark Energy Survey (DES), including cosmic shear, galaxy clustering and galaxy - galaxy lensing correlation function measurements (ABBOTT et AL. 2018). As we will see later on, all these probes are complementary and once combined provide constraints on the nature of gravity and dark energy, and on the energy budget we reviewed in Chapter 1.

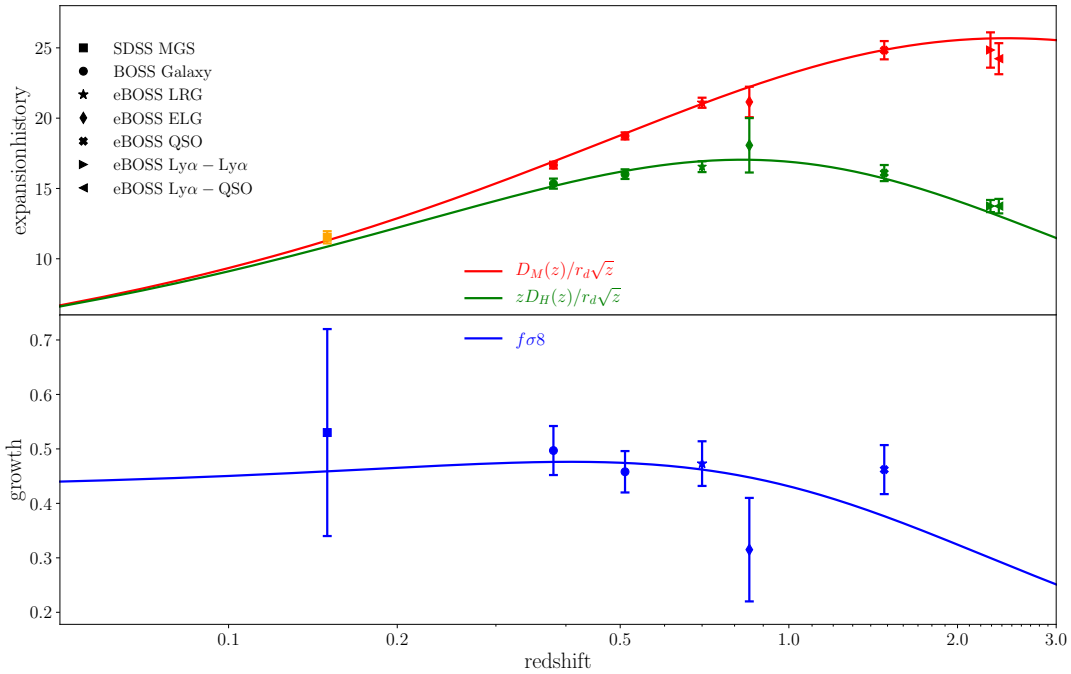

FIGURE 4.17 – SDSS BAO and growth rate measurements used in the final cosmological analysis. The continuous lines corresponds to Planck prediction for a flat ΛCDM cosmology (PLANCK COLLABORATION 2018). The MGS D_v measurement plotted in orange have been translated to a D_M measurement for a flat ΛCDM model for illustration. Taken from (EBOSS COLLABORATION 2021)

Extension to the flat ΛCDM cosmology were also investigated in (EBOSS COLLABORATION 2021). More specifically, an open ΛCDM model (oΛCDM; with free curvature), a ΛCDM model with varying equation of state (EoS) (wCDM), an open CDM with free dark energy (DE) EoS (owCDM), a CDM model with DE EoS given by CPL paremetrisation (w0waCDM),a open CDM model with DE EoS given by the CPL paremetrisation with a DE EoS given by the CPL parametrisation (ow0waCDM) and a CDM model with varying neutrino mass ($\nu\Lambda$CDM, νwCDM). In this section, σ_8 and all density parameters are taken at $z = 0$, and we will omit the subscript ,0 to ease notations. The precision of LSS surveys which aim to constraint dark-energy is usually quantified in terms of the Figure-of-Merit (FoM) as defined by the Dark Energy Task Force (DEFT, ALBRECHT et AL. 2006). The FoM [5] is defined in the CPL parameterization as

$$FoM = \frac{1}{\sqrt{det[Cov(w_0, w_a)}} \tag{4.22}$$

where the curvature parameter is left free. The DETF defines 4 stages. Stage II experiments correspond to SDSS-I-II with a FoM of 11 (SULLIVAN et AL. 2011). Stage III experiments are those improving upon the Stage II FoM by at least a factor of 3, and include the BOSS and eBOSS experiments, while Stage-IV experiments will improve this FoM by a factor of 10, which will be reach by DESI (DESI COLLABORATION 2016) and EUCLID (AMENDOLA et AL. 2018).

5. We can define the pivot w_p such that the covariance matrix is diagonal and then FoM = $1/(\sigma_{w_a}\sigma_{w_b})$]

4.4.1 BAO constraints

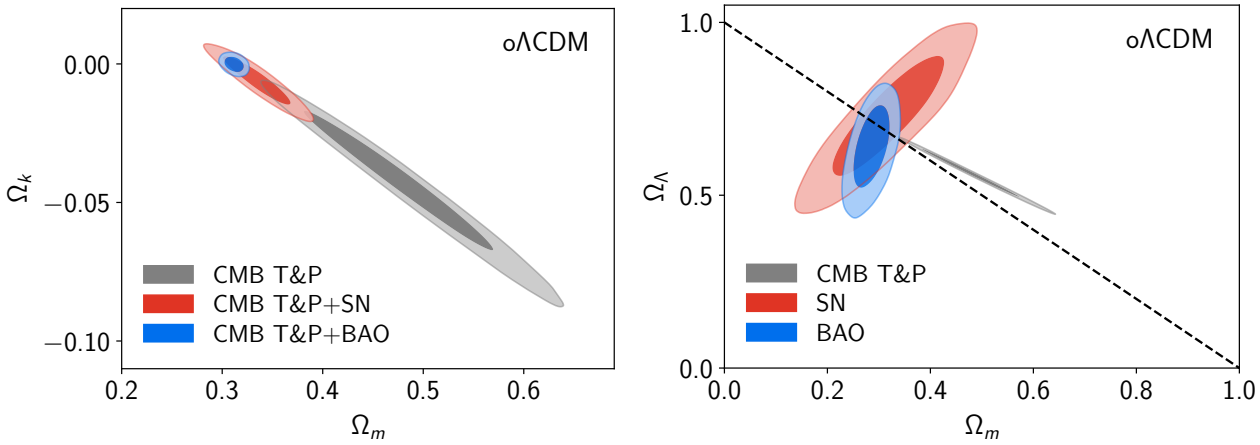

FIGURE 4.18 – Cosmological constraints under the assumption of a ΛCDM model with a $w = -1$ with free curvature (oΛCDM) Right : 68% and 95% constraints on $\Omega_m - \Omega_\Lambda$, from the Planck CMB temperature and polarization data (gray), Pantheon SNe Ia sample (red), and SDSS BAO-only measurements (blue). The dashed line represents a model with zero curvature. Left : The $\Omega_m - \Omega_K$,constraints for the combination of CMB (gray), CMB + SN (red), and CMB + BAO (blue). Taken from (EBOSS COLLABORATION 2021)

I present in Fig. 4.18 the contours of BAO, SN and CMB Temperature and Polarization (T&P CMB lensing information is mostly useful for gravity test) posteriors in the $\Omega_m - \Omega_\Lambda$, and the combination of these measurements in the $\Omega_m - \Omega_K$ plane. Combination of BAO measurements at differents redshifts enables us to break the degeneracy between Ω_m and Ω_K yielding $\Omega_\Lambda = 0.637^{0.084}_{0.074}$, with a much better precision that SN measurement alone $\Omega_\Lambda = 0.73 \pm 0.11$. Both cosmological probes are compatible with a flat Universe. Combining BAO measurement with Planck T&P (which favours a closed Universe) push the curvature parameter towards zero yielding $\Omega_K = -0.0001 \pm 0.0018$, in excellent agreement with a flat Universe.

BAO and SN data can also be used to set constraints on H_0 through the inverse distance ladder. Specifically, given a value of r_d, BAO provide measurements of cosmological distances which enable to calibrate SN luminosity distances to constraint H_0. Given a mean CMB temperature under the standard Big Bang nucleosynthesis (BBN) model, one can infer the value of r_d given ω_c and ω_b. Taking for these parameters priors from CMB T&P, BAO and SN data provides percent constraints on the current value of the expansion rate. As we can see from Fig. 4.19, the measurement of H_0 is stable with respect to dark energy and curvature assumption, yielding $H_0 = 67.87 \pm 0.86$ km s^{-1} Mpc^{-1} for a o$w_0 w_a CDM$ model. To make sure that the measured value of H_0 is insensitive to CMB anisotropies, ω_b can be constrained by BBN with a radiation density given by COBE (FIXSEN 2009) with ω_c constrained by BAO alone. Fig. 4.19 shows that the constraining power of BAO is due to high redshift measurements (QSO and Lyman-α forest) having a different degeneracy in the $\Omega_m - H_0$ plane than low redshift ones. With a BBN prior within a flat ΛCDM model, $H_0 = 67.35 \pm 0.97$ km s^{-1} Mpc^{-1}, in very good agreement with the value quoted above. This value of the Hubble constant is in tension with late time measurements. Indeed, WONG et AL. 2019 find from the combination of SH0ES (RIESS et AL. 2018,SNIa luminosity) and H0LiCOW measurements $H_0 = 73.8 \pm 1.1$ km s^{-1} Mpc^{-1}, in 5σ tension with the measurements above.

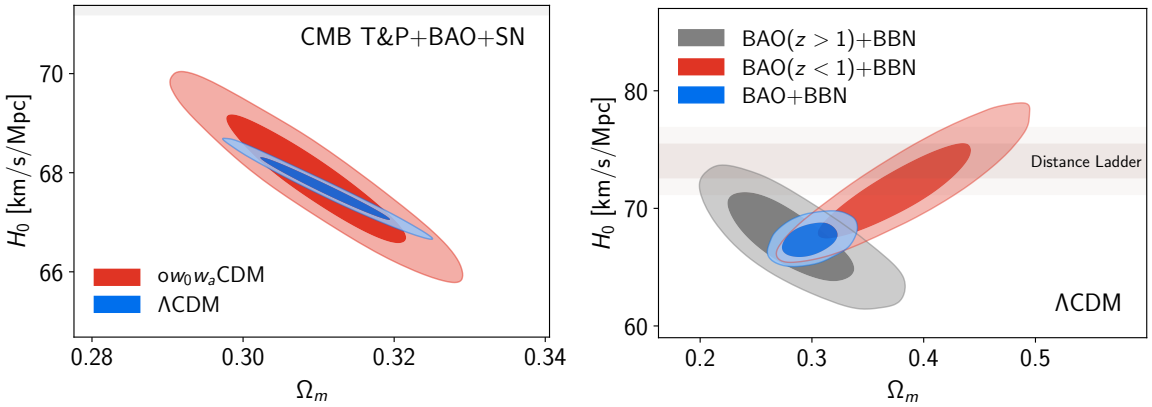

FIGURE 4.19 – Left : H_0 versus Ω_m from the inverse distance ladder (CMB+BAO+SN) for the ΛCDM and the ow0waCDM model. Right : H_0 versus Ω_m from the combination of BAO and BBN, in a ΛCDM model (blue). The red (gray) contours show the results when using only BAO measurements below (above) $z = 1$, which corresponds respectively to galaxy and quasars (both clustering and lyman-α) samples. The horizontal shaded area shows the (68%, 95%) measurement of H_0 from (RIESS et AL. 2019).Taken from (EBOSS COLLABORATION 2021).

4.4.2 RSD constraints

RSD measurements are a powerful way constrain the DE EoS. Lower w value imply larger cosmic acceleration, and thus lower $f\sigma_8$ value at low redshift. Hence, RSD reduce uncertainty on w by more than a factor of two over CMB data, as we can see from the upper left panel of Fig. 4.20 yielding $w = -1.09 \pm 0.11$ fully compatible with a cosmological constant. RSD and weak lensing measurements also provide constraints in the $\Omega_m - \sigma_8$ plane, as shown in the right upper panel of Fig. 4.20. The growth of structure, probed by RSD, galaxy and CMB weak lensing, is consistent (although with large contours) with that inferred from the early Universe assuming a ΛCDM model (such that $f \approx \Omega_m^{\alpha}$), providing a strong consistency test of this cosmological model. Finally, the growth of structure is also a powerful tool to test variation from GR. Following the notation of ABBOTT et AL. 2018, let's introduce the parameters $\mu(a)$ and $\Sigma(a)$, such that the Poisson equation 2.11 takes the forms

$$k^2\Phi = -4\pi G a^2(1+\mu)\bar{\rho}\delta \tag{4.23}$$

$$k^2(\Phi+\Psi) = -8\pi G a^2(1+\Sigma)\bar{\rho}\delta \tag{4.24}$$

where we recall that Ψ and Φ are the Bardeen potentials, related to the time and spatial part of the metric. The time dependence of $\mu(a)$ and $\Sigma(a)$ is parametrized as

$$\mu(a) = \mu_0 \frac{\Omega_\Lambda(a)}{\Omega_\Lambda}, \quad \Sigma(a) = \Sigma_0 \frac{\Omega_\Lambda(a)}{\Omega_\Lambda} \tag{4.25}$$

In GR, $\Psi = \Phi$ and therefore $\mu_0 = \Sigma_0 = 0$. In the non relativist limit, RSD is only sensitive to Φ and can only constraint μ_0. Weak lensing measurements probe the propagation of light, which is sensitive to $\Psi + \Phi$ and can thus constraint Σ_0. As we can see from the bottom panel of Fig. 4.20, combining RSD and lensing measurements yields $\mu_0 = 0.04 \pm 0.25$ and $\Sigma_0 = 0.024 \pm 0.054$, consistent with GR predictions.

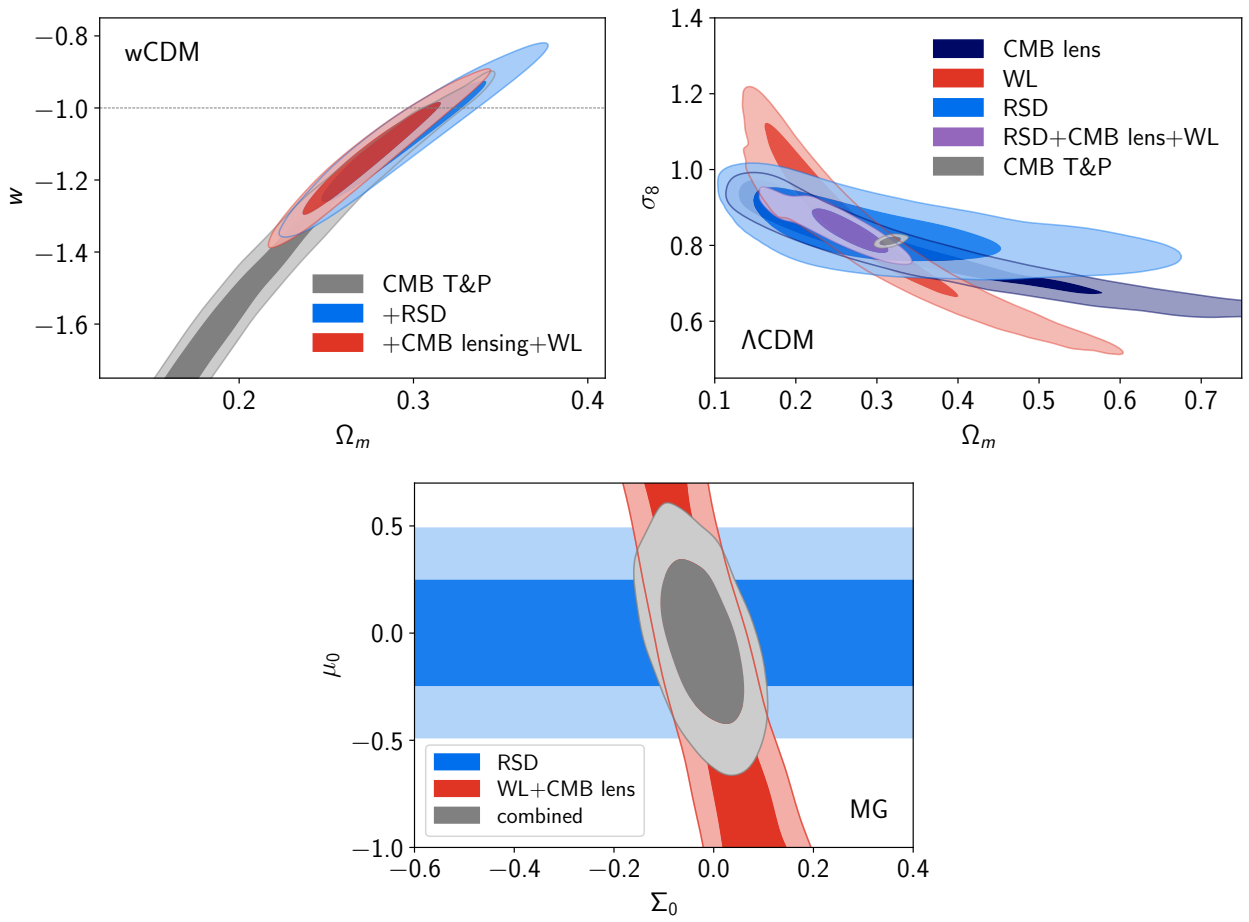

FIGURE 4.20 – In each panel are shown the 68% and 95% confidence intervals for each sample. Upper left : $\Omega_m - w$ constraints for a flat wCDM cosmology. The gray contours represent P&T data, while the blue(red) contours show the results including RSD(RSD+WL) data. Upper right : $\Omega_m - \sigma_8$ constraints for a flat ΛCDM cosmology. Blue contours represents RSD data, red contours represents WL lensing, dark blue contours represents Planck lensing light purple represent the combination of RSD, DES WL, and Planck lensing. The gray contours represent the predictions from P&T data. Bottom : The $\Sigma_0 - \mu_0$ constraints for a cosmology with a fixed cosmological constant. Blue contours for RSD, red for DES WL + Planck lensing, while gray contours represents the combination of the three posteriors. Taken from (EBOSS COLLABORATION 2021).

4.4.3 Full cosmological fit

After investigating the constraining power of growth measurements and expansion history on cosmology, we then proceeded with a full cosmological fit combining Planck (P&T + lensing), SDSS BAO and RSD, DES y1 3 × 2pt (cosmic shear, galaxy clustering, galaxy-galaxy lensing) and Pantheon SNIa measurements. We started by deriving cosmological parameters in the simplest flat ΛCDM model, with fixed neutrinos mass ($\sum m_\nu = 0.06$eV). We then expanded cosmological models to put constraints on the curvature, the dark energy EoS and the neutrinos mass. I first present the compatibility between the different probes in Fig. 4.21. For both DES and SDSS contours, priors on ω_b and n_s are those of PLANCK COLLABORATION 2018, $n_s = 0.96 \pm 0.02$, $\omega_b = 0.0222 \pm 0.0005$ given by BBN. The baryonic fraction does not impact DES contours, but is correlated with SDSS contours, through the determination of r_d which depends on the sound speed c_s. We can see that SDSS measurements are fully compatible with the best-fit model from Planck, specially for Ω_m and H_0 (see right panel of Fig. 4.21). SDSS however predict a higher value for σ_8, but the shift remains small. DES

Tableau 4.14 – Marginalized values and 68% confidence limits for models using Planck, Pantheon SNe, SDSS BAO+RSD, and DES 3×2pt data. Extracted from (eBOSS COLLABORATION 2021)

	Ω_{DE}	H_0	σ_8	Ω_K	w_0	w_a	Σm_ν [eV]
ΛCDM	0.6959 ± 0.0047	68.19 ± 0.36	0.8073 ± 0.0056	-	-	-	-
oΛCDM	0.6958 ± 0.0048	68.21 ± 0.55	0.8076 ± 0.0065	0.0001 ± 0.0017	-	-	-
wCDM	0.6992 ± 0.0066	68.64 ± 0.73	0.8128 ± 0.0092	-	-1.020 ± 0.027	-	-
owCDM	0.6997 ± 0.0069	68.59 ± 0.73	0.8127 ± 0.0091	-0.0004 ± 0.0019	-1.023 ± 0.030	-	-
$w_0 w_a$CDM	0.6971 ± 0.0069	68.47 ± 0.74	0.8139 ± 0.0093	-	-0.939 ± 0.073	$-0.31^{+0.28}_{-0.24}$	-
o$w_0 w_a$CDM	0.6988 ± 0.0072	68.20 ± 0.81	0.8140 ± 0.0093	-0.0023 ± 0.0022	-0.912 ± 0.081	$-0.48^{+0.36}_{-0.30}$	-
$\nu\Lambda$CDM	0.6975 ± 0.0053	68.34 ± 0.43	$0.8115^{+0.0092}_{-0.0068}$	-	-	-	< 0.111 (95%)
νwCDM	0.6993 ± 0.0067	68.65 ± 0.73	$0.813^{+0.011}_{-0.0098}$	-	$-1.019^{+0.034}_{-0.029}$	-	< 0.161 (95%)

y1 measurements give lower value of Ω_m compared to PLANCK COLLABORATION 2018 which can be seen in the $\Omega_m - \sigma_8$ plane. The new y3 measurements presented in (DES COLLABORATION 2021) yield $\Omega_m = 0.327 \pm 0.028, \sigma_8 = 0.754^{+0.040}_{-0.044}$ for the 3×2 point function (including non-linear bias), in much better agreement with Planck value without lensing, $\Omega_m = 0.3166 \pm 0.0084, \sigma_8 = 0.8120 \pm 0.0073$, hence showing no strong evidence of tension with Planck. We can see that DES y3 measurements predict a larger value of Ω_m correlated with a lower value of σ_8, due to the observed degeneracy in the $\Omega_m - \sigma_8$ plane. The Pantheon SNIa measurement of Ω_m is fully compatible with measurements of other probes. The ΛCDM fit combining all probes is presented in the first row of Table 4.14. We find $\Omega_{DE} = 0.6959 \pm 0.0047$, with a dark energy density constrained at the 0.7% level. The local expansion rate we derived $H_0 = 68.19 \pm 0.36$, still in tension with the distance ladder measurements in the local Universe.

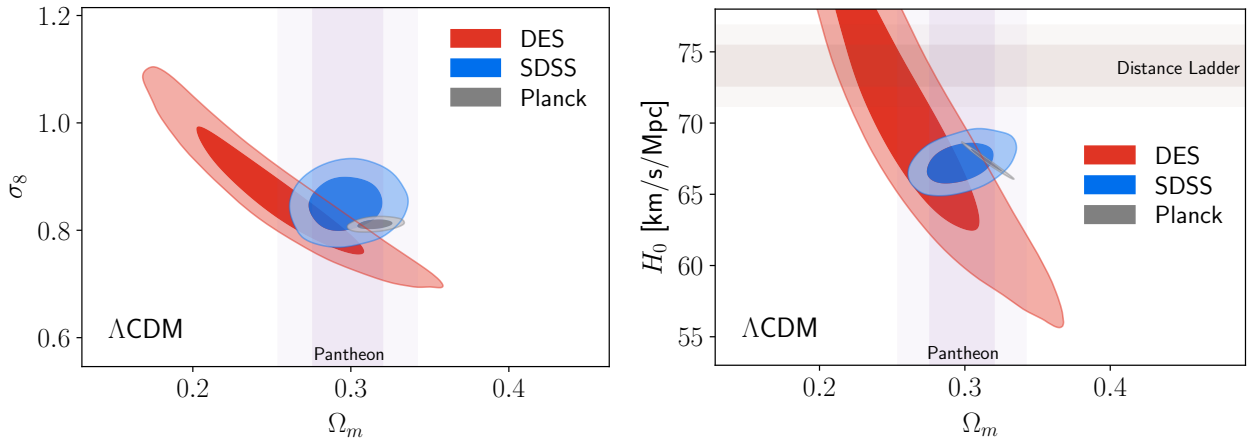

FIGURE 4.21 – Left : Constraints on the $\Omega_m - \sigma_8$ for a ΛCDM model. Right : H_0 versus Ω_m for a ΛCDM model. In both panels, the 68% and 95% confidence intervals for the BAO+RSD data are shown in blue, the DES 3×2pt data in red, and the Planck CMB and lensing data in gray. The vertical bands represent the Pantheon constraints, $\Omega_m = 0.298 \pm 0.022$ (SCOLNIC et AL. 2018) while the horizontal line in the right panel, represent the SNIa constraints from (RIESS et AL. 2019), $H_0 = 74.03 \pm 1.42 kms^1 Mpc^1$. Taken from (eBOSS COLLABORATION 2021)

We then proceeded with full CDM fit, presented in Table 4.14. Regardless of the considered model, cosmological parameters remain stable and consistent with ΛCDM. Errors on DE density and H_0 increase at most by a factor 2.5 when considering a $ow_0 w_a$CDM model. Fig. 4.22 presents the posterior contours for different combinations of cosmological probes. In the $w_0 - w_a$ plane, CMB + SN provide more powerful constraints to the DE EoS than CMB + SDSS, while CMB + SDSS (thought

the BAO signal) provide better constraints on curvature. Measurement are consistent with a flat ΛCDM model : w_0, w_a and Ω_K are 1.1,1.3 and 1.0 σ away from -1, 0 and 0 respectively. Combining Planck and SDSS data, the FoM in is 38.4, adding lensing and supernovae measurements increase the FoM by another factor of 3.5, yielding a FoM of 134. This value lower to 92 in the $o w_0 w_a$CDM model.

The combination of cosmological probes can also be used to constrain neutrino mass. The sum of neutrino mass, previously fixed to 0.06 eV, is left free in the different CDM models. The constraints are presented in Table 4.15 assuming one massive and two massless neutrinos and a prior $\sum m_\nu > 0$. The combination of all dataset yield $\sum m_\nu < 0.111$eV for ΛCDM which degrade to $\sum m_\nu < 0.161$eV for a free DE EoS, at 95% confidence level, with a preference for negative value for the sum of the neutrinos masses. Fig. 4.23 illustrates the constraining power of neutrinos mass as a function of

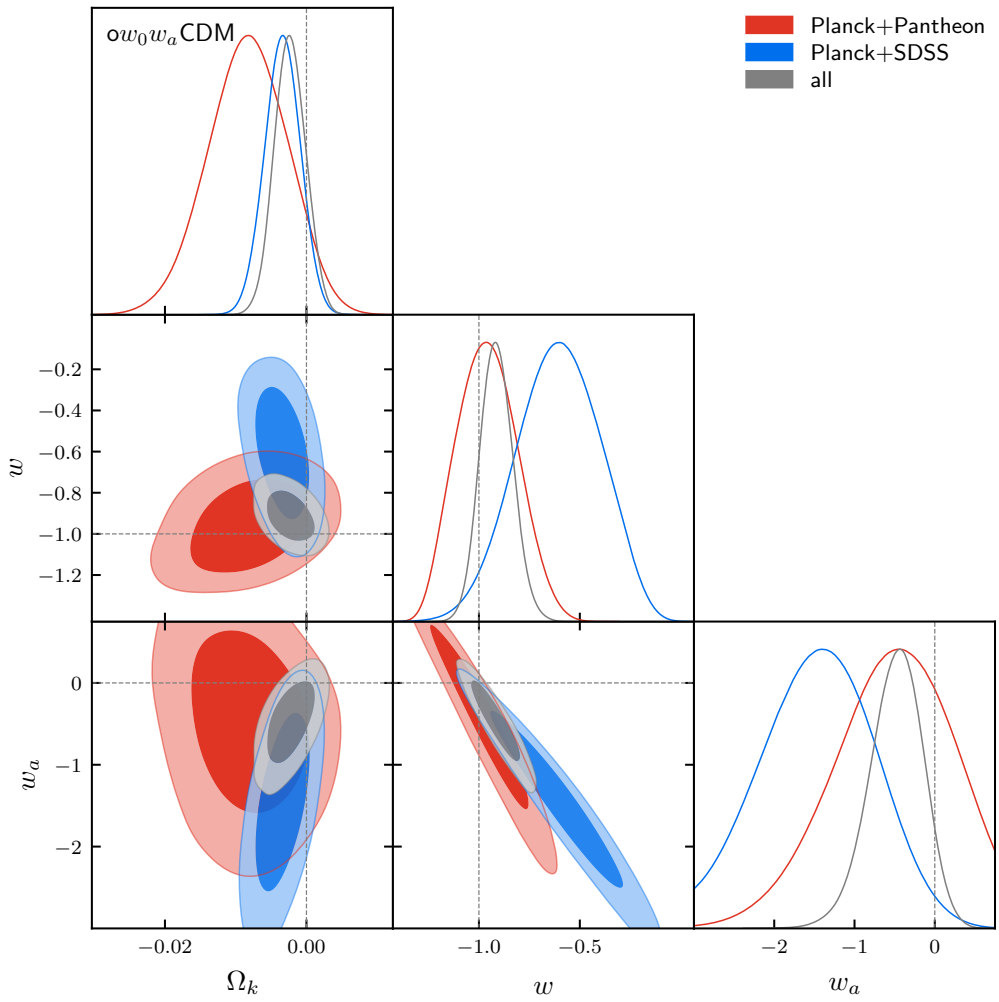

FIGURE 4.22 – Contours on w_0, w_a, and Ω_K under the assumption of an $o w_0 w_a$CDM model. The one-dimensional constraints on each independent parameter are presented in the top panels. The red contours represent the 68% and 95% constraints from Planck and the Pantheon SNIa measurement. The blue contours represent the constraints from Planck and SDSS BAO+RSD, while the gray contours represent the combination of all measurements presented in the beginning of the section. Taken from (EBOSS COLLABORATION 2021).

the different probes. Improvement in constraining power over Planck is mainly driven by BAO, through the impact of neutrino masses on the expansion rate, a factor 2 in gain is achieved. RSD add another 20% reduction in uncertainty, through the damping effect of neutrino free-streaming

on the growth of structure. Adding lensing measurements slighlty degrades the constraints on $\sum m_\nu$ from 0.099 eV to 0.111eV due to preferred lower Ω_m value, this would potentially be mitigated with DES y3 measurement. The neutrino mass hierarchy is one of the remaining undetermined fundamental features of the neutrino standard model. i.e., whether the ν_3 neutrino mass eigenstate is heavier or lighter than the ν_1 and ν_2 mass eigenstates. For each scenerio, the minimum sum of neutrino mass is given by

$$\sum m_\nu > 0.0588\,\mathrm{eV} \quad \text{normal hierarchy,} \tag{4.26}$$
$$\sum m_\nu > 0.0995\,\mathrm{eV} \quad \text{inverted hierarchy.} \tag{4.27}$$

where lower bound are fixed by the observation of neutrinos oscillations. From these lower bound, we can define the following integrated probability

$$P_\mathrm{norm} = \int_{0.0588\,\mathrm{eV}}^{\infty} p(m_\nu)\mathrm{d}m_\nu, \tag{4.28}$$
$$P_\mathrm{inv} = \int_{0.0995\,\mathrm{eV}}^{\infty} p(m_\nu)\mathrm{d}m_\nu, \tag{4.29}$$
$$P_\mathrm{unphy} = \int_{0}^{0.0588\,\mathrm{eV}} p(m_\nu)\mathrm{d}m_\nu. \tag{4.30}$$

We see in Table 4.15 that these probabilities are always indecisive, there doesn't seem to be strong evidence from cosmology on a preference for a normal hierarchy, an inverted hierarchy, or a model with a very low neutrino mass.

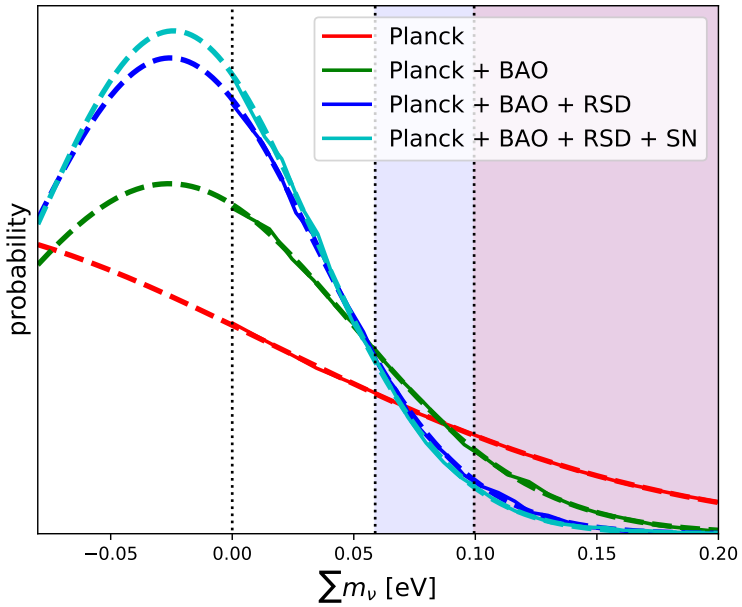

FIGURE 4.23 – Posteriors of the sum of the neutrino masses, within the ΛCDM model. Dashed lines are Gaussian fits. Purple and red regions are low limits on the sum of the neutrinos mass given the normal and inverse hierarchy respectively

Tableau 4.15 – Constraints on neutrino masses and relative probabilities of neutrino models with $\nu\Lambda$CDM and νwCDM cosmological models. Extracted from (eBOSS COLLABORATION 2021)

Data	95% upper limit [eV]	$P_{\rm inv}/P_{\rm norm}$	$P_{\rm unphy}$	Gaussian fit [eV]
Planck	0.252	0.64	0.43	
Planck + BAO	0.129	0.36	0.64	-0.026 ± 0.074
Planck + BAO + RSD	0.102	0.24	0.76	-0.026 ± 0.060
Planck + SN	0.170	0.49	0.56	-0.076 ± 0.106
Planck + BAO + RSD + SN	0.099	0.22	0.78	-0.024 ± 0.057
Planck + BAO + RSD + SN + DES	0.111	0.27	0.71	-0.014 ± 0.061
Planck + BAO + RSD + SN (νwCDM)	0.139	0.40	0.61	-0.033 ± 0.082
Planck + BAO + RSD + SN + DES (νwCDM)	0.161	0.48	0.56	-0.048 ± 0.097

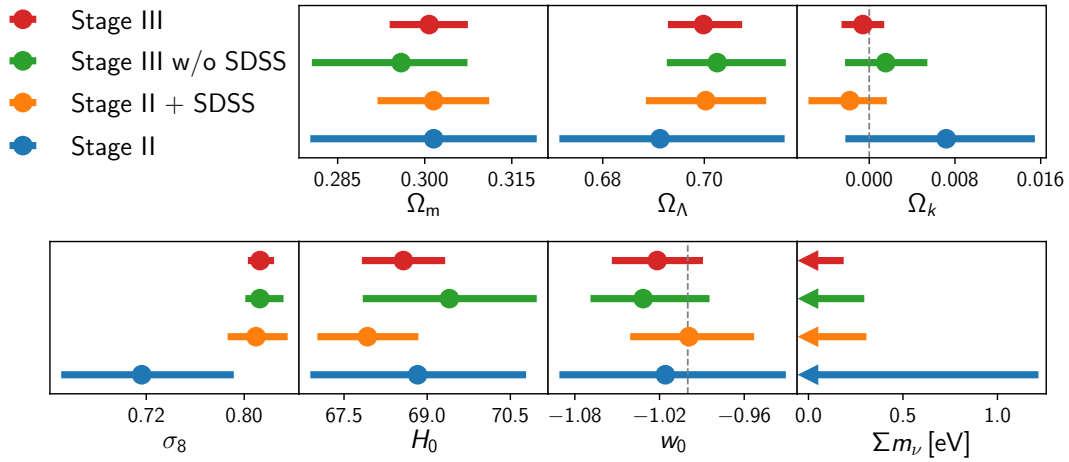

FIGURE 4.24 – Uncertainties in parameters of the νowCDM model with Stage-II and Stage-III experiments. Limits on the sum of neutrino masses are given at the 95% confidence level. Taken from (eBOSS COLLABORATION 2021)

Finally, it is interesting to look at the evolution of the cosmological constraints during the past decades. Stage-II consist of the combination of CMB data from WMAP (HINSHAW et AL. 2013; BENNETT et AL. 2013), supernovae from the JLA sample (BETOULE et AL. 2014), and BAO measurements from SDSS DR7 (PERCIVAL et AL. 2010) and from the 2-degree Field Galaxy Redshift Survey (COLLESS et AL. 2001). Stage II + SDSS replace BAO measurements by the final SDSS BAO+RSD measurements. Stage-III without SDSS is obtained by replacing the final SDSS BAO + RSD measurement by the previous BAO measurements. Stage-III measurements are fully compatible with Stage-II results, the largest deviation being for σ_8, which can be explain by the lack of robust RSD and WL constraints. Stage-III measurement are fully compatible with a flat ΛCDM with w_0 and Ω_K moving toward -1 and 0 respectively while bounds on the sum of neutrino masses have become significantly tighter. The precision on the cosmological parameters has increased by at least a factor of 2.5 from Stage II to Stage III, the largest reduction of uncertainties corresponding to Ω_K (4.5), σ_8 (7.0) and $\sum m_\nu$ (7.1). The FoM in the w_0,Ω_m,$\sum m_\nu$,σ_8 and H_0 space, defined as the inverse of the determinant of the N = 5 parameter to the power 1/(-2N), has increased from 11 to 44 between Stage-II and Stage-III. Including only SDSS measurements to Stage-II increase the FoM by a factor of 2.1, which demonstrate the significant impact of BAO and RSD measurements in constraining cosmology. The role played by LSS cosmological measurements will become significantly important with the Stage-IV galaxy surveys, such as DESI. During my last year of PhD, i have been involved in the mock

Tableau 4.16 – Summary statistics of the different DESI samples. Extracted from (DESI COLLABORATION 2016)

Galaxy samples	Redshift range	Good Redshift
LRGs	0.4-1.0	4.0 M
ELGs	0.6-1.4	17.1 M
QSOs	< 2.1	1.7 M
QSOs lyman-α	> 2.1	0.7 M
BCGs	0.05-0.4	9.8 M

challenge of DESI with goals to minimize systematic budget for future observations.

4.4.4 The DESI survey

The DESI (Dark Energy Spectroscopic Instrument) survey (DESI COLLABORATION 2016) has started operating end 2020 and is designed to observed at least 10 times mores galaxy than all gathered previous SDSS samples. We will first introduce the DESI survey, its expected constraining power in cosmology, and we will present the perspectives along with future challenges that such a gigantic project will bring to the scientific community. DESI will measure spectra during approximately five years. Observations will be carried out with the 4m Mayall telescope located at Kill Peak, Arizona, with a FoV of 7.5 deg^2. The footprint of 14 000 deg^2 will be covered by 2000 tiles, what is called a layer, given the FoV of the telescope. DESI will target four classes of tracers; already observed with previous BOSS/eBOSS program. Bright galaxies (equivalent of to the MGS), LRGs, ELGs and QSOs. The requirements after the five year observations are given in Table 4.16. Five tiling layers (approximately one per year), will be performed during DESI operations. The moon will be below the horizon during 80% of the spectroscopic observations. In dark time, LRG and QSO will be targeted in priority. The DESI LRG sample will contain 4M redshift, 3 times more than combined BOSS and eBOSS LRG. The QSO sample for clustering observations will contain 1.7M redshifts, 5 times more than the SDSS sample, while Lyman-α QSOs will contain and 0.7M redshift,3 times more than SDSS. During gray time will be oberved ELG, less contimated by sky subtraction due to strong emission features in the spectra. 17.1M redshift will be obtained, 100 times more than for SDSS. Bright galaxy (BGS) in the local Universe will be observe during bright time for a total of 10M redshift, 10 times larger than the SDSS MGS sample.

The statistical precision of the cosmological measurement that will be achieved by the DESI survey is determined with the Fisher matrix. This matrix corresponds to the expectation value of the second derivative matrix of the log likelihood with respect to parameters of interest (FONT-RIBERA et AL. 2014)

$$F_{AB} = -\left\langle \frac{\partial^2 L}{\partial A \partial B} \right\rangle, \tag{4.31}$$

with L the likelihood, A and B are parameters, and the average is performed over all possible realisations of the data given a fiducial model. Under Gaussian likelihood assumption, $F_{AA}^{-1/2}$ represents the excepted error on parameter A, assuming the other values of parameter are know, while $(F_{AA}^{-1})^{1/2}$ is the marginalized error on parameter A. For a observed vector $\mathbf{O}$, for which we assume the likelihood to be Gaussian, with vector of mean, $\bar{\mathbf{O}}$, predictable given parameters θ, and covariance C assumed independent of the parameter, the Fisher matrix can be written as (FONT-RIBERA et AL. 2014)

$$F_{ij} = \frac{\partial \bar{\mathbf{O}}^T}{\theta_i} C \frac{\partial \bar{\mathbf{O}}}{\theta_i}. \tag{4.32}$$

In general, the Covariance matrix does depend on the parameters, but the dependence becomes

Tableau 4.17 – DESI forecasts for the FoM, the error w_p at the pivot scalar a_p, and the error on the curvature energy density Ω_K at the 68% confidence level. All lines includes DESI galaxy observation with LRGs, ELGs, QSOs and BGCs, combined with BOSS in $0.45 < z < 0.60$ in non-overlapping regions and Planck measurement of 2014 (PLANCK COLLABORATION 2016). Extracted from (DESI COLLABORATION 2016)

data	FoM	a_p	$\sigma(w_p)$	$\sigma(\Omega_K)$
Planck + galaxy BAO	133	0.69	0.023	0.0013
Planck + galaxy BAO + gal broadband up to k < 0.1 h^{-1} Mpc	332	0.74	0.0015	0.0009
Planck + galaxy BAO + gal broadband up to k < 0.2 h^{-1} Mpc	704	0.73	0.011	0.0007

subdominant once the parameters are precisely determined (EIFLER, SCHNEIDER et HARTLAP 2009). For the fishier matrix evaluation, a baseline ΛCDM is assumed, with fiducial cosmology given by the measurements of PLANCK COLLABORATION 2014. Linear perturbation is performed with CMBFAST (SELJAK et ZALDARRIAGA 1996). We present the DESI fisher forecast errors bars in Fig. 4.25, provided in the Tables 2.3 and 2.4 of (DESI COLLABORATION 2016). In the scenario where the maximum wavenumber is $k_{max} = 0.2h\text{Mpc}^{-1}$ in Fourier Space analysis, the forecast relative uncertainty in $f\sigma_8, D_H/r_d, D_M/r_d$ is ≈ 2% for $z = 0.1$ redshift slices in the range $0.05 < z < 1.85$. We present in Table 4.17 the forecast for the excepted FoM of the DEFT (ALBRECHT et AL. 2006). Even with galaxy BAO measurements alone, the FoM is 133, above the threshold value of 110 for a Stage-IV experiment. By adding the information of the full-shape broadband [6] power spectrum, yields an improvement up to 704 for the FoM.

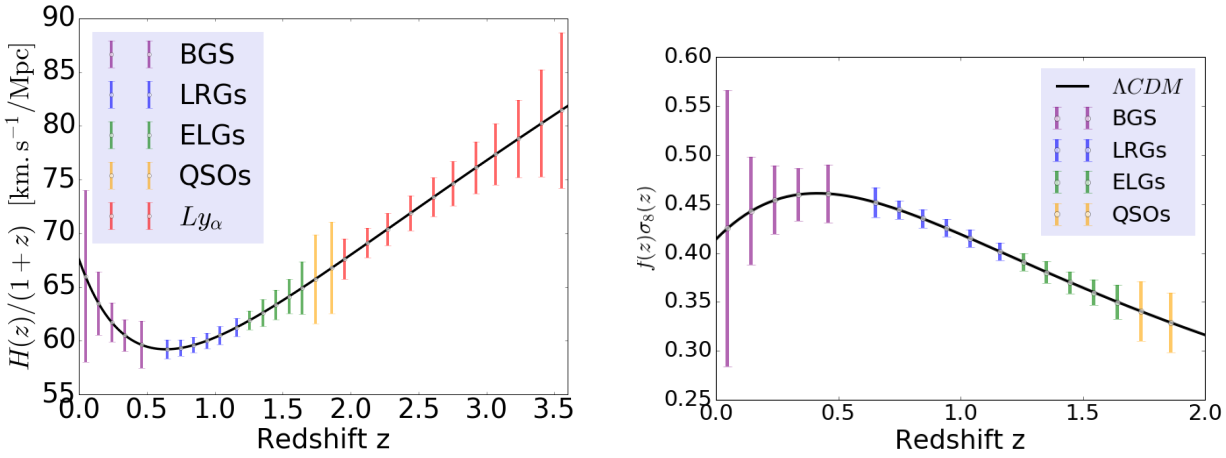

FIGURE 4.25 – Forecast on errors estimation for the Hubble parameter (left) and the growth rate(right) for DESI observations. Values are taken from Table 2.3 and Table 2.4 of (DESI COLLABORATION 2016). Taken from (VARGAS-MAGANA et AL. 2019)

Including Lyman-α forest measurements in top of the galaxy BAO measurements does not improve cosmological measurement if the broadband power spectrum is combined with other probes. Apart constraining the dark energy EoS, DESI will also constraint inflation, primordial non-Gaussianity, and the sum of neutrinos mass. DESI will be able to measure n_s and the running α_s with a precision of 0.19% (once marginalising over the sum of neutrino mass), an improvement of 1.7 and 2.7 % over (PLANCK COLLABORATION 2016). Also, DESI alone will constraint f_{NL}^{LOCAL} [7] with

6. The broadband power spectrum corresponds to the measurement of the redshift space power spectrum in wavenumber and redshift slice, $P(k, \mu, z)$.

7. There exist two convention for f_{NL}, f_{NL}^{LOCAL} is when ϕ corresponds the primordial potential, or f_{NL}^{LSS} where ϕ is extrapoled at the current time, $f_{NL}^{LSS} = g(\infty)/g(0) f_{NL}^{LOCAL} \approx 1.3 f_{NL}^{LOCAL}$ (MUELLER et AL. 2021)

a precision $\sigma(f_{\rm NL}^{\rm LOCAL}) = 5$ similar to (PLANCK COLLABORATION 2016) alone, which will improve the precision by a factor 2 when combining both dataset. Finally, DESI will put tight constraints on the sum of the neutrino mass. Planck and DESI combined will yield measurements with uncertainties of 0.020 eV, most of the constraining power coming from the galaxy broadband power spectrum (DESI COLLABORATION 2016). This precision would allow to dissociate between normal or inverted hierarchy, being an huge step forward in cosmology and particle physics.

Conclusion

My PhD work was dedicated to the statistical analysis of galaxy clustering in the eBOSS sample of luminous red galaxies, and the extraction of the most accurate cosmological constraints. I first developed the theoretical models that describe the two main cosmological features in the two-point correlation function : redshift-space distortions and baryonic acoustic oscillations. These were tested on realistic galaxy mock samples of the eBOSS survey in order to quantify the possible modelling systematic errors. We demonstrated that current semi-linear RSD models are accurate enough for the statistical precision of eBOSS galaxies. We also found a strong correlation between dynamical $f\sigma_8$ and geometrical $\alpha_{\rm iso}$ cosmological parameters (GIL-MARIN et AL. 2020; BAUTISTA et AL. 2021) that needs to be corrected by changing the scale at which σ_8 is evaluated, hence reducing the modelling systematic of $f\sigma_8$ to 2%. Observational systematic errors were mitigated by weighting galaxies according to their redshift failure probability as well as angular completeness weights. This was notably studied by implementing observational artefacts in the mock. In the end, we found that observational systematic errors represent a non-negligible source of uncertainties, up to 1.0%, 1.5% and 1.8% for $\alpha_\perp, \alpha_\parallel$ and $f\sigma_8$ parameters respectively.

I developed in parallel a modified two-point statistic in configuration space that erases angular modes, and that we called the angular-mode free correlation function. This statistics is very efficient at removing angular contamination, in particular for the eBOSS ELG sample (TAMONE et AL. 2020). Given a survey geometry and selection function, I developed an analytical model that can reproduce very accurately this new statistic and be used for cosmology inference. I tested it against galaxy mock samples, and found that our method gives quasi-unbiased results compared to the standard statistic, with a bias below the percent level on $\alpha_\perp$ and $f\sigma_8$ in RSD analysis.

I performed the final RSD and BAO cosmology analysis of the sample of 377 458 CMASS and LRG galaxies at redshift $0.6 < z < 1.0$ assembled by the BOSS and eBOSS surveys. The configuration space results that we obtained in (BAUTISTA et AL. 2021) were combined with the Fourier-space results of (GIL-MARIN et AL. 2020). The consensus results measurements are $D_m/r_d = 17.65 \pm 0.30$, $D_H/r_d = 19.77 \pm 0.47$ and $f\sigma_8 = 0.473 \pm 0.044$ at an effective $z_{\rm eff} = 0.70$, putting new and precise constraints on the expansion rate and growth of structure. Those results were combined with the cosmological measurements from the others eBOSS tracers, to investigated cosmological constraints and possible deviations from the λCDM cosmological model with General Relativity. For this, we included the external constraints from Planck CMB (PLANCK COLLABORATION 2020), Pantheon SNIa (SCOLNIC et AL. 2018), and Year-1 weak lensing results from DES (ABBOTT et AL. 2018). We found that our BAO and RSD measurements provide cosmological constraints in line with ΛCDM and General Relativity predictions. The eBOSS BAO measurements put tight constraints on the expansion history and curvature of the Universe. We found that the history of universal expansion can be well described with a cosmological constant, Λ, and favour a flat Universe with $\Omega_{\rm K} = -0.0001 \pm 0.0018$. We also investigated the nature of gravity, with a simple parameterization (ABBOTT et AL. 2018) and found that our results are consistent with General Relativity predictions. Our RSD constraints are not precise enough for the moment to see deviations from standard gravity. We further showed that the study of large scales structure can put constraint on neutrino masses, inflation and primordial non-gaussianity.

In the near future, the DESI experiment will probe the Universe over the redshift range $0.05 < z < 3.5$, measuring a tremendous amount of galaxy and quasar redshifts during its five years of operation. Most of the constraining power comes from the measurement of the broadband power spectrum and two-point correlation function. Nonetheless, given the exquisite statistical precision that it will reach, very careful clustering analysis will be crucial. In particular, on very large scales, wide-angle corrections (GIL-MARIN et AL. 2020; DE MATTIA et AL. 2021), radial integral constraint corrections and relativistic effect will need to be corrected for (M. WANG, BEUTLER et BACON 2020). On semi-linear and non-linear scales, a correct modelling of redshift-space distortions and non-linear bias using in part on galaxy halo occupation model will be mandatory to properly model this range of scale. State-of-the-art eBOSS modelling systematic errors is of the order of 2% for $f\sigma 8$ (GIL-MARIN et AL. 2020; BAUTISTA et AL. 2021), which is equal to the expected statistical errors of each redshift bin in DESI, as shown in Fig. 4.25. These systematic errors might be divided by nearly a factor of two by varying the template model correlation function with cosmology in the cosmological inference (i.e. a full cosmological fit, see for example CHUDAYKIN et AL. 2020). As a remark, template fit and full cosmological fit both usually assume a fiducial ΛCDM cosmology.

Finally, observational systematic errors will need to be understood in very detail. eBOSS observational systematic errors were of the order of 2-3% (NEVEUX et AL. 2020; HOU et AL. 2021; GIL-MARIN et AL. 2020; BAUTISTA et AL. 2021),to 9% (TAMONE et AL. 2020), which is too large compared to DESI expected precision. On small scales, fibre collisions will play an important role, which can be modelled with the method of (MOHAMMAD et AL. 2020). On large scales, clustering measurement will be mostly affected by non-cosmological fluctuations due to the quality of the imaging. Deep-learning techniques might a powerful tool to properly account for these observational artefacts (REZAIE et AL. 2020), while pure angular systematic errors could also be mitigated using novel methods such as (PAVIOT et AL. 2021; DE MATTIA et RUHLMANN-KLEIDER 2019). Nevertheless, DESI and EUCLID will probe an enormous volume of the Universe in the upcoming years, and we except considerable breakthrough in cosmology within the next decades.

Résumé

Durant ces trois années de thèse, j'ai effectué l'analyse de la fonction de corrélation à deux points des galaxies rouges (LRGs) du programme spectroscopique eBOSS de la collaboration SDSS. J'ai mesuré, dans la distribution spatiale des LRG dans le décalage vers le rouge entre $0.6 < z < 1.0$, les oscillations acoustiques des baryons et le taux d'accroissement des structures. Ces études, qui cherchent à comprendre la formation et l'évolution des grandes structures, sont communément appelés étude de *clustering*. Dans ce résumé, je vais introduire les élements fondamentaux de la cosmologie moderne. J'introdurai ensuite la théorie d'évolution des pertubations primordiales, qui permet de modéliser la fonction de corrélation à deux points dans l'espace réel. Par la suite, je montrerai comment modéliser les oscillations acoustiques ainsi que le décalage vers le rouge pour des objects biasées comme les galaxies. Basé sur ces théories, je décrirai par la suite l'analyse du catalogue de LRGs. Cette thèse se termine sur les implications cosmologiques des surveys BOSS et eBOSS, ainsi que sur les perspectives futures du sondage DESI.

4.5 Le modèle standard de la cosmologie

Dans cette section, je décris les élements clés de la cosmologie moderne.

4.5.1 Le principe cosmologique

Le principe cosmologique est l'hypothèse, qu'à très grand échelle, l'Univers peut être assumé isotrope et homogène. Une cartographie de l'Univers est presentée sur la Fig. 4.26. Nous pouvons observer qu'à des échelles inférieures à 100 Mpc, l'Universe est hétérogène : on observe des filaments connectants des zones de surdensités : les galaxies et amas de galaxies. Cependant, à des échelles plus grandes, l'Univers parait en effet homogène et isotrope, car nous n'observons pas de directions préférentielles. Dans le modèle standard de la cosmologie, la géometrie ainsi que l'évolution de l'Univers est décrite dans le cadre de la relativité Générale d'Einstein. Avant cette théorie, le temps était supposé universel car s'écoulant de la même manière à n'importe quel endroit de l'Univers. Einstein a cependant démontré que ce n'était pas le cas : le temps t est en réalité une variable, au même titre que les coordonées spatiales x, y et z, et la géometrie de l'espace-temps est totalement déterminée par le contenue et la distribution énergetique de L'Univers. Cette géometrie est décrite par une métrique g, qui dans le cadre d'un Universe homogène et isotrope prend la forme suivante

$$\mathrm{d}s^2 = a^2(\tau)[-\mathrm{d}\tau^2 + \mathrm{d}\chi^2 + f_k^2(\chi)(\mathrm{d}\theta^2 + \sin^2\theta\mathrm{d}\phi^2)], \tag{4.33}$$

Cette métrique est la métrique de Friedmann-Lemaître-Robertson-Walker (FLRW). a est le facteur d'échelle, χ est une coordonnée spatiale, Ω est l'angle solide et τ est appelé le temps conforme. Il est relié au temps cosmique t par la relation $\mathrm{d}\tau = \mathrm{d}t/a$. f_k est une fonction de χ est de K, la courbure de l'Univers. Je suppose dans la suite le cas ou l'Univers est plat, où $K = 0$ et $f_k(\chi) = \chi$. Ceci est confirmée par les observations du fond diffus cosmologique par Planck combiné avec les observations des BAO et RSD dans les galaxies BOSS et eBOSS, comme nous le verrons dans la section 4.8.2.

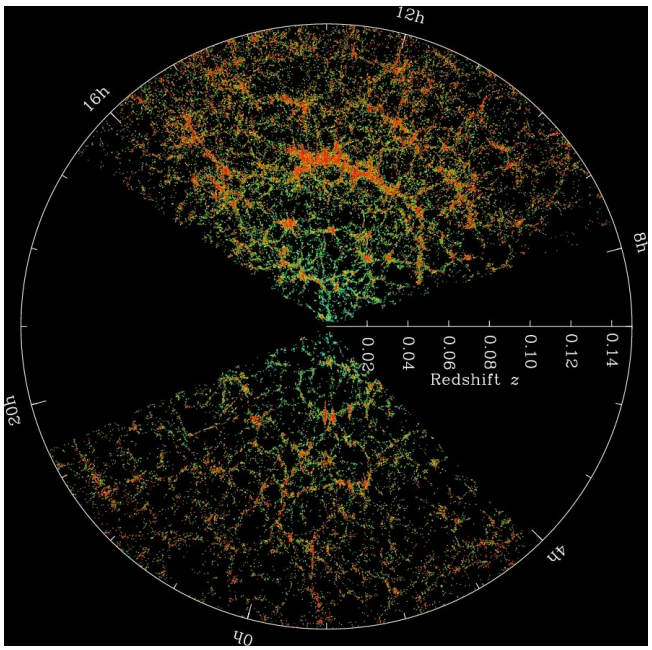

FIGURE 4.26 – La distribution des galaxies observées par le sondage Baryon Oscillations Spectroscopic Survey (BOSS) du Sloan Digital Sky Survey (SDSS)-III. Credit : Pris sur https://www.sdss.org/science/

4.5.2 La composition de l'Univers

Durant le dernier siècle, de nombreuses découvertes nous ont permit de faire d'incroyable avancées dans notre compréhension de l'Univers. En 1929, Erwin Hubble (HUBBLE 1929) fut le premier à observer que l'Univers était en expansion. Plus tard, la découverte du fond diffus cosmologique, nous a permit de comprendre que l' Univers priomordial était chaud et dense, favorisant l'hypothèse du Big Bang. En 1937, ZWICKY 1937 fût l'un des premiers à soumettre l'hypothèse qu'une partie de la matière était noire, ayant très peu d'interaction avec la matière, la lumière et elle-même. Cette matière est nécessaire afin de comprendre la dynamique et la formation des grandes structures. Cependant, celle-ci n'est pas prédit par le modèle actuel de la physique des particules, réprésentant néanmoins environ 27% du budjet énergetique totale dans le modèle standard (PLANCK COLLABORATION 2018). Le modèle standard assume que cette matière est composée de particules massives, la matière noire froide (CDM). Un autre composant de l'Univers fût également découvert pour la première fois par (PERLMUTTER et AL. 1999) : l'énergie noire. Cette énergie serait responsable de l'accélération de l'expansion de l'Univers et représenterait envrion 70% du budget totale. Cette énergie noire est principalement modélisée par une constante cosmologique Λ. Bien que pré-dominant aux débuts de l'Univers, les espèces relativistes tels que les neutrinos et les photons, sont de nos jours négligables. Dans la suite, nous assumerons l'Univers tel qu'il est définit dans le modèle standard de la cosmologie, plus communement écrit ΛCDM. Je détaille sur la Table 4.18 les valeurs exactes des paramètres cosmologiques.

Tableau 4.18 – Paramètres cosmologiques déterminés par PLANCK COLLABORATION 2018 CMB (TT, TE, EE, lowE + lentille + BAO). Les densités physiques sont définit par la relation $\omega_{Y,0} = \Omega_{Y,0} h^{-2}$.

Parameter	Notation	Value
constante de hubble réduite	h	0.6766 ± 0.0042
densité de matière	$\omega_{m,0}$	0.14240 ± 0.00087
densité de matière noire	$\omega_{c,0}$	0.11933 ± 0.00091
densité de baryons	$\omega_{b,0}$	0.02242 ± 0.00014
densité de photons	$\omega_{\gamma,0}$	$(2.4729 \pm 0.0022) \times 10^5$
densité de curvature	$\Omega_{K,0}$	0.0007 ± 0.0019
constante cosmologique	$\Omega_{\Lambda,0}$	0.6889 ± 0.0056

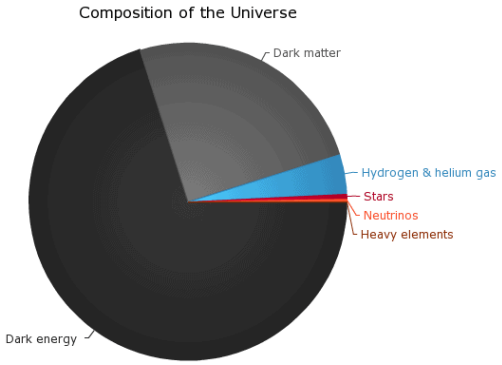

FIGURE 4.27 – La composition de l'Univers. Credit : Pris sur https://nineplanets.org/the-universe/

4.5.3 Distances à échelle cosmologique

En pratique, il peut être difficile de déterminer de manière directe la distance relative de galaxies lointaine par rapport à la Voie lactée. L'une des méthodes la plus directe, est la détection des décalages spectraux de raies d'absorptions/ émissions dans le spectre de galaxies, dues aux effets Doppler. Comme l'Univers est en expansion toute les galaxies, à part la galaxie d'Andromeda qui s'approche vers nous, ont un spectre décalé vers le rouge. Un photon émit par une galaxie à une longueur d'onde λ_e et à un temps t_e et recu à un temps t_0 est dilaté par un facteur

$$1 + z \equiv \frac{\lambda_o}{\lambda_e} = \frac{a(t_o)}{a(t_e)}, \tag{4.34}$$

ou z est le décalage spectral. A partir du facteur d'échelle, nous pouvons définir le taux d'expansion à un facteur d'echelle a donné par

$$H(z) = \frac{\dot{a}}{a}, \tag{4.35}$$

ou le point correspond à des dérivés par rapport au temps cosmique. Pour des raisons historiques, sa valeur dans l'Univers local, i.e $z = 0$, s'écrit H_0, et est nomée la constante d'Hubble. Une notation courante est d'écrire $H_0 = 100h\text{kms}^{-1}\text{Mpc}^{-1}$. PLANCK COLLABORATION 2018 mesure à partir du CMB et des BAO un taux d'expansion $h = 0.6766$. La distance radiale comobile D_c d'un objet à un décalage spectral z_e correspond à l'intégrale selon une géodesique nulle $\mathrm{d}s^2 = 0$

$$D_c(z) = \int_0^z \frac{\mathrm{d}z}{H(z)}. \tag{4.36}$$

La distance angulaire comobile D_M relie la distance comobile angulaire d'un objet avec surface comobile dS_e à son angle solide observé $d\Omega_o$, $dS_e = D_M^2 d\Omega_o^2$. A partir de l'Eq. 4.33, il est clair que

$$D_M(z) = f_k(D_c(z)). \tag{4.37}$$

Afin de calculer ses distances, il faut déterminer l'évolution de $H(z)$ en fonction du temps. Les équations d'Einstein appliqués à une métrique FLRW déterminent cette évolution,

$$H(z) = H_0 E(z) = H_0 \sqrt{\Omega_{\mathrm{m},0}(1+z)^3 + \Omega_{\mathrm{r},0}(1+z)^4 + \Omega_{\mathrm{k},0}(1+z)^2 + \Omega_{\Lambda,0}}. \tag{4.38}$$

Ici, $\Omega_{\mathrm{m},0}$, $\Omega_{\mathrm{r},0}$,$\Omega_{\Lambda,0}$ et $\Omega_{K,0}$ correspondent respectivement aux densités d'énergies de la matière, de la radiation, de l'énergie noire et de la courbure de l'Univers à $z = 0$. La somme de ces densités d'énergies est égale par définition à 1. Je présente sur la Fig. 4.28 l'évolution de ces paramètres de densités en fonction du décalage spectral. L'Univers jeune est dominé par la radiation. Celui-ci est alors chaud et dense, de tel sorte que matière et lumière sont couplés l'un à l'autre. De par son expansion, l'Univers refroidit jusqu'au point où électron et proton se recombine pour former des atomes d'hydrogène. Les photons sont donc libres de se propager dans l'Univers, ce qui correspond à l'observation du fond diffus cosmologique, la première lumière visible dans l'Univers. L'Univers devient ensuite dominé par la matière, puis de nos jours par l'énergie noire, ce qui implique potentiellement que son expansion finira par être exponentielle.

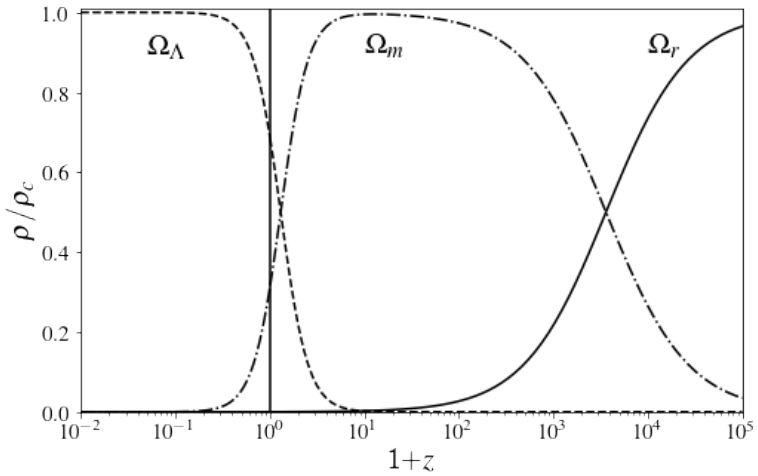

FIGURE 4.28 – Variation des paramètres cosmologiques en fonction du décalage spectral. Nous avons assumer un espace plat avec $\Omega_{\mathrm{m}}+\Omega_\Lambda+\Omega_{\mathrm{r}}+\Omega_\nu = 1$, valeurs prises dans (PLANCK COLLABORATION 2018). Pour simpliciter, nous avons assumer les neutrinos ν sans masses.

4.5.4 Pertubations primordiales

L'Univers est assumé isotrope et homogène à grand échelle. A plus petite échelle, nous pouvons observer des fluctuations dans le champ densité,

$$\delta = \frac{\rho - \bar{\rho}}{\rho} \tag{4.39}$$

ou ρ est le champ de densité, et $\bar{\rho}$ sa moyenne dans l'Universe. Nous supposerons le principe d'ergodicité, qui stipule équivalence entre $\bar{\rho}$ et $\langle\rho\rangle$, sa moyenne d'ensemble. Par définition le moment d'ordre un du champ de densité, $\langle\delta\rangle = 0$. On peut observer sur la Fig. 4.29 les fluctuations de densité, de l'ordre de puissance d'environ 10^{-5}, observées dans le fond diffus cosmologique. Ces

fluctuations ont été générées dans l'Univers primordial au cours d'une phase d'expansion accélerée appellée l'inflation. Ces fluctuations suivent une statistique quasi-gaussienne. Un champ gaussien est entièrement déterminé par son moment d'ordre 2

$$\xi(\mathbf{s}) = \langle \delta(\mathbf{x})\delta(\mathbf{x}+\mathbf{s})\rangle, \tag{4.40}$$

ou par sa transformé de Fourier,

$$\langle \delta(\mathbf{k},\mathbf{k}')\rangle = (2\pi)^3\delta^D(\mathbf{k}-\mathbf{k}')P(\mathbf{k}), \quad P(\mathbf{k}) = \int \xi(x)\exp^{-i\mathbf{kx}}\mathrm{d}x^3. \tag{4.41}$$

$\xi(\mathbf{s})$ et $P(\mathbf{k})$ sont appelées respectivement la fonction de corrélation à deux points et le spectre de puissance. Ces fonctions ne dépendent que de la norme de $\mathbf{s}$ et $\mathbf{k}$ dans un Univers isotrope. L'inflation prédit un spectre de puissance de la forme $P(k) \propto k^{n_s}$ avec n_s l'index spectral, mesuré $n_s = 0.9665 \pm 0.0038$ par PLANCK COLLABORATION 2018. L'inflation prédit également une faible variation de cette index en fonction du vecteur d'onde k.

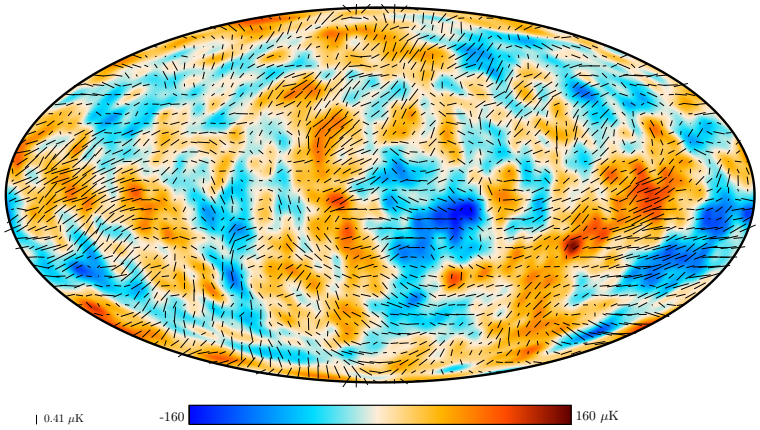

FIGURE 4.29 – Planck 2018 map of the polarized CMB anisotropies. The direction and lengths of the rods represents the direction and amplitude of the polarized photons. With this map, (PLANCK COLLABORATION 2018) measured the cosmological parameters given in Table 1.2. Taken from https://www.cosmos.esa.int/web/planck/picture-gallery

4.6 La structure à grand échelle de l'Univers

Les pertubations primordiales, initialement dans le regime linéaire ou $\delta \ll 1$, vont croître sous l'effet de la gravité jusqu'au point ou celles-ci ne seront plus négligeables $\delta \approx 1$. Il conviendra donc de décrire l'évolution des pertubations jusqu'au régime quasi non-linéaire. Nous allons principalement travailler dans un cadre Eulérien, où un fluide est décrit de manière discrète dans l'espace. Il est également possible de décrire l'évolution des constrastes de densité dans un cadre Lagrangian, ou le fluide est décrit par l'ensemble des particules qui le compose.

4.6.1 La théorie des pertubations

Dans le régime linéaire, l'évolution des perturbations s'écrit de la manière suivante (BERNARDEAU et AL. 2002)

$$\text{Equation de continuité} \quad \frac{\partial \delta}{\partial \tau} + \theta = 0, \tag{4.42}$$

$$\text{Equation d'Euler} \quad \frac{\partial \theta}{\partial \tau} + \mathscr{H}\theta + \frac{3}{2}\Omega_{\rm m}(\tau)\mathscr{H}^2\delta = 0 \tag{4.43}$$

$$\text{Equation de Poisson} \quad \nabla^2\Phi = 4\pi G\bar{\rho}a^2\delta = \frac{3}{2}\Omega_{\rm m}(\tau)\mathscr{H}^2\delta, \tag{4.44}$$

où $\mathscr{H}$ est le temps conforme, $\mathscr{H} = aH$ et θ est la divergence du champ de vitesse $\theta = \nabla \cdot \mathbf{v}$. La divergence apparait naturellement dans les équations car le rotationnel du champ de vitesse tend vers zero dans le régime linéaire. On peut re-écrire le système d'équations 4.42-4.42 en espace de Fourier comme

$$\frac{\partial^2 \delta_{\mathbf{k}}}{\partial^2 \tau} + \mathscr{H}\frac{\partial \delta_{\mathbf{k}}}{\partial \tau} - \frac{3}{2}\Omega_{\rm m}(\tau)\mathscr{H}^2\delta_{\mathbf{k}} = 0 \tag{4.45}$$

Dans le régime linéaire, chaque mode k de fluctuations évoluent indépendamments. Les solutions générales sont données par $\delta(t,\mathbf{k}) = \delta_+(\mathbf{k})D_+(t) + \delta_-(\mathbf{k})D_-(t)$, avec D_+ et D_- les solutions croissantes et décroissantes. Dans un Univers dominé par la matière, le mode croissant croît comme $D_+ \propto a \propto t^{2/3}$. Le taux de croissance des structures est définit comme étant la dérivée logarithmique du facteur de croissance $g(a) \equiv D(a)/a$,

$$f \equiv \frac{{\rm d}lnD}{{\rm d}lna} \tag{4.46}$$

Le taux de croissance f peut être approximé comme $f \approx \Omega_{\rm m}(z)^\gamma$ Dans le cadre de la relativité générale, assumé par ΛCDM, $\gamma \approx 0.545$. Cette valeur peut différer de 30% en fonction du modèle de gravité assumé (LINDER et CAHN 2007). L'équation de continuité Eq. 4.42 peut s'écrire

$$\nabla \cdot \mathbf{v} = -aH\delta f(\Omega_{\rm m}), \tag{4.47}$$

Cette description des perturbations dans le régime linéaire n'est seulement valide dans un Univers dominé par la matière pour des échelles où la causalité entre deux évenements peut être considérée instantanée. A plus grand échelle, au dessus de l'*horizon*, ou lorsque l'Univers est dominé par la radiation, ce traitement n'est plus valide. Pour déterminer l'évolution des pertubations dans l'Univers primordial, dominée par la radiation, il faudrait prendre en compte chaque composant énergétiques, dans le cadre de la relativité générale, comme dans de l'Eq. 4.38. Seule la matière noire peut s'agréger pendant cette ère, car les baryons sont couplés aux photons, et ne tombent dans les régions de surdensités qu'après recombination. A l'intérieur de l'horizon des évènements, les fluctuations de matières noires δ_c croissent de manière logarithmique pendant l'ère dominée par la radiation et comme $\propto \mathscr{H}^{-2}$ dans l'ère dominée par la matière. En dehors de l'horizon des évènements, les pertubations de matière noire évoluent dans chaque ère comme $\propto \mathscr{H}^{-2}$. Ainsi, en fonction du mode k d'oscillation, le spectre de puissance linéaire va prendre la forme

$$P_{\rm lin}(k) \approx \begin{cases} k^{n_s} & \left(\frac{k}{k_{eq}}\right) \ll 1, \\ k^{n_s-4} & \left(\frac{k}{k_{eq}}\right) \gg 1. \end{cases} \tag{4.48}$$

ou k_{eq} marque la transition entre l'ère de la radiation et l'ère de la matière. Cette transition est observée dans le spectre de puissance de la matière à une echelle $\approx 0.2h{\rm Mpc}^{-1}$ comme on peut le voir sur la Fig. 4.30.

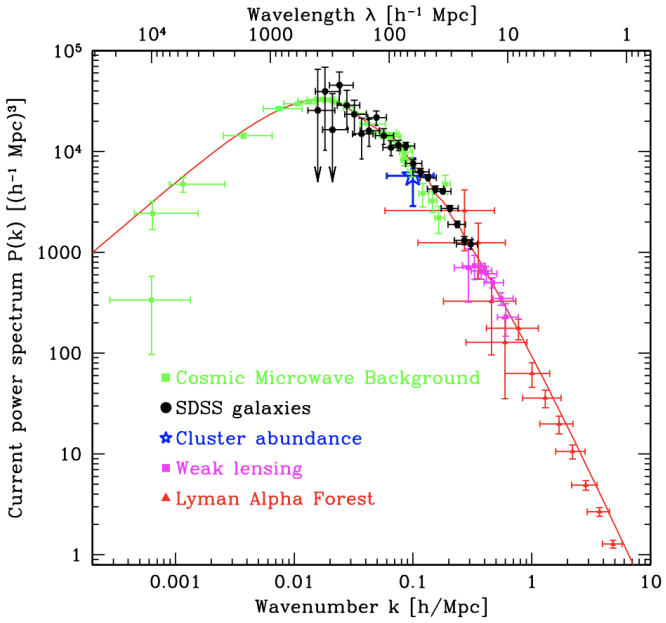

FIGURE 4.30 – Spectre de puissance de la matière, observé à partir de différents sondage. Pris à partir du papier de TEGMARK et AL. 2012.

Jusqu'à maintenant, nous avons seulement considéré les fluctuations de densité de matière noire. Dans l'ère de la radiation, les baryons et photons sont couplés et interagissent entre eux par diffusion Thomson, de manière (quasi)-indépendantes de la matière noire. On peut montrer qu'à une certaine échelle en dessous de l'horizon, le constraste de densité des photons suit une loi d'oscillateur harmonique. Les oscillations produites dans ce fluide sont appellées oscillations acoustiques des baryons (BAO). Après re-combination, au moment du découplage entre baryon et photon, la matière baryonique aura parcouru dans le fluide une distance moyenne

$$r_d = \int_{z_d}^{\infty} \frac{c_s(z)}{H(z)} \mathrm{d}z, \tag{4.49}$$

autour des pertubations initiales du fluide baryon-photon. r_d est appellé l'horizon du son à l'époque de découplage, et est mesuré à une très grande précision par (PLANCK COLLABORATION 2018), $r_d = 147.21 \pm 0.23$Mpc. En réalité, le fluide baryon-photon interagit de manière faible sur les pertubations de matière noire. Les baryons, sous effet gravationnel seront légèrement attirés par les puits de potentiel de la matière noire, alors que les photons par amortissement de Silk, vont applatir ces zones de sur-densités. Après recombination, la matière baryonique va imprimer l'échelle acoustique r_d dans la distribution de matière. (EISENSTEIN et HU 1998) fournit des expressions analytiques qui prennent en compte les interactions physiques entre les différents composants primordiaux. Pour avoir une description encore plus précise de l'évolution des constrates de densités primordiaux, il est courant de résoudre numériquement les équations de Boltzmann relativiste

$$\left(p^\mu \delta_\mu - \Gamma^i_{\mu\nu} p^\mu p^\nu \frac{\delta}{\delta p^\mu} \right) f = C(f), \tag{4.50}$$

ou $f(x, \mathbf{p})$ est la fonction de distribution, $p^\mu = (p^0, \mathbf{p})$ est le moment et C le terme de collision. De nombreux codes publiques comme CAMB (LEWIS et AL. 2000) or CLASS (LESGOURGUES 2011), résolvent les equations de Botlzmann, et fournissent une estimation du spectre de puissance linéaire des fluctuations au moment du découplage en prenant comme argument une cosmologie ΛCDM donnée. Toujours dans le régime linéaire, il est facile de déterminer le spectre de puissance à n'importe quel décalage spectral, $P_{\rm lin}(k,t) = D^2(t) P_{\rm lin}(k, t_{\rm ini})$. Lorsque les constrastes de densité

ne deviennent plus négligeables, $\delta, \theta \approx 1$, le système d'équation 4.42-4.43 devient (ASSASSI et AL. 2014)

$$\frac{\partial \delta}{\partial \tau} + \theta = [\delta * \theta], \tag{4.51}$$

$$\frac{\partial \mathbf{v}}{\partial \tau} + \mathscr{H}\mathbf{v} + \frac{3}{2}\Omega_{\rm m}(\tau)\mathscr{H}^2\delta = [\theta * \theta], \tag{4.52}$$

ou le terme de gauche est la solution linéaire et le terme de droite correspond à des convolutions non linéaires entre différents modes k. Dans un Univers dominé par la matière, les solutions de ce système peuvent être déterminées par une approche pertubative

$$\delta(\mathbf{x}, \tau) = \sum_{i=1}^{n} a^n(\tau)\delta^{(n)}(\mathbf{x}, \tau_{\rm ini}), \quad \theta(\mathbf{x}, t) = -\mathscr{H}\sum_{i=1}^{n} a^n(\tau)\theta^{(n)}(\mathbf{x}, \tau_{\rm ini}), \tag{4.53}$$

ou les champs $\delta^{(n)}$ and $\theta^{(n)}$ sont données en fourier space par les relations

$$\delta^{(n)}(\mathbf{k}, \tau_{\rm ini}) = \int_{\mathbf{q}_1} .. \int_{\mathbf{q}_n} (2\pi)^3 \delta^{\rm D}(\mathbf{q}_1 + .. \mathbf{q}_n - \mathbf{q}) F_n(\mathbf{q}_1, ..., \mathbf{q}_n) \delta_{\mathbf{q}_1} \delta^{(1)}_{\mathbf{q}_1}(\mathbf{k}, \tau_{\rm ini}) .. \delta^{(1)}_{\mathbf{q}_n}(\mathbf{k}, \tau_{\rm ini}), \tag{4.54}$$

$$\theta^{(n)}(\mathbf{k}, \tau_{\rm ini}) = \int_{\mathbf{q}_1} .. \int_{\mathbf{q}_n} (2\pi)^3 \delta^{\rm D}(\mathbf{q}_1 + .. \mathbf{q}_n - \mathbf{q}) G_n(\mathbf{q}_1, ..., \mathbf{q}_n) \delta_{\mathbf{q}_1} \delta^{(1)}_{\mathbf{q}_1}(\mathbf{k}, \tau_{\rm ini}) .. \delta^{(1)}_{\mathbf{q}_n}(\mathbf{k}, \tau_{\rm ini}), \tag{4.55}$$

ou les kernels F_n et G_n peuvent être calculés de manière itérative (BERNARDEAU et AL. 2002). (CROCCE et Román SCOCCIMARRO 2006) montrent qu'afin d'avoir une bonne estimation du spectre de puissance à l'échelle des BAO, il est nécéssaire de fournir une approche pertubative à l'ordre 2. Dans ce manuscrit l'estimation du spectre de puissance non linéaire de la matière, notée $P_{\delta\delta}$, est basée sur le formalisme de RESPRESSO (Rapid and Efficient SPectrum calculation based on RESponSe functiOn) (NISHIMICHI et AL. 2017). La fonction de réponse determines les variations du spectre de puissance non linéaire par rapport à de petites variations du spectre de puissance linéaire.

$$\delta P_{\delta\delta}(k; z) = \int {\rm d}\ln q K(q, k; z) \delta P_{\rm lin}(k; z). \tag{4.56}$$

ou l'expression de $K(q, k; z)$ a été déterminée à l'aide de simulations numériques. Son expression est donnée par

$$K_{\rm model}(k, q) = \left[\left(1 + \beta_{k,q} + \frac{1}{2}\beta^2_{k,q}\right) K^{\rm SPT}_{\rm tree}(k, q) + (1 + \beta_{k,q}) K^{\rm SPT}_{\rm 1\text{-}loop}(k, q) + K^{\rm SPT}_{\rm 2\text{-}loop}\right] D(\beta_{k,q}), \tag{4.57}$$

ou les expressions de $K^{\rm SPT}$, $\beta_{k,q}$ peuvent être trouver dans (NISHIMICHI et AL. 2017).

4.6.2 Bias des galaxies

Dans l'Univers, le champ de matière δ n'est pas directement observable : seuls les objets émettant ou absorbant de la lumière sont visibles. Les galaxies, composées de millions d'étoiles, sont observables à de très grandes distances et sont ainsi parfaites pour tracer le champs de matière. Une hypothèse courante est d'assumer qu'il existe une relation entre le champ de galaxie δ_g et le champ de matière δ. Par une approche pertubative, il est possible de déterminer une telle relation en prenant en compte les valeurs locales du champ de potentiel gravitationnel Φ et du champ de potentiel de vitesse Φ_v. A l'ordre 3, l'expression du champ δ_g est donnée par (ASSASSI et AL. 2014; SIMONOVIĆ 2018)

$$\delta_{\rm g} = b_1\delta + \frac{b_2}{2}\delta^2 + b_{\mathscr{G}_2}\mathscr{G}_2 + b_{\Gamma_3}\Gamma_3, \tag{4.58}$$

ou les fonctions $\mathscr{G}_2$ et Γ_3 sont fonction de Φ et Φ_v. Avec cette expression, les spectres de puissanses non-linéaire sont donnés par (SIMONOVIĆ 2018; BAUTISTA et AL. 2021)

$$\begin{aligned} P_{gg}(k) &= b_1^2 P_{\delta\delta}(k) + b_2 b_1 I_{\delta^2}(k) + 2 b_1 b_{\mathscr{G}_2} I_{\mathscr{G}_2}(k) \\ &\quad + 2\left(b_1 b_{\mathscr{G}_2} + \frac{2}{5} b_1 b_{\Gamma_3}\right) F_{\mathscr{G}_2}(k) + \frac{1}{4} b_2^2 I_{\delta^2\delta^2}(k) \\ &\quad + b_{\mathscr{G}_2}^2 I_{\mathscr{G}_2\mathscr{G}_2}(k) + \frac{1}{2} b_2 b_{\mathscr{G}_2} I_{\delta_2\mathscr{G}_2}(k) \end{aligned} \tag{4.59}$$

$$\begin{aligned} P_{g\theta}(k) &= b_1 P_{\delta\theta}(k) + \frac{b_2}{4} I_{\delta^2\theta}(k) + b_{\mathscr{G}_2} I_{\mathscr{G}_2\theta}(k) \\ &\quad + \left(b_{\mathscr{G}_2} + \frac{2}{5} b_{\Gamma_3}\right) F_{\mathscr{G}_2\theta}(k). \end{aligned} \tag{4.60}$$

ou j'ai introduit le spectre de puissance croisée entre matière et θ, $P_{\delta\theta}$, et le spectre de puissance de θ, $P_{\theta\theta}$. $P_{\theta\theta}$ et $P_{\theta\theta}$ sont déterminés à partir des fonctions de BEL et AL. 2018,

$$\begin{aligned} P_{\theta\theta}(k) &= P_L(k) e^{-k(a_1 + a_2 k + a_3 k^2)}, \\ P_{\delta\theta}(k) &= \left(P_{\delta\delta}^{HF}(k) P_{\rm lin}(k)\right)^{\frac{1}{2}} e^{-\frac{k}{k_\delta} - bk^6}, \end{aligned} \tag{4.61}$$

ou les variables a_1, a_2, k_δ et b sont des variables dont l'expression peut être trouvé dans BEL et AL. 2018. Les équations Eqs. 4.59 et 4.60 fournissent une description théorique à l'évolution du champ de galaxie au cours du temps.

4.6.3 Le décalage dans l'espace spectral

L'observation d'un spectre d'une galaxie nous permet de déterminer son décalage spectral z. A partir de ce décalage, l'Eq. 4.36 nous permet de calculer sa distance à partir d'une cosmologie donnée, qui fournit une fois stipulée l'évolution du taux d'expansion $H(z)$. Cependant, les galaxies ont des vitesses intrinsèques, due aux variations locales du potentiel gravitionnel, qui dévit de l'expansion pûre. Ceci va créer une distortion entre l'espace des décalages spectraux et l'espace réel (RSD),

$$\mathbf{s} = \mathbf{x} - f u_z(\mathbf{x}) \hat{\mathbf{z}} \tag{4.62}$$

ou $u_z(\mathbf{x}) \equiv -\mathbf{v}\cdot\hat{\mathbf{z}}/(aH(a)f)$ et $\hat{z}$ est le vecteur normé de la ligne de visée. La conservation du nombre de galaxies entre les deux espaces s'écrit $[1+\delta^s(\mathbf{s})]\mathrm{d}^3 s = [1+\delta(\mathbf{r})]\mathrm{d}^3 r$, et le spectre de puissance dans l'espace des décalages spectraux prend la forme

$$P^s(\mathbf{k}) = \int_0^\infty \frac{\mathrm{d}^3 r}{(2\pi)^3} e^{-i\mathbf{kr}} \langle e^{if k\mu\Delta U_z} [\delta(\mathbf{x}) + f\Delta_z u_z(\mathbf{x'})][\delta(\mathbf{x'}) + f\Delta_z u_z(\mathbf{x})]\rangle, \tag{4.63}$$

ou $\Delta U_z = u_z(\mathbf{x}) - u_z(\mathbf{x'})$. Cette expression est exacte dans l'approximation de plan parallèle, lorsque la distance relative entre deux galaxies est négligable par rapport à la distance de la ligne de visée. On peut observer deux phénomènes distincts : à grand échelle $s > 30 - 40h^{-1}$Mpc, dans le régime linéaire, les vitesses des galaxies sont cohérentes et l'amplitude du spectre de puissance est accru d'un facteur $(1+\mu^2 f)^2$, c'est l'effet Kaiser (KAISER 1987). A plus petite échelle, le terme exponentiel dans l'accolade amortit le spectre de puissance, c'est l'effet Finger-of-God (FoG, JACKSON 1972). Ces distortions sont directement visibles dans l'espace des configurations comme on peut le voir dans sur l'image à gauche de la Fig. 4.31, qui répresente la fonction de corrélation à deux points des galaxies LRG de BOSS et eBOSS.

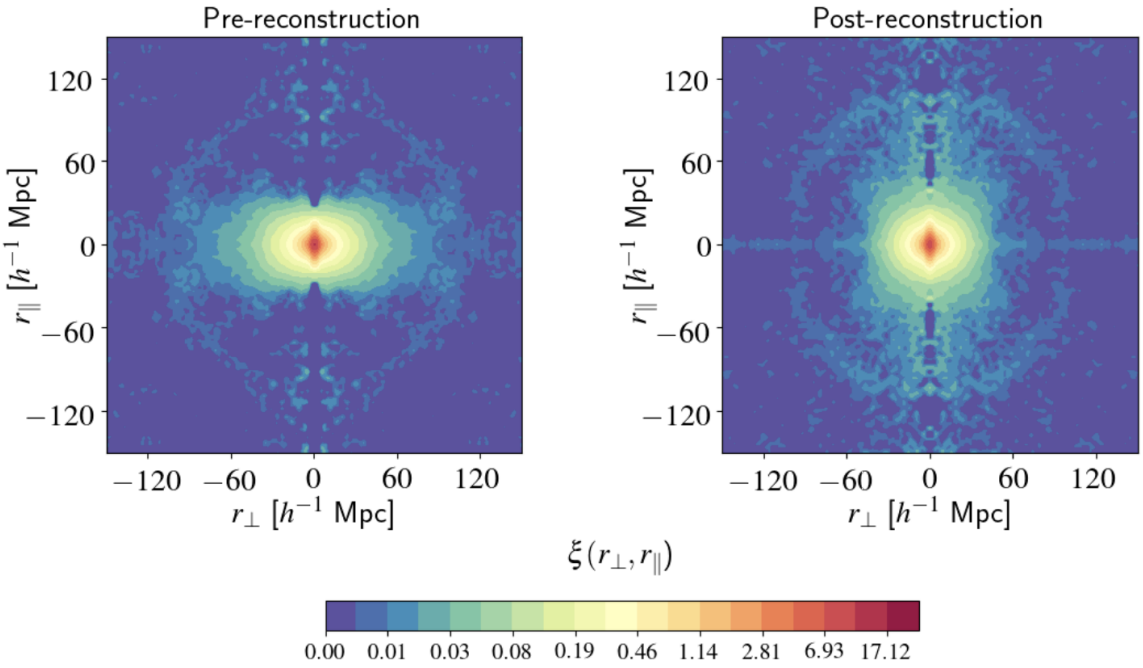

FIGURE 4.31 – Fonction de corrélation à deux points dans l'espace des décalages spectraux dans la tranche $0.6 < z < 1.1$. A gauche (droite) nous pouvons observer la fonction de corrélation avant (après) la reconstruction, (BAUTISTA et AL. 2021)

Ces corrélations sont observées en 2d en fonction de la distance transverse et radiale par rapport à la ligne de visée. A grande échelle, l'effet Kaiser se traduit par un aplatissement de l'amplitude des corrélations selon la ligne de visée, dûes aux vitesses cohérentes des galaxies qui tombent dans les potentiels gravitationels de plus grandes structures, tel que des groupes ou des amas de galaxies. A plus petite échelle, les galaxies sont dans ces amas, et leurs vitesses ne sont plus négligables comparé à la vitesse d'expansion. Ces vitesses sont maintenant aléatoires et incohérentes, ce qui crée une élongation des corrélations selon la ligne de visée. L'un des modèles utilisé dans l'analyse de la fonction de corrélation des galaxies dans l'espace du décalage spectral de BAUTISTA et AL. 2021 est le modèle TNS (TARUYA, NISHIMICHI et SAITO 2010) qui dérive une expression approximée de l'Eq. 4.63 en prenant en compte le couplage entre le FoG et l'effet Kaiser,

$$P_{\rm g}^s(k,\mu) = D(k\mu\sigma_v)\left[P_{\rm gg}(k) + 2\mu^2 f P_{{\rm g}\theta} + \mu^4 f^2 P_{\theta\theta}(k) + C_A(k,\mu,f,b_1) + C_B(k,\mu,f,b_1)\right], \tag{4.64}$$

ou les termes $C_A(k,\mu,f,b_1)$ et $C_B(k,\mu,f,b_1)$ sont des termes correctifs dont les expressions peuvent être trouver dans (TARUYA, NISHIMICHI et SAITO 2010). J'ai pris comme Finger of God une forme lorentzienne de la forme $D(k,\nu,\sigma_v) = (1 + k^2\nu^2\sigma_v^2/2)^{-2}$ L'information 2d modélisée est compresée en multipôles à l'aide de la base de Legendre,

$$P^s(k) = \sum L_l(\mu) P_\ell^s(k) \quad P_\ell^s(k) = \frac{2\ell+1}{2}\int_{-1}^{1} P^s(k,\mu) L_\ell(\mu)\, {\rm d}\mu, \tag{4.65}$$

ou L_ℓ sont les polynômes de Legendre. Nous assumerons une symétrie selon la ligne de visée, ainsi seul les multipoles pairs jusqu'à $\ell = 8$ sont non nuls. L'analyse de BAUTISTA et AL. 2021 se fait en espace de configuration, et nos mesures sont ensuite combinées avec les mesures dans l'espace de Fourier de GIL-MARIN et AL. 2020. A partir du modèle dans l'espace de Fourier, les multipoles dans l'espace des configurations s'obtiennent par transformation d'Hankel

$$\xi_\ell(r) = \frac{i^\ell}{2\pi^2}\int_0^\infty k^2 j_\ell(kr) P_\ell(k)\, {\rm d}k, \tag{4.66}$$

Dans l'espace des configurations, l' Eq. 4.63 peut être écrite comme une convolution (SCOCCIMARRO 2004)

$$1+\xi^s(s_\perp,s_\parallel)=\int_{-\infty}^{\infty}\mathrm{d}r_\parallel[1+\xi(r)]p(s_\parallel-r_\parallel|\mathbf{r}), \tag{4.67}$$

ou p est la fonction de distribution de probabilité des vitesses selon la LOS par paire à une séparation $\mathbf{r}$. Ce type de modèle est généralement appelé modèle de flux. Le second modèle de RSD considéré dans (BAUTISTA et AL. 2021) utilise une distribution de propabilité gaussiènne (GS) (REID et AL. 2011), ou le champs de densité et de vitesse dans l'espace réel est prédit par la théorie des pertubations de convolutions Lagrangiennes (CLPT) de (L. WANG et AL. 2014).

4.6.4 Les effets de géometrie

Dans un sondage spectroscopique, la position angulaire des galaxies combinée avec l'observation du décalage spectral z, nous permet de déterminer les positions 3D dans l'espace du décalage spectral. Pour se faire, il faut assumer une cosmologie, dîte "fiduciaire", pour convertir z en distance radiale. L'échelle des BAO, présente dans la distribution spatiale des galaxies, est mesurée de manière anisotrope et décomposée en un composant transverse (sensible à D_m) et radial (sensible à H). De manière plus spécifique, ce qui est mesuré est l'écart relatif de la position des BAO par rapport à leur estimations dans la cosmologie fiduciaire. Ces distortions, indépendantes des RSD, sont paramétrés par les variables sans dimension,

$$\alpha_\perp=\frac{D_M(z_{\rm eff})/r_d}{D_M^{\rm fid}(z_{\rm eff})/r_d^{\rm fid}},\quad \alpha_\parallel=\frac{D_H(z_{\rm eff})/r_d}{D_H^{\rm fid}(z_{\rm eff})/r_d^{\rm fid}}, \tag{4.68}$$

avec $D_H(z)=c/H(z)$. Afin de modéliser ces distortions, l'équation Eq. 4.63 est re-écrite comme,

$$P_\ell(k)=\frac{2\ell+1}{2\alpha_\perp\alpha_\parallel^2}\int_{-1}^{1}\mathrm{d}\mu\mathscr{L}_\ell(\mu)P[k'(k,\mu),\mu'(\mu)], \tag{4.69}$$

avec

$$k' = \frac{k}{\alpha_\perp}\left[1+\mu^2\left(\frac{1}{F_\epsilon^2}-1\right)\right]^{1/2}, \tag{4.70}$$

$$\mu' = \frac{\mu}{F_\epsilon}\left[1+\mu^2\left(\frac{1}{F_\epsilon^2}-1\right)\right]^{-1/2}, \tag{4.71}$$

L'image de droite de la Fig. 4.31, réprésente la fonction de corrélation après reconstruction du champ de densité. Dans le régime linéaire, on peut utiliser l'équation de continuité, Eq. 4.47 assumant une valeur de f, afin de déterminer le champs de vitesse à partir du champ de densité de galaxie. Une fois que l'on a determiné les vitesses particulières des galaxies, on peut modifier leur décalage spectral afin de supprimer les distortions apparentes due à l'accroisement des structures. Cette reconstruction est particulièrement importante afin de mesurer un signal BAO clair et isotrope, comme on peut le voir sur la Fig. 4.31. La modélisation de l'échelle des BAO est plus phénoménologique que la modélisation des distortions dans l'espace spectral. Le modèle pour le spectre de puissance dans l'espace du décalage spectral $P^s(k,\mu)$ s'écrit

$$P^s(k,\mu)=\frac{b^2\left[1+\beta(1-S(k))\mu^2\right]^2}{(1+k^2\mu^2\Sigma_s^2/2)}\times\left[P_{\rm no\ peak}(k)+P_{\rm peak}(k)e^{-k^2\Sigma_{\rm nl}^2(\mu)/2}\right]. \tag{4.72}$$

avec b le bias linéaire, $\delta_g=b\delta$ et $\beta=f/b$. L'assouplisement non-linéaire du peak BAO est modélisée par une distribution gaussienne $\Sigma_{\rm nl}^2(\mu)=\Sigma_\parallel^2\mu^2+\Sigma_\perp^2(1-\mu^2)$, et le spectre de puissance linéaire est

décomposé en une partie avec et sans signal BAO. Le terme $S(k)$ modelise le lissage du champ de densité des galaxies, nécessaire pour la reconstruction. Les distortions géometriques ne sont appliqués seulement au signal BAO, $P_{\rm peak}(k)$. Le modèle final pour les BAO dans l'espace des configuration s'écrit

$$\xi_\ell^t(r) = \xi_\ell(\alpha_\perp, \alpha_\parallel, r) + \sum_{i=i_{\rm min}}^{i_{\rm max}} a_{\ell,i} r^i, \tag{4.73}$$

comme la combinaison des multipoles de l'equation Eq. 4.72 et de fonctions continue en fonction de la séparation, nécéssaire pour marginaliser selon les effets non-linéaires restants. La cosmologie fiduciaire assumé dans ce manuscript pour les analyses des BAO et des RSD est la cosmologie suivante

$$\Omega_m = 0.310 \quad \Omega_c = 0.260 \quad \Omega_b = 0.048 \quad \Omega_\nu = 0.0014 \quad h = 0.676 \quad n_s = 0.970 \quad s_8 = 0.80, \tag{4.74}$$

ou σ_8 correspond à la normalisation du spectre de puissance, qui pour des raison historiques, correspond à l'amplitude des fluctuations de matière observées dans une fênêtre d'observation circulaire de rayon 8 h^{-1}Mpc. Dans la suite, le spectre de puissance linéaire fiduciaire est déterminé avec CAMB. Comme f et σ_8 sont fortement dégénérés, σ_8 est maintenu fixe à sa valeur fiduciaire dans l'analyse. Cependant, nous montrerons dans la Section 4.8.1 que les contraintes sur $f\sigma_8$ dépendent fortement de la cosmologie lorsque $\alpha = \alpha_\parallel^{1/3}\alpha_\perp^{2/3}$. s'écarte trop de l'unité. Nous pouvons réduire cette dépendance en recalculant σ_8 avec $R = 8\alpha h^{-1}$Mpc.

4.7 La construction d'un catalog de galaxie

Maintenant que le coté théorique a été introduit, je vais maintenant discuter de la stratégie observationnelle du sondage SDSS-III BOSS et SDSS-IV eBOSS (DAWSON et AL. 2013; DAWSON et AL. 2016).

4.7.1 Photométrie et Spectroscopie

Le sondage SDSS (YORK et AL. 2000) a été conçue dans les années 80 comme un sondage spectroscopique et d'imagerie multi-bandes sur une large zone (10.000 degrés carrés) avec pour objectif principal de comprendre la structure à grande échelle de l'Univers. Un télescope dédié de 2,5 mètres (GUNN et AL. 2006) a été conçu et construit par la collaboration SDSS à l'Apache Point Observatory (APO), Sunspot, Nouveau Mexique. Les observations spectroscopiques ont été réalisées avec deux spectrographes jumeaux multi-objets alimentés par fibre (SMEE et AL. 2013). Afin de déterminé les positions 3D des galaxies dans l'espace des décalages spectraux, il faut déterminé le décalage spectral z pour une population donnée de galaxie. Cependant, des milliards de galaxies sont observables dans le ciel, et ca serait une tache trop grande d'observer un spectre pour chacune d'entre elle. La stratégie des sondages à grande échelle de BOSS et d'eBOSS, fût d'abord de réaliser un sondage photométrique du ciel. Les photos nous fournissent des informations sur le flux des object observés dans le ciel dans différentes bandes passantes, ce qui fournit à posteriori des informations sur leurs couleurs. Ces informations peuvent être utiliser afin de cibler une population de galaxie particulière à un décalage spectrale souhaité. En effet, la distribution spectrale d'une galaxie, qu'elle soit rouge et elliptique ou bleu et spirale, peut être déterminé à partir de modéle de formation et d'évolution stellaire. Il suffit ensuite de prendre en compte l'expansion de l'Univers, afin d'observer une population de galaxie à un décalage spectrale souhaité à partir de sélection en couleur et magnitude. Trois types de de galaxies ont été ciblées par BOSS et eBOSS : les galaxies lumineuses

rouges (LRG), les galaxies à raies d'emission bleus (ELG) et les quasars (QSO) [8].

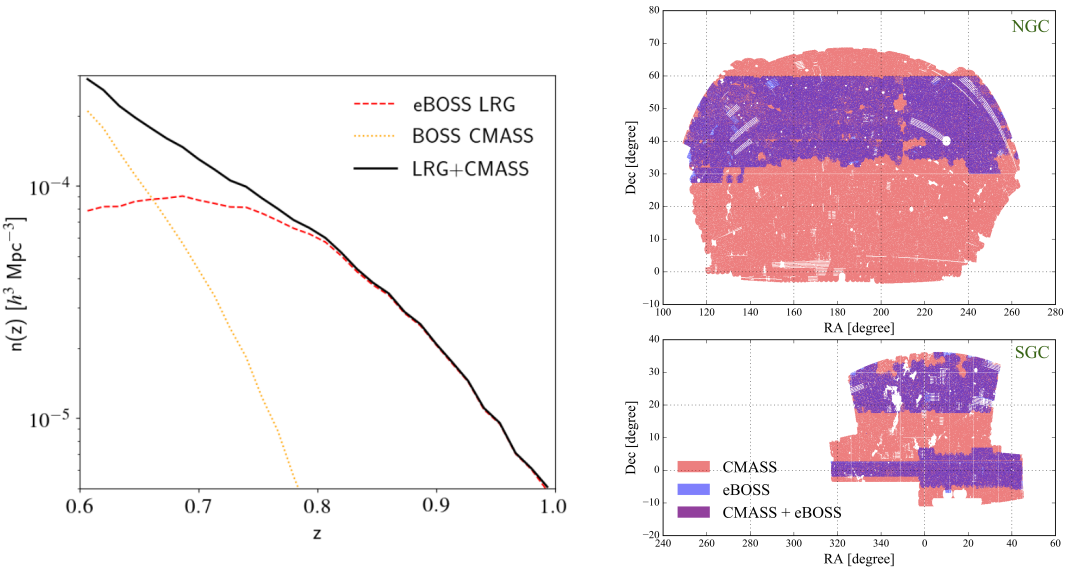

FIGURE 4.32 – Distribution radiales des CMASS observées par BOSS et des LRG observées par eBOSS dans la tranche $0.6 < z < 1.0$. Taken from (BAUTISTA et AL. 2021)

Le décalage spectrale est ensuite mesuré, à partir de l'observation du spectre de chaque objet ciblé, avec le code REDROCK. Le spectre mesuré est comparé à une combinaison linéaire de modèles spectraux. Les modèles spectraux sont construits à partir de 3 classes différentes, STAR, GALAXIE et QUASAR, en utilisant une analyse en composantes principales (ACP) appliquée à un échantillon d'entraînement basé sur les spectres observés d'étoiles, de quasars et de galaxies. Les modèles d'étoiles et de galaxies sont construits à une résolution supérieure à celle du spectrographe BOSS. Les modèles à haute résolution sont ensuite convolués avec la résolution de l'instrument et la position dans le plan focal pour correspondre aux observations de eBOSS. En plus des modèles empiriques BOSS, de nouveaux modèles PCA ont été dérivés de 20 000 spectres théoriques de galaxies qui couvrent l'âge stellaire, la métallicité et la formation des étoiles (ROSSI et AL. 2021). 30 000 spectres ont également été produits pour des étoiles de masse et de stade évolutif différents. Les meilleures mesures (z, dz et classe spectrale) sont celles qui minimisent le χ^2. Une seconde minimisation du χ^2 dans l'entourage des 3 meilleures solutions est effectuée, cette fois-ci à partir de modèle de classe spectrale individuel, de tel sorte d'éliminer les modèles non-physiques. Le meilleur χ^2 nous donne la mesure de z, cette méthode fournit environ 97% de décalage spectrale correctement mesurée pour les LRG d'eBOSS. Je présente sur la Fig. 4.32, la distribution radiale (à gauche) des galaxies à masse constante (CMASS) observés par BOSS et des galaxies LRG (en rouge) observés par eBOSS ainsi que la fenêtre d'observation pour chaque type de galaxie. On peut voir à l'intérieur de la fênêtre d'observation des régions masquées dûe à la fois à une mauvaise qualité de l'imagerie et à des collision avec des cibles de quasars. Ce catalogue de galaxie est composé de 174 816 LRG et de 202 642 CMASS.

4.7.2 Estimation de la fonction de corrélation à deux points

Maintenant que nous avons accès aux positions 3D d'un catalogue de galaxie dans l'espace des décalage spectraux, on peut maintenant estimer la fonction de corrélation à deux points. Le champ

8. Les Quasars sont des galaxies avec un trou noir supermassif actif, qui émet une large majorité de la lumière dans celle-ci.

de constraste de galaxie est définit (KAISER 1987 ; Andrew HAMILTON 1998)

$$\delta^s_{\mathbf{obs}}(\mathbf{s}) = \frac{n^s(\mathbf{s}) - P(\mathbf{s})}{P(\mathbf{s})}, \tag{4.75}$$

où $P(\mathbf{s}) \equiv \bar{n}^s(\mathbf{s})$ et $n^s(\mathbf{s})$ sont la fonction de sélection (la densité moyenne de galaxies à une distance radiale donnée) et la densité de galaxies à la position $\mathbf{s}$ dans l'espace des décalages spectral. La fonction de corrélation à deux point peut alternativement être définit comme l'excès de probabilité, comparé à une distribution aléatoire, d'observer deux objets séparés par une distance s,

$$\delta P = \bar{n}^2 \delta V_1 \delta V_2 (1 + \xi(s)), \tag{4.76}$$

où $\bar{n}$ est la densité moyenne de galaxie, et les δV_i sont des volumes infinidésimaux. Cet excès de probabilité peut être calculé de manière effective en comparant le nombre de paires de galaxies à une séparation s donnée par rapport un procédé aléatoire. Pour se faire, un catalogue aléatoire de galaxies est crée avec exactement la même fonction de sélection et la même fênêtre d'observation que les données. La fonction de sélection est prise comme étant exactement la distribution radiale observée sur la Fig. 4.32. Ceci va entrainé une modification des fluctuations δ mesurées, comme on peut le voir à partir de l'Eq. 4.75, car la réelle fonction de sélection n'est pas connue à priori. Cet effet peut être corrigé en imposant des contraintes d'intégration radiales (RIC), comme le montre DE MATTIA et RUHLMANN-KLEIDER 2019. Chaque galaxie du catalogue random se voit attribuer un décalage spectral, à partir de la méthode dîte *shuffle*, en piochant aléatoire un décalage spectral dans le catalogue de galaxie. La mesure de la fonction de corrélation à deux points se fait à partir de l'estimateur de LANDY et SZALAY 1993 (LS),

$$\xi(s,\mu) = \frac{DD(s,\mu) - 2DR(s,\mu) + RR(s,\mu)}{RR(s,\mu)}. \tag{4.77}$$

Ici, les paires de galaxies sont groupés en fonction de leur distances relative s et de l'angle μ entre la LoS $\mathbf{s} = (\mathbf{s}_1 + \mathbf{s}_2)/2$ et $\mathbf{s}_2$. On peut ainsi estimer les multipoles de la fonction de corrélation à partir d'une somme de Riemmann

$$\xi_\ell(s) = (2\ell + 1) \sum_i \xi(s,\mu_i) L_\ell(\mu_i) \mathrm{d}\mu \tag{4.78}$$

Ce sont les multipoles mesurés de la fonction de corrélation des LRGs et CMASS qui vont être comparés aux modèles théoriques. Cependant, la mesure de de cette fonction de corrélation est biasée par différents effets observationelles qui vont entrâiner des modifications apparentes, d'origine non cosmologiques, dans le champ de constraste δ_g.

4.7.3 Les systématiques observationnelles

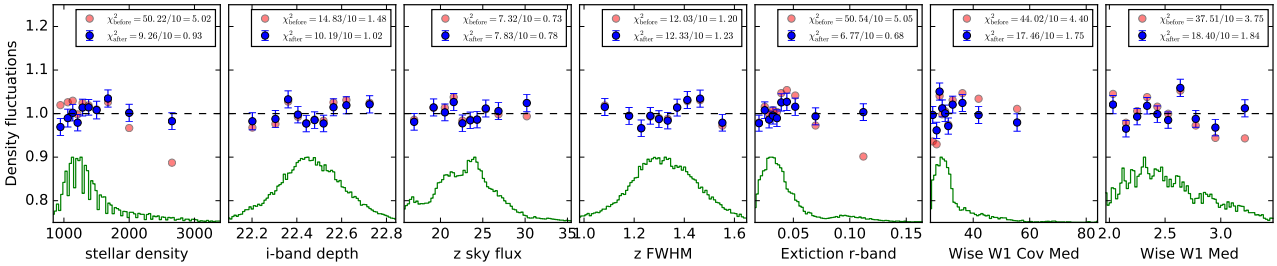

FIGURE 4.33 – Fluctuations de la densité de nombre de galaxies en fonction de différentes variables photométriques pour le pôle nord. Les points rouges (bleus) indiquent les fluctuations avant/après les corrections. L'histogramme des galaxies par rapport aux mêmes quantités est représenté en vert. L'ajustement est effectué simultanément sur toutes les cartes. Pris à partir BAUTISTA et AL. 2018

Les principales systématiques observationnelles sont

— les effets de collisions de fibres. Les observations spectroscopiques sont effectuées à l'aide de plaques, dans lesquelles des trous y sont percés et des fibres optiques assignées. De part la taille physique des fibres, deux galaxies ne peuvent pas être observées dans le ciel à une distance inférieure de $62''$. Nous avons donc appliqué la correction suivante : pour les objets de $N_{\rm targ}$ d'un groupe de collision donné pour lesquels $N_{\rm spec}$ ont un spectre, tous les objets sont pondérés par $w_{\rm cp} = N_{\rm targ}/N_{\rm targ}$.

— les effets de décalage spectraux incorrects. Certaines galaxies se voit attribuer un mauvais décalage spectral. Un modèle d'efficacité est déterminé à partir des observations, ce modèle dépend de la position de la fibre dans le plan focal, ainsi que du secteur observé dans le ciel. Chaque galaxie observée et aléatoire se voit assigner un poids $w_{\rm noz}$.

— les effets dû à la qualité de l'image. Je montre sur la Fig. 4.33 les constrastes de densité de galaxies en fonction de variables photométriques. Comme on peut le voir avant correction (points rouge), il existe de fortes corrélations, par exemple entre δ_g et la densité d'étoile ou entre δ_g et l'extinction de la voie lactée. Le champ de densité observé $\delta_{\rm phot}$ est modélisé comme une combinaison linéaire des cartes m_i, $\delta_{\rm phot}(RA, Dec) = p_0 + \sum_{i=1}^{n} p_i m_i(RA, Dec)$ où p_0 est la densité moyenne sur l'ensemble du relevé, et les p_i sont les coefficient qui minimisent le $\chi^2 = (\delta - \delta_{\rm phot})^2/\sigma_i^2$. Chaque galaxie recoit ensuite le poids $w_{\rm syst} = 1/\delta_{\rm phot}$ ce qui corrige une grande partie des fluctuations (points bleu).

En plus des poids que nous venons de décrire, nous avons également utilisé dans notre analyse le poids introduit par (FELDMAN, KAISER et PEACOCK 1994) qui optimise le rapport signal/bruit du clustering pour un relevé avec une densité moyenne variable $\bar{n}(z)$ en fonction du redshift. Les poids FKP sont définit comme

$$w_{\rm fkp}(z) = \frac{1}{1 + \bar{n}(z) P_0}. \tag{4.79}$$

avec P_0 variant de 4000 à 10000 $h^3\ Mpc^{-3}$ en fonction du traceur considéré. Pour résumé, nous pondérons chaque galaxie observée et aléatoire par le poids total [9].

$$w = w_{\rm cp}\, w_{\rm noz}\, w_{\rm syst}\, w_{\rm fkp} \tag{4.80}$$

pour tenir compte à la fois des collisions de fibre, de la défaillance des décalages spectraux et des fluctuations parasites dues aux cartes systématiques. Le redshift effectif d'un catalogue de galaxie

9. Pour BOSS, la convention est différente, $w = w_{\rm syst}\, w_{\rm fkp}(w_{\rm cp} + w_{\rm noz} - 1)$

est défini comme le redshift moyen pondéré des paires de galaxie,

$$z_{\rm eff} = \frac{\sum_{i>j} w_i w_j (z_i + z_j)/2}{\sum_{i>j} w_i w_j}, \tag{4.81}$$

où w_i (w_j) est le poids total de la galaxie $i(j)$. Nous n'incluons que les paires de galaxies dont la séparation est comprise entre 25 et 130 h^{-1} Mpc, ce qui correspond à la plage utilisée dans notre analyse de forme complète (voir la section 4.2.2.1). Nous obtenons $z_{\rm eff} = 0.698$ pour l'échantillon combiné eBOSS + CMASS. Étant donné le poids total de l'équation 3.33, nous definissons le volume effectif d'un échantillon de galaxie par

$$V_{\rm eff} = \int_{z=z_{\rm min}}^{z_{\rm max}} \left(\frac{\bar{n}(z) P_0}{1 + \bar{n}(z) P_0} \right)^2 A_{\rm eff} R^2(z) dR(z), \tag{4.82}$$

avec $R(z)$ la distance comobile au décalage vers le rouge z et $A_{\rm eff}$ la surface effective de l'échantillon. Pour les pôles Nord et Sud combinés, nous trouvons un volume effectif de 2,72 Gpc^3.

4.7.4 La fonction de corrélation avec modes angulaires annulés

Dans PAVIOT et AL. 2021, je réintroduis et modélise une statistique modifiée du champ du densité : la fonction de corrélation avec modes angulaires annulés (AMF). Cette statistique a l'avantage d'être non biasée par rapport à n'importe quelle source de contamination angulaire. Elle fût introduit par BURDEN et AL. 2014 et modélisée de manière simplifié dans (TAMONE et AL. 2020), afin de mesurer les distortions géométriques $\alpha_\perp$ et $\alpha_\parallel$ et le taux d'accroissement des structures $f\sigma_8$ à partir catalogue d'ELG d'eBOSS. Afin de supprimer les corrélations angulaires, on peut modifier l'estimateur LS en introduisant un catalogue aléatoire auxiliaire. Ce dernier a exactement la même distribution angulaire que les données mais avec une réalisation aléatoire de la distribution radiale. Il est facilement construit en assignant de manière aléatoire les positions angulaires des galaxies observées aux nouveaux points aléatoires. Nous l'appellerons le catalogue aléatoire mélangé, S, dans la suite. On peut donc concevoir un estimateur LS modifié tel que (BURDEN et AL. 2017)

$$\tilde{\xi}(s,\mu) = \frac{DD(s,\mu) - 2DS(s,\mu) + SS(s,\mu)}{RR(s,\mu)}. \tag{4.83}$$

Dans cet estimateur, le catalogue aléatoire standard au numérateur est remplacé par le catalogue aléatoire mélangé, tandis qu'il est conservé au dénominateur. Il est clair qu'en imprimant le signal angulaire des galaxies dans le catalogue aléatoire, nous supprimons le signal angulaire et les erreurs systématiques potentielles associées, mais au prix de la suppression d'une partie de l'information cosmologique, qu'il convient donc de modéliser. Afin de modéliser la fonction de corrélation AMF, nous suivons la définition de BURDEN et AL. 2017 et définissons le champ de sur-densité de l'AMF

$$\tilde{\delta}(\mathbf{r}) \equiv \frac{n(\mathbf{r}) - \tilde{n}(\mathbf{r})}{\bar{n}(\mathbf{r})} \tag{4.84}$$

où $n(\mathbf{r})$, $\tilde{n}(\mathbf{r})$ et $\bar{n}(\mathbf{r})$ correspondent respectivement à la densité de galaxie, de points aléatoire mélangé et de point aléatoire standard à la position comobile $\mathbf{r}$. La fonction de corrélation AMF est définit comme

$$\tilde{\xi}(\mathbf{s}) \equiv \frac{\langle F(\mathbf{r}) F(\mathbf{r}+\mathbf{s}) \rangle}{\langle P(\mathbf{r}) P(\mathbf{r}+\mathbf{s}) \rangle}, \tag{4.85}$$

où

$$F(\mathbf{r}) = P(\mathbf{r})\delta(\mathbf{r}) - P(\mathbf{r}) \int \mathrm{d}r'' \bar{n}(r'') \delta(\mathbf{r}''), \tag{4.86}$$

avec $\mathbf{r}$ et $\mathbf{r}''$ partagant la même ligne de visée. Après quelques calculs, la fonction de corrélation AMF anisotropique s'écrit

$$\tilde{\xi}(s,\mu) = \xi(s,\mu) - \frac{C(s,\mu)}{W(s,\mu)} + \frac{A(s,\mu)}{W(s,\mu)} \tag{4.87}$$

où

$$C(s,\mu) = \sum_{\ell=0}^{\infty} \left(\int_0^{\infty} \mathrm{d}\Delta \sum_{p=0}^{\infty} \Delta\xi_p(\Delta) \mathcal{W}_{C\ell p}(s,\Delta) \right) L_\ell(\mu), \tag{4.88}$$

$$A(s,\mu) = \sum_{\ell=0}^{\infty} \left(\int_0^{\infty} \mathrm{d}\Delta \sum_{p=0}^{\infty} \Delta\xi_p(\Delta) \mathcal{W}_{A\ell p}(s,\Delta) \right) L_\ell(\mu) \tag{4.89}$$

$$W(s,\mu) = \sum_{\ell=0}^{\infty} \mathcal{W}_\ell(s) L_\ell(\mu), \tag{4.90}$$

$$\mathcal{W}_{C\ell p}(s,\Delta) = \mathcal{W}_{C_1\ell p}(s,\Delta) + \mathcal{W}_{C_2\ell p}(s,\Delta), \tag{4.91}$$

avec

$$\mathcal{W}_{C_1\ell p}(s_{\min}, s_{\max}, \Delta) = \frac{2\ell+1}{2} \int_0^{\infty} \mathrm{d}r\, r^2 \bar{n}(r) \int_{s_{\min}}^{s_{\max}} \mathrm{d}s \int_{-1}^{1} \mathrm{d}\mu\, \Phi(\theta)\, \bar{n}(r_s) L_\ell(\mu_s) \times \frac{\bar{n}\left(r\cos\theta + \sqrt{\Delta^2 - r^2\sin^2\theta}\right) L_p(\mu_{\Delta-}) + \bar{n}\left(r\cos\theta - \sqrt{\Delta^2 - r^2\sin^2\theta}\right) L_p(\mu_{\Delta-})}{\sqrt{\Delta^2 - r^2\sin^2\theta}}, \tag{4.92}$$

$$\mathcal{W}_{C_2\ell p}(s_{\min}, s_{\max}, \Delta) = \frac{2\ell+1}{2} \int_0^{\infty} \mathrm{d}r\, r^2 \bar{n}(r) \int_{s_{\min}}^{s_{\max}} \mathrm{d}s \int_{-1}^{1} \mathrm{d}\mu\, \Phi(\theta)\, \bar{n}(r_s) L_\ell(\mu_s) \times \frac{\bar{n}\left(r_s\cos\theta + \sqrt{\Delta^2 - r_s^2\sin^2\theta}\right) L_p(\mu_{\Delta'+}) + \bar{n}\left(r_s\cos\theta - \sqrt{\Delta^2 - r_s^2\sin^2\theta}\right) L_p(\mu_{\Delta'-})}{\sqrt{\Delta^2 - r_s^2\sin^2\theta}}, \tag{4.93}$$

$$\mathcal{W}_{A\ell p}(s_{\min}, s_{\max}, \Delta) = \frac{2\ell+1}{2} \int_0^{\infty} \mathrm{d}r\, r^2 \bar{n}(r) \int_{s_{\min}}^{s_{\max}} \mathrm{d}s \int_{-1}^{1} \mathrm{d}\mu\, \Phi(\theta)\, \bar{n}(r_s) \int_0^{\infty} \mathrm{d}r'\, \bar{n}(r') L_\ell(\mu_s) \times \frac{\bar{n}\left(r'\cos\theta + \sqrt{\Delta^2 - r'^2\sin^2\theta}\right) L_p(\mu_{\Gamma+}) + \bar{n}\left(r'\cos\theta - \sqrt{\Delta^2 - r'^2\sin^2\theta}\right) L_p(\mu_{\Gamma-})}{\sqrt{\Delta^2 - r'^2\sin^2\theta}}, \tag{4.94}$$

ou les expressions des différentes valeurs μ peuvent être trouvés dans PAVIOT et AL. 2021. Nous utilisons une méthode similaire à celle présentée dans BRETON et DE LA TORRE 2021 pour calculer les kernels du modèle complet. Nous construisons d'abord des cartes angulaires HEALPIX (GÓRSKI et AL. 2005) à partir des de la fenêtre d'observations. Ces cartes sont utilisées pour estimer la fonction de corrélation de sélection angulaire, $\Phi(\theta)$, avec le code POLSPICE (SZAPUDI, PRUNET et COLOMBI 2001 ; CHON et AL. 2004). Les $\bar{n}(\chi)$ sont estimés à partir des catalogues aléatoires. Les décalages spectraux sont convertis en distances cosmiques à l'aide d'une cosmologie fiduciaire donnée. À partir de ces deux ingrédients, les kernels peuvent être évalués numériquement à l'aide de méthodes d'intégration Monte-Carlo multidimensionnelles. Plus précisément, nous utilisons la bibliothèque CUBA (T. HAHN 2005) de la même manière que dans BRETON et DE LA TORRE 2021 pour résoudre numériquement les intégrales. Un code permettant de calculer ces kernels pour toute géométrie sera disponible publiquement sur le lien [10]. Une fois les kernels calculés, la

10. https://github.com/mianbreton/RR_code

corrélation croisée et les termes angulaires sont obtenus en intégrant sur Δ les kernels multipliés par la fonction de corrélation standard du modèle. En pratique, cette intégrale est réalisée sous la forme d'une somme de Riemmann. Nous constatons qu'un binning de Δ de 1 Mpc/h est suffisant pour obtenir une estimation numériquement stable du modèle. L'estimation des corrélations de la fonction de sélection $W(s,\mu) \equiv \langle P(\mathbf{s}_1)P(\mathbf{s}_2)\rangle$ se fait suivant la méthode de BRETON et DE LA TORRE 2021. Il est intéressant de voir formellement que la surdensité AMF supprime toute contamination angulaire additive. En effet, si on écrit la surdensité contaminée $\delta(\mathbf{r}) + c(\mathbf{r})$, où c est un champ de contamination qui ne dépend que de la direction de la ligne de visée, on a pour la surdensité AMF fenêtrée,

$$F(\mathbf{r}) = P(\mathbf{r})(\delta(\mathbf{r}) + c(\mathbf{r})) - P(\mathbf{r}) \int \mathrm{d}r' \bar{n}(r')(\delta(\mathbf{r}') + c(\mathbf{r}')) \tag{4.95}$$

$$N = P(\mathbf{r})\delta(\mathbf{r}) - P(\mathbf{r}) \int \mathrm{d}r' \bar{n}(r')\delta(\mathbf{r}'). \tag{4.96}$$

Par définition de c et le fait que $\mathbf{r}$ et $\mathbf{r}'$ partagent la même ligne de visée, $c(\mathbf{r}') = c(\mathbf{r})$. Néanmoins, si le champ de contamination module le nombre de galaxies observé, comme par exemple dans le cas de la variation de la profondeur du relevé ou de l'extinction galactique (SHAFER et HUTERER 2015), des composantes additives et multiplicatives apparaîtront, et la composante multiplicative ne sera pas effacée (elle factorisera $F(\mathbf{r})$).

Test du modèle

Afin de tester notre méthodologie, nous avons comparés les predictions de notre model à la mesure de la fonction de corrélation AMF dans des simulations réalistes. Pour ce faire, nous avons utilisé deux types de simulations : les NSERIES et les EZMOCK. Les NSERIES sont des simulations à N-Corps conçues pour reproduire les propriétés de statistiques à deux point des galaxies CMASS de BOSS. Les simulations à N-Corps évoluent un ensemble de particule de matière noire par gravité, à partir de conditions initiales ($z \approx 100$) spécifiées par un constraste de densité gaussien avec pour variance le spectre de puissance linéaire de la matière, estimé avec CAMB ou CLASS. Ces simulations fournissent à grande échelle des structures similaires à celle observée dans l'Univers : des amas de matière noire, appellés *halo*, connectés entre eux par des filaments. Afin de simuler la formation de galaxie, des es simulations *hydrodynamiques* sont nécéssaires afin d'incorporer les différents effets physiques qui agiront sur la matière baryonique. Cependant ces simulations sont très longues et ne permettent pas actuellement de simuler des volumes assez grand. Une alternative est une approche statistique qui vise à peupler les halos de matière noire des simulations à N-Corps avec des galaxies, appellé le modèle de *distribution d'occupation d'halo* (DOH). Les modèles de DOH décrivent la fonction de distribution de probabilité $P(N_\mathrm{g}|M_\mathrm{h})$ d'avoir un nombre N_g de galaxie dans des halos de masse M_h. Cette probabilité est souvent répartie entre les galaxies centrales et les galaxies satellites, orbitant autour des galaxies centrales, de sorte que

$$\langle N_\mathrm{g}|M_\mathrm{h}\rangle = \langle N_\mathrm{cen}|M_\mathrm{h}\rangle + \langle N_\mathrm{sat}|M_\mathrm{h}\rangle. \tag{4.97}$$

Pour fournir cette description, il faut supposer une loi de probabilité complète (Poisson, Gaussienne, binomiale négative, etc., voir AVILA et AL. 2020 et ROSSI et AL. 2021) pour les galaxies centrales et satellites. Les modèles et paramètres DOH peuvent également être adaptés à des modèles semi-analytiques de formation de galaxies (AVILA et AL. 2020) ou aux propriétés d'assemblages. Une fois les halos peuplés, on peut par la suite effectuer une analyse de BAO et RSD sur l'ensemble de galaxies. Les EZMOCK sont un ensemble de simulations approximé basé sur la théorie des pertubations Lagrangiene à l'ordre 1 : l'approximation de Zel'Dovich. Ces simulations sont très rapides, et reproduisent dans l'espace des décalages spectraux, le monopole ($\ell = 0$) et le quadrupole ($\ell = 2$) de la fonction de corrélation à deux points des galaxies à 1% pour $s < 10h^{-1}$Mpc. Elles sont

utilisées afin de fournir des matrices de covariances réalistes pour l'analyse des galaxies eBOSS. Dans la suite de ce résumé, je vais seulement présenter les résultats pour les simulations les plus précises : les NSERIES.

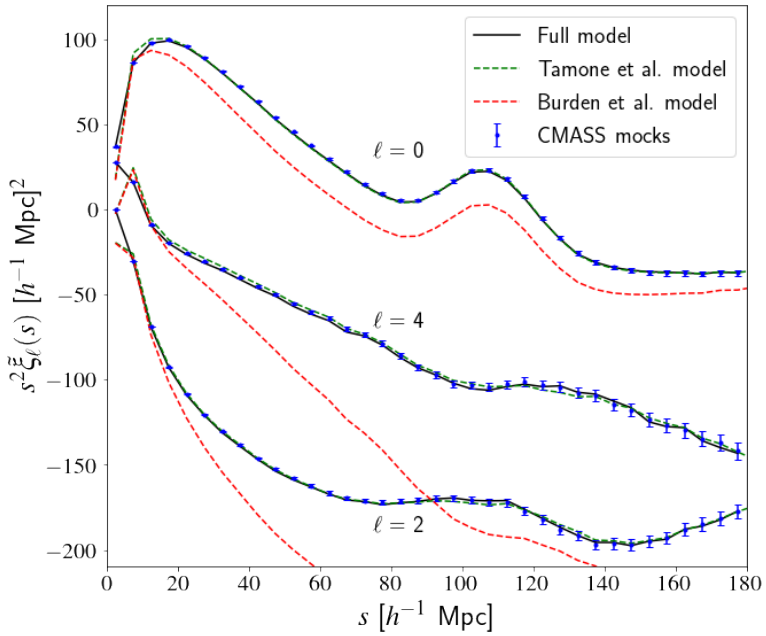

FIGURE 4.34 – Comparaison entre les prédictions des modèles AMF du monopole, quadripôle et hexadécapôle ($\ell = 4$) et de la mesure moyenne des mocks CMASS. La ligne noire continue correspond au modèle complet, la ligne verte à pointillés courts au modèle TAMONE et AL. 2020, et la ligne rouge à pointillés longs à l'ansatz original BURDEN et AL. 2017.

Je présente dans la Fig. 4.34 la comparaison entre l'ansatz original de BURDEN et AL. 2017, le modèle utilisé dans TAMONE et AL. 2020, le modèle complet présenté dans cet article, et les prédictions fictives. Nous pouvons voir que l'ansatz original ne permet de récupérer que qualitativement les moments mutipolaires de la fonction de corrélation de l'AMF simulée, avec un décalage significatif de l'amplitude. Inversement, le TAMONE et AL. 2020, et le modèle complet fournissent des prédictions similaires, très proches de la mesure fictive. En examinant de près les différences entre ces deux modèles, on constate que le modèle complet est le plus performant, en particulier aux plus petites échelles du monopole et de l'hexadécapole. Il est utile de rappeler que le modèle TAMONE et AL. 2020, possède un paramètre libre, $\tilde{\chi}$, que nous avons optimisés ici pour reproduire au mieux la fonction de corrélation AMF simulée mesurée.

Nous avons ensuite effectué une analyse de BAO et de RSD des fonctions de corrélations à deux points AMF et standard. La modélisation des RSD et des BAO AMF s'effectue en utilisant l'Eq. 4.87 avec pour argument le modèle théorique ξ donné par Eq. 4.63) et Eq. 4.72. L'inférence des paramètres cosmologiques est effectuée au moyen de l'analyse de vraisemblance des données. La vraisemblance $\mathscr{L}$ est supposée être gaussienne

$$-2\ln\mathscr{L}(\theta) = \sum_{i,j}^{N_p} \vec{\Delta}_i(\theta)\hat{\Psi}_{ij}\vec{\Delta}_j(\theta), \tag{4.98}$$

où θ est le vecteur des paramètres, $\vec{\Delta}$ est le vecteur de différence données-modèle et N_p est le nombre total de points que l'on cherche à modéliser. Une estimation de la matrice de précision $\hat{\Psi} = (1-D)\hat{C}^{-1}$ est obtenue à partir de la covariance $\hat{C}$ de 2048 simulations MD-PATCHY, des simulations approximés qui ont la même fênetre d'observation et distribution radiale que les NSERIES, où

Tableau 4.19 – Résultats des BAO et RSD pour les simulations NSERIES. Nous assumons comme cosmologie fiduciaire la cosmologie de la simulation donnée par $\Omega_m = 0.286, \Omega_b = 0.047, \Omega_\nu = 0, h = 0.7, n_s = 0.96, \sigma_8 = 0.823$. Nous nous attendons donc à ce que les paramètres de distorsion, $\alpha_\parallel$ et $\alpha_\perp$, soient égaux à 1. Pour le taux de croissance, la valeur attendue est $f\sigma_8 = 0.469$.

Method	$\alpha_\perp$	$\alpha_\parallel$	$f\sigma_8$
RSD standard	0.9972 ± 0.0019	1.0032 ± 0.0032	0.4700 ± 0.0044
RSD AMF	0.9962 ± 0.0023	0.9987 ± 0.0038	0.4686 ± 0.0067
BAO standard	1.0056 ± 0.0022	1.0007 ± 0.0044	
BAO AMF	1.0043 ± 0.0026	1.0011 ± 0.0046	

$D = (N_p + 1)/(N_{\text{mocks}} - 1)$. Les moments monopole, quadripôle et hexadécapôle sont adaptés au modèle TNS dans la plage $25 < r < 150\ h^{-1}$Mpc.

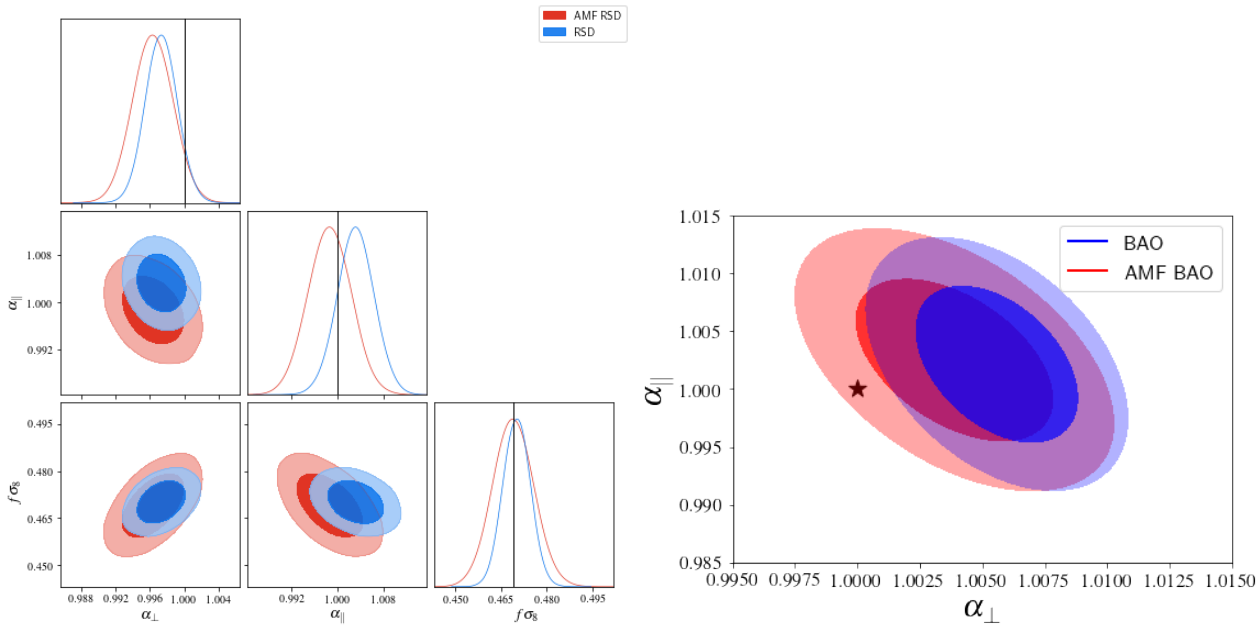

FIGURE 4.35 – Posterior likelihood contours on $\alpha_\parallel$, $\alpha_\perp$ and $f\sigma_8$ obtained when fitting standard (blue) and AMF (red) multipole moments in the full-shape RSD analysis on the CMASS sample

Les contraintes sur $\alpha_\parallel, \alpha_\perp, f\sigma_8$ que nous obtenons sont données dans le Tableau 4.19. Nous constatons que la fonction de corrélation AMF, comparée à la fonction de corrélation standard, fournit une estimation non biaisée de $f\sigma_8$ et de $\alpha_\perp$. La valeur centrale de $\alpha_\parallel$ récupérée présente un léger décalage de $1{,}4\sigma$ par rapport à l'analyse standard, mais elle est néanmoins proche de la valeur de référence, tout comme l'analyse standard. Les erreurs statistiques de 1σ obtenues sur les paramètres dans l'analyse AMF sont augmentées de 20%, 10% et 50% pour $\alpha_\parallel$, $\alpha_\perp$, et $f\sigma_8$ respectivement. Les contours de probabilité postérieure pour toutes les combinaisons de paramètres sont illustrés sur l'image de gauche de la Fig. 4.35. Ces contours sont obtenus avec l'échantillonneur d'ensemble ZEUS (KARAMANIS et AL. 2020 ; KARAMANIS et AL. 2021). Nous pouvons voir que, bien que l'analyse AMF montre des contours plus larges par rapport à l'analyse standard, les directions de dégénérescence entre les paramètres sont les mêmes.

Nous effectuons ensuite une analyse des BAO uniquement sur les fonctions de corrélation standard et AMF simulées moyennes. Nous ne considérons ici que les fonctions de corrélation sans schéma de reconstruction. Nous ajustons le monopôle et le quadripôle dans la plage $40 < s <$

150 h^{-1}Mpc. Les contraintes que nous obtenons sur $\alpha_\parallel$ et $\alpha_\perp$ sont données dans le Tableau 3.3. Les valeurs centrales sur $\alpha_\parallel$ et $\alpha_\perp$ sont à moins de 1σ de celle de l'analyse standard. L'incertitude statistique sur les paramètres augmente de moins de 5%. Dans l'ensemble, l'analyse BAO seule de la fonction de corrélation de l'AMF est presque aussi efficace que l'analyse BAO standard de pré-reconstruction. Les contours de probabilité postérieure conjointe pour $\alpha_\parallel$ et $\alpha_\perp$ sont présentés sur l'image de droite de la Fig. 4.35. Ces contours ont été calculés à l'aide de l'algorithme de minimisation IMINUIT [11]

Par construction, la fonction de corrélation à deux points AMF est moins contraignante que la fonction de corrélation standard. Néanmoins, cette approche peut être avantageusement utilisée dans le cas d'échantillons inhomogènes, ou dans le cas de relevés avec une fonction de sélection angulaire complexe et mal comprise (TAMONE et AL. 2020). Enfin, il est important de souligner que l'approche AMF est complémentaire à l'approche standard, dans le sens où elle peut être utilisée comme un test de validation croisée. En effet, elle permet d'étudier l'impact des erreurs systématiques angulaires dans l'analyse standard et peut être utilisée comme référence pour vérifier si toutes les erreurs systématiques angulaires sont bien prises en compte. Si l'on constate que les paramètres cosmologiques récupérés sont les mêmes avec les deux approches, on valide l'exactitude du schéma de correction du biais observationnel utilisé dans l'analyse standard.

4.8 L'analyse cosmologique des galaxies rouges lumineuses

Je vais maintenant résumé l'analyse cosmologique des galaxies lumineuses rouges (LRG) observés par eBOSS et BOSS [12].

4.8.1 Mesures des BAO et des RSD

Avant de mesurer les paramètres cosmologiques $\alpha_\perp, \alpha_\parallel$ et $f\sigma_8$ à partir des observations, il est nécessaire de déterminer avec soin les biais potentiels induit par notre méthodologie. Spécifiquement, il existe quatre sources de biais majeures qui vont influencuer notre mesure

— Biais de modélisation. Ce biais est déterminé en mesurant les paramètres cosmologiques sur les simulations. Dans ce cas, on assume comme cosmologie fiduciaire la cosmologie de la simulation, et les différences observés sont directement due à la modélisation des RSD et des BAO.
— Biais de cosmologie. Nous avons observer une dépendance entre la cosmologie fiduciaire assumée, et la mesure de paramètres cosmologiques. Nous avons pu réduire cette dépendance d'un facteur 2 sur $f\sigma_8$ en modifiant la valeur de σ_8, comme expliqué dans la Section 4.6.4.
— Biais observationnels. Les poids introduits dans l'Eq. 4.80 afin de corriger les différents effets observationnels ne sont pas parfaits. Afin de déterminer le potentiel biais introduit par cette méthode, nous avons mesuré les paramètres cosmologiques sur des simulations avec et sans poids. La différence relative entre les deux mesures nous fournit l'écart attendue pour les données.
— Biais lié à l'effet de contrainte intégrale radiale. Cet effet n'a pas été modélisé, car faible pour notre catalogue de galaxie. En analysant des simulations avec et sans RIC, on peut le quantifier simplement.

Les biais dûes à la modélisation et à la cosmologie fiduciaire ont été déterminés à partir des simulations NSERIES, bien plus réaliste et fiable que les EZMOCK. Les biais observationnelles et liée à la RIC ont été testé sur les EZMOCKS, car ils correspondent à des effets géometriques qui ne

11. https://iminuit.readthedocs.io/
12. 25 % des galaxies CMASS sont néanmoins bleu. Pour faciliter les notations, nous omettrons ce détail

Tableau 4.20 – Résumé des erreurs systématiques obtenues avec les modèle TNS à partir de tests avec les simulations NSERIES et EZMOCK catalogues fictifs. L'erreur systématique totale $\sigma_{\rm syst}$ est la somme quadratique de chaque contribution. Les dernières lignes affichent l'erreur finale qui est une somme quadratique d'erreurs statistiques et erreurs systématiques.

Type	$\sigma_{\alpha_\perp}$	$\sigma_{\alpha_\parallel}$	$\sigma_{f\sigma_8}$
Modelling	0.004	0.006	0.009
Fid. cosmology	0.005	0.008	0.012
Obs. effects	0.010	0.014	0.018
$\sigma_{\rm syst}$	0.012	0.017	0.023
$\sigma_{\rm stat}$	0.018	0.031	0.040
$\sigma_{\rm syst}/\sigma_{\rm stat}$	0.65	0.55	0.58
$\sigma_{\rm tot} = \sqrt{\sigma^2_{\rm syst} + \sigma^2_{\rm stat}}$	0.021	0.035	0.046

demande pas une description précise du clustering des galaxies afin d'être quantifier. Nous avons également étudier le biais introduit par la méthode de population d'halo à partir des simulation OUTERRIM (HEITMANN et AL. 2019; ROSSI et AL. 2021). Nous n'avons pas trouvé de biais majeur concernant ce paramètre. Pour les BAO seul le biais induit par la modélisation est non-négligeable, il a été montrer par (CARTER et AL. 2020) que l'effet de la cosmologie fiduciaire est très faible. Les effets de RIC et de systématiques observationnels sont également faible (BAUTISTA et AL. 2021). Les biais systématiques avec le modèle de BAO (en post-reconstruction) sont

$$\text{BAO}: \ \sigma_{\rm syst,model} = (0.0014, 0.0021), \tag{4.99}$$

très faible par rapport aux erreurs statistiques des données. Nous présentons sur la Table 4.20 les biais introduits sur l'analyse de forme complète de la fonction de corrélation à deux points des galaxies pour le modèle TNS. Les erreurs les plus importantes sont les erreurs liées aux effets d'observations, qui répresente environ 50 % des erreurs statistiques totales pour chaque paramètre. L'erreur systémaique totale est calculé en additionnant toutes les contributions en quadrature, en supposant qu'elles sont toutes indépendantes. En comparant les erreurs systématiques avec l'erreur statistique provenant des ajustements de base aux données, nous constatons que les erreurs systématiques sont loin d'être négligeables : plus de 50 pour cent des erreurs statistiques pour tous les paramètres. Les erreurs systématiques sont ajoutés en quadrature à la diagonale de la covariance de chaque mesure. Nous ne cherchons pas à calculer la covariance entre les erreurs systématiques et cette approche est plus conservatrice (elle ne sous-estime pas les erreurs). Je présente sur la Fig. 4.36 les résultats finaux de ce travail obtenus par la combinaison des analyses BAO et RSD dans les espaces de configuration et de Fourier (voir GIL-MARIN et AL. 2020 pour plus de détail sur l'analyse de l'espace de Fourier). Les mesures de $\alpha_\perp$ et $\alpha_\parallel$ ont été convertis en mesures de D_m/r_d et D_H/r_d avec $D_H = c/H(z)$. Ces mesures concordent bien avec les prédictions de PLANCK COLLABORATION 2018, qui prévoient à $z_{\rm eff} = 0.698$: 17.48, 20.23 et 0.462, respectivement, pour un modèle ΛCDM plat supposant que la gravité est décrite par la relativité générale. Ces valeurs sont représentées par l'étoile sur la Fig. 4.36. Les erreurs sur D_m/r_d, D_H/r_d, $f\sigma_8$ sont respectivement de 1.7, 2.4 et 9.4 %, les mesures les plus précises à nos jour à ce décalage spectral.

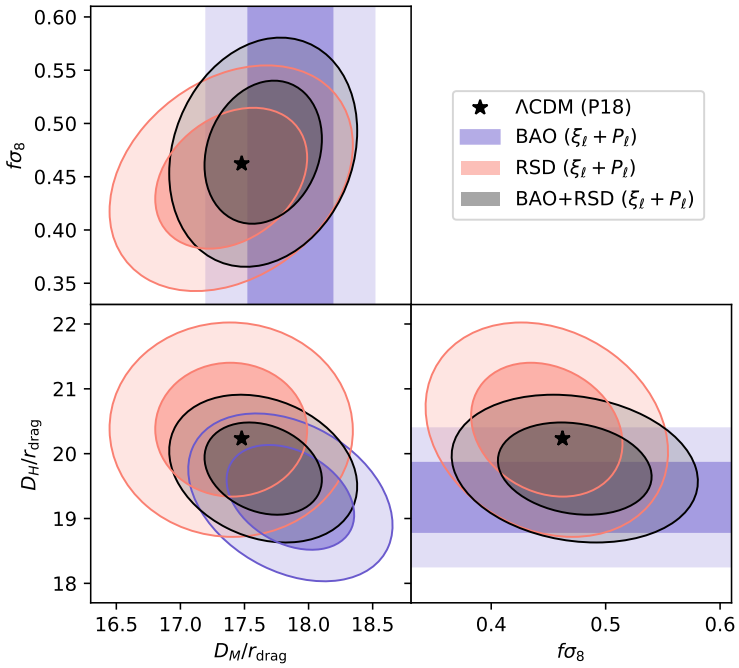

FIGURE 4.36 – Mesure finales de $D_M/r_d, D_H/r_d, f\sigma_8$ à un décalage vers le rouge effectif de $z = 0.698$. L'étoile montre la prédiction de Planck.

$$\mathbf{D}_{\rm LRG} = \begin{pmatrix} D_M/r_d \\ D_H/r_d \\ f\sigma_8 \end{pmatrix} = \begin{pmatrix} 17.65 \pm 0.30 \\ 19.77 \pm 0.47 \\ 0.473 \pm 0.044 \end{pmatrix} \tag{4.100}$$

4.8.2 Implications cosmologiques de SDSS

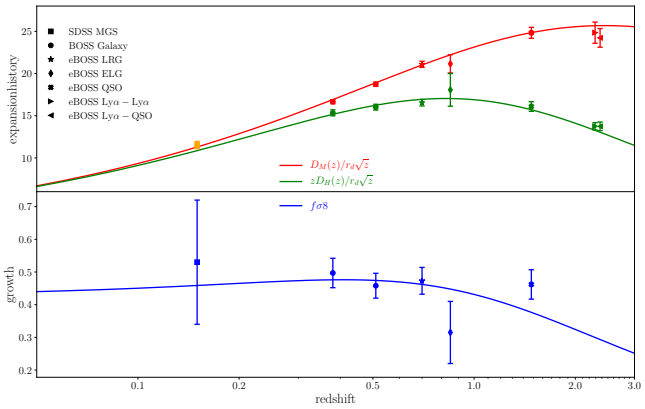

FIGURE 4.37 – SDSS BAO and growth rate measurements used in the final cosmological analysis. The continuous lines corresponds to Planck prediction for a flat ΛCDM cosmology (PLANCK COLLABORATION 2018). The MGS D_v measurement plotted in orange have been translated to a D_M measurement for a flat ΛCDM model for illustration. Taken from (EBOSS COLLABORATION 2021)

Les mesures du taux d'expansion et du taux d'accroissement de BOSS et eBOSS, présentés sur la Fig. 4.37, ont été combinées avec les observations du CMB de PLANCK COLLABORATION 2018,

des supernovas SCOLNIC et AL. 2018, et avec la première année des observations de cisaillement cosmique, de clustering et de lensing galaxie-galaxie de DES ABBOTT et AL. 2018. Cette section est basée sur le papier de EBOSS COLLABORATION 2021.

Je présente sur la Fig. 4.38 les contours de la température et de la polarisation de BAO, du SN et du CMB (les informations sur l'effet de lentille du CMB sont surtout utiles pour le test de gravité) dans le plan $\Omega_{\rm m} - \Omega_\Lambda$, et la combinaison de ces mesures dans le plan $\Omega_{\rm m} - \Omega_{\rm K}$. La combinaison des mesures BAO à différents décalages vers le rouge nous permet de rompre la dégénérescence entre Ω_m et $\Omega_{\rm K}$, ce qui donne $\Omega_\Lambda = 0.637^{0.084}_{0.074}$, avec une précision bien meilleure que la mesure SN seule $\Omega_\Lambda = 0.73 \pm 0.11$. Les deux sondes cosmologiques sont compatibles avec un Univers plat. En combinant la mesure de BAO avec le T&P de Planck (qui favorise un Univers fermé), le paramètre de courbure est poussé vers zéro, ce qui donne $\Omega_{\rm K} = -0.0001 \pm 0.0018$, en excellent accord avec un Univers plat. Les données BAO et SN peuvent également être utilisées pour établir des contraintes sur H_0 à travers l'échelle de distance inverse. Plus précisément, étant donné une valeur de r_d, les BAO fournissent des mesures de distances cosmologiques qui permettent de calibrer les distances de luminosité des SN pour contraindre H_0. Étant donné une température moyenne du CMB dans le cadre du modèle standard de nucléosynthèse du Big Bang (BBN), on peut déduire la valeur de r_d à partir de $\omega_{\rm c}$ et $\omega_{\rm b}$. En calibrant ces paramètres à partir des observations T&P du CMB, les BAO et SN fournissent des contraintes précise sur la valeur actuelle du taux d'expansion, $H_0 = 67.35 \pm 0.97$ km s^{-1} Mpc^{-1}. Comme nous pouvons le voir sur la Fig. 4.19, la mesure de H_0 est stable par rapport à l'énergie sombre et à l'hypothèse de courbure, donnant $H_0 = 67,87 \pm 0,86$ km s^{-1} Mpc^{-1} pour un modèle o$w_0 w_a CDM$ (un modèle CDM avec l'équation d'état de l'énergie noire et la curvature libre), en excellent accord avec la valeur de H_0 cité juste avant.

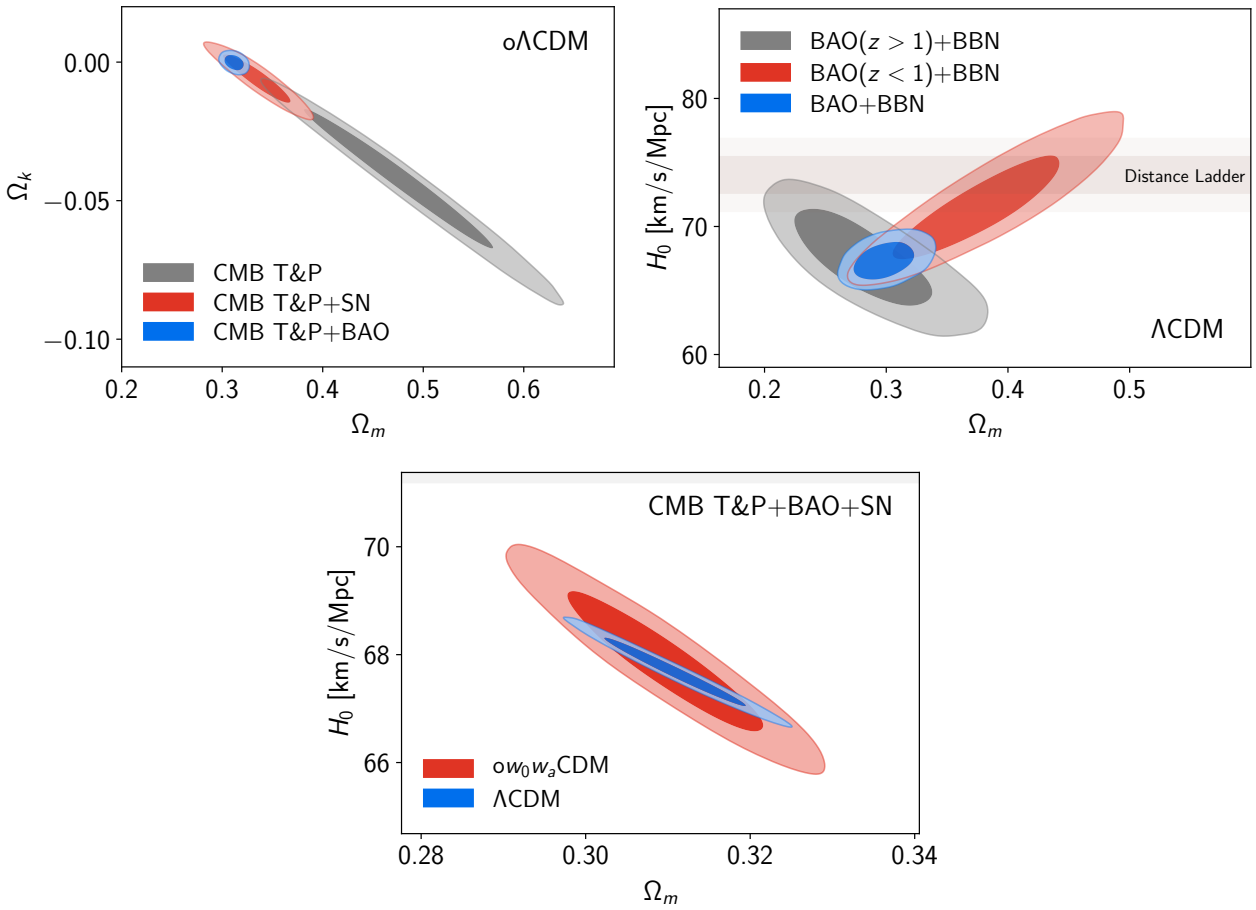

FIGURE 4.38 – Contraintes cosmologiques sous l'hypothèse d'un modèle ΛCDM avec un $w = -1$ à courbure libre (oΛCDM) En haut à gauche : contraintes à 68 % et 95 % sur le modèle $\Omega_m - \Omega_\Lambda$, à partir des données de température et de polarisation du CMB de Planck (en gris), de l'échantillon Pantheon SNe Ia (rouge), et des mesures SDSS BAO uniquement (bleu). La ligne pointillée représente un modèle à courbure nulle. En haut à droite : Contraintes dans le plan H_0-Ω_m,contraintes avec un BBN prior sur la densité baryonique. En bas : H_0-Ω_m pour le modèle ΛCDM et le modèle ow_0w_aCDM. Tiré de (EBOSS COLLABORATION 2021)

Les mesures de RSD sont un moyen puissant de contraindre l'équation d'état de l'énergie noire. Une valeur de w plus faible implique une accélération cosmique plus importante, et donc une valeur de $f\sigma_8$ plus faible à faible décalage vers le rouge. Par conséquent, la RSD réduit l'incertitude sur w de plus d'un facteur deux par rapport aux données du CMB, comme nous pouvons le voir dans l'image de droite de la Fig. 4.39 donnant $w = -1.09 \pm 0.11$ entièrement compatible avec une constante cosmologique. La croissance des structures est également un outil puissant pour tester la variation par rapport à la GR. En suivant la notation de (ABBOTT et AL. 2018), nous introduisons les paramètres $\mu(a)$ et $\Sigma(a)$ de sorte que les équations de Poisson 4.44 prennent les formes suivantes

$$k^2\Phi = -4\pi G a^2(1+\mu)\bar{\rho}\delta \tag{4.101}$$

$$k^2(\Phi+\Psi) = -8\pi G a^2(1+\Sigma)\bar{\rho}\delta \tag{4.102}$$

où nous rappelons que Ψ et Φ sont le potentiels de Bardeen (BARDEEN 1980) et sont liés à la partie temporelle et spatiale de la métrique. La dépendance temporelle de $\mu(a)$ et $\Sigma(a)$ est paramétrée comme suit

$$\mu(a) = \mu_0 \frac{\Omega_\Lambda(a)}{\Omega_\Lambda}, \quad \Sigma(a) = \Sigma_0 \frac{\Omega_\Lambda(a)}{\Omega_\Lambda} \tag{4.103}$$

En relativité générale, $\Psi = \Phi$ et donc $\mu_0 = \Sigma_0 = 0$.

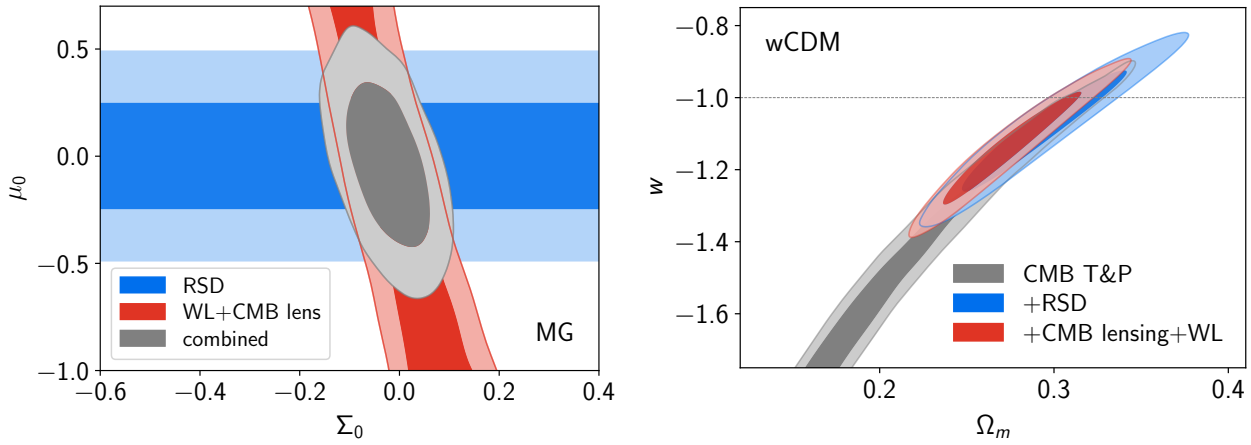

FIGURE 4.39 – Les contraintes $\Sigma_0 - \mu_0$ pour une cosmologie avec une constante cosmologique fixe et un espace plat, $K = 0$. Contours bleus pour RSD, rouges pour DES WL + lentille de Planck, tandis que les contours gris représentent la combinaison des trois postérités. Tiré de (EBOSS COLLABORATION 2021).

Dans la limite non relativiste, les RSD ne sont sensiblent qu'à Φ et ne peuvent que contraindre μ_0. Les mesures de lentille faible sondent la propagation de la lumière sensible à $\Psi + \Phi$ et peuvent donc contraindre Σ_0. Comme nous pouvons le voir sur la Fig. 4.39, la combinaison des mesures de RSD et de l'effet de lentille donne $\mu_0 = 0.04 \pm 0.25$ et $\Sigma_0 = 0.024 \pm 0.054$, en accord avec la théorie de la relativité générale.
Il est également intéressant de vérifier si nos mesures sont en accord avec le modèle ΛCDM standard. Pour ce faire, nous assumons un modèle avec une paramétrisation modifiée de l'énergie noire donnée par CHEVALLIER et POLARSKI 2001, $w(a) = w_0 + (1-a)w_a$. Dans le cas d'une constante cosmologique, $w_a = 0$ et $w_0 = -1$.. De plus nous laissons la curvature libre dans notre analyse. Les résultats sont présentés sur la Fig. 4.40. Les mesures sont cohérentes avec un modèle plat ΛCDM : w_0, w_a et Ω_k sont éloignés de 1,1, 1,3 et 1,0 σ de -1, 0 et 0 respectivement. On peut observer l'impact important des BAO et des RSD dans la détermination de la curvature Ω_k et dans la détermination de l'équation d'état de l'énergie noire w. Bien qu'en accord avec le modèle standard, ces mesures ont de larges barres d'erreurs. Les sondages futurs tels que DESI DESI COLLABORATION 2016 ou Euclid AMENDOLA et AL. 2018 observeront une centaines de fois plus de décalage spectral que les sondages BOSS et eBOSS cumulés. Avec cette précision, il sera vraiment possible de discriminer entre les différents modèles cosmologiques afin de mieux comprendre la nature de la gravité et celle de l'énergie noire. D'ici là, il est important de comprendre et de corriger le mieux possible les erreurs systématiques que nous avons décrits précèdemmment.

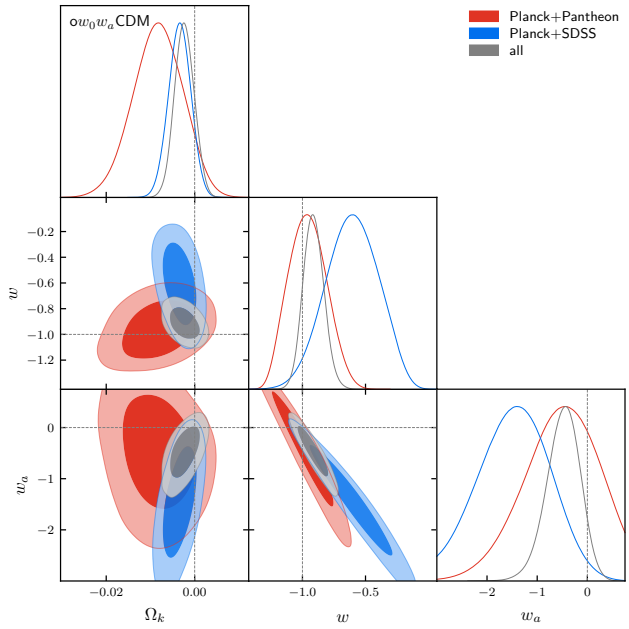

FIGURE 4.40 – Contours sur w_0, w_a, et Ω_k. Les contours rouges représentent les contraintes de Planck et Panthéon. Les contours bleus représentent les contraintes de Planck et SDSS BAO+RSD, tandis que les contours gris représentent la combinaison de toutes les mesures. Tiré de (EBOSS COLLABORATION 2021).

Table des figures

Liste des tableaux

Bibliographie

[Aa04] Kevork ABAZAJIAN et AL. « The Second Data Release of the Sloan Digital Sky Survey ». In : *Astrophysical Journal* 128.1 (juil. 2004), p. 502-512. DOI : 10.1086/421365. arXiv : astro-ph/0403325 [astro-ph] (cf. p. 100).

[Aa18a] T ABBOTT et AL. « Dark Energy Survey year 1 results : Cosmological constraints from galaxy clustering and weak lensing ». In : *Physical Review D* 98.4, 043526 (août 2018), p. 043526. DOI : 10.1103/PhysRevD.98.043526. arXiv : 1708.01530 [astro-ph.CO] (cf. p. 168, 171, 180, 205, 206).

[Aa01] Qasid AHMAD et AL. « Measurement of the Rate of $\nu_e + d \rightarrow p + p + e^-$ Interactions Produced by 8B Solar Neutrinos at the Sudbury Neutrino Observatory ». In : *Physical Review Letters, vol. 87, Issue 7, id. 071301* (2001). DOI : 10.1103/PhysRevLett.87.071301 (cf. p. 36).

[Aa20a] Romina AHUMADA et AL. « The 16th Data Release of the Sloan Digital Sky Surveys : First Release from the APOGEE-2 Southern Survey and Full Release of eBOSS Spectra ». In : *The Astrophysical Journal Supplement Series* 249.1, 3 (juil. 2020), p. 3. DOI : 10.3847/1538-4365/ab929e. arXiv : 1912.02905 [astro-ph.GA] (cf. p. 104).

[Aa11] Hiroaki AIHARA et AL. « The Eighth Data Release of the Sloan Digital Sky Survey : First Data from SDSS-III ». In : *The Astrophysical Journal Supplement, Volume 193, Issue 2, article id. 29, 17 pp. (2011).* (2011). DOI : 10.1088/0067-0049/193/2/29 (cf. p. 99, 114).

[Aa17] Shadab ALAM et AL. « The clustering of galaxies in the completed SDSS-III Baryon Oscillation Spectroscopic Survey : cosmological analysis of the DR12 galaxy sample ». In : *Monthly Notices of the Royal Astronomical Society, Volume 470, Issue 3, p.2617-2652* (2017). DOI : 10.1093/mnras/stx72 (cf. p. 85, 86, 108, 148, 159, 167, 168).

[Aa06a] Andreas ALBRECHT et AL. « Report of the Dark Energy Task Force ». In : *arXiv e-prints*, astro-ph/0609591 (sept. 2006), astro-ph/0609591. arXiv : astro-ph/0609591 [astro-ph] (cf. p. 169, 178).

[AP01] Charles ALCOCK et Bohdan PACZYŃSKI. « An evolution free test for non-zero cosmological constant ». In : *Nature volume 281, pages358–359* (2001). DOI : https://doi.org/10.1038/281358a0 (cf. p. 85).

[Ald81] Robert ALDER. « The Geometry of Random Fields ». In : (1981) (cf. p. 66).

[Alo12] David ALONSO. « CUTE solutions for two-point correlation functions from large cosmological datasets ». In : *arXiv e-prints*, arXiv :1210.1833 (oct. 2012), arXiv :1210.1833. arXiv : 1210.1833 [astro-ph.IM] (cf. p. 107).

[Aa18b] Luca AMENDOLA et AL. « Cosmology and fundamental physics with the Euclid satellite ». In : *Living Reviews in Relativity* 21.1, 2 (avr. 2018), p. 2. DOI : 10.1007/s41114-017-0010-3. arXiv : 1606.00180 [astro-ph.CO] (cf. p. 66, 169, 207).

[Aa14a] Lauren ANDERSON et AL. « The clustering of galaxies in the SDSS-III Baryon Oscillation Spectroscopic Survey : measuring D_A and H at z = 0.57 from the baryon acoustic peak in the Data Release 9 spectroscopic Galaxy sample ». In : *Monthly Notices of the Royal Astronomical Society* 439.1 (mar. 2014), p. 83-101. DOI : 10.1093/mnras/stt2206. arXiv : 1303.4666 [astro-ph.CO] (cf. p. 87).

[Aa14b] Valentin ASSASSI et AL. « Renormalized halo bias ». In : *Journal of Cosmology and Astroparticle Physics, Issue 08, article id. 056* (2014). DOI : 10.1088/1475-7516/2014/08/056 (cf. p. 63, 74, 84, 90, 189).

[Aa06b] P ASTIER et AL. « The Supernova Legacy Survey : measurement of Ω_M, Ω_Λ and w from the first year data set ». In : *Astronomy and Astrophysics* 447.1 (fév. 2006), p. 31-48. DOI : 10.1051/0004-6361:20054185. arXiv : astro-ph/0510447 [astro-ph] (cf. p. 18).

[Aa20b] Marie AUBERT et AL. « The Completed SDSS-IV Extended Baryon Oscillation Spectroscopic Survey : Growth rate of structure measurement from cosmic voids ». In : *arXiv e-prints*, arXiv :2007.09013 (juil. 2020), arXiv :2007.09013. arXiv : 2007.09013 [astro-ph.CO] (cf. p. 90).

[Aa15] Erik AVER et AL. « The effects of He I λ10830 on helium abundance determinations ». In : *Journal of Cosmology and Astroparticle Physics, Issue 07, article id. 011, (2015)* (2015). DOI : 10.1088/1475-7516/2015/07/011 (cf. p. 37).

[Aa20c] S. AVILA et AL. « The Completed SDSS-IV extended Baryon Oscillation Spectroscopic Survey : exploring the halo occupation distribution model for emission line galaxies ». In : *Monthly Notices of the Royal Astronomical Society* 499.4 (déc. 2020), p. 5486-5507. DOI : 10.1093/mnras/staa2951. arXiv : 2007.09012 [astro-ph.CO] (cf. p. 96, 199).

[Bah96] Neta BAHCALL. « Clusters and superclusters of galaxies ». In : (1996). URL : arXiv:astro-ph/9611148 (cf. p. 37).

[Bar80] James BARDEEN. « Gauge-invariant cosmological perturbations ». In : *Phys. Rev. D 22, 1882* (1980). DOI : https://doi.org/10.1103/PhysRevD.22.1882 (cf. p. 51, 75, 206).

[Ba18a] Julian BAUTISTA et AL. « The SDSS-IV Extended Baryon Oscillation Spectroscopic Survey : Baryon Acoustic Oscillations at Redshift of 0.72 with the DR14 Luminous Red Galaxy Sample ». In : *Astrophysical Journal* 863.1, 110 (août 2018), p. 110. DOI : 10.3847/1538-4357/aacea5. arXiv : 1712.08064 [astro-ph.CO] (cf. p. 87, 103, 112-115, 165, 196).

[Ba21] Julian BAUTISTA et AL. « The completed SDSS-IV extended Baryon Oscillation Spectroscopic Survey : measurement of the BAO and growth rate of structure of the luminous red galaxy sample from the anisotropic correlation function between redshifts 0.6 and 1 ». In : *Monthly Notices of the Royal Astronomical Society, Volume 500, Issue 1, pp.736-762* (2021). DOI : 10.1093/mnras/staa2800 (cf. p. 70, 72, 76, 87, 89, 103, 104, 111, 135, 140, 168, 180, 181, 190-192, 194, 203).

[Ba18b] Julien BEL et AL. « Accurate fitting functions for peculiar velocity spectra in standard and massive-neutrino cosmologies ». In : *Astronomy Astrophysics, Volume 622, id.A109, 8 pp.* (2018). DOI : 10.1051/0004-6361/201834513 (cf. p. 71, 73, 190).

[Ba13] C. L. BENNETT et AL. « Nine-year Wilkinson Microwave Anisotropy Probe (WMAP) Observations : Final Maps and Results ». In : *The Astrophysical Journal Supplement* 208.2, 20 (oct. 2013), p. 20. DOI : 10.1088/0067-0049/208/2/20. arXiv : 1212.5225 [astro-ph.CO] (cf. p. 176).

[Ba20] José BERNAL et AL. « Robustness of baryon acoustic oscillation constraints for early-Universe modifications of Λ CDM cosmology ». In : *Physical Review D, Volume 102, Issue 12, article id.123515* 102.12, 123515 (déc. 2020), p. 123515. DOI : 10.1103/PhysRevD.102.123515. arXiv : 2004.07263 [astro-ph.CO] (cf. p. 144).

[Ba02] F BERNARDEAU et AL. « Large-scale structure of the Universe and cosmological perturbation theory ». In : *Physics Reports* 367.1-3 (sept. 2002), p. 1-248. DOI : 10.1016/S0370-1573(02)00135-7. arXiv : astro-ph/0112551 [astro-ph] (cf. p. 44, 63-65, 68, 89, 187, 189).

[Ba08] Francis BERNARDEAU et AL. « Multipoint propagators in cosmological gravitational instability ». In : *Physical Review D* 78.10, 103521 (nov. 2008), p. 103521. DOI : 10.1103/PhysRevD.78.103521. arXiv : 0806.2334 [astro-ph] (cf. p. 69).

[Ba14a] M. BETOULE et AL. « Improved cosmological constraints from a joint analysis of the SDSS-II and SNLS supernova samples ». In : *Astronomy Astrophysics* 568, A22 (août 2014), A22. DOI : 10.1051/0004-6361/201423413. arXiv : 1401.4064 [astro-ph.CO] (cf. p. 176).

[Ba14b] Marc BÉTOULE et AL. « Improved cosmological constraints from a joint analysis of the SDSS-II and SNLS supernova samples ». In : *Astronomy Astrophysics, Volume 568, id.A22, 32 pp* (2014). DOI : 10.1051/0004-6361/201423413 (cf. p. 18).

[BP17] Davide BIANCHI et Will PERCIVAL. « Unbiased clustering estimation in the presence of missing observations ». In : *Monthly Notices of the Royal Astronomical Society* 472.1 (nov. 2017), p. 1106-1118. DOI : 10.1093/mnras/stx2053. arXiv : 1703.02070 [astro-ph.CO] (cf. p. 116).

[Ba03] Michael BLANTON et AL. « An Efficient Targeting Strategy for Multiobject Spectrograph Surveys : the Sloan Digital Sky Survey "Tiling" Algorithm ». In : *The astrophysical Journal* 125.4 (avr. 2003), p. 2276-2286. DOI : 10.1086/344761. arXiv : astro-ph/0105535 [astro-ph] (cf. p. 103).

[Blo10] W.J.G de BLOK. « The Core-Cusp Problem ». In : *Advances in Astronomy, 2010, article id. 789293* (2010). DOI : 10.1155/2010/789293 (cf. p. 39).

[Ba12] Adam BOLTON et AL. In : *Astrophysical Journal* 144.5, 144 (nov. 2012), p. 144. DOI : 10.1088/0004-6256/144/5/144. arXiv : 1207.7326 [astro-ph.CO] (cf. p. 103, 104).

[Bou96] F. R. BOUCHET. « Introductory Overview of Eulerian and Lagrangian Perturbation Theories ». In : *Dark Matter in the Universe*. Sous la dir. de S. BONOMETTO, J. R. PRIMACK et A. PROVENZALE. Jan. 1996, p. 565. arXiv : astro-ph/9603013 [astro-ph] (cf. p. 64).

[BM14] David BRANCH et Douglas.L MILLER. « Type IA Supernovae as Standard Candles ». In : *Astrophysical Journal Letters v.405, p.L5* (2014). DOI : 10.1086/186752 (cf. p. 19).

[Ba19] Michel-Andrès BRETON et AL. « Imprints of relativistic effects on the asymmetry of the halo cross-correlation function : from linear to non-linear scales ». In : *Monthly Notices of the Royal Astronomical Society* 483.2 (fév. 2019), p. 2671-2696. DOI : 10.1093/mnras/sty3206. arXiv : 1803.04294 [astro-ph.CO] (cf. p. 75).

[Bd21] Michel-Andrès BRETON et Sylvain DE LA TORRE. « Fast analytical calculation of the random pair counts for realistic survey geometry ». In : *Astronomy and Astrophysics* 646, A40 (fév. 2021), A40. DOI : 10.1051/0004-6361/202039603. arXiv : 2010.02793 [astro-ph.CO] (cf. p. 125, 126, 198, 199).

[Ba14c] Angela BURDEN et AL. « Efficient reconstruction of linear baryon acoustic oscillations in galaxy surveys ». In : *Monthly Notices of the Royal Astronomical Society, Volume 445, Issue 3, p.3152-3168* (2014). DOI : 10.1093/mnras/stu1965 (cf. p. 86, 197).

[Ba17] Angela BURDEN et AL. « Mitigating the impact of the DESI fiber assignment on galaxy clustering ». In : *Journal of Cosmology and Astroparticle Physics* 2017.3, 001 (mar. 2017), p. 001. DOI : 10.1088/1475-7516/2017/03/001. arXiv : 1611.04635 [astro-ph.CO] (cf. p. 117-119, 126, 129, 130, 137, 197, 200).

[Ca13] Jordan CARLSON et AL. « Convolution Lagrangian perturbation theory for biased tracers ». In : *Monthly Notices of the Royal Astronomical Society* 429.2 (fév. 2013), p. 1674-1685. DOI : 10.1093/mnras/sts457. arXiv : 1209.0780 [astro-ph.CO] (cf. p. 70).

[Car92] Sean CARROLL. « The Cosmological Constant ». In : *Annual Review of Astronomy and Astrophysics* (1992). DOI : https://doi.org/10.1146/annurev.aa.30.090192.002435 (cf. p. 47).

[Car97] Sean CARROLL. « Lecture Notes on General Relativity ». In : *arXiv* (1997). URL : https://arxiv.org/abs/gr-qc/9712019 (cf. p. 13).

[Ca20a] Paul CARTER et AL. « The impact of the fiducial cosmology assumption on BAO distance scale measurements ». In : *Mon.Not.Roy.Astron.Soc. 494 2, 2076-2089* (2020). DOI : 10.1093/mnras/staa761 (cf. p. 87, 144, 203).

[CL11] Anthony CHALLINOR et Antony LEWIS. « Linear power spectrum of observed source number counts ». In : *Physical Review D* 84.4, 043516 (août 2011), p. 043516. DOI : 10.1103/PhysRevD.84.043516. arXiv : 1105.5292 [astro-ph.CO] (cf. p. 75).

[Ca12] Kwan CHAN et AL. « Gravity and large-scale nonlocal bias ». In : *Physical Review D, vol. 85, Issue 8, id. 083509* (2012). DOI : 10.1103/PhysRevD.85.083509 (cf. p. 81).

[CP01] Michel CHEVALLIER et David POLARSKI. « Accelerating Universes with Scaling Dark Matter ». In : *International Journal of Modern Physics D, Volume 10, Issue 02, pp. 213-223* (2001). DOI : 10.1142/S0218271801000822 (cf. p. 40, 207).

[Ca04] Gayoung CHON et AL. « Fast estimation of polarization power spectra using correlation functions ». In : *Monthly Notices of the Royal Astronomical Society* 350.3 (mai 2004), p. 914-926. DOI : 10.1111/j.1365-2966.2004.07737.x. arXiv : astro-ph/0303414 [astro-ph] (cf. p. 126, 198).

[Ca15] Chia-Hsun CHUANG et AL. « EZmocks : extending the Zel'dovich approximation to generate mock galaxy catalogues with accurate clustering statistics ». In : *Monthly Notices of the Royal Astronomical Society* 446.3 (jan. 2015), p. 2621-2628. DOI : 10.1093/mnras/stu2301. arXiv : 1409.1124 [astro-ph.CO] (cf. p. 109).

[Ca20b] Anton CHUDAYKIN et AL. « Nonlinear perturbation theory extension of the Boltzmann code CLASS ». In : *Physical Review D* 102.6, 063533 (sept. 2020), p. 063533. DOI : 10.1103/PhysRevD.102.063533. arXiv : 2004.10607 [astro-ph.CO] (cf. p. 73, 181).

[Ca00] Shaun COLE et AL. « Hierarchical galaxy formation ». In : *Monthly Notices of the Royal Astronomical Society* 319.1 (nov. 2000), p. 168-204. DOI : 10.1046/j.1365-8711.2000.03879.x. arXiv : astro-ph/0007281 [astro-ph] (cf. p. 95).

[Ca05] Shaun COLE et AL. « The 2dF Galaxy Redshift Survey : power-spectrum analysis of the final data set and cosmological implications ». In : *Monthly Notices of the Royal Astronomical Society, Volume 362, Issue 2, pp. 505-534.* (2005). DOI : 10.1111/j.1365-2966.2005.09318.x (cf. p. 85).

[CJ91] Peter COLES et Bernard JONES. « A lognormal model for the cosmological mass distribution. » In : *Monthly Notices of the Royal Astronomical Society* 248 (jan. 1991), p. 1-13. DOI : 10.1093/mnras/248.1.1 (cf. p. 105, 106).

[Ca19] Jacques COLIN et AL. « Evidence for anisotropy of cosmic acceleration ». In : *Astronomy Astrophysics, Volume 631, id.L13, 6 pp.* (2019). DOI : 10.1051/0004-6361/201936373 (cf. p. 41).

[Ca01] Matthew COLLESS et AL. « The 2dF Galaxy Redshift Survey : spectra and redshifts ». In : *Monthly Notices of the Royal Astronomical Society* 328.4 (déc. 2001), p. 1039-1063. DOI : 10.1046/j.1365-8711.2001.04902.x. arXiv : astro-ph/0106498 [astro-ph] (cf. p. 176).

[Ca18] Ryan COOKE et AL. « One Percent Determination of the Primordial Deuterium Abundance ». In : *The Astrophysical Journal, Volume 855, Issue 2, article id. 102, 16 pp* (2018). DOI : 10.3847/1538-4357/aaab53 (cf. p. 36).

[Cou91] H. M. P. COUCHMAN. « Mesh-refined P 3M : A Fast Adaptive N-Body Algorithm ». In : *The Astrophysical Journal Letters* 368 (fév. 1991), p. L23. DOI : 10.1086/185939 (cf. p. 92).

[CS06] Martín CROCCE et Román SCOCCIMARRO. « Renormalized cosmological perturbation theory ». In : *Physical Review D, vol. 73, Issue 6, id. 063519* (2006). DOI : 10.1103/PhysRevD.73.063519 (cf. p. 68, 189).

[Ca08] Weiguang CUI et AL. « An Ideal Mass Assignment Scheme for Measuring the Power Spectrum with Fast Fourier Transforms ». In : *The Astrophysical Journal* 687.2 (nov. 2008), p. 738-744. DOI : 10.1086/592079. arXiv : 0804.0070 [astro-ph] (cf. p. 92).

[DP83] M DAVIS et P PEEBLES. « A survey of galaxy redshifts. V. The two-point position and velocity correlations. » In : *The Astrophysical Journal* 267 (avr. 1983), p. 465-482. DOI : 10.1086/160884 (cf. p. 106).

[Da85] M. DAVIS et AL. « The evolution of large-scale structure in a universe dominated by cold dark matter ». In : *The astrophysical Journal* 292 (mai 1985), p. 371-394. DOI : 10.1086/163168 (cf. p. 94).

[Da13] Kyle DAWSON et AL. « The Baryon Oscillation Spectroscopic Survey of SDSS-III ». In : *Astrophysical Journal* 145.1, 10 (jan. 2013), p. 10. DOI : 10.1088/0004-6256/145/1/10. arXiv : 1208.0022 [astro-ph.CO] (cf. p. 85, 99, 113, 193).

[Da16] Kyle DAWSON et AL. « The SDSS-IV Extended Baryon Oscillation Spectroscopic Survey : Overview and Early Data ». In : *The Astronomical Journal, Volume 151, Issue 2, article id. 44, 34 pp.* (2016). DOI : 10.3847/0004-6256/151/2/44 (cf. p. 35, 85, 99, 102-104, 193).

[da13] Sylvain DE LA TORRE et AL. « The VIMOS Public Extragalactic Redshift Survey (VIPERS) . Galaxy clustering and redshift-space distortions at z 0.8 in the first data release ». In : *Astronomy Astrophysics* 557, A54 (sept. 2013), A54. DOI : 10.1051/0004-6361/201321463. arXiv : 1303.2622 [astro-ph.CO] (cf. p. 116).

[da17] Sylvain DE LA TORRE et AL. « The VIMOS Public Extragalactic Redshift Survey (VIPERS). Gravity test from the combination of redshift-space distortions and galaxy-galaxy lensing at 0.5 < z < 1.2 ». In : *Astronomy Astrophysics* 608, A44 (déc. 2017), A44. DOI : 10.1051/0004-6361/201630276. arXiv : 1612.05647 [astro-ph.CO] (cf. p. 79, 90).

[da21] Arnaud DE MATTIA et AL. « The completed SDSS-IV extended Baryon Oscillation Spectroscopic Survey : measurement of the BAO and growth rate of structure of the emission line galaxy sample from the anisotropic power spectrum between redshift 0.6 and 1.1 ». In : *Monthly Notices of the Royal Astronomical Society, Volume 501, Issue 4, pp.5616-5645* (2021). DOI : 10.1093/mnras/staa3891 (cf. p. 69, 74, 80, 81, 107, 121, 134, 137, 168, 181).

[dR19] Arnaud DE MATTIA et Vanina RUHLMANN-KLEIDER. « Integral constraints in spectroscopic surveys ». In : *Journal of Cosmology and Astroparticle Physics* 2019.8, 036 (août 2019), p. 036. DOI : 10.1088/1475-7516/2019/08/036. arXiv : 1904.08851 [astro-ph.CO] (cf. p. 106, 107, 117, 118, 124, 127, 150, 181, 195).

[Deh01] Walter DEHNEN. « Towards optimal softening in three-dimensional N-body codes - I. Minimizing the force error ». In : *Monthly Notices of the Royal Astronomical Society* 324.2 (juin 2001), p. 273-291. DOI : 10.1046/j.1365-8711.2001.04237.x. arXiv : astro-ph/0011568 [astro-ph] (cf. p. 91).

[DES21] DES COLLABORATION. « Dark Energy Survey Year 3 Results : Cosmological Constraints from Galaxy Clustering and Weak Lensing ». In : *arXiv e-prints*, arXiv :2105.13549 (mai 2021), arXiv :2105.13549. arXiv : 2105.13549 [astro-ph.CO] (cf. p. 173).

[DES16] DESI COLLABORATION. « The DESI Experiment Part I : Science,Targeting, and Survey Design ». In : *arXiv e-prints*, arXiv :1611.00036 (oct. 2016), arXiv :1611.00036. arXiv : 1611.00036 [astro-ph.IM] (cf. p. 66, 169, 177-179, 207).

[Da19] Arjun DEY et AL. « Overview of the DESI Legacy Imaging Surveys ». In : *The Astronomical Journal, Volume 157, Issue 5, article id. 168, 29 pp.* (2019). DOI : 10.3847/1538-3881/ab089d1 (cf. p. 99).

[Da18] Suhail DHAWAN et AL. « Measuring the Hubble constant with Type Ia supernovae as near-infrared standard candles ». In : *Astronomy Astrophysics* 609, A72 (jan. 2018), A72. DOI : 10.1051/0004-6361/201731501. arXiv : 1707.00715 [astro-ph.CO] (cf. p. 19).

[Dre80] A. DRESSLER. « Galaxy morphology in rich clusters : implications for the formation and evolution of galaxies. » In : *The Astrophysical Journal* 236 (mar. 1980), p. 351-365. DOI : 10.1086/157753 (cf. p. 101).

[da20] Hélion DU MAS DES BOURBOUX et AL. « The Completed SDSS-IV Extended Baryon Oscillation Spectroscopic Survey : Baryon Acoustic Oscillations with Lyα Forests ». In : *The Astrophysical Journal* 901.2, 153 (oct. 2020), p. 153. DOI : 10.3847/1538-4357/abb085. arXiv : 2007.08995 [astro-ph.CO] (cf. p. 168).

[eBO21] EBOSS COLLABORATION. « Completed SDSS-IV extended Baryon Oscillation Spectroscopic Survey : Cosmological implications from two decades of spectroscopic surveys at the Apache Point Observatory ». In : *Physical Review* 103.8, 083533 (avr. 2021), p. 083533. DOI : 10.1103/PhysRevD.103.083533. arXiv : 2007.08991 [astro-ph.CO] (cf. p. 141, 167-174, 176, 204-208).

[ESH09] T EIFLER, P SCHNEIDER et J HARTLAP. « Dependence of cosmic shear covariances on cosmology. Impact on parameter estimation ». In : *Journal of Cosmology and Astroparticle Physics* 502.3 (août 2009), p. 721-731. DOI : 10.1051/0004-6361/200811276. arXiv : 0810.4254 [astro-ph] (cf. p. 178).

[Ea98] Daniel EISENSTEIN et AL. « Cosmic Complementarity : H_0 and Ω_m from Combining Cosmic Microwave Background Experiments and Redshift Surveys ». In : *The Astrophysical Journal* 504.2 (sept. 1998), p. L57-L60. DOI : 10.1086/311582. arXiv : astro-ph/9805239 [astro-ph] (cf. p. 88).

[Ea01] Daniel EISENSTEIN et AL. « Spectroscopic Target Selection for the Sloan Digital Sky Survey : The Luminous Red Galaxy Sample ». In : *The Astronomical Journal, Volume 122, Issue 5, pp. 2267-2280.* (2001). DOI : 10.1086/323717 (cf. p. 99, 101).

[Ea05] Daniel EISENSTEIN et AL. « Detection of the Baryon Acoustic Peak in the Large-Scale Correlation Function of SDSS Luminous Red Galaxies ». In : *The Astrophysical Journal, Volume 633, Issue 2, pp. 560-574.* (2005). DOI : 10.1086/466512 (cf. p. 99, 101).

[Ea11] Daniel EISENSTEIN et AL. « SDSS-III : Massive Spectroscopic Surveys of the Distant Universe, the Milky Way, and Extra-Solar Planetary Systems ». In : *The Astronomical Journal, Volume 142, Issue 3, article id. 72, 24 pp* (2011). DOI : 10.1088/0004-6256/142/3/72 (cf. p. 99).

[EH98] Daniel EISENSTEIN et Wayne HU. « Baryonic Features in the Matter Transfer Function ». In : *The Astrophysical Journal* 496.2 (mar. 1998), p. 605-614. DOI : 10.1086/305424. arXiv : astro-ph/9709112 [astro-ph] (cf. p. 61, 188).

[FKP94] Hume FELDMAN, Nick KAISER et John PEACOCK. « Power-Spectrum Analysis of Three-dimensional Redshift Surveys ». In : *The Astrophysical Journal* 426 (mai 1994), p. 23. DOI : 10.1086/174036. arXiv : astro-ph/9304022 [astro-ph] (cf. p. 114, 196).

[Fis+94] Karl B. FISHER, Marc DAVIS, Michael A. STRAUSS et al. « Clustering in the 1.2-Jy IRAS Galaxy Redshift Survey. I - The redshift and real space correlation functions ». In : *Monthly Notices of the Royal Astronomical Society* 266 (jan. 1994), p. 50. DOI : 10.1093/mnras/266.1.50. arXiv : astro-ph/9307001 [astro-ph] (cf. p. 119).

[Fix09] D. J. FIXSEN. « The Temperature of the Cosmic Microwave Background ». In : *The Astrophysical Journal* 707.2 (déc. 2009), p. 916-920. DOI : 10.1088/0004-637X/707/2/916. arXiv : 0911.1955 [astro-ph.CO] (cf. p. 31, 170).

[Fa14] Andreu FONT-RIBERA et AL. « DESI and other Dark Energy experiments in the era of neutrino mass measurements ». In : *Journal of Cosmology and Astroparticle Physics* 2014.5, 023 (mai 2014), p. 023. DOI : 10.1088/1475-7516/2014/05/023. arXiv : 1308.4164 [astro-ph.CO] (cf. p. 177).

[Fa13] Daniel FOREMAN-MACKEY et AL. « emcee : The MCMC Hammer ». In : *Publications of the Astronomical Society of the Pacific* 125.925 (mar. 2013), p. 306. DOI : 10.1086/670067. arXiv : 1202.3665 [astro-ph.IM] (cf. p. 140).

[Gai18] GAIA COLLABORATION. « Gaia Data Release 2. Summary of the contents and survey properties ». In : *Astronomy Astrophysics* 616, A1 (août 2018), A1. DOI : 10.1051/0004-6361/201833051. arXiv : 1804.09365 [astro-ph.GA] (cf. p. 103).

[GSW05] Liang GAO, Volker SPRINGEL et Simon WHITE. « The age dependence of halo clustering ». In : *Monthly Notices of the Royal Astronomical Society* 363.1 (oct. 2005), p. L66-L70. DOI : 10.1111/j.1745-3933.2005.00084.x. arXiv : astro-ph/0506510 [astro-ph] (cf. p. 94, 96).

[Ga20] Hector GIL-MARIN et AL. « The Completed SDSS-IV extended Baryon Oscillation Spectroscopic Survey : measurement of the BAO and growth rate of structure of the luminous red galaxy sample from the anisotropic power spectrum between redshifts 0.6 and 1.0 ». In : *Monthly Notices of the Royal Astronomical Society, Volume 498, Issue 2, pp.2492-2531* (2020). DOI : 10.1093/mnras/staa2455 (cf. p. 74, 88, 141, 150, 152-154, 156, 158, 159, 165, 168, 180, 181, 191, 203).

[Ga15] Héctor GIL-MARIN et AL. « The power spectrum and bispectrum of SDSS DR11 BOSS galaxies - II. Cosmological interpretation ». In : *Monthly Notices of the Royal Astronomical Society* 452.2 (sept. 2015), p. 1914-1921. DOI : 10.1093/mnras/stv1359. arXiv : 1408.0027 [astro-ph.CO] (cf. p. 89).

[GNa15] Héctor GIL-MARIN, NOREÑA et AL. « The power spectrum and bispectrum of SDSS DR11 BOSS galaxies - I. Bias and gravity ». In : *Monthly Notices of the Royal Astronomical Society* 451.1 (juil. 2015), p. 539-580. DOI : 10.1093/mnras/stv961. arXiv : 1407.5668 [astro-ph.CO] (cf. p. 89).

[Ga05] K GÓRSKI et AL. « HEALPix : A Framework for High-Resolution Discretization and Fast Analysis of Data Distributed on the Sphere ». In : *The Astrophysical Journal* 622.2 (avr. 2005), p. 759-771. DOI : 10.1086/427976. arXiv : astro-ph/0409513 [astro-ph] (cf. p. 117, 126, 198).

[Ga06] James GUNN et AL. « The 2.5 m Telescope of the Sloan Digital Sky Survey ». In : *The Astronomical Journal, Volume 131, Issue 4, pp. 2332-2359.* (2006). DOI : 10.1086/500975 (cf. p. 98, 99, 193).

[Ga12] Stephen GWYN et AL. « The Canada-France-Hawaii Telescope Legacy Survey : Stacked Images and Catalogs ». In : *The Astronomical Journal, Volume 143, Issue 2, article id. 38, 22* (2012). DOI : 10.1088/0004-6256/143/2/38 (cf. p. 102).

[Ha16a] Salman HABIB et AL. « HACC : Simulating sky surveys on state-of-the-art supercomputing architectures ». In : *New Astronomy* 42 (jan. 2016), p. 49-65. DOI : 10.1016/j.newast.2015.06.003. arXiv : 1410.2805 [astro-ph.IM] (cf. p. 108).

[HA16] Oliver HAHN et Raul E. ANGULO. « An adaptively refined phase-space element method for cosmological simulations and collisionless dynamics ». In : *Monthly Notices of the Royal Astronomical Society* 455.1 (jan. 2016), p. 1115-1133. DOI : 10.1093/mnras/stv2304. arXiv : 1501.01959 [astro-ph.CO] (cf. p. 92).

[Hah05] T. HAHN. « CUBA—a library for multidimensional numerical integration ». In : *Computer Physics Communications* 168.2 (juin 2005), p. 78-95. DOI : 10.1016/j.cpc.2005.01.010. arXiv : hep-ph/0404043 [hep-ph] (cf. p. 125, 126, 198).

[Ham93] A HAMILTON. « Toward Better Ways to Measure the Galaxy Correlation Function ». In : *The Astrophysical Journal* 417 (nov. 1993), p. 19. DOI : 10.1086/173288 (cf. p. 106).

[Ham98] Andrew HAMILTON. « Linear Redshift Distortions : a Review ». In : (1998). DOI : 10.1007/978-94-011-4960-0_17 (cf. p. 77, 195).

[Ham00] Andrew HAMILTON. « Uncorrelated modes of the non-linear power spectrum ». In : *Monthly Notices of the Royal Astronomical Society, Volume 312, Issue 2* (2000). DOI : https://doi.org/10.1046/j.1365-8711.2000.03071.x (cf. p. 80).

[Ha96] Mario HAMUY et AL. « The Absolute Luminosities of the Calan/Tololo Type IA Supernovae ». In : *Astronomical Journal* 112 (déc. 1996), p. 2391. DOI : 10.1086/118190. arXiv : astro-ph/9609059 [astro-ph] (cf. p. 39).

[Ha07] J HARTLAP et AL. « Why your model parameter confidences might be too optimistic. Unbiased estimation of the inverse covariance matrix ». In : *Astronomy and Astrophysics* 464.1 (mar. 2007), p. 399-404. DOI : 10.1051/0004-6361:20066170. arXiv : astro-ph/0608064 [astro-ph] (cf. p. 140, 141).

[Ha15a] Andrew HEARIN et AL. « Beyond halo mass : galactic conformity as a smoking gun of central galaxy assembly bias ». In : *Monthly Notices of the Royal Astronomical Society* 452.2 (sept. 2015), p. 1958-1969. DOI : 10.1093/mnras/stv1358. arXiv : 1404.6524 [astro-ph.CO] (cf. p. 108, 109, 151).

[Hea77] D HEATH. « The growth of density perturbations in zero pressure Friedmann-Lemaitre universes. » In : *Monthly Notices of the Royal Astronomical Society* 179 (mai 1977), p. 351-358. DOI : 10.1093/mnras/179.3.351 (cf. p. 47).

[Ha19] Katrin HEITMANN et AL. « The Outer Rim Simulation : A Path to Many-core Supercomputers ». In : *The Astrophysical Journal Supplement Series* 245.1, 16 (nov. 2019), p. 16. DOI : 10.3847/1538-4365/ab4da1. arXiv : 1904.11970 [astro-ph.CO] (cf. p. 108, 203).

[Hew82] P. C. HEWETT. « The estimation of galaxy angular correlation functions ». In : *Monthly Notices of the Royal Astronomical Society* 201 (déc. 1982), p. 867-883. DOI : 10.1093/mnras/201.4.867 (cf. p. 106).

[Ha13] G HINSHAW et AL. « Nine-year Wilkinson Microwave Anisotropy Probe (WMAP) Observations : Cosmological Parameter Results ». In : *The Astrophysical Journal Supplement* 208.2, 19 (oct. 2013), p. 19. DOI : 10.1088/0067-0049/208/2/19. arXiv : 1212.5226 [astro-ph.CO] (cf. p. 176).

[Ha21] Jiamin HOU et AL. « The completed SDSS-IV extended Baryon Oscillation Spectroscopic Survey : BAO and RSD measurements from anisotropic clustering analysis of the quasar sample in configuration space between redshift 0.8 and 2.2 ». In : *Monthly Notices of the Royal Astronomical Society, Volume 500, Issue 1, pp.1201-1221* (2021). DOI : 10.1093/mnras/staa3234 (cf. p. 70, 72, 73, 79, 145, 168, 181).

[Ha15b] Cullan HOWLETT et AL. « The clustering of the SDSS main galaxy sample - II. Mock galaxy catalogues and a measurement of the growth of structure from redshift space distortions at z = 0.15 ». In : *Monthly Notices of the Royal Astronomical Society* 449.1 (mai 2015), p. 848-866. DOI : 10.1093/mnras/stu2693. arXiv : 1409.3238 [astro-ph.CO] (cf. p. 168).

[Hub29] Edwin HUBBLE. « A relation between distance and radial velocity among extra-galactic nebulae ». In : *PNAS* (1929). DOI : https://doi.org/10.1073/pnas.1424299112 (cf. p. 19, 183).

[Ha16b] Timothy HUTCHINSON et AL. In : *The astrophysical Journal* 152.6, 205 (déc. 2016), p. 205. DOI : 10.3847/0004-6256/152/6/205. arXiv : 1607.02432 [astro-ph.IM] (cf. p. 104).

[Ia20] M ICAZA-LIZAOLA et AL. « The clustering of the SDSS-IV extended Baryon Oscillation Spectroscopic Survey DR14 LRG sample : structure growth rate measurement from the anisotropic LRG correlation function in the redshift range 0.6 < z < 1.0 ». In : *Monthly Notices of the Royal Astronomical Society* 492.3 (mar. 2020), p. 4189-4215. DOI : 10.1093/mnras/stz3602. arXiv : 1909.07742 [astro-ph.CO] (cf. p. 147, 148, 161, 165, 166).

[Ia09] Olivier ILBERT et AL. « Cosmos Photometric Redshifts with 30-Bands for 2-deg2 ». In : *The Astrophysical Journal, Volume 690, Issue 2, pp. 1236-1249* (2009). DOI : 10.1088/0004-637X/690/2/1236 (cf. p. 102).

[Jac72] J. C. JACKSON. « A critique of Rees's theory of primordial gravitational radiation ». In : *Monthly Notices of the Royal Astronomical Society* 156 (jan. 1972), 1P. DOI : 10.1093/mnras/156.1.1P. arXiv : 0810.3908 [astro-ph] (cf. p. 76, 190).

[JR75] F. JAMES et M. ROOS. « Minuit - a system for function minimization and analysis of the parameter errors and correlations ». In : *Computer Physics Communications* 10.6 (déc. 1975), p. 343-367. DOI : 10.1016/0010-4655(75)90039-9 (cf. p. 135, 140).

[Kai87] Nick KAISER. « Clustering in real space and in redshift space ». In : *Monthly Notices of the Royal Astronomical Society* 227 (juil. 1987), p. 1-21. DOI : 10.1093/mnras/227.1.1 (cf. p. 77, 78, 190, 195).

[Kaj98] Takaaki KAJITA. « Atmospheric neutrino results from Super-Kamiokande and Kamiokande - Evidence for $\nu\mu$ oscillations ». In : *Nuclear Physics B Proceedings Supplements, Volume 77, Issue 1-3, p. 123-132.* (1998). DOI : 10.1016/S0920-5632(99)00407-7 (cf. p. 36).

[Ka20] Minas KARAMANIS et AL. « Ensemble slice sampling : Parallel, black-box and gradient-free inference for correlated multimodal distributions ». In : *arXiv preprint arXiv : 2002.06212* (2020) (cf. p. 134, 201).

[Ka21] Minas KARAMANIS et AL. « zeus : A Python implementation of Ensemble Slice Sampling for efficient Bayesian parameter inference ». In : *arXiv preprint arXiv :2105.03468* (2021) (cf. p. 134, 201).

[Ka09] Richard KESSLER et AL. « First-Year Sloan Digital Sky Survey-II Supernova Results : Hubble Diagram and Cosmological Parameters ». In : *The Astrophysical Journal Supplement* 185.1 (nov. 2009), p. 32-84. DOI : 10.1088/0067-0049/185/1/32. arXiv : 0908.4274 [astro-ph.CO] (cf. p. 18).

[Ka13] David KIRKBY et AL. « Fitting methods for baryon acoustic oscillations in the Lyman-α forest fluctuations in BOSS data release 9 ». In : *Journal of Cosmology and Astroparticle Physics* 2013.3, 024 (mar. 2013), p. 024. DOI : 10.1088/1475-7516/2013/03/024. arXiv : 1301.3456 [astro-ph.CO] (cf. p. 87, 88).

[Ka14] F KITAURA et AL. « Modelling baryon acoustic oscillations with perturbation theory and stochastic halo biasing. » In : *Monthly Notices of the Royal Astronomical Societyo* 439 (mar. 2014), p. L21-L25. DOI : 10.1093/mnrasl/slt172. arXiv : 1307.3285 [astro-ph.CO] (cf. p. 108).

[Kur20] Hannu KURKI-SUONIO. « Cosmological Perturbation Theory, part 1 ». In : (2020) (cf. p. 44, 51, 52, 54).

[LL59] Lev Davidovich LANDAU et E LIFSHITZ. *Fluid mechanics*. 1959 (cf. p. 29).

[LS93] Stephen D. LANDY et Alexander S. SZALAY. « Bias and Variance of Angular Correlation Functions ». In : *The Astrophysical Journal* 412 (juil. 1993), p. 64. DOI : 10.1086/172900 (cf. p. 106, 195).

[La11] Alexie LEAUTHAUD et AL. « A Theoretical Framework for Combining Techniques that Probe the Link Between Galaxies and Dark Matter ». In : *The Astrophysical Journal* 738.1, 45 (sept. 2011), p. 45. DOI : 10.1088/0004-637X/738/1/45. arXiv : 1103.2077 [astro-ph.CO] (cf. p. 108, 109, 151).

[Les11] Julien LESGOURGUES. « The Cosmic Linear Anisotropy Solving System (CLASS) I : Overview ». In : *arXiv :1104.2932* (2011) (cf. p. 62, 66, 188).

[La00] Antony LEWIS et AL. « Efficient Computation of Cosmic Microwave Background Anisotropies in Closed Friedmann-Robertson-Walker Models ». In : *Astrophys.J. 538 473-476* (2000). DOI : 10.1086/309179 (cf. p. 61, 62, 66, 188).

[LV17] LIGO-COLLABORATION et The VIRGO-COLLABORATION. « GW170817 : Observation of Gravitational Waves from a Binary Neutron Star Inspiral ». In : *Physical Review Letters, Volume 119, Issue 16, id.161101* (2017). DOI : 10.1103/PhysRevLett.119.161101 (cf. p. 42).

[Lim53] D. Nelson LIMBER. « The Analysis of Counts of the Extragalactic Nebulae in Terms of a Fluctuating Density Field. » In : *The Astrophysical Journal* 117 (jan. 1953), p. 134. DOI : 10.1086/145672 (cf. p. 119).

[LC07] Eric LINDER et Robert CAHN. « Parameterized beyond-Einstein growth ». In : *Astroparticle Physics, Volume 28, Issue 4-5, p. 481-488* (2007). DOI : 10.1016/j.astropartphys.2007.09.003 (cf. p. 48, 187).

[La96] Charley LINEWEAVER et AL. « The Dipole Observed in the COBE DMR 4 Year Data ». In : *Astrophysical Journal v.470, p.38* (1996). DOI : 10.1086/177846 (cf. p. 13).

[La18] X LURI et AL. « Gaia Data Release 2 : Using Gaia parallaxes ». In : *Astronomy Astrophysics, Volume 616, id.A9, 19 pp* (2018). DOI : 10.1051/0004-6361/201832964 (cf. p. 19).

[Ma02] Gianpiero MANGANO et AL. « A precision calculation of the effective number of cosmological neutrinos ». In : *Physics Letters B, Volume 534, Issue 1-4, p. 8-16.* (2002). DOI : 10.1016/S0370-2693(02)01622-2 (cf. p. 36).

[Ma09a] Claudia MARASTON et AL. « Modelling the colour evolution of luminous red galaxies - improvements with empirical stellar spectra ». In : *Monthly Notices of the Royal Astronomical Society : Letters, Volume 394, Issue 1* (2009). DOI : 10.1111/j.1745-3933.2009.00621.x (cf. p. 100, 101).

[Mas11] Karen L.and al. MASTERS. « The morphology of galaxies in the Baryon Oscillation Spectroscopic Survey ». In : *Monthly Notices of the Royal Astronomical Society* 418.2 (déc. 2011), p. 1055-1070. DOI : 10.1111/j.1365-2966.2011.19557.x. arXiv : 1106.3331 [astro-ph.CO] (cf. p. 101).

[Mat08] Takahiko MATSUBARA. « Resumming cosmological perturbations via the Lagrangian picture : One-loop results in real space and in redshift space ». In : *Physical Review D* 77.6, 063530 (mar. 2008), p. 063530. DOI : 10.1103/PhysRevD.77.063530. arXiv : 0711.2521 [astro-ph] (cf. p. 81).

[Ma09b] Patrick MCDONALD et AL. « Clustering of dark matter tracers : generalizing bias for the coming era of precision LSS ». In : *Journal of Cosmology and Astroparticle Physics, Issue 08, id. 020* (2009). DOI : 10.1088/1475-7516/2009/08/020 (cf. p. 73).

[MBW12] Houjun MO, Franck van den BOSCH et Simon WHITE. *Galaxy formation and evolution*. 2012. DOI : https://doi.org/10.1017/CBO9780511807244 (cf. p. 13, 34, 44, 45, 77, 94).

[Ma18] Faizan MOHAMMAD et AL. « The VIMOS Public Extragalactic Redshift Survey (VIPERS). Unbiased clustering estimate with VIPERS slit assignment ». In : *Astronomy Astrophysics* 619, A17 (nov. 2018), A17. DOI : 10.1051/0004-6361/201833853. arXiv : 1807.05999 [astro-ph.CO] (cf. p. 116).

[Ma20] Faizan MOHAMMAD et AL. « The completed SDSS-IV extended baryon oscillation spectroscopic survey : pairwise-inverse probability and angular correction for fibre collisions in clustering measurements ». In : *Monthly Notices of the Royal Astronomical Society* 498.1 (oct. 2020), p. 128-143. DOI : 10.1093/mnras/staa2344. arXiv : 2007.09005 [astro-ph.CO] (cf. p. 116, 117, 167, 181).

[Ma15] Surhud MORE et AL. « The Splashback Radius as a Physical Halo Boundary and the Growth of Halo Mass ». In : *The astrophysical Journal* 810.1, 36 (sept. 2015), p. 36. DOI : 10.1088/0004-637X/810/1/36. arXiv : 1504.05591 [astro-ph.CO] (cf. p. 94).

[Ma21] Eva-Maria MUELLER et AL. « The clustering of galaxies in the completed SDSS-IV extended Baryon Oscillation Spectroscopic Survey : Primordial non-Gaussianity in Fourier Space ». In : *arXiv e-prints*, arXiv :2106.13725 (juin 2021), arXiv :2106.13725. arXiv : 2106.13725 [astro-ph.CO] (cf. p. 35, 178).

[NK05] Daisuke NAGAI et Andrey V. KRAVTSOV. « The Radial Distribution of Galaxies in Λ Cold Dark Matter Clusters ». In : *The astrophysical Journal* 618.2 (jan. 2005), p. 557-568. DOI : 10.1086/426016. arXiv : astro-ph/0408273 [astro-ph] (cf. p. 94).

[NFW96] Julio NAVARRO, Carlos FRENK et Simon WHITE. « The Structure of Cold Dark Matter Halos ». In : *Astrophysical Journal v.462, p.563* (1996). DOI : 10.1086/177173 (cf. p. 39).

[Na20] Richard NEVEUX et AL. « The completed SDSS-IV extended Baryon Oscillation Spectroscopic Survey : BAO and RSD measurements from the anisotropic power spectrum of the quasar sample between redshift 0.8 and 2.2 ». In : *Monthly Notices of the Royal Astronomical Society, Volume 499, Issue 1, pp.210-229* (2020). DOI : 10.1093/mnras/staa2780 (cf. p. 69, 74, 80, 145, 168, 181).

[Na17] Takahiro NISHIMICHI et AL. « Moving around the cosmological parameter space : A nonlinear power spectrum reconstruction based on high-resolution cosmic responses ». In : *Physical Review D, Volume 96, Issue 12, id.123515* (2017). DOI : 10.1103/PhysRevD.96.123515 (cf. p. 69, 70, 189).

[Pa12] Nikhil PADMANABHAN et AL. « A 2 per cent distance to z = 0.35 by reconstructing baryon acoustic oscillations - I. Methods and application to the Sloan Digital Sky Survey ». In : *Monthly Notices of the Royal Astronomical Society* (2012). DOI : 10.1111/j.1365-2966.2012.21888.x (cf. p. 87).

[Pa21] Romain PAVIOT et AL. « Angular systematics-free cosmological analysis of galaxy clustering in configuration space ». In : *To be submitted to MNRAS* (2021) (cf. p. 117, 181, 197, 198).

[Pee74] Hauser PEEBLES. « Statistical Analysis of Catalogs of Extragalactic Objects. III. The Shane-Wirtanen and Zwicky Catalogs ». In : *The Astrophysical Journal Supplement* 28 (nov. 1974), p. 19. DOI : 10.1086/190308 (cf. p. 106).

[Pee80] P PEEBLES. *The large-scale structure of the universe*. 1980 (cf. p. 48, 66, 119).

[Pa10] Will PERCIVAL et AL. « Baryon acoustic oscillations in the Sloan Digital Sky Survey Data Release 7 galaxy sample ». In : *Monthly Notices of the Royal Astronomical Society* 401.4 (fév. 2010), p. 2148-2168. DOI : 10.1111/j.1365-2966.2009.15812.x. arXiv : 0907.1660 [astro-ph.CO] (cf. p. 176).

[Pa14] Will PERCIVAL et AL. « The clustering of Galaxies in the SDSS-III Baryon Oscillation Spectroscopic Survey : including covariance matrix errors ». In : *Monthly Notices of the Royal Astronomical Society* 439.3 (avr. 2014), p. 2531-2541. DOI : 10.1093/mnras/stu112. arXiv : 1312.4841 [astro-ph.CO] (cf. p. 141).

[PB17] Will PERCIVAL et Davide BIANCHI. « Using angular pair upweighting to improve 3D clustering measurements ». In : *Monthly Notices of the Royal Astronomical Society* 472.1 (nov. 2017), p. L40-L44. DOI : 10.1093/mnrasl/slx135. arXiv : 1703.02071 [astro-ph.CO] (cf. p. 117).

[Pa99] Saul PERLMUTTER et AL. « Measurements of Ω and Λ from 42 High-Redshift Supernovae ». In : *The Astrophysical Journal, Volume 517, Issue 2, pp. 565-586.* (1999). DOI : 10.1086/307221 (cf. p. 39, 40, 183).

[PU12] Patrick PETER et Jean-Phillipe UZAN. « Cosmologie primordiale ». In : *The Astrophysical Journal, Volume 517, Issue 2, pp. 565-586.* (2012). DOI : 10.1086/307221 (cf. p. 34).

[Pa18] Annalisa PILLEPICH et AL. « Simulating galaxy formation with the IllustrisTNG model ». In : *Monthly Notices of the Royal Astronomical Society* 473.3 (jan. 2018), p. 4077-4106. DOI : 10.1093/mnras/stx2656. arXiv : 1703.02970 [astro-ph.GA] (cf. p. 93).

[Pa17] Lucas PINOL et AL. « Imprint of DESI fiber assignment on the anisotropic power spectrum of emission line galaxies ». In : *Journal of Cosmology and Astroparticle Physics* 2017.4, 008 (avr. 2017), p. 008. DOI : 10.1088/1475-7516/2017/04/008. arXiv : 1611.05007 [astro-ph.CO] (cf. p. 117).

[Pla14] PLANCK COLLABORATION. « Planck 2013 results. XVI. Cosmological parameters ». In : *Astronomy and Astrophysics* 571, A16 (nov. 2014), A16. DOI : 10.1051/0004-6361/201321591. arXiv : 1303.5076 [astro-ph.CO] (cf. p. 89, 178).

[Pla16] PLANCK COLLABORATION. « Planck 2015 results. XIII. Cosmological parameters ». In : *Astronomy and Astrophysics* 594, A13 (sept. 2016), A13. DOI : 10.1051/0004-6361/201525830. arXiv : 1502.01589 [astro-ph.CO] (cf. p. 90, 178, 179).

[Pla18] PLANCK COLLABORATION. « Planck 2018 results. VI. Cosmological parameters ». In : *Astronomy and Astrophysics* 641, A6 (sept. 2018), A6. DOI : 10.1051/0004-6361/201833910. arXiv : 1807.06209 [astro-ph.CO] (cf. p. 20, 25, 31, 32, 36, 40, 41, 66, 85, 158, 164, 168, 169, 172, 173, 183-186, 188, 203, 204).

[Pla20] PLANCK COLLABORATION. « Planck 2018 results. V. CMB power spectra and likelihoods ». In : 641, A5 (sept. 2020), A5. DOI : 10.1051/0004-6361/201936386. arXiv : 1907.12875 [astro-ph.CO] (cf. p. 168, 180).

[Pa16] Abhishek PRAKASH et AL. « The SDSS-IV Extended Baryon Oscillation Spectroscopic Survey : Luminous Red Galaxy Target Selection ». In : *The Astrophysical Journal Supplement Series, Volume 224, Issue 2, article id. 34, 14 pp* (2016). DOI : 10.3847/0067-0049/224/2/34 (cf. p. 99, 101, 102).

[PS74] William PRESS et Paul SCHECHTER. « Formation of Galaxies and Clusters of Galaxies by Self-Similar Gravitational Condensation ». In : *The astrophysical Journal* 187 (fév. 1974), p. 425-438. DOI : 10.1086/152650 (cf. p. 94).

[Ra17a] Anand RAICHOOR et AL. « The SDSS-IV extended Baryon Oscillation Spectroscopic Survey : final emission line galaxy target selection ». In : *Monthly Notices of the Royal Astronomical Society, Volume 471, Issue 4, p.3955-3973* (2017). DOI : 10.1093/mnras/stx1790 (cf. p. 99).

[Ra11] Beth REID et AL. « Towards an accurate model of the redshift-space clustering of haloes in the quasi-linear regime ». In : *Monthly Notices of the Royal Astronomical Society* 417.3 (nov. 2011), p. 1913-1927. DOI : 10.1111/j.1365-2966.2011.19379.x. arXiv : 1105.4165 [astro-ph.CO] (cf. p. 81, 192).

[Ra16] Beth REID et AL. « SDSS-III Baryon Oscillation Spectroscopic Survey Data Release 12 : galaxy target selection and large-scale structure catalogues ». In : *Monthly Notices of the Royal Astronomical Society, Volume 455, Issue 2, p.1553-1573* (2016). DOI : 10.1093/mnras/stv2382 (cf. p. 99-101, 103, 113, 115).

[Ra20a] Mehdi REZAIE et AL. « Improving galaxy clustering measurements with deep learning : analysis of the DECaLS DR7 data ». In : *Monthly Notices of the Royal Astronomical Society, Volume 495, Issue 2, pp.1613-1640* 495.2 (juin 2020), p. 1613-1640. DOI : 10.1093/mnras/staa1231. arXiv : 1907.11355 [astro-ph.CO] (cf. p. 181).

[Ra07] Adam RIESS et AL. « New Hubble Space Telescope Discoveries of Type Ia Supernovae at z >= 1 : Narrowing Constraints on the Early Behavior of Dark Energy ». In : *The Astrophysical Journal* 659.1 (avr. 2007), p. 98-121. DOI : 10.1086/510378. arXiv : astro-ph/0611572 [astro-ph] (cf. p. 18).

[Ra18] Adam RIESS et AL. « Milky Way Cepheid Standards for Measuring Cosmic Distances and Application to Gaia DR2 : Implications for the Hubble Constant ». In : *The Astrophysical Journal, Volume 861, Issue 2, article id. 126, 13 pp.* (2018). DOI : 10.3847/1538-4357/aac82e (cf. p. 19, 170).

[Ra19] Adam RIESS et AL. « Large Magellanic Cloud Cepheid Standards Provide a 1% Foundation for the Determination of the Hubble Constant and Stronger Evidence for Physics beyond ΛCDM ». In : *The Astrophysical Journal, Volume 876, Issue 1, article id. 85, 13 pp.* (2019). DOI : 10.3847/1538-4357/ab1422 (cf. p. 20, 171, 173).

[Ra12] Ashley ROSS et AL. « The clustering of galaxies in the SDSS-III Baryon Oscillation Spectroscopic Survey : analysis of potential systematics ». In : *Monthly Notices of the Royal Astronomical Society* 424.1 (juil. 2012), p. 564-590. DOI : 10.1111/j.1365-2966.2012.21235.x. arXiv : 1203.6499 [astro-ph.CO] (cf. p. 106, 113).

[Ra14] Ashley ROSS et AL. « The clustering of galaxies in the SDSS-III DR10 Baryon Oscillation Spectroscopic Survey : no detectable colour dependence of distance scale or growth rate measurements ». In : *Monthly Notices of the Royal Astronomical Society, Volume 437, Issue 2, p.1109-1126* (2014). DOI : 10.1093/mnras/stt1895 (cf. p. 99, 101).

[Ra15a] Ashley ROSS et AL. « The clustering of the SDSS DR7 main Galaxy sample - I. A 4 per cent distance measure at z = 0.15 ». In : *Monthly Notices of the Royal Astronomical Society* 449.1 (mai 2015), p. 835-847. DOI : 10.1093/mnras/stv154. arXiv : 1409.3242 [astro-ph.CO] (cf. p. 168).

[Ra15b] Ashley ROSS et AL. « The information content of anisotropic Baryon Acoustic Oscillation scale measurements ». In : *Monthly Notices of the Royal Astronomical Society* 451.2 (août 2015), p. 1331-1340. DOI : 10.1093/mnras/stv966. arXiv : 1501.05571 [astro-ph.CO] (cf. p. 142).

[Ra17b] Ashley ROSS et AL. « The clustering of galaxies in the completed SDSS-III Baryon Oscillation Spectroscopic Survey : observational systematics and baryon acoustic oscillations in the correlation function ». In : *Monthly Notices of the Royal Astronomical Society* 464.1 (jan. 2017), p. 1168-1191. DOI : 10.1093/mnras/stw2372. arXiv : 1607.03145 [astro-ph.CO] (cf. p. 87, 145).

[Ra20b] Ashley ROSS et AL. « The Completed SDSS-IV extended Baryon Oscillation Spectroscopic Survey : Large-scale structure catalogues for cosmological analysis ». In : *Monthly Notices of the Royal Astronomical Society, Volume 498, Issue 2, pp.2354-2371* (2020). DOI : 10.1093/mnras/staa2416 (cf. p. 99, 103, 104, 134).

[Ra21] Graziano ROSSI et AL. « The completed SDSS-IV extended Baryon Oscillation Spectroscopic Survey : N-body mock challenge for galaxy clustering measurements ». In : *Monthly Notices of the Royal Astronomical Society* 505.1 (juil. 2021), p. 377-407. DOI : 10.1093/mnras/staa3955. arXiv : 2007.09002 [astro-ph.CO] (cf. p. 96, 108, 109, 151, 194, 199, 203).

[Sa14] Shun SAITO et AL. « Understanding higher-order nonlocal halo bias at large scales by combining the power spectrum with the bispectrum ». In : *Phys.Rev.D 90 (2014) 12, 123522* (2014). DOI : 10.1103/PhysRevD.90.123522 (cf. p. 81).

[SP16] Pablo.F de SALAS et Sergio PASTOR. « Relic neutrino decoupling with flavour oscillations revisited ». In : *Journal of Cosmology and Astroparticle Physics, Issue 07, article id. 051* (2016). DOI : 10.1088/1475-7516/2016/07/051 (cf. p. 36).

[Sa17a] Ariel SÁNCHEZ et AL. « The clustering of galaxies in the completed SDSS-III Baryon Oscillation Spectroscopic Survey : Cosmological implications of the configuration-space clustering wedges ». In : *Monthly Notices of the Royal Astronomical Society* 464.2 (jan. 2017), p. 1640-1658. DOI : 10.1093/mnras/stw2443. arXiv : 1607.03147 [astro-ph.CO] (cf. p. 81, 141).

[Sa19] Elena SARPA et AL. « BAO reconstruction : a swift numerical action method for massive spectroscopic surveys ». In : *Monthly Notices of the Royal Astronomical Society, Volume 484, Issue 3, p.3818-3830* (2019). DOI : 10.1093/mnras/stz278 (cf. p. 87).

[Sa17b] Siddharth SATPATHY et AL. « The clustering of galaxies in the completed SDSS-III Baryon Oscillation Spectroscopic Survey : on the measurement of growth rate using galaxy correlation functions ». In : *Monthly Notices of the Royal Astronomical Society* 469.2 (août 2017), p. 1369-1382. DOI : 10.1093/mnras/stx883. arXiv : 1607.03148 [astro-ph.CO] (cf. p. 148).

[Sa98] David SCHLEGEL et AL. « Maps of Dust Infrared Emission for Use in Estimation of Reddening and Cosmic Microwave Background Radiation Foregrounds ». In : *The Astrophysical Journal, Volume 500, Issue 2, pp. 525-553.* (1998). DOI : 10.1086/305772 (cf. p. 98).

[Sch09] Bernard SCHUTZ. « A First Course in General Relativity ». In : (2009). DOI : https://doi.org/10.1017/CBO9780511984181 (cf. p. 13).

[Sco04] R SCOCCIMARRO. « Redshift-space distortions, pairwise velocities, and nonlinearities ». In : *Physical Review D* 70.8, 083007 (oct. 2004), p. 083007. DOI : 10.1103/PhysRevD.70.083007. arXiv : astro-ph/0407214 [astro-ph] (cf. p. 68, 79, 81, 192).

[Sa99] Román SCOCCIMARRO et AL. « The Bispectrum as a Signature of Gravitational Instability in Redshift Space ». In : *The Astrophysical Journal* 517.2 (juin 1999), p. 531-540. DOI : 10.1086/307220. arXiv : astro-ph/9808305 [astro-ph] (cf. p. 79).

[Sa18] Daniel SCOLNIC et AL. « The Complete Light-curve Sample of Spectroscopically Confirmed SNe Ia from Pan-STARRS1 and Cosmological Constraints from the Combined Pantheon Sample ». In : *The Astrophysical Journal, Volume 859, Issue 2, article id. 101, 28 pp. (2018)*. (2018). DOI : 10.3847/1538-4357/aab9bb (cf. p. 40, 168, 173, 180, 205).

[SZ96] Uros SELJAK et Matias ZALDARRIAGA. « A Line-of-Sight Integration Approach to Cosmic Microwave Background Anisotropies ». In : *Astrophysical Journal* 469 (oct. 1996), p. 437. DOI : 10.1086/177793. arXiv : astro-ph/9603033 [astro-ph] (cf. p. 178).

[Sa16] Hee-Jong SEO et AL. « Modeling the reconstructed BAO in Fourier space ». In : *Monthly Notices of the Royal Astronomical Society* 460.3 (août 2016), p. 2453-2471. DOI : 10.1093/mnras/stw1138. arXiv : 1511.00663 [astro-ph.CO] (cf. p. 87, 143).

[SH15] Daniel SHAFER et Dragan HUTERER. « Multiplicative errors in the galaxy power spectrum : self-calibration of unknown photometric systematics for precision cosmology ». In : *Monthly Notices of the Royal Astronomical Society* 447.3 (mar. 2015), p. 2961-2969. DOI : 10.1093/mnras/stu2640. arXiv : 1410.0035 [astro-ph.CO] (cf. p. 127, 199).

[SR98] Joseph SILK et Martin J. REES. « Quasars and galaxy formation ». In : *Astronomy and Astrophysics* 331 (mar. 1998), p. L1-L4. arXiv : astro-ph/9801013 [astro-ph] (cf. p. 95).

[Sa12] Vimal SIMHA et AL. « Testing subhalo abundance matching in cosmological smoothed particle hydrodynamics simulations ». In : *Monthly Notices of the Royal Astronomical Society* 423.4 (juil. 2012), p. 3458-3473. DOI : 10.1111/j.1365-2966.2012.21142.x. arXiv : 1011.4964 [astro-ph.CO] (cf. p. 96).

[Sim07] P. SIMON. « How accurate is Limber's equation ? » In : *Astronomy and Astrophysics* 473.3 (oct. 2007), p. 711-714. DOI : 10.1051/0004-6361:20066352. arXiv : astro-ph/0609165 [astro-ph] (cf. p. 119).

[Sim18] Marko SIMONOVIĆ. « Cosmological perturbation theory using the FFTLog : formalism and connection to QFT loop integrals ». In : *Journal of Cosmology and Astroparticle Physics, Issue 04, article id. 030* . (2018). DOI : 10.1088/1475-7516/2018/04/030 (cf. p. 74, 189, 190).

[SG20] Manodeep SINHA et Lehman H. GARRISON. « CORRFUNC - a suite of blazing fast correlation functions on the CPU ». In : *Monthly Notices of the Royal Astronomical Society* 491.2 (jan. 2020), p. 3022-3041. DOI : 10.1093/mnras/stz3157 (cf. p. 107).

[Sa13] Stephen SMEE et AL. « The Multi-object, Fiber-fed Spectrographs for the Sloan Digital Sky Survey and the Baryon Oscillation Spectroscopic Survey ». In : *The Astronomical Journal, Volume 146, Issue 2, article id. 32, 40 pp. (2013)*. (2013). DOI : 10.1088/0004-6256/146/2/32 (cf. p. 98, 99, 101, 113, 193).

[Sa20] Alex SMITH et AL. « The completed SDSS-IV extended Baryon Oscillation Spectroscopic Survey : N-body mock challenge for the quasar sample ». In : *Monthly Notices of the Royal Astronomical Society* 499.1 (nov. 2020), p. 269-291. DOI : 10.1093/mnras/staa2825. arXiv : 2007.09003 [astro-ph.CO] (cf. p. 150).

[Spr05] Volker SPRINGEL. « The cosmological simulation code GADGET-2 ». In : *Monthly Notices of the Royal Astronomical Society* 364.4 (déc. 2005), p. 1105-1134. DOI : 10.1111/j.1365-2966.2005.09655.x. arXiv : astro-ph/0505010 [astro-ph] (cf. p. 92).

[Sa05] Volker SPRINGEL et AL. « Simulations of the formation, evolution and clustering of galaxies and quasars ». In : *Nature* 435.7042 (juin 2005), p. 629-636. DOI : 10.1038/nature03597. arXiv : astro-ph/0504097 [astro-ph] (cf. p. 92).

[Ste06] Gary STEIGMAN. « Primordial Nucleosynthesis : Successes And Challenges ». In : *International Journal of Modern Physics E, Volume 15, Issue 01, pp. 1-35* (2006). DOI : 10.1142/S0218301306004028 (cf. p. 36).

[Sa02] Michael STRAUSS et AL. « Spectroscopic Target Selection in the Sloan Digital Sky Survey : The Main Galaxy Sample ». In : *The Astronomical Journal* 124.3 (sept. 2002), p. 1810-1824. DOI : 10.1086/342343. arXiv : astro-ph/0206225 [astro-ph] (cf. p. 99).

[Sa11] M. SULLIVAN et AL. « SNLS3 : Constraints on Dark Energy Combining the Supernova Legacy Survey Three-year Data with Other Probes ». In : *The Astrophysical Journal* 737.2, 102 (août 2011), p. 102. DOI : 10.1088/0004-637X/737/2/102. arXiv : 1104.1444 [astro-ph.CO] (cf. p. 169).

[Sa08] M SWANSON et AL. « Methods for rapidly processing angular masks of next-generation galaxy surveys ». In : *Monthly Notices of the Royal Astronomical Society* 387.4 (juil. 2008), p. 1391-1402. DOI : 10.1111/j.1365-2966.2008.13296.x. arXiv : 0711.4352 [astro-ph] (cf. p. 103).

[SPC01] I SZAPUDI, S PRUNET et S COLOMBI. « Fast Clustering Analysis of Inhomogeneous Megapixel CMB maps ». In : *arXiv e-prints*, astro-ph/0107383 (juil. 2001), astro-ph/0107383. arXiv : astro-ph/0107383 [astro-ph] (cf. p. 126, 198).

[Ta12a] Ryuichi TAKAHASHI et AL. « Revising the Halofit Model for the Nonlinear Matter Power Spectrum ». In : *The Astrophysical Journal, Volume 761, Issue 2, article id. 152, 10 pp* (2012). DOI : 10.1088/0004-637X/761/2/152 (cf. p. 71).

[Ta20] Amélie TAMONE et AL. « The completed SDSS-IV extended baryon oscillation spectroscopic survey : growth rate of structure measurement from anisotropic clustering analysis in configuration space between redshift 0.6 and 1.1 for the emission-line galaxy sample ». In : *Monthly Notices of the Royal Astronomical Society* 499.4 (déc. 2020), p. 5527-5546. DOI : 10.1093/mnras/staa3050. arXiv : 2007.09009 [astro-ph.CO] (cf. p. 107, 117, 120, 121, 126, 129-131, 134, 137, 168, 180, 181, 197, 200, 202).

[Ta12b] Atsushi TARUYA et AL. « Direct and fast calculation of regularized cosmological power spectrum at two-loop order ». In : *Physical Review D, vol. 86, Issue 10, id. 103528* (2012). DOI : 10.1103/PhysRevD.86.103528 (cf. p. 68, 69, 72, 73).

[Ta13a] Atsushi TARUYA et AL. « Precision modeling of redshift-space distortions from a multipoint propagator expansion ». In : *Physical Review D* 87.8, 083509 (avr. 2013), p. 083509. DOI : 10.1103/PhysRevD.87.083509. arXiv : 1301.3624 [astro-ph.CO] (cf. p. 80, 84).

[TNS10] Atsushi TARUYA, Takahiro NISHIMICHI et Shun SAITO. « Baryon acoustic oscillations in 2D : Modeling redshift-space power spectrum from perturbation theory ». In : *Physical Review D, vol. 82, Issue 6, id. 063522* (2010). DOI : 10.1103/PhysRevD.82.063522 (cf. p. 79, 80, 191).

[Ta12c] Max TEGMARK et AL. « The Three-Dimensional Power Spectrum of Galaxies from the Sloan Digital Sky Survey ». In : *The Astrophysical Journal, Volume 606, Issue 2, pp. 702-740.* (2012). DOI : 10.1086/382125 (cf. p. 67, 188).

[Ta13b] Jeremy TINKER et AL. « Evolution of the Stellar-to-dark Matter Relation : Separating Star-forming and Passive Galaxies from z = 1 to 0 ». In : *The Astrophysical Journal* 778.2, 93 (déc. 2013), p. 93. DOI : 10.1088/0004-637X/778/2/93. arXiv : 1308.2974 [astro-ph.CO] (cf. p. 108, 109, 151).

[TF77] Brent TULLY et Richard FISHER. « A new method of determining distance to galaxies ». In : *Astronomy and Astrophysics, Vol. 500, p. 105-117 (2009)* (1977) (cf. p. 19).

[Va19] Mariana VARGAS-MAGANA et AL. « Unraveling the Universe with DESI ». In : *arXiv e-prints*, arXiv :1901.01581 (jan. 2019), arXiv :1901.01581. arXiv : 1901.01581 [astro-ph.IM] (cf. p. 178).

[Va13] M. VARGAS-MAGAÑA et AL. « An optimized correlation function estimator for galaxy surveys ». In : *Astronomy Astrophysics* 554, A131 (juin 2013), A131. DOI : 10.1051/0004-6361/201220790. arXiv : 1211.6211 [astro-ph.CO] (cf. p. 105).

[Wa14] Lile WANG et AL. « An analytic model for redshift-space distortions ». In : *Monthly Notices of the Royal Astronomical Society* 437.1 (jan. 2014), p. 588-599. DOI : 10.1093/mnras/stt1916. arXiv : 1306.1804 [astro-ph.CO] (cf. p. 70, 192).

[WBB20] Mike WANG, Florian BEUTLER et David BACON. « Impact of relativistic effects on the primordial non-Gaussianity signature in the large-scale clustering of quasars ». In : *Monthly Notices of the Royal Astronomical Society* 499.2 (déc. 2020), p. 2598-2607. DOI : 10.1093/mnras/staa2998. arXiv : 2007.01802 [astro-ph.CO] (cf. p. 181).

[WT18] Risa WECHSLER et Jeremy TINKER. « The Connection Between Galaxies and Their Dark Matter Halos ». In : *Annual Review of Astronomy and Astrophysics* 56 (sept. 2018), p. 435-487. DOI : 10.1146/annurev-astro-081817-051756. arXiv : 1804.03097 [astro-ph.GA] (cf. p. 96).

[Whi94] Simon WHITE. « Formation and Evolution of Galaxies : Les Houches Lectures ». In : *arXiv e-prints*, astro-ph/9410043 (oct. 1994), astro-ph/9410043. arXiv : astro-ph/9410043 [astro-ph] (cf. p. 91).

[Wa19] Kenneth WONG et AL. « HOLiCOW XIII 2.4% measurement of HO from lensed quasars : 5.3σ tension between early and late-Universe probes ». In : *Astronomy Astrophysics, Volume 609, id.A72, 13 pp.* (2019). DOI : 10.1051/0004-6361/201731501 (cf. p. 20, 170).

[Wa10] Edward WRIGHT et AL. « The Wide-field Infrared Survey Explorer (WISE) : Mission Description and Initial On-orbit Performance ». In : *The Astronomical Journal, Volume 140, Issue 6, pp. 1868-1881* (2010). DOI : 10.1088/0004-6256/140/6/1868 (cf. p. 99, 102, 114).

[Xa13] Xiaoying XU et AL. « Measuring DA and H at z = 0.35 from the SDSS DR7 LRGs using baryon acoustic oscillations ». In : *MNRAS 431, 2834–2860* (2013). DOI : doi:10.1093/mnras/stt379 (cf. p. 88).

[Ya00] Donald YORK et AL. « The Sloan Digital Sky Survey : Technical Summary ». In : *The Astronomical Journal, Volume 120, Issue 3, pp. 1579-1587.* (2000). DOI : 10.1086/301513 (cf. p. 98, 193).

[Za18] Pauline ZARROUK et AL. « The clustering of the SDSS-IV extended Baryon Oscillation Spectroscopic Survey DR14 quasar sample : measurement of the growth rate of structure from the anisotropic correlation function between redshift 0.8 and 2.2 ». In : *Monthly Notices of the Royal Astronomical Society* 477.2 (juin 2018), p. 1639-1663. DOI : 10.1093/mnras/sty506. arXiv : 1801.03062 [astro-ph.CO] (cf. p. 147).

[Za17a] Anatoly ZASOV et AL. « Dark matter in galaxies ». In : *Physics Uspekhi* (2017). DOI : 10.3367/UFNe.2016.03.037751 (cf. p. 38).

[Za70] Y ZEL'DOVICH et AL. « Gravitational instability : an approximate theory for large density perturbations. » In : *Astronomy and Astrophysics, Vol. 5, p. 84 - 89* (1970) (cf. p. 49, 87).

[Za17b] Zhongxu ZHAI et AL. « The Clustering of Luminous Red Galaxies at z ~ 0.7 from EBOSS and BOSS Data ». In : *The Astrophysical Journal* 848.2, 76 (oct. 2017), p. 76. DOI : 10.3847/1538-4357/aa8eee. arXiv : 1607.05383 [astro-ph.CO] (cf. p. 82).

[Za21] Cheng ZHAO et AL. « The completed SDSS-IV extended Baryon Oscillation Spectroscopic Survey : 1000 multi-tracer mock catalogues with redshift evolution and systematics for galaxies and quasars of the final data release ». In : *Monthly Notices of the Royal Astronomical Society* 503.1 (mai 2021), p. 1149-1173. DOI : 10.1093/mnras/stab510. arXiv : 2007.08997 [astro-ph.CO] (cf. p. 103, 110).

[Za13] HongSheng ZHAO et AL. « Testing gravity theories via transverse Doppler and gravitational redshifts in galaxy clusters ». In : *Physical Review D* 88.4, 043013 (août 2013), p. 043013. DOI : 10.1103/PhysRevD.88.043013. arXiv : 1206.5032 [astro-ph.CO] (cf. p. 75).

[Za07] Zheng ZHENG et AL. « Galaxy Evolution from Halo Occupation Distribution Modeling of DEEP2 and SDSS Galaxy Clustering ». In : *The Astrophysical Journal* 667.2 (oct. 2007), p. 760-779. DOI : 10.1086/521074. arXiv : astro-ph/0703457 [astro-ph] (cf. p. 108).

[Zwi37] Fritz ZWICKY. « On the Masses of Nebulae and of Clusters of Nebulae ». In : *Astrophysical Journal, vol. 86, p.217* (1937). DOI : 10.1086/143864 (cf. p. 37, 183).